Optical interferometric detection of young giant exoplanets at the astronomical unit scale

Nicolas Pourré

THÈSE

Pour obtenir le grade de

DOCTEUR DE L'UNIVERSITÉ GRENOBLE ALPES

École doctorale : PHYS - Physique
Spécialité : Astrophysique et Milieux Dilués
Unité de recherche : Institut de Planetologie et d'Astrophysique de Grenoble

Détection par interférométrie optique d'exoplanètes géantes jeunes à l'échelle de l'unité astronomique

Optical interferometric detection of young giant exoplanets at the astronomical unit scale

Présentée par :

Nicolas POURRÉ

Direction de thèse :

Karine PERRAUT ASTRONOME, UNIVERSITE GRENOBLE ALPES	Directrice de thèse
Jean-Baptiste LE BOUQUIN ASTRONOME ADJOINT, Université Grenoble Alpes	Co-encadrant de thèse

Rapporteurs :

ANTHONY BOCCALETTI
DIRECTEUR DE RECHERCHE, CNRS ILE-DE FRANCE MEUDON
LAURENT PUEYO
ASTRONOME ADJOINT, SPACE TELESCOPE SCIENCE INSTITUTE

Thèse soutenue publiquement le **10 juillet 2024**, devant le jury composé de :

NADEGE MEUNIER, ASTRONOME, UNIVERSITE GRENOBLE ALPES	Présidente
ANTHONY BOCCALETTI, DIRECTEUR DE RECHERCHE, CNRS ILE-DE FRANCE MEUDON	Rapporteur
LAURENT PUEYO, ASTRONOME ADJOINT, SPACE TELESCOPE SCIENCE INSTITUTE	Rapporteur
ELODIE CHOQUET, ASTRONOME ADJOINTE, AIX-MARSEILLE UNIVERSITE	Examinatrice
LAURA KREIDBERG, FULL PROFESSOR, UNIVERSITÄT HEIDELBERG	Examinatrice

"Hold on - hold on
Wait, maybe the answer's
Looking for you
Hold on - hold on
Sunshine shine on through"

Yes. "Hold On". 90125. Atco, 1983.

Remerciements

Immense merci à Jean-Baptiste Le Bouquin et Karine Perraut de m'avoir guidé, soutenu, relu, motivé, avec beaucoup de bienveillance à travers ce voyage de trois ans,

À Mathias Nowak, Sylvestre Lacour, Jens Kammerer, Thomas Winterhalder, Anne-Lise Maire, et tout le consortium ExoGRAVITY,

À Julien Woillez, Sylvain Oberti, Taïssir Heritier, Pierre Bourget, tout le monde à Garching et à Paranal, pour les moments formidables à l'ESO,

À Tituan Allain, Myriam Bonduelle, Hugo Nowacki, Adrien Hours, Lucie Leboulleux, la coloc de Montréal, pour leur amitié et leur soutien infini,

À Nicolás Cuello, Arseniy Kuznetsov, Jonah Mauxion, Adrien Soudais, Guillaume Bourdarot, Lionel Vacher, Antonia Drescher, Felix Widmann, Tadeja Veršič, Célia Desgrange, Thomas Jannaud, Alexis Bidot, soeurs et frères thésard·es et post-doctorants (ou ex-post-docs),

À Gaël Chauvin et David Mouillet, pour m'avoir accompagné au travers du Comité de Suivi Individuel,

À Jean Philippe Berger, Julien Milli, Faustine Cantalloube, Alexis Carlotti, Laurent Jocou, Pierre Kern, Alain Delboulbe, Eric Stadler, toute l'équipe CHARM pour la passion de la lumière, des miroirs et des gâteaux, merci aussi à Carine Babusiaux, Mickaël Bonnefoy, Xavier Bonfils, Marie-Hélène Sztefek, David Gillier, et toutes les personnes de l'IPAG,

À tou·te·s les enseignant·es du master de physique de l'université Grenoble Alpes, dans le parcours recherche fondamentale de la faculté PhiTEM,

À toute l'équipe de football du laboratoire, le Red Star IPAG, surtout Antoine Alaguero, Maxime Roumesy, Rajeev Manick, Nicolas Balducci et Gaspard Duchêne, pour les entraînements malgré le froid, la pluie et le vent, et pour les frissons dans le tournoi de l'UGA,

À Monique Pourré, Georges Pourré, Arielle Pourré, Éléonore Delenne, Zélie Delenne, Hortense Delenne, Geoffrey Delenne, Yohann Petit-Brasier, Brigitte Vialle, Pascal Pourré, Karine Morange, Ghislaine Boyé, Patrick Boyé, Julien Boyé, Hugo Boyé, Odette Vialle, Marcel Vialle, Maria Pourré, François Pourré, Tatie Jeannette, Bernard Gabay, Hélène Lasserre, Jean-Marc Lasserre, Roxane Lasserre, Mathieu Bruguera, Titouan Bruguera, Marie-Françoise Prissé, Fernande et Jean-Marie Pourré, ma famille, pour m'avoir donné le goût de la connaissance de soi et de la connaissance du monde,

À Clément Vessella, Simon Rispal, Ugo Vincent, Nicolas Pellegrini, Nicolas Lemoine, Élisa Tripotin, Chafik Lekouara, Benoit Moreau, Simon Moulin, Anthony Bernigaud, Raphaël Stayeart, Kipré Lago, Fábio da Silva Costa, Arnaud Jolly, Edgar Mauricio Loza Ramirez, Francesco Vercesi, pour être mes boussoles à chaque instant de ma vie,

Enfin, pour leur inépuisable source de joie, d'inspiration, d'énergie, de mélancolie, d'élévation, Johann Sebastian Bach, Terje Bakken, Tony Banks, Phil Collins, Olve Eikemo, Keith Emerson, Girolamo Frescobaldi, Robert Fripp, Peter Gabriel, Philip Glass, Paul Hindemith, Keith Jarrett, Stu Mackenzie, Kali Malone, Brad Mehldau, Pat Metheny, Harald Nævdal, Anton Newcombe, Esbjörn Svensson, Hiromi Uehara, Christian Vander et Steven Wilson.

Abstract

Direct observations provide key information about exoplanetary systems. By analyzing the position of planets at different times, we can determine their orbits and trace the dynamic history of the systems. By analyzing their emission spectra, we can determine the temperature of exoplanets, as well as the chemical composition of their atmosphere, containing tracers of their formation mechanism.

However, direct observations are currently limited. Angular resolution limits allow us to observe only the exoplanets furthest from their star, generally more than 10 astronomical units away. Also, the limits of contrast with the host star mean that we can only observe young giant exoplanets, less than 15 Myr, whose infrared thermal radiation is still strong due to their recent formation. To better understand the formation and evolution of planetary systems, these limits must be pushed back to enable direct observations of gas giants on the scale of the astronomical unit.

Since 2019, the GRAVITY instrument installed on the Very Large Telescope Interferometer in Chile has made it possible to observe exoplanets at angular separations previously unattainable by conventional direct imaging instruments. Recently, the instrument enabled the first direct observations of the planets β Pictoris c and HD 206893 c, respectively 8.2 and 12.7 masses from Jupiter, and 2.7 and 3.5 astronomical units from their star.

In summer 2024, the GRAVITY+ upgrade will install new adaptive optics crucial for obtaining better contrast and making observations of less massive exoplanets closer to their star. In 2026, the Gaia space telescope will publish a new list of exoplanets discovered around 2 astronomical units from their star using absolute astrometry. GRAVITY+ will be an instrument of choice for characterizing these planets, measuring their mass and spectrum at wavelengths close to 2 µm.

My thesis involves understanding the current limitations of GRAVITY, and preparing the GRAVITY+ upgrade to enable direct observation of "young Jupiters" as close as possible to their star. My thesis was divided into three parts.

Firstly, I analyzed data from archival observations to quantify GRAVITY's current limitations in contrast and angular separation. I was able to determine that we could observe exoplanets 30,000 times fainter than their star, down to 50 milli-arcseconds.

Secondly, I worked on observational data reduction to understand the source of systematic noise that pollutes exoplanet spectra. I was able to determine the conditions under which these noises appear and their impact on observations.

Thirdly, I worked directly on the instrument to implement a high-contrast mode for GRAVITY+. This specific mode for exoplanet observations involves optical aberration correction and wavefront control. The high-contrast mode will limit the impact of host starlight, enabling us to observe less massive and younger exoplanets.

In the years to come, the synergy between Gaia and GRAVITY+ will allow us to finely characterize many young giant exoplanets, and certainly transform our vision of how planetary systems form and how they evolve.

Résumé

Les observations directes fournissent des informations capitales sur les systèmes exoplanétaires. Par l'analyse de la position des planètes à différentes époques, nous pouvons déterminer leur orbite et remonter à l'histoire dynamique des systèmes. Par l'analyse de leur spectre en émission, nous pouvons déterminer la température des exoplanètes ainsi que la composition chimique de leur atmosphère, contenant des traceurs de leur mécanisme de formation.

Seulement, les observations directes sont actuellement limitées. Les limites en résolution angulaire des instruments nous permettent d'observer uniquement les exoplanètes les plus éloignées de leur étoile, généralement à plus de 10 unités astronomiques. Aussi, les limites de contraste avec l'étoile hôte ne nous permettent que d'observer des exoplanètes géantes jeunes, de moins de 15 millions d'années, dont le rayonnement thermique infrarouge est encore fort du fait de leur formation récente. Pour mieux comprendre la formation et l'évolution des systèmes planétaires, ces limites doivent être repoussées pour permettre des observations directes de planètes géantes gazeuses à l'échelle de l'unité astronomique.

Depuis 2019, l'instrument GRAVITY installé sur le Very Large Telescope Interferometer au Chili permet d'observer des exoplanètes à des séparations angulaires jusqu'ici inatteignables par les instruments d'imagerie directe classique. Récemment, l'instrument a permis de réaliser les premières observations directes des planètes β Pictoris c et HD 206893 c, respectivement de 8.2 et 12.7 masses de Jupiter et à 2.7 et 3.5 unités astronomiques de leur étoile.

Dès l'été 2024, la mise à jour de l'instrument GRAVITY+ va inclure des nouvelles optiques adaptatives cruciales pour obtenir un meilleur contraste et réaliser des observations d'exoplanètes moins massives et plus proches de leur étoile. En 2026, le télescope spatial Gaia publiera une nouvelle liste d'exoplanètes découvertes dans un rayon de 2 unités astronomiques autour de leur étoile par méthode d'astrométrie absolue. GRAVITY+ sera un instrument de choix pour caractériser ces planètes, mesurer leur masse et leur spectre à des longueurs d'onde proches de 2 µm.

Ma thèse consiste à comprendre les limites actuelles de l'instrument GRAVITY et à préparer la mise à jour GRAVITY+ afin de permettre l'observation directe de "Jupiters jeunes" au plus proche de leur étoile. Pour ceci, ma thèse s'est déroulée selon 3 axes.

Premièrement, j'ai analysé des données d'observations passées pour quantifier les limites actuelles de GRAVITY en contraste et séparation angulaire. J'ai pu déterminer que l'instrument nous permettait d'observer des exoplanètes 30 000 fois moins brillantes que leur étoile, et ce jusqu'à 50 milli-arcseconde d'angle.

Deuxièmement, j'ai travaillé sur la réduction des données d'observations afin de comprendre la source des bruits systématiques qui polluent les spectres d'exoplanètes. J'ai pu déterminer à quelles

conditions ces bruits apparaissent et leur impact sur les observations.

Troisièmement, j'ai travaillé directement sur l'instrument pour implémenter un mode haut-contraste pour GRAVITY+. Ce mode spécifique pour les observations d'exoplanètes implique une correction des aberrations optiques ainsi qu'un contrôle du front d'onde. Le mode haut-contraste limitera l'impact de la lumière des étoiles hôtes et donc permettra d'observer des exoplanètes moins massives et moins jeunes.

Dans les années à venir, la synergie entre Gaia et GRAVITY+ va permettre de caractériser finement de nombreuses exoplanètes géantes jeunes, et certainement transformer notre vision de la manière dont les systèmes planétaires se forment et évoluent.

Acronyms

AT Auxiliary Telescope

DIT Detector Integration Time

ELT Extremely Large Telescope

FDDL Fibered Differential Delay Lines

FT GRAVITY Fringe Tracker arm

GPAO GRAVITY+ Adaptive Optics

KL Karhunen-Loève modal basis

LWE Low Wind Effect

NCPA Non-Common Path Aberrations

NDIT Number of detector integration

OPD Optical Path Difference

PA Positional Angle

PSF Point Spread Function

SC GRAVITY SCience arm

SCAR Single-mode Complex Amplitude Refinement

SNR Signal to Noise Ratio

TT Tip-Tilt

UT Unit Telescope

VLTI Very Large Telescope Interferometer

Contents

Foreword

I structured my PhD manuscript thematically, with two introduction chapters (1 and 2) and three chapters that summarize my own contributions (3, 4 and 5). Then, the reader should not be surprised if there is often no chronological order in the presented work.

In my PhD manuscript, the term ExoGRAVITY must be understood in the sense of "exoplanets observations with GRAVITY". This term is declined into variations, like "ExoGRAVITY technique" for the specifics of the exoplanets observations with the instrument, "ExoGRAVITY consortium" for the group of researchers and engineers working on exoplanets observations with GRAVITY, "ExoGRAVITY pipeline", etc.

Observation dates follow the ESO standard YYYY-MM-DD, and the date of the observation night is the date at noon that day (e.g. 2022-10-23 is the night from the 23rd to the 24th). The obsevation data are structured in NFILES×NDIT×DIT, where DIT is the detector integration time of single exposures, NDIT is the number of exposures in the file and NFILES is the number of files recorded during this observation.

Finally, I call "discovery" the first detection that confirmed an exoplanet. So, "detection" refers to the ability of a specific technique or instrument to observe an exoplanet (e.g. "β Pic c has been discovered by radial velocity. Later, in 2020, it has been detected with GRAVITY.").

Chapter 1

Introduction

Contents

1.1 A photon, from the exoplanet to the detector

At 19 parsecs from here, in the haze of the exoplanet β Pictoris c,

a molecule falls to a lower energy level,

and releases a near-infrared photon.

The energy released travels in free space for 62 years under the form of an electromagnetic wave, and eventually reaches the Earth.

It passes through the Earth atmosphere, and reaches the top of Cerro Paranal, in north Chile. Here two telescopes collect it with their 50 m^2 primary mirror and reflect it to their secondary mirror, then their respective M3, M4,... In total it is reflected by 30 mirrors before the electromagnetic wave captured by each telescope is recombined.

The journey ends at the instrument detector, where the wave collapses on a particle that deliver its energy to an electron of the HgCdTe valence band of a specific pixel. The electron is excited to the conduction band of the semi-conductor, and creates a signal.

Wave after wave, photon after photon, the distribution of illuminated pixels on the detector encodes the direction where this electromagnetic light comes from.

Adding the flux at K-band ($\lambda \sim 2.2$ µm) from the brightest exoplanets directly observed, I find a total flux of $3{\times}10^4$ photons.s^{-1}.m^{-2}, so $4{\times}10^{18}$ photons of exoplanets falling on the Earth surface each second.

These photons contain information on the position of exoplanets, and information on their atmosphere temperature, composition and dynamics. From this, we can discover the variety of planetary systems in our galactic neighborhood, understand how they form, and how they evolve.

Information from distant worlds rains down upon us. For nearly 30 years now, astronomers have imagined and created remarkably ingenious instruments to make the best use of this incoming light.

1.2 Exoplanets: a brief overview

Here, at the beginning of the present manuscript, I wish to propose a very concise overview of our current knowledge and the hot topics in exoplanet research.

1.2.1 Definition

The International Astronomical Union (IAU) is an acknowledged authority for standards and definitions in the astronomy and astrophysics community. According to Lecavelier des Etangs and Lissauer (2022), their current definition of an exoplanet is:

- an object less massive than 13 Jupiter mass ($M_{\rm Jup}$). Above this mass an object of solar-metallicity starts to trigger thermonuclear fusion of deuterium and is considered a brown-dwarf, or a star.
- that orbits "stars, brown dwarfs or stellar remnants". The mass ratio between the object and the central mass must be below 1/25. Above this mass ratio, the Lagrangian points L4 and L5 become unstable.
- massive enough to match the definition of a planet in our solar system (hydrostatic equilibrium shape, orbit mostly cleared from other objects).

This definition excludes:

- dwarf planets, analogue of our solar-system trans-Neptunian objects Pluto and Eris or Ceres in the asteroid belt. To my knowledge, no dwarf exoplanet has been detected yet,
- rogue planets, wandering in the interstellar space and not gravitationally bound to a star,

- low-mass binaries, where the mass ratio is above 1/25.

I will follow this exoplanet definition throughout this manuscript, and it will not prevent me from describing observations of other non-planetary companions, such as brown dwarfs (e.g. Sect. 5.4.2 and 5.4.3).

1.2.2 Formation processes

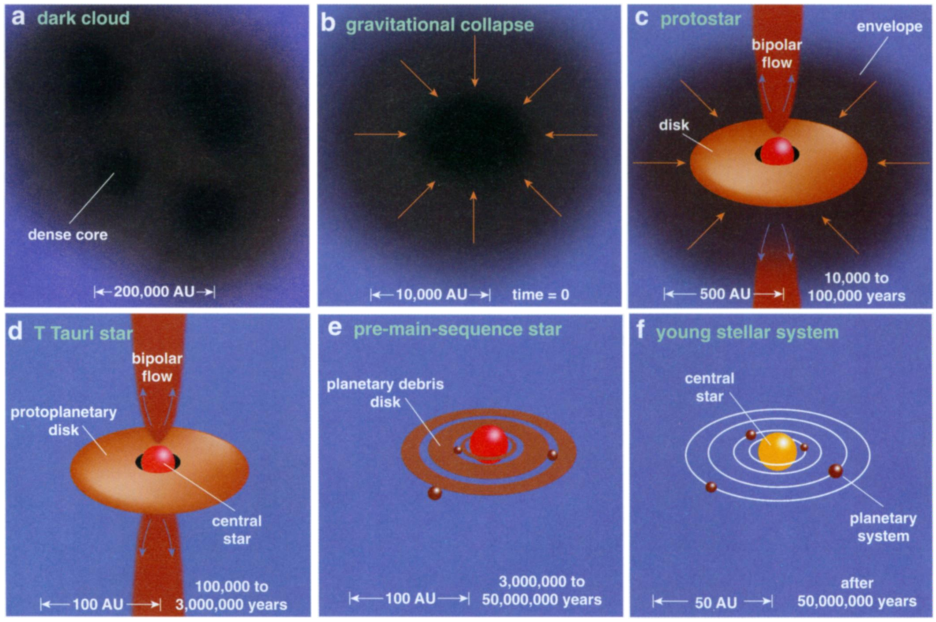

Figure 1.1 – Stages of the formation of planetary systems around sun-like stars (Greene, 2001).

Birth of a planetary system

The history of an exoplanet starts at the birth of its host-star (Fig. 1.1). The interstellar medium contains molecular clouds that are dense enough to host simple molecules like H_2, CO, but also around 1% of dust (silicates, carbonaceous grains). These clouds are not homogeneous, they contain dense cores, pre-stellar cores, that eventually shrink because of self-gravity. After around 30 000 years, the gravitational collapse leads to dense objects where the temperature reaches at least 10 million degrees, enough to start hydrogen fusion. A protostar is born.

During the collapse, the 10^4 astronomical unit (au) pre-stellar core has shrunk to a few 10^2 au. Because of angular momentum conservation, the initial rotation of the pre-stellar core concentrates in the protostar and its envelope. Perpendicular to the rotation axis, the centrifugal force counteracts the gravitational collapse and forms a disk of gas and dust, the protoplanetary disk.

In this protoplanetary disk, the heaviest particules, dust and ice, settle in the mid-plane. Here, for around one million years, these particles encounter and aggregate by Van der Waals forces to form bigger grains (Weidenschilling, 1980), that in turn aggregate into larger objects, the planetesimals. Several planetesimals form in the disk and accrete material along their orbit thanks to gravitational

attraction. The biggest planetesimals accrete more material and eventually enter a process of runaway growth (Kokubo and Ida, 2000). This hierarchical process continues until planet-size bodies are formed. It is commonly acknowledged that terrestrial planets form below the ice-line, where the H_2O is sublimated by the star's radiation and cannot exist at ice state. On the other side, beyond the ice-line, the planetesimal can accrete more solid elements, resulting in a faster growth. The protoplanet core can exceed the estimated limit of 10 $M_\oplus$(Earth mass) necessary for triggering runaway gas accretion and form a giant gaseous planet.

Around 10 million years after the initial core collapse, the disk is a debris disk, where gas has been either accreted or ejected, and only young planets and debris belts remain. From this state, the system evolves to a more mature planetary system, with the debris being accreted in asteroids or ejected by the gravitational influence of the planets. The central star enters the main-sequence of stellar evolution.

Open questions

This is a schematic view of the formation of a planetary system. I did not mention the influence of magnetic field on the young stellar object and its surroundings. The bipolar outflow of the early protostar is the most visible feature created by the magnetic field influence on the disk (Blandford and Payne, 1982). The magnetic field is also expected to induce turbulence in the protoplanetary disk and have a direct influence on planet formation (Wardle, 2007).

I also considered the simple case of a single central star, but 50% of the stars are in multiple systems (Duchêne and Kraus, 2013). The influence it can have on the efficiency of planet formation is debated, but it is generally accepted that the presence of multiple massive hosts is an obstacle to the aggregation of dust and pebbles in larger bodies (Marzari and Thebault, 2019).

Even without considering additional magnetic field or multiple stellar hosts, the growth of micrometer dust grains into planetesimals is far from easy. Especially, there is a difficult transitional regime between small grains coupled with the gas and larger bodies following a Keplerian orbit. In the disk, the gas angular orbital speed is sub-Keplerian. Large kilometric bodies are decoupled from the gas and are not affected by this low headwind. However, in a typical disk, it is not the case for objects from millimeter to meter-size that are slowed down by the gas and should drift toward the central star on timescales of 100 years. This phenomenon is known as the radial-drift barrier (Weidenschilling, 1977; Laibe et al., 2012), and it is a major limitation to the classical accretion theory. This problem finds partial solutions in adding more complexity to the model, either disc instabilities decoupling the small bodies from the gas (Johansen et al., 2006), or considering back-reaction from the dust onto the gas (Gonzalez et al., 2017).

For the giant planets, the specific formation processes at work are not well known. They can form by core accretion, as described in the previous section, slowly accreting material up to a threshold mass (Mizuno, 1980) from which a runaway gas accretion occurs (Pollack et al., 1996). But this is not the only possible process. Another explanation could be gravitational instabilities in the disk (Boss, 1997). Under certain conditions of pressure and temperature, the protoplanetary disk can become locally unstable and collapse to form a dense core. In this theory, the giant planets are formed faster than in the core accretion paradigm. The gravitational instability would be the favored mechanism to

form giant planets more massive that 1 M_{Jup} at more than 10 au from the star. But which formation mechanism dominates for which kind of objects is still poorly constrained. Marley et al. (2007) show that these formation models lead to different mass-luminosity and luminosity-age (cooling curves) relationships. These parameters can be observed, especially by direct observations (Sect. 1.3.4), and, in the future, will help to better determine the formation pathways for giant exoplanets. For now, the direct observation techniques are limited to the observation of the more massive gaseous giants on distant orbits (> 10 au). Allowing direct observations of Jupiter-mass planets on 2 to 5 au orbits by optical interferometry is the major scientific motivation of my thesis.

1.2.3 Exoplanets' population

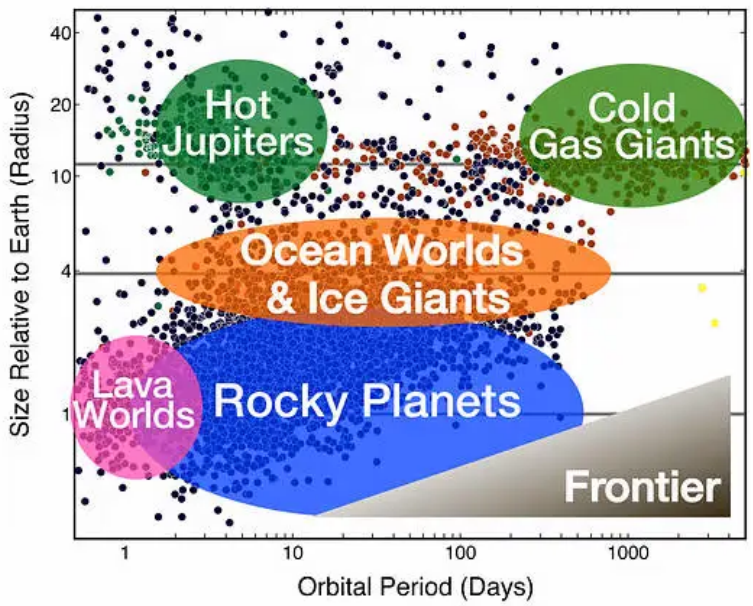

Figure 1.2 – Radius-period diagram of all planet detected so far (2024, April). The grey triangle depicts the zone of this parameter space currently out of reach for current instruments. (NASA/Ames Research Center/Natalie Batalha/Wendy Stenzel, 2017)

Since 1995 and the first detection of an exoplanet around a main sequence star (Mayor and Queloz, 1995), a total of 5654 exoplanets have been discovered and confirmed (April 2, 2024 number). This explosion of discoveries has unveiled an impressive diversity that we could never have imagined from the observation of our own solar system. Figure 1.2 shows how the different types of discovered exoplanet dispatch on a radius-period parameter space. On top of the well-known rocky planets, ice giants and gas giants, we discovered giant planets of a few days orbital period (hot-jupiters), terrestrial planets so close from their star that they undergo intense radiation and tidal forces (lava worlds) and planets essentially composed of water potentially liquid on surface or below an ice surface (ocean worlds). Overall, statistical studies on planets detected by transit (Sect. 1.3.1) show that 75% of FGK stars have planets, with an average of 2.7 planet per system (Yang et al., 2020; Kunimoto and Matthews, 2020). These studies also show that 50% of the solar-type stars harbor super-Earth planets with a radius between 1.25 and 2 times the Earth radius. Therefore, the solar system, with its small terrestrial planets inward and giant gaseous planets and ice giants in the outskirts, appears

to be relatively different from the bulk of exoplanetary systems discovered so far.

Fernandes et al. (2019) combined transit and radial-velocity observations to determine the radial distribution of giant exoplanets. Figure 1.3 shows a peak of giant planet occurrence close to 2 au, at the expected position of the ice-line around young sun-like stars. This result is challenged by Lagrange et al. (2023), arguing that the planet population beyond 5 au is poorly sampled by the existing techniques. Still, they confirm that the giant planets are preferably found beyond 1 au and stress the need for expanding the instruments sensitivity to the 5 to 10 au range. However, direct imaging shows that giant planets are relatively rare in the outskirts of planetary systems. The survey SHINE (Vigan et al., 2021) shows that only about 6% of FGK stars have a companion more massive than 1 M_{Jup} beyond 5 au. In this manuscript, I will show that GRAVITY+ is tailored to provide direct observations of young giants in the critical 1 to 5 au range (Chapters 3 and 5). In a near future, it shall significantly improve our knowledge of the giant planet population.

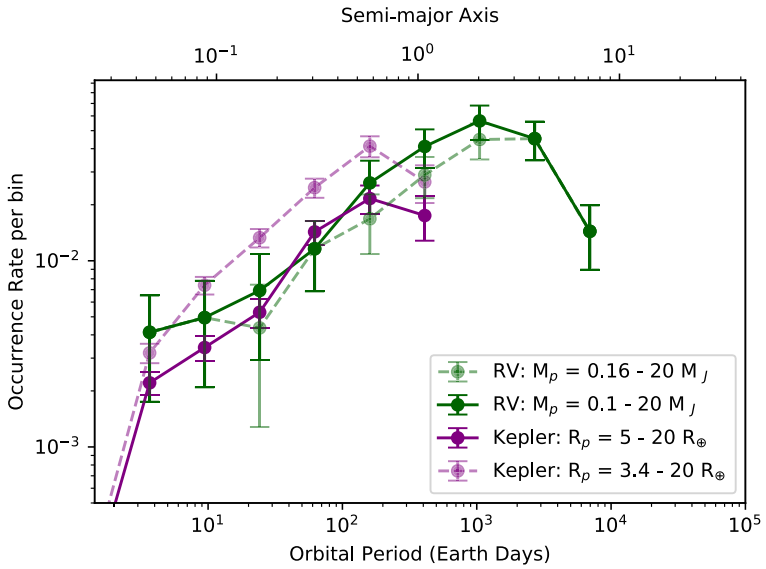

Figure 1.3 – (From Fernandes et al., 2019) Occurrence rate of giant planets from the radial-velocity survey of Mayor et al. (2011), and from Kepler transit survey.

In the previous section, I already mentioned that giant planets can only form beyond the ice-line, where there is enough solid material to grow rapidly. For this reason, the discovery of the hot-jupiter population was a challenge to the theory. It indicates that planets do not stay where they form, but can migrate over time.

1.2.4 Exoplanets' dynamical history

Indeed, planets change their orbit during their lifetime. It can happen from the protoplanet stage via gravitational interactions of the body with the disk (Baruteau et al., 2014). On evolved systems, migration can be triggered by dynamical interaction with debris disk or the influence of the other planets.

Even the solar system has probably experienced a spectacular migration event described by the Nice model (Tsiganis et al., 2005; Morbidelli et al., 2005; Gomes et al., 2005). Originally, Jupiter, Saturn, Uranus and Neptune may have been on closer circular orbits, at less than 17 au from the sun.

Their interaction with an external planetesimal disk has eventually triggered a massive migration process leading to the formation of the actual solar-system shape, with Neptune and Uranus at 19 and 30 au, the Kuiper belt, and the resonance of the trans-Neptunian objects orbit. This is a remarkable example of how giant planets can shape their planetary system.

For the extra-solar systems we discovered, it is common to analyze the dynamical stability of multiple systems thanks to the observed relative astrometry of the different bodies (Wang et al., 2018; Lacour et al., 2021). We generally expect to find dynamically stable systems, as it is the most probable configuration. If a system would happen to be observed in a dynamically unstable configuration it might mean we have an incomplete view with other planet yet to be found.

In addition, as I will briefly discuss in Sect. 5.4.2, the shape of the orbits can contain information about how the planets formed, and GRAVITY is proving to be very powerful at fine-scale measurements of orbital parameters.

1.2.5 Exoplanets' atmosphere

As the exoplanets' observations provide more and more data, it becomes relevant to use tools previously dedicated to the solar-system planets. Especially, the fine transit spectroscopy of hot-Jupiters now allows for comparisons with 3D global-circulation models to determine the key atmosphere dynamics and meteorology (Tan and Komacek, 2019; Parmentier et al., 2021; Teinturier et al., 2024). Also, from the transit-spectroscopy of exoplanets ranging from super-Earths to hot-giants, we can identify the species present in the planets' atmosphere, like the first unambiguous detection of CO_2 in WASP-39b (JWST Transiting Exoplanet Community Early Release Science Team et al., 2023), or the constrain on the water vapor content in the atmosphere of 55Cnc e (Esteves et al., 2017), and the chemical processes at work, like the iron precipitation on the night side of WASP-76b (Ehrenreich et al., 2020).

The emission spectroscopy of longer period exoplanets is not yet as precise as the transit-spectroscopy for atmosphere characterization. It is limited to young giant exoplanets of less than 15 million years, a population poorly probed by the other techniques, so it is particularly indicated for the study of the planet formation. Young giants are still in the process of contracting, and the release of gravitational energy heats their atmosphere to temperatures reaching 1800 K (β Pic b: GRAVITY Collaboration et al., 2020b). So, giant exoplanets are not yet observed thanks to their reflected light but thanks to their infrared thermal emission. However, this emission is faint, so analyzing it at high resolution is at best challenging. Still, it allows for comparison with spectra from atmospheric models like DRIFT-PHOENIX (Woitke and Helling, 2003), BT-Settl (Allard et al., 2012) or ExoREM (Charnay et al., 2018). From fitting of the exoplanets' spectra with the model grids, one can retrieve the temperature of the exoplanet atmosphere, a mass estimate, and quantify tentative tracers of the formation history like the C/O ratio.

Indeed, the C/O ratio observed on an exoplanet is expected to trace the orbital distance where the planet formed. A formation before or after the H_2O, CO or CO_2 ice-lines should impact the global C/O ratio of a planet (Öberg et al., 2011). This C/O ratio is appealing because it is a metric that is possible to extract even from medium resolution spectra and that is assumed to give precious hints on the planet formation. However, there are more and more criticism against conclusions drawn

too fast on stellar or substellar C/O ratios. The measurements probe only the C/O ratio on the upper atmosphere of the planet and it seems generally over-simplistic to expand it to the bulk of the giant planet without independent hints on eventual mixing processes. As I mentioned previously, the mass-luminosity relationship is a more robust formation tracer, but it still requires a precise calibration and exoplanets with a precise mass measurement are still too few.

Finally, the James Webb Space Telescope (JWST) has made an impressive leap in the spectral resolution of exoplanet emission spectra. For example, within 6-hour integration time, they obtained a high signal-to-noise (SNR) infrared spectrum of VHS 1256 b from 1 to 20 µm with a resolution power from 1000 to 3700 (Miles et al., 2023). This opens the way for a fine spectral characterization of exoplanets from space-based observatories. Soon, the Nancy Grace Roman space telescope will be launched (2027) and shall bring the first observation of reflected light of giant exoplanets by direct imaging (Bailey et al., 2023). In the decades to come, there are projects of space telescopes like the Habitable World Observatory (HWO: Gaudi et al., 2020) or the Large Interferometer For Exoplanets (LIFE: Quanz et al., 2022), whose goal is to characterize the atmosphere of telluric planets and eventually identify bio-signatures. On the ground, the most ambitious projects are linked to the Extremely Large Telescope (ELT, Gilmozzi and Spyromilio, 2007), the 39-meter diameter optical telescope under construction in Chile. After a first generation of instruments that are expected to bring observations of young giants at only a few au from their star (ex. HARMONI: Thatte et al., 2021), the Planetary Camera and Spectrograph (PCS Kasper et al., 2021) shall bring atmosphere observation of exoplanets down to Earth-size. We can expect the question of the detectability of bio-signatures in exoplanets' atmosphere spectra to be increasingly important in years to come.

1.3 Observation techniques

Different observation techniques have been developed to detect and characterize exoplanets. One way or another, all these techniques rely on resolving the planet, either photometrically, spectroscopically, temporally or angularly. In this section, I develop the key elements to understand the position of optical interferometry in exoplanet science. Indeed, all the different methods open a different parameter space for the measurement of the exoplanets' mass, radius, age and semi-major axis. Their different approach is crucial to reveal the diversity of extra-solar planets.

Figure 1.4 shows a representation of the yield of the major detection techniques in term of semi-major axis and mass. In this section, I will describe the different detection and observation methods, sorted by discovery yield.

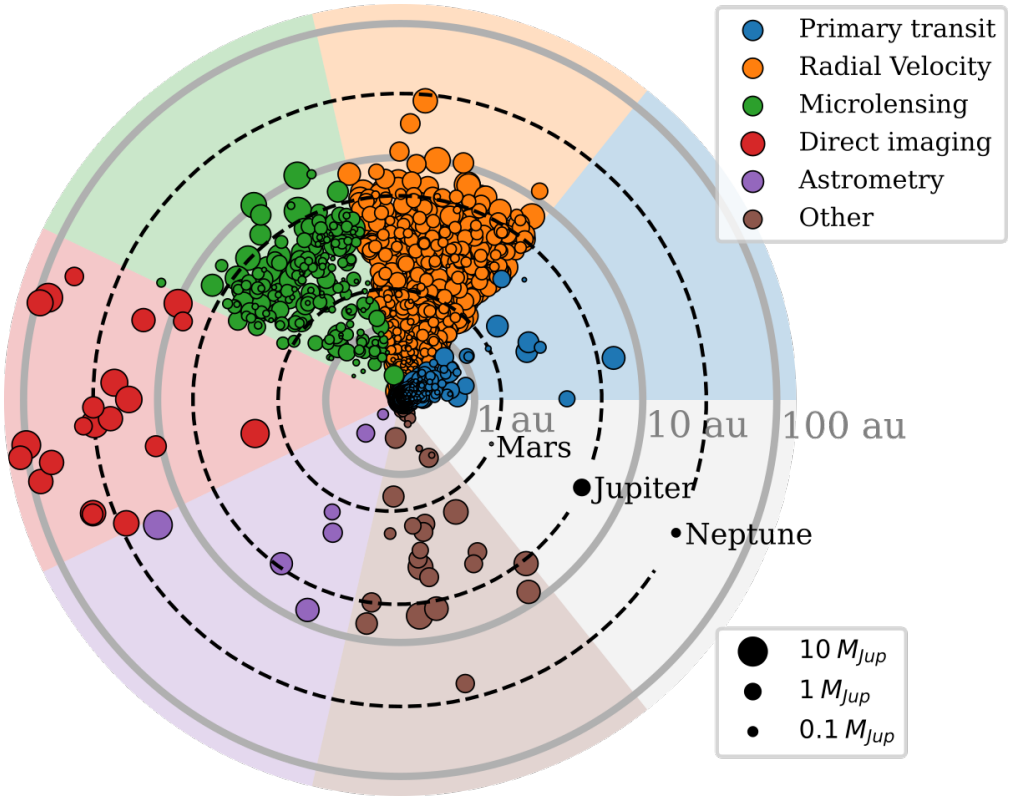

Figure 1.4 – Comparison of the discovery yield of the major exoplanet detection techniques. (circles) All exoplanets confirmed with an estimate of semi-major axis and mass, according to `https://exoplanet.eu`. Circle width represents the planet mass on a square root scaling. Planets of the solar system are shown for reference.

1.3.1 Primary transit

The detection by primary transit consists in observing the eclipse of a star by an exoplanet. A small fraction of the starlight is not propagated during the transit and induces a photometry gap that can be detected even with 1 meter size telescopes. Detection by primary transit provides a measurement of the orbital period and of the exoplanet radius, as the transit depth is determined by the relative radii of the planet and the star.

The probability ρ for a random planet to be favorably aligned for a transit is (from Borucki and Summers, 1984):

$$\rho = \frac{R_*}{a},$$

with R_* the star's radius and a the planet semi-major axis. Therefore, the method is most sensitive to closely packed planets (as shown on Fig. 1.4). Indeed, 50% of the exoplanets detected by primary transit are below 0.07 au from their star.

By observing a transit over a spectral range, one can measure the amount of chemical species that is present in the exoplanet's atmosphere. It is a powerful technique for atmosphere characterization of exoplanets, especially now on the JWST (e.g. JWST Transiting Exoplanet Community Early Release Science Team et al., 2023).

The most prolific instruments dedicated to detection by primary transit are space based to benefit

from the stable photometry (Kepler: Borucki et al. (2010), TESS: Ricker et al. (2015)).

This method discovered 69% of the exoplanets actually known.

1.3.2 Radial-velocity

The detection by radial-velocity consists in detecting the Doppler shift of the star spectrum due to its orbital motion around the system center of mass. For one planet of mass M_p, of period P, and eccentricity e around a star of mass M_*, the semi-amplitude of the radial-velocity variation is (from Cumming et al., 1999):

$$K = v_r \sin i = \left(\frac{2\pi G}{P}\right)^{1/3} \frac{M_p \sin i}{(M_* + M_p)^{2/3}} \frac{1}{(1-e^2)^{1/2}}.$$

The method is mostly sensitive to high planet-to-star mass ratio on short orbital period. This is why the first ever exoplanet discovered around a solar-type star was 51 Peg b, a gas giant of 0.5 M_{Jup} on a 4-day orbit (Mayor and Queloz, 1995). The detection of long period companions (beyond 5 au) is limited by both the reduced radial-velocity amplitude and the duration of the surveys. So far, 50% of planets detected by radial-velocities are closer than 1 au from their star.

The radial-velocity observations provide measurements of the orbital period and eccentricity, but also of the mass ratio between the planet and the star (proportionnaly to sin i). From an assumption of M_* by the star's spectral type, one can obtain $M_p \sin i$.

The most notable instruments for radial-velocity measurements are dedicated high resolution spectrographs like HARPS (Pepe et al., 2002) or ESPRESSO (Pepe et al., 2021).

This method discovered 19% of the exoplanets actually known.

1.3.3 Microlensing

The detection by gravitational microlensing uses a general relativity principle. The matter has the property to distort space-time, and doing so, bend light rays. When we observe a star, that we call star A, for example at 8 kpc, imagine that another star B crosses the line of sight between star A and us. The image of star A will be distorted by the bending of the light rays due to the lensing effect induced by star B. For a star B of 1 $M_\odot$ (solar mass), the distorted secondary image of star A appears at a separation of the order of 1 mas and cannot be resolved by single telescopes (Perryman, 2018). However, the photometry of star A is amplified by the transit, following a well identified curve. If a planet orbits star B, it will also leave a signature under the form of bends or cusps in the star A light curve during the microlensing event. From this, we can extract an estimate of the exoplanet mass, and its projected separation with the host star during the event. One significant drawback is that the observation is not repeatable as a second gravitational lensing event of the same star B has very little chance to happen.

The gravitaional microlensing is mostly sensitive to planets in the 1 to 10 au range, and down to 2 $M_\oplus$ (Gould et al., 2014). The accessible companions are much less massive than those accessible by the radial-velocity in the same semi-major axis range.

Detection by gravitational microlensing detects planets around more distant stars than other

techniques. Its detection distribution peaks at 7 kpc, at the edge of the galactic bulge. For comparison, 90% of exoplanets detected by primary transit are within 1.4 kpc, and 90% of exoplanets detected by radial velocity are within 300 pc.

This method has gained importance in the recent years thanks to dedicated projects using 1-meter class telescopes and covering wide field of view (OGLE: Udalski et al. (2015), KMTNET: Kim et al. (2016)).

This method discovered 5% of the exoplanets actually known.

1.3.4 Direct exoplanet imaging

The detection by direct imaging is the simplest in principle but not in practice: make pictures of the planetary systems. It requires high-angular resolution capabilities, to be able to differentiate the star from the planet, and high-contrast, to reveal faint objects around the bright host.

High-angular resolution Let me take an example, an exoplanet on a 2 au circular orbit around a star at 10 pc has a planet-star angular separation of 200 mas. But, for ground-based observations, the Earth atmosphere turbulence distorts the light wavefront from astronomical objects. Even on the best sites, it limits the maximal angular separation we can measure between two objects at about 500 mas in the visible (seeing). However, thanks to the advent of adaptive optics applied to astronomy, it is now possible to correct part the atmosphere turbulence and enable higher angular resolution (see Sect. 2.2.1). Wave optics shows that the fundamental resolution limit θ is set by the diffraction of the telescope pupil such that:

$$\theta = 1.22\frac{\lambda}{D}\,[\text{rad}] \tag{1.1}$$

at wavelength λ for a round pupil of diameter D. Technical progress in adaptive optics brought 8-meter class telescopes close to their diffraction limit in the near-infrared (41 mas in H-band, λ=1.6 µm).

High-contrast From its reflected light in the visible, Jupiter has a flux contrast estimated to 1.4×10^{-9} compared to the solar visible flux (Traub and Oppenheimer, 2010). This is currently out of reach for direct imaging instruments. In the infrared, the exoplanet flux is dominated by the thermal emission. So the contrast is:

$$C_{IR} = \frac{B_\lambda(T_p)\,R_p^2}{B_\lambda(T_*)\,R_*^2} \tag{1.2}$$

with T_p and T_* the temperature of the planet and the star respectively, R_p the planet radius, and assuming blackbody emissions as:

$$B_\lambda(T) = \frac{2hc^2}{\lambda^5\left(e^{hc/\lambda k_B T}-1\right)}. \tag{1.3}$$

The contrast rises with the temperature difference between the planet and the star, and giant planets have a higher temperature when they are young (Sect. 1.2.5). For this reason, the first exoplanet directly observed by Chauvin et al. (2004) was a young ($\sim$ 5 Myr) 5 M_{Jup} planet with a surface temperature of 1200 K orbiting a brown dwarf with 2700 K surface temperature. The contrast was observed around 10^{-2}. Since then, contrast limits have gone deeper, down to a few 10^{-7} in the near-infrared. The development of coronagraphy has been a key for pushing the contrast limit, but the direct imaging is still only able to observe young giant gaseous planets.

Post-processing To disentangle the star light from the planet light, astronomers use every piece of differential information between the two. First, the angular-differential imaging technique (ADI: Marois et al., 2006) uses the angle variation due to sky rotation during the observation. It helps revealing the planet (rotation with the sky) from the residual star light diffraction after the coronagraph, called speckles (static in the instrument reference frame). Second, the spectral-differential imaging (SDI: Racine et al., 1999) uses the difference in chromatic dispersion between speckles (originating from star light, dispersed at the planet position) and the planet (not dispersed). Finally, reference-differential imaging (RDI: Soummer et al., 2014) uses a library of single star images to identify the best calibration for subtracting the star contribution in the image. The ADI and SDI bring the most contrast improvement but are less efficient at short separations. A promising way to push direct imaging at shorter separations is the molecular mapping technique. It combines the image with high spectral resolution information at each pixel to cross-match an expected planet spectrum and identify the position in the image with the highest overlap (Snellen et al., 2015). This method has no fundamental limit at short separations, except the stellar photon noise, and is gaining importance for new and future instruments (Mâlin et al., 2023; Houllé et al., 2021).

Detections For the instrumental and post-processing reasons mentioned above, the direct imaging technique is limited to exoplanets at large separations, namely, with semi-major axis beyond 5 au. Moreover, the need for a contrast above 10^{-7} limits the technique to the detection of young giant planets. The detection parameter space in mass-semi-major-axis is clearly visible in Fig. 1.4.

Observations Detection is difficult, but the price is well worth it. From the direct imaging of a system at different epochs, one can achieve orbit characterization that, unlike radial-velocity observations, is not affected by undetermined inclination. Moreover, measuring directly the exoplanet flux, one can infer the planet surface temperature and, if the spectral resolution is high enough, the chemical composition of the exoplanet atmosphere.

Extensive surveys have been conducted on the major direct imaging instruments like SPHERE (Beuzit et al., 2019) with the SHINE survey (Desidera et al., 2021; Langlois et al., 2021; Vigan et al., 2021), GPI with the GPIES survey (Nielsen et al., 2019) and the Large Binocular Telescope with the LEECH survey (Stone et al., 2018).

This method discovered 4% of the exoplanets actually known.

In the wake of direct imaging In the same family of direct imaging techniques, we can consider instruments that rely on high angular resolution to observe the exoplanet light but without the

imaging capability. It is the case of fiber fed instruments like KPIC (Delorme et al., 2021a) and HiRISE (Vigan et al., 2024), that use adaptive optics and planet light injection in a single-mode fiber to feed a spectrometer and obtain high-resolution spectra. This is also the case of GRAVITY (Gillessen et al., 2010) at the Very Large Telescope Interferometer (VLTI), the central topic of this manuscript, that uses injection in single-mode fibers before optical interferometric recombination. Despite not providing images of the field, these techniques share the majority of the instrumental challenges and limitations of the direct imaging. The question is still to find how to reduce the impact of the host star light to provide exoplanets' observations at high contrast. One of the biggest limitations is the small field of view of single-mode fibers. Because of this, these instruments are poorly suited for first exoplanets' discoveries. However, their interest comes from their powerful characterization capabilities. In this manuscript, I call direct observation all the techniques of direct imaging and direct GRAVITY-like or KPIC-like observations that rely on high-angular resolution to measure the exoplanet light.

1.3.5 Astrometry

The detection by absolute astrometry uses measurements of the reflex motion of the primary under the gravitational interaction with a companion. On single stars, precise measurements of the star's photocenter position on sky at different epochs provides the proper motion, the angular velocity of the star displacement with respect to a fixed reference frame. If the star has a companion, one can measure a periodic perturbation of the proper motion. The angular semi-amplitude α of this perturbation scales as (Perryman, 2018):

$$\alpha[\text{arcsec}] = \frac{\mathrm{M}_p}{\mathrm{M}_* + \mathrm{M}_p} \frac{a[\text{au}]}{d[\text{pc}]} \tag{1.4}$$

with a the companion semi-major axis and d the star distance. Observations by the astrometric technique can provide the seven Keplerian elements of a single companion (a, e, t_p, i, Ω, ω, P) and fully constrain the orbit (see Keplerian orbit Appendix A.1). Only remains a 180° degeneracy on the ascending node Ω.

The companion mass can be estimated by derivating the photometric mass of the star by its spectral type. Combining astrometry and radial velocities, one can obtain an independent mass measurements that can confirm the planetary nature of the companion.

Strictly speaking, the astrometric method does not measure the star absolute position but the position of the photocenter of the star-companion system. A bright companion on close orbit may not be resolved by the telescope but contribute to bias the photocenter position. Therefore, one key point for description of a planetry system including astrometric data is to confirm that the companion does not contribute significantly to the total flux observed.

As shown by Eq. 1.4, the astrometric method is mostly sensitive to massive planets with large semi-major-axis and orbiting nearby stars. However, there is a cut-off in the sensitivity to large semi-major axis planets due to the limited duration of the surveys. Sozzetti (2010) shows that the sensitivity of the Gaia space telescope (Gaia Collaboration et al., 2016) peaks at 2∼3 au and would detect planets down to 100 $\mathrm{M}_\oplus$ (0.31 $\mathrm{M}_{\mathrm{Jup}}$). Figure 3.20 shows an example of Gaia sensitivity curve.

Gaia is already a game changer for our understanding of the Milky Way. In 2026, they will release the data covering 5.5 years of observation (DR4). It is expected to provide thousands of astrometric detection of potential planetary mass companions (Perryman et al., 2014).

To this day, this method discovered 23 exoplanets (according to `https://exoplanet.eu`).

1.3.6 Other techniques

On top of the major exoplanet detection techniques described above, I would like to mention other interesting methods.

Binary astrometry By precise astrometric measurements of binary stars orbits (∼10 µas), one can reveal the pertrubation caused by a third body, possibly of sub-stellar nature. Such measurements can be performed by optical interferometry. The most notable examples are the ARMADA survey at the Center for High Angular Resolution Astronomy (CHARA) (Gardner et al., 2021, 2022) and the PHASES survey on the Palomar Testbed Interferometer (PTI) (Muterspaugh et al., 2010). So far, these surveys did not detect planetary mass companions. However, very recently, with this technique the GRAVITY team claimed the detection of a Neptune-mass exoplanet orbiting the binary M-dwarf Gliese 65 AB (GRAVITY Collaboration et al., 2024a).

Timing The timing methods focus on temporal anomalies in the primary light to detect companions. This method discovered the first ever exoplanets by analyzing anomalies in the frequency of a pulsar host (Wolszczan and Frail, 1992). It can also detect exoplanets via variation anomalies of variable stars or in the timing of eclipsing binaries.

The most prolific timing method so far is the transit timing variation (TTV). It is able to detect non-transiting companions thanks to anomalies on transiting companions of the same system. In resonant systems like Trappist-1, it can even provide mass estimates for the companions of the system (Teyssandier et al., 2022). It discovered 29 exoplanets so far (e.g. Wittrock et al., 2023).

Secondary transit The secondary transit method observes the drop of luminosity when the exoplanet passes behind its host star. The transit depth is more difficult to detect than for the primary transit, so there is no claim of exoplanet discovery with this technique so far. However, this is one of the few methods that has directly observed visible photons from the reflected light of an exoplanet.

1.4 GRAVITY

Bracewell and MacPhie (1979) had foreseen it: interferometry in the infrared has a role to play for exoplanet observations. Given the angular resolution needed to differentiate a planet from its host-star, it was clear that interferometers with long baselines would have an edge on single-telescope instruments for disentangling starlight from planet light.

It took the construction of the Very Large Telescope (VLT) and VLTI from 1991, a first generation of interferometric instruments (VINCI: Kervella et al. (2003), MIDI: Leinert et al. (2003), AMBER:

Petrov et al. (2007)), and in 2016 the first-light of GRAVITY. Two years after, HR 8799 e was the first exoplanet ever directly observed by interferometry (GRAVITY Collaboration et al., 2019).

GRAVITY is a second-generation instruments at VLTI. It recombines either the four 8-meter diameter Unit Telescopes (UT) or the smaller relocatable 1.8-meter Auxiliary Telescopes (AT). It observes in the K-band ($\lambda \sim 2.2$ µm) and has launched optical interferometry into the realm of faint objects (K<19 mag). I detail the instrument specificities in Chapter 2. Here, let us focus on the achievements of GRAVITY observations.

Figure 1.5 – Twilight on the Very Large Telescope (picture: G.Hüdepohl/ESO).

1.4.1 Science cases' overview

The main science case of GRAVITY is the study of the Galactic Center (Eisenhauer et al., 2005). The instrument is able to measure the relative astrometry of stars orbiting the central black hole Sgr A* at an exquisite precision of 50 µas. Moreover, it can detect gravitational redshifts in the stars' spectra (GRAVITY Collaboration et al., 2018a, 2020a) and monitor matter distribution close to the last stable orbit (GRAVITY Collaboration et al., 2018b). This brought direct confirmation that Sgr A* is a supermassive black hole and allowed for a validation of General Relativity principles. The next exciting goal is to determine the spin of the black hole from the orbits of stars on close orbit (Gravity+ Collaboration et al., 2022).

The study of active galactic nuclei is another important science case of GRAVITY. Observations can resolve the broad-line region extension around black holes at the center of distant galaxies (up to z=2). Together with the velocity gradients estimated from the shape of the K-band emission, one can measure the mass of the central supermassive black holes and bring information on how black holes shape their galaxy evolution (Abuter et al., 2024a).

GRAVITY also brought major breakthroughs to the study of young stellar objects. The high angu-

lar resolution of the instrument at K-band allows for resolving the innermost region of protoplanetary disks at a fraction of au. This allows for analyses of dust distribution (GRAVITY Collaboration et al., 2021b) and temporal variability of the infrared emission close to the star (Gravity Collaboration et al., 2024). Also, the analysis of emission lines from the magnetospheric gas accretion and/or ejection brings precious information on the complex processes at play on T-Tauri stars (Bouvier et al., 2020; Gravity Collaboration et al., 2023).

Finally, but of primary importance here, GRAVITY has enabled the first direct observations of exoplanets by interferometry. GRAVITY was designed for observing faint infrared point-sources, so the ability of the instrument to observe planetary mass companions was already predicted at the beginning of the GRAVITY project (Eisenhauer et al., 2005). Since 2018, GRAVITY has observed and characterized 13 young exoplanets. This has been possible thanks to the ExoGRAVITY large programme and the community that gathered around this new observation technique.

1.4.2 ExoGRAVITY

For observing exoplanets by interferometry, having a sensitive instrument was a requirement. But it was not the only one. We also needed: observing strategies, a dedicated data reduction pipeline, and observation time (Lacour et al., 2020). The ExoGRAVITY project was created by Sylvestre Lacour, and accreted more and more researchers over the years to form the ExoGRAVITY consortium ($\sim$ 100 people). They developed observing strategies and the ExoGRAVITY pipeline (GRAVITY Collaboration et al., 2020b) I will describe later in Chapter 2. In 2019, they obtained a large programme of observation (ID: 2104.C-5046(A)) that lasted from February 2020 to September 2023. During my PhD, I contributed to some of these observing nights by reducing the data in real time. A lot of the work I will describe here is based on data from the large programme (Chapters 3 and 4). Now that the large programme is over, several smaller open-time programmes are conducted by members of the consortium.

In terms of scientific output, ExoGRAVITY observations provide the relative astrometry between the host star and the planet at 50 µas precision, 20 times more precise than classical imaging. This great precision allows for constraining exoplanets' orbits (e.g. semi-major axis, eccentricity, inclination) even on a relatively short temporal baseline. The observations also provide K-band spectra at a resolution power of 500 (routinely) or 4000 (on brightest companions). This contains information on the planet's atmosphere (Sect. 1.2.5) where we can extract the companion's temperature, radius, metallicity, and C/O ratio.

Combined with radial-velocity or absolute astrometry observations, the ExoGRAVITY relative astrometry provides direct dynamical mass measurements at a precision and a robustness greatly improved compared to spectroscopy mass estimations. For a proper estimation of the companion mass and orbit, we use Markov Chain Monte Carlo codes like `orbitize!` (Blunt et al., 2020) that provide the probability distribution of the parameters given a set of observational constraints.

Radial-velocity and absolute astrometry are also used with GRAVITY to identify new targets. The science fiber of GRAVITY has a limited field of view, so, we need a prior estimate on the companion's projected position on sky before an observation (Sect. 2.5.1).

Finally, the observation of more massive substellar companions, like brown dwarfs, is also a

significant fraction of the ExoGRAVITY activities. It uses the same observation strategy and pipelines, and from it, we can study the continuum of substellar objects from planets to main-sequence stars.

1.4.3 Harvest of substellar companions

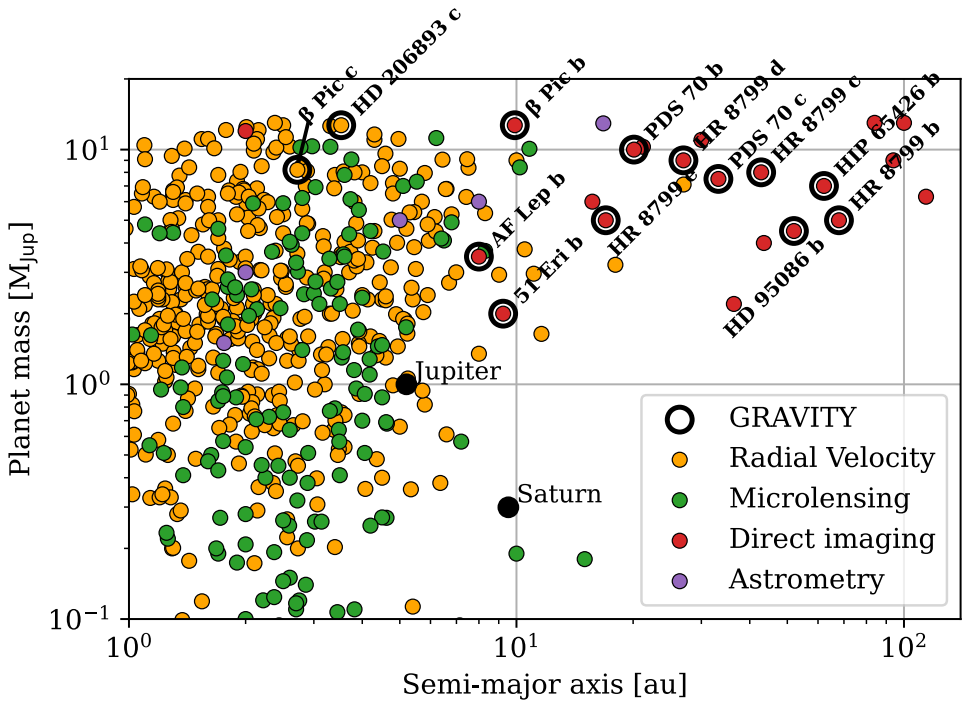

Figure 1.6 – All planets detected with a mass and semi-major axis estimate according to `https://exoplanet.eu` (April 2024). The colored dots show the discovery method. The black circles show the exoplanets observed with GRAVITY. Jupiter and Saturn are shown for reference.

ExoGRAVITY has directly observed 13 sub-stellar companions that are confirmed as exoplanets. Most of them are exoplanets discovered by direct imaging:

- β Pic b: GRAVITY Collaboration et al. (2020b)
- HR 8799 bcde: Nasedkin et al. (submitted)
- PDS 70 bc: Wang et al. (2021b)
- HIP 65426 b: Blunt et al. (2023)
- HD 95086 b: unpublished
- AF Lep b: Balmer et al. (in prep.)
- 51 Eri b: unpublished

We also made the first direct detection of exoplanets discovered by radial velocity:

- β Pic c: Nowak et al. (2020)
- HD 206893 c: Hinkley et al. (2023).

Figure 1.6 shows the planets observed with GRAVITY. The majority of the exoplanets detected with GRAVITY are on more distant orbits than Jupiter, and all are more massive than Jupiter. The two exoplanets closest to their star have a semi-major axis around 3 au. They have been discovered by the radial-velocity technique, and, indeed, radial-velocity planets are mostly in a 1 to 10 au

semi-major axis range. All planets observed with GRAVITY are young (< 15 Myr) self-luminous planet.

Observations of young Jupiter-mass planets at 5 au (Jupiter analogues) and closer companions are needed to complete the picture of giant planet formation and dynamic evolution. For observing exoplanets so close to their star, we will not be able to rely on a previous discoveries by direct imaging. The classical imaging technique is not yet capable of detecting companions in this parameter space. Radial-velocity technique has already discovered Jupiter analogues, but this technique disfavors young systems due to their higher stellar activity that disturbs radial-velocity measurements. The microlensing technique is also sensitive to these Jupiter analogues, but, as shown in Sect. 1.3.3, they are detected at distance around 7 kpc. The projected separation of a planet orbiting at 5 au from its star at 7 kpc from earth is 0.7 mas, inaccessible by direct observation techniques. For these low mass planetary companions observations at the au-scale, GRAVITY relies on the planets discovered by absolute astrometry. And hopefully, these planets will be revealed by the next Gaia data release, the Gaia DR4, in 2026 (see Sect. 3.6).

Before the expected harvest of Gaia exoplanets, we already use the information of the Non-Single-Stars (NSS) catalogue of Gaia DR3 released in 2022 to infer the on-sky position of companion brown dwarfs and observe them with GRAVITY (Winterhalder et al., 2024; Pourré et al., 2024). It adds up to notable brown dwarf observations of the ExoGRAVITY consortium, like HD 72946 B (Balmer et al., 2023), HD 136164 Ab (Balmer et al., 2024) and HD 206893 B (Kammerer et al., 2021) with an extensive study of their orbit and atmosphere that helps to constrain mass-luminosity relationships and cooling curves. From these observations, we also gather indications on the brown dwarfs' formation process and the impact they can have on protoplanetary discs (e.g. HD 142527 B Nowak et al., 2024b).

Hold your breath...

... before a deep dive in the instrument.

In this chapter, I focused only on the yield of the different exoplanet detection methods, but all these methods rely on cutting-edge instruments designed to push the sensitivity limits and expand the detection parameter space.

In the next chapter, I will describe how GRAVITY achieve the direct observations of exoplanets by optical interferometry.

Chapter 2

Observing planets with GRAVITY

Contents

If GRAVITY achieved the first direct observations of an exoplanet by optical interferometry, it is thanks to instrumental breakthroughs and a remarkable instrumental design. In this chapter, I start by wave optics to outline the theory of single-mode interferometry. Then I describe the GRAVITY subsystems, all are crucial building blocks of the instrument sensitivity and astrometric precision. Finally, I detail the ExoGRAVITY observation strategy and data reduction pipeline to achieve interferometric light deconvolution.

2.1 Theory of optical interferometry

2.1.1 Simple model

Let me first describe the simple case of an interferometer with two telescopes[1], observing the same unresolved source. Each telescope receives the electric field:

$$E_{\mathrm{T}_1}(t,\lambda) = E_0 \ \exp\left(i\frac{2\pi}{\lambda}(\mathbf{k}(t)\cdot\mathbf{x}_{\mathrm{T}_\mathbf{1}})\right) \ \exp(-i\omega t) \tag{2.1}$$

$$E_{\mathrm{T}_2}(t,\lambda) = E_0 \ \exp\left(i\frac{2\pi}{\lambda}(\mathbf{k}(t)\cdot\mathbf{x}_{\mathrm{T}_\mathbf{2}})\right) \ \exp(-i\omega t) \tag{2.2}$$

with E_0 the electric field amplitude, λ the wavelength, $\mathbf{k}(t)$ the unit vector in the source direction (in the following all vectors and matrices are printed in bold), $\mathbf{x}_{\mathrm{T}_\mathbf{1}} = (x_{\mathrm{T}_1}, y_{\mathrm{T}_1}, z_{\mathrm{T}_1}), \mathbf{x}_{\mathrm{T}_\mathbf{2}} = (x_{\mathrm{T}_2}, y_{\mathrm{T}_2}, z_{\mathrm{T}_2})$ the two telescopes' position in space, and $\omega = 2\pi f$ the light pulsation. Combining the two electric fields, we obtain the intensity:

$$I_{\mathrm{T}_1\mathrm{T}_2}(t,\lambda) = |E_{\mathrm{T}_1}(t,\lambda) + E_{\mathrm{T}_2}(t,\lambda)|^2 \tag{2.3}$$

$$= |E_0|^2 \ |\exp(-i\omega t)|^2 \ \left|\exp\left(i\frac{2\pi}{\lambda}(\mathbf{k}(t)\cdot\mathbf{x}_{\mathrm{T}_\mathbf{1}})\right) + \exp\left(i\frac{2\pi}{\lambda}(\mathbf{k}(t)\cdot\mathbf{x}_{\mathrm{T}_\mathbf{2}})\right)\right|^2 \tag{2.4}$$

$$= 2I_0 + 2I_0 \ \cos\left(\frac{2\pi}{\lambda}[\mathbf{k}(t)\cdot(\mathbf{x}_{\mathrm{T}_\mathbf{2}} - \mathbf{x}_{\mathrm{T}_\mathbf{1}})]\right). \tag{2.5}$$

So, the intensity is the sum of two terms: the simple addition of the intensity of the two electric fields, and an oscillating interference term. Converting $\mathbf{k}$ to its expression in the appropriate spherical coordinates system fixed with respect to the celestial sphere, and hereafter called "the pointing direction", Eq. C.4 becomes:

$$I_{\mathrm{T}_1\mathrm{T}_2}(t,\lambda) = 2I_0 + 2I_0 \ \cos\left(\frac{2\pi}{\lambda}[\Delta\mathrm{RA}(x_{\mathrm{T}_2} - x_{\mathrm{T}_1}) + \Delta\mathrm{Dec}(y_{\mathrm{T}_2} - y_{\mathrm{T}_1}) + (z_{\mathrm{T}_2} - z_{\mathrm{T}_1})]\right), \tag{2.6}$$

with ΔRA and ΔDec angles corresponding respectively to small right-ascension and declination offsets. The term $(z_{\mathrm{T}_2} - z_{\mathrm{T}_1})$ is the geometrical delay due to the path difference between the two telescopes. In the cases where the apertures are on the same plane perpendicular to $\mathbf{k}$, like single-telescope aperture masking or interferometry at the Large Binocular Telescope, this term is null by design. On VLTI or CHARA, the telescopes are not on the same mount, so this term is non-zero but is compensated by delay-lines.

The U_b and V_b coordinates for the baseline b formed by T_1 and T_2 are defined as:

$$U_b = x_{\mathrm{T}_2} - x_{\mathrm{T}_1} \tag{2.7}$$

$$V_b = y_{\mathrm{T}_2} - y_{\mathrm{T}_1} \tag{2.8}$$

[1] Following an outline close to Nowak (2019).

so Eq. 2.6 becomes:

$$I_{\mathrm{T_1T_2}}(t,\lambda) = 2I_0 + 2I_0\ \cos\left(\frac{2\pi}{\lambda}[\Delta\mathrm{RA}\ U_b(t) + \Delta\mathrm{Dec}\ V_b(t)]\right). \tag{2.9}$$

The telescopes' position $(x_{\mathrm{T_1}}, y_{\mathrm{T_1}}, z_{\mathrm{T_1}})$ and $(x_{\mathrm{T_2}}, y_{\mathrm{T_2}}, z_{\mathrm{T_2}})$ expressed in the pointing direction coordinate system are fixed with respect to the celestial frame, and therefore change with Earth rotation. So the UV coordinates change with time with respect to the target direction ΔRA and ΔDec. Here, the useful astrophysical information is ΔRA and ΔDec, the position of the object on the celestial sphere with respect to the pointing direction. It is the only unknown, and it is encoded in the intensity as a cosine oscillation.

2.1.2 Reveal the interference term

If we consider a monochromatic, mono-axial observation (fixed $\mathbf{k}$), with a fixed baseline, the Eq. 2.9 is sterile. The purpose of an interferometer is to measure the interference term by adding some diversity in the cosine term. For this at least two solutions exist.

OPD scan

Modifying the optical path difference (OPD) is the most obvious solution to reveal the interference pattern. Under its simplest form, it is the Young's two slits experiment (Fig. 2.1). The centeral pixel of the detector is at zero OPD, but, as we move away from the centeral pixel, we induce a path difference d between the two apertures of the interferometer:

$$I_{\mathrm{T_1T_2}}(d) = 2I_0 + 2I_0\ \cos\left(\frac{2\pi}{\lambda}[\Delta\mathrm{RA}\ U_b + \Delta\mathrm{Dec}\ V_b + d]\right). \tag{2.10}$$

For apertures small with respect to the apertures distance (baseline), the interference pattern is directly visible as a cosine modulating the intensity on the detector.

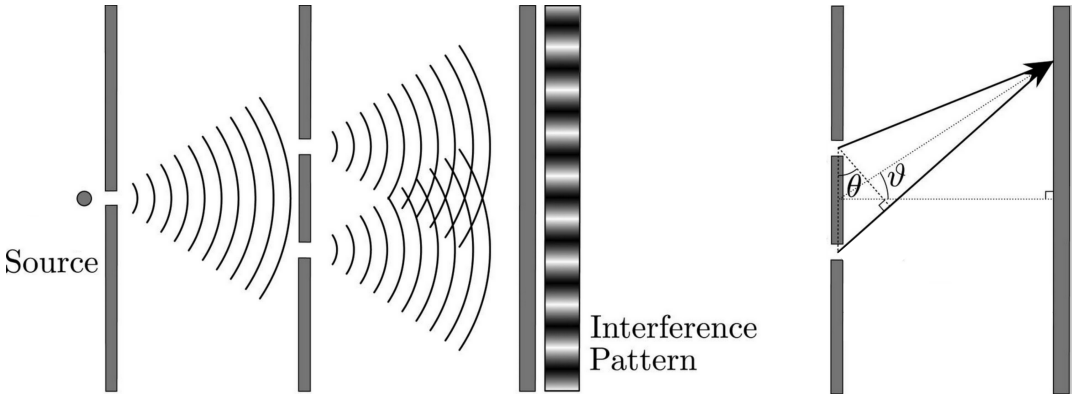

Figure 2.1 – Schematic for the interference pattern on a detector for different angle ϑ. Zero OPD is at $\vartheta = 0$. (From Bopp et al., 2018)

On PIONIER at VLTI (Le Bouquin et al., 2011), the recombination does not occur on the detector itself. The electric field from the individual telescopes is injected in single-mode fibers and

the recombination is performed in integrated optics (Benisty et al., 2009). Because of the single-mode nature of the instrument, the angle on the detector does not correspond to a different observation direction **k**, and so, does not convey any OPD meaning. In order to scan the fringes, an OPD d must be introduced before recombination. In PIONIER, this is performed by independent piezo-controlled mirrors on each incoming beam from individual telescopes. In this case, the detector records the temporal variation of intensity during the OPD scan and reveals the interference term (Fig. 2.2).

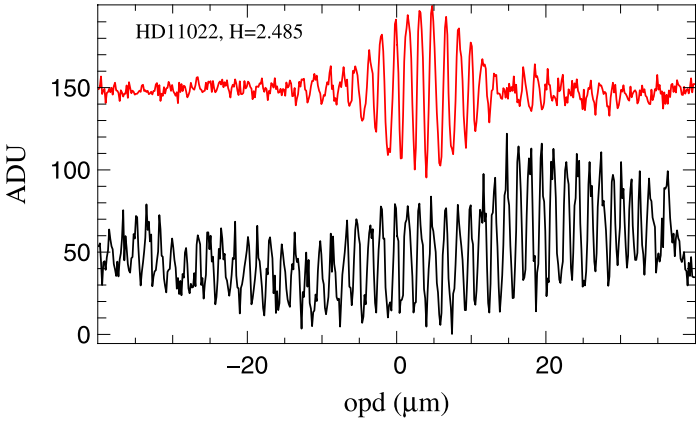

Figure 2.2 – Intensity measured on one baseline on PIONIER at H-band for different OPD. (Red) summing the 7 spectral channels. (black) on a single spectral channel (From Le Bouquin et al., 2011)

In practice, the scan of OPDs is disturbed by the OPD contribution of the Earth atmosphere (see Sect. 2.2.2 on the fringe tracker). Still, one can detect short separation binary stars by closure phase. It consists in adding the phase measured on three baselines forming a closed path to eliminate the atmosphere contribution and retrieve the relative astrometry $(\Delta\mathrm{RA}, \Delta\mathrm{Dec})$ between the two bodies (e.g. Le Bouquin and Absil, 2012; Marion et al., 2014). This technique hardly detects binaries at contrasts less than 10^{-2}, and is therefore not favored for exoplanet observations.

Wavelength dispersion

Like PIONIER, GRAVITY is a single-mode interferometer with recombination by integrated optics (Perraut et al., 2018). However, in GRAVITY the interference pattern is not revealed by a scan in OPD but by dispersion of wavelengths in the K-band:

$$I_{\mathrm{T_1T_2}}(\lambda) = 2I_0 + 2I_0 \cos\left(\frac{2\pi}{\lambda}[\Delta\mathrm{RA}\, U_b + \Delta\mathrm{Dec}\, V_b]\right) \quad \text{with} \quad 1.95\ \mu\mathrm{m} < \lambda < 2.45\ \mu\mathrm{m}. \tag{2.11}$$

As shown by Fig. 2.3, at OPD=0 (ΔRA=ΔDec=0) we are on the white fringe and the intensity does not vary with the wavelength. When we consider non-zero OPD, the intensity starts to modulate with the wavelength.

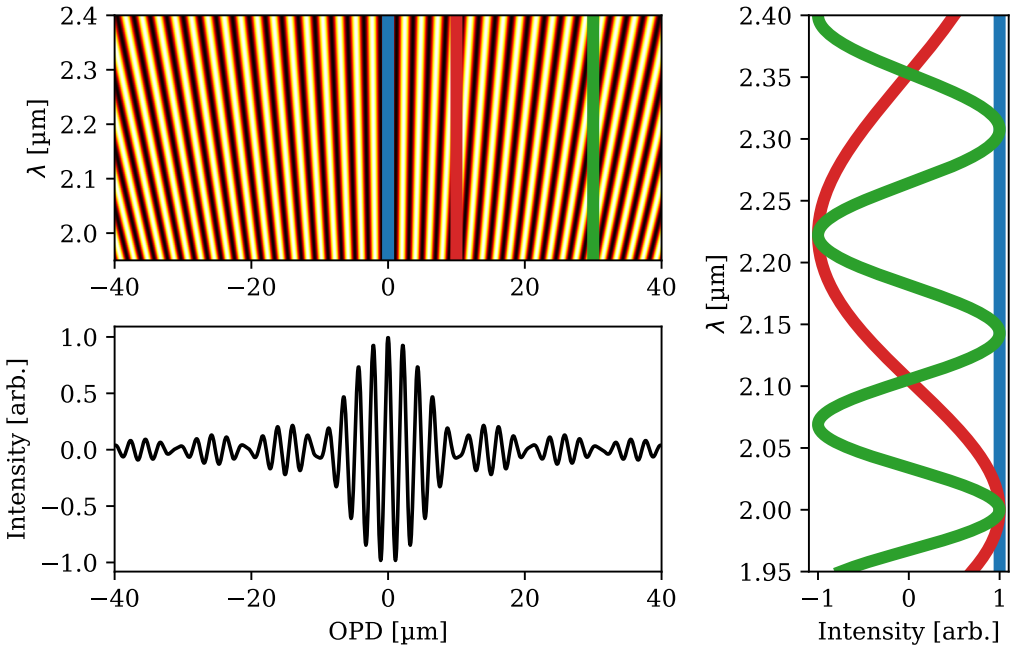

Figure 2.3 – (Top) Interference term intensity dependence with λ. (Bottom) Fringes averaged over the whole K-band. (Right) Interference term intensity at given OPD 0, 10 and 30 µm.

The intensity variations at different wavelengths and at different OPD values are precisely what is recorded by the GRAVITY science camera. The wavelength dispersion of the interference term at only one OPD value is not sufficient to determine the relative astrometry (ΔRA, ΔDec) of the light source. If we consider an object aligned with our unique baseline, the Eq. (2.11) becomes:

$$I_{\mathrm{T_1T_2}}(\lambda) = 2I_0 + 2I_0 \cos\left(\frac{2\pi}{\lambda}\Delta\mathrm{RA}\, U_b\right) \quad \text{with} \quad 1.95\ \mu\mathrm{m} < \lambda < 2.45\ \mu\mathrm{m}. \tag{2.12}$$

Due to the parity of the cosine function, there is a fundamental indetermination on the sign of ΔRA. This provides relative astrometry modulo 180°. To lift this indetermination, an additional technique is required.

2.1.3 Complex visibility in GRAVITY

GRAVITY not only relies on the wavelength dispersion to reveal the interference term, but also uses a technique called ABCD recombination. The ABCD recombination consists in having four separate recombination channels that each introduces a different phase ϕ_A, ϕ_B, ϕ_C and ϕ_D.

Still considering a simple two-telescope interferometer observing the same unresolved source, we

obtain:

$$I_A(\lambda) = 2I_0 + 2I_0 \cos\left(\frac{2\pi}{\lambda}[\Delta\text{RA}\, U_b + \Delta\text{Dec}\, V_b] + \phi_A\right), \tag{2.13}$$

$$I_B(\lambda) = 2I_0 + 2I_0 \cos\left(\frac{2\pi}{\lambda}[\Delta\text{RA}\, U_b + \Delta\text{Dec}\, V_b] + \phi_B\right), \tag{2.14}$$

$$I_C(\lambda) = 2I_0 + 2I_0 \cos\left(\frac{2\pi}{\lambda}[\Delta\text{RA}\, U_b + \Delta\text{Dec}\, V_b] + \phi_C\right), \tag{2.15}$$

$$I_D(\lambda) = 2I_0 + 2I_0 \cos\left(\frac{2\pi}{\lambda}[\Delta\text{RA}\, U_b + \Delta\text{Dec}\, V_b] + \phi_D\right). \tag{2.16}$$

With the phases $\phi_A = 0$, $\phi_B = \frac{\pi}{2}$, $\phi_C = \pi$ and $\phi_D = \frac{3\pi}{2}$ rad, it becomes:

$$I_A(\lambda) = 2I_0 + 2I_0 \cos\left(\frac{2\pi}{\lambda}[\Delta\text{RA}\, U_b + \Delta\text{Dec}\, V_b]\right), \tag{2.17}$$

$$I_B(\lambda) = 2I_0 - 2I_0 \sin\left(\frac{2\pi}{\lambda}[\Delta\text{RA}\, U_b + \Delta\text{Dec}\, V_b]\right), \tag{2.18}$$

$$I_C(\lambda) = 2I_0 - 2I_0 \cos\left(\frac{2\pi}{\lambda}[\Delta\text{RA}\, U_b + \Delta\text{Dec}\, V_b]\right), \tag{2.19}$$

$$I_D(\lambda) = 2I_0 + 2I_0 \sin\left(\frac{2\pi}{\lambda}[\Delta\text{RA}\, U_b + \Delta\text{Dec}\, V_b]\right). \tag{2.20}$$

From these four terms, we can identify:

$$\underline{V}(\lambda) = \frac{I_A - I_C}{2} + i \times \frac{I_D - I_B}{2} = 2I_0 \exp\left(i\left[\frac{2\pi}{\lambda}(\Delta\text{RA}\, U_b + \Delta\text{Dec}\, V_b)\right]\right), \tag{2.21}$$

with $\underline{V}$ the complex visibility. Here and in the following notations, underlined variables indicate complex quantities. This quantity is not degenerate in the (ΔRA,ΔDec) sign, as individual intensities I_A, I_B, I_C and I_D can be. In this respect, the ABCD recombination can be seen as a scanning at four different OPDs to fully constrain the fringes' dispersion shown on Fig. 2.3 (top).

One baseline at a given time t only provides the projection of $(\Delta\text{RA}, \Delta\text{Dec})$ on its orientation (U_b, V_b) but not yet the individual relative astrometry ΔRA and ΔDec. For this, more than two telescopes are needed. At VLTI, we have four UTs (or ATs) that observe simultaneously the same target; they form six baselines of different lengths and different orientations. Moreover, the length and orientation of the baselines projected in the target direction $\mathbf{k}$ changes with time as the Earth rotates with respect to the celestial sphere. The set of all U_b and V_b coordinates probed during the time of the observation forms the UV plane. Each baseline provides complex visibilities $\underline{V}(b, t, \lambda)$, so the relative astrometry ΔRA and ΔDec of the object is fully constrained by the observation.

This is all that is needed to understand the basics of how to observe exoplanets with GRAVITY. As we observe objects that we do not resolve (stars and planets), this simple plane-wave formalism is sufficient and there is no need to introduce the Zernike-Van Cittert general theorem that describes the visibility drop for any intensity distribution on-sky (see Monnier (2003) for a concise description or Thompson et al. (2017) for a complete derivation).

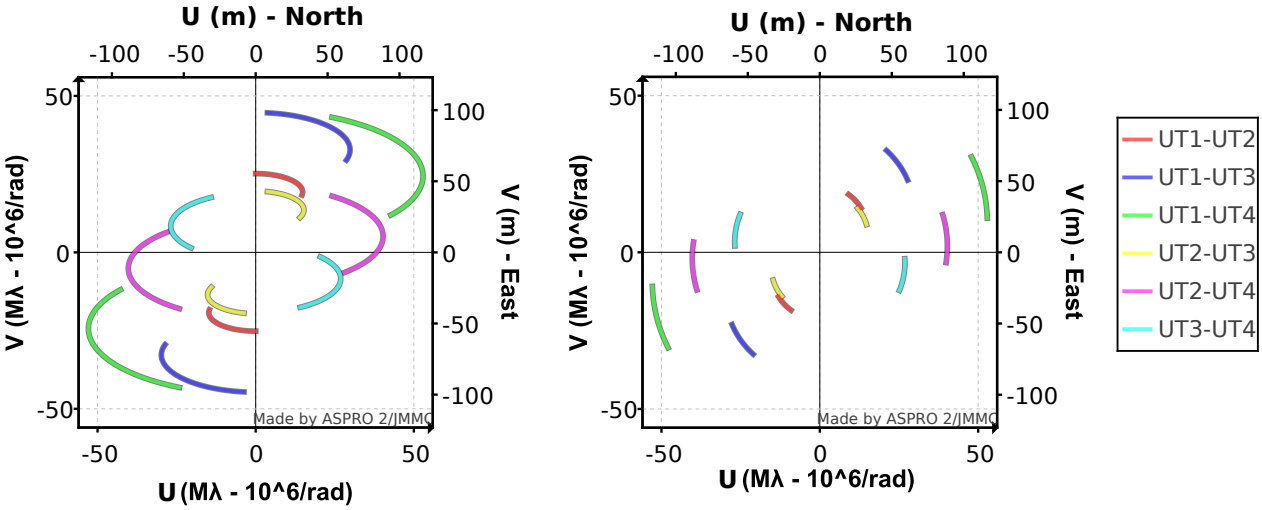

(a) (b)

Figure 2.4 – UV plane examples at VLTI on the UTs. (a) Observing a target for 6.5 hours with elevation from 45 to 89°. (b) Observing a target for 1.5 hours at 45° elevation. UV planes from ASPRO2.

2.2 GRAVITY sub-systems

GRAVITY is a complex instrument. The Eq. (2.21) defining the complex visibilities is in an ideal case, without the Earth atmosphere, and without undesired instrumental OPD contributions. In order to measure the ($\Delta\text{RA}\, U_b + \Delta\text{Dec}\, V_b$) term in real conditions various instrumental subsystems are required (Fig. 2.5 and 2.6).

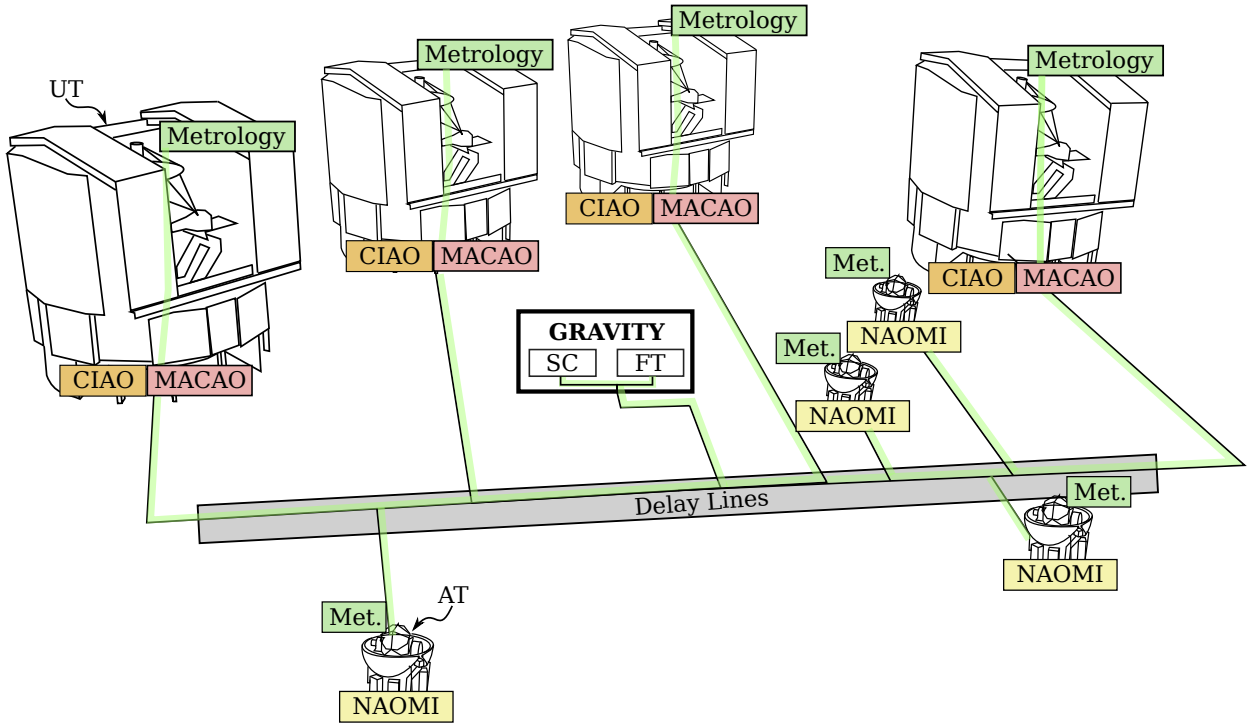

Figure 2.5 – Simplified schematic of GRAVITY at VLTI. Highlighted: the adaptive optics CIAO, MACAO and NAOMI, the metrology sub-system and the delay-lines.

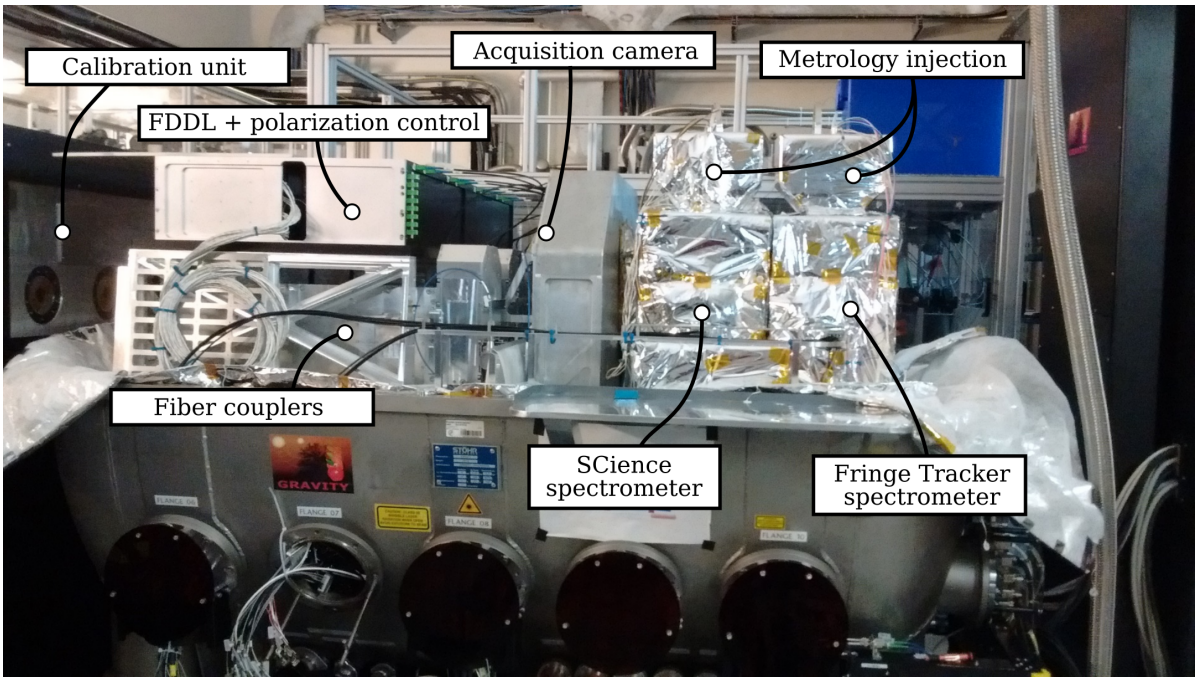

Figure 2.6 – GRAVITY with the cryostat open, in the VLTI lab (photo K. Perraut).

2.2.1 Adaptive optics

Before any interferometric considerations, we must collect the light from the individual telescopes. The telescope's pupil transmission function $A(u, v)$ is:

$$A(u,v) = \begin{cases} 1, & \text{if } u, v \text{ in the UT (or AT) pupil (Fig. 2.7)} \\ 0, & \text{otherwise} \end{cases} \tag{2.22}$$

where u and v are the coordinates in the pupil plane.

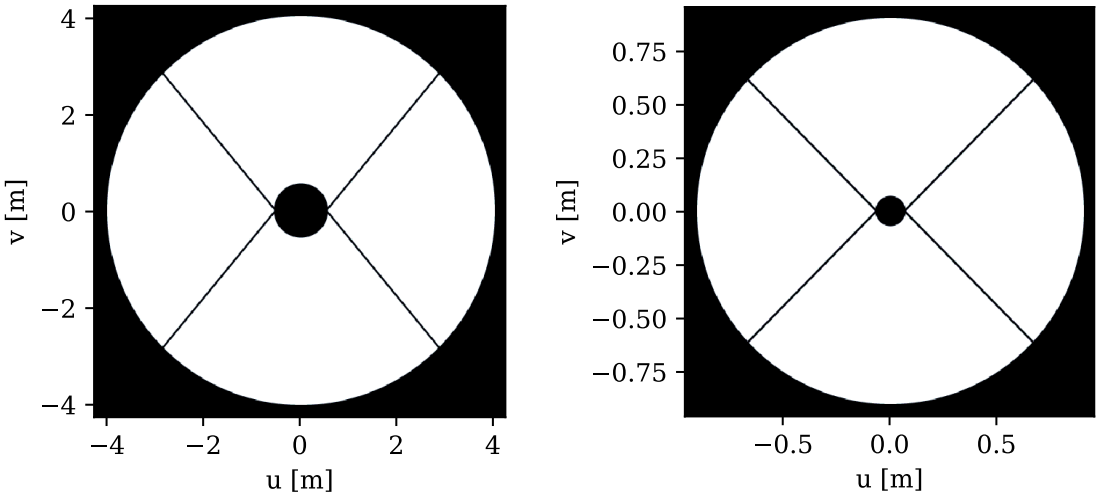

(a) UT pupil (b) AT pupil

Figure 2.7 – Modeled pupil of the VLTI telescopes.

Back to Eq. (2.1) describing a plane-wave arriving at a telescope, I now take into account the pupil A and obtain:

$$\underline{E}(t,u,v) = A(u,v)\ E_0\ \exp\left(i\frac{2\pi}{\lambda}(\mathbf{k}(t)\cdot\mathbf{x})\right)\ \exp(-i\omega t). \tag{2.23}$$

Considering timescales far longer than the light period $2\pi/\omega$, and neglecting the delay term $\mathbf{k}(t)\cdot\mathbf{x}$ that is irrelevant for a single telescope, we simply obtain:

$$E(u,v) = A(u,v)\ E_0. \tag{2.24}$$

In the Fraunhofer diffraction approximation for far fields, the corresponding intensity I_F at the focal plane (x, y) is:

$$I_F(x,y)\ =\ ||\ \mathcal{F}[E_0\ A(u,v)]\ ||^2, \tag{2.25}$$

with $\mathcal{F}$ the Fourier transform. I_F is called the point spread function (PSF) of the telescope. This determines the diffraction limit of the instrument (Fig. 2.8a).

In real ground-based conditions, turbulence in the Earth atmosphere distorts the incoming

wavefront and adds undesired OPD $\Phi_{\rm atm}$ at different points u, v in the pupil:

$$\underline{E}(t,u,v) = A(u,v)\ E_0\ \exp\left(i\frac{2\pi}{\lambda}\Phi_{\rm atm}(t,u,v)\right). \tag{2.26}$$

The temporal and spatial content of $\Phi_{\rm atm}$ is well approximated by the turbulent energy cascade theory of Kolmogorov (Fried, 1965). We usually describe the atmosphere turbulence by its coherence time τ_0, the typical timescale during when the phase of a given point u, v changes by 1 rad, and the Fried parameter r_0, the typical length at a given time where the phase changes by 1 rad. Both τ_0 and r_0 are defined for $\lambda = 500$ nm. At Paranal, the coherence time τ_0 can vary between 1 and 20 ms depending on the weather, and the spatial coherence r_0 can vary between 5 and 30 cm. In the following, I use the seeing at $\lambda = 500$ nm instead of r_0: it is defined as $S_e = 0.98 \times \lambda/r_0$.

The atmosphere OPD, $\Phi_{\rm atm}$, is responsible for degradation of the PSF. In the focal plane, instead of the characteristic pattern of the diffraction limit of Fig. 2.8a, we obtain a PSF that resembles Fig. 2.8b that is more extended and displays satellite blobs structures called "speckles". The Strehl ratio is a metric for the wavefront quality; it is the ratio between the peak intensity in the image and the peak intensity at the diffraction limit. On Fig. 2.8a the Strehl ratio is 100%, on Fig. 2.8b I estimate the Strehl ratio around 30%

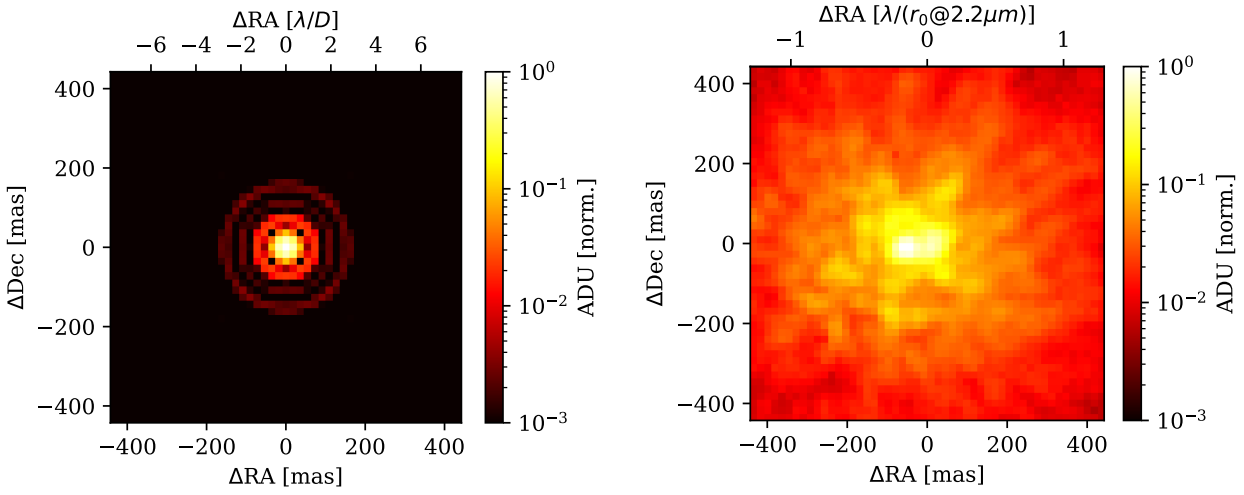

(a) Simulation (b) On-sky

Figure 2.8 – Image of a star in H-band (1.6 µm) on the acquisition camera of GRAVITY. (a) in simulations on a UT pupil with $D = 8$ m and the same pixel scale as the GRAVITY acquisition camera. (b) 0.7 s acquisition on-sky with MACAO on β Pic with an excellent seeing of 0.45 arcsec.

The correction of the atmosphere's impact on the wavefront has motivated the development of adaptive optics for astronomy since the end of the 1980s (Roddier, 1988). Under its most simple form, adaptive optics relies on the real-time measurement of $\Phi_{\rm atm}$ that is applied as a correction on a deformable mirror in a closed control loop. The frequency of the correction loop must be high enough to capture a significant fraction of the turbulence (τ_0=5 ms corresponds to 200 Hz variation of the atmosphere state). Similarly, the adaptive optics better captures the turbulence if it corrects a wide range of aberrations at the pupil plane. The aberrations are generally decomposed on orthogonal bases like the Zernike basis (Zernike, 1934) or the Karhunen–Loève basis (KL, e.g. Roddier et al., 1991). For example, SPHERE (Beuzit et al., 2019) has arguably one of the most advanced adaptive

optics currently in operation (Fusco et al., 2014), it obtains routinely Strehl ratios of 90% in the near-infrared with a loop running at 1380 Hz and correcting close to 1000 KL modes on the UT3 pupil.

At VLTI, the adaptive optics on the UTs are:

- MACAO, Multi Application Curvature Adaptive Optics (Arsenault et al., 2003), that couples a bimorph mirror with a curvature sensor in the visible. It controls 50 modes at 500 Hz.
- CIAO, Coudé Infrared Adaptive Optics (Kendrew et al., 2012), that uses the same bimorph mirror as MACAO but with a Shack-Hartmann wavefront sensor operating in the range $1.4 < \lambda < 2.4$ µm. It also controls 50 modes at 500 Hz.

On the ATs, the adaptive optics are:

- NAOMI, New Adaptive Optics Module for Interferometry (Woillez et al., 2019), the deformable mirror is a reflective surface with magnetic actuators and the wavefront sensor is a Shack-Hartmann in the visible. It controls 14 modes at 500 Hz.

MACAO is the only adaptive optics used for exoplanets' observations with GRAVITY so far.

The progress in adaptive optics have been of paramount importance for the ground-based direct imaging of exoplanets. Although, it is clear from Fig. 2.8b that the MACAO adaptive optics does not correct enough atmosphere turbulence to permit direct observations of exoplanets on a single UT. On GRAVITY, the direct observation of exoplanets is made possible by the interferometric deconvolution technique described in Sect. 2.5. The adaptive optics serves two purposes for optical interferometry: first, it concentrates the light of the astronomical targets to better match the single-mode of the fibers. This way, we have more flux from the science object, that is crucial for observing faint sources as exoplanets. Second, it limits the amount of starlight that leaks in the science fiber when we observe the planet. This starlight is responsible for noise in the visibilities that ultimately set the detection limits of the instrument (see Chapter 3).

2.2.2 Fringe tracker

The Earth atmosphere is not only distorting the images from individual telescopes. It also contribute to an additional OPD term (piston) between telescopes. Back to Eq. (2.21), it becomes:

$$\underline{V}(b,t,\lambda) = 2I_0 \exp\left(i\left[\frac{2\pi}{\lambda}(\Delta\mathrm{RA}\, U_b(t) + \Delta\mathrm{Dec}\, V_b(t) + \Delta\Phi_{\mathrm{atm},\pi}(b,t))\right]\right), \tag{2.27}$$

with $\Delta\Phi_{\mathrm{atm},\pi}(b,t) = \Phi_{\mathrm{atm},\pi,\mathrm{T}_1}(t) - \Phi_{\mathrm{atm},\pi,\mathrm{T}_2}(t)$ the difference of atmospheric piston between the two telescopes forming the baseline b. I mentioned in the previous section that the atmosphere turbulence over Paranal has a spatial coherence length r_0 at most of 30 cm in the visible, so 1.8 m at K-band (scaling in $\lambda^{6/5}$). This is much smaller than the smallest UT baseline (≈30 m). So each telescope is affected by a totally different turbulence outcome that is responsible for a differential delay $\Delta\Phi_{\mathrm{atm},\pi}$ affecting the interferometric complex visibilities. The differential delay between the two telescopes is changing on timescale of the coherence time of the atmosphere, that is around 60 ms in K-band. This is a problem by many aspects.

First, it adds an OPD term that pollutes the astronomical OPD ($\Delta\text{RA}\, U_b + \Delta\text{Dec}\, V_b$) that we want to measure. Second, the atmospheric piston prevents any long integration of the fringes. Integrating for more than the atmosphere coherence time results in the fringes to blur. For this reason, VLTI instruments like VINCI (Kervella et al., 2003) and PIONIER (Le Bouquin et al., 2011) have to make short integrations of the order a few milliseconds to "freeze" the turbulence (Fig. 2.9), which limits the achievable magnitude of these instruments (K=9 mag on VINCI, H=7 mag on PIONIER).

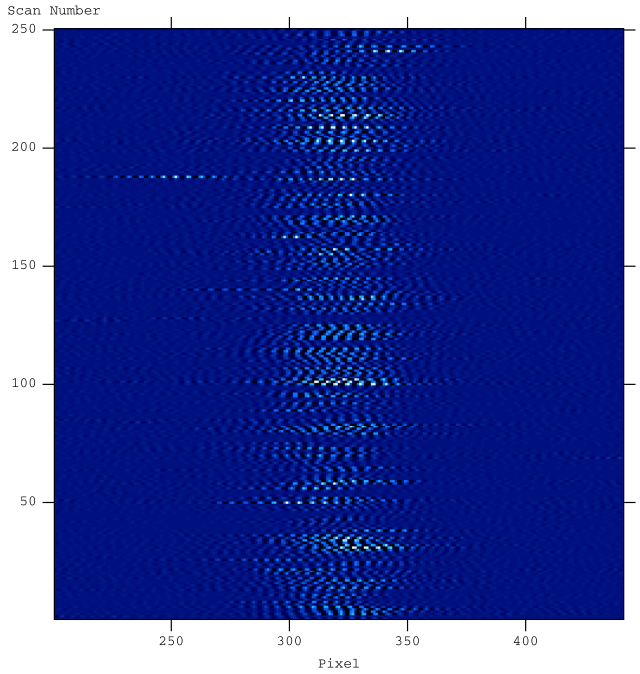

Figure 2.9 – K-band fringes on VINCI at VLTI. VINCI had no fringe tracker, so the fringes are shifted from one exposure to the other by atmospheric pistons (From Glindemann et al., 2003)

The solution adopted for GRAVITY directly follows the adaptive optics philosophy. The fringe tracker (FT, Lacour et al., 2019) is an interferometric arm of the instrument that is fed by single-mode fibers and has its own ABCD combiner (see Sect. 2.1.3). The FT observes a bright target (K<10 mag) and measures the fringes at a rate up to 1 kHz. It sends correction commands to a fast piezo-controlled mirror for each beam that adjusts the piston in real-time to lock the fringes at a given position. The FT is in the GRAVITY cryostat, therefore it is also sensitive to the differential pistons induced by the VLTI vibrations, and it can correct them.

In parallel, since the fringes are locked and the $\Delta\Phi_{\text{atm},\pi}(b,t)$ term is compensated, the science arm (SC) of GRAVITY can integrate on a target with exposures up to 300 s. The science object cannot be picked arbitrary far from the guide star of the fringe tracker. Like in adaptive optics, the distance between the guide star and the science object is limited by the isoplanetic angle (Tallon and Foy, 1990). On GRAVITY+ and in the WIDE mode (see Sect. 2.6), it is recommended not to exceed 30 arcsec between the FT star and the SC target.

Overall, the fringe tracker implementation has been a game changer for optical interferometry, pushing the magnitude limits of science objects down to K=19 mag. Since 2023, the fringe tracker of GRAVITY is used to stabilize the fringes during MATISSE observations (GRA4MAT mode, Lagarde

et al., 2022). This gives access to fainter targets in L ($\lambda = 3.5$ µm) and M-band ($\lambda = 4.7$ µm), and launches another instrument into the direct observations of exoplanets by optical interferometry.

2.2.3 Metrology system and other loops

The FT can be understood as a piston-adaptive optics for interferometry. As any adaptive optics, it is subject to non-common path aberrations (NCPA). At VLTI, non-common path pistons are a major problem that greatly limits the astrometric accuracy. GRAVITY has a metrology system (Lippa et al., 2016) dedicated to measure the non-common path piston between the FT and the SC.

Metrology

As already shown in Eq. (2.27), each telescope is affected by different atmospheric pistons $\Phi_{\mathrm{atm},\pi}$. Again, following a formalism close to Nowak (2019), we can add Φ_{DL}, a delay term that encompasses delay lines tracking and the correction of the atmospheric piston by the actuator of the FT, and $\Phi_{\mathrm{prop,SC}}$ or $\Phi_{\mathrm{prop,FT}}$ the delays induced by the specific propagation in the SC or the FT arm of GRAVITY. This way, the total piston for the SC and FT of Telescope 1 is:

$$\Phi_{\mathrm{SC,T_1}} = \Phi_{\mathrm{atm},\pi,\mathrm{T_1}} + \Phi_{\mathrm{DL,T_1}} + \Phi_{\mathrm{prop,SC,T_1}} \tag{2.28}$$

$$\Phi_{\mathrm{FT,T_1}} = \Phi_{\mathrm{atm},\pi,\mathrm{T_1}} + \Phi_{\mathrm{DL,T_1}} + \Phi_{\mathrm{prop,FT,T_1}}. \tag{2.29}$$

So, the OPD between Telescope 1 and Telescope 2 is:

$$\Delta\Phi_{\mathrm{SC}} = \Phi_{\mathrm{SC,T_2}} - \Phi_{\mathrm{SC,T_1}} = \Delta\Phi_{\mathrm{atm},\pi} + \Delta\Phi_{\mathrm{DL}} + \Delta\Phi_{\mathrm{prop,SC}} \tag{2.30}$$

$$\Delta\Phi_{\mathrm{FT}} = \Phi_{\mathrm{FT,T_2}} - \Phi_{\mathrm{FT,T_1}} = \Delta\Phi_{\mathrm{atm},\pi} + \Delta\Phi_{\mathrm{DL}} + \Delta\Phi_{\mathrm{prop,FT}}. \tag{2.31}$$

The angular separations considered in this work (<0.5 arcsec) are much smaller than the piston atmospheric isoplanetic angle (>10 arcsec). Therefore, we can consider that the SC and FT experience the same propagation in the atmosphere. By principle, the FT keeps $\Delta\Phi_{\mathrm{FT}} = 0$, so:

$$\Delta\Phi_{\mathrm{atm},\pi} + \Delta\Phi_{\mathrm{DL}} = -\Delta\Phi_{\mathrm{prop,FT}}, \tag{2.32}$$

and the OPD for the science arm can be written:

$$\Delta\Phi_{\mathrm{SC}} = \Delta\Phi_{\mathrm{prop,SC}} - \Delta\Phi_{\mathrm{prop,FT}}. \tag{2.33}$$

Back to a telescope by telescope expression, it becomes:

$$\Delta\Phi_{\mathrm{SC}} = \underbrace{\left(\Phi_{\mathrm{prop,SC,T_2}} - \Phi_{\mathrm{prop,FT,T_2}}\right)}_{\text{Telescope 2}} - \underbrace{\left(\Phi_{\mathrm{prop,SC,T_1}} - \Phi_{\mathrm{prop,FT,T_1}}\right)}_{\text{Telescope 1}} \tag{2.34}$$

So, the OPD $\Delta\Phi_{\mathrm{SC}}$ that affects the astrometry can be corrected if we can measure the OPD between the propagation in the FT and in the SC.

In GRAVITY, this measurement is done by the metrology system. It injects a laser in the SC and

FT beam combiners that retro-propagates through the whole GRAVITY and VLTI optical chain to the individual telescopes. On the telescope pupil, it forms fringes whose frequency encodes the OPD ($\Phi_{\mathrm{prop,SC,T_1}} - \Phi_{\mathrm{prop,FT,T_1}}$). On the spiders of each telescope (UT and AT) there are four receiving diodes that measure these fringes and, therefore, properly measure $\Delta\Phi_{\mathrm{SC}}$.

GRAVITY has benefited from the lessons learned in the PRIMA instrument at VLTI (Eisenhauer et al., 2023). Indeed, PRIMA had a metrology system that went from the instrument to the coudé focus of each telescope. It was insufficient to fully probe the non-common path pistons and the accuracy of the instrument was limited to 3 mas instead of the expected 10 to 50 µas (Woillez et al., 2014). The experience acquired during the PRIMA project motivated an extensive work on the error budget for the astrometry at VLTI (Lacour et al., 2014), and concluded that the metrology must measure the full non-common path in the telescope, up to the M1 space, at the very location of the telescope aperture.

Acquisition camera loops

In practice, the metrology system of GRAVITY captures correctly the OPD $\Delta\Phi_{\mathrm{SC}}$ only if the SC and the FT pupils are matching on the diode receivers of the telescopes spiders. If the SC and FT pupils are not matching, the metrology diodes probe different part of the pupil, and any optical aberration (higher than piston) translates into errors in the differential piston measurement. In GRAVITY, there is a pupil tracking system that images four emitting diodes placed at the telescopes spiders and adjusts variable curvature mirrors to prevent any drift.

The pupil diodes are imaged on the acquisition camera of GRAVITY (Anugu et al., 2018). This camera receives the H-band (λ=1.6 µm) photons and serves many purposes (Fig. 2.10). It is not only the sensor for the pupil tracking system, but also the sensor for a field guiding that uses a focal plane image to correct tip-tilt drifts at less than 1 Hz frequency.

Additionally, the acquisition camera has a Shack-Hartmann wavefront sensor per beam that is not (yet) used in operation, and provides an image of the four pupils.

The fringe-tracker, the metrology system, the pupil guiding and the field guiding are necessary subsystems for achieving astrometry measurements at 10 µas accuracy. Altogether, they rigidify the instrument, against most of the jitters and drifts to provide the most stable and unbiased wavefront to the SC.

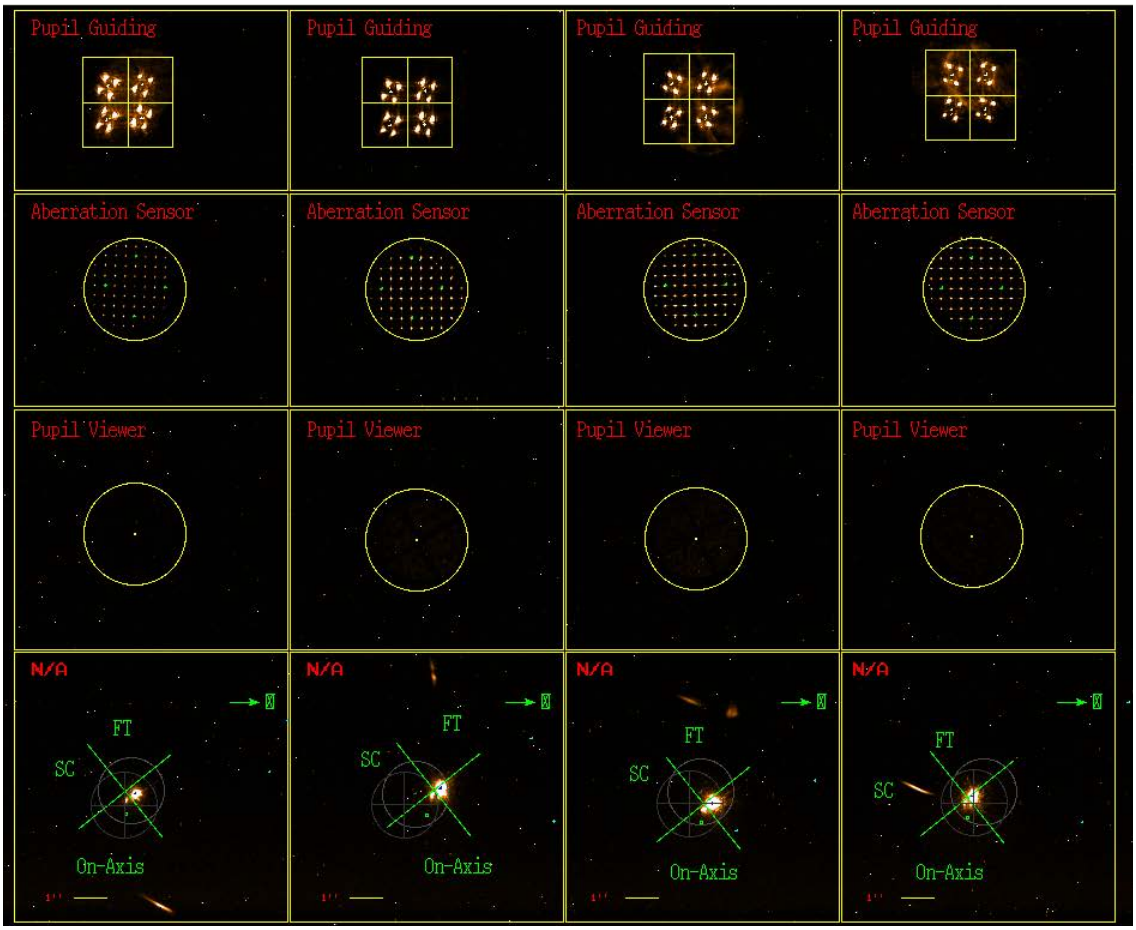

Figure 2.10 – Real-time display of the GRAVITY acquisition camera. Each column corresponds to one telescope. Vertical lines from top to bottom is: pupil beacons, internal Shack-Hartmann wavefront sensor, pupil viewer, and field image (From Anugu, 2016)

2.2.4 Science arm

The science arm of GRAVITY collects the K-band flux from each telescope of the array, recombines the beams with an integrated optics combiner, and then disperses the fringes chromatically on the spectrometer camera[2].

The beam from individual telescopes is injected in a single-mode fiber after an off-axis parabola (Fig. 5.2). The intensity injected in the SC corresponds to the convolution of the Gaussian mode with the electric field at the focal plane. I give more details on the SC fiber injection of GRAVITY at Sect. 5.3. Once the light is injected in the SC fibers, a fine tuning of the OPD is performed by the Fibered Differential Delay Lines (FDDL). This subsystem stretchs the fibers to adjust the pointing of GRAVITY.

The core of GRAVITY is the interferometric recombiner. Building up on the developments in integrated optics for PIONIER (Benisty et al., 2009), GRAVITY recombiner is an integrated ABCD combiner (Perraut et al., 2018) with four inputs (the four telescopes) and 24 outputs (6 baselines ×

[2]The FT arm has a similar design but the chromatic dispersion is only at low spectral resolution (R=23) and the camera is a SAPHIRA detector (Finger et al., 2016a).

4 ABCD). The integrated optics chip is very compact (5 cm long) compared to recombination in bulk optics. This permits to enclose the recombination stage in a cryostatic stable environment.

After the integrated optics, the combined light of each baseline is dispersed by prism or grisms, depending on the spectral resolution. Finally, the flux from the 24 outputs dispersed in wavelength is recorded on the SC camera, a HAWAII-2RG detector (Loose et al., 2003). The integration time ranges from 0.3 to 300 s, and is chosen by the observer to maximize the signal-to-noise ratio (SNR) without saturating the detector.

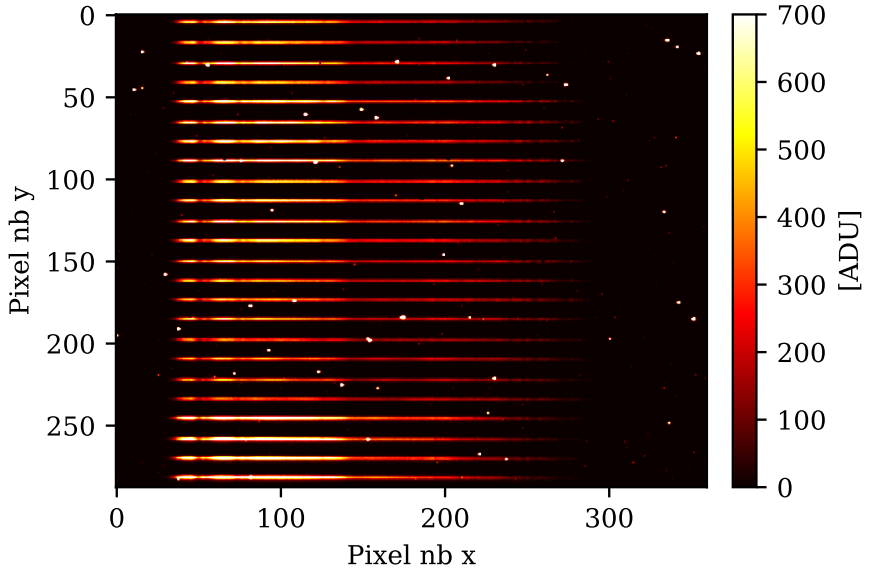

Figure 2.11 – Example of SC camera image during an observation of β Pic b at MEDIUM resolution (R∼500).

2.3 Observation modes

GRAVITY has several observation modes that can be chosen by the observer depending on the object observed and the scientific goal.

2.3.1 Spectral resolution

The instrument has three spectral resolutions available: LOW at R∼20, MEDIUM at R∼500 and HIGH at R∼4000. The LOW resolution mode is used for the observation of stars around the Galactic Center to maximize the SNR. For exoplanet observations, experience from the ExoGRAVITY large programme shows that the LOW resolution is not optimal for the interferometric deconvolution of the star's light and the planet's light. For this reason, we commonly use the MEDIUM resolution that appears to be better for both the detection and the spectral characterization. The HIGH resolution is used only on the brightest exoplanets. To my knowledge, the only satisfactory spectrum obtained with the HIGH resolution is on the bright β Pic b (K=12 mag). The GRAVITY+ upgrade (Sect. 2.6), and especially the new adaptive optics, will improve the transmission and the Strehl. It will certainly enable more HIGH resolution observations of exoplanets in years to come.

2.3.2 Polarization

GRAVITY offers the possibility to separate the two linear polarizations (GRAVITY Collaboration et al., 2024) in a SPLIT observation mode. The polarization separation is done by a Wollaston prism inserted after the prism/grism of the SC and of the FT. For exoplanets observations, we use in general the COMBINED mode, where polarizations are not separated. As planets are detected via their thermal emission, the fraction of polarized light is expected to be null or low. Combining the two polarizations provides more flux in each spectral channel, and thus a better SNR for faint objects like exoplanets.

2.3.3 Field separation

As already mentioned, GRAVITY has two interferometric arms operating in parallel. The light from the VLTI must be split in the instrument in order to feed both SC and FT.

SINGLE

The most simple mode of GRAVITY is the SINGLE field mode. In this configuration, the FT and the SC have the same field of view. In other words, the FT guide star is also the science star. The beams are separated by a 50/50 beamsplitter.

This mode is not used for exoplanets' observations but this is the mode favored for observation of young-stellar objects (e.g. GRAVITY Collaboration et al., 2024b).

DUAL ON-AXIS

One of the major strength of GRAVITY is the possibility to observe a different field of view on the SC and on the FT. This is the DUAL field mode. For separations of less than 600 mas between the FT and the SC field, the split between the two fields is done by the 50/50 beamsplitter and is called DUAL ON-AXIS. Figure 2.12a illustrates how the SC fiber can point to a different location than the FT and observe a science target that is not the FT guide star. This is the mode we use for direct observation of exoplanets and other substellar companions at short separations (e.g. Nowak et al., 2020; Winterhalder et al., 2024).

By design, 50% of the SC target flux is lost in DUAL ON-AXIS mode.

DUAL OFF-AXIS

For more than 300 mas separation between the FT and the SC fields of view, one can split the two beams with a roof-mirror instead of the beamsplitter. This mode is called DUAL OFF-AXIS and is illustrated in Fig. 2.12b. Contrary to the DUAL ON-AXIS, in DUAL OFF-AXIS all the flux from the science target is transmitted to the SC. This is why, this mode is favored for observing exoplanets and brown dwarfs beyond 300 mas (e.g. Blunt et al., 2023).

The beam propagated from one UT has a 2×2 arcsec field of view at the VLTI lab (4×4 arcsec on ATs). It sets the upper separation limit of the DUAL OFF-AXIS mode at 2 arcsec on the UT.

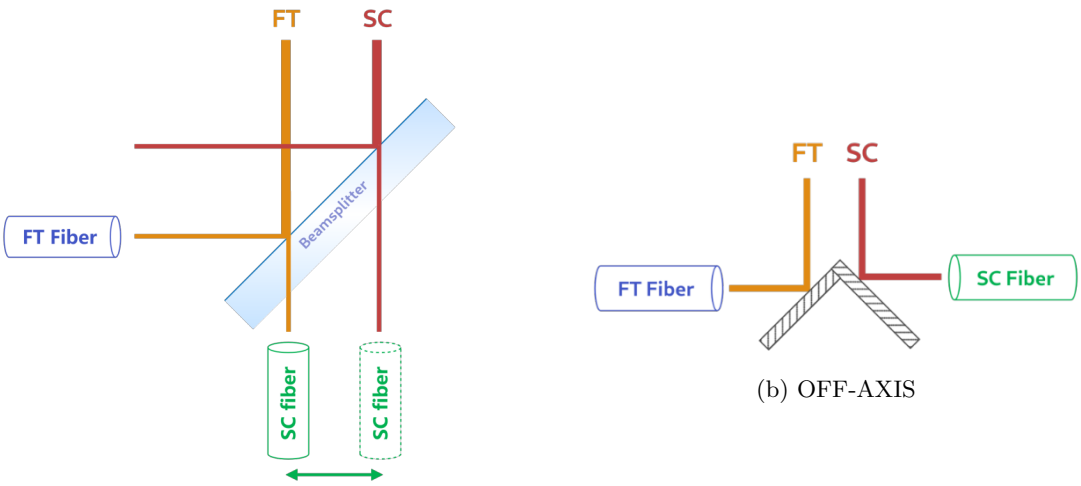

(a) ON-AXIS

(b) OFF-AXIS

Figure 2.12 – Schematic description of the two methods available in GRAVITY for separating the FT and SC. (From Nowak et al., 2024a)

DUAL WIDE

The DUAL WIDE (GRAVITY+ Collaboration et al., 2022) is a new mode developed as part of the GRAVITY+ upgrade (Sect. 2.6) and operational since 2022. In this mode, the star-separator system (STS, Delplancke et al., 2004) at the coudé focus of each telescope propagates two different fields of view of 2×2 arcsec for the UTs (4×4 arcsec on ATs). It now makes possible to have a FT guiding star on one field of view, the SC target on the other, and allows for increasing the distance between the FT and the SC beyond what was possible with the DUAL OFF-AXIS mode.

Being able to pick a guide star for the FT and the adaptive optics at up to 30 arcsec from the SC target has improved the sky coverage of the instrument. It has already permitted important extragalactic observations, for example the observation of the broad line region around a supermassive black-hole at z=2 (Abuter et al., 2024b).

To my knowledge, this mode is not used for exoplanets' observations. Usually, substellar companions remain in the 2 × 2 arcsec of a single field of view around their host-star. Also, in DUAL WIDE mode the metrology link between the FT and the SC is lost as well as the absolute measure of visibilities. It makes it impractical for measurement of relative astrometry between the star and the companion.

Summary

Figure 2.13 summarizes the separation ranges of the different modes. My PhD is focused on exoplanet observations at short separation; below 200 mas. So, in all my work I used only observations in the DUAL ON-AXIS mode.

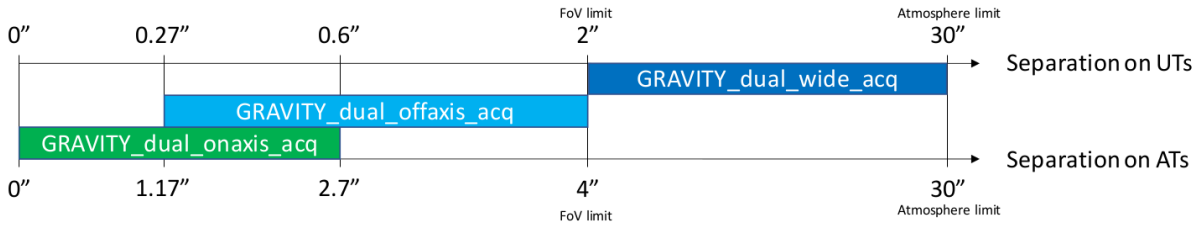

Figure 2.13 – Range of separations accessible on the UTs and the ATs on the different ON-AXIS, OFF-AXIS and WIDE modes (From ESO website)

A description of the GRAVITY hardware that makes possible the ON-AXIS and OFF-AXIS separation of the FT and SC fields is in Pfuhl et al. (2014).

2.4 Observables

GRAVITY provides one observable: the complex visibilities of the science object referenced to the position of the FT object.

P2VM

The pixel-to-visibility-matrix (P2VM) is crucial to obtain the complex visibilities from the SC and the FT camera. The method to obtain the P2VM is close to the AMBER data reduction (Tatulli et al., 2007). As detailed in Lacour et al. (2008), the relationship between the intensities of the ABCD outputs at the different wavelengths and the complex visibilities is linear. Therefore, a single linear operation with the SC images provides the complex visibilities on all the baselines, as well as the total incoming flux for each telescope. This linear operation is performed thanks to the P2VM.

GRAVITY has a calibration unit (Blind et al., 2014), placed at the output of the cryostat (Fig. 2.6). It is used for calibrations and health-checks. The P2VM is computed on the calibration unit before and after each observing night. This way, it is closest to the state of the instrument at the moment of the observation. The visibility-to-pixel-matrix (V2PM) is measured on the internal calibration lamp by sequentially measuring the flux on SC camera with only one incoming beam, and then for the six different baselines. The P2VM is obtained by inversion of the V2PM. The P2VM is simply the generalisation of Eq. (2.21) but for the cases where A, B, C and D outputs are not exactly measured at phases of 0, $\pi/2$, π and $3\pi/2$.

The P2VM is the cornerstone of the GRAVITY pipeline (Lapeyrere et al., 2014) that converts the raw data into `astroreduced.fits` that are used for the science analysis of the observations.

Observation files

An observation is composed of NDIT exposures on the SC assembled in NFILES files. The number of NDIT per files has to be a multiple of four because of a dithering pattern on the detector that repeats every four exposures.

The GRAVITY pipeline provides an `astroreduced.fits` for each NFILES of the observation. It contains nine different tables, the most important for us here are: the `OI_WAVELENGTH` table with the wavelength λ and the error on λ, the `OI_VIS` that contains the complex visibilities at each λ on

the SC and FT and the associated error for each baseline and each NDIT, the `OI_VIS` also contains information on the metrology OPD and the FDDL position; finally, the `OI_FLUX` contains the total flux from individual telescopes at each λ.

Referencing the visibilities

The complex visibilities `VISDATA` in the `OI_VIS` are not referenced. Back to Eq. (2.21), it means that the angles ΔRA and ΔDec do not correspond yet to the relative astrometry with respect to an identified position on sky.

In order to reference the raw visibilities, it is necessary to add a phase term[3]:

$$\phi_p(b,t,\lambda) = PHASE\_REF - PHASE\_MET\_TELFC - \frac{2\pi}{\lambda} OPD\_DISP \tag{2.35}$$

where $PHASE\_REF$ is the phase measured by the fringe tracker, $PHASE\_MET\_TELFC$ the phase measured by the metrology between the fiber couplers and the telescopes, and OPD_DISP the OPD induced by the FDDL.

We obtain the complex visibilities referenced on a point determined by the metrology, $\underline{V}_m(b,t,\lambda)$, by applying:

$$\underline{V}_m(b,t,\lambda) = \texttt{VISDATA} \times e^{i\phi_p}. \tag{2.36}$$

With this correction, we obtain a phase-referenced visibility, therefore static in a celestial reference frame. However, these complex visibilities still contain a static term, possibly very large (mm), coming from the unknown zero-point of the metrology. This unknown offset disappears if we reference the observations with respect to each other. For example, considering one observation $\underline{V}_{1,m}$ on a star and another observation $\underline{V}_{2,m}$ on a companion at a relative astrometry (ΔRA, ΔDec), both referenced at the same metrology point:

$$\underline{V}_{1,m}(b,t,\lambda) = \texttt{VISDATA}_1 \times e^{i\phi_p} \tag{2.37}$$

$$\underline{V}_{2,m}(b,t,\lambda) = \texttt{VISDATA}_2 \times e^{i\phi_p}. \tag{2.38}$$

We can reference $\underline{V}_2$ with respect to the star and obtain $\underline{V}_{2,s}$:

$$\underline{V}_{2,s}(b,t,\lambda) = \underline{V}_{2,m} \times e^{-i\arg(\underline{V}_{1,m})}. \tag{2.39}$$

Now, the phase of $\underline{V}_{2,s}$ is the pure astronomical OPD term ($\Delta\text{RA}\, U_b + \Delta\text{Dec}\, V_b$), and from this we can extract the relative astrometry of the companion with respect to the star (see ExoGRAVITY pipeline Sect. 2.5.2). An example of companion phase referenced to the star is shown in Fig. 2.16b.

By definition, the observation on the star (V_1) referenced to itself is:

$$\underline{V}_{1,s}(b,t,\lambda) = \underline{V}_{1,m} \times e^{-i\arg(\underline{V}_{1,m})}. \tag{2.40}$$

and has a phase equal to zero on all baselines, at all wavelength λ and all time t. Similarly, if we

[3]Detailed at Sect 10.26.1 of the GRAVITY Pipeline user manual.

reference the observation $\underline{V_2}$ with respect to the companion position (relative astrometry), the phase of the companion will be zero at all b, λ and t.

The work with complex visibilities often requires to switch from one referential to another. In this manuscript, I will mostly use visibilities referenced to the star, or referenced to the planet, and occasionally visibilities referenced to the position of the center of the SC fiber or referenced to the speckles. I will refer to it as "referenced to the (star/planet/fiber/speckles)", "phased on the (star/planet/fiber/speckles)", or "in the (star/planet/fiber/speckles) reference frame". All these expressions convey the same meaning of referencing the phase of the complex visibilities with respect to a position on-sky.

2.5 The ExoGRAVITY technique

GRAVITY was not specifically designed for exoplanets' observations. However, it was designed for enabling observation of faint point sources in the K-band. At the beginning of ExoGRAVITY, Sylvestre Lacour and Mathias Nowak developed a specific observation strategy and a dedicated pipeline to turn GRAVITY into a powerful instrument for direct observation of exoplanets.

2.5.1 Observation strategy

Let me first describe the basics of planning and performing exoplanet observations with GRAVITY.

Position the SC fiber

Before the observing night, we must determine the position of the SC on-sky. Due to the injection in single-mode fibers in the SC arm, GRAVITY has a field of view limited to 65 mas on the UT and 290 mas on the AT (full-width at half maximum of the Gaussian mode in intensity). Because of this limitation, we never make an observation without at least a guess on the companion (planet or brown dwarf) position around its host-star. If the companion has already been detected by direct imaging, its relative astrometry is often enough constrained to enable observations with GRAVITY (GRAVITY Collaboration et al., 2020b; Blunt et al., 2023). We keep track of the best up-to-date orbit predictions in `http://whereistheplanet.com/` (Wang et al., 2021a).

For companions that have never been directly imaged, we can rely on trends in the Hipparcos-Gaia proper motion of the host star as well as radial-velocity data if the companion has a semi-major axis smaller than 10 au. This was the case of the first direct detection of HD 206893 c in September 2021 (Hinkley et al., 2023), it took seven pointings at different positions on the UTs to pave the field and finally detect the planet. We were not so lucky with the search for HIP 77718 b or HR 8799 f where we did not detect the companion despite several pointing attempts.

For higher-mass companions like brown-dwarfs, the Gaia DR3 Non-Single Stars catalog (Halbwachs et al., 2023) provides orbits of tentative detections that, given some assumptions on their brightness, are often constrained well enough for the GRAVITY field of view (Winterhalder et al., 2024).

Observation sequence

In every direct observations of exoplanet with GRAVITY, the host star is the FT guide star. The fiber of the FT arm of GRAVITY stays centered on the star during the whole observation. For the SC, the observation sequence is different if we are in DUAL ON-AXIS or OFF-AXIS mode.

During observations in DUAL ON-AXIS mode, we alternate between acquisitions with the SC centered on the star, the SC centered on the expected position of the planet, and the SC away from the star and the planet (SKY). The observation on the star is used as a phase reference (Sect. 2.4) and a spectrum reference (Sect. 2.5.2). For both observations on star and on the planet, the detector integration time (DIT) must be chosen carefully to avoid saturation of the SC camera[4].

A typical observation sequence on the UTs is:

- SC on-star: NDIT={16, 32, 64} and DIT={0.3, 1, 3}s
- SC on-SKY: NDIT={16, 32, 64} and DIT={0.3, 1, 3}s
- SC on-planet: NDIT={8, 12, 32} and DIT={10, 30, 100}s
- SC on-SKY: NDIT={8, 12, 32} and DIT={10, 30, 100}s
- SC on-planet: ··· ···
- SC on-planet: ··· ···
- SC on-planet: ··· ···
- SC on-star: NDIT={16, 32, 64} and DIT={0.3, 1, 3}s

This sequence is repeated for the duration of the observation. Without the overheads, 20 min total integration time on planet(NFILES×NDIT×DIT) can be enough for obtaining the relative astrometry of a bright companion (K<15). For obtaining companion's spectra at high-SNR, the total integration time of the observation can be of the order of 2 or 3 hours.

In OFF-AXIS mode, the calibration of the metrology zero-point by observing the FT object is impossible. Instead a "swap" is executed where the FT is fed by the science object and the SC is fed by the tracking object. Such a swap is obviously impossible for exoplanets, which are too faint for fringe tracking; so the observation sequence must include a "swap" on a known calibrator (Nowak et al., 2024a). I did not use this mode during my PhD, all the observations I worked on were at short separations with the DUAL ON-AXIS mode.

2.5.2 Pipeline

The reduction of the raw observation data is done by the GRAVITY pipeline (Lapeyrere et al., 2014). It provide the `astroreduced.fits` files already described in Sect. 2.4.

The relative astrometry and the spectra of exoplanets are obtained with a second reduction stage, the ExoGRAVITY pipeline. This section is a summary of the ExoGRAVITY pipeline description in Nowak (2019) and GRAVITY Collaboration et al. (2020b). This pipeline was developed at least two years before my PhD. However, I wish to give some details of the underlying mathematics that will be necessary to understand the modification I propose at the end of Chapter 4 (Sect. 4.6.4).

The total process for ExoGRAVITY reduction is illustrated in Fig. 2.14. The `astroreduced.fits` of both observations on-star and on-planet are used in the script `astrometry_reduce.py` to obtain

[4]GRAVITY template manual, Fig. 2 and 3

the relative astrometry of the planet with respect to its star. This relative astrometry is used in a second script, `spectrum_reduce.py`, that measures the planet-to-star contrast spectrum.

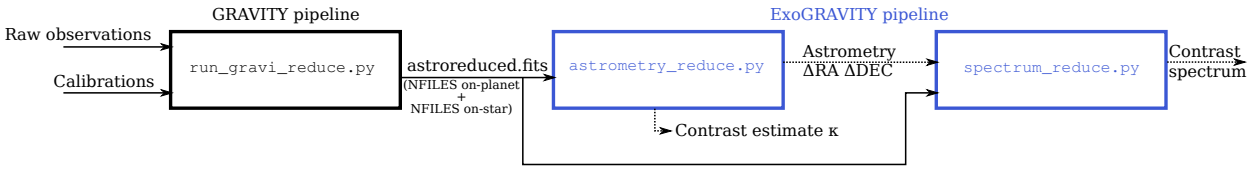

Figure 2.14 – Block diagram for the reduction process of exoplanet observations with GRAVITY

Preamble

Following a formalism close to Pourré et al. (2024), the total flux injected in the SC fiber when we observe the planet is:

$$F_{\text{onplanet}}(m,t,\lambda) = F_*(\lambda)T(m,\boldsymbol{\Delta\alpha},t,\lambda) + F_p(\lambda)T(m,\mathbf{0},t,\lambda) \tag{2.41}$$

with m the telescope, $\boldsymbol{\Delta\alpha} = (\Delta\text{RA}, \Delta\text{Dec})$ the relative astrometry, F_* and F_p respectively the true star and planet flux (unaffected by the instrument nor the atmosphere), and T a transmission term containing the atmosphere and the instrumental transmission. It also includes the loss due to the Gaussian field of view of the SC. Therefore, $T(m,\boldsymbol{\Delta\alpha},t,\lambda)$ is the transmission of an object at an angular distance $\boldsymbol{\Delta\alpha}$ from the SC fiber center, and $T(m,\mathbf{0},t,\lambda)$ is the transmission of an object located directly under the SC fiber. The total flux is not the observable of interest in GRAVITY; however, the star flux injected in the fiber at the planet position is responsible for photon noise and systematic noise in the complex visibilities.

A fraction of the total flux is coherent between two telescopes and contributes to the complex visibilities observed with the SC on planet:

$$\underline{V}_{\text{onplanet}}(b,t,\lambda) = \underbrace{\underline{V}_*(b,t,\lambda)G(b,\boldsymbol{\Delta\alpha},t,\lambda)}_{\text{speckle}} + \underbrace{\underline{V}_p(b,t,\lambda)G(b,\mathbf{0},t,\lambda)}_{\text{planet}} \tag{2.42}$$

with $\underline{V}_*$ and $\underline{V}_p$ respectively the true complex visibilities for the star and the planet, and G an interferometric transmission term. Like T, G includes transmission losses from the Earth atmosphere, the instrument and the distance $\boldsymbol{\Delta\alpha}$ from the center of the Gaussian field of view. The Equation (2.42) shows clearly the term V_p that we want to measure, and the undesired speckle term.

Like any deconvolution technique for direct imaging, the aim of the ExoGRAVITY pipeline is to disantangle the speckle from the planet signal and provide an estimation of V_p. If we consider the complex visibilities referenced to the star, the planet complex visibility is:

$$\underline{V}_p(b,t,\lambda) = S_p(\lambda)\exp\left(i\frac{2\pi}{\lambda}\left[\boldsymbol{\Delta\alpha}\,\mathbf{U}(t)\right]\right) \tag{2.43}$$

with S_p the planet's spectrum and $\mathbf{U} = (U_b, V_b)$ the UV plane coordinates. Moreover, in the

ExoGRAVITY pipeline, the speckle term is modeled with:

$$\underline{V}_*(b,t,\lambda)G(b,\boldsymbol{\Delta\alpha},t,\lambda) = \underline{P}(b,t,\lambda)\underline{V}_{\text{onstar}}(b,t,\lambda), \tag{2.44}$$

where $\underline{P}$ is a complex polynomial and $\underline{V}_{\text{onstar}}$ is the complex visibility measured when the SC fibers are centered on the star. $\underline{V}_{\text{onstar}}$ can be written:

$$\underline{V}_{\text{onstar}}(b,t,\lambda) = J(b,t,\lambda)G(b,\mathbf{0},t,\lambda)S_*(\lambda), \tag{2.45}$$

where S_* is the star's spectrum and J is a function accounting for the drop of star's visibilities if the star is resolved by the interferometer. The resolution limit in the K-band on the longest baselines B of VLTI is:

$$\theta = \frac{\lambda}{2B} = \frac{2.2\times10^{-6}}{2\times130} = 8.5\times10^{-9}\text{ rad} = 1.7\text{ mas}. \tag{2.46}$$

The star observed during the ExoGRAVITY large program with the highest apparent angular diameter is β Pic with θ_d =0.9 mas. In the following, I will consider that the objects are not resolved and take $J = 1$.

Introducing the contrast spectrum:

$$C(\lambda) = \frac{S_p}{S_*}, \tag{2.47}$$

we can rewrite Eq. (2.42):

$$\underline{V}_{\text{onplanet}}(b,t,\lambda) = \underline{P}(b,t,\lambda)\underline{V}_{\text{onstar}}(b,t,\lambda) + C(\lambda)\underline{V}_{\text{onstar}}(b,t,\lambda)\exp\left(i\frac{2\pi}{\lambda}\left[\boldsymbol{\Delta\alpha}\,\mathbf{U}(t)\right]\right). \tag{2.48}$$

This equation holds under three assumptions:

- the host star is not resolved by the interferometer,
- the modulation of $\underline{V}_{\text{onstar}}$ by the polynomial $\underline{P}$ is a good model for the coherent flux $\underline{V}_*$ effectively injected in the SC at the planet position,
- the transmission G (including the Earth atmosphere transmission and the instrumental transmission) has not changed significantly between the on-planet observation and the on-star observation.

Experience have shown that a 4^{th} or 6^{th} degree polynomials are enough for $\underline{P}$ to effectively model the speckle term. In the following, we take for $\underline{V}_{\text{onstar}}$ the average of the visibilities in the two FILES observed on-star directly before and directly after the acquisition on-planet considered.

Equation (2.48) is what we want to solve with the ExoGRAVITY pipeline. The script `astrometry_reduce` recovers $\boldsymbol{\Delta\alpha}$ and the script `spectrum_reduce` recovers $C(\lambda)$.

Astrometry fit

As shown by Eq. (2.48), there are two unknowns, the contrast spectrum and the planet relative astrometry. It means that we must make an assumption on the contrast spectrum in order to

obtain the astrometry. Either we already know the contrast spectrum of the planet from previous observations, or we make the assumption of a flat contrast spectrum. Experience shows that the shape of the contrast spectrum has only a small impact on the astrometry fit, so in almost all cases we make the flat contrast assumption in `astrometry_reduce`.

Following notations close to Nowak (2019), we can express Eq. (2.48) in matrix form for a given baseline b and time t, it becomes:

$$\underline{\mathbf{V}}_{b,t,\text{onplanet}} = \underbrace{\sum_{k=0}^{k_{\max}} \underline{a}_k \mathbf{\Lambda}^k \, \underline{\mathbf{V}}_{b,t,\text{onstar}}}_{\text{speckles}} + \underbrace{\kappa \underline{\mathbb{V}}_{b,t,\text{onstar}} \underline{\mathbf{\Theta}}_{b,t}}_{\text{planet}} \tag{2.49}$$

where:

- $\underline{\mathbf{V}}_{b,t,\text{onplanet}}$ and $\underline{\mathbf{V}}_{b,t,\text{onstar}}$ are vectors of length (n_λ), with n_λ the number of spectral channels ($n_\lambda = 233$ in MEDIUM resolution),
- $\underline{\mathbb{V}}_{\text{onstar}}$ is a $(n_\lambda \times n_\lambda)$ matrix, with $\underline{\mathbf{V}}_{b,t,\text{onstar}}$ on the diagonal and zero everywhere else,
- $\sum_{k=0}^{k_{\max}} \underline{a}_k \mathbf{\Lambda}^k$ is the complex polynomial $\underline{P}$ of order $k_{\max}$ with coefficients $\underline{a}_k$. $\mathbf{\Lambda}$ is a $(n_\lambda \times n_\lambda)$ matrix with wavelengths λ on the diagonal and zero everywhere else,
- κ is the scalar contrast value for the flat contrast,
- $\underline{\mathbf{\Theta}}_{b,t}$ is the exponential term of Eq. (2.48) depending on the UV plane and the relative astrometry of the planet, it is a complex vector of length (n_λ).

In linear algebra language, Eq. (2.49) shows that the visibilities observed with the SC on the planet exist in two subspaces: one in the speckle's subspace formed by the observation on-star modulated by a polynomial in λ that takes different values for each b and t, the other is the planet subspace formed by the visibilities that have the same instrumental and telluric transmission as $\underline{\mathbf{V}}_{b,t,\text{onstar}}$ (G in Eq. (2.45)) but with the phase $\underline{\mathbf{\Theta}}_{b,t}$ of the planet. This last term contains the relative astrometry that we want to measure, but it is in a complex exponential that is not compatible with a linear fit. We fix this problem with the most straightforward solution: a brute force grid exploration of all possible separations. Once we fixed a position $\mathbf{\Delta\alpha} = (\Delta\text{RA}, \Delta\text{Dec})$, the rest of the fit is linear and provides a χ^2 value quantifying the accordance of the fixed relative astrometry with the data. At the end, we obtain a χ^2 grid were we can find the astrometry that best fits the visibilities (see Fig. 2.15).

I will detail here how we perform the linear fit for a given relative astrometry $\mathbf{\Delta\alpha}$. If the speckles' subspace and the planet's subspace are identical, there is no hope to disentangle the planet from the speckles' visibilities. However, we have good reason to believe that the two subspaces are different. The main reason is that the planet can have a phase that modulates on spectral frequencies greater than frequencies accessible by a 4^{th} or 6^{th} order polynomial[5]. Also, expressed in the star's reference frame, the planet visibilities follow the temporal variation of the UV plane due to sky rotation. In the star's reference frame, the speckles are not affected by the UV plane, so this diversity further helps to disentangle the planet's signal from the speckle's signal. In this sense, it is very close to the

[5]I will show in Sect 3.5.1 that the inner working-angle of ExoGRAVITY is reached when this frequency dichotomy ceases to hold.

angular differential imaging technique used for direct imaging of exoplanets on single telescopes.

From the speckles' term, we can compute $\underline{\mathbf{P}}^{\perp}_{b,t}$ the projector matrix orthogonal to the speckle's subspace. By definition:

$$\underline{\mathbf{P}}^{\perp}_{b,t} \left(\sum_{k=0}^{k_{\max}} \underline{a}_k \mathbf{\Lambda}^k \, \underline{\mathbf{V}}_{b,t,\text{onstar}} \right) = 0, \tag{2.50}$$

so, when we apply $\underline{\mathbf{P}}^{\perp}_{b,t}$ to Eq. 2.49 we obtain:

$$\underline{\mathbf{P}}^{\perp}_{b,t} \underline{\mathbf{V}}_{b,t,\text{onplanet}} = \kappa \underline{\mathbf{P}}^{\perp}_{b,t} \underline{\mathbb{V}}_{b,t,\text{onstar}} \underline{\mathbf{\Theta}}_{b,t} \tag{2.51}$$

The Eq. (2.51) seems easier to solve than Eq. (2.49), but, since the projection matrix for a given b and t is necessarily of order less than n_λ, Eq. (2.51) is not invertible. This is why we use a decomposition of $\underline{\mathbf{P}}^{\perp}_{b,t}$:

$$\underline{\mathbf{H}}_{b,t} \, \underline{\mathbf{P}}^{\perp}_{b,t} \underline{\mathbf{H}}^{\dagger}_{b,t} = \underline{\mathbf{D}}_{b,t} \tag{2.52}$$

where $\underline{\mathbf{H}}_{b,t}$ is an Hermitian matrix and $\underline{\mathbf{H}}^{\dagger}_{b,t}$ its complex transpose, $\underline{\mathbf{D}}_{b,t}$ is the diagonal expression of $\underline{\mathbf{P}}^{\perp}_{b,t}$ in the basis defined by $\underline{\mathbf{H}}_{b,t}$. From Eq. (2.52) we can identify:

$$\underline{\mathbf{H}}_{b,t} \, \underline{\mathbf{P}}^{\perp}_{b,t} = \underline{\mathbf{D}}_{b,t} \, \underline{\mathbf{H}}_{b,t}, \tag{2.53}$$

so Eq. (2.51) can be written:

$$\underline{\mathbf{D}}_{b,t} \, \underline{\mathbf{H}}_{b,t} \, \underline{\mathbf{V}}_{b,t,\text{onplanet}} = \kappa \underline{\mathbf{D}}_{b,t} \, \underline{\mathbf{H}}_{b,t} \, \underline{\mathbb{V}}_{b,t,\text{onstar}} \underline{\mathbf{\Theta}}_{b,t}. \tag{2.54}$$

Because $\underline{\mathbf{P}}^{\perp}_{b,t}$ was an orthogonal projector, the matrix $\underline{\mathbf{D}}_{b,t}$ is diagonal with values $(1, \cdots, 1, 0, \cdots, 0)$. So we can identify blocks in $\underline{\mathbf{D}}_{b,t}$ and $\underline{\mathbf{H}}_{b,t}$ such that:

$$\underline{\mathbf{D}}_{b,t} = \begin{pmatrix} \mathbf{I}_d & 0 \\ 0 & 0 \end{pmatrix} \tag{2.55}$$

$$\underline{\mathbf{H}}_{b,t} = \begin{pmatrix} \underline{\mathbf{H}}_{b,t11} & \underline{\mathbf{H}}_{b,t12} \\ \underline{\mathbf{H}}_{b,t21} & \underline{\mathbf{H}}_{b,t22} \end{pmatrix}. \tag{2.56}$$

Equation (2.54) becomes:

$$\begin{pmatrix} \underline{\mathbf{H}}_{b,t11} & \underline{\mathbf{H}}_{b,t12} \end{pmatrix} \underline{\mathbf{V}}_{b,t,\text{onplanet}} = \kappa \begin{pmatrix} \underline{\mathbf{H}}_{b,t11} & \underline{\mathbf{H}}_{b,t12} \end{pmatrix} \underline{\mathbb{V}}_{b,t,\text{onstar}} \underline{\mathbf{\Theta}}_{b,t}. \tag{2.57}$$

We can express the last equation under the form:

$$\underline{\mathbf{Q}}_{b,t} = \kappa \underline{\mathbf{R}}_{b,t} \tag{2.58}$$

with,

$$\underline{\mathbf{Q}}_{b,t} = \left(\underline{\mathbf{H}}_{b,t11} \quad \underline{\mathbf{H}}_{b,t12}\right) \underline{\mathbf{V}}_{b,t,\text{onplanet}}, \tag{2.59}$$

that is a vector of length equal to the rank r of $\underline{\mathbf{H}}_{b,t}$. For example, for a 4^{th} order polynomial the number of polynomial parameters is 4+1, and the rank of $\underline{\mathbf{H}}_{b,t}$ is $r = n_\lambda - 5$, so $r = 228$ in MEDIUM resolution. The right hand term of the equation is:

$$\underline{\mathbf{R}}_{b,t} = \left(\underline{\mathbf{H}}_{b,t11} \quad \underline{\mathbf{H}}_{b,t12}\right) \underline{\mathbb{V}}_{b,t,\text{onstar}} \underline{\mathbf{\Theta}}_{b,t} \tag{2.60}$$

that is a vector also of length r.

We have to keep in mind that the Eq. (2.58) is very incomplete, it is for only one baseline and time. Due to the projection perpendicular to the speckles' subspace, a part of the planet signal may have been lost and cannot be recovered from this equation alone. To recover all the planet's information, we must use all the diversity we have between the speckles' subspace and the planet's subspace, that means, taking into account the full set of visibilities on all b and for all exposures. By doing so, we expect that the planet signal can be fully disentangled from the speckles.

I do not detail here the calculations necessary for propagating the errors along the astrometry fit procedure. It is all described in Nowak (2019) at Sect. 12.5. But, in the maximum likelihood formalism detailed at Eq. (B.46) of Nowak (2019), the astrometry dependent part of χ^2 for the fit on all b and t can obtained by:

$$\chi^2 = -\left[\sum_{b,t} \underline{\mathbf{R}}^\dagger_{2,b,t} \, \underline{\mathbf{W}}^{-1}_{2,b,t} \underline{\mathbf{Q}}_{2,b,t}\right]^2 \left(\sum_{b,t} \underline{\mathbf{R}}^\dagger_{2,b,t} \, \underline{\mathbf{W}}^{-1}_{2,b,t} \underline{\mathbf{R}}_{2,b,t}\right)^{-1} \tag{2.61}$$

and the contrast κ is estimated by:

$$\kappa = \left(\sum_{b,t} \underline{\mathbf{R}}^\dagger_{2,b,t} \, \underline{\mathbf{W}}^{-1}_{2,b,t} \underline{\mathbf{Q}}_{2,b,t}\right) \left(\sum_{b,t} \underline{\mathbf{R}}^\dagger_{2,b,t} \, \underline{\mathbf{W}}^{-1}_{2,b,t} \underline{\mathbf{R}}_{2,b,t}\right)^{-1}, \tag{2.62}$$

where $\underline{\mathbf{R}}_2$ and $\underline{\mathbf{Q}}_2$ are vectors of length $2r$ such that:

$$\underline{\mathbf{R}}_2 = \begin{pmatrix} \underline{\mathbf{R}} \\ \underline{\mathbf{R}}^* \end{pmatrix} \qquad \underline{\mathbf{Q}}_2 = \begin{pmatrix} \underline{\mathbf{Q}} \\ \underline{\mathbf{Q}}^* \end{pmatrix} \tag{2.63}$$

The matrix $\underline{\mathbf{W}}_2$ is an expression of the error covariance described at Eq. (12.60) of (Nowak, 2019).

Now that we have a linear fit that provides a χ^2 for each given position ΔRA, ΔDec of the planet, we can try different positions and search for the one that provides the best fit (minimal χ^2).

Astrometry outputs

The `astrometry_reduce` script produces the result of the astrometry fit in $(\Delta\text{RA}, \Delta\text{Dec})$ maps. Each position on the map is assigned a periodogram power p_w corresponding to:

$$p_w(\Delta\text{RA}, \Delta\text{Dec}) = \chi^2_0 - \chi^2(\Delta\text{RA}, \Delta\text{Dec}), \tag{2.64}$$

where χ^2_0 is the χ^2 obtained under the null hypothesis, i.e., that there is no planet signal in the data. The peak periodogram power p_w on the map indicates the position where the planet has been detected. Assuming Gaussian noise, this peak power scales with the square of the SNR, so, a high periodogram power p_w is an indicator for a strong planet signal in the data correctly fitted by the reduction script.

Figure 2.15 shows examples of periodogram maps. A periodogram map is obtained for each NFILES of the observation, and finally summed to form the combined periodogram map. The best astrometric fit is extracted from the combined periodogram map and the error on the astrometry is estimated from the dispersion of the peak periodogram power position in the periodogram maps of individual NFILES. The combined periodogram map is statistically equivalent to a fit on all NFILES, thus taking full account of the diversity brought by the sky rotation. We can notice that the peak periodogram power is always surrounded by bright side lobes. This corresponds to the "dirty beam" of the VLTI, in other words, the PSF of the instrument given the UV plane orientation. To assess the robustness of a detection, one can also examine the periodogram from the fit of the separate NFILES. If they all point to the same best fit spot (as on Fig. 2.15), the detection is robust. It is also common to check if the fit from the different baselines agree to the same solution. However, this file-by-file analysis is possible only for targets bright enough to be detected on individual NFILES. For the faintest targets, or targets far from the SC fiber field-of-view, the combined periodogram map is the only source of information.

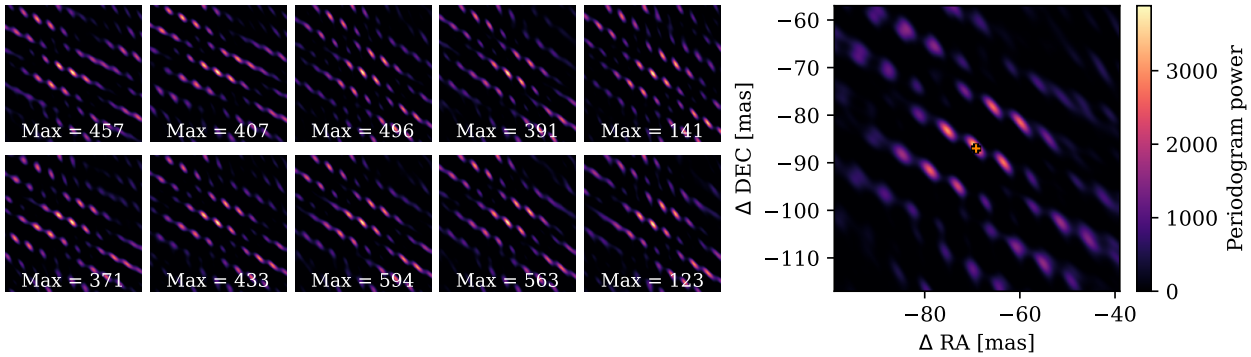

Figure 2.15 – Periodogram maps from an observation on HD 206893 c the 2021-10-16. (left) periodogram map for each of the 10 NFILES composing the observation. The white numbers correspond to the peak periodogram power of the maps. (right) combined periodogram map corresponding of the sum of the 10 individual periodogram maps. The orange cross shows the fiber position during the observation.

To understand better the data behind the astrometry fit, we can look at the best planet fit and speckle fit. Figure 2.16 shows the speckle and the planet fit of complex visibilities for the same observation as the periodograms of Fig. 2.15. It contains the real and imaginary part of the fits for all 6 baselines and all NDITs. In this example, the speckle fit captures most of the observed

complex visibilities ($\underline{\mathbf{V}}_{\text{onplanet}}$), if the visibilities data and the speckle fit were side-by-side, we could not easily tell the difference. However, a small part of the visibilities (here $\sim$1%) is not captured by the speckle fit, this signal is captured by the planet fit. Due to the sky rotation, we can notice that the frequency of planet spectral oscillations drifts with time and this is well captured by the pipeline. Appendix A.2 shows another example of how the polynomial modulation fit the speckle and can reveal the exoplanet's visibilities.

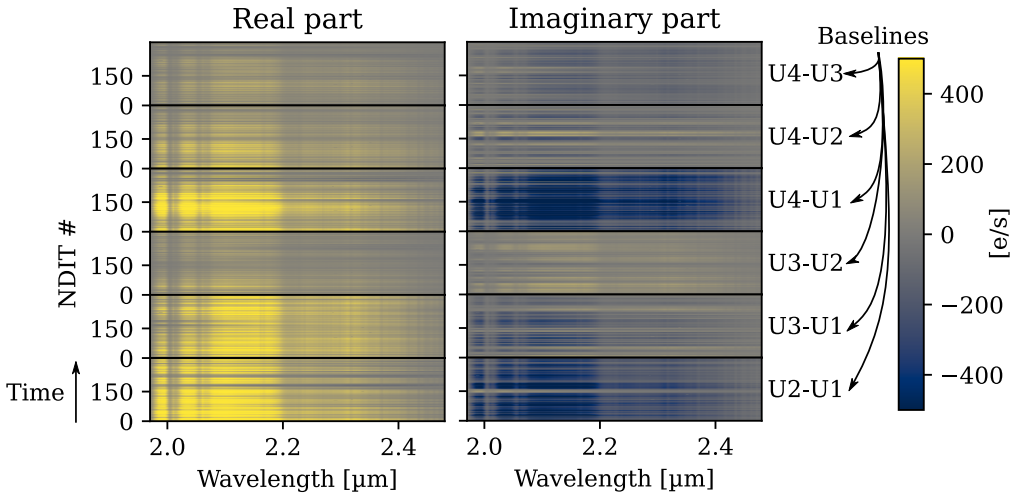

(a) Speckle fit

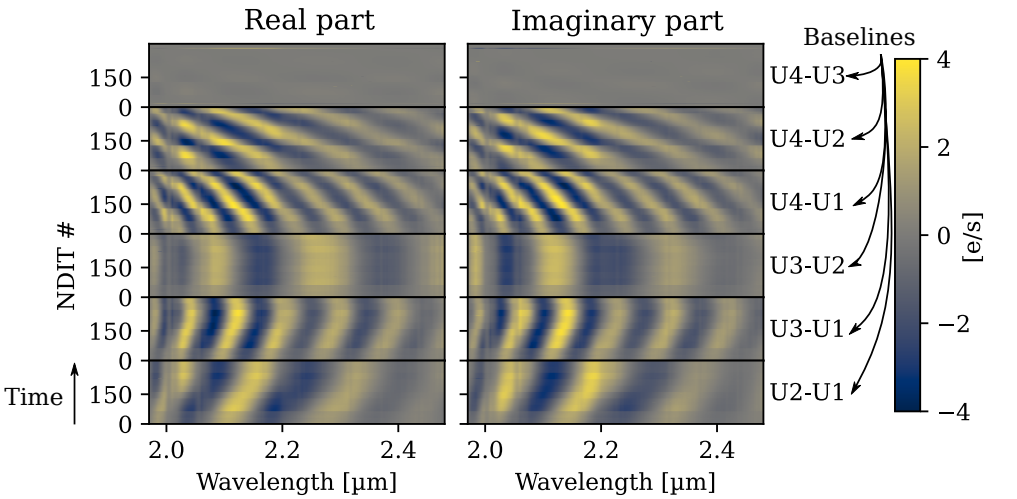

(b) Planet fit

Figure 2.16 – Best fit for the speckles (a) and the planet (b) phased on the star, in HD 206893 c observation the 2021-10-16. The observation contains 10 files of 32 exposures, hence the total of 320 NDITs.

Similarly as the χ^2, we obtain an estimation κ of the planet contrast at each $(\Delta\text{RA}, \Delta\text{Dec})$ tested during the script. Then, it is possible to obtain the κ from the best fit in individual NFILES and then average the κ values obtained. Another solution is to rely on the contrast κ at the best fit in the combined periodogram. If the companion is not detected on individual NFILES but is only revealed when we combine all the periodogram maps, it is advisable to rely on the κ value computed on combined periodogram. Either way, this contrast estimation is just an indication. The total contrast spectrum $C(\lambda)$ is provided by the second part of the pipeline.

Spectrum fit

The `spectrum_reduce` part of the ExoGRAVITY pipeline relies on the companion astrometry $(\Delta\text{RA}, \Delta\text{Dec})$ measured by the `astrometry_reduce` script. So $\underline{\mathbf{\Theta}}_{b,t}$ is fixed to:

$$\underline{\mathbf{\Theta}}_{b,t} = \exp\left(i\frac{2\pi}{\lambda}\left[\Delta\text{RA}\, U_b(t) + \Delta\text{Dec}\, V_b(t)\right]\right). \tag{2.65}$$

Contrary to the astrometry fit, here we do not make any assumption on the planet contrast. Also, in `spectrum_reduce`, the contrast is obtained for the whole set of NFILES combined in one single linear fit, and not in a fit of separated files of the observations. Otherwise, the method is the same as `astrometry_reduce`: we search the contrast spectrum $\mathbf{C}(\lambda)$ in the subspace perpendicular to the speckles' subspace.

For the contrast spectrum fit, we express all the visibilities in the companion reference frame. In the following, a tilde $\sim$ indicate visibilities phase referenced on the planet. Back to Eq. (2.54) for a given baseline b and time t, it now becomes:

$$\begin{pmatrix}\underline{\widetilde{\mathbf{H}}}_{b,t11} & \underline{\widetilde{\mathbf{H}}}_{b,t12}\end{pmatrix}\underline{\widetilde{\mathbf{V}}}_{b,t,\text{onplanet}} = \mathbf{C}(\lambda)\begin{pmatrix}\underline{\widetilde{\mathbf{H}}}_{b,t11} & \underline{\widetilde{\mathbf{H}}}_{b,t12}\end{pmatrix}\underline{\widetilde{\mathbf{V}}}_{b,t,\text{onstar}} \tag{2.66}$$

To obtain a single linear expression for all b and t, we assemble all the $\underline{\widetilde{\mathbf{H}}}_{b,t}$ matrices such that:

$$\underline{\mathbf{H}} = \begin{pmatrix} (\underline{\widetilde{\mathbf{H}}}_{b_1,t_1})_{11}(\underline{\widetilde{\mathbf{H}}}_{b_1,t_1})_{12} & 0 & \cdots & 0 \\ 0 & (\underline{\widetilde{\mathbf{H}}}_{b_2,t_1})_{11}(\underline{\widetilde{\mathbf{H}}}_{b_2,t_1})_{12} & \cdots & \vdots \\ \vdots & \cdots & \ddots & 0 \\ 0 & \cdots & 0 & (\underline{\widetilde{\mathbf{H}}}_{b_6,t_{\text{NDIT}}})_{11}(\underline{\widetilde{\mathbf{H}}}_{b_6,t_{\text{NDIT}}})_{12} \end{pmatrix} \tag{2.67}$$

and all the observed visibilities such that:

$$\underline{\mathbf{V}} = \begin{pmatrix} \underline{\widetilde{\mathbf{V}}}_{b_1,t_1,\text{onplanet}} \\ \vdots \\ \underline{\widetilde{\mathbf{V}}}_{b_6,t_1,\text{onplanet}} \\ \vdots \\ \underline{\widetilde{\mathbf{V}}}_{b_6,t_{\text{NDIT}},\text{onplanet}} \end{pmatrix}. \tag{2.68}$$

From this, we can form a matrix $\underline{\mathbb{Q}}$ as:

$$\underline{\mathbb{Q}} = \underline{\mathbf{H}}\,\underline{\mathbf{V}}. \tag{2.69}$$

Also, we form:

$$\underline{\mathbb{R}} = \begin{pmatrix} \left((\underline{\tilde{\mathbf{H}}}_{b_1,t_1})_{11} \quad (\underline{\tilde{\mathbf{H}}}_{b_1,t_1})_{12}\right) \underline{\tilde{\mathbf{V}}}_{b_1,t_1,\text{onstar}} \\ \left((\underline{\tilde{\mathbf{H}}}_{b_2,t_1})_{11} \quad (\underline{\tilde{\mathbf{H}}}_{b_2,t_1})_{12}\right) \underline{\tilde{\mathbf{V}}}_{b_2,t_1,\text{onstar}} \\ \vdots \\ \left((\underline{\tilde{\mathbf{H}}}_{b_6,t_{\text{NDIT}}})_{11} \quad (\underline{\tilde{\mathbf{H}}}_{b_6,t_{\text{NDIT}}})_{12}\right) \underline{\tilde{\mathbf{V}}}_{b_6,t_{\text{NDIT}},\text{onstar}} \end{pmatrix} \tag{2.70}$$

And finally, the Eq. (2.66) becomes:

$$\underline{\mathbb{Q}} = \underline{\mathbb{R}}\, \mathbf{C}(\lambda). \tag{2.71}$$

This Eq. (2.71) is the equivalent of the previous Eq. (2.58), excepted that this time the information in $\underline{\mathbb{Q}}$ and $\underline{\mathbb{R}}$ is not incomplete as were $\underline{\mathbf{Q}}_{b,t}$ and $\underline{\mathbf{R}}_{b,t}$. We can arrange $\underline{\mathbb{Q}}$ and $\underline{\mathbb{R}}$ in such a way ($\underline{\mathbb{Q}}_2$ and $\underline{\mathbb{R}}_2$) that we obtain the contrast for each of the n_λ spectral channels by:

$$\mathbf{C}(\lambda) = \text{Re}\left(\underline{\mathbb{Q}}_2^\dagger \underline{\mathbb{W}}_2^{-1} \underline{\mathbb{R}}_2\right) \left[\text{Re}\left(\underline{\mathbb{R}}_2^\dagger \underline{\mathbb{W}}_2^{-1} \underline{\mathbb{R}}_2\right)\right]^{-1} \tag{2.72}$$

with $\underline{\mathbb{W}}_2$ an expression of the spectrum errors that I do not detail here.

Spectrum outputs

The `spectrum_reduce` script provides the companion-to-star contrast spectrum in the K-band (see an example in Fig. 2.17) and the spectrum covariance matrix between each spectral channel (see Fig. 2.18). The covariance includes all the correlated errors provided by the GRAVITY pipeline and propagated through the ExoGRAVITY pipeline.

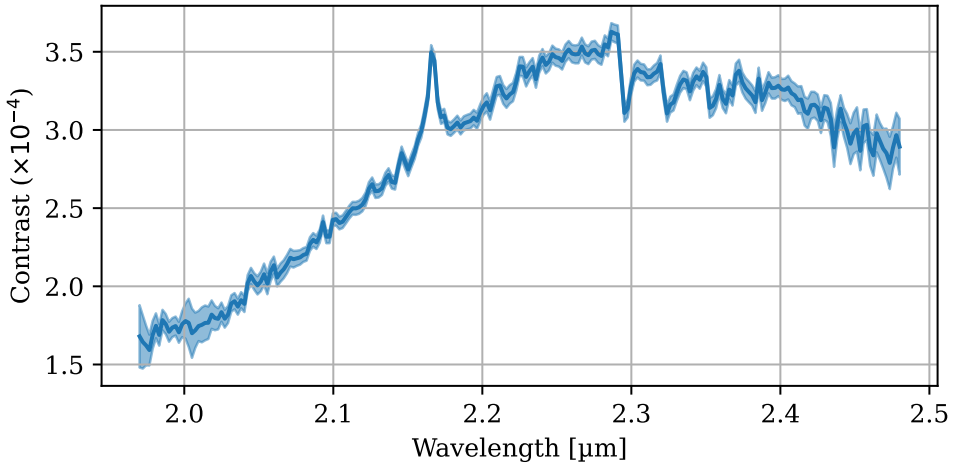

Figure 2.17 – Contrast spectrum of β Pic b for an observation of 7 NFILES×32 NDIT×10 s on 2021-01-06. The lighter blue area corresponds to the 1σ error artificially inflated ×2.

We can obtain the spectrum of the exoplanet by multiplying the contrast spectrum with a synthetic stellar spectrum (e.g. NextGen, Hauschildt et al., 1999) at the same effective temperature, metallicity and $log(g)$ as the primary. Then we can compare the planet spectrum with synthetic grids

of planet spectra (e.g. ExoREM Charnay et al., 2018) to retrieve some of the exoplanet atmosphere properties (temperature, radius, metallicity, C/O ratio, $log(g)$).

The covariance matrix (Fig. 2.18) is dominated by the variance (diagonal term) but also include the covariance between all the spectral channels. This covariance is non-zero and is especially prominent at the lower and higher ends of the spectrum.

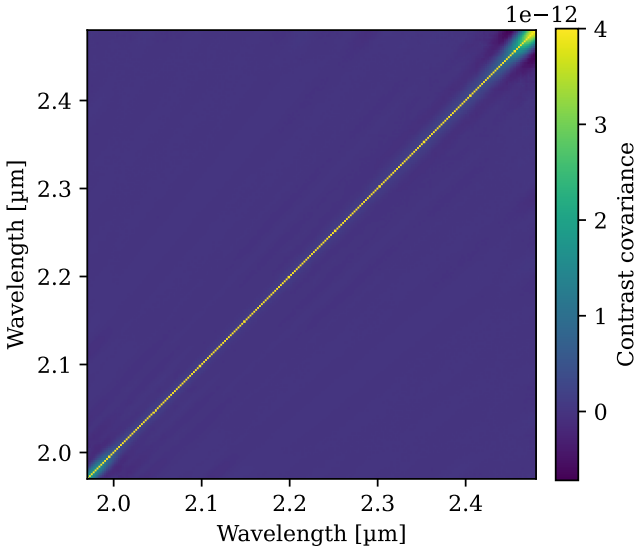

Figure 2.18 – Covariance matrix for the spectrum of β Pic b shown in Fig. 2.17.

Thanks to the dedicated observation strategy and the ExoGRAVITY pipeline, GRAVITY is now a recognized instrument for direct observation of exoplanets.

2.6 Towards GRAVITY+

The multiple successes of GRAVITY have motivated an upgrade of the instrument and of the VLTI infrastructure. The project GRAVITY+ started in 2019 and includes several major improvements (Fig. 2.19).

WIDE, FAINT and vibrations The first phase of implementation focused on the commissioning of the DUAL-WIDE mode (Sect. 2.3.3), called GRAVITY WIDE, and on activities dedicated to improve the instrument sensitivity, called GRAVITY FAINT, including the replacements of the grisms, implementation of a procedure to limit the metrology laser noise, and improvement of the fringe tracker software. At the time of writing this manuscript, these items are completed and operational. The improved vibration control of the VLTI is still in progress (Bigioli et al., 2022).

GPAO The second phase of implementation is the replacement of the 20 years old MACAO by the new adaptive-optics GPAO at the coudé focus of each UT. I have shown in Sect. 2.8 that the actual atmosphere correction provided by MACAO leaves much to be desired. GPAO will bring us closer to the extreme adaptive optics world, with a design close to the SAXO adaptive optics of SPHERE (Fusco et al., 2014) and the adaptive optics of ERIS (Davies et al., 2023). The wavefront sensors

of GPAO are Shack-Hartmanns with 40×40 lenslets (for natural guide stars) and the deformable mirrors are from ALPAO and have 1432 actuators. These new adaptive optics will correct more than 800 modes (MACAO corrects 50 modes) at around 1 kHz (MACAO 500 Hz). It will routinely provide Strehl of 80% in the K-band and significantly improve the injection in the FT and SC, as well as limiting the amount of star-light injected in the SC when we observe exoplanets. With GPAO, we expect to be able to close the FT loop on fainter guide stars (down to K=13 mag) and to be able to detect fainter K-band science objects, down to K=22 mag (actually limited to K=19 mag). The new adaptive optics are currently assembled at the Max Planck Institute for Extraterrestrial Physics in Garching (wavefront sensors), IPAG in Grenoble (corrective optics: deformable mirrors and mounts), LESIA in Paris (real-time controller) and the Lagrange laboratory in Nice (final test bench). It will be commissioned at VLTI during summer 2024 and should be operational in October 2024.

Laser guide stars In a third phase, the GRAVITY+ project will install laser guide stars on UT1, 2 and 3 (UT4 is already equipped with the 4LGSF). This will allow for closing the adaptive optics loop in regions of the sky where we lack bright stars in the visible to serve as guide stars. The expected Strehl is around 60% at K-band. However, we will still need a natural FT guide star as the artificial laser-guide-stars do not allow for fringe tracking, and a natural guide star for tip-tilt control. Still, with the DUAL WIDE mode that allows to pick a FT guide star at up to 30 arcsec from the SC target, the laser guide stars will greatly improve the sky coverage of GRAVITY.

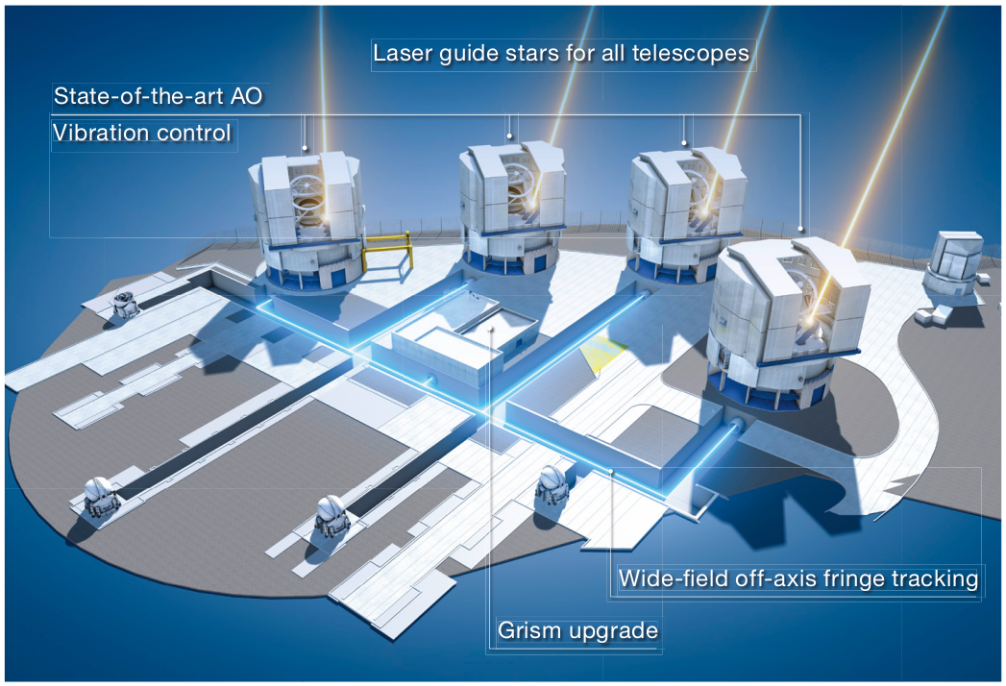

Figure 2.19 – Improvements of the GRAVITY+ project. (From Gravity+ Collaboration et al., 2022)

For the exoplanets' science case, we will benefit from all the efforts to limit the noises at VLTI (metrology back-propagation, vibrations) and to improve the instrument transmission. However, the breakthrough is expected from new adaptive optics GPAO that will stabilize the wavefront against

atmosphere turbulence, allow for fine aberrations control, and thus limit the stellar photon noise and other systematic noises in our exoplanets' observations. It shall enable observations of lower-mass companions closer to their star.

The direct observations of exoplanets focus on nearby stars that are generally bright enough to be guide stars for the adaptive optics. For this reason, the implementation of the laser guide stars is not as crucial for our science case as it is for the observation of active galactic nuclei or low-mass young stellar objects still embedded in their parent clouds. Still, the lasers might improve the observations of exoplanets around young stars like PDS 70 (Wang et al., 2021b) that are faint in the visible and expand our capacity to directly exoplanets in young systems.

My role in the GRAVITY+ project was not to directly contribute to the development of GPAO, but rather to already prepare the ground for an optimal use of the new adaptive optics once it is installed. In this manuscript, I call the instrument GRAVITY+ when mentioning instrument after the GPAO commissioning.

2.7 Here it starts

Here starts my PhD, on this new technique for direct observations of exoplanets: the optical interferometry. The recent breakthroughs in this science case on GRAVITY leads us to imagine that the instrument might play a big role in exoplanets' characterization in years to come. I conducted my PhD is this context, in the very last years before the commissioning of the new adaptive optics of GRAVITY+ and before the release of the Gaia Data Release 4. GPAO will be crucial for high-contrast observations with GRAVITY+, and the Gaia DR4 will give us thousands of targets to characterize, including young Jupiter analogues that are so important for our understanding of the formation and dynamical history of planetary systems.

From the hardware of the instrument, to the data reduction and the observation strategies, I have shown in this chapter that GRAVITY is a sophisticated instrument that includes a wide range of subsystems and real grasp on the telescopes' infrastructure. This provided me several routes to investigate to improve the capabilities of the instrument for exoplanets' observations, and a 3-year PhD is not enough to cover everything. Nevertheless, I made progress on our understanding of the instrument limits in high-contrast conditions (Chapter 3), on the "wiggles" systematics that pollute our K-band spectra (Chapter 4) and I worked on a high-contrast mode dedicated to exoplanet observations on GRAVITY+ (Chapter 5).

Chapter 3

Detection limits of ExoGRAVITY

Contents

Any mature instrument dedicated to direct observations of exoplanet must have a thorough estimation of its sensitivity and detection limits. It serves at least three purposes. First, it allows for identifying synergies between instruments. Detection curves do not say everything about an instrument's capabilities, but comparing their different limitations with their specific strengths outlines the overall potential of the community to investigate this science field. Second, a detection limit is very useful for optimizing the observation strategy, especially for challenging targets. Third, getting the detection limits brings us to understand what the limitations are. This helps for getting the best from an existing instrument, and, even more, for wisely guiding instrumental upgrades towards tackling the biggest problems.

GRAVITY is very young as an exoplanet observer, and its detection capabilities had so far not been assessed. During the second year of my PhD, I took it upon myself to investigate which exoplanets GRAVITY can detect, which it can't, and what the main limitations are.

My related publications

- (Pourré et al., 2024) : Pourré, N., Winterhalder, T. O., Le Bouquin, J.-B., Lacour, S., et al. (2024). High contrast at short separation with VLTI/GRAVITY: bringing Gaia companions to light. A&A, 686:A258.

- (Pourré et al., in prep.): Pourré, N., Palma-Bifani, P., Bonnefoy, M., et al. (in prep.). Constraints on the moon-forming disk around GQ Lup B with VLTI/GRAVITY. A&A.

3.1 The most challenging exoplanets observed

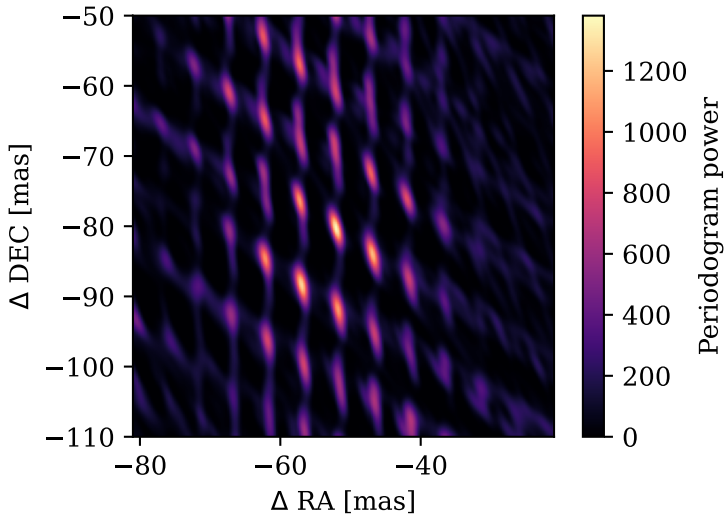

Figure 3.1 – Periodogram from the `astrometry_reduce` script for the β Pic c observation of 2021-01-05. I kept only 6×32×10 s to check the detection over ∼ 30 min exposure. The full dataset for this observation is 18×32×10 s (∼1h30).

Prior to my work quantifying the detection limits of the ExoGRAVITY technique, we could only rely on rough quantitative estimates of the instrument's capabilities. This was provided by successful observations of exoplanets that seem to have a lower SNR because of their high contrast in flux with their primary, or because of their short separation. In Sect. 1.4.3, I already listed the exoplanets observed directly with GRAVITY. Among these observations, the most challenging ones were β Pic c and 51 Eri b.

β Pic c has a K-band contrast of $(4.8 \pm 0.4) \times 10^{-5}$ (Nowak et al., 2020) and apparent magnitude $m_k = 14.3 \pm 0.1$. With the ExoGRAVITY large programme, we observed it down to 94 mas separation (Lacour et al., 2021). At this separation, the detection is clear when combining the periodogram maps over 30 min integration time, but strong side lobes are present around the periodogram peak (Fig. 3.1) and there are heavy systematics in the visibilities (see Sect. 4). We somewhat feel that

the noise floor is close, and that we would not be able to detect much fainter companion at this separation.

51 Eri b has a K-band contrast around 2.5×10^{-6} and an apparent magnitude $m_k = 18.5$. We observed it down to 300 mas thanks to an on-going monitoring programme lead by William Balmer. The detection is difficult and seems to require exquisite atmosphere conditions. It is at the limit of the instrument capabilities in DUAL OFF-AXIS.

These observations were the first hints we had of our detection limits. From these two challenging observations, we could estimate the ExoGRAVITY limits around 4×10^{-5} contrast at 94 mas, and 2×10^{-6} at 300 mas.

3.2 Injection method

Injection of a planet

Injection of synthetic companions in observation data and retrieval attempts with the reduction pipeline is a standard technique to quantify the detection limits of an instrument. In ExoGRAVITY, this technique had never been used before my PhD. I developed it first with the goal to understand the impact of systematics on observables (Sect. 4), but it also appeared to be the simplest solution for testing detections.

In all my work, I injected planets in DUAL ON-AXIS data at MEDIUM resolution. I inject the planets in the `astroreduced.fits` files produced by the GRAVITY pipeline (Fig. 3.2). The `OI_VIS` table of the `astroreduced` contains `VISDATA`, the complex coherent flux measured in SC for each baseline and each NDIT. I inject the synthetic planet model in the star reference frame:

$$V_{\text{syntheticcomp}} = C\, V_{\text{onstar}}\; e^{-i\frac{2\pi}{\lambda}\,[\mathbf{U}(t)\boldsymbol{\Delta\alpha}]}\; e^{-i\phi_p}. \tag{3.1}$$

For V_{onstar}, I use the average of the two nearest host-star observations with the SC. $\mathbf{U}(t)$ are the UV plane coordinates included in the `UCOORD` and `VCOORD` columns in the `VISDATA` table. I choose the relative position of the planet with respect to the star with $\boldsymbol{\Delta\alpha} = (\Delta\text{RA}, \Delta\text{Dec})$. In all this chapter, the planets are injected with a flat contrast spectrum for the sake of simplicity, so C is scalar. Later on, in Sect. 4, I also will inject planets with $C(\lambda)$ of the shape of the β Pic b contrast spectrum.

In this chapter, with a flat contrast spectrum, it is the same model of an off-axis point source that is used for the retrieval in `astrometry_reduce` script of the ExoGRAVITY pipeline. As already discussed in Sect. 2.5.2, the complex visibilities in `VISDATA` must be rephased by a ϕ_p in order to be referenced to a meaningful on-sky position (the metrology reference point). So, here we must proceed the other way round and dephase the synthetic planet signal to match the raw data phase.

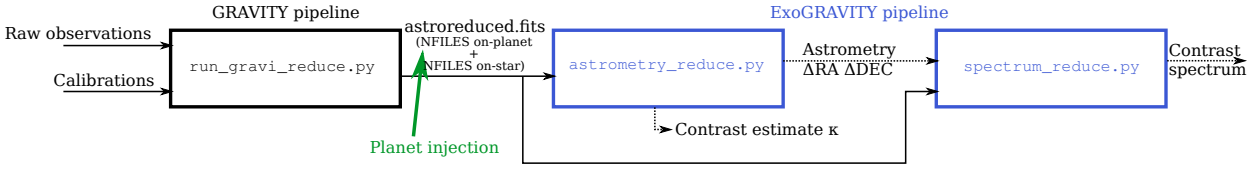

Figure 3.2 – Block diagram from raw observations to planet contrast spectrum. The planet injection is done after the GRAVITY pipeline.

Finally, for each file, we have a (NDIT×NBASES×N_λ) matrix that we add to the data:

$$\texttt{VIS\_DATA} += V_{\text{syntheticcomp}} \times \text{DIT}. \tag{3.2}$$

The data in `VIS_DATA` are in unit of number of electron on the SC camera, but V_{onstar} as extracted by the `cleanGRAVITY` tools[1] is in e/s. This is why a multiplication by DIT is required in Eq. 3.2. In all this work NBASES=6 (the six baselines of VLTI) and N_λ=233 channels (MEDIUM resolution mode). After this process, the data contains the original speckles and noises (detector, photon-noise, background,...) together with a synthetic planet at a known position and contrast.

Subtraction of a planet

Under its current form, the ExoGRAVITY is not able to retrieve several planets in the SC fiber field-of-view. For this reason, and to avoid adding unnecessary complexity, I inject the planets in planet-free datasets. It can be non-detection datasets taken during the search of an exoplanet, or datasets where I subtracted the companion. To subtract a companion signal in the data, I follow the block diagram of Fig. 3.3. From the `astroreduced` files produced by the GRAVITY pipeline, I run a first `astrometry_reduce` with the `gofast` option that averages NDIT in each NFILES to speed-up the reduction. At this point, we do not have the planet contrast spectrum, so the best astrometry is fitted under a flat contrast assumption. The best (ΔRA, ΔDec) astrometry is then used as an input for the `spectrum_reduce` script. Here, two possibilities: we can either use the astrometry fit for each file, or the global astrometry from the combination of each file. In this chapter I always used the astrometry per file, it makes sense if the companion is bright enough to be detected in each file. If the companion is not detected in each NFILES, the astrometry fit is erratic and it might lead to a biased contrast spectrum. Once completed, the `spectrum_reduce` script execution produces a unique contrast spectrum that we use in a final run of `astrometry_reduce` instead of the flat contrast assumption. For a better subtraction, we need a separate planet fit for each NDIT and not a global one for the whole file. The last step is to subtract the NFILES planet fit of size (NDIT×NBASES×N_λ) into the corresponding `VIS_DATA` column of each `astroreduced.fits`. As for the injection, a dephasing by $-\phi_p$ is needed to match the raw data state:

$$\texttt{VIS\_DATA} -= \text{PLANETFIT} \times \text{DIT} \times e^{-i\phi_p} \tag{3.3}$$

The dataset we obtain is subtracted from our best fit of the companion signal in the data. Careful checks of the `astrometry_reduce` outputs on the planet-subtracted datasets show no remaining signal of the subtracted planet.

Be it for injection or subtraction of a planet companion, I expect no methodology difference on the AT or the UT, although I never tested it on AT data.

[1] `https://gitlab.obspm.fr/mnowak/cleanGravity`

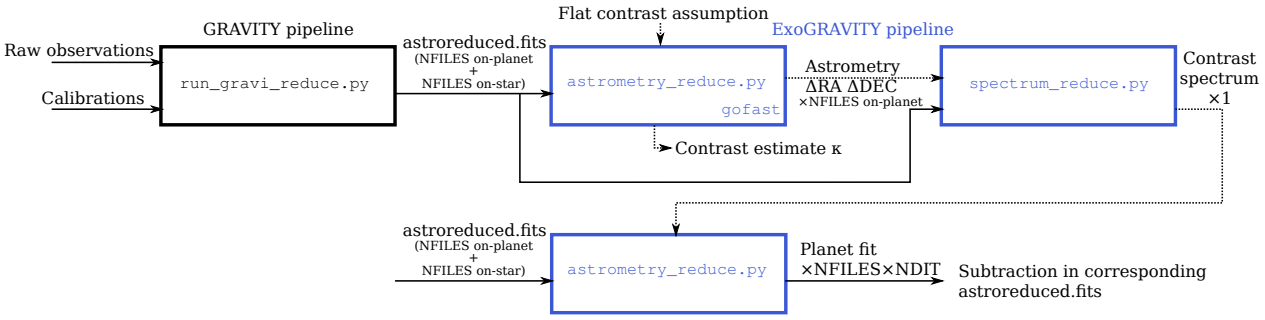

Figure 3.3 – Block diagram for the planet subtraction in a `astrometry_reduce`→`spectrum_reduce`→`astrometry_reduce` process.

3.3 Determine what is a detection

At the beginning of my PhD, we had no method established to determine the robustness of ExoGRAVITY detections. For the attempts to detect new exoplanets or brown dwarfs, and for the challenging known targets, we relied on the visual inspection of the astrometry fit outputs by the most experienced eyes of Sylvester Lacour and Mathias Nowak. Eventually, a small hint of detection was ruled out, or confirmed, by the comparison of the reduction between the ExoGRAVITY pipeline and the Sylvestre own reduction pipeline. The detection was decided by the inspection of the periodogram maps provided by the astrometry fit. Figure 3.4 shows examples of clear detection and non-detection periodograms. As shown on Fig. 3.4b, for a non-detection, the periodogram map has no peak standing above the rest. The grid-like structure of the spots is characteristic of the pipeline fitting noise. The periodogram power remains to low values, despite summing the periodograms from all NFILES (5 in this example).

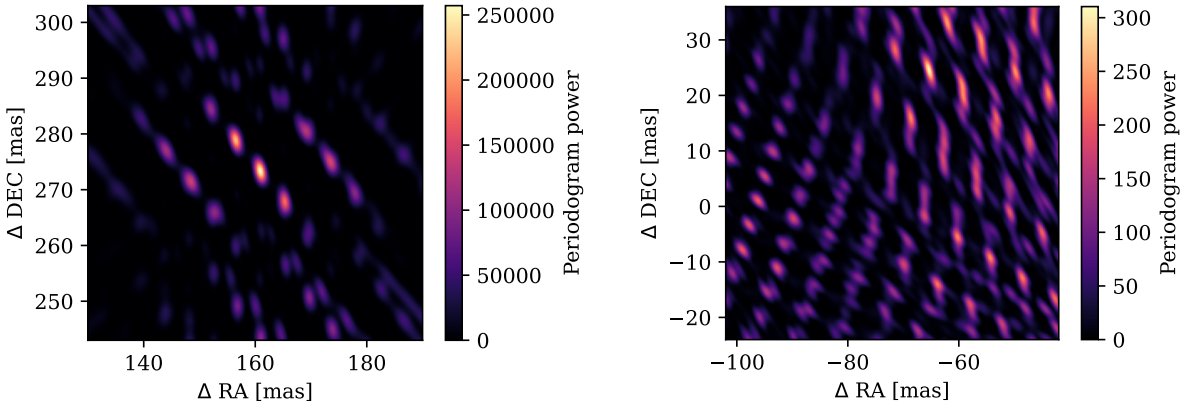

(a) β Pic b detection (b) Non-detection around HD 206893

Figure 3.4 – Comparison of the periodograms summed for all NFILES for a clear detection and a non-detection. (a) Clear detection of β Pic b the 2020-02-10 on a $2 \times 32{\times}10$ s (10 min) dataset. (b) Non-detection during the search for HD 206893 c the 2021-08-27 on a $5 \times 32{\times}10$ s (27 min) dataset.

I have to note here that in the ExoGRAVITY framework, the detection is not easy to link to the SNR of visibilities provided by the GRAVITY pipeline. The general pipeline provides error bars that take only into account the detector noise and photon noise. But the visibilities are also affected by systematics (Sect. 4), especially for high-contrast observations in DUAL-ON-AXIS mode. This is why we rely only on the outputs of our reduction pipeline to take a decision on the detection or

non-detection of the target.

3.3.1 Preliminary attempt

During the first few months of my PhD, I carried out a study to determine the integration time necessary for detecting a planet at a given K magnitude. For this, I used the ExoGRAVITY observations listed in Table 3.1. It is a mixture of actual planets' observations and non-detection pointings where I injected planets.

Table 3.1 – Dataset for the sensitivity analysis

Companion	Date	K mag comp.	K mag *	Contrast	Sep. [mas]	τ_0 [ms]	Seeing [arcsec]
β Pic c	2020-02-11	14.3	3.5	4.7×10^{-3}	130	12	0.49
β Pic b	2021-01-07	12.3	3.5	2.9×10^{-4}	411	7	0.54
β Pic b	2021-08-26	12	3.5	3.9×10^{-4}	464	1.8	1.6
HD 206893 (inj.)	2021-08-27	15.6	5.6	1×10^{-4}	75	4	0.7
...	...	14.8	...	2×10^{-4}	...	...	...
...	...	13.1	...	1×10^{-3}	...	...	...
...	...	11.9	...	3×10^{-3}	...	...	...
HD 206893 c	2021-10-16	15.9	5.6	7.8×10^{-5}	111	2.5	0.53
HD 72946 B	2022-01-25	13.8	5.5	4.7×10^{-4}	163	7	0.6
HD 136164 b	2022-02-20	14.3	7.3	1.6×10^{-3}	104	12	0.39
PDS 70 b	2022-02-21	16.4	8.5	6.9×10^{-4}	160	7	0.8
PDS 70 c	2022-02-21	17	8.5	3.8×10^{-4}	211	6	0.7
HIP 77718 (inj.)	2022-02-21	15.8	5.8	1×10^{-4}	203	3	0.9
...	...	15	...	2×10^{-4}	...	...	...
...	...	13.3	...	1×10^{-3}	...	...	...
...	...	12.1	...	3×10^{-3}	...	...	...

I estimated at that time that a periodogram power of more than 500 on the combined map was a satisfactory criterion for detection. My method was to reduce iteratively each observation presented on Table 3.1 with the `astrometry_reduce` script of the ExoGRAVITY pipeline. For each observation, if the periodogram maximum was above 500, I ran again the reduction with subtracting exposures (NDIT) to artificially restrain the observing integration time. I stopped at the last reduction that provides a periodogram power above 500. The results obtained are shown in Fig. 3.5a. It shows that the integration time versus companion K band magnitude follows line $2.9 \times 10^{-4} \times 10^{\mathrm{K\,mag}/2.5}$. With this detection criterion, I saw no clear influence of the separation on the integration time necessary for detection of the real companions' observations. However, for the injected companions, the observation at 75 mas required systematically twice more integration time than the injection at 203 mas. The outlier observation of β Pic b has a seeing of 1.6 arcsec and shows a possible strong influence of the weather conditions on the detection.

In Fig. 3.5b, I show the integration time necessary for a detection does not scale with the contrast. If injected companions show a trend towards higher integration time for deeper contrasts, it is only because they are all injected around stars of similar magnitude (K= 5.6 $\sim$ 5.8). For the whole dataset that include host star magnitude ranging from 8.5 to 3.5, the integration time does not seem to scale with the planet-to-star contrast.

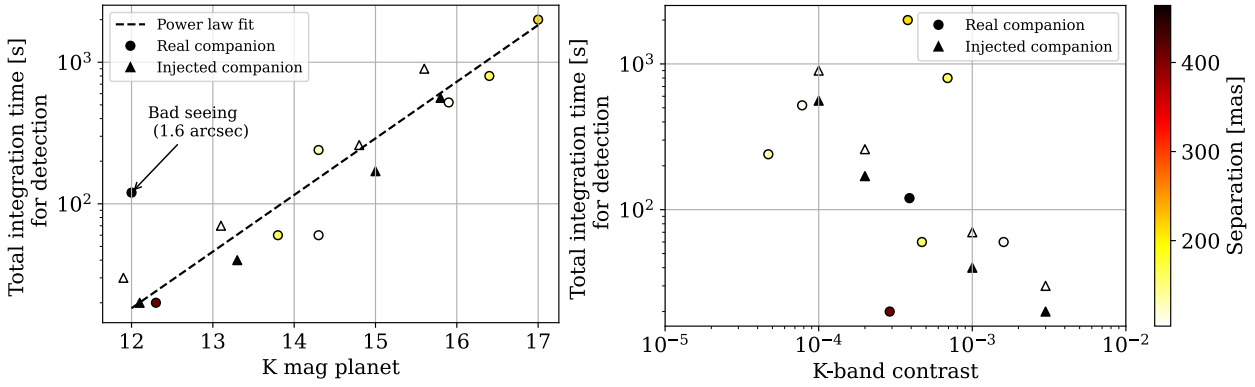

(a) (b)

Figure 3.5 – Minimal integration time needed to have a periodogram power of minimum 500. (a) Expressed in companion magnitude, ranging from 12 to 17. (b) Expressed in companion-to-star contrast at K-band.

The empirical relationship linking planet magnitude and integration time has been very useful for building observation proposals and has been widely used in the ExoGRAVITY consortium. Looking back to it, it has severe limitations. The periodogram power is based on a χ^2 computation using the errors on visibilities given by the GRAVITY pipeline. These errors only take into account photon noise and detector noise, but we know that we also have correlated noise that is sometimes the dominant contributor. In these conditions, the χ^2 is not necessarily representative of the SNR.

It was a first step that was very useful, but later on I developed another strategy providing more reliable SNR estimation.

3.3.2 New proposition

The ExoGRAVITY consortium needs to have a robust quantitative estimate of planet detection SNR. Unlike the previous technique (Sect. 3.3.1), this new proposition is not only based on the peak periodogram power but also estimates the noise from the periodogram map.

Method

The method uses only the combined periodogram maps produced by the `astrometry_reduce` script. It can me summarized as:

- Step 1: Run `astrometry_reduce` on the observation data. The investigated range in (ΔRA, ΔDec) must cover the fiber field of view (50% injection limit). It is 65 mas on the UT and 290 mas on the AT, centered on the SC fiber position. The number of (ΔRA, ΔDec) on the map must be sufficient to properly sample the periodogram peaks. 150 points for 65 mas is a good number.
- Step 2: Find $p_{\max}$, the peak periodogram power in the map.
- Step 3: Subtract the planet from the data following the process of Fig. 3.3.
- Step 4: Run `astrometry_reduce` on the data with the planet subtracted. Keep the same range of (ΔRA, ΔDec) as step 1.
- Step 5: Find $p_{0,\max}$, the peak periodogram power in the new map.
- Repeat steps 3 to 5 to subtract the brightest "blob" fit found at step 5, and obtain $p'_{0,\max}$.

The SNR of the companion detection is:

$$\mathrm{SNR}_{\mathrm{det}} = \sqrt{\frac{p_{\max}}{p_{0,\max}}}. \tag{3.4}$$

The ratio $\mathrm{SNR}_0 = \sqrt{p_{0,\max}/p'_{0,\max}}$ is a check that there is not another companion in the data. I assume that SNR_0 <1.5 is a good sanity check that there is no major problem in the companion subtraction. On my laptop (CPU i9-11950H), the full process takes around 20 min for NFILES∼10. To save computation time and avoid memory overload, the companion subtractions (step 3) must be done on a small (ΔRA, ΔDEC) grid centered on the companion position, with no more than 50×50 grid points.

Unlike the previous detection criterion (Sect. 3.3.1), this method takes into account the systematics and not only the provided error bars. It is then more representative of the actual detection status.

Example: β Pic c

The β Pic c observation of 2020-03-07 is emblematic of high-contrast with GRAVITY. It was taken under the ExoGRAVITY large programme. The instrument mode is DUAL-ON-AXIS and MEDIUM resolution. The planet is at 4.7×10^{-5} contrast and 138 mas separation. The data are heavily affected by the systematics (the "wiggles") discussed in Sect. 4. The observing log is on Table 3.2.

Table 3.2 – Log for the GRAVITY observations of β Pic c on the UT.

Date: 2020-03-07			
Observing time	Airmass	τ_0	Seeing
00:15:44/01:41:47	1.13-1.27	6.1-12.6 ms	0.49-0.99"
Target	ΔRA/ΔDEC[2]	NFILES/NDIT/DIT	
β Pic	0/0 mas	8/64/0.3 s	
β Pic c	-72/-118 mas	12/32/10 s	

Figure 3.6 shows the periodogram maps used for SNR computation. The periodogram with the planet (Fig. 3.6a) peaks at $p_{\max} = 9904$. Once the planet best fit is subtracted from the data, the periodogram peak is at $p_{0,\max} = 224$. Then, the detection SNR for this observation is:

$$SNR = \sqrt{\frac{p_{\max}}{p_{0,\max}}} = 6.6 \tag{3.5}$$

The SNR_0 between the planet subtracted and the bightest-blob subtracted periodograms is 0.9. We can conclude that there is no other planet in the data, and that the β Pic c subtraction brought us to the noise level.

[2]Fiber position.

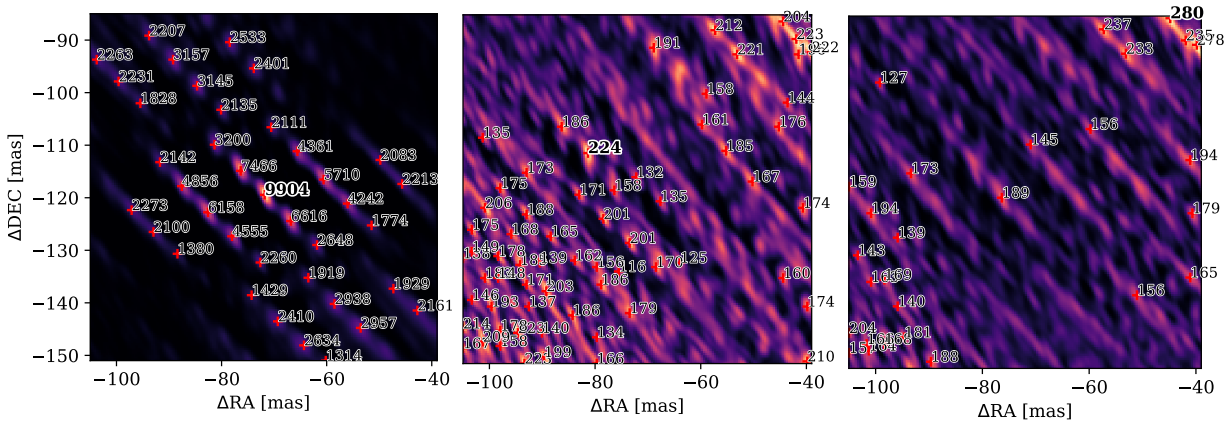

(a) β Pic c (b) Planet subtracted (c) Brightest blob subtracted

Figure 3.6 – Periodogram maps for the β Pic c observation of 2020-03-07. The periodogram main peak is shown in bold for each map. (a) Original with planet, with peaks higher than 1000 (periodogram power) plotted with red crosses. (b) After subtraction of best β Pic c fit, with peaks higher than 100 plotted. (c) After subtraction of the brightest blob fit, peaks higher than 100.

Example: AF Lep b

The observation of AF Lep b of 2023-12-23 is a good example of an observation of a faint companion at more than 300 mas. There are no wiggles in the data at this separation. The observation is part of the programme 0112.C-2396(C) led by William Balmer. As it is recent unpublished observations, I do not disclose the precise planet position that has little importance here. The instrument mode is DUAL-ON-AXIS and MEDIUM resolution. The companion was observed at a contrast of 1.5×10^{-5}. The observing log is on Table 3.3.

Table 3.3 – Log for the GRAVITY observations of AF Lep b on the UT.

Date: 2023-12-23			
Observing time	Airmass	τ_0	Seeing
03:20:45/06:35:24	1.04-1.31	4.9-10.8 ms	0.37-0.68”
Target	ΔRA/ΔDEC[3]	NFILES/NDIT/DIT	
Af Lep	0/0 mas	4/16/3 s	
Af Lep b	∼320 mas	22/12/30 s	

Figure 3.7 shows the periodograms map for the AF Lep b observation. The detection is at SNR=6.3. I run a second reduction on the dataset where the planet is subtracted. The brightest blob of the planet-free periodogram is at SNR=1.1, so no other planet is detected in the data.

[3]Fiber position.

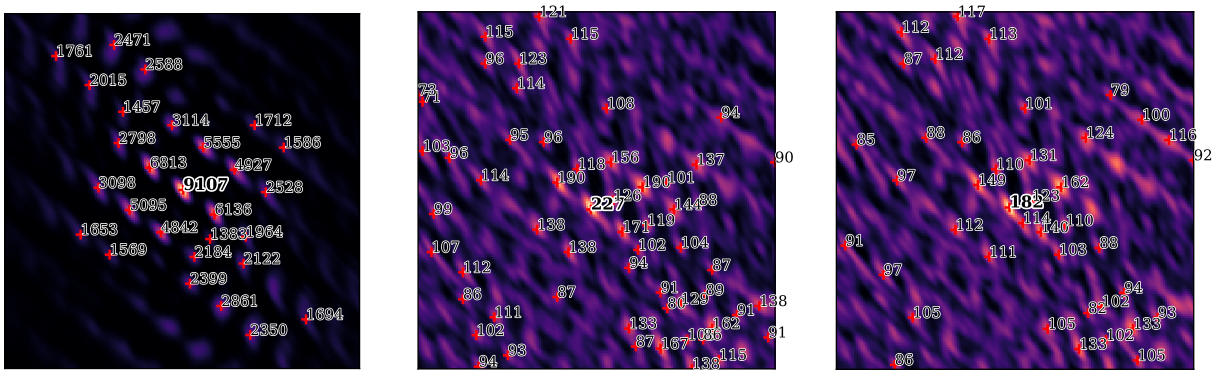

(a) AF Lep b (b) Planet subtracted (c) Brightest blob subtracted

Figure 3.7 – Periodogram maps 66×66 mas for the AF Lep b observation of 2023-12-23. (a) Original with planet, with peaks higher than 1000 plotted with red crosses. (b) After subtraction of best AF Lep b fit, with peaks higher than 60 plotted. (c) After subtraction of the brightest blob fit, peaks higher than 60.

Summary and other examples

Let me summarize here the tested detection of β Pic c and of AF Lep b, and add two other examples from the ExoGRAVITY large programme.

Table 3.4 – Summary of quantified detections

Companion	Date	K mag comp.	Contrast	Separation [mas]	NFILES×NDIT×DIT [min]	SNR
β Pic c	2020-03-07	14.3	4.7×10^{-5}	138	64	6.6
AF Lep b	2023-12-23	17.0	1.5×10^{-5}	320	132	6.3
β Pic b	2020-02-10	12.3	3×10^{-4}	319	11	11.2
PDS 70 b	2022-02-20	16.4	7.2×10^{-4}	160	80	7.2

These results tend to confirm that fainter companions require more integration time than brigher companions to reach the same SNR.

Conclusion

I plan to include a script doing this SNR computation in the ExoGRAVITY pipeline. It will be a useful add-on for planet-search and for first observations with GRAVITY, when the planet position is not well known. If Gaia DR4 brings the expected yield, GRAVITY+ will routinely confirm Gaia companions and a robust SNR estimate will help to confirm the companions, and determine if we have sufficient confidence to publish their direct detection.

For the first-pass of the SNR procedure (steps 1 to 5), I do not expect it to reveal planets that have not been identified before. The visual inspection was not quantitative but it was reliable. However, it is possible that we have missed second companions when a bright companion was already seen in the field of view. For this, my method that subtracts the bright companion and re-runs the reduction could reveal a companion signal that was previously hidden. Especially on observations on the AT where the wider field of view is more likely to contain several companions. We could imagine doing a consistent re-reduction of all ExoGRAVITY archival data with my technique, and hopefully have good surprises.

On SPHERE, they developed the powerful reduction algorithm PACO (Flasseur et al., 2020) that motivated to reduce again the data of the SHINE survey (Chomez et al., 2023a). Last year, Antoine Chomez discovered an additional companion to HIP 81208, already a three-body system (Chomez et al., 2023b). This new planetary mass companion orbits at 20 au (137 mas) around the brown-dwarf (HIP 81208 C) and was previously hidden by its host. This is just one shining example of what new reduction of archival data can bring.

3.4 ExoGRAVITY contrast curve

The injection/retrieval method is usually the best way to estimate the sensitivity limit of exoplanet imagers. It allows for testing the retrieval pipelines on realistic noise from the observations, but in a controlled environment where we know the ground truth (planet position and magnitude). Before my PhD, it was already clear that GRAVITY could observe planets at close separation that are out of reach for classical imaging techniques. But there was no quantitative study to show how close and how deep GRAVITY could observe around a bright host star. I proved in the previous sections that my methods of injection and subtraction of companion in the GRAVITY data were reliable. So the path is now clear for determining the contrast curve of GRAVITY with the ExoGRAVITY observation technique. I recently published these results in Pourré et al. (2024).

3.4.1 Choice of a dataset

The first step was to choose a dataset that will be the basis of this analysis. I had access to the full ExoGRAVITY database, not only from the large programme but also smaller open time and technical time programmes from the consortium. Sylvestre Lacour reduces all these data uniformly with the lastest GRAVITY pipeline. In total, the 7th January 2024 it contained 2950 files for 317 observations from 2017-09-05 to 2023-12-29 (if three targets are observed during the same night, I count three observations). Among these observations, 141 had the SC fiber below 400 mas separation. For my analysis, a collection of several observations was needed to cover a given range in separation because of the restricted field of view of each individual observation. I first focused on observations from 30 to 150 mas for my injection/retrieval, because it is the most relevant separations for observing Gaia candidates and possibly Jupiter-mass planets at the au scale. Only in a second phase, I added an observation at 320 mas to have a measure of ExoGRAVITY limit at longer separation. I wanted it to be as uniform as possible, with bright host stars and good atmospheric conditions to be sure that the adaptive optics was performing at the nominal regime. I also chose the dataset so that they are uniform in NFILES×NDIT×DIT. Table 3.5 summarizes the data I chose.

All the data below 150 mas have 1600 s integration time (27 min). The AF Lep dataset at 320 mas is the same as the one presented in Sect. 3.3.2 but limited to $5 \times 12 \times 30$ s (30 min). For all the data, the 5 NFILES span over one hour observation time. In the table, the “Sky rot.” column gives the variation of parallactic angle along the observations. Unfortunately, it is not consistent between observations, it ranges from 16 to 91°. For classical imaging instruments, it would be important since the sky rotation affects a lot the deconvolution power of ADI. For our ExoGRAVITY technique, it is not yet clear whether it is of critical importance. The fact that the sky rotation does not match

Table 3.5 – Dataset for the ExoGRAVITY contrast curve

Injection range [mas]	SC sep. [mas]	Star	Date	K mag *	Seeing [arcsec]	τ_0 [ms]	Sky rot. [deg]	Integr. time NFILES×NDIT×DIT
30 to 45	54	HD 17155	2022-08-19	6.5	0.54	9-18	36	$5 \times 32 \times 10$ s
45 to 70	72	HD 206893	2021-08-28	5.6	0.62	2-8	48	$5 \times 32 \times 10$ s
70 to 100	92	β Pic	2021-01-06	3.5	0.45	8-12	45	$5 \times 32 \times 10$ s
100 to 130	111	HD 206893	2021-10-16	5.6	0.50	2-4	91	$5 \times 32 \times 10$ s
130 to 150	136	β Pic	2020-02-09	3.5	0.81	6-15	16	$5 \times 32 \times 10$ s
320	320	AF Lep	2023-12-23	4.9	0.52	5-10	16	$5 \times 12 \times 30$ s

between the chosen datasets should give us indication on the role it plays in the interferometric deconvolution.

3.4.2 Method

Injection separation Here, I will first describe where I inject the planets. Despite the access to so many ExoGRAVITY archival observations, it was impossible to find SC pointing at all 5 mas separation interval between 30 to 150 mas. The observations I selected for the injection/retrieval are separated by 20 mas one from another. To obtain a continuous contrast curve, I took the liberty to inject companions not only at the exact separation of the SC fiber but also on a range of 20∼30 mas around the fiber center. I will show in Chapter 5 (Fig. 5.5) that the star flux injection in SC with respect to separation forms a plateau from 80 to 150 mas. As we expect our dominant source of noise to be related to the amount of star flux injected in the fiber at the planet position, a 15 mas difference between the companion and the fiber position does not make a significant difference in the observed noise. More, I show in Chapter 5 Sect. 5.4 that it is in our best interest to off-point the fiber from the companion at separations below 80 mas. I use this in the present work. As Table 3.5 shows, for the planets injected from 30 to 45 mas, the actual fiber position is at 54 mas, and for planets injected from 45 to 70 mas, the SC fiber is at 72 mas. This simulates the off-pointing strategy described in Sect. 5.4.

Injection PA Also, from my very first injection/retrieval with this dataset, it appears clearly that the positional angle (PA) had a strong influence on the detection limits. This comes from the inhomogeneous UV plane drawn by the UTs. Figure 3.8 shows that the longest projected baselines (UT1-UT4 or UT1-UT3) are oriented east/west or north-east/south-west. The perpendicular direction is probed only by shorter baselines. If the star-companion couple is oriented perpandicular to the longest baselines, the sensitivity at short separation is affected. For this reason, in this work I inject the companions either at the PA parallel to the longest baselines (most favorable position), or at the PA perpendicular to the longest baselines (worst position). I do not necessarily inject the companion at the PA where the SC was positioned during the observation, but I adapt the `astroreduced.fits` headers so that the ExoGRAVITY pipeline behaves as if the SC was at the simulated position. The method holds if the noise in the SC does not depend on PA; this is a reasonable assumption and the results we obtained gave us no reason for challenging it.

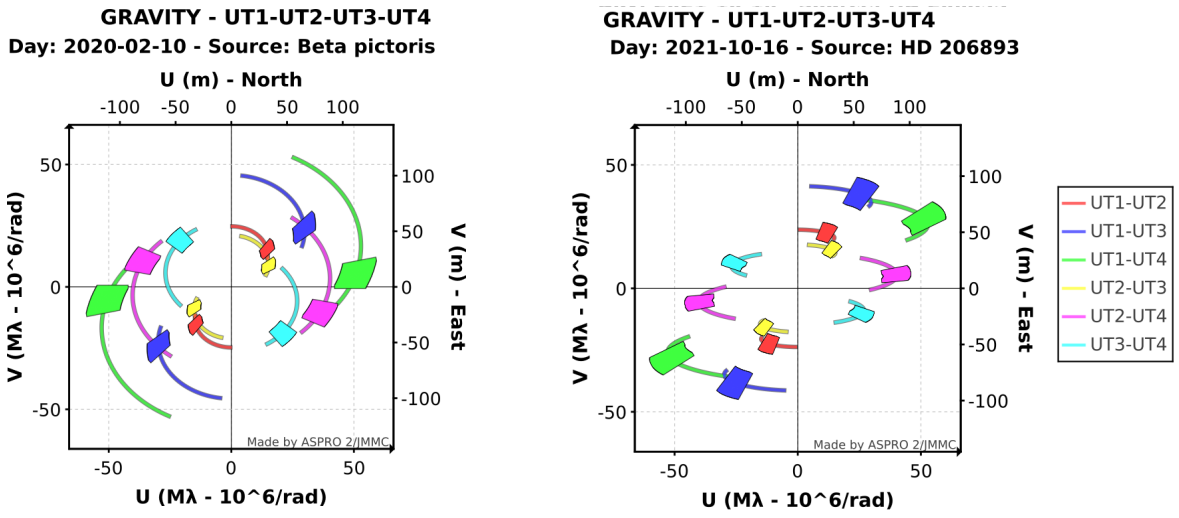

(a) (b)

Figure 3.8 – VLTI UV plane as shown by Aspro2 for two targets of the dataset. Radial segments shows the UV plane coverage during the acquisitions in MEDIUM resolution.

Strategy and detection criterion For the retrieval, I use the `astrometry_reduce` script of the ExoGRAVITY pipeline, averaging NDIT in each NFILES. The range of (ΔRA,ΔDec) is a 60×60 mas grid centered on the injected planet, excepted for injections below 45 mas where the grid is shifted to avoid the 10 mas region around the star that can provide strong and erroneous signal (Fig. 3.9). This comes from the impossible planet/star deconvolution at short separation that I describe later in Sect. 3.5.1. I use the combined periodogram for extracting both the astrometry and the companion contrast. I use a 4^{th} order polynomial for the speckle fit. In this analysis, I consider that a retrieval is successful if the planet is retrieved at less than 3 mas than the injected position, and if the contrast is retrieved with less by 50% error. The 3 mas criterion comes from the typical spot size on periodogram maps (e.g. Fig. 3.4). If the planet is retrieved with an error on astrometry of more than the typical spot size, I have good reason to believe that the retrieval failed.

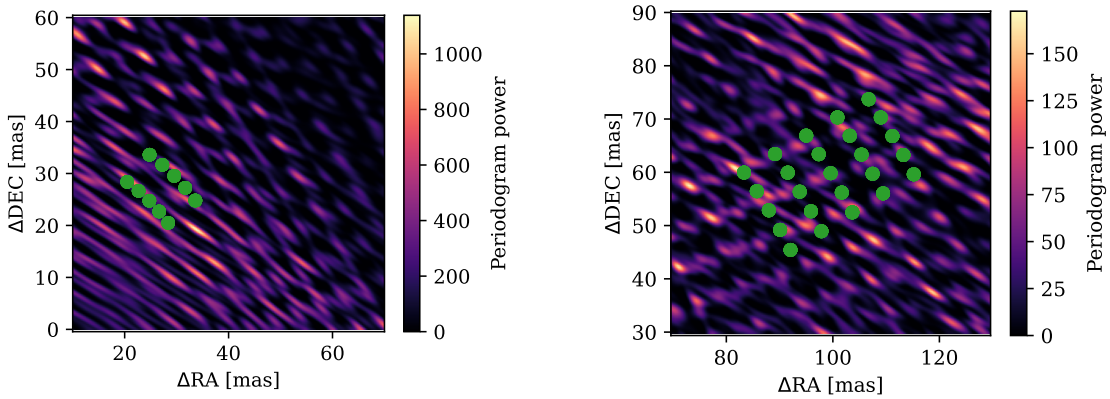

(a) HD 17155 dataset (b) HD 206893 (Oct. 2021) dataset

Figure 3.9 – Examples of planet injections for the contrast curve at the most favorable PA. (Green dots) position of planets injected. (Background image) Periodograms when no planet is injected. (a) Injections at less than 45 mas in HD 17155 dataset. (b) Injections from 100 to 130 mas in HD 206893 dataset of 2021-10-16.

To reveal the contrast curve, I inject 5 companions per separation and contrast, each at a different

PA of maximum $\pm 10^{\circ}$ around the best (or worst) PA with respect to the UV plane. This shuffles the effect of individual blobs in the periodogram that could affect one particular position. I consider that the 1σ limit is reached at a given separation when I retrieve successfully at least four companions out of five. Injecting more companions per position and contrast would be too intensive computationally, it would also make companions too close from each other and therefore not statistically independent (several planets under the same blob). Already, under these conditions, obtaining the ExoGRAVITY contrast curve with the PA parallel or perpendicular to the longest baselines required around 72 hours of computation on my laptop.

3.4.3 Contrast curves

Curves analysis The ExoGRAVITY contrast curve for 27 min integration time and in good atmospheric conditions are shown in Fig. 3.10. It shows that we can reach contrasts of 6×10^{-5} down to 50 mas separation. Below 50 mas the sensitivity drops fast (see Sect. 3.5.1 on inner working angle). Between 100 and 140 mas, the contrast limit reaches a plateau at 2.5×10^{-5}. This is for the most favorable PA, for the less favorable PA; the dependence on the orientation of the star-to-companion axis with respect to the UV plane is striking. Compared to the best orientation, when the PA is perpendicular to the longest baselines the contrast limit is $\times20$ less deep at 35 mas and still $\times3$ less deep at 90 mas. At separations larger than 130 mas there is no influence of the UV plane orientation. It means that, above 130 mas, even the shortest baselines have sufficient signal to enable the interferometric deconvolution. This sensitivity dependence with the PA was quantified before my analysis. It must be taken into account for the future observations at less than 130 mas, and some companions may remain undetected by GRAVITY because their unfavorable PA puts them in the blind spot of VLTI.

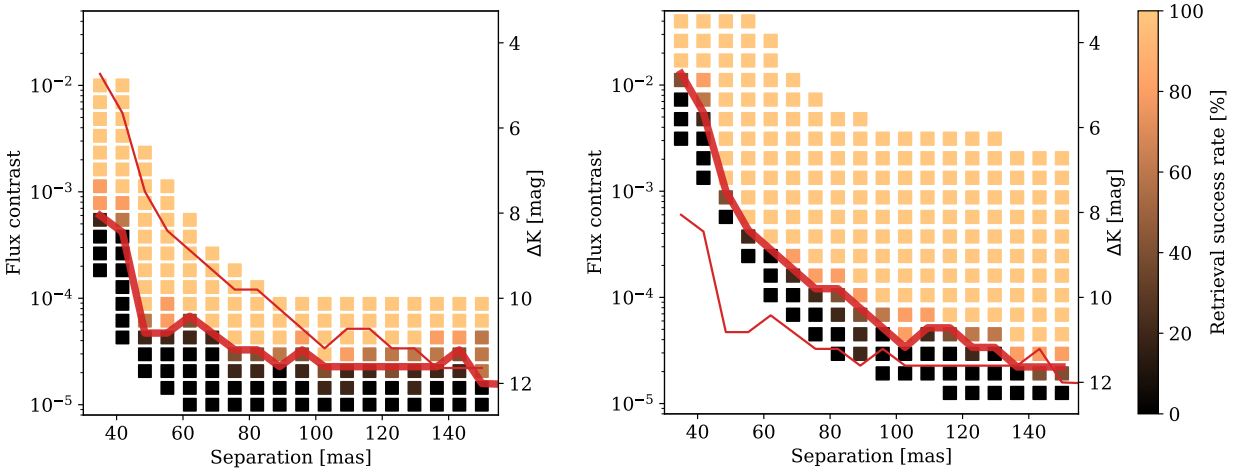

(a) Parallel to longest baselines

(b) Perpendicular to longest baselines

Figure 3.10 – (From Pourré et al., 2024) Empirical contrast curves for ExoGRAVITY from the injection/retrieval analysis. The red lines outline the 1σ limits for the PA parallel to the longest baselines and the PA perpendicular to the longest baselines, thin or thick depending on the background plot.

Fundamental limitations Another important fact from these contrast curves, is their remarkable smoothness with separation despite the fact that I used 5 different observations around different host stars. It is a first clue that, below 150 mas, we are not limited by stellar photon noise. For example,

at 100 mas we pass from a dataset with a host star at 3.5 mag to a host-star at 5.6 mag (×7 fainter). If the detection in the two datasets were dominated by photon noise, we would see a step in the detection limit contrast by $\sqrt{7} \approx 2.6$ at 100 mas (Fig. 3.16). There is no such step in the contrast curve, showing that either we are limited by systematics that scale with the stellar flux instead of scaling with the square root of the stellar flux, or the higher amount of sky rotation in the faint star dataset (see Table 3.5) compensates for the sensitivity step. I further investigate the limitations in Sect. 3.5.

Limit further away In the dataset at 320 mas around AF Lep, the detection limit at the most favorable PA is at 5.1×10^{-6} for 30 min integration time (see Fig. 3.19). It is a good indication of the contrast we can reach around 300 mas. It also shows that the contrast limit decreases with the separation, and thus again points towards a limitation that is related to the star flux injected in the SC.

3.5 Fundamental limitations

After determining the contrast curve, the next step was to investigate the fundamental limitations that prevents the detection of fainter and closer-separation companions.

3.5.1 Inner working angle

A deconvolution limit

In classical Lyot coronagraphic imaging, there is a mechanical inner working angle determined by the size of the focal plane mask. In this configuration, the planet photons get masked from a given separation and there is zero throughput below this limit. On top of that, deconvolution techniques such as ADI and SDI also have a drop in efficiency at lower separations and lead to self-subtraction of the planet signal. Unlike coronagraphic imaging, the dual-fied interferometry with GRAVITY does not have a mechanical inner working angle, the short separation limit is set by the limit of the deconvolution technique.

As already explained in Sect. 2.5.2, the coherent flux injected when the SC fiber is observing the companion is (Eq. (2.48)):

$$\underline{V}_{\text{onplanet}}(b,t,\lambda) = \underline{P}(b,t,\lambda)\underline{V}_{\text{onstar}}(b,t,\lambda) + C(\lambda)\underline{V}_{\text{onstar}}(b,t,\lambda)\exp\left(i\frac{2\pi}{\lambda}\left[\boldsymbol{\Delta\alpha}\,\mathbf{U}(t)\right]\right). \quad (3.6)$$

The deconvolution relies on the fact that the polynomial $\underline{P}$ modulates on low spectral frequencies when the planet signal $\underline{\Theta}(b,t,\lambda) = e^{i\frac{2\pi}{\lambda}[\boldsymbol{\Delta\alpha}\,\mathbf{U}(t)]]}$ modulates on higher spectral frequencies. Going down to shorter separations, the planet signal will modulate on lower and lower frequencies, and ultimately be completely captured by $\underline{P}$ in the speckle fit. This is the fundamental limit of the ExoGRAVITY technique in term of inner working angle. The separation range where it happens depends on the order of the polynomial, more degrees of freedom for $\underline{P}$ encompass higher spectral frequencies and are more likely to capture part of the planet signal. It also depends on the projection

of the planet signal on the UV plane, that determines the planet modulation frequencies on the different baselines.

Tests

I investigated for the loss of planet signal to the polynomial fit. For this, I used an average UV plane representative of the observations with the UT (Fig. 3.11b) and computed the term $\underline{\Theta}$ for several separations and PA. For each planet injected, I obtained a complex planet signal of size (NBASES$\times$N$_\lambda$) and I measured its rms amplitude as:

$$\mathrm{rms}(\underline{\Theta}) = \sum_{b_0}^{\mathrm{NBASES}} \left[\sqrt{\frac{1}{N_\lambda} \sum_{N_\lambda} (\mathrm{Re}(\underline{\Theta}(\lambda)|_{b_n})^2)} + \sqrt{\frac{1}{N_\lambda} \sum_{N_\lambda} (\mathrm{Im}(\underline{\Theta}(\lambda)|_{b_n})^2)} \right]. \tag{3.7}$$

Then, I fit a polynomial of a given order on $\underline{\Theta}(\lambda)$, separately on the real and imaginary part of each baseline. I removed this fit to $\underline{\Theta}$ and obtained the filtered version $\widehat{\underline{\Theta}}$ that represents the residual planet signal after the speckle fit. I computed the residual fraction as $\mathrm{rms}(\widehat{\underline{\Theta}})/\mathrm{rms}(\underline{\Theta})$.

The results are shown on Fig. 3.11. I computed the residual fraction of planet signal $\underline{\Theta}$ for separations from 0 to 200 mas, for three different PA from 60° (optimal) to 120°, and four different polynomial orders from 3 to 8. At PA=60° with a 4$^{\mathrm{th}}$ order polynomial, that is the most commonly used, half of the planet signal is lost below 35 mas. Above 100 mas, almost no signal is lost. this tendency is the same at PA=90° because the planet still induces a signal on all baselines, including the longest. But at PA=120°, the losses are important even at 200 mas separation because the planet is perpendicular to three baselines and the projected length of the three other baselines is reduced. The planet signal modulates on very low frequencies and is captured by the polynomial even at 200 mas separation. Loosing some planet signal to the polynomial does not directly entail that the planet contrast is underestimated by the pipeline. Indeed, the real observations are generally not a static snapshot at one position of the UV plane. There are different baselines orientations along the observations due to sky rotation and this diversity is crucial for the pipeline to retrieve the full planet astrometry and contrast. Even if part of the planet signal is missing in each file due to the capture by the polynomial, the fit can still properly fit the planet and retrieve the right contrast as long as the missing information is not the same in each file. However, at short separations the information loss can be drastic and this capture of the planet signal by the polynomial is responsible for the sudden loss of sensitivity showed in the contrast curves. It happens at 45 mas when the planets are injected parallel to the longest baselines (Fig. 3.10a), at this separation even the signal from the longest projected baselines start to be lost in the fit. When the planets are injected perpendicular to the longest baselines (Fig. 3.10b) the loss is not sharp at 45° but more progressive from 35 to 100 mas.

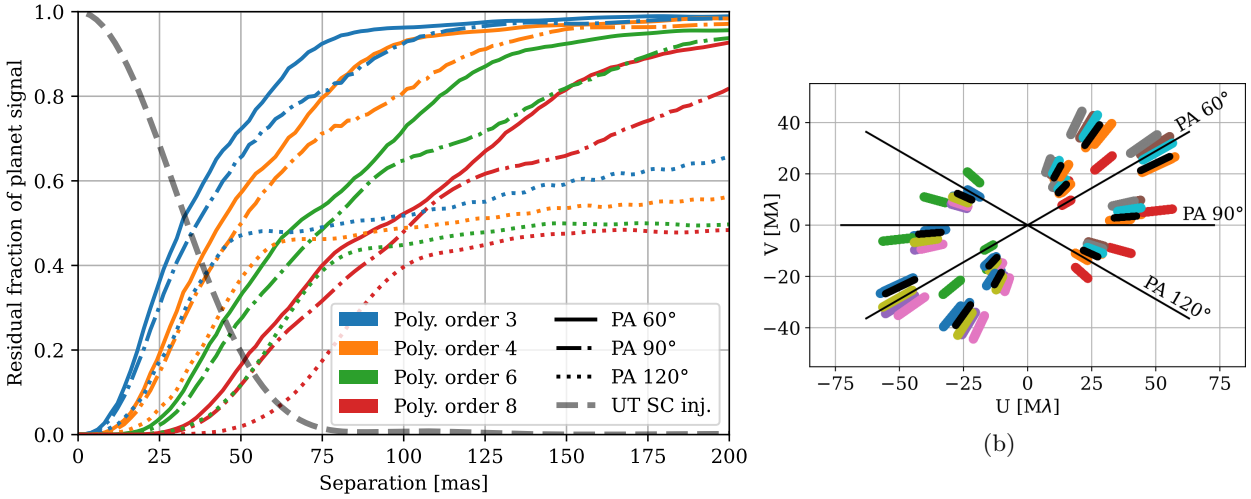

(a) (b)

Figure 3.11 – Influence of the polynomial order on the planet signal subtraction. (a) Simulations. Fraction of planet signal left after speckle subtraction for different polynomial orders and PA. The gray dashed line shows the intensity injected in SC on the UT at diffraction limit, for reference. (b) (color dots) UV plane for the 6 observations used for the contrast curve (Table 3.5). (black dots) Average UV plane used for the simulations of Fig (a).

Towards the 3rd order

This analysis shows that there is an interest in reducing the polynomial order to push the inner working angle. Historically, during the ExoGRAVITY large programme, the default polynomial order was 4. Lower order polynomials proved not sufficient for fitting speckles, and gave erratic results. The situation changed from November 2022 when Sylvestre Lacour, Mathias Nowak and Julien Woillez upgraded the GRAVITY FT in the context of the GRA4MAT commissioning. Before that, the fringe tracker was frequently jumping from one fringe to the neighbor. On GRAVITY, it was responsible for low order features at the border of the K-band that were captured by the polynomial in the ExoGRAVITY pipeline. On MATISSE, it was a major limitation to the data exploitation and thus needed to be solved. The 2022-11-09, during a technical run for the FT upgrade (60.A-9102), Sylvestre observed a brown dwarf at 35 mas separation with PA=27°. This observation is treated in detail in Sect. 5.4.3. Reducing the data, I realized that a 3rd order polynomial provided a stronger companion signal and a slightly more constrained position on the periodogram. Indeed, the FT upgrade was so successful that we obtained this unexpected side effect: the features at the K-band border are greatly reduced and we can use a 3rd order polynomial at short separations.

I made an injection/retrieval test on the 2022-11-09 data to test if the inner-working angle was effectively pushed by the use of the diminution of the polynomial order. I subtracted the companion signal from the data and injected successively companions at 2.7×10^{-3} contrast (same as the brown dwarf detected) from 30 to 58 mas. For each separation, I injected 3 companions at different PA around 27° (the actual fiber PA during the observation). Figure 3.12 shows the results of the retrievals. It shows clearly that below 45 mas the `astrometry_reduce` fit with 4th order polynomials is less reliable than with the 3rd order for retrieving the companion at the right position and contrast. The fit with the 3rd order polynomial detects the three companions injected down to 34 mas, where the 4th order fit is clearly erratic. Above 45 mas, the fit with the 4th order polynomial appears to be

slightly more a accurate. I tested 2nd order polynomials for the sake of completeness but it provided very unstable results. My recommendation would be to use a 4th order polynomial above 45 mas and a 3rd order polynomial below 45 mas. However, this cannot be a strict rule as it depends on the PA of the target. For close companions, or particularly badly oriented ones, the 3rd order polynomial is now an option for achieving better detections even above 45 mas separation.

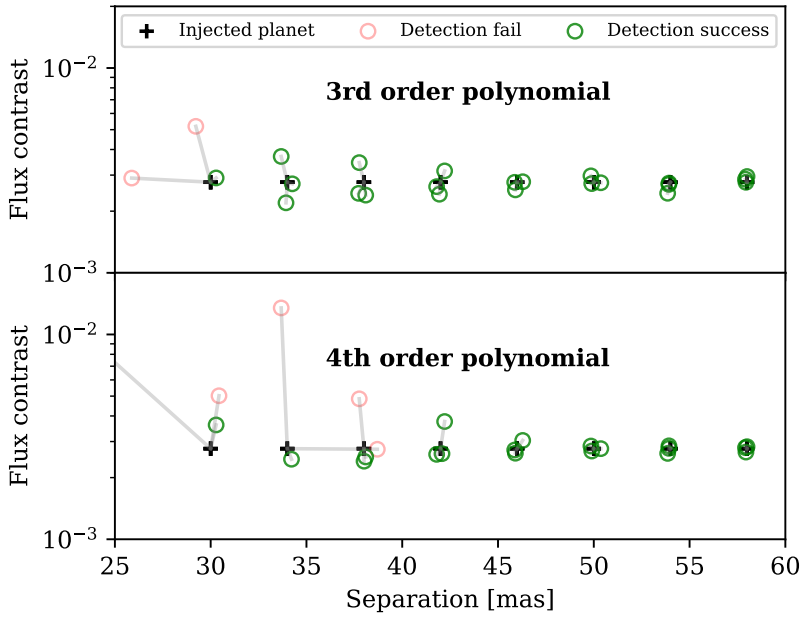

Figure 3.12 – (From Pourré et al., 2024) Injection and retrieval of a companion at 2.7×10^{-3} and different separations. Comparison of the reduction with a (top) 3rd order polynomial and (bottom) 4th order polynomial.

Prospects

A question arises very often in the ExoGRAVITY consortium: "Would you rather have longer baselines or bigger telescopes?". This analysis provides part of the answer. Our observations of exoplanets on the UT at VLTI suffer from non-homogeneously populated UV plane. The PA from 100° to 180 ° (±180°) are poorly probed due to the lack of long baselines in this direction. So, rather than longer baselines, we could use another UT adequately positioned to fill the north/south, north-west/south-east gap. Moreover, the interferometric deconvolution would be increased by the 4 additional baselines. Otherwise, Fig. 3.11a shows that the full-width at half maximum of central lobe of the UT PSF injection matches exactly the point where half of the planet signal is lost due to its interplay modulation with the speckles. I doubt it was foreseen by the visionary creators of VLTI, but it shows that the 8-meters UTs are a reasonable choice for working with 130 meter baselines in the near-infrared. For more answers to this question, a thorough study of the fundamental noises limiting the detection is required.

3.5.2 Photon-noise or systematics limited?

I have shown in the previous section that the polynomial speckle fit was limiting the exoplanets' detections at separations below 45 mas. The fundamental limitation on the plateau from 50 to 150 mas is still left to determine.

Comparison of two photon regimes

Method A simple look at the contrast curves of Fig. 3.10 shows that the contrast limit decreases with separation, the injection/retrieval at 320 mas makes it even more visible (full contrast curve in Fig. 3.19). It is a good indication that we are not limited by detector noise, but by a noise source related to the stellar flux injected in SC. To determine if the limitation comes from photon noise, I made another test based on injection/retrieval. I selected the two datasets of Table 3.5 where the SC fiber is around 100 mas: β Pic (K*=3.5 mag) with the fiber at 92 mas and a total of 13×32×10 s (69 min) integration, and HD 206893 (K*=5.6 mag) with the fiber at 111 mas and a total of 27×32×10 s (144 min) integration. For each dataset, I simulated shorter integration times by selecting a limited number of successive NFILES among the total NFILES×NDIT×DIT available. Then, I injected 7 planets at 100 mas and different PA around the most favorable orientation with respect to the UV plane. Starting from injections at a contrast where I was sure to retrieve all the injections, I decreased the contrast by steps of 1×10^{-6} until I retrieved less than 5 companions over the 7 injected (1σ limit). The conditions for successful retrieval are the same as previously: less than 3 mas from the injected position, less than 50% error on contrast. I recorded the contrast limit for different exposure times on each dataset.

Results The results for these tests are shown in Fig. 3.13. There are two ways to plot the contrast limit, either as a function of the number of star's photons injected in the SC (Fig. 3.13a), or as a function of the integration time (Fig. 3.13b). When plotted in number of photons, we can see that the contrast limits on HD 206893 do not align with the contrast limits on β Pic. If the observations were limited by the stellar photon noise, they would align proportionally to the inverse square root of the number of stellar photons injected (Poisson statistics). This is a proof that, at 100 mas, we are not at the fundamental limit of photon noise. Instead, when I plot the contrast limit with respect to the total integration time, we can see that it aligns well along a line of equation $1.5 \times 10^{-3} \times (\sqrt{t})^{-1}$. It shows that increasing the observing time pushes down the detection floor, down to 1.6×10^{-5} contrast for 144 min total exposure time.

Analysis Since the detection limit seems to depend solely on the integration time and not on the host star magnitude, I conclude that we are limited by systematics that scale with the number of injected photons. I see two possible reasons that could explain why the contrast limit decreases with integration time. First, the systematics can vary with their own coherence time and a longer exposure time averages them out. This is similar to direct imaging observations limited by the coherence time of speckles for detection with differential techniques. Second, even on static systematics, the sky rotation adds some diversity between the noise and the signal and can explain the benefit of longer observations. The β Pic observation has a total sky rotation (variation of parallactic angle) of 60° and the HD 206893 observation has 115° sky rotation. This could explain why β Pic contrast limits lie above the HD 206893 limits. These two reasons are not exclusive, and both phenomena could play a role in our detections.

I show here that the contrast limit at 100 mas depends fully on the integration time. This result does not match the result I obtained in Sect. 3.3.1, where I showed that the detection limit depended

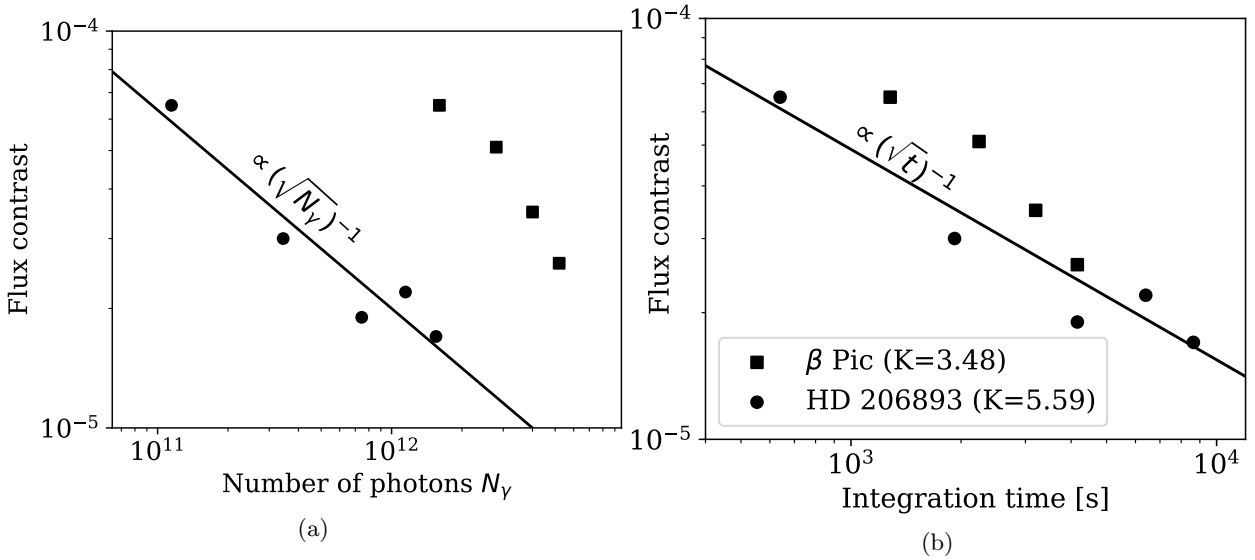

(a) (b)

Figure 3.13 – Detection limits for different integration times on two datasets: HD 206893 (2021-10-16) and β Pic (2021-01-06). Planets injected at 100 mas. (a) Expressed in number of photons estimated from the star's magnitude, the VLTI transmission and loss of injection at 100 mas. (b) (From Pourré et al., 2024) Expressed in integration time.

on the companion magnitude but not on the contrast. However, this previous study was fully based on the periodogram power that takes into account only the error bars computed by the GRAVITY pipeline (photon noise, read-out noise). I believe that the results presented in the current section are more reliable, since they are based on retrieval of the injected planet properties (position and contrast) and, thus, take into account the noise structures that are not captured in the error bars. To confirm the conclusion I draw here, it would be interesting to develop this study at different separation and with data around different host stars.

The level of statistical noise

To identify the nature of the limiting noise, I performed another test. It consisted in adding Gaussian noise to the data and measuring the impact on the detection limit.

Method For this, I used the HD 206893 (2021-10-16) dataset limited to $5 \times 32 \times 10$ s, the same exposure time used for the contrast curve computation of Sect. 3.4.3. I wanted to measure the noise rms in the data without the contribution of the low frequency systematics. For this, I collected the residual noise from the observations without planet injected, real and imaginary part separately, and I filtered to keep only the higher half of spectral frequencies. Then I found the level of white Gaussian noise required to have the same power in the high frequencies. I call this level the normalized rms noise. Then I added the white noise to the `VISDATA`. Each NFILES, NDIT, baseline, and real and imaginary parts have a different realization of the noise. The final step is to launch the injection/retrieval to find the new detection limit.

Results and analysis Figure 3.14 shows the results of this analysis. It shows that the detection limit is not directly affected by the addition of white noise. It has a small plateau between 1 (original

noise) and ×2∼3 normalized rms noise. After this plateau, the contrast limit rises proportionally with the noise and indicates that the SNR is driven by the Gaussian noise added. This analysis tends to show that the statistical noise floor is only $\times 2 \sim 3$ below the limiting systematics. I confirmed this result by measuring the contrast limit of fully synthetic data, namely, with only Gaussian noise and a synthetic planet signal in the `VISDATA`. The Gaussian noise is at the same normalized rms as the real data. In this case, I found a 1σ contrast limit at 9×10^{-6} instead of the original 2.5×10^{-5}. It shows that, additional to the statistical noise, there are structures in the visibilities that limit the achievable contrast.

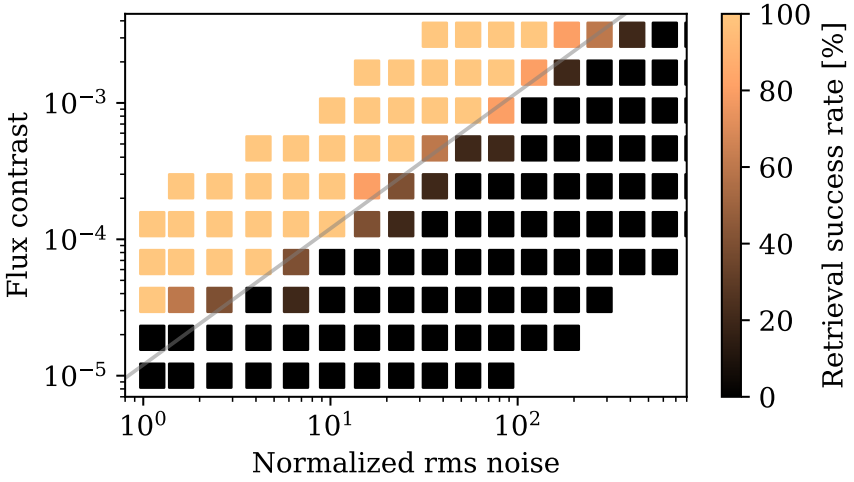

Figure 3.14 – Retrieval success rate at 100 mas when injecting additional Gaussian noise in the HD 206893 (2021-10-16) dataset. Normalized rms noise of 1 is the original noise in the data. Normalized rms noise of 10 is ×10 the original noise rms amplitude. (gray line) ax line for reference.

Conclusion

The conclusions are illustrated in Fig. 3.15. I have shown that the exoplanet observations with GRAVITY are limited at 100 mas by systematics that scale with the amount of star flux injected in the SC fiber when it points at the exoplanet. This is a good sign, since the new GRAVITY+ adaptive optics will reduce the amount of star flux injected and have a direct linear impact on the contrast limit. Then, I showed that the statistical noise floor was $\times 2 \sim 3$ below the contrast limit in the HD 206893 dataset of 27 min. I know from discussions on this topic with Frank Eisenhauer that observations of the galactic center stars reach a noise floor at K=19 mag. The statistical noise floor I measured (red in Fig. 3.15) is at K=18.2 mag. It would be very interesting to make the same analysis as Fig. 3.14 on the β Pic dataset. If the statistical noise appears to be at the same magnitude (around K=18.2 mag) it would be a confirmation that we reached a floor that is not related to star flux, maybe the same floor that limits the observation of faint free-floating objects with GRAVITY.

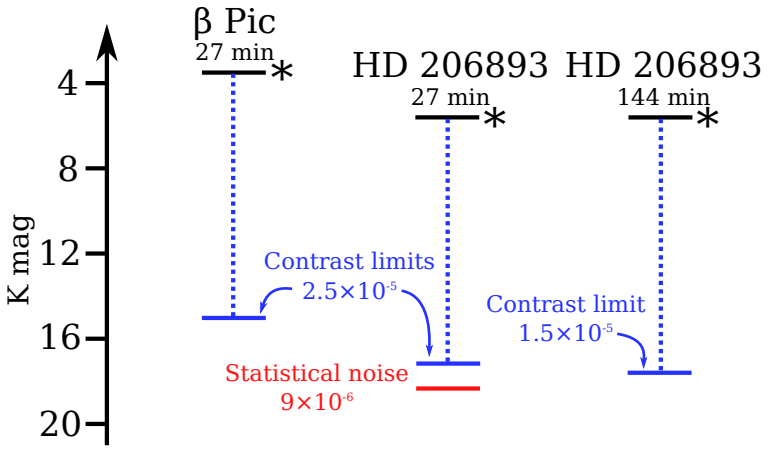

Figure 3.15 – Schematic summary of the detection limits at 100 mas measured in this section.

3.5.3 Theoretical noise level

So far, I have determined the limits of the ExoGRAVITY observations with an empirical method based on injection/retrieval. However, it is also possible to draw the contrast curve theoretically with an estimate of each noise contributor. Especially, we can learn a lot from the comparison between the empirical and theoretical methods. I was very lucky that, at this point of my PhD, Alexis Bidot was also willing to estimate the theoretical noise in GRAVITY. Alexis was a PhD student[4] working on an analytical model for estimating molecular mapping limitations in the instrument HARMONI (Bidot et al., 2024) on the Extremely Large Telescope (ELT) and he wanted to expand his analysis to other instruments observing exoplanets. We worked together on the theoretical noise level of GRAVITY.

Method The first step is to estimate the theoretical flux F_s for a star of a given magnitude m_k. It is:

$$F_s = Z_p \times 10^{-\frac{m_k}{2.5}} \times B_w \times \frac{1}{E_\gamma} \times f_{ill} \times \frac{\pi\, D^2}{4} \tag{3.8}$$

with:

- $Z_p = 4.29 \times 10^{-10}$ W.m^{-2}.µm^{-1}, the zero-point flux of the 2MASS K-band.
- $B_w = 0.4$ µm, the bandwidth of the K-band.
- $E_\gamma = \frac{h\,c}{\lambda_0} = 9.2 \times 10^{-20}$ J, the energy of a photon of $\lambda_0 = 2.2$ µm.
- $f_{ill} = 0.97$, the effective factor of surface on the UT that is not obscured by the M2 and the spiders.
- $D = 8$ m, the diameter of the UT primary mirror.

For example, for HD 206893 of magnitude $m_k = 5.6$, each UT receives a flux in K-band:

$$F_s = 5.23 \times 10^8 \text{ photons.s}^{-1}$$

[4]He defended his PhD successfully in November 2023

The theoretical SNR taking into account the photon noise and the detector noise is:

$$\text{SNR} = \frac{\text{planet signal}}{\sqrt{(\text{Photon noise})^2 + (\text{Read-out noise})^2}} \tag{3.9}$$

$$= \frac{\eta\, T\, v_i\ (\sum_{\text{tel}} C_\sigma\ F_s)\ \text{DIT}\ \text{NDIT}_{\text{tot}}}{\sqrt{\xi(s)\ T\ (\sum_{\text{tel}} F_s)\ \text{DIT}\ \text{NDIT}_{\text{tot}} + \text{RON}^2\, N_{\text{pixels}}\, \text{NDIT}_{\text{tot}}}} \tag{3.10}$$

with η the fraction of the planet signal that is not captured by the polynomial fit (see Sect. 3.5.1), T the total transmission of the VLTI and GRAVITY, v_i is the instrumental visibility, $\sum_{\text{tel}}$ is the sum over the 4 telescopes, C_σ the planet contrast, ξ the fraction of star flux injected in the SC at the separation s, RON the read-out noise of the camera and N_{pixels} the number of useful pixels read on the camera. For a given SNR, we can estimate the corresponding contrast:

$$C_\sigma(s) = \text{SNR}\ \frac{\sqrt{\xi(s)\ T\ (\sum_{\text{tel}} F_s)\ \text{DIT}\,\text{NDIT}_{\text{tot}} + \text{RON}^2\, N_{\text{pixels}}\, \text{NDIT}_{\text{tot}}}}{\eta\, T\, v_i\ (\sum_{\text{tel}} F_s)\ \text{DIT}\,\text{NDIT}_{\text{tot}}}. \tag{3.11}$$

In this analysis, we use the following values:

- $\xi(s)$ is estimated thanks to measurements of total flux at different separations. I simulated a continuous injection profile with HCIPy (more details in Sect. 5.4.1).
- $T = 0.01$, this is the common value for the fraction of K-band photons that reaches the SC detector. I verified this number by comparing the theoretical flux F_s per telescope (Eq. 3.8) and the flux measured in the SC. I obtained values between 0.008 and 0.015 depending on the observation.
- DIT=10 s.
- NDIT_{tot}= NFILES×NDIT=5×32=160.
- RON = 9 photons/DIT on the Hawaii-2RG detector.
- N_{pixels}=6 baselines× 4 ABCD channels× 233 pixels of the spectrum (MEDIUM res.) × 2 pixels width = 11184 pixels. The useful pixels on the detector.
- η is the fraction of the planet signal that is not captured by the polynomial speckle fit. It is similar to the profiles shown on Fig. 3.11a. Here we considered 4^{th} order polynomials and only baselines of 100 m.
- v_i=0.8. The estimated fraction of total flux that makes fringes. Thanks to this, we can estimate the level of planet coherent flux from stellar total flux F_s and the contrast C_σ.

Results The results for the theoretical contrast limit with respect to separation are on Fig. 3.16. There is a crenelation pattern on the theoretical curves because I used different star magnitudes with respect to separation (Table 3.5). This is to match the setup of the empirical curve and be representative of where the empirical curve should be if it was limited by photon noise. Indeed, for a brighter host star there is more star flux injected in the SC and the photon noise level follows the square root of this flux. Hence, expressed in flux contrast, the noise level is lower on brighter star. I definitely conclude that ExoGRAVITY observations at less than 150 mas are not limited by photon noise because this crenelation is not visible on the empirical contrast curve. The theoretical

curve at SNR=3 is given for reference, but this is the curve at SNR=1 that directly compares to the empirical curve. At SNR=1, the theoretical contrast limit lies well below the empirical contrast. For HD 206893 at 100 mas, it is a factor 10. For β Pic at 95 mas, it is a factor 37. From Fig. 3.16, I also conclude that the photon noise dominates largely the read-out noise. It is therefore the main noise contributor in our theoretical analysis.

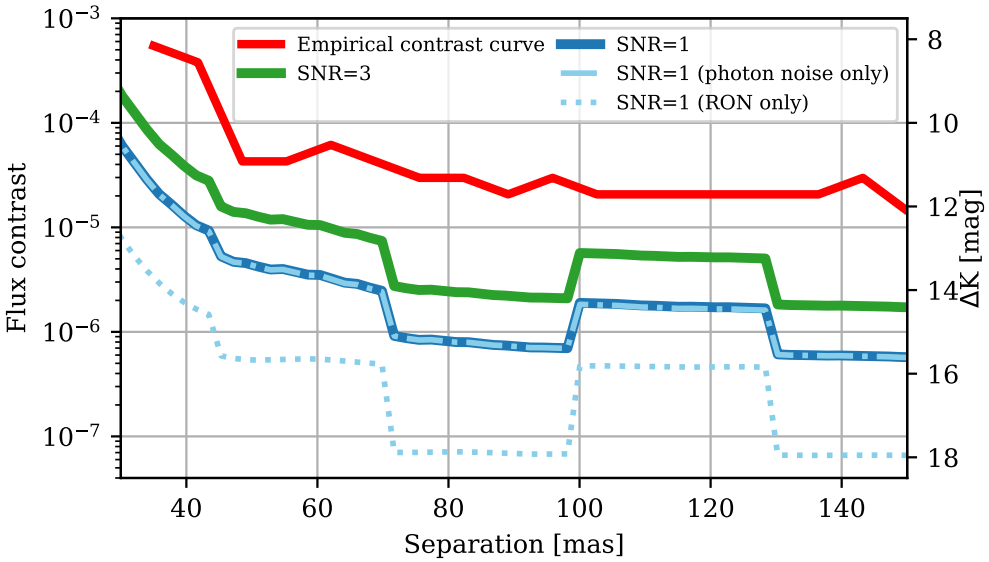

Figure 3.16 – Comparison of theoretical curves at SNR 1 and 3 with the empirical contrast curve derived at 1σ by injection/retrieval with a favorable PA. The separate contributions of read-out noise (RON) and photon noise are shown for SNR=1.

Conclusion Computing the theoretical photon noise level is an additional proof that the current observations are limited by systematics that scale with the star flux. Here, I found that the photon noise was $\times 10$ below the empirical contrast limit. However, in the previous section, I found that the statistical noise level at 100 mas was $\times 2 \sim 3$ below the effective contrast limit in HD 206893 observations. It shows that our theoretical noise analysis miss an important noise contributor, maybe the same noise floor that we know is limiting the observations of faint stars that are not in a high-contrast regime.

3.5.4 Noise level in the data

One last possibility to determine the noise limit in ExoGRAVITY observations is the most straightforward: measure the noise level in the data.

Method For this, I analyzed the observations around β Pic on 2021-01-06 with the fiber at 92 mas and HD 206893 on 2021-10-16 with the fiber at 111 mas (same as Sect. 3.5.2). The `OI_VIS` table in the `astroreduced` files contains the referenced complex visibilities. From these data of each NFILES of the observations, I subtracted the speckle fit and the planet fit I obtained thanks to the `astrometry_reduce` script of the ExoGRAVITY pipeline. This way, I obtained the residual from the observation data. This is the process described in Eq. 4.1 that is of paramount importance in the next chapter (Chapter 4). Since the planet and the speckle fit are removed, the residuals contain

only the noise (statistical and systematics). The intensity in each spectroscopic channel is stored in unit of photo-electrons in the `OI_VIS` table. So, I computed the noise $\mathcal{N}_{\rm res}$ in the complex visibilities residuals R as:

$$\mathcal{N}_{\rm res}(b,\lambda) = \frac{1}{\text{NFILES} \times \text{NDIT}} \sum_t |R(b,t,\lambda)|, \tag{3.12}$$

with b the baseline and t the observing time composed of NFILES×NDIT exposures. So the noise $N_{\rm res}$ is representative of the noise level on one exposure of 10 s.

The `astroreduced` file also includes the `OI_FLUX` table compiling the individual total flux F_1, F_2, F_3 and F_4 received by each telescope, as computed from fluxes measured on the SC camera. From this, I can estimate $\mathcal{N}_{\rm phot}$ the photon noise associated:

$$\mathcal{N}_{\rm phot}(b,\lambda) = \frac{1}{\text{NFILES} \times \text{NDIT}} \sum_t \sqrt{\frac{F_{b1}(t,\lambda) + F_{b2}(t,\lambda)}{3}}, \tag{3.13}$$

where F_{b1} and F_{b2} are the respective flux on the two telescopes constituting the baseline b. The division by 3 accounts for the split of each telecope flux to form the 3 related baselines.

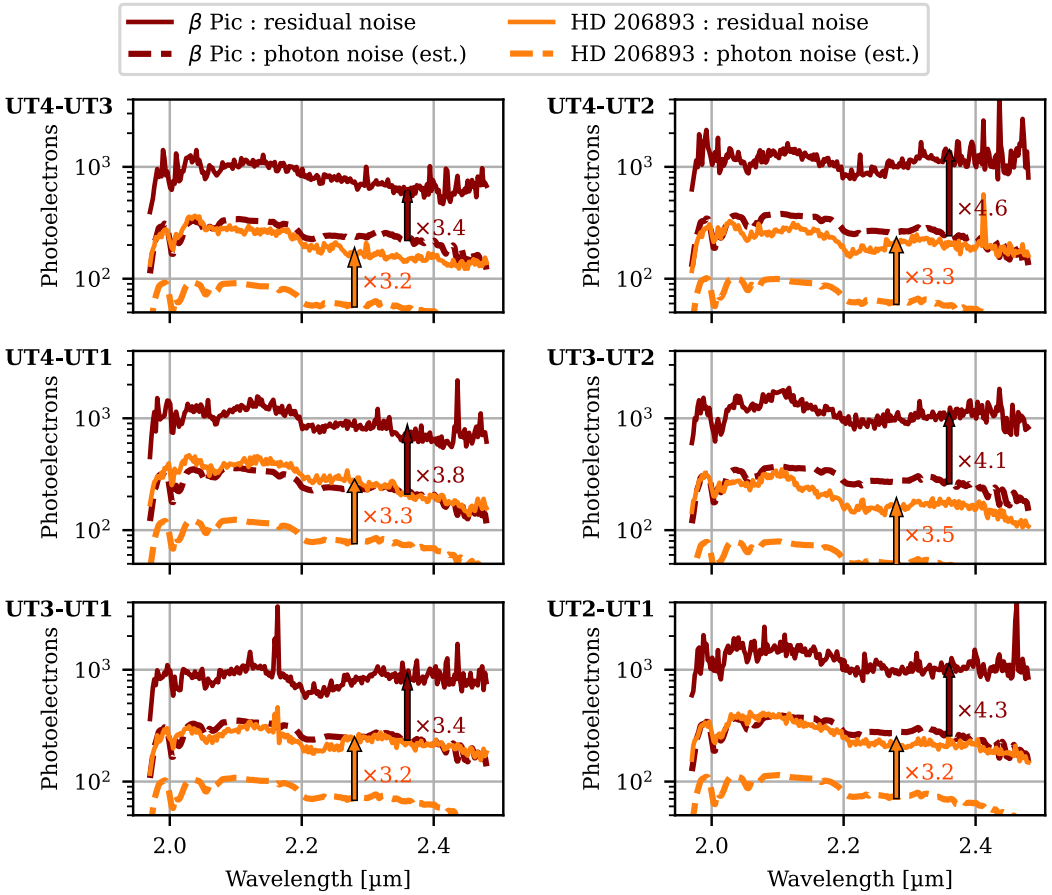

Figure 3.17 – Comparison of the residual noise amplitude in the complex visibilities with the estimated photon noise from the observed flux. Both represent the average noise level over 160 exposures of 10 s. The orange and red numbers corresponds to the average scaling between the residual noise and the estimated noise.

Results The results are shown in Fig. 3.17. The actual noise in our observations residuals is ×3.3 above the photon noise for HD 206893 and ×4 above for β Pic. The data are in full accordance with the previous analysis, so everything shows that the noise level in the data is above the photon noise level. Also, I found that the photon noise estimated from the observed fluxes (dashed on Fig. 3.17) matches well the theoretical noise computed in Sect. 3.5.3.

Conclusion

My analysis of the fundamental limitations for exoplanet observations with GRAVITY conclude that we are currently limited by systematics that scale with the star flux injected in the SC fiber when we observe the companion.

Despite my detailed analysis, I did not yet obtained a complete view on the noise contributors at 100 mas in the specific dataset of HD 206893 on 2021-10-16. As shown in Fig. 3.18, the residuals observed in the data at Sect. 3.5.4 are ×3 higher than the photon noise, not enough to fill the ×10 gap we found theoretically at Sect. 3.5.3. The theoretical noise level and the measurements of residuals in the data were only taking into account the norm of the complex visibilities $\underline{V}$. For future work, it would be interesting to investigate if structures in the phase of $\underline{V}$ could be responsible for the gap between the empirical contrast limit and the residuals level in the data.

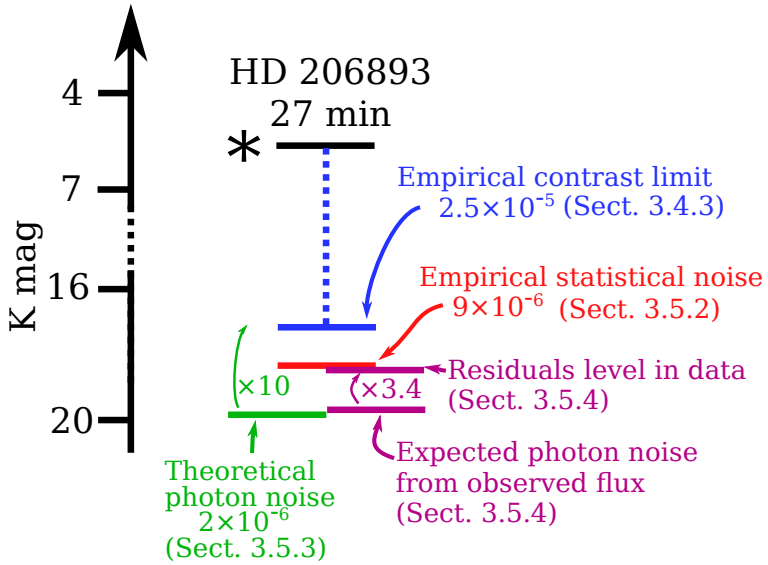

Figure 3.18 – Summary of the noise levels estimated or measured in this chapter in the HD 206893 dataset of 2021-10-16.

As the situation is about to change at VLTI, with the upgrade from GRAVITY to GRAVITY+. I would recommend to replicate this analysis and push it further with new data collected after the adaptive optics commissioning.

3.6 Comparison with other instruments and techniques

Drawing the ExoGRAVITY contrast curve is useful not only for identifying the main limitations of the technique, but also allows for comparisons with other instruments.

I have to remind here that the GRAVITY curve I computed focuses on the shortest separations achievable with the instrument on the UT, from 30 to 300 mas. It represents only the innermost region of the DUAL-ON-AXIS mode and does not include the detection of binaries down to 2 mas using closure-phase, the outer ON-AXIS (up to 600 mas), and the OFF-AXIS mode (up to 2000 mas).

Comparison at short separation

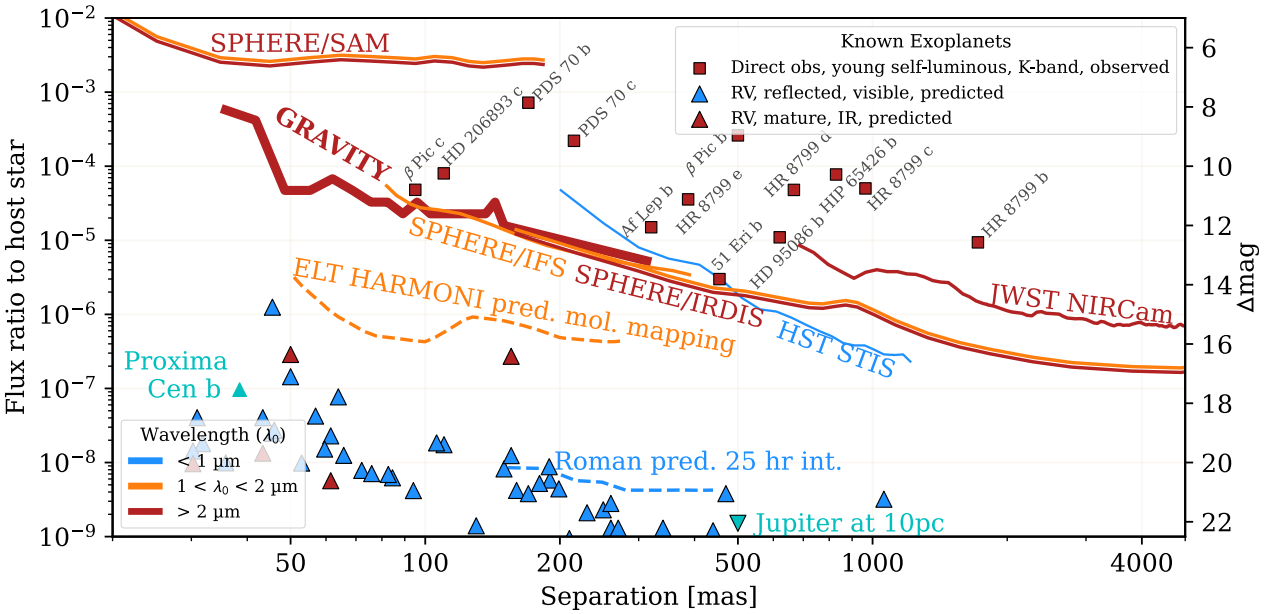

Figure 3.19 – Contrast curves for some instruments dedicated to direct observations of exoplanets. Adapted from `https://github.com/nasavbailey/DI-flux-ratio-plot`. SPHERE/IFS in YJH and IRDIS in HK bands from Chomez et al. (2023a). SPHERE/SAM from Stolker et al. (2024). ELT/HARMONI from Houllé et al. (2021). HST/STIS from Ren et al. (2017). JWST/NIRCAM from Carter et al. (2023). Roman space telescope prediction for 25 hours exposure time (from personal communication of V. Bailey). (red squares) Exoplanets directly observed with GRAVITY, contrast at K-band as measured on GRAVITY. (blue triangles) Visible contrast estimation for exoplanets detected by radial-velocity cataloged in the NASA exoplanet archive. The estimation follows a Lambertian model assuming radii of 1 R_{Jup} and geometric albedo of 0.5. (red triangle) Infrared contrast estimated for exoplanets detected by radial-velocity. Computed from estimated equilibrium temperature and assuming radii of 1 R_{Jup}. All visible and infrared contrast calculations are based on Traub and Oppenheimer (2010).

Figure 3.19 shows the contrast curve of several instruments dedicated to direct observations of substellar companions. First, it shows that GRAVITY is the only instrument that can directly observe planetary-mass companions below 100 mas. It demonstrates that infrared interferometry unlocks a parameter space at short separations that was previously unprobed by direct imaging techniques.

The single-telescope aperture masking on SPHERE (SAM) is capable of probing very short separations, but the contrast limit is ×100 above the GRAVITY limit. It highlights the benefits from interferometric deconvolution on 130 m baselines compared to UT aperture baselines. Compared to classical coronagraphic imaging, the GRAVITY curve aligns well with the SPHERE/IFS and IRDIS contrast curves above 100 mas. So far, β Pic c and HD 206893 c have only been directly observed by GRAVITY. The SPHERE/IFS curve seems to imply that both planets are in the reach

of SPHERE, but the IFS curve is at YJH bands and the planets are plotted with their K-band flux. From discussions with Antoine Chomez and Philippe Delorme, we concluded that the contrast of these two planets at YJH-bands was much less favorable than at K-band. This explains why these two exoplanets have never been observed by SPHERE.

In the future, the high-contrast mode of HARMONI and the molecular mapping technique might reach direct imaging at separations comparable with GRAVITY and down to 3×10^{-6} contrast at H-band (Houllé et al., 2021).

Until now, spatial imaging with HST or JWST has never been able to reach the inner-working angle of ground-based instruments. This is due to both limited size primary mirrors (HST: 2.4 m, JWST: 6.5 m) and lack of adaptive optics for fine aberration control. Future space observatories (Roman space telescope, HWO) will have to bridge this gap in order to fulfill their ambitious goal of detecting solar-system planet analogues in reflected light.

Instrumental synergies

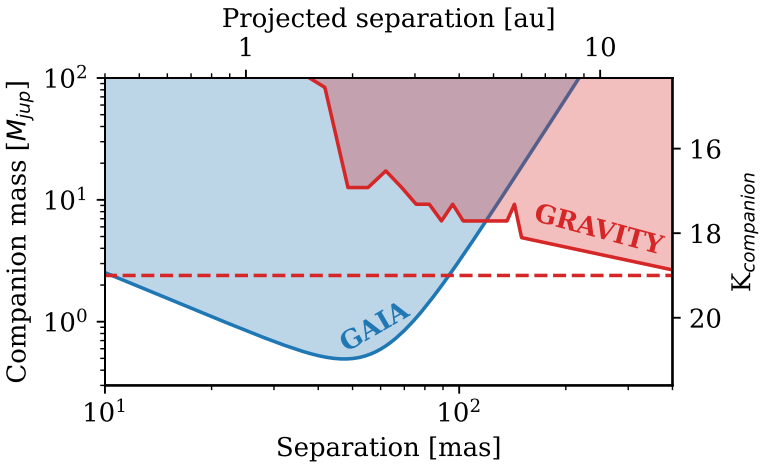

Figure 3.20 – (From Pourré et al., 2024) Comparison of the Gaia and GRAVITY sensitivity in a mass-vs-projected-separation plot for a star of K=6 mag at 40 pc. The Gaia curve is from Sozzetti (2010). I scaled the GRAVITY contrast curve in companion mass using previous substellar companion observations characterized with the ExoGRAVITY program. (red dashed) Estimation of the fundamental limit of GRAVITY observation for free-floating objects.

One of the biggest limitations of these contrast curve comparisons is that it put asides the specificity of each instrument, and thus the possible fruitful synergies. For example, GRAVITY has comparable detection limits as SPHERE but has a limited field of view that makes it poorly suitable for blind search of exoplanets. However, once the planets have been located by SPHERE, GRAVITY is able to get the relative astrometry at an unchallenged 50 µas precision, and obtain the companion K-band spectrum at $R \sim 500$ during the same observations. Similarly with the ELT instruments like HARMONI, GRAVITY will not compete with their field-of-view, but will remain an excellent tool for exoplanet characterization. As already discussed in Chapter 1, the most promising synergy foreseen is with the space telescope Gaia that will deliver astrometric detection of thousands of exoplanets with the data release 4 in 2026. Figure 3.20 shows an estimate of the sensitivity overlap between Gaia and GRAVITY. It shows that thanks to its ability to detect down to 50 mas, GRAVITY will

be able to characterize a significant fraction of exoplanets whose positions have been previously deduced by Gaia absolute astrometry. The actual number of exoplanets directly observed is less than 20. Thanks to Gaia, we can expect that this number will explode in the 5 years to come and GRAVITY+ will make this possible even before the first light of ELT instruments.

3.7 Zoom-in: (non-)detection of a circum-companion disk

Introduction

In the young stellar objects and exoplanet communities, there is a growing interest to obtain direct constraints on the presence of disks around sub-stellar companions. It has been a few years that the presence of material orbiting companion exoplanets and brown-dwarfs has been established from the analysis of infrared excess and accretion signature in emission lines (e.g. GQ Lup B: Seifahrt et al. (2007), Marois et al. (2007), Demars et al. (2023); GSC 06214-00210 b: Bowler et al. (2011); Delorme 1(AB)b: Eriksson et al. (2020)). This matter is expected to form a circum-companion disk, the kind of disks where satellites can form (Canup and Ward, 2002). These circum-companion disks are necessarily compact because of the low mass of companions (below 100 $M_{\rm Jup}$) and the gravitational influence of the host star. It is commonly acknowledged that the disk cannot be more extended than 1/3 of the Hill radius (Ayliffe and Bate, 2009), this predicts disks of radius of at most a few au. To obtain direct observations of these disks, astronomers naturally turned to interferometry. Benisty et al. (2021) describes a detection of unresolved material around PDS 70 b and c with ALMA. Wang et al. (2021b) observed the same PDS 70 b and c with GRAVITY and the UT from 2018 to 2020. On GRAVITY, they used the visibilities per baseline to determine an upper limit for the circum-planetary disks' extension. They did not detect any loss of visibility that would betray a spatial extension of the planets' light distribution. Still, they could constrain the maximal disk extension, and assuming a bright disk they found a 3σ limit at 0.14 au for b and 0.24 au for c.

Observations of GQ Lup B

At the beginning of my PhD, Mickaël Bonnefoy brought to my attention that the companion brown-dwarf GQ Lup B would be an ideal target for a tentative detection of circum-companion disk with GRAVITY. We know that it is accreting thanks the observations of Hα and Paschen β lines observed by (Marois et al., 2007) on Subaru and HST, and by (Seifahrt et al., 2007) and Demars et al. (2023) on VLT/SINFONI. It orbits at 700 mas from the host-star, at this separation the disentanglement with stellar light is not challenging. Also it has a mass estimated between 10 and 42 $M_{\rm Jup}$ that lets us hope for a more extended disk than the PDS 70 planets. I submitted a proposal as PI to apply for GTO NAOMI time on GRAVITY and the AT. Unfortunately, it was rejected. However, a brown-dwarf monitoring programme led by Jason Wang started at the same time on GRAVITY/AT, and GQ Lup B was on the target list. His goal was to get the brown-dwarf astrometry at different epochs. So, at each epoch, he was doing integrations of 27 min in total in the astrometric array configuration. This is enough for a good detection and astrometry, but for a characterization of the companion disk I would rather have had two times 2 hours integrations, one with the astrometric array to benefit from the long baselines of the AT, one with the small array to

Date	Target	Airmass	τ_0 [ms]	Seeing [arcsec]	ΔRA/ΔDEC	NFILES/NDIT/DIT
2022-08-14	GQ Lup A	1.10-1.23	3.6-5.0	0.5-0.7	0/0 mas	5/4/30 s
	GQ Lup B	···	···	···	-700/109 mas	4/4/100 s
2022-09-06	GQ Lup A	1.21-1.47	3.8-6.7	0.7-1.2	0/0 mas	5/4/30 s
	GQ Lup B	···	···	···	-700/109 mas	4/4/100 s
2023-03-19	GQ Lup A	1.17-1.32	4.8-6.4	0.9-1.2	0/0 mas	5/4/30 s
	GQ Lup B	···	···	···	-700/109 mas	3/4/100 s

Table 3.6 – Observing log for the GQ Lup B observations on GRAVITY and the AT.

have a full coverage of the UV plane. Be that as it may, Jason Wang kindly handed me his data so I could run my analysis. He used the DUAL-ON-AXIS mode of the instrument with the MEDIUM resolution. The observing log is on Table 3.6.

Data reduction and disk model

For the data reduction, I used the ExoGRAVITY pipeline. By ignoring all baselines but one, we can obtain the contrast per baseline and the 1σ error based on the contrast standard deviation on separate NFILES. To overcome the lack of short baselines (Fig. 3.21b), I used the K-band contrast of GQ Lup B measured by Neuhäuser et al. (2008) on VLT/NACO as a 0m-baseline visibility, the contrast is $(3.28\pm0.67)\times10^{-3}$. All points are shown on Fig. 3.21a. On GRAVITY visibilities from the three epochs and the 0m-photometry, I fit a model composed of a point source and a Gaussian disk in the UV plane. The model is:

$$M(B, F_p, F_d, W_d) = F_p + F_d \exp\left[-\frac{\pi^2}{4\ln 2}\left(\frac{B}{\lambda}\right)^2 W_d^2\right] \tag{3.14}$$

with B the baseline length, F_p the point source flux, F_d the peak flux of the Gaussian disk and W_d the full-width at half-maximum of the disk in the object space (light distribution on-sky). The three parameters for the fit are W_d, the flux ratio $R = F_d/F_p$ and the total flux $F_t = F_d + F_p$. I vary these three parameters in the ranges $W_d = [0, 1.42]$ au, $R = [0, 0.5]$ and $F_t = [1.8, 4.8] \times 10^{-3}$ contrast with the primary GQ Lup A. To obtain a reduced χ^2 equal to one for the best fit, I had to shrink the error bars by a ratio of 0.785. Since the errors are only computed from the dispersion of small samples (NFILES=4 or 3), it was expected that the error bars would need some adjustement to be statistically meaningful. With these data and the model, I obtained the χ^2 map showed in Fig. 3.22.

Results

This analysis leads to a non-detection, the best fit is obtained with a zero disk flux ($F_d = 0$). However it puts constraints on the maximal extent the disk can have. For example, Fig. 3.22 shows that a disk of 0.5 au width and contributing to $\times0.45$ of the companion flux would have been detected with a 2σ confidence level. The 1σ limit indicates that assuming a flux ratio of 0.15, the disk is not wider that 0.3 au. Because we lack visibilities at baselines shorter than 50 m, a bright disk of more than 0.8 au width is compatible with the data. As shown with the dashed line on Fig. 3.21a, a

bright extended disk can induce the visibility loss between 0 and 40 m baselines, where we have no measurements, and have constant visibilities for longer baselines. This explains the loosening of the disk constraints for more than 0.8 au wide disk on Fig. 3.22.

The Hill radius r_H of GQ Lup B is:

$$r_H = a(1-e)\sqrt[3]{\frac{M_\mathrm{B}}{3M_\mathrm{A}}} \qquad \text{For } M_\mathrm{B} = 10\,M_\mathrm{Jup} \Rightarrow r_H = 13\,\mathrm{au} \qquad \text{For } M_\mathrm{B} = 40\,M_\mathrm{Jup} \Rightarrow r_H = 21\,\mathrm{au}, \tag{3.15}$$

where M_B is the mass of GQ Lup B, $M_\mathrm{A} = 1.02\,M_\odot$ (MacGregor et al., 2017) the mass of the primary, $a = 117^{+24}_{-23}$ au (Stolker et al., 2021) the semi-major axis and $e = 0.24^{+0.32}_{-0.17}$ the eccentricity of B orbit (Stolker et al., 2021). For the Hill radius of GQ Lup B with the lightest mass this corresponds to a theoretical diameter limit of $(13/3) \times 2 \approx 9$ au for the circum-companion disk. New observations with shorter baselines would help to draw a conclusion on the wide-disk hypothesis.

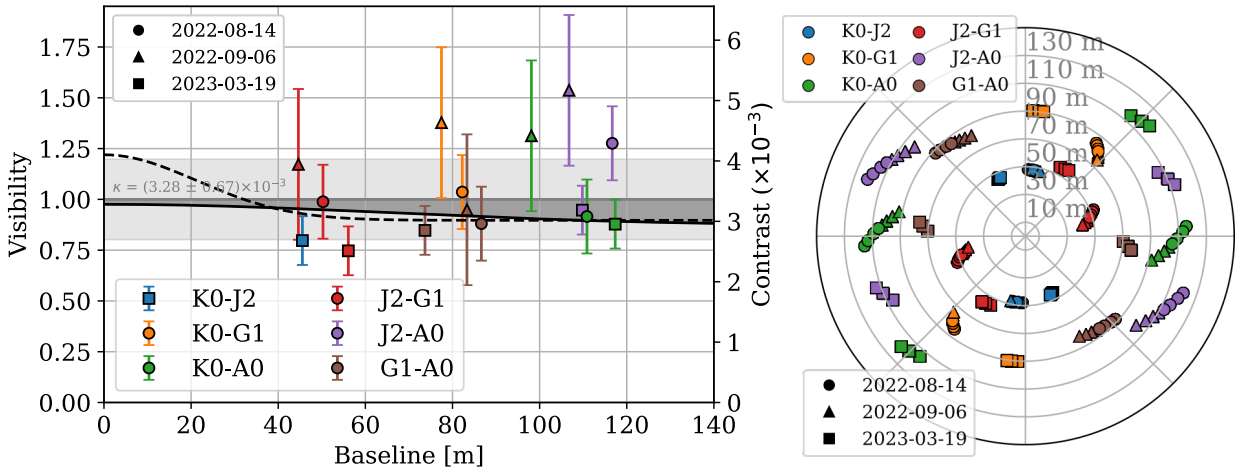

(a) (b)

Figure 3.21 – (From Pourré et al., in prep.)Observations with GRAVITY on GQ Lup B with the AT. (a) Visibilities observed on three epochs of the astrometric configuration of the AT. (grey line and light grey area) Zero-baseline photometry from Neuhäuser et al. (2008). (solid black line) Gaussian disk model at 1σ and 0.4 au width. (dashed black line) Gaussian disk model at 1σ and 1.2 au width. (b) UV plane at the three epochs.

Conclusion on this analysis

This analysis was initially part of paper in preparation (Pourré et al., in prep.) with Paulina Palma-Bifani and Mickaël Bonnefoy. Half of the paper was about the GRAVITY observations detailed here, the other half was a revised spectrum fit with ForMoSA (Petrus et al., 2023) from 0.6 to 5 µm. For the second part, we used improved calibrations and scaling of the available spectra and photometry that challenged the tentative detection of Stolker et al. (2021) of a disk of radius 65 R_Jup (0.03 au) at 460 K around GQ Lup B. The situation changed very recently when JWST/MIRI observations of GQ Lup B from 4.8 to 11.7 µm confirmed the infrared excess from a circum-companion disk (Cugno et al., 2024). The spectrum analysis of our paper is now obsolete. It is left to determine if my paper on preparation can stand on one leg with the interferometric detection limit alone.

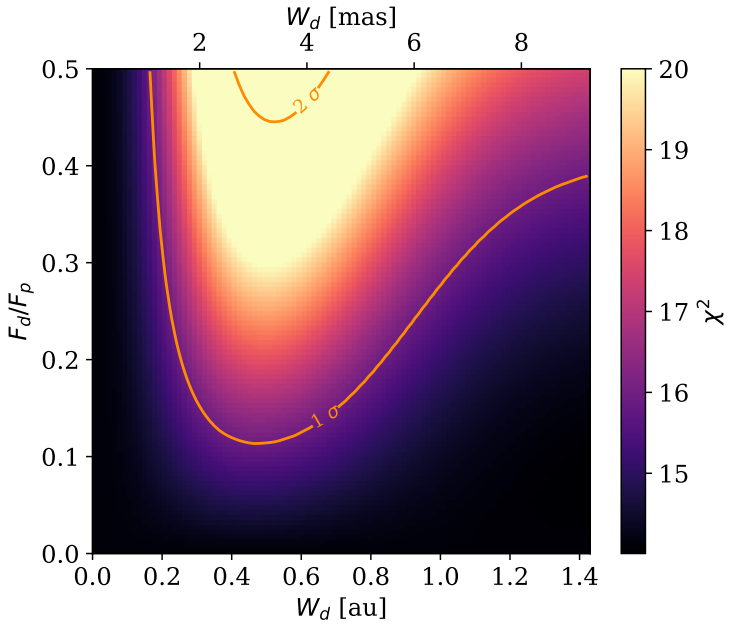

Figure 3.22 – (From Pourré et al., in prep.) χ^2 map from the GQ Lup B visibilities fit with the Gaussian disk model.

The results presented in this section are not only interesting for the disk of GQ Lup B, it is also an example of the constrains we can put on a circum-companion disk with the AT and GRAVITY. However, the K-band is probably not optimal for probing cold disks around companions. The new GRA4MAT mode of MATISSE at the longer wavelengths of L and M-bands is more promising to one day bring a detection.

3.8 Conclusion of the chapter

I developed new tools based on injection, subtraction and retrieval of exoplanets signal in GRAVITY data. With these tools I proposed a solution to quantify detections SNR, and I used archival data to determine the contrast limit of the ExoGRAVITY technique.

My work on the detection limits concludes that we are currently limited by systematics that scale with the star flux. I conclude that the priority is to limit the injection of stellar flux in the SC fiber at the planet position. This will improve with the new adaptive optics GPAO and I expose my preliminary work on a dedicated high-contrast mode for GRAVITY in Chapter 5.

Regarding the tools, the next step is to make the injection/subtraction scripts available in the ExoGRAVITY pipeline such that any user can quantify the significance of their detections.

Concerning the GRAVITY contrast curve, it represents the actual capabilities of the instrument but it will soon be outmatched by the upgrade GRAVITY+. Spending 3 hours on-sky, in good atmosphere conditions, at the end of GPAO commissioning would be enough to provide an updated contrast curves and quantify the new capabilities of the instrument. At the end Chapter 5, I give an estimation of the contrast curve we can expect on GRAVITY+ .

Chapter 4

Systematics in the K-band visibilities

Contents

The previous chapter showed that the exoplanet detection limit below 150 mas on GRAVITY was not due to statistical photon noise. Instead, we showed that we were limited by systematics whose amplitude scales with the host star flux injected in the SC. One particular type of systematics was identified before the present work, from the beginning of the ExoGRAVITY large program in 2020, and these features were thought to be the cause of correlated noise in exoplanet spectra. In the ExoGRAVITY consortium, these systematics are called "wiggles".

Reproducing the problem on the GRAVITY calibration unit, I showed it was not a feature created by ExoGRAVITY pipeline, and I investigated for the problem source on the hardware. However, at the time of writing this manuscript, we still have no explanation for the nature of the phenomenon.

Working with Mathias Nowak on the ExoGRAVITY pipeline, we converged to a promising strategy that uses the wiggles-vs-planet phase diversity to reduce the amount of static systematics mixing with the planet signal.

4.1 Unexpected spectral oscillations: a common problem

The apparition of systematics under the form of clear oscillations above the statistical noise is an ubiquitous problem in high-precision astronomy.

Before GRAVITY, it already affected AMBER at VLTI with beating in the phases across the K-band (Millour et al., 2008). The cause of the problem has been identified: it came from the polarizers at the entrance of the intrument. Air-blades were responsible for a Fabry-Perot effect on each separated beam, and created a more complex beating signal after beam recombination (Malbet et al., 2008).

More recently, I had the opportunity to discuss with Kevin Barjot and Manon Lallement, both PhD students on the single telescope interferometric instrument FIRST installed at Subaru (Vievard et al., 2023), and Sebastien Vievard, astronomer at the Subaru telescope. Wiggles also appeared on the test bench of FIRSTv2, in a band around λ =675 nm, and appeared to be a serious problem for the detection of protoplanet signal. Fortunately, they identified the cause of the problem. Again, it came from the polarizers located on the separated beams before recombination (Barjot, 2023).

Spectral oscillation systematics do not appear only in interferometry but also on one-telescope instruments. The planet characterizer Keck/KPIC suffers the same problem in a narrow band around λ =2.3 µm. It comes from Fary-Perot effect in the dichroics that is mitigated a posteriori in the data (Finnerty et al., 2023).

Finally, the James Webb Space Telescope is not spared by fringing effects. It appeared pre-launch on the detector of the MIRI instrument in a band around λ =5.3 µm (Argyriou et al., 2020). Reflections between the different layers of the cameras is responsible for a fringing that is not totally corrected by the standard calibration. The problem is field dependent and depends also on the intensity distribution of the object observed. By collecting data on internal source in various configurations, they obtained a better understanding of the fringing structure and developed a model that reduces by 50% the fringes' amplitude after post-processing.

4.2 Apparition of the wiggles in ExoGRAVITY

In February and March 2020, the ExoGRAVITY large program performed a series of observations to bring the first direct observation of the planet β Pic c. The search for this faint companion revealed an unexpected signal in the complex visibilities.

The archetypal example of the wiggles is the β Pic c observation of the 2020-03-07 (Tab. 4.1). The SC fibers were positioned at 138 mas from the star, and the data reduction with the ExoGRAVITY pipeline revealed a clear detection of the companion (SNR=6.6). The β Pic c contrast is measured at $(4.8 \pm 0.5) \times 10^{-5}$.

The astrometry fit of the complex visibilities gives the speckle fit of the stellar flux injected in the SC fibers when observing the planet (Fig. 4.1a) and the planet fit (Fig. 4.1b). We can see the sky rotation in the planet signal, the oscillations evolve as the six baselines rotate with respect to the star-to-planet axis.

Table 4.1 – Log for the β Pic c observations of 2020-03-07.

Date: 2020-03-07				
Observing time	Airmass	τ_0	Seeing	Sky rotation
00:15 / 01:41	1.13-1.27	6-13 ms	0.49-0.99”	34 deg
Target	ΔRA/ΔDEC	NFILES/NDIT/DIT		
β Pic A	0/0 mas	8/64/0.3 s		
β Pic c	-72/-118 mas	12/32/10 s		

We can compute the residuals $\underline{r}$ of these observations. In the case of ExoGRAVITY observations, the classical $r = \text{Signal} - \text{Model}$, is:

$$\underline{r}(b,t,\lambda) = \underline{V}_{oncompanion}(b,t,\lambda) - \underline{V}_{speckle\_fit}(b,t,\lambda) - \underline{V}_{companion\_fit}(b,t,\lambda). \quad (4.1)$$

The residual for the β Pic c observation are shown on Fig. 4.1c. The “wiggles” correlated structures appear clearly above the noise. It is composed of oscillations that remain static, when referenced on the star, over the 1.5 hour observation. The wiggles are similar in spectral frequency and phase on all baselines. These two properties already discard the hypothesis of an astrophysical nature of the signal, as no intensity distribution on-sky can induce the same static signal on baselines of different length whose projection evolves with time.

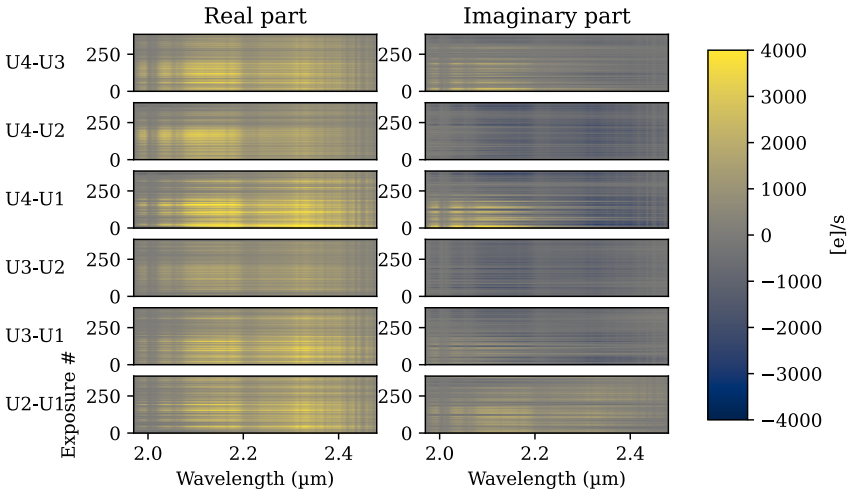

(a) Speckle fit

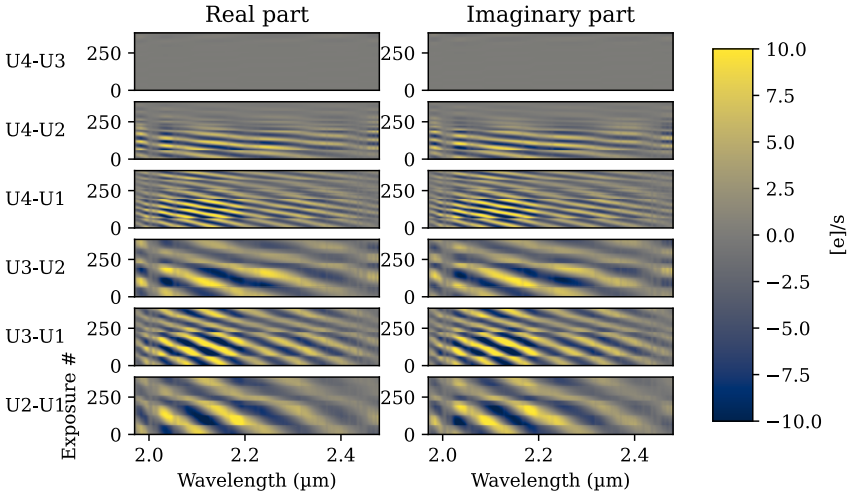

(b) Planet fit

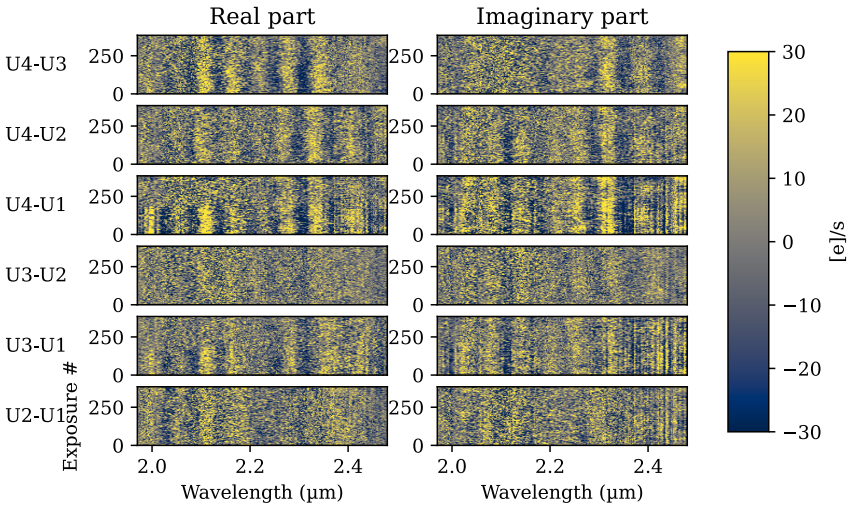

(c) Residuals

Figure 4.1 – (a) Speckle fit, (b) planet fit, (c) residuals, on the complex visibilities, with phase centered on the star. For each baseline, the 384 exposures (NFILES×NDIT) are stacked on the vertical axis. From β Pic c observations the 2020-03-07.

Figure 4.2 shows the same residual in amplitude and phase of the complex visibilities. The wiggles are clearly visible in the phase, and only slightly visible in the amplitude (on baseline U3-U1). At this moment, the favored hypotheses were that either the feature was created by the data reduction, or originated from an instrumental problem.

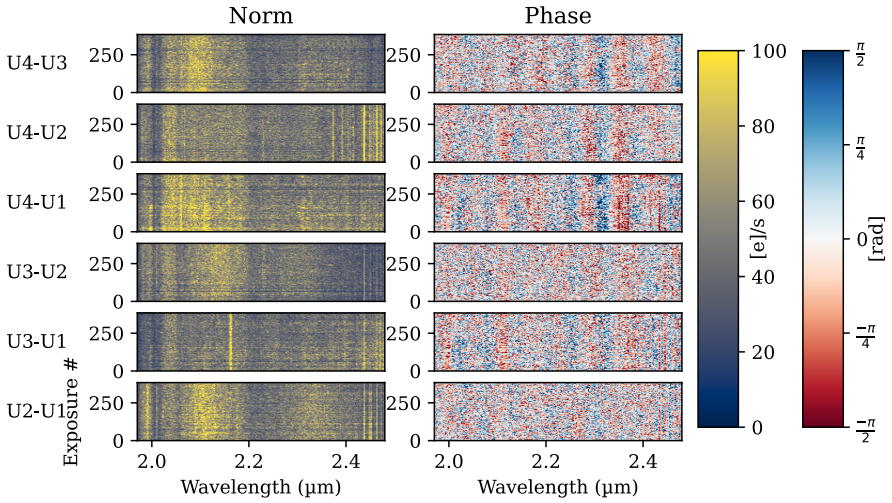

Figure 4.2 – Residuals (Norm/Phase) in the complex visibilities, phase centered on the star. From β Pic c observations the 2020-03-07.

The amplitude of these correlated structures can reach three times the planet signal amplitude on certain baselines. Since the "wiggles" are stable in time and on all baselines, the signal decouples easily from the planet signal in the astrometry fit and did not affect the β Pic c detection. However, a correlation was identified between the presence of wiggles in the data and oscillating features in the extracted K-band spectrum of the planet. Figure 4.3 shows the spectrum of β Pic c obtained from the February and March 2020 observations. Figure 4.4 shows the spectrum of HD 206893 c whose observations also contain strong wiggles. These features prevent detailed analyses of the planet atmosphere from the GRAVITY spectrum alone.

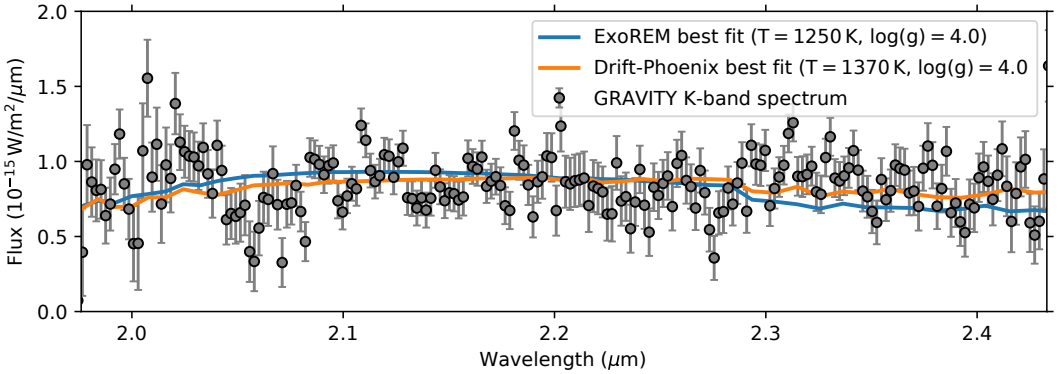

Figure 4.3 – β Pic c K-band MEDIUM (R∼500) resolution spectrum from Nowak et al. (2020)

The "wiggles" appeared systematically on ExoGRAVITY observations around bright stars (β Pic: K=3.5; HD206893: K=5.6; HR8799: K=5.2) at separation from 80 to 140 mas. They were identified as the main limitation for the spectral characterization of short separation exoplanets.

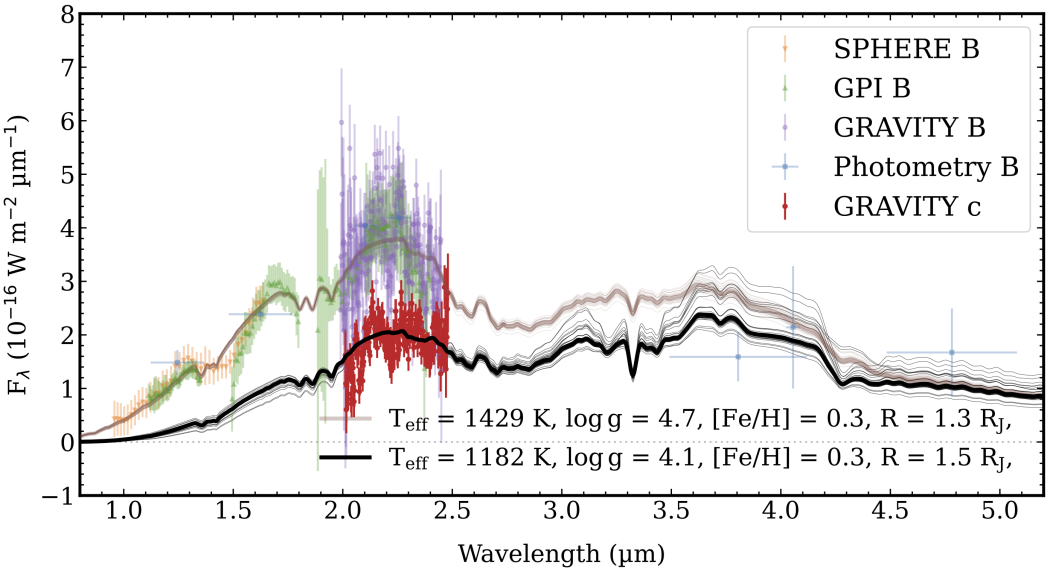

Figure 4.4 – HD 206893 c K-band MEDIUM (R∼500) resolution spectrum (red) from Hinkley et al. (2023)

4.3 Impact on observables

We have seen that the "wiggles" signal is very different from a planet signal. However, the wiggles amplitude can be higher than the planet signal amplitude and, at some point, affect the observables. To test the wiggles impact on the relative astrometry and K-band contrast spectrum, I used purely synthetic data to simulate the observations and a wiggles' model. The synthetic observations include Gaussian noise and an injected planet with a flat contrast spectrum. The planet injection follows the procedure described in Sect. 3.2. I modeled the wiggles in the star's referential as a Fabry-Perot pure phase effect:

$$\underline{V}_{wiggles}(\lambda) = A \times e^{i\frac{2\pi}{\lambda}\sigma} \tag{4.2}$$

with A the amplitude and σ the size of the Fabry-Perot cavity. I injected the same wiggles model on each baseline. The wiggles in the β Pic observation presented in the previous section have an amplitude contrast with respect to the star around 1.7×10^{-4}.

To match the noise and wiggles' properties, I computed the power spectral density of the residual on β Pic. I performed the Fourier transform using Welch's method (`scipy.signal.welch`) along the spectral direction, separately on each exposure and baseline, and separately on the real and imaginary part. The power spectra are on Fig. 4.5. The wiggles are clearly visible with a peak at 17 µm^{-1} on baselines U4-U3, U4-U1 and U4-U2, that corresponds to a $\sigma \approx 84$ µm in the Fabry-Perot model. The drop below 4 µm^{-1} comes from the 4$^{\text{th}}$ order polynomial that captures all the low frequencies in the speckle fit. We have no explanation for the drop above 100 µm^{-1}, it may come from a spectral channel smoothing in the GRAVITY pipeline. In my synthetic observations, the noise I injected is Gaussian with 51 e/s rms filtered by an order 1 Butterworth low-pass filter with a cutoff frequency at 100 Hz. I injected separate outcomes of this noise in the real and imaginary parts of individual exposures.

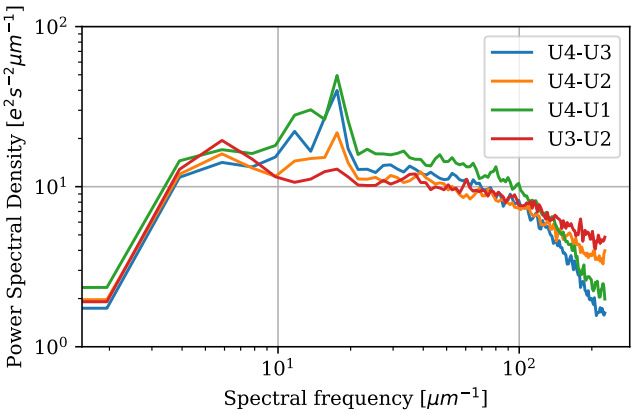

Figure 4.5 – Power spectral densities of the residuals on four baselines on β Pic c observations the 2020-03-07. Only real part.

To keep a reasonable computation time, the following data reductions use the `go_fast` mode of the ExoGRAVITY pipeline that averages the NDIT of each file.

4.3.1 On relative astrometry

The first part of the ExoGRAVITY pipeline is the `astrometry_reduce`. It provides the relative astrometry (ΔRA, ΔDec) and a planet contrast, assuming a flat contrast spectrum. As discussed in Sect. 2.5.2, these observables can be estimated either on the individual NFILES and then averaged, or estimated on the fit maps of all NFILES combined. For this test, we use the combined fit maps as they give more robust detection of faint companions. I injected a planet at the same separation (138 mas) and contrast (5×10^{-5}) as β Pic c. The UV plane and NFILES$\times$NDIT$\times$DIT are the same as the 2020-03-07 observation on β Pic c shown in the previous section. The observables retrieved by the pipeline for the synthetic observations, with Gaussian noise and increasing wiggles amplitude, are on Fig. 4.6. The script converges to the same astrometry for wiggles of less than 1.4×10^{-3} contrast with respect to the star flux (28 times the planet amplitude). Even so, the error on ΔRA and ΔDec increases from 0.2 mas with no wiggles to 1.8 mas with wiggles at 1.4×10^{-3} contrast. For wiggles' amplitude higher than 1.4×10^{-3}, the astrometry fit becomes completely biased by the systematics and does not converge on the injected planet. The planet contrast measured remains within 20% error as long as the fit converges to the right astrometry.

Figure 4.7 shows the periodogram maps from the χ^2 fit for the different wiggles' amplitude. It shows that wiggles tend to disturb the relative power of the primary and secondary peaks, ultimately making the script converge to the wrong astrometry.

I concluded that, for a planet at 5×10^{-5} contrast and 138 mas separation, the `astrometry_reduce` script is robust against wiggles. The outputs deviate from the injected value only for wiggles of 28 times the planet amplitude. On some baselines, the wiggles modulate on a similar spectral frequency as the planet on some baselines. However, the sky-rotation makes the planet signal evolve with time, and as the wiggles are static, then it is easy for the code to disentangle the planet and the wiggles. We can make the hypothesis that the wiggles can have more impact on the astrometry if the planet and the wiggles modulate on the same spectral frequencies on several baselines and if there is less sky-rotation to add temporal diversity between the planet and the systematics.

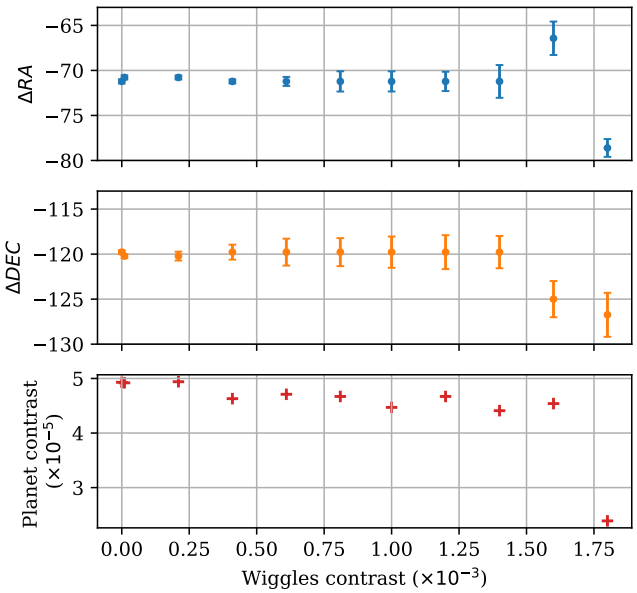

Figure 4.6 – Outputs of the `astrometry_reduce` for increasing wiggles amplitude. The planet is injected at ΔRA = -71 mas, ΔDec = -120 mas at 5×10^{-5} contrast.

4.3.2 On K-band spectrum

The results of the `spectrum_reduce` of the ExoGRAVITY pipeline with different wiggles' amplitude are on Fig. 4.8. The planet is injected at a 5×10^{-5} contrast, close to β Pic c contrast at K-band. We can see that the flat spectrum is affected by significant features for a wiggles' amplitude close to the β Pic c observation of 2020-03-07 (1.7×10^{-4} contrast). These features peak at 1.5×10^{-5} above the planet contrast and significantly above the statistical errors estimated in the GRAVITY pipeline from read-out noise and photon noise. As expected, the features in the spectrum grow stronger as the Fabry-Perot signal grow stronger, up to 160% relative error on the flat spectrum for wiggles of 4×10^{-4} contrast.

The impact on the spectrum is more and more problematic as we stack observations. This reduces the statistical noise but, if the wiggles are stable from one observation or one night to another, only make the features more prominent.

I also performed synthetic observations with $C(\lambda)$ as a β Pic b spectrum instead of a flat spectrum. The contrast spectrum is accumulated from several nights to have a high SNR (> 100), it is close to the spectrum published in GRAVITY Collaboration et al. (2020b). For setting $C(\lambda)$, I divided the β Pic b spectrum by its average over λ and multiplied this normalized contrast spectrum by a scalar setting the average contrast value.

For this test, I added no statistical Gaussian noise. The results for different wiggles' amplitude is shown on Fig. 4.9. It shows that the CO absorption at 2.3 µm is strongly disturbed by the wiggles effect on the spectrum. For wiggles at 1.7×10^{-4} contrasts, this test simulates the spectrum one can achieve on β Pic b if observed at 140 mas, for an observing time long enough to be dominated by systematics. It highlights how the extraction of spectral information of astrophysical interest can be disturbed, or made impossible, by the wiggles presence in the data.

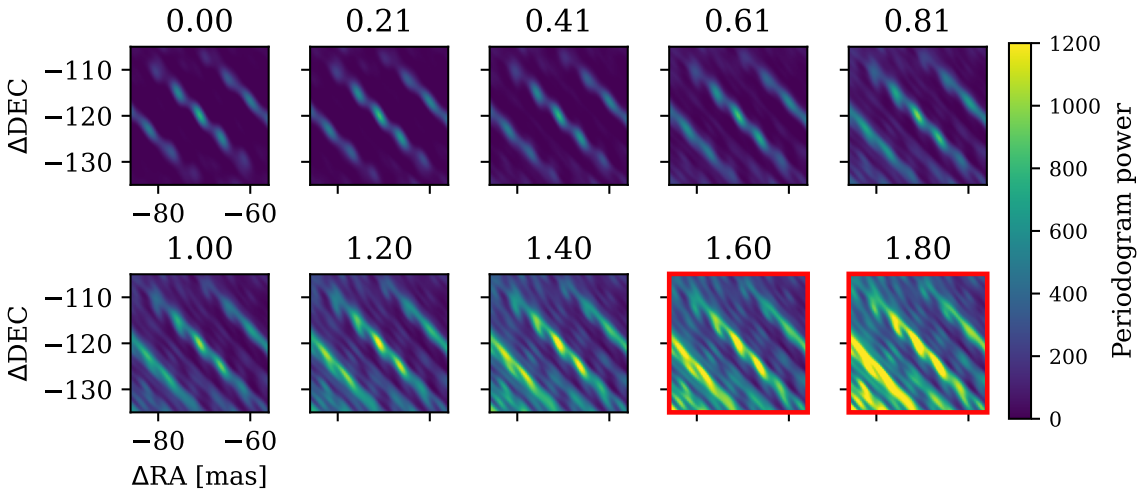

Figure 4.7 – $(\Delta RA, \Delta DEC)$ maps from the astrometry fit. Panel's titles correspond to the wiggles' contrast ($\times 10^{-3}$). Panels with a red frame highlight the reductions that did not converge to the right astrometry.

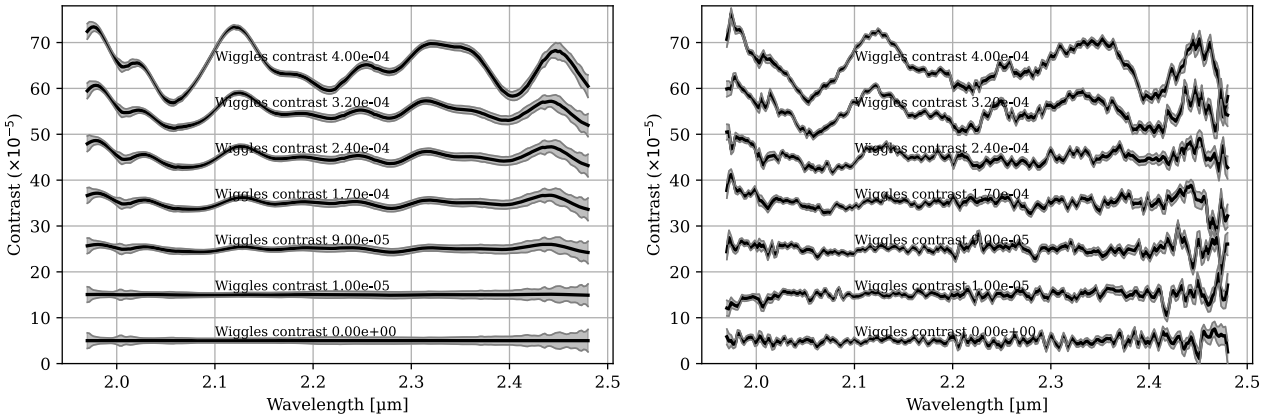

(a) Planet+wiggles (b) Planet+wiggles+noise

Figure 4.8 – Contrast spectrum retrieved on synthetic observations with a flat contrast spectrum at 5×10^{-5}. The gray fill shows the 1σ error bar amplitude as estimated by the GRAVITY pipeline. The spectra have an artificial waterfall offset of 10×10^{-5}.

Conclusion

To conclude, this study shows that the planet detection and astrometry measurement are more robust to the wiggles effect than the planet spectrum. I have shown in Chapter 3 that the planet detection in the instrument was limited by systematics. We can wonder if the wiggles are this limiting noise. For a specific case of a planet at 138 mas, I have shown in Sect.4.3.1 that the wiggles can set a detection limit 25 times below their amplitude on 1.5 hours observing time. Back to the archetypal case of the 2020-03-07 observation, it would set a planet detection limit at 6×10^{-6}. Testing the detection limit with the code used in Sect. 3.5.2, I found a detection limit at 2.5×10^{-5} on this dataset. It indicates that the wiggles are not the limiting noise for detection, or at least that the Fabry-Perot model is not representative of the systematics that are limiting the planet detection.

For the planets observed with GRAVITY below 150 mas, the wiggles' amplitude is never high enough to disturb the astrometry fit. However, the wiggles disturb the planet spectrum retrieval and this fact alone motivates to calibrate or suppress the source of these systematics in GRAVITY data.

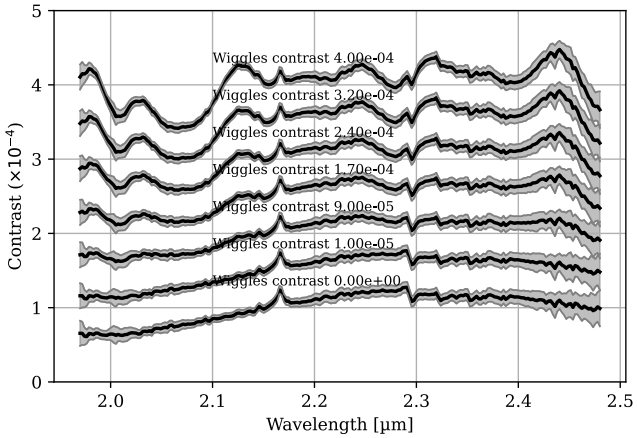

Figure 4.9 – Contrast spectrum of the shape of β Pic b injected at 1×10^{-4} in synthetic observations with different wiggles' amplitude. No noise added. The spectra have an artificial waterfall offset of 0.5×10^{-4}.

4.4 Search for the wiggles' source: on-sky data

I analyzed on-sky archival data from the ExoGRAVITY large programme to understand the nature of the wiggles and find a way to mitigate them. Because it is polluting the coherent flux, the picture of one telescope beam undergoing a Fabry-Perot reflection generating the wiggles is too simplistic. We must keep in mind that the effect we observe is a differential effect between the four beams recombined in GRAVITY. Therefore, it can be complex to pinpoint the physical source of the problem.

4.4.1 Method

To quantify the impact of wiggles in residuals, I fitted the wiggles separately for the real part and imaginary part with a low-pass filter on the data. I used the model W:

$$W = \underbrace{|P(b,t,\lambda)V_{\text{onstar}}|}_{\text{speckle fit}} \times [A_s \times \sin(2\pi\sigma/\lambda) + A_c \times \cos(2\pi\sigma/\lambda)], \tag{4.3}$$

with A_s and A_c scalar amplitudes and σ the OPD. The speckle fit comes from the `astrometry_reduce` script. I fit σ on the residuals with testing 1000 values from 1 to 100 µm and selecting the one that provides the lowest χ^2. Amplitudes A_s and A_c come from a linear fit. Thanks to this model, we can quantify the frequency and amplitude (rms(W)) of the wiggles. I found the phase of the model (arctan[A_c/A_s]) not robust enough for looking at phase drifts. Figure 4.10 shows that this model captures well the wiggles in the residuals.

I collected 11 ExoGRAVITY observations, from 2020 to 2022, at separations lower than 140 mas (DUAL-ONAXIS mode), all at MEDIUM resolution (Table. 4.2). These observations are all around bright stars, ranging from K=3.5 mag to K=5.8 mag. It ticks all the boxes for wiggles to dominate the residuals. I reduced the data with the ExoGRAVITY pipeline, averaged the residuals over the NFILES×NDIT, and fitted the residuals with Eq. (4.3) on separate baselines.

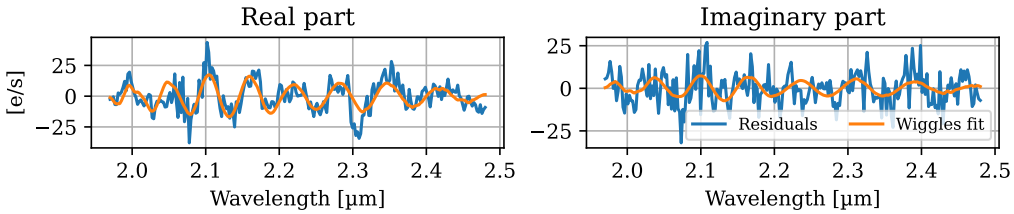

Figure 4.10 – Example of wiggles fit on baseline U4-U3 of the β Pic c observations of 2020-03-07 (Fig. 4.1c). The residuals are averaged over the whole observation (NFILES and NDIT).

Table 4.2 – Dataset for wiggles analysis ExoGRAVITY

Star	K mag star	Date	τ_0 [ms]	Seeing [arcsec]	NFILES/NDIT/DIT	Fibers position	Planet?
β Pic	3.5	2020-02-11	11∼18	0.49∼0.72	$10 \times 32 \times 10s$	131 mas, PA 211°	Yes
β Pic	3.5	2020-03-07	6∼12	0.50∼0.89	$12 \times 32 \times 10s$	138 mas, PA 211°	Yes
CPD-36 6759	5.8	2021-02-28	4∼6	0.83∼1.10	$12 \times 32 \times 10s$	69 mas, PA 279°	No
CPD-36 6759	5.8	2021-03-29	3∼4	0.69∼0.84	$6 \times 32 \times 10s$	69 mas, PA 279°	No
HD 206893	5.6	2021-08-26	4∼7	0.46∼0.77	$4 \times 32 \times 10s$	75 mas, PA 344°	No
···	5.6	···	4∼7	0.54∼0.78	$4 \times 32 \times 10s$	74 mas, PA 318°	No
···	5.6	···	4∼6	0.54∼0.84	$4 \times 32 \times 10s$	76 mas, PA 293°	No
HD 206893	5.6	2021-09-27	2∼3	0.74∼1.13	$8 \times 32 \times 10s$	72 mas, PA 245°	No
···	5.6	···	2∼3	0.70∼1.11	$12 \times 32 \times 10s$	109 mas, PA 223°	Yes
HD 206893	5.6	2021-10-16	2∼3	0.47∼0.60	$27 \times 32 \times 10s$	111 mas 218°	Yes
HR 8799	5.2	2022-08-17	3∼7	0.84∼1.56	$12 \times 12 \times 30s$	131 mas, PA 15°	No

4.4.2 Wiggles' occurrence

The analysis of the wiggles' amplitude with respect to the amount of coherent flux $|\underline{V}_{\text{onplanet}}|$ injected in the SC is shown on Fig. 4.11. In all observations of the dataset, the coherent flux is largely dominated by the host star flux (the planet is faint). This analysis tends to indicate that the wiggles' amplitude scales with the coherent flux injected in the SC. For the outliers observations on HD 206893 at 293° and 318° PA, the coherent flux increased drastically (up to 4 times) compared to the observation at 344° PA the same night. This increase in coherent flux does not entail an increase in the wiggles' amplitude. Considering all other observations, the wiggles appear to have an amplitude around 0.5% of the coherent flux in SC. It is an indication that these systematics originate from the flux of the star injected in the fibers at the planet position.

The wiggles' fit on this dataset also gives the spectral frequency, under the form of the OPD parameter σ in Eq. (4.3). The Figure 4.12 shows that the wiggles are consistently appearing at $\sigma = 78 \pm 11$ nm. I have seen no correlation with the separation or the coherent flux injected.

Some of the observations chosen for this analysis do not contain a companion signal (e.g. HD 206893 on 2021-08-26). They were taken while searching for a planet with loose constrain on the relative astrometry. Wiggles are clearly visible in the residuals of these observations too. This excludes the hypothesis of an origin from the companion signal. Overall, I concluded from this analysis that the wiggles are compatible with an origin as a reflection in some dichroics or other optical parts in the VLTI or in the instrument.

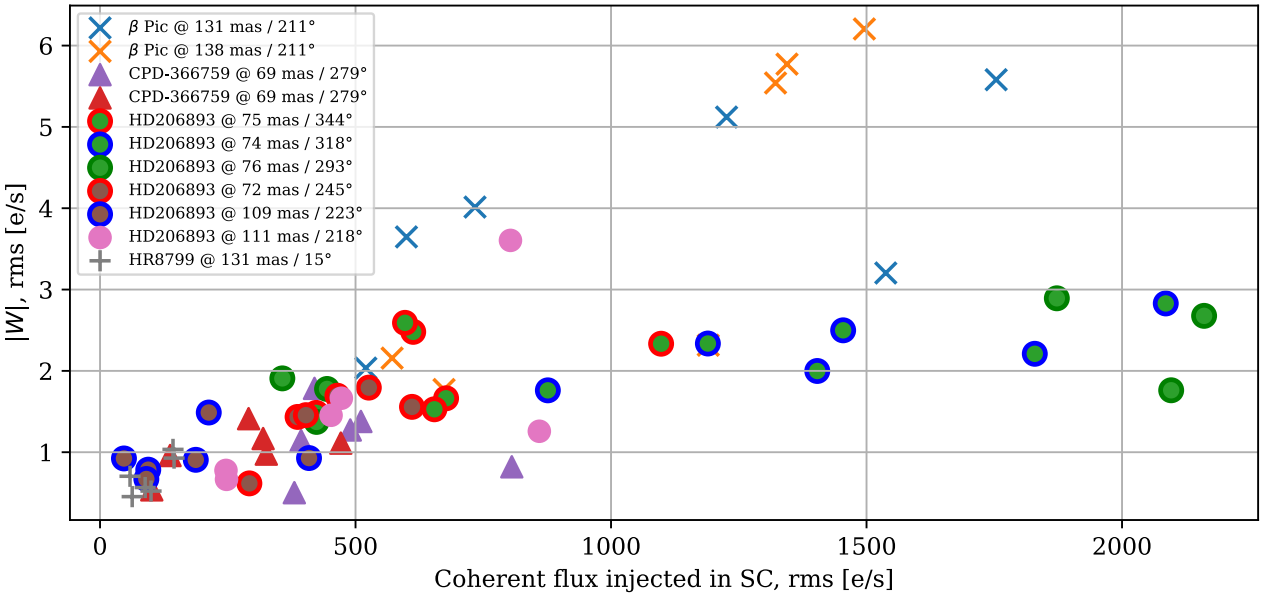

Figure 4.11 – Amplitude of wiggles fitted on the residuals with respect to coherent flux injected in SC, for 11 different observations. Markers' shape differentiate the host stars and markers colors differentiate the observing nights. All six baselines are plotted separately for each observation.

4.4.3 Wiggles in HIGH resolution

On 2022-01-24, I participated to an ExoGRAVITY observing night (remotely, in delegated visitor mode) to reduce the data collected as we observed. One goal of this run was to obtain the first HIGH resolution (R∼4000) K-band spectra for β Pic b and β Pic c. It was a success for β Pic b, as it has a favourable contrast (2.5×10^{-4}) and was at large separation (494 mas). The analysis of the spectrum is actually part of the PhD of Matthieu Ravet[1]. However, the observation on β Pic c was much more challenging. It was at 91 mas from the star and the contrast is know to be 4.5×10^{-5} at K-band. The planet c was detected during this run, showing that the HIGH resolution mode is also suitable for planet detection at less than 100 mas, but the spectrum was extremely noisy. It brought no improvement compared to the previous MEDIUM resolution spectrum (Fig.4.3).

From this HIGH resolution observation, on the top of the exoplanets spectra, there was also something to learn about the wiggles. Interestingly, the residuals showed a wiggles structure comparable with the one observed in MEDIUM resolution. From the wiggles' fit, I obtained an average $\sigma = 79$ nm, and, on the most affected baseline (U4-U3), an amplitude rms of 0.4% of the coherent flux injected (rms). This is an important result. In HIGH resolution mode, the light is projected over 1628 pixels of the SC camera in the spectral direction (see Fig. 2.11), against only 233 pixels in MEDIUM resolution mode. The wiggles have the similar properties with both modes, this discards the hypothesis of wiggles originating from reflection in the camera coating or fringing in the CCD (like on JWST/MIRI, Argyriou et al. (2020)). Also, diagnostic tools of the GRAVITY pipeline show that pixels are below the saturation threshold for all observations where wiggles are the most prominent. I concluded that wiggles do not originate from a saturation of the camera, for both MEDIUM and HIGH resolution mode.

[1]Supervised by Gaël Chauvin and Mickaël Bonnefoy.

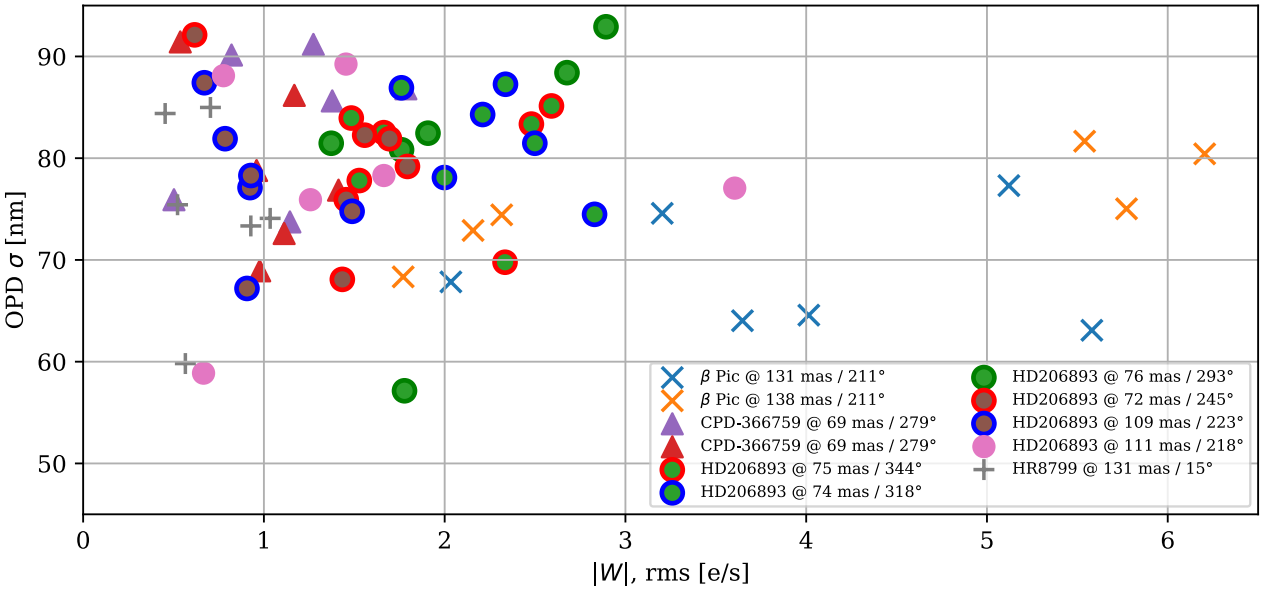

Figure 4.12 – σ parameter of the wiggles' model with respect to the wiggles' amplitude, for 11 different observations. Markers' shape differentiate the host stars and points of the same color are from the same observing night. All six baselines are plotted separately for each observation.

4.4.4 First basic tests on the ExoGRAVITY pipeline

In the attempt to understand the source of the wiggles, I carried out simple tests on the ExoGRAVITY reduction of on-sky data, with β Pic 2020-03-07 and HD 206893 2021-09-27 data.

Polynomial fit The first test was to investigate the possible influence of the polynomial $P(\lambda)$ used for speckle fitting. We suspected that fitting 4^{th} or 6^{th} order polynomials separately on the real and imaginary parts could result in unexpected phase effects. I compared the residuals with the 4^{th} and 6^{th} order in ExoGRAVITY reduction: the wiggles stay the same in both cases. The script reaches a limit for polynomial order 17^{th} due to a conditioning of matrix inversion for the speckle basis. At order 17^{th}, the wiggles in the residuals are attenuated because partially fitted by the polynomial, but their frequency and phase are unchanged. At least an order 23^{th} is required for totally fitting the wiggles, but it would wash out the planet signal in the speckle fit. To conclude, the wiggles are not an artifact from the technique of polynomial modulation of on-star observation for the speckle fit.

Wiggles at zero-separation The second basic test was on the planet-star separation. So far, the wiggles were only observed at separation from 70 to 140 mas. We did not know if the wiggles were still visible at shorter separations, and even at 0 mas. To answer this question, I reduced on-star observations as if it was on-planet observations and looked at the residuals produced. The β Pic 2020-03-07 contains 8 observation files on the star (separation 0 mas), interleaved with the 12 observation files on the planet c (separation 138 mas). I discarded the observations on the planet and chose 4 observations on the star to be the new "science". I reduced these 4 on-star files with the ExoGRAVITY pipeline with the other 4 neighbor on-star files as phase reference and contrast spectrum reference. The outputs of `astrometry_reduce` show that, obviously, we have more coherent

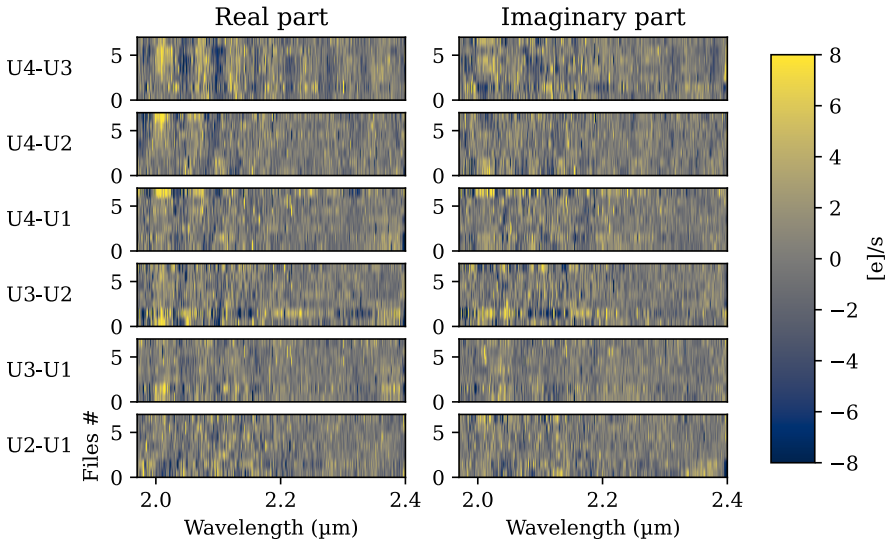

Figure 4.13 – Residuals from β Pic c observation at HIGH resolution the 2022-01-24. Averaged over the NDIT.

flux injected than the observation on-planet, but residuals do not contain any wiggles. This is a surprising result. Previous analysis, like the one presented on Fig. 4.11, have shown that the more coherent flux in the observation from 75 to 140 mas, the higher the wiggles in the residuals. The fact that they are not observed in SINGLE-FIELD (separation 0 mas) challenges the hypothesis of a source in a dichroic reflection.

Star reference Third, I wanted to check if the wiggles can originate from bad star reference. I made two tests that discard this hypothesis:

- Test #1. I reduced the data with stellar reference not as the average of the nearest observation on-star (default mode), but with only one reference for the whole dataset, or only the average of the first with the last on-star observation. In all these tests, the wiggles in the residuals appeared unchanged.
- Test #2. Before reduction, I fitted the phase of the star reference of each baseline with a 10^{th} order polynomial and I replaced the phase reference by the polynomial fit[2]. This have the effect of filtering out an eventual wiggle in the reference phase. Then, the reduction of the planet observations with this filtered star reference exactly displays the same wiggles in the residuals.

Modifications or deliberate alteration of the on-star reference do not affect the wiggles. This is not the origin of our systematics problem. This is also a strong argument against the optical reflection hypothesis, that would affect both the star reference and the planet.

For further investigations on the wiggles' cause, I turned to the GRAVITY calibration unit that allows for daytime tests on the instrument itself.

[2]The polynomial fit is performed in the star referential, de-wrapped from the metrology phase, FT phase, and dispersion. The polynimal is then re-wrapped to mimic normal visibility reference for the ExoGRAVITY pipeline.

4.5 Search for the wiggles' source: on calibration unit

The GRAVITY calibration unit (see Fig. 2.6) allows us to fully operate the instrument independently from VLTI and provide daytime observations on the calibration source in a controlled and replicable environment.

During the technical time slot for GRAVITY+ commissioning from the 26$^{\text{th}}$ May to the 2$^{\text{nd}}$ June 2023, Sylvestre Lacour and I managed to produce daytime ExoGRAVITY-like observations, at short separations, on the calibration unit. This opened the way to an extensive investigation of the wiggles' source in the GRAVITY optics.

4.5.1 Procedure

We setup the instrument in SINGLE-FIELD, MEDIUM resolution mode and manually set the SC fibers' position in the beam combiner parameters. We ran acquisitions with the SC on the calibration lamp to mimic the on-star observations, and acquisitions with the SC of each channel at a given positional offset (unit of acquisition camera pixels, 1px=17.78 mas sky UT). For SKY observations, we take a SINGLE-FIELD acquisition with the whole field away from the fibers by 2 arcsec. For data reduction by the GRAVITY and ExoGRAVITY pipelines, the following header keys must be modified:

- `DPR TYPE`: to `OBJECT,DUAL` or `SKY,DUAL`
- `INS SOBJ X` and `INS SOBJ Y`: to the separation set in the beam combiner settings (in mas sky UT)
- `INS SOBJ SWAP`: to "NO"

The data obtained were reduced with the most recent P2VM, and the SKY taken instead of the calibration DARK. With the default lamp power, sequences of 64×1 s and the SC at 50 mas, we obtained wiggles at the highest SNR ever observed (Fig. 4.14). Both the ratio with respect to coherent flux and the spectral frequency of the systematics make us confident this is the same wiggles phenomenon as observed on-sky. There are no planet in our observations on the calibration source, still we will continue to use the nomenclature described in Sect. 2.5.2, especially $\underline{V}_{\text{onplanet}}$ for the observations with the SC offseted from the on-star axis.

I made the following tests in Garching, at the ESO Headquarters, where the Garching Remote Access Facility allows for a control of VLT/VLTI instruments and telescopes. The test sessions were part of technical time for the GRAVITY+ commissioning during the slot of October 2023 and January 2024.

4.5.2 Wiggles: a creation of the ExoGRAVITY pipeline?

This was a question that was still pending. I have previously shown that the polynomial order in `astrometry_reduce` and the on-star reference had no influence on the wiggles. By proving this, I did not totally excluded a creation of the systematics in the ExoGRAVITY pipeline.

Thanks to the high SNR of the wiggles in the observations on the calibration unit, I was able to definitely discard a cause in the ExoGRAVITY pipeline. I showed that the wiggles are already present in the phase of $\underline{V}_{\text{onplanet}}$ even before the ExoGRAVITY reduction and the planet fit. Figure 4.15

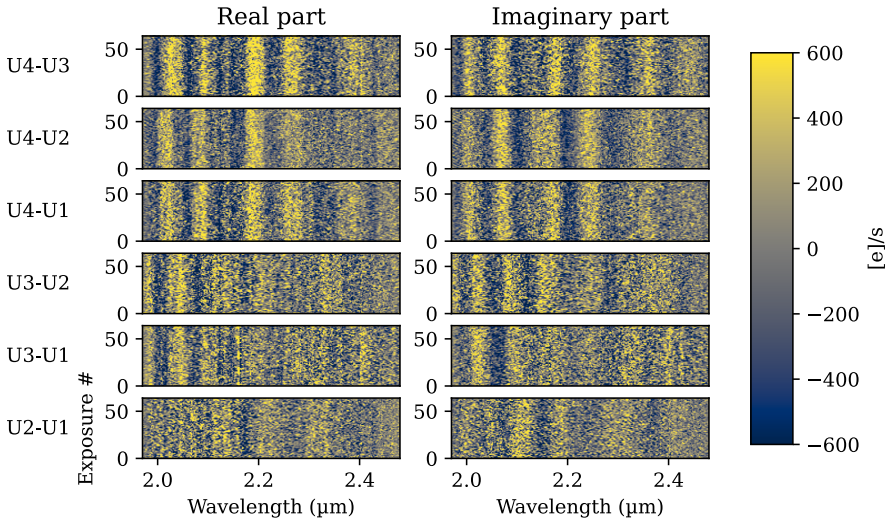

Figure 4.14 – Residuals from calibration unit. SC fibers at 50 mas, 1 s DIT.

shows that if we subtract a polynomial on the phase of $\underline{V}_{\text{onplanet}}$, the wiggles directly appear in the phase. It also shows that the features in the phase are the same as the wiggles observed in the post-`astrometry_reduce`.

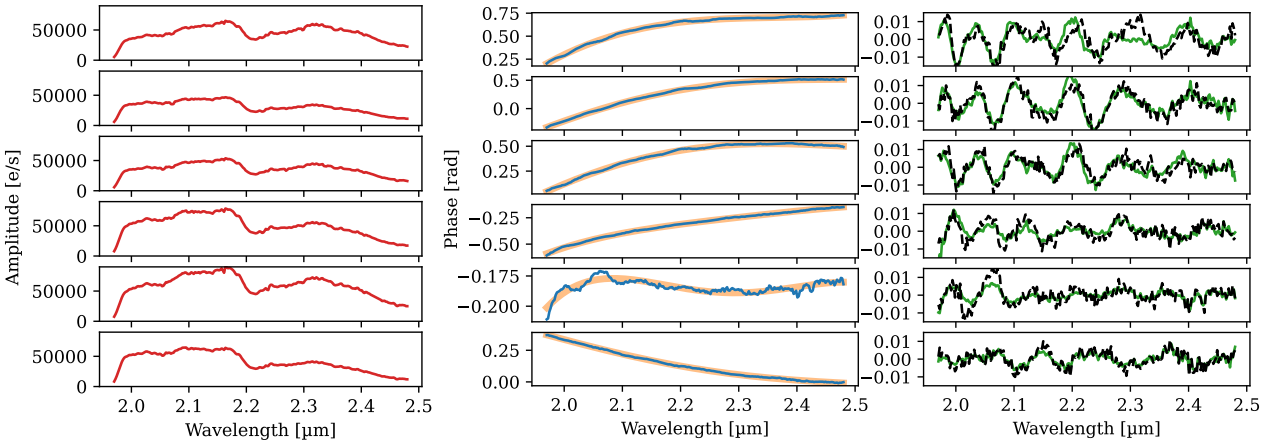

(a) Amplitude of $V_{onplanet}$ (b) Phase of $V_{onplanet}$

Figure 4.15 – Amplitude (a) and phase (b) of $V_{onplanet}$ averaged over the NDIT for the measurement at 50 mas also displayed on Fig. 4.14. (b left): Blue line, raw phase centered on the star. Orange line, 4^{th} order polynomial fit. (b right): Green line, raw phase - polynomial fit. Black dashed, residuals post `astrometry_reduce` $\times$ 0.01.

Thanks to this test, I proved that the wiggles come either from the instrument or from the GRAVITY pipeline, but is not a feature from the ExoGRAVITY pipeline.

4.5.3 The wiggles' field

I used the calibration unit to make 48 observations with the SC fibers positioned on a grid from -150 to 150 mas in both directions, with 50 mas steps. This took more than two hours, and therefore could hardly be done on-sky on the UT, even on technical time. I reduced all pointings separately with the ExoGRAVITY pipeline and fitted the wiggles model W on the post-astrometry residuals. Thanks to this study we can quantify the wiggles amplitude and frequency on the field close to the

"star" (calibration lamp).

For the wiggles' amplitude, the results are on Fig. 4.16. This is, to my knowledge, the first ever map of interferometric speckle field. On these maps, the wiggles' amplitude and the coherent flux are averaged over the NDIT, over the baselines and over the real/imaginary parts. It is striking how the wiggles' amplitude map (Fig. 4.16a) follows closely the coherent flux amplitude map (Fig. 4.16b). This is an additional argument that the wiggles are issued from star coherent flux injected at the SC fibers' position. The closer we observe to the star, the higher the wiggles' amplitude. Also, the Fig. 4.16c shows the ratio between wiggles amplitude and coherent flux across the field. First, we recover the 0.5% ratio around 100 mas observed on sky. Second, it shows that the closer we observe to the star, the smaller the ratio between coherent flux and wiggles' amplitude. It falls down to 0.13% at 50 mas in these tests. This fact is consistent with the absence of wiggles at separation 0 mas (Sect. 4.4.4). In SINGLE-FIELD, either the ratio is null or it is so small that the wiggles are buried in the photon noise. The maps also show that the wiggles' amplitude can slightly vary with the PA, a fact also observed on-sky.

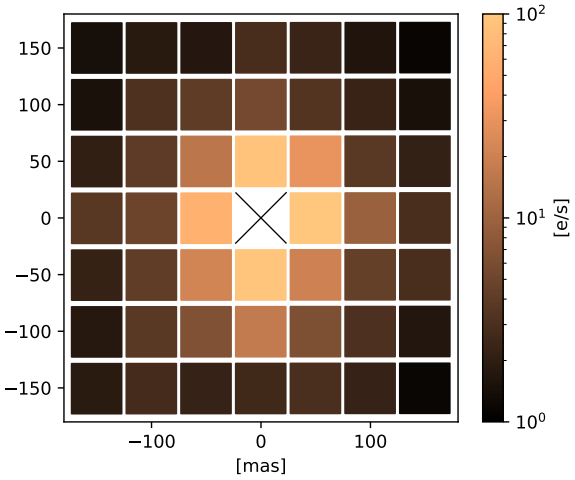

(a) Wiggles' amplitude rms [e/s]

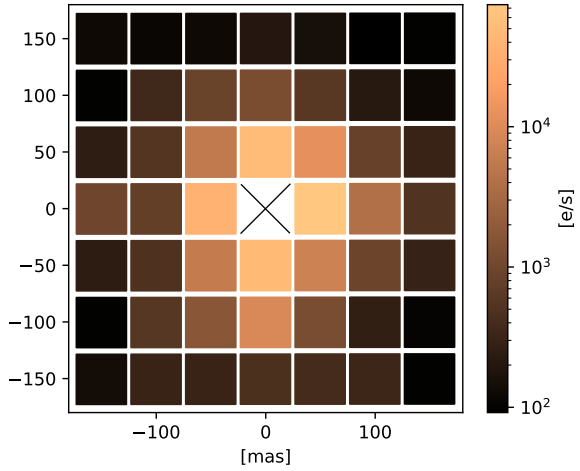

(b) Coherent flux amplitude rms [e/s]

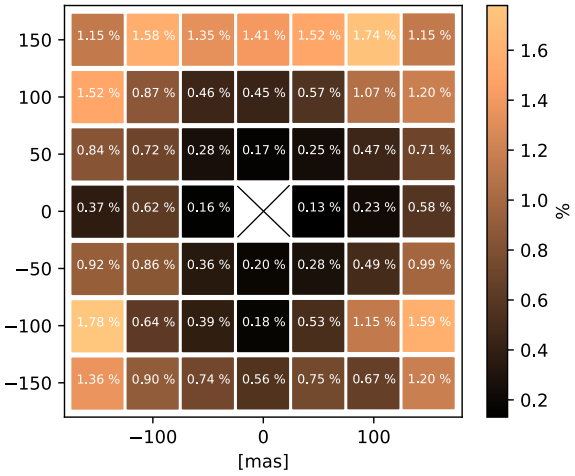

(c) Wiggle amp./coherent flux ratio

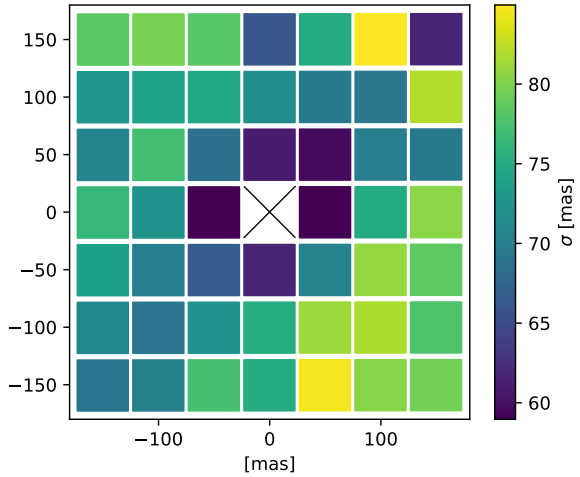

(d) Wiggle frequency σ

Figure 4.16 – Results, on wiggle amplitude (a), (b) and (c), and on wiggle spectral frequency (d), of paving the field with the SC on the calibration unit.

Second output of the wiggles fit, the frequency. The evolution of the wiggles' spectral frequency across the field is shown on Fig. 4.16d. A slight trend towards lower frequency emerges as we approach the star. This tendency is also difficult to reconcile with the hypothesis of wiggles originating from reflection in the instrument.

4.5.4 Phase

Change with SC position. I investigated how the phase of the wiggles changes with the SC position in the field. The phase of the wiggles must be understood here in the sense of the oscillation position along the K-band. Figure 4.17 shows the residuals for different SC positions separated by 5 mas. On some baselines, we see that the wiggles remain similar in structure, only reducing amplitude as we increase the separation (it appears clearly on U3-U1). On some others, the wiggles change in shape and phase drastically when the fibers are offset by 5 mas (U3-U2). This indicates that the wiggles can have a high sensitivity to the fibers' position. This may prevent any calibration by observing the sky out of the planet position. As all different positions are reduced with the same reference on-star but still display very different wiggles' shape and amplitude, it is an additional proof that the wiggles do not come from a bad on-star reference.

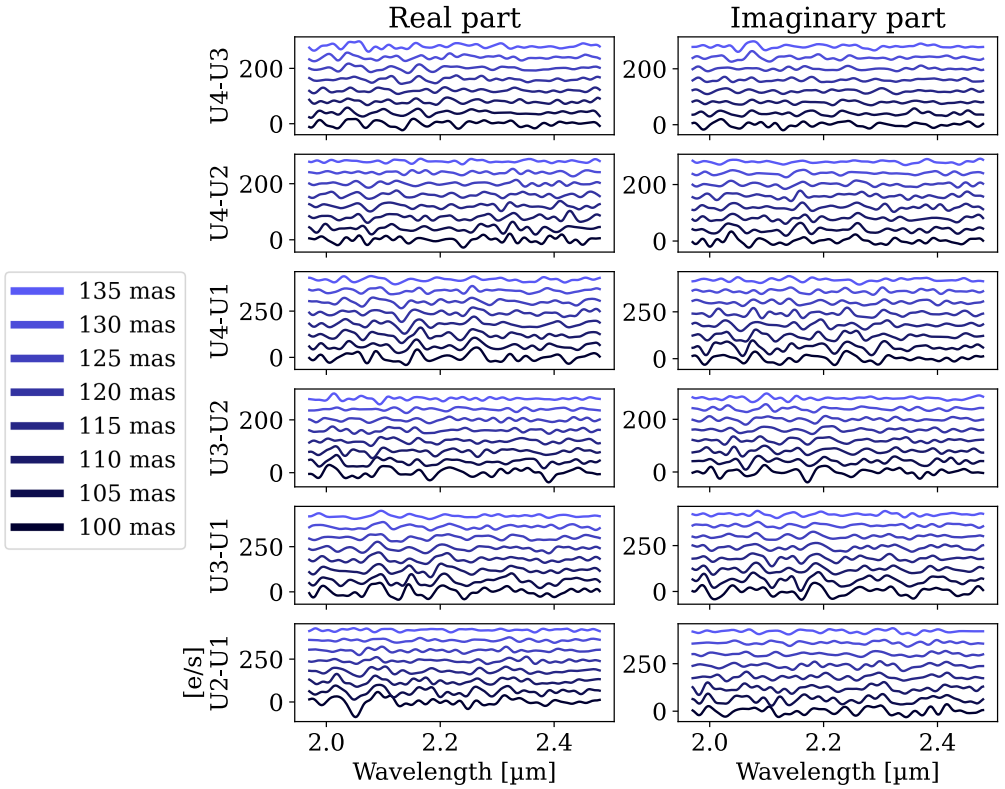

Figure 4.17 – Post `astrometry_reduce` residuals (same as Fig. 4.14 but averaged over NDITs) by 5 mas increment of the SC position in the radial direction from 100 mas. High-frequencies filtered. Calibration unit. Artificial waterfall offset.

Temporal evolution. I collected data on the calibration unit at the same SC fibers' position and same NDIT×DIT (64×1 s) at 87-days intervals. The wiggles' comparison is shown on Fig. 4.18.

Most of the bigger structures in residuals are consistent between the two dates (e.g. U3-U1, U4-U1).

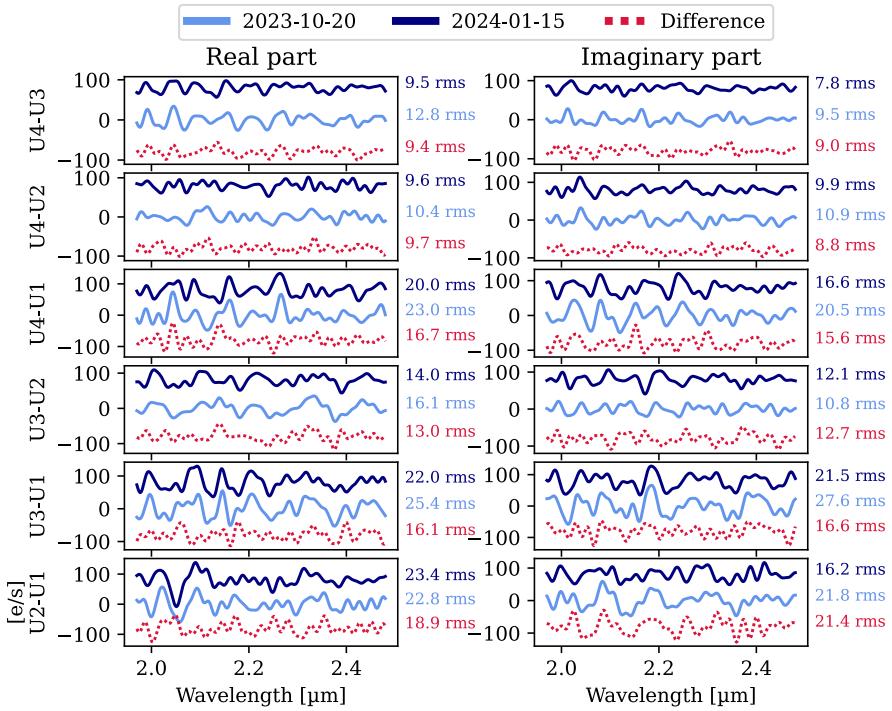

Figure 4.18 – Residuals at the same SC position at 100 mas in October 2023 and January 2024. High-frequencies filtered. Calibration unit. Artificial waterfall offset.

So, the wiggles appear to be relatively similar if taken 3 months apart, but can change with the fine position of the SC fibers in the field. This last fact prevents to make a calibration map to apply to the on-sky observations. It would require a field sampling of at least 2.5 mas steps from -150 to 150 mas separation, and at least two minutes per position. It would take 512 hours of daytime and possibly would need to be updated every year or so. More realistically, we can imagine a solution where the GRAVITY calibrations at the end of the night include DUAL-ONAXIS observations at the exact SC position of the exoplanet observations of the run. This could be used as wiggles' calibration at the ExoGRAVITY reduction stage.

4.5.5 Investigate the wiggles' source

The GRAVITY calibration unit is a remarkable laboratory for day-time tests. It allows for replicating observations with various operational modes of the instrument, but also for changing the optical parts setup or adding/removing it from the beams. I used the calibration unit to investigate for the source of the wiggles. Thanks to this, I excluded some possible contributors to the wiggles problem.

Wollaston prism. As recalled in Sect. 4.1, the polarizing elements have been identified in other instruments as the source of oscillations in the visibilities. In GRAVITY, there are two observing modes, one where polarizations are combined (COMBINED mode), and another where the two linear polarization states are separated by a Wollaston prism and recorded separately (SPLIT mode). All

ExoGRAVITY observations use the COMBINED mode, as this mode is preferred for faint sources with low polarization fraction expected. I used the calibration unit with the SC fibers at 125 mas from the "star" and recording 16×10 s acquisitions in both COMBINED and SPLIT modes. I also took acquisitions "on-star" with the two modes. After separate reduction by the ExoGRAVITY pipeline, I saw wiggles in the residuals with both COMBINED and SPLIT modes. Moreover, the wiggles were identical in amplitude, frequency and phase with both modes and on the two polarization states. I concluded that the Wollaston have no influence on the wiggles.

Half-wave plate. The half-wave plate in GRAVITY is used to control the linear polarization orientation. It can be rotated at different angles. In usual ExoGRAVITY observations it is left at 0°. I used the same setup as for the Wollaston test (fibers at 125 mas) and recorded acquisitions of 8×10 s for half-wave plate angles successively at 0°, 20° and 40°. The wiggles residuals remained unchanged for each half-wave plate angle. I concluded it has no effect on our systematics residuals.

Fibered Differential Delay Lines. One possible source of the wiggles is the fibered differential delay lines (FDDL). Fibers have birefringence and, according to Sylvestre Lacour, it could cause undesired phasing effects between the two polarizations that could generate wiggles after the recombination. These delay lines are in the GRAVITY cryostat and perform the last fine tuning of the OPD in the instrument, with delays up to 6 mm on each beam. I tested, still on the calibration unit, if setting different set-points on the FDDL has an impact on the wiggles.

For this, I put the SC fibers at 53 mas separation from the "star" and took a 64×3 s acquisitions. During the acquisition, I added an offset of 3 µm every 30 s on the input 1 (UT4) of the FDDL. This way, the fibers' length increased on only one telescope and, if the FDDL are the problem, it would have an impact on the wiggles.

I reduced the data with the ExoGRAVITY pipeline. As the wiggles remained unchanged along the whole sequence, at that time I concluded that the FDDL was not the source of our problem. But moving only one telescope, we could not change the set point over a large amplitude before loosing the fringes. Another interesting test would be to change the FDDL setpoint for all telescopes simultaneously, this way we could safely reach ±200 µm offsets and cover a more significant fraction of the FDDL stroke. If the wiggles remain unchanged even after such drastic offsets of the FDDL, I would conclude that the FDDLs are not the cause of our problem.

Derotator. At the entrance of the GRAVITY cryostat, there are four K-mirrors, one for each input beam. Their role is to stabilize the field against sky rotation. Here, on the calibration unit, there is no sky rotation to counter. So K-mirrors rotate the entire field as seen by the instrument. To test the impact of the derotator angle on the wiggles, I put the SC fibers at 100 mas separation. I ran acquisitions of 64×1 s for derotator angles 0°, 5°, 10°, 20°, 40° and 80° (mechanical angle), successively. The fibers position are fixed in the instrument, only the derotator moves. This is also what happens during the on-sky observations. Figure 4.19 shows how residuals evolve with K mirror rotation. They are relatively unchanged on all baselines from the original position (0°) to 5° rotation. However, for 10° and more the residual drastically change. Between 0° and 80° the wiggles' amplitude drops linearly by 50%. A high frequency appears in the residuals for baselines U3-U2, U3-U1 and

U2-U1. I have no explanation for these higher-frequency wiggles but changing the "on-star" reference (one taken at 0°, the other one at 80°) for the ExoGRAVITY reduction has an impact on their amplitude.

These tests on the GRAVITY derotators are preliminary results. I did not have the opportunity yet to replicate them, so, at this point I cannot draw a conclusion. However, it seems to indicate that a field rotation seems to have an impact on the wiggles' amplitude and shape.

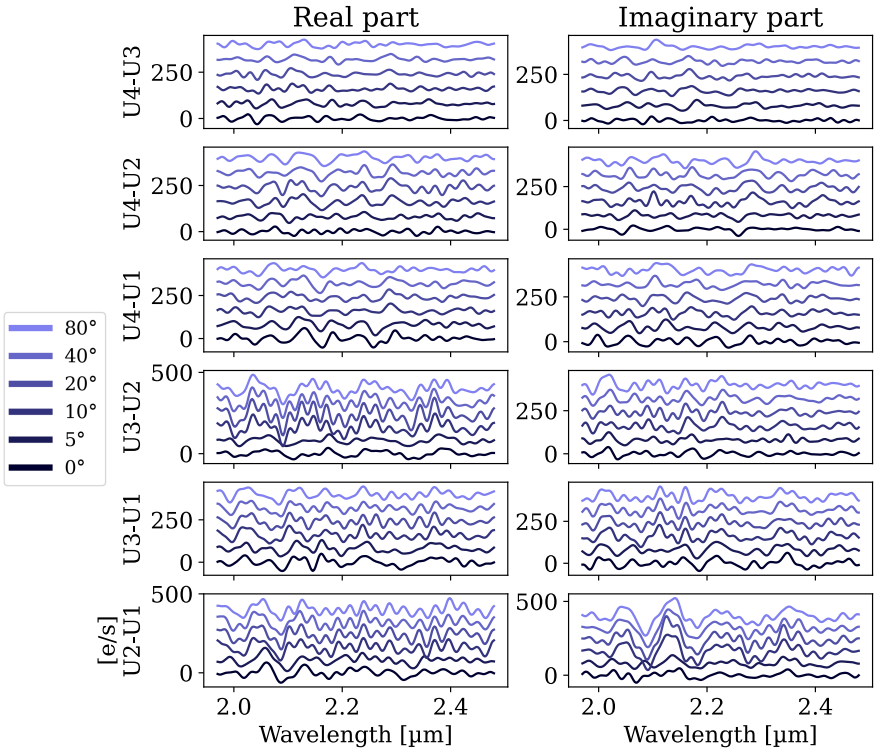

Figure 4.19 – Post `astrometry_reduce` residuals for different derotator angles. SC fibers at 100 mas. High-frequencies filtered. Calibration unit. Artificial waterfall offset.

P2VM calibration At the end of each night, a new P2VM matrix is measured in the calibration unit of the instrument. This matrix is crucial for GRAVITY data reduction (Sect. 2.4). Julien Woillez brougth to my attention that the P2VM are always measured in the OFF-AXIS mode of the instrument (with the FT-SC fields separated by the roof mirror), even for data reduction of ON-AXIS observations (FT-SC separated by a beam-splitter). If the wiggles come from a reflection in the beam-splitter, it would not be captured in the calibration. Thanks to the Paranal staff, we immediately obtained a ON-AXIS P2VM (taken on 2023-11-17) that I could use to reduce again the data affected by wiggles. I started by the archetypal 2020-03-07 run on β Pic c. Unfortunately, this calibration was not valid anymore, 3.5 years distance between the observation and the P2VM calibration was too long. Only the U4-U3 baseline reduced correctly, and wiggles appeared the same as with the classic OFF-AXIS P2VM. However, the new ON-AXIS P2VM proved to be a good calibrator on the daytime data collected during the technical run of October 2023. It further showed that the wiggles were the same with the ON-AXIS or OFF-AXIS P2VM. This test tends to eliminate the hypothesis of a cause in a reflection of the ON-AXIS beam splitter.

4.5.6 Conclusion

I tested different optics configuration in GRAVITY to identify the instrumental parameters that have an impact on the wiggles. Of all components tested, only the derotator has an impact on the residuals systematics. It is a promising direction for further tests. The objective of these studies was to better understand the wiggles, how they change with time, with position in the field, etc. Unfortunately, these tests did not yet provide a solid physical explanation for the apparition of the wiggles in the ExoGRAVITY residuals. At this point of our knowledge, given all the experience collected on the wiggles' condition for appearance, I would discard the hypothesis of a source in star-light reflection in dichroics or in the beam combiner.

I would rather advocate for a cause in the off-centered light injection in the SC fiber. I have shown in this section that wiggles are a fraction of the starlight injected in the SC. As shown in Fig. 4.20, under realistic atmosphere residuals, between 1 and 10% of the starlight is injected even when the SC fiber is at 100 mas from the star. If a fraction of this off-axis light is affected by some OPD, it could have a wiggle effect in the phase. It would also explain why we do not see wiggles at separation 0 mas, because at this position most of the flux is injected directly at the fiber center and is not affected by this OPD. We could imagine that, as we move the fiber away from the star, the off-axis OPD problem gets more prominent, until we are far enough from the star for the problematic flux fraction to fall below other noise sources. It could explain why we see the wiggles only from 50 to 140 mas separation. However, this theory fails to explain other wiggles' properties. For example, I do not know any physical process that could add 80 µm OPD in an off-centered fiber injection, let alone producing a differential 80 µm OPD on the six baselines.

The cause of the wiggles in GRAVITY is still under investigation.

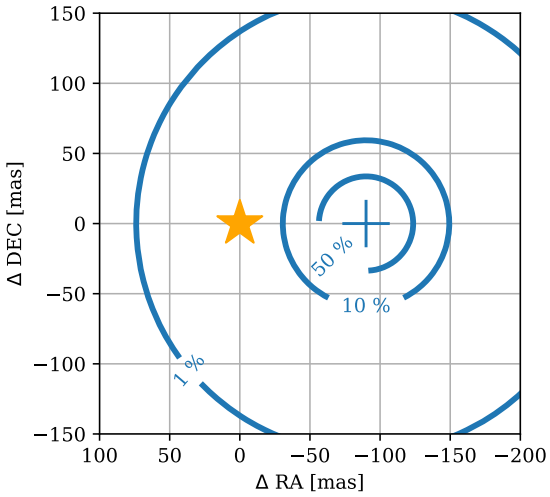

Figure 4.20 – Contour flux injection of the SC fiber including realistic atmosphere residuals.

4.6 Calibration attempts

In order to obtain cleaner and unbiased exoplanet spectra with GRAVITY, there is another way besides correcting the physical source of the wiggles. This other solution is to remove the unwanted signal at the data reduction stage. As shown in Sect. 4.1, this solution has often been favored for

mitigating fringes effects in non-interferometric instruments. These methods must be implemented carefully, to avoid any distortion or masking of the signal of interest. The calibration can bring two equally good solutions: either it corrects the wiggles' effect in spectra, or it corrects the spectrum covariance matrix $\mathbf{C}_{\rm ov}$ such that the wiggles are properly included in the correlated errors.

In the following, the $\chi^2_{\rm red}$ are calculated as:

$$\chi^2_{\rm red} = \frac{[C_{\rm mes} - C_{\rm inj}]\mathbf{C}_{\rm ov}^{-1}[C_{\rm mes} - C_{\rm inj}]^T}{DOF}, \tag{4.4}$$

with $C_{\rm mes}(\lambda)$ the contrast spectrum at the `spectrum_reduce` output, $C_{\rm inj}(\lambda)$ the contrast spectrum injected, and DOF the number of degrees of freedom. Here DOF is taken to 233-5 (number of channels in spectrum - parameters of speckle fit). Thus, the $\chi^2_{\rm red}$ calculation takes fully account of the covariance matrix. The errors for the 233 channels of the spectrum are provided by the GRAVITY pipeline and only account for photon noise and read-out noise (here photon noise dominates). I tested this $\chi^2_{\rm red}$ by injecting bright companions at 10^{-3} contrast in data not affected by wiggles, at 300 mas from the star. I obtained $\chi^2_{\rm red}$=1.7 with the full spectrum and $\chi^2_{\rm red}$=1.3 by cutting the spectrum edges by 30 channels on each side (and adapting DOF accordingly). The spectra edges seem affected by systematics even in no-wiggles conditions.

For all the following calibration attempts, I used on-sky data on HD 206893 c taken on 2021-10-16 in an extensive 27 × 32 × 10 s observation. I removed the planet observed at 111 mas and I injected a planet at PA=+45° but at the same separation as HD 206893 c. I injected it at 8×10^{-5} contrast with a contrast spectrum of the same shape as β Pic b (see Fig. 4.9). This way, my dataset is representative of the kind of long ExoGRAVITY observations we make for obtaining faint exoplanets spectra. For the data reduction, I used the fast mode of the ExoGRAVITY pipeline (average of all NDIT in individual NFILES).

4.6.1 Self calibration

One of my first attempts for the wiggles' calibration was to use the post-`astrometry_reduce` residuals R themselves for cleaning the data before the spectrum reduction.

Remove all residuals

First of all, I made a rudimentary test. This consists in running the `astrometry_reduce` with the default flat contrast assumption and completely remove the residuals from the data before `spectrum_reduce` (Fig. 4.21). The phase term φ_p (REFTOphasingdata) must be added to the residuals to express it in the same referential as the VISDATA. This way the residuals can be suppressed from the `astroreduced` file in a meaningful way.

This procedure removes the wiggles from the data, but, by definition, it also removes everything that is not a planet with a flat contrast spectrum. Indeed, the astrometry fit assumes a flat contrast for the planet, so the post-`astrometry_reduce` residuals contain the planet signal that could not be captured with a flat contrast spectrum. So, unsurprisingly, when we subtract the residuals from the data, the `spectrum_reduce` outputs what is left in the data, namely, a perfectly flat contrast spectrum. I tried different contrast assumptions in the `astrometry_reduce` to obtain different residuals. Each

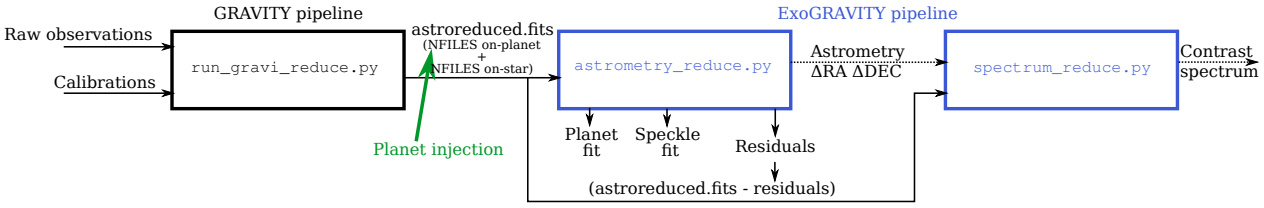

Figure 4.21 – Block diagram from raw observations to planet contrast spectrum with removing residuals before spectrum reduction.

time, the spectrum obtained at the end of the process matches exactly the spectrum assumption provided in the astrometry fit. There is no improvement of the spectrum to expect by this technique but it is a good starting point for the description of more promising calibration solutions.

Remove residual average over time

A slightly more sophisticated solution is to take the temporal average of the post-`astrometry_reduce` residuals over the whole observation. The observation lasts 3.5 hours for a total of 2.4 hours integration time, so, in the star reference, the planet imprint in complex visibilities varies a lot with time (e.g. Fig. 4.1b). From this, I expected that the residuals' average contains most of the wiggles and not too much planet signal not captured by the astrometry fit. Again, I obtained the residuals under the flat contrast spectrum assumption in `astrometry_reduce`. I used the same workflow as Fig. 4.21.

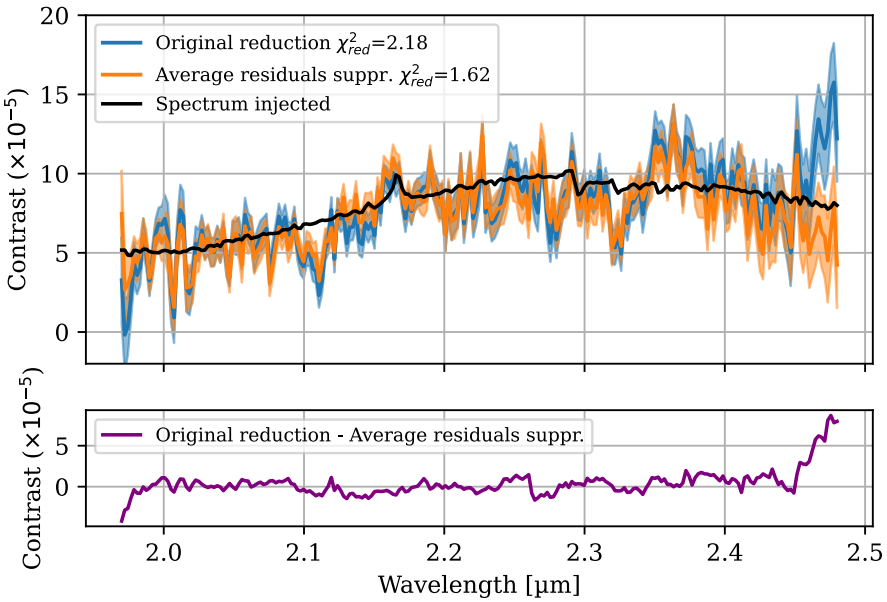

Figure 4.22 – Contrast spectra comparison for the injected planet, with and without removing the residuals average from the data. Blue and orange envelopes show the errors from the GRAVITY pipeline.

Figure 4.22 shows the results of this calibration on the final contrast spectrum. The calibration damps most features, especially at the band borders. This results in a more accurate spectrum with $\chi^2_{\text{red}} = 1.62$ instead of $\chi^2_{\text{red}} = 2.18$. The original spectrum fit gives an average contrast of 7.8×10^{-5} and the calibrated spectrum gives 7.4×10^{-5}, indicating that part of the planet spectrum have been suppressed. In this calibration attempt, the covariance matrix is unchanged.

Modulate the residuals in the joint fit

Instead of suppressing the residuals' average in the `VISDATA`, I attempted a more subtle method. I included the residuals into the fit of `spectrum_reduce` that jointly fits the planet and the speckle term. I added the possibility for the fit to modulate the average residuals by a 4$^{\text{th}}$ degree polynomial P_w, separately on the real and imaginary part of each baseline and file. On our typical ExoGRAVITY observation formula (Eq. (2.48)), it gives:

$$\underline{V}_{\text{onplanet}}(b,t,\lambda) = \underbrace{\underline{P}(b,t,\lambda)\underline{V}_{\text{onstar}}(b,t,\lambda)}_{\text{speckles}} + \underbrace{\underline{P}_w(b,t,\lambda)\left[\sum_t \underline{r}(b,t,\lambda)\right]}_{\text{wiggles}} + \underbrace{\underline{C}(\lambda)\underline{V}_{\text{onstar}}(b,t,\lambda)e^{i\frac{2\pi}{\lambda}[\boldsymbol{\Delta\alpha}\,\mathbf{U}(t)]}}_{\text{planet}} \tag{4.5}$$

This polynomial modulation for the wiggles' fit is additional to the polynomial modulation for the speckle fit. It offers new degrees of freedom to the fit for evacuating systematics.

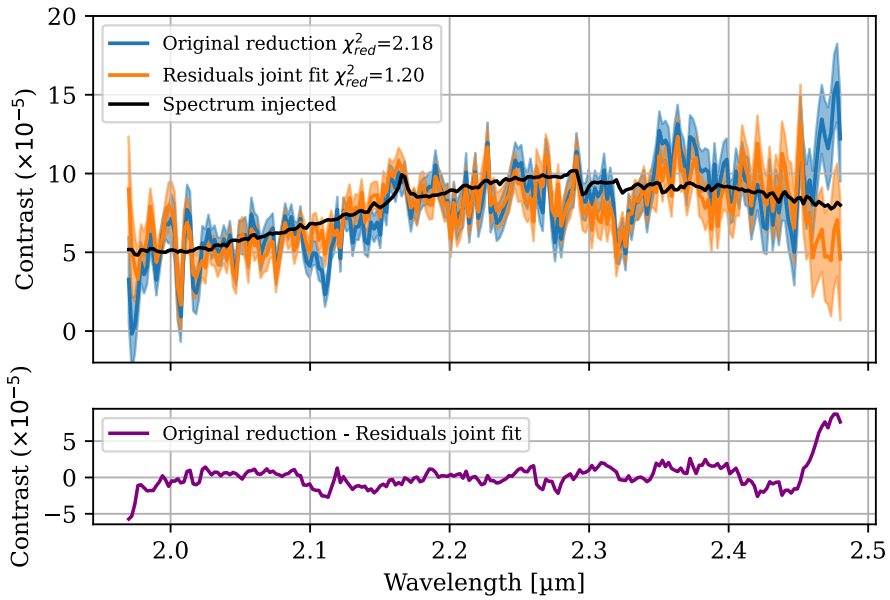

Figure 4.23 – Contrast spectra comparison for the injected planet, with and without adding the residuals fitting in `spectrum_reduce`. Blue and orange envelopes show the errors from the GRAVITY pipeline.

This calibration gives good results, with a $\chi^2_{\text{red}} = 1.20$ (Fig. 4.23). Including new parameters in the spectrum fit modifies the covariance matrix. However, the better χ^2 is not an effect from the covariance matrix alone. Indeed, the squared distance to the injected spectrum is reduced by 37% compared to the classical reduction without wiggles' fit. Attempts with polynomial modulations of order 6 and 8 deteriorated the spectrum. With a 4$^{\text{th}}$ order polynomial modulation, this is a promising calibration solution that seems to efficiently reduce the systematics impact.

4.6.2 Model calibration

Suppressing the model

I tried another calibration solution based on the Fabry-Perot phase model described in Eq. (4.3). I fitted the model on the residuals averaged in NDIT for each of the individual 27 files of the dataset. Visual inspection showed that this fit captured efficiently the wiggles with OPD around 80 µm. Then, I removed this fit, file by file in the `astroreduced` before the spectrum reduction, in the same spirit as previous tests (Fig. 4.21).

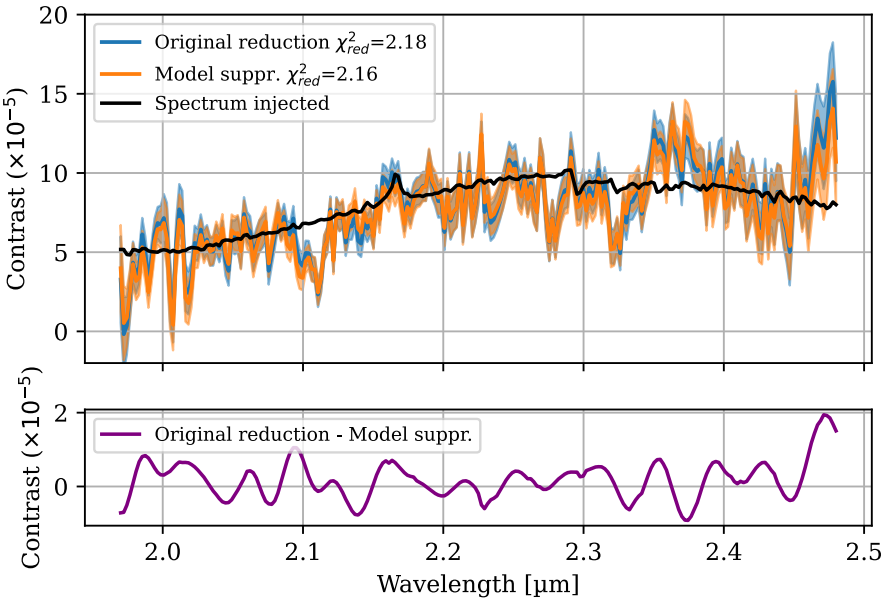

Figure 4.24 – Contrast spectra comparison for the injected planet, with and without removing the Fabry-Perot model from the data. Blue and orange envelopes show the errors from the GRAVITY pipeline.

This model calibration did not change the spectrum significantly (Fig. 4.24). The average contrast retrieved is 7.6×10^{-5} accounting again for a slight loss of planet signal.

Adding the model to the joint fit

Similarly to Sect. 4.6.1, I included the wiggles' model into the fit of `spectrum_reduce` that jointly fit the planet and the speckle term:

$$\underline{V}_{\text{onplanet}}(b,t,\lambda) = \underbrace{\underline{P}(b,t,\lambda)\underline{V}_{\text{onstar}}(b,t,\lambda)}_{\text{speckles}} + \underbrace{\underline{P}_w(b,t,\lambda)W(b,t,\lambda)}_{\text{wiggles}} + \underbrace{\underline{C}(\lambda)\underline{V}_{\text{onstar}}(b,t,\lambda)e^{i\frac{2\pi}{\lambda}[\boldsymbol{\Delta\alpha}\,\mathbf{U}(t)]}}_{\text{planet}} \tag{4.6}$$

The wiggles' model W from Eq. (4.3) cannot be fitted linearly because of the σ parameter in the sine and cosine. So, in a first step, I fitted the wiggles' model on the post-`astrometry_reduce` residuals R, on each file separated, and, in a second step I inject this fit of W to the spectrum fit. As a result, the `spectrum_reduce` cannot modify the frequency of the wiggles' model, but it can modulate the amplitude with a low order polynomial.

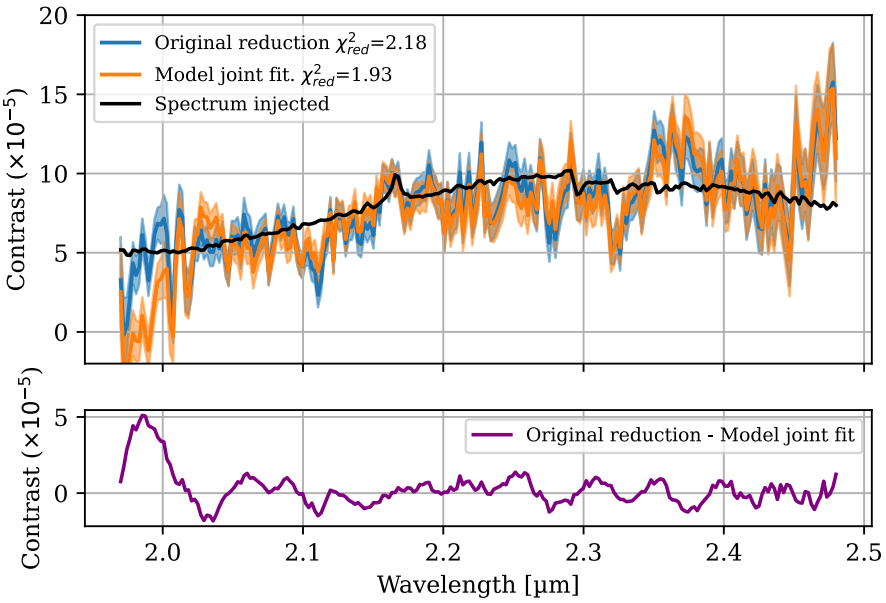

Figure 4.25 – Contrast spectra comparison for the injected planet, with and without adding the Fabry-Perot fitting in `spectrum_reduce`. Blue and orange envelopes show the errors from the GRAVITY pipeline.

Adding these new parameters to the spectrum fit provided a slightly better χ^2_{red} even if the calibration deteriorated the lower end of the contrast spectrum. Indeed, the calibration changed the covariance matrix and thus achieved to reduce the χ^2 while deteriorating the spectrum. This calibration method is not reliable.

I draw two possible conclusions from these model driven calibrations.

- This calibration method is too rigid, with the σ parameters issued from the residuals fit. It would certainly benefit from non-linear additional fit of these parameters in the spectrum reduction.
- The Fabry-Perot model may not capture the most problematic properties of the systematics, and so, fails to significantly improve the contrast spectra.

4.6.3 Off-pointing calibration

Inspired by the SKY acquisitions on GRAVITY and chopping strategy for observations in the mid-infrared, we wanted to investigate the possibility to calibrate the wiggles by observations taken out of the planet position.

The dataset I used in this section do not include pointings at another position than on the planet. To test the possibility of the off-pointing calibration, I used an observation taken on the same star but 20 days before, on the 2021-09-27. It is an acquisition of $8 \times 32 \times 10$ s taken at 71 mas separation, where no planet was found (Fig. 4.26).

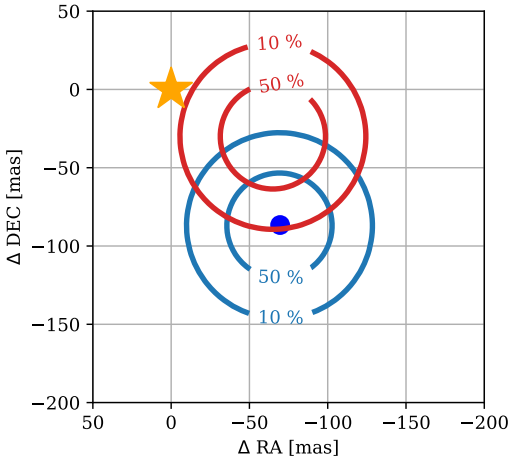

Figure 4.26 – SC fibers' transmission for the observation on planet HD 206893 c (blue dot) the 2021-10-16 (blue contour), and the calibration observation off-planet the 2021-09-27 (red contour). Injection dependence with separation is for coherent flux under standard atmosphere residuals (see Sect. 5.4.1).

I included the off-planet visibilities $\underline{V}_{\rm off}$ into the `spectrum_reduce` script, I took the temporal average (phased on star) over NFILES and NDIT, and added the possibility to modulate this average by a $4^{\rm th}$ order polynomial, similarly to previous add-on to the joint fit:

$$\underline{V}_{\rm onplanet}(b,t,\lambda) = \underbrace{\underline{P}(b,t,\lambda)\underline{V}_{\rm onstar}}_{\text{speckles}} + \underbrace{\underline{P}_w(b,t,\lambda)\left[\sum_t \underline{V}_{\rm off}(b,t,\lambda)\right]}_{\text{wiggles}} + \underbrace{C(\lambda)\underline{V}_{\rm onstar}e^{i\frac{2\pi}{\lambda}[\boldsymbol{\Delta\alpha}\mathbf{U}(t)]}}_{\text{planet}} \quad (4.7)$$

The modulation was done separately on real and imaginary part.

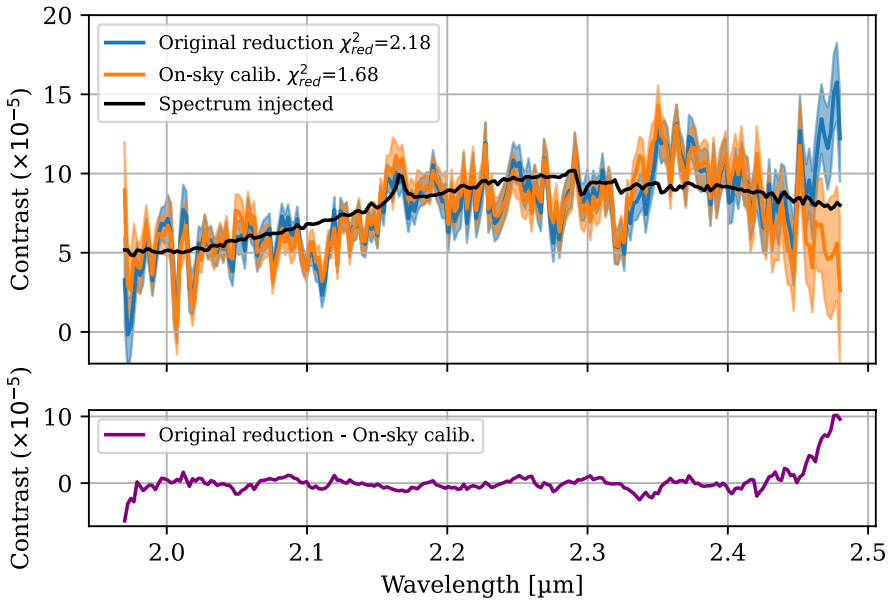

Figure 4.27 – Contrast spectra comparison for the injected planet, with and without calibrating on an off-planet observation. Blue and orange envelopes show the errors from the GRAVITY pipeline.

The results for this on-sky calibration attempt is on Fig. 4.27. The $\chi^2_{\rm red}$ is improved to 1.74 and the squared distance to injected spectrum is improved by 15%. The calibration performance is less

than the previous test with modulation of the residuals of the same observation night at the same fiber position (Sect. 4.6.1). I have shown on the calibration unit that wiggle's phase is changing with the fiber position in the field. On some baselines, wiggles are already changing in phase, amplitude and frequency when moving the SC fibers on a 10 mas scale. This is therefore not surprising that an observation taken at 57 mas distance, additionally at a different separation from the star and at a different date, do not capture well the systematics.

4.6.4 Use planet-VS-speckles diversity

Building up on the previous calibration attempts and the subsequent discussions they triggered, Mathias Nowak and I developed another promising solution based on a modification of the `spectrum_reduce` script.

The wiggles' model for this new solution follows these assumptions that are consistent with the observations:

- wiggles are static in the speckles' referential,
- wiggles can have different amplitudes depending on the baseline.

The speckles' referential is slightly different from the star's referential. It is illustrated in Appendix A.3. The speckles' referential is close to the star's referential but there is an additional low-order modulation that comes from polynomial speckle fit. Empirically, we have verified that the solution better captured the wiggles when we considered that the wiggles are static in the speckles' referential, rather than static in the star's referential.

In the script `spectrum_reduce`, we cannot implement a model for static wiggles in the same way we implemented new degrees of freedom in the previous sections. When we added new degrees of freedom to the joint fit in Eq. (4.5), (4.6) and (4.7), it was always in the philosophy of adding a new term that resembles the speckles term, and to fit it in the same way we fit the speckles. This time, we did not want to modulate a signal with a polynomial, we rather wanted to capture what is static in the speckles' referential. To achieve this, the right way to proceed is to add a term that resembles the planet term. Our first attempt was of the form:

$$\underline{V}_{\text{onplanet}}(b,t,\lambda) = \underbrace{\underline{P}(b,t,\lambda)\underline{V}_{\text{onstar}}}_{\text{speckles}} + \underbrace{\underline{C}(\lambda)|\underline{V}_{\text{onstar}}|e^{i\frac{2\pi}{\lambda}[\mathbf{\Delta\alpha U}(t)]}}_{\text{planet}} + \underbrace{\underline{C}_w(b,\lambda)|\underline{V}_{\text{onstar}}|e^{-i\arg(\underline{P}(b,t,\lambda))}}_{\text{wiggles}}. \tag{4.8}$$

In this equation, the planet term captures the fraction of V_{onplanet} that is referenced on the planet position (complex exponential term) and that has the same transmission as V_{onstar}. The transmission can vary with λ and with the baseline b. It holds under the assumption that the instrument and atmosphere transmission have not changed too much in time between the acquisition on planet and the acquisitions on star. In this referential and with this transmission, the script can output the planet-to-star contrast $C(\lambda)$.

Similarly, the wiggles' term captures the fraction of V_{onplanet} that has the same transmission as V_{onstar} but that is referenced on the speckles. The additional output is the wiggles' contrast $C_w(b,\lambda)$. Contrary to $C(\lambda)$, the wiggles' contrast $C_w(b,\lambda)$ has a real and imaginary part. Before the joint fit, we need to obtain the polynomial phase $\arg(P(b,t,\lambda))$ necessary for a phasing at the speckle

referential. The cleanest way to obtain it is to use the polynomials obtained for the speckle fit at the previous stage, in the `astrometry_reduce` script.

This new model implemented in the ExoGRAVITY script[3] opens new possibilities for tests. The use of $|V_{\text{onstar}}|$ for the wiggles' transmission was motivated by the assumption that the wiggles originate from star flux. In practice, I found that using the residuals post-`astrometry_reduce` $|r|$ instead of $|V_{\text{onstar}}|$ captured better the wiggles. Therefore, for the following test on the synthetic planet I used:

$$\underline{V}_{\text{onplanet}}(b,t,\lambda) = \underbrace{\underline{P}(b,t,\lambda)\underline{V}_{\text{onstar}}}_{\text{speckles}} + \underbrace{\underline{C}(\lambda)\underline{V}_{\text{onstar}}e^{i\frac{2\pi}{\lambda}[\mathbf{\Delta\alpha U}(t)]}}_{\text{planet}} + \underbrace{\underline{C}_w(b,\lambda)|\underline{r}(b,t,\lambda)|e^{-i\arg(\underline{P}(b,t,\lambda))}}_{\text{wiggles}} \tag{4.9}$$

In this equation, the contrasts $C_w(b,\lambda)$ can be understood as the best fit for everything that is static in the speckles referential, given a transmission corresponding to the features present in post-`astrometry_reduce` residuals. Implementation wise, it consists is in modifying the matrix $\underline{\mathbb{R}}$ presented in Eq. (2.70). I give the details on the implementation in Appendix A.4.

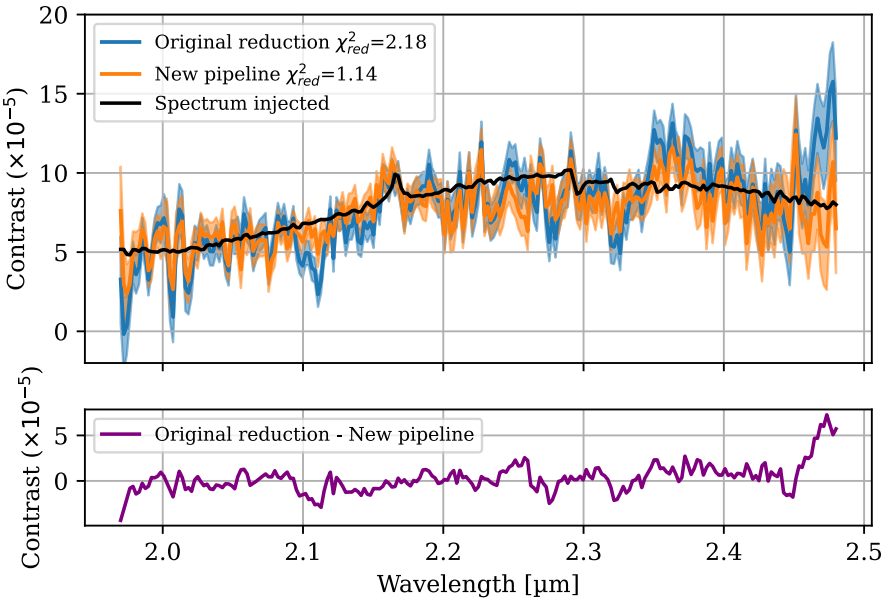

Figure 4.28 – Contrast spectra comparison for the injected planet, with the original and with the new pipeline version. Blue and orange envelopes show the errors from the GRAVITY pipeline.

The result for this calibration strategy is shown in Fig. 4.28. The χ^2_{red} is equal to 1.14, that is the closest to 1 I achieved in all my tests. Moreover, the square-distance to the injected spectrum is reduced by 49% compared to the classical reduction without wiggles' fit. The covariance matrix of the planet spectrum is modified by the addition of the wiggles term and we believe that it new covariance matrix better capture the correlated errors in the signal.

This method relies on the difference between the planet's referential and the speckles' referential.

[3] in the branch `newstyle` of the ExoGRAVITY pipeline

The speckles' referential is slowly evolving with time but stays close to the star's referential, so the efficiency of the method relies on the diversity of the planets referential due to the UV plane change with time. In the long dataset I used for these tests, the sky rotation (variation of parallactic angle) is 115°, and the spectrum looks significantly improved by the additional wiggles' fit. I tested this wiggles' fit on a shorter dataset with only $\sim 40°$ sky rotation, and, on the contrary, the spectrum improvement was marginal.

4.6.5 Summary of calibration attempts

Here end our explorations on calibration techniques to remove the wiggles' impact on the contrast spectrum. Table 4.3 shows a summary of the spectrum improvement with the different techniques.

Table 4.3 – Result from calibrations attempts

	$(C - C_{\texttt{inj}})^2$	χ^2_{red}	Cov. matrix	Average contrast
Original reduction	8.9×10^{-8}	2.18	—	7.8×10^{-5}
Calibrations	Relative sq. dist.[§]			
Removed residuals average	-35%	1.62	Unchanged	7.4×10^{-5}
Modulated residuals average	-37%	1.2	Modified	7.5×10^{-5}
Removed model	-11%	2.16	Unchanged	7.6×10^{-5}
Modulated model	+38%	1.93	Modified	7.5×10^{-5}
Off-pointing calibration	-15%	1.68	Modified	7.6×10^{-5}
Planet-vs-speckles diversity	**-49%**	**1.14**	**Modified**	$\mathbf{7.5 \times 10^{-5}}$

The proposed new version of the `spectrum_reduce` presented in Sect. 4.6.4 is the most promising pipeline solution against the wiggles. Based on additional spectrum retrieval on synthetic Gaussian-noise (not detailed here), I believe that the corrected spectrum is cleaned from systematics, and therefore, close to the statistical noise limit.

4.7 Towards a solution

All the studies I conducted for understanding the wiggles' source and for finding the best way to calibrate it did not yet converged to an operational solution. However, I now see promising ways forward for limiting the impact of systematics on ExoGRAVITY spectra.

4.7.1 Upgrade of the ExoGRAVITY pipeline

In the previous section, I showed that we found a promising solution that reduces the impact of wiggles and other static systematics in the pipeline. This solution still needs to be tested in different configurations, on true planets and injected, before being implemented in the ExoGRAVITY pipeline.

Already, we can test this new version on the spectra of exoplanets observed with the ExoGRAVITY large program. I reduced the ExoGRAVITY observations of HD 206893 c separately with the classical pipeline and with the solution proposed to fit the wiggles (new pipeline). The observation includes

[§]Square distance to the injected spectrum, relative to the original reduction.

2.4 hours on target. Figure 4.29 shows the comparison of the contrast spectra obtained. Here we do not have the ground truth so we cannot compute a χ^2 or a squared distance. By qualitative inspection, I notice that the wiggles' fit of the new pipeline tends to reduce the prominence of some features, for example at 2.13 µm and 2.27 µm. Also, it significantly damps the increase of the contrast at the band border above 2.4 µm.

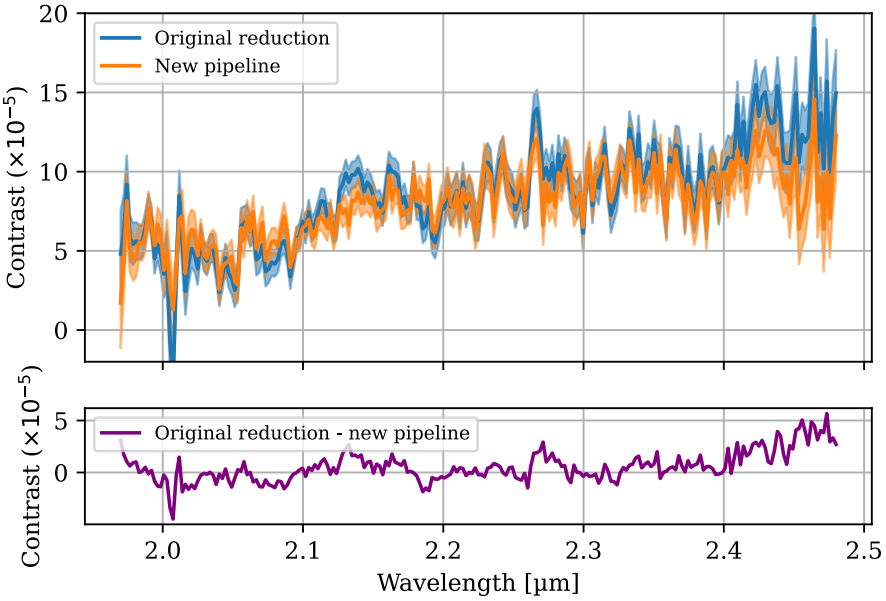

Figure 4.29 – Contrast spectrum of HD 206893 c, comparison with and without the wiggles' correction of the new pipeline.

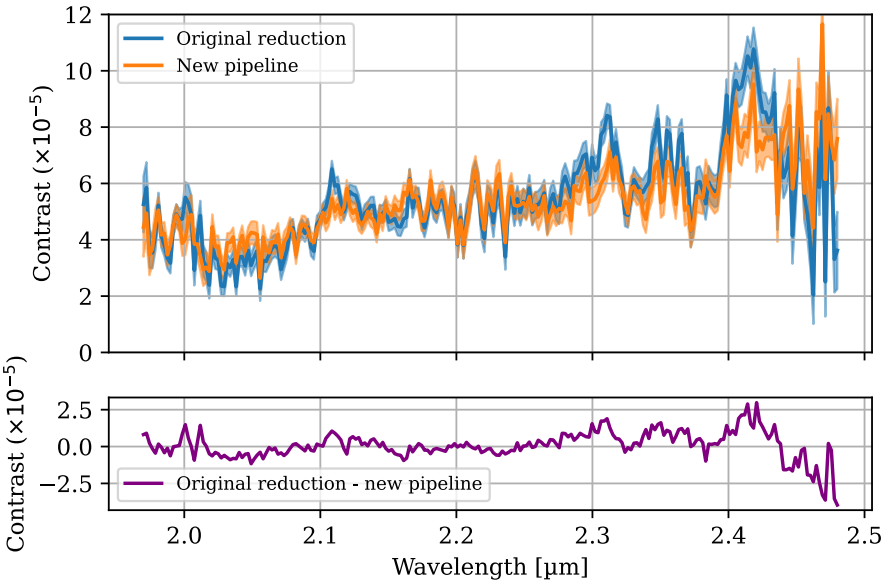

Figure 4.30 – Contrast spectrum of β Pic c, comparison with and without the wiggles' correction of the new pipeline.

I repeated this comparison for β Pic c observation combining three runs on target for a total of 2.8 hours integration. The comparison is in Fig. 4.30, the amplitude of the correction is similar to

the previous comparison on HD 206893 c. Similarly, some features are reduced in the spectrum and, again, the biggest correction is at the higher-end of the contrast spectrum.

From these spectra comparison alone, we cannot push the analysis much further. An interesting way forward would be to measure the impact of the wiggles' correction on the exoplanets' characteristics measured by atmosphere fitting. In the two cases tested here, the wiggles' correction does not seem to significantly change the slope of the contrast spectra, so I do not expect a big effect on the exoplanet temperature. However, measuring the potential change in other parameters like the $\log(g)$, the metallicity or the C/O ratio would help us to determine what is robust against the wiggles, and what is not. More importantly, I also believe that the atmosphere parameters obtained on the corrected spectrum would be more accurate.

According to me, this wiggles' fit improves the spectrum quality even in non-wiggles cases. I have preliminary results from retrieval of injected spectra in AF Lep B observation where we see no wiggles in the residuals. In this case, the wiggles' fit still brings better retrieval, especially by correcting the features at the K-band borders.

4.7.2 Instrumental solutions

In Sect. 4.4 and 4.5, I have shown that the wiggles roughly scale with the coherent flux from the light that is injected at the planet position. Moreover, I will show in Chapter 5 that GPAO and the high-contrast mode shall reduce the star injection at the planet position by a factor close to 10 at separations from 80 to 150 mas. So, we can expect that the wiggles' amplitude and any systematics that scale with the star flux will be reduced by a same amount. With both GPAO and a high-contrast mode implemented in GRAVITY+ in the months to come, it will be worth to observe again the actually challenging planets β Pic c and HD 206893 c and obtain higher SNR K-band spectra. For the new fainter exoplanets we will certainly discover at separations closer than 150 mas, it is still to be determined if wiggles will still be a significant problem.

Apart from the new adaptive optics, another solution against the wiggles has been imagined by Sylvestre Lacour and Guillaume Bourdarot and will soon be tested on technical time. It consists in a pupil modulation during the planet observation. The modulation pattern changes the imaging baselines (Woillez and Lacour, 2013) by a controlled amount $\boldsymbol{\mu}(t)$ of maximum $\pm$50 cm and so the exoplanet signal changes accordingly:

$$\underline{V}_{\text{onplanet}}(b,t,\lambda) = \underline{P}(b,t,\lambda)\underline{V}_{\text{onstar}} + C(\lambda)|\underline{V}_{\text{onstar}}|e^{i\frac{2\pi}{\lambda}[\boldsymbol{\Delta\alpha}(\mathbf{U}(t)+\boldsymbol{\mu}(t))]} \tag{4.10}$$

As the wiggles are generated in the instrument, they are independent from the baseline, so they would not be affected by the pupil modulation. This technique can be interpreted as a way to force planet-wiggles diversity, and not just relying on sky and UV plane rotation to disentangle the planet from the systematics. It may even help recovering the planet signal in other systematic noise, even in observations that are not affected by the wiggles, and thus improving the detection limits at little cost.

4.8 Conclusion

Now we have a better understanding of the correlated structures in the K-band visibilities of GRAVITY. From the analysis of on-sky and calibration unit data, I conclude that the wiggles originate from stellar flux leaking in the SC fiber. From tests on the calibration unit, I could conclude that the wiggles' problem comes from GRAVITY itself, and not from the VLTI. I could exclude a cause in most of the optical parts of the instrument, only a field rotation with the K-mirror changes the wiggles' shape in the residuals of internal ExoGRAVITY-like observations. But, at this time, we did not yet pinpoint the cause of the wiggles.

I tested different calibration strategies in the ExoGRAVITY pipeline, and eventually we found a promising solution that seems to efficiently disentangle the wiggles from the planet. According to me, implementing it in the `master` branch of the ExoGRAVITY pipeline is a priority.

In the future, we can reasonably expect that with the higher Strehl of GPAO, less stellar light will leak in the SC fiber and the wiggles' amplitude will be significantly reduced.

Chapter 5

GRAVITY+ high-contrast mode

Contents

The injection of host star light in the SC at the planet position is the unanimous limit for planet detection and characterization with GRAVITY. It is a fact I demonstrated in Chapter 3 and Chapter 4. Since I have identified this single major limitation, we can put all our efforts towards limiting as much as possible the speckles' injection in the SC fiber. This is timely with the commissioning of the new GRAVITY+ adaptive optics GPAO this year in 2024. The new AO is expected to routinely provide K-band Strehl of 80% against the actual ∼30% with MACAO, and thus make a big leap towards the diffraction limit of the UT. This better atmosphere correction will already contribute to reduce the star light injected in the SC fiber during planet observations. It will also open the way for wavefront control and Non Common-Path Aberrations (NCPA) control solutions that are expected to bring remarkable improvement. This chapter describes the work I did to prepare the ground for a high-contrast mode before the advent of GPAO.

In this chapter, I first describe the increasing importance of techniques to create high-contrast zones (dark holes) in direct imaging (Sect. 5.1, Sect. 5.2) and fibered instruments (Sect. 5.2.2). Then, I describe a rudimentary but efficient strategy to improve the contrast already on GRAVITY, the tip-tilt dark hole (Sect. 5.4). After this, I explore phase apodizations for digging dark holes with GRAVITY+ (Sect. 5.5, Sect. 5.6). I finish the chapter with a description of my work on aberration control and beam-stabilization (Sect. 5.7, Sect. 5.8).

My related publications

- (Pourré et al., 2022c) : Pourré, N., Le Bouquin, J.-B., Woillez, J., et al. (2022c). Digging a dark hole in GRAVITY: towards Jupiter-like observations at the astronomical unit scale. In Mérand, A., Sallum, S., & Sanchez-Bermudez, J., editors, Optical and Infrared Interferometry and Imaging VIII, volume 12183 of Society of Photo-Optical Instrumentation Engineers (SPIE) Conference Series, page 121830V.

- (Pourré et al., 2024) : Pourré, N., Winterhalder, T. O., Le Bouquin, J.-B., Lacour, S., et al. (2024). High contrast at short separation with VLTI/GRAVITY: bringing Gaia companions to light. A&A, 686:A258.

- (Pourré et al., 2022a) : Pourré, N., Le Bouquin, J. B., Milli, J., et al. (2022a). Low-wind-effect impact on Shack-Hartmann-based adaptive optics. Partial control solution in the context of SPHERE and GRAVITY+. A&A, 665:A158.

- (Pourré et al., 2022b) : Pourré, N., Le Bouquin, J. B., Milli, J., et al. (2022b). Understand and correct for the low wind effect on the SPHERE and GRAVITY+ adaptive optics. In Schreiber, L., Schmidt, D., & Vernet, E., editors, Adaptive Optics Systems VIII, volume 12185 of Society of Photo-Optical Instrumentation Engineers (SPIE) Conference Series, page 121855C.

5.1 From extreme AO to dark holes

For the past fifteen years, the AO technologies improved a lot on the number of actuators of the deformable mirrors and on the wavefront sensors sensitivity. Now, the most advanced AO instruments are called Extreme Adaptive Optics, like SPHERE (Beuzit et al., 2019), GPI 2.0 (Chilcote et al., 2020), SCExAO (Jovanovic et al., 2015). They are characterized by fast ($>$ 1 kHz) and high order ($\sim$1000 modes) atmosphere correction and specific control of vibration and NCPA. After the post-processing techniques of angular-differential imaging (Marois et al., 2006), reference differential imaging (Lafrenière et al., 2007) and spectral differential imaging (Racine et al., 1999), they can detect exoplanets at 10^{-6} contrast at 1 arcsec in the near infrared.

Their biggest limitations now are servolag from the adaptive optics (wind-driven halo, Cantalloube et al., 2020) and quasi-static aberrations from NCPA (Vigan et al., 2022) or low-wind effect (LWE, Sauvage et al., 2016; Milli et al., 2018). Against the wind-driven halo, the chosen solution on SPHERE is to build a faster, pyramid-based, second stage of adaptive optics (Boccaletti et al., 2020a). Against static and quasi-static aberrations, one solution is to measure them directly on the science camera with a Zernike phase mask (N'Diaye et al., 2013a). Another solution is to design focal-plane wavefront sensing algorithms, that together with phases introduced by the pupil-plane deformable mirror, can converge to reducing the speckle impact on the whole field or on a given field area.

These high-contrast strategies are called wavefront-control techniques. If they correct speckles of the whole focal plane, these algorithm coupled to a pupil plane deformable mirror can only correct for phase aberrations. However, if they focus on reducing the speckles impact only in a specific region they can correct both amplitude and phase aberrations to reach deeper contrasts. The high-contrast zone created is called "dark hole" (Malbet et al., 1995). The wavefront control technique has been designed and tested on SPHERE (Potier et al., 2020, 2022) with reduction up to $\times$5 of the speckles intensity on sky. It is also developed on SCExAO (Ahn et al., 2023) where they reach $\times$100 to 500 on internal source and on MagAO-X (Haffert et al., 2023) with promising results on test bench.

5.2 Dark-holes theory

5.2.1 Electric field conjugation

The theory of wavefront control writes as:

$$E_P = Ae^{\nu+i\phi}e^{i\phi_{DM}} \tag{5.1}$$

with E_P the electric field in the pupil, A the pupil transmission, ν the amplitude aberrations, ϕ the phase aberrations and ϕ_{DM} the phase introduced by the deformable mirror. In the small phase approximation, the first order expansion gives:

$$E_P = A + iA\phi_{DM} + A(\nu + i\phi) \tag{5.2}$$

The electric field at the focal plane is then:

$$E_F = \mathcal{F}[A] + i\mathcal{F}[A\phi_{DM}] + \mathcal{F}[A\nu] + i\mathcal{F}[A\phi] \tag{5.3}$$

$$= E_D + E_{DM} + E_A \tag{5.4}$$

with $\mathcal{F}$ the Fourier transform, E_D the electric field induced by the pupil diffraction, E_{DM} the electric field induced by the deformable mirror and E_A the electric field induced by the aberrations. The goal of the electric field conjugation is to minimize $||E_{DM} + E_D + E_A||^2$, the light's intensity, at a given position of the focal plane. It is how dark holes are created.

Going back to Eq. 5.3, we can break Φ_{DM}, ν and Φ in odd and even components:

$$E_F = \underbrace{\mathcal{F}[A]}_{\text{Re}} + \underbrace{i\mathcal{F}[A\phi_{DM,o}]}_{\text{Re}} + \underbrace{i\mathcal{F}[A\phi_{DM,e}]}_{\text{Im}} + \underbrace{\mathcal{F}[A\nu_o]}_{\text{Im}} + \underbrace{\mathcal{F}[A\nu_e]}_{\text{Re}} + \underbrace{i\mathcal{F}[A\phi_o]}_{\text{Re}} + \underbrace{i\mathcal{F}[A\phi_e]}_{\text{Im}} \tag{5.5}$$

The core of most wavefront control algorithm is to identify the phase ϕ_{DM} to apply on the deformable mirror to tackle the focal plane impact of aberrations ν and ϕ. We need odd modes on the deformable mirror to tackle the pupil diffraction, the even amplitude aberrations ν_e and odd phase aberrations ϕ_o. We need even modes to tackle odd amplitude aberrations ν_o and the even phase aberrations ϕ_e.

On high-contrast imaging instruments, the electric field aberrations are measured thanks to probes sent with the deformable mirror. In the pairwise probing technique (described in Give'on et al., 2007; Potier et al., 2020), two probes of opposite amplitude are applied successively, and an image is recorded for each one. If we have a good knowledge of the influence functions of the deformable mirror, it is then possible to have an estimate of E_D and E_A. All that is left, is to apply the opposite phase $(-E_D - E_A)$ on the deformable mirror to create the dark zone with reduced speckles amplitude.

5.2.2 Specifics for fiber instruments

Some high-contrast instruments, like Keck/KPIC (Delorme et al., 2021b) or GRAVITY, do not have a camera at their science focal plane but a single-mode fiber. For KPIC, this is to enable high resolution spectroscopy (R>30 000). For GRAVITY, this is to enable interferometric beam recombination by integrated optics. This poses specific questions in the context of wavefront control for creating dark holes.

In fibered instruments, the only field location where we are interested in reducing the speckles impact is in the fiber field-of-view. This relaxes the degree of freedom of the problem, and the stroke required on the deformable mirror for the correction. However, the only information we have from the electric field is the intensity of the light injected at different wavelengths (and eventually the phase in GRAVITY, see Sect. 5.9). There are different approaches for creating dark holes in single-mode instruments.

Phase apodization

First, we can inject a pre-defined OPD map that is designed to create a null at the fiber location. This resembles the phase apodization developed for imaging (Guyon, 2003; Yang and Kostinski, 2004), however, the light coupling in the fiber's mode offers specific possibilities. This is the technique chosen by Emiel Por and Sebastiaan Haffert in their instrumental concept Single-mode Complex Amplitude Refinement (SCAR, Por and Haffert, 2020; Haffert et al., 2020). The instrument is composed of six micro-lenses that each feed a fixed single-mode fiber at 1.6 λ/D separation. They used simulations and Gurobi minimizers together with the method for coronagraph optimization of Carlotti et al. (2013). At the diffraction limit, they found that best solution is to join the first zero and the second zero of the diffraction pattern to create a dark hole at a short separation. As shown on Fig. 5.1a, in unaberrated conditions and at a single wavelength, the light injection in a single-mode fiber reaches a perfect null when the fiber overlaps the first zero of the diffraction pattern. One way to widen the null and make it more robust to tip-tilt jitter and chromaticity is to join the first and second null under the fiber mode. This strategy applies to our case on GRAVITY.

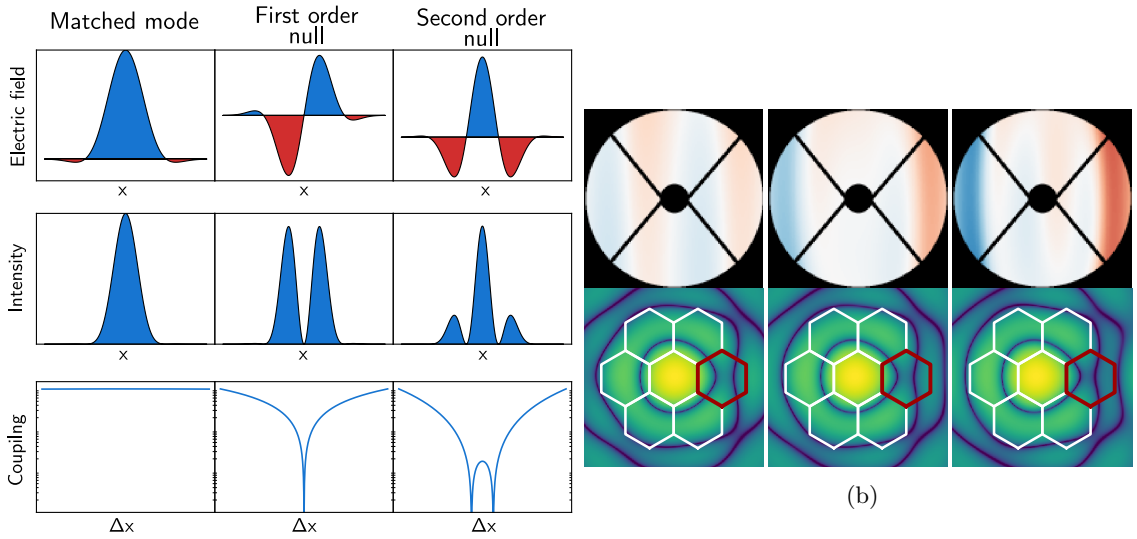

Figure 5.1 – From Por and Haffert (2020), Fig. 2 and 8. (a) Coupling efficiency in a single-mode fiber when centered on a star (left), when overlapping a zero (center) and when overlapping two zeros (right). (b) The SCAR optimal modes for average normalized star flux injected of 1×10^{-4}, 3×10^{-5} and 1×10^{-5}. These simulations include a 20% bandwidth.

They obtained the best OPD offset to tackle the diffraction of a VLT/UT pupil at $\lambda = 750\ nm$ (Fig. 5.1b), and this for different bandwidths. They tested it on bench and achieved $\times50$ reduction of the star injection in the off-axis fiber. The major drawback of the static apodization is that it assumes a diffraction limited system and does not adapt to instrumental changes, like quasi-static NCPA.

Semi-analytical model

In a forthcoming paper, Sylvestre Lacour and Mathias Nowak will publish a semi-analytical model, close to speckle-nulling, for the optimal phase apodization in the context single-mode fiber

injection for optical interferometry. The strategy focuses on reducing the stellar flux injected in the SC for individual telescopes. In this respect, this is not specific to interferometry but could also apply to other single-telescope instruments.

Expressed at pupil plane, the stellar intensity in the single mode fiber, when observing a planet at a separation $\boldsymbol{\Delta\alpha}$, is:

$$I_{P*} = \left| \iint A\, M_P\, \exp\left(i\left[\phi(\mathbf{u}) + \phi_{DM}(\mathbf{u}) - k\boldsymbol{\Delta\alpha}\cdot\mathbf{u}\right]\right) \mathrm{d}\mathbf{u} \right|^2, \tag{5.6}$$

with u the spatial coordinates in the pupil, ϕ the residual phase aberrations from the atmosphere or NCPA, ϕ_{DM} a phase apodization induced by the deformable mirror and k the wavenumber. They want to find the apodization ϕ_{DM} that minimizes I_{P*}. For this, they assume that ϕ_{DM} respects two symmetries:

$$\phi_{DM}(\mathbf{u}) = \phi_{DM}(\mathbf{u}') \quad \text{if} \quad \boldsymbol{\Delta\alpha}\cdot\mathbf{u} = \boldsymbol{\Delta\alpha}\cdot\mathbf{u}' \tag{5.7}$$

$$\phi_{DM}(\mathbf{u}) = -\phi_{DM}(\mathbf{u}') \quad \text{if} \quad \boldsymbol{\Delta\alpha}\cdot\mathbf{u} = -\boldsymbol{\Delta\alpha}\cdot\mathbf{u}'. \tag{5.8}$$

Equation 5.7 forces the phase to be equal along the direction perpendicular to the star-planet axis. Equation 5.8 forces the phase function to be odd along the star-planet axis. Also, they want the apodization to be as small as possible in order to preserve the Strehl and, consequently, the planet injection. This adds to the constraints:

$$\iint |\phi_{DM}(\mathbf{u})|^2 \mathrm{d}\mathbf{u} \approx 0. \tag{5.9}$$

Finally, they we consider that the fiber apodization M_P is 1 over the whole pupil.

With these assumptions, they develop an analytical solution that lead them to an apodization of the shape:

$$\phi_{DM}(u) = k[a\sin(k\boldsymbol{\Delta\alpha}\cdot\mathbf{u}) + b(k\boldsymbol{\Delta\alpha}\cdot\mathbf{u})\cos(k\boldsymbol{\Delta\alpha}\cdot\mathbf{u})]. \tag{5.10}$$

The two parameters a and b can either be estimated in simulation or optimized iteratively to reduce star injection. This apodization is based on first order linear approximations but the model can be enhanced by adding higher order terms at the price of additional parameters to optimize. In the spirit of "simple is better", at least for a first try, I tested the focal plane impact of the two parameters model of Eq. (5.10) in simulation in Sect. 5.5.

Iterative algorithms

To have a dark-hole less rigid than a static phase apodization, it is possible to use iterative algorithms that actively adapt the OPD map applied on the deformable mirror to the instrumental conditions. This is the route taken by Llop-Sayson et al. (2019), Llop-Sayson et al. (2022) in the visible with a pair-wise probing and electric field conjugation adapted to a single-mode fiber at the focal plane. The formalism is the following (adapted from Llop-Sayson et al., 2019). From Eq. 5.4,

the first order expansion of the intensity I_F injected in a single-mode fiber is:

$$I_F = \left| \iint (E_D + E_{DM} + E_A)\, M_F \, \mathrm{d}\mathbf{x} \right|^2 , \tag{5.11}$$

with M_F the fiber mode shape at focal plane and $\mathbf{x}$ the focal plane coordinates. A probe injected on the deformable mirror induces the electric field E_p, so I_F can be written:

$$\begin{aligned} I_F = &\left| \iint (E_D + E_A)\, M_F \, \mathrm{d}\mathbf{x} \right|^2 + \left| \iint E_p \, M_F \, \mathrm{d}\mathbf{x} \right|^2 \\ &+ 2\mathrm{Re}\left(\iint (E_D + E_A)\, M_F \, \mathrm{d}\mathbf{x} \times \iint E_p \, M_F \, \mathrm{d}\mathbf{x} \right). \end{aligned} \tag{5.12}$$

And, the intensity difference for a pair of probes of opposite amplitude is:

$$\begin{aligned} \Delta I_F &= 4\mathrm{Re}\left(\iint (E_D + E_A)\, M_F \, \mathrm{d}\mathbf{x} \times \iint E_p \, M_F \, \mathrm{d}\mathbf{x} \right) \\ &= 4 \iint \mathrm{Re}(E_D + E_A)\, M_F \, \mathrm{d}\mathbf{x} \times \iint \mathrm{Re}(E_p)\, M_F \, \mathrm{d}\mathbf{x} \\ &\quad + 4 \iint \mathrm{Im}(E_D + E_A)\, M_F \, \mathrm{d}\mathbf{x} \times \iint \mathrm{Im}(E_p)\, M_F \, \mathrm{d}\mathbf{x}, \end{aligned} \tag{5.13}$$

which gives for n pair of probes:

$$\begin{bmatrix} \Delta I_1 \\ \vdots \\ \Delta I_n \end{bmatrix} = 4 \begin{bmatrix} \iint \mathrm{Re}(E_{p,1})\, M_F \, \mathrm{d}\mathbf{x} & \iint \mathrm{Im}(E_{p,1})\, M_F \, \mathrm{d}\mathbf{x} \\ \vdots & \vdots \\ \iint \mathrm{Re}(E_{p,n})\, M_F \, \mathrm{d}\mathbf{x} & \iint \mathrm{Im}(E_{p,n})\, M_F \, \mathrm{d}\mathbf{x} \end{bmatrix} \times \begin{bmatrix} \iint \mathrm{Re}(E_D + E_A)\, M_F \, \mathrm{d}\mathbf{x} \\ \iint \mathrm{Im}(E_D + E_A)\, M_F \, \mathrm{d}\mathbf{x} \end{bmatrix}. \tag{5.14}$$

This last equation is a linear equation of the form $B = Cx$, where B is the observation, C the expected probe impact on focal plane and x the unknown overlap integral with the electric field from diffraction and aberrations. The estimation $\hat{x}$ is obtained by:

$$\hat{x} = C^+ B, \tag{5.15}$$

where C^+ is the pseudo-inverse of C. The last step is the electric field conjugation. We want to minimize the cost function that is:

$$Y = \left| \iint (E_D + E_A + E_{DM})\, M_F \, \mathrm{d}\mathbf{x} \right|^2 . \tag{5.16}$$

The command to send to the deformable mirror is computed thanks to the transformation matrix from the field space (injected in the fiber) to the actuators voltages. This matrix comes from simulations of the optical system. The probing, flux recording and corrections are iterated until convergence. With this technique, the null in the fiber is not achieved by nulling the intensity over the whole fiber field of view. Instead, it adapts the phase under the fiber to make it asymmetric and cancel the light coupling by phase opposition (as shown for SCAR, on Fig. 5.1a).

An iterative algorithm using a more straightforward speckle-nulling technique has been tested by Xin et al. (2023) for dark-hole creation in the K-band on KPIC. They injected four probes with the deformable mirror to recover the phase of the electric field coupling in the fiber. Then they applied the corresponding correction on the deformable mirror. They tested it on-sky with observations of HD 206893 c at 98 mas ($2\ \lambda/D$) and achieved a moderate $\times 2.7$ star flux reduction. It took 4 iterations to converge on an internal source and the same number of iterations on-sky. To my knowledge, this is the closest experiment to what we want to do on GRAVITY, given the single-mode fiber, the wavelength and the planet separation.

It is still debated if an iterative algorithm like these can be used on GRAVITY in the future (see Sect. 5.9).

5.3 Fiber injection in GRAVITY

I want to build a realistic simulation of the fiber coupling stage of GRAVITY to enable meaningful wavefront control simulations.

5.3.1 Optical properties of the fiber coupler

In GRAVITY, the incoming beam from each individual telescope is injected into two single-mode fibers, the FT and the SC. It is performed by off-axis parabolic mirrors (M12 in Fig. 5.2).

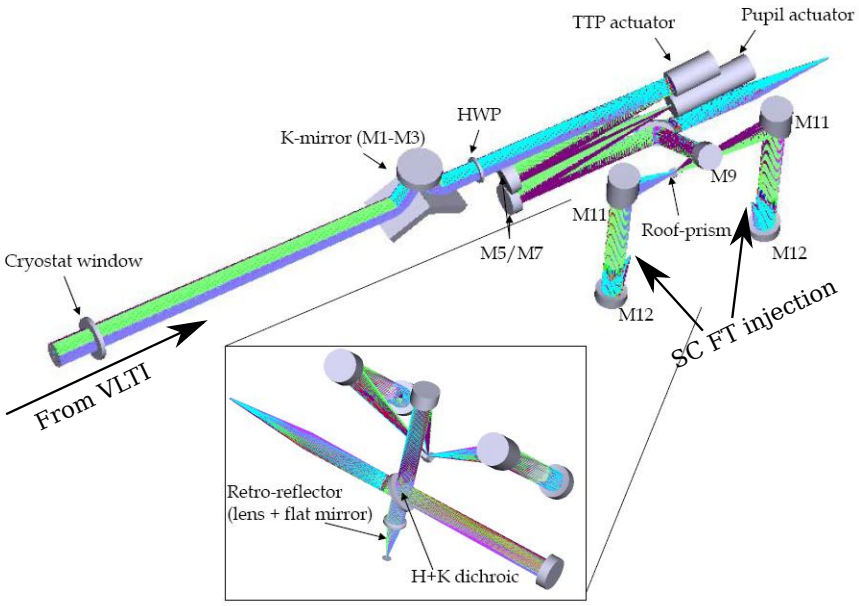

Figure 5.2 – The fiber coupler of GRAVITY. From Pfuhl et al. (2012)

I will focus here on the SC fiber. I approximate the mode shape of the fiber by a Gaussian beam. The Fourier transform of a Gaussian is another Gaussian such that:

$$\mathcal{F}(e^{-\alpha x^2})(u) = \sqrt{\frac{\pi}{\alpha}} e^{-\frac{u^2}{4\alpha}} \tag{5.17}$$

Therefore a Gaussian in focal plane is a Gaussian on pupil plane with a different width.

In the Gaussian beam framework, the fiber beam is described by the mode-field-radius w_0 and the wavelength λ. The mode-field-radius is the distance from the propagation axis z for which the intensity decays by $1/e^2$ of the peak intensity at $z = 0$, where the beam waist is the narrowest (Fig. 5.3). With these parameters we can find the beam radius dependence with the distance z from the fiber.

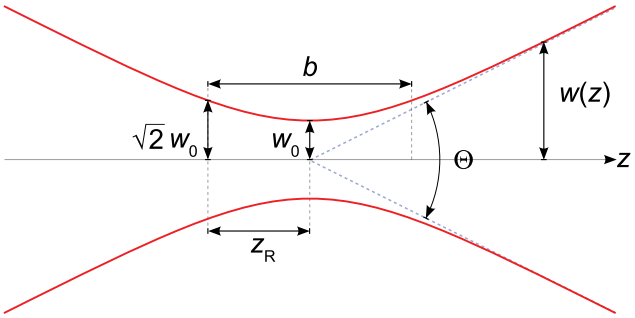

Figure 5.3 – Evolution of w with the distance z for a Gaussian beam. With z_R the Rayleigh length, Θ the angular spread (figure by Rodolfo Hermans for Wikipedia.)

The Rayleigh length z_R is equal to:

$$z_R = \frac{\pi w_0^2}{\lambda} \tag{5.18}$$

and the beam-waist-radius $w(z)$ equals:

$$w(z) = w_0 \sqrt{1 + \left(\frac{z}{z_R}\right)^2} \tag{5.19}$$

It leads us to the optimisation part to be sure that the fiber will collect as much light as possible. A wide field-of-view in the focal plane (a wide Gaussian) results in a narrow Gaussian on pupil plane and is a sub-optimal coupling. Conversely, a narrow field-of-view in the focal plane will result of loss in the injected light. There is an optimum to be found here.

The key parameters for our study are in Pfuhl et al. (2012):

- the wavelength $\lambda = 2.15$ μm, the center of the K-band.
- the mode-field-radius $w_0 = 3.83$ μm
- the beam diameter at the entrance of the instrument $d = 18.0 \pm 0.3$ mm
- the radius of curvature of M9 is $R_{c9} = 200$ mm
- the off-axis distance for M9 is $do_9 = 40.00$ mm
- the radius of curvature of M11 is $R_{c11} = 200$ mm
- the off-axis distance for M11 is $do_{11} = 105.55$ mm
- the radius of curvature of M12 is $R_{c12} = 104.35$ mm
- the off-axis distance for M12 is $do_{12} = 28.00$ mm

As shown in Fig. 5.2, the beam coming from the VLTI is focused by the M5 and recollimated by the M7. M5 and M7 have the same curvature radius and off-axis distance so the beam size is preserved. However, M9 focuses the beam and M11 recollimates but M9 and M11 do not have the same focal

length. The focal length of off-axis parabolas is:

$$f_s = \frac{R_c}{1 + \cos(\sin^{-1}\left(\frac{d}{f_s}\right))} \tag{5.20}$$

that we can numerically iterate to find the focal length f_s. It gives $f_9 = 104$ mm and $f_{11} = 127.8$ mm. The magnification is then:

$$M_{9/11} = \frac{f_{11}}{f_9} = 1.229 \tag{5.21}$$

So after M11 the beam diameter is $d' = M_{9/11}d = 22.1$ mm. In GRAVITY the numerical aperture of the fiber injection is optimized to $F = 2.5$. So:

$$F = \frac{f_{12}}{d'} \quad \Leftrightarrow \quad f_{12} = d' \times F = 55 \text{ mm} \tag{5.22}$$

with f_{12} the focal length of M12. Ultimately, the focal length of M12, the last off-axis parabola, determines the size of the fiber mode on the pupil.

I then wanted to check that I could find the same optimum in simulation. I used the values describing the fiber coupler and kept the f_{12} as a free parameter. I ran the optimization at pupil plane. So the problem was to find for what value of f_{12} the following integral reaches its maximum:

$$C = |\iint A(u,v) \cdot M_P(u,v,w_z)\mathrm{d}\mathbf{u}|^2 = |\iint A(u,v) \cdot \frac{e^{-\left(\frac{\sqrt{u^2+v^2}}{w_z}\right)^2}}{\sqrt{m}w_z}\mathrm{d}\mathbf{u}|^2 \tag{5.23}$$

with A the aperture (here 8 m circular aperture with a circular central obscuration of 1.116 m to match the UT pupil), and M_P the electric mode of the fiber at the pupil plane. The integral of M_P^2 and A^2 are normalised to 1. So C corresponds to the coupling rate, m is the normalisation factor of M_P, and w_z is linked to f_{12} by Eq. 5.19. Exploring f_{12} values from 0.1 mm to 200 mm I found that the maximum for C is reached for $f_{12} = 55$ mm. It matches the value in the instrument. For this optimal value, I foundd a coupling rate of 77.9% in intensity (Pfuhl et al. (2012) gives a 77.8% coupling rate).

In my simulations, most of the time I used the single-mode optimum derived in this section. Sometimes, I used a common approximation in the GRAVITY consortium for the fiber mode on the pupil plane:

$$M_P(d) = \exp(-0.078\ d^2), \tag{5.24}$$

with d the distance from the pupil center in meter. I could verify that the approximation was very close to the physical approach and leads to similar results.

5.3.2 Implementation in simulation

I call "injection map" the flux injected in the fiber at the different positions on the focal plane. To simulated it, I use:

$$E_F^{\text{inj}}(\mathbf{x}_0) = \iint E_F(\mathbf{x}) M_F(\mathbf{x} - \mathbf{x}_0) \mathrm{d}x \tag{5.25}$$

with E_F^{inj} the electric field injected in the fiber at the position $\mathbf{x}_0 = (x_0, y_0)$, $\mathbf{x} = (x, y)$ the focal plane coordinates, and M_F the fiber mode at the focal plane. This is a convolution product:

$$E_F^{\text{inj}}(\mathbf{x}_0) = \{E_F(\mathbf{x}) * M_F(\mathbf{x})\}(\mathbf{x}_0) \tag{5.26}$$

$$= \mathcal{F}[\mathcal{F}\{E_F(\mathbf{x})\}\mathcal{F}\{M_F(\mathbf{x})\}]. \tag{5.27}$$

We can replace $\mathcal{F}\{E(\mathbf{x})\} = A(\mathbf{u})$ the electric field at the pupil plane and $\mathcal{F}\{M_F(\mathbf{x})\} = M_P(\mathbf{u})$ the fiber mode at the pupil plane to obtain:

$$E_F^{\text{inj}}(\mathbf{x}_0) = \mathcal{F}[A(\mathbf{u}) M_P(\mathbf{u})] \tag{5.28}$$

and

$$I_F^{\text{inj}}(\mathbf{x}_0) = ||E_F^{\text{inj}}||^2 \tag{5.29}$$

The UT pupil with the fiber mode and the corresponding injection map are shown on Fig. 5.4.

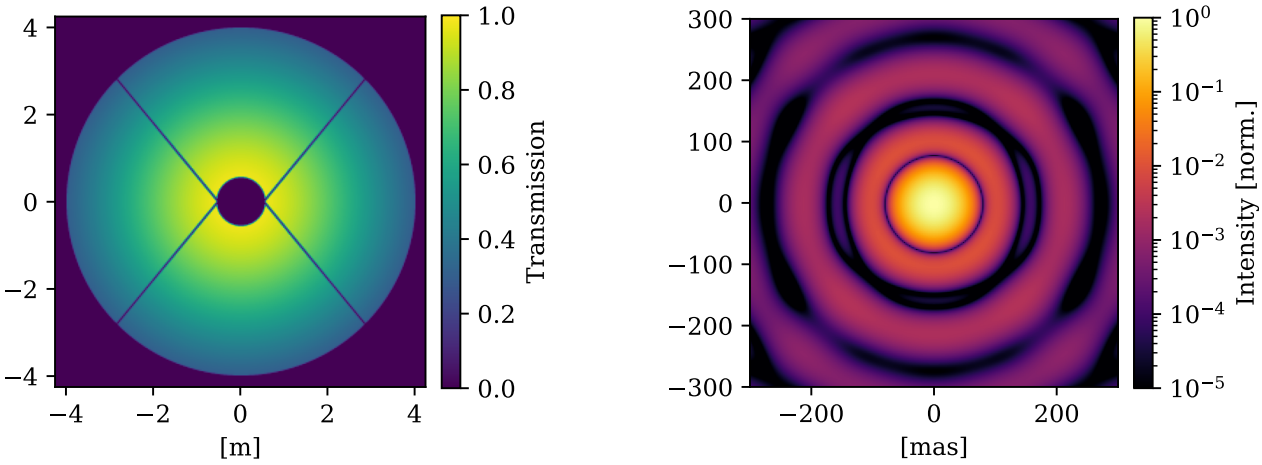

(a) $A(\mathbf{u})M_P(\mathbf{u})$ (b) I_F^{inj}

Figure 5.4 – (Left) Amplitude of UT pupil with the SC fiber mode. (Right) Corresponding injection intensity map at focal plane. Each point of the map represents the injection intensity in the SC fiber for a given position around the star.

It shows that the fiber injection map can be computed from pupil plane directly, in an efficient way. It opened the way for testing strategies to reduce the stellar light injection in simulations.

5.4 Tip-tilt dark hole: from simulations to operation

I have shown in Chapter 3 that GRAVITY has the unique capability to directly observe planets below 100 mas separation. This motivates us to increase the planet-to-star contrast at less than $2\lambda/D$ (113 mas on the UT). At these short separations, we identified that the lowest order Zernike modes played the main role. Here, I describe the key impact of the modes of lowest possible order (piston excluded), tip and tilt.

Straight from the first injection simulations, Jean-Baptiste Le Bouquin identified a regime at short separation where a moderate amount of tip-tilt offset could increase significantly the planet-to-star contrast. Close to diffraction limit the star injection decreases sharply in a separation range from 0.5 to 1.5 λ/D. At the same time, when the SC fiber is pointed on the off-axis planet, the planet injection is relatively stable, up to field offsets of $\pm 0.5\lambda/D$. I tested if it could be used in actual GRAVITY observations, and I quantified the improvement. These results are part of a SPIE proceeding (Pourré et al., 2022c) and a publication in A&A (Pourré et al., 2024).

5.4.1 Simulations for GRAVITY

The first step is to determine the on-sky injection map on GRAVITY using the UT and MACAO. For this, I used archival data to get a realistic estimate of the flux injection dependence with separation. The dataset is composed of observations around bright stars (3.5 >K> 7.5) with the SC fiber at separation from 55 to 411 mas. The atmosphere conditions are from normal to good (0.4" <seeing< 1.0") and are representative of the usual conditions at Paranal.

The `astroreduced` files contain the total flux per telescope for each exposure (`OI_FLUX`) and the coherent flux per baseline for each exposure (`OI_VIS`). I used end-to-end adaptive optics simulations with HCIPy (Por et al., 2018) to obtain a continuous injection profile that matches the observations. I simulated a low order adaptive optics controlling 50 modes (like MACAO) and a Kolmogorov turbulence. I included 20% bandwidth to account for the GRAVITY band from 1.95 to 2.4 µm. The actual tip-tilt jitter in the VLTI tunnels is referenced at 10 mas rms (Anugu et al., 2018), in the simulations I included 8 mas rms instead. It is a conservative value for the residuals we expect with an operational fast guiding system in GRAVITY (Sect. 5.8.1). From this realistic simulation, I adjusted the atmosphere parameters and the adaptive optics loop gain to obtain the best match for the total flux and coherent flux respectively. The result is shown on Fig. 5.5. Continuous profiles match remarkably the observations from short to longer separations.

Now that I have a realistic injection profile, I can make predictions. In operation, we will not use the deformable mirrors to introduce field offset. Instead, the "tip-tilt" will be introduced by changing the SC position in the field by some determined offset. Figure 5.6 shows the example of a planet at 56 mas (1 λ/D). At this separation, a fiber offset of 25 mas in the radial direction opposite to the star allows for a increase of the planet-to-star flux ratio of $\times 1.9$ in total flux and $\times 4.3$ in coherent flux. This simulation also predicts that the flux ratio would be increased by $\times 15.8$ in an unaberrated case. This situation close to the diffraction limit represents the best we could achieve with GPAO with a control of the internal aberrations and extremely good atmospheric conditions.

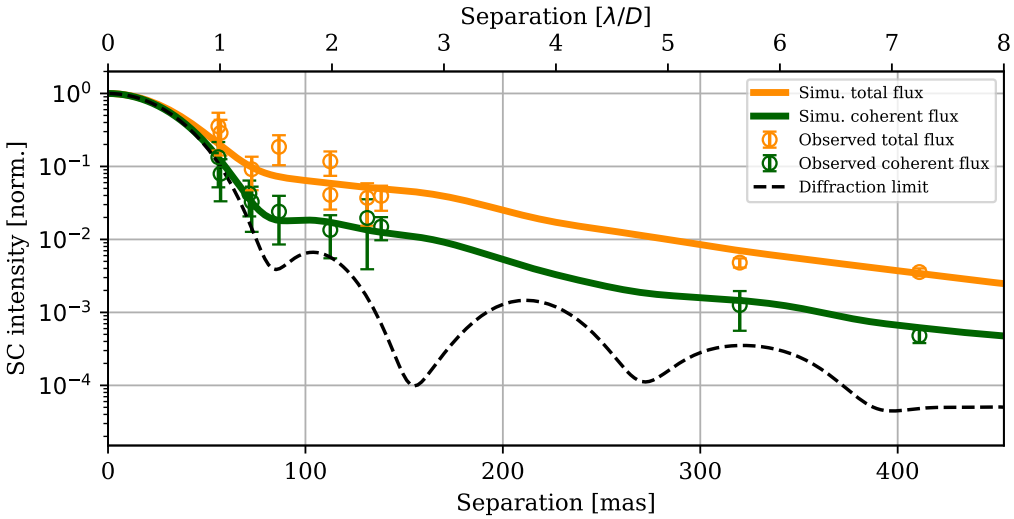

Figure 5.5 – SC injection profiles for total flux and coherent flux based on observations on the UT. The diffraction limit is for 20% bandwidth and 8 mas rms tip-tilt jitter.

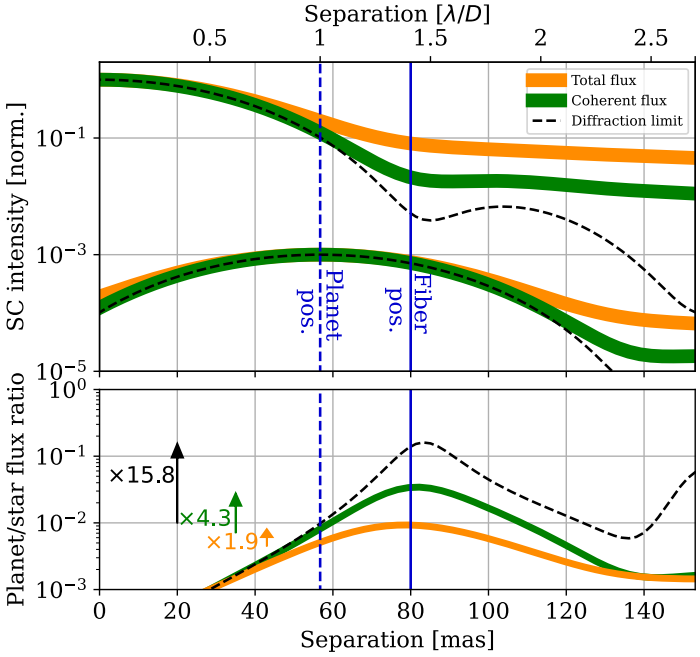

Figure 5.6 – Example of the flux ratio improvement by fiber off-pointing for a planet at 1 λ/D on the UT. (Top) Slices of the total flux, coherent flux, and diffraction limit injection along the planet-star axis. (Bottom) Flux ratio for all possible fiber position. The best position with the fiber at +25 mas is in solid blue line.

I can expand these simulations to any planet position. I search for the best fiber position in a -25 mas to +25 mas range around the planet. This maximal offset corresponds to 73% of planet flux injected (100% is for the fiber on the planet) and it appeared not safe to offset the fiber further away due to aberrations in off-axis fiber injection (GRAVITY Collaboration et al., 2021a). Figure 5.7 shows that the technique brings the most improvement in total flux (×2.3) for a planet at 40 mas and in coherent flux (×5) for a planet at 50 mas. It shows that no improvement can be expected for planets at more than 83 mas. The positioning strategy for the SC fiber can be summarized this way:

- Planet at less than 58 mas : fiber at planet position +25 mas

- Planet between 58 and 83 mas : fiber at 83 mas
- Planet at more than 83 mas : fiber on planet

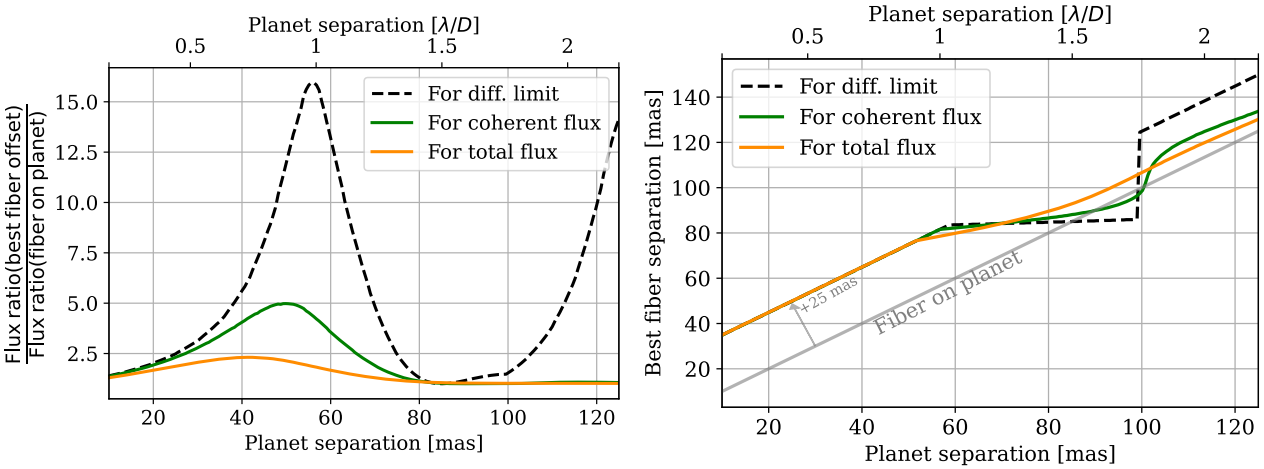

(a) (b)

Figure 5.7 – Fiber off-pointing technique improvement for all planets from 10 to 125 mas on the UT. (a) Improvement of the flux ratio compared to fiber pointing on planet. (b) Best fiber positions.

I have drawn the same study for the AT. To my knowledge, these smaller telescopes have never been used for exoplanet direct observations, but they are routinely used for brighter sub-stellar companions observations (brown-dwarfs, e.g. Nowak et al., 2024a). I used on-sky observations I acquired during technical time to obtain the continuous injection profiles. The injection in SC on the AT with the NAOMI adaptive optics is slightly closer to the diffraction than the injection on the UT with MACAO. Figure 5.8 summarizes the improvement the technique can bring on the AT. It shows that, here, the fiber is better left at 400 mas separation when observing companions from 300 to 400 mas. The predicted flux ratio improvement is close to the prediction for the UT.

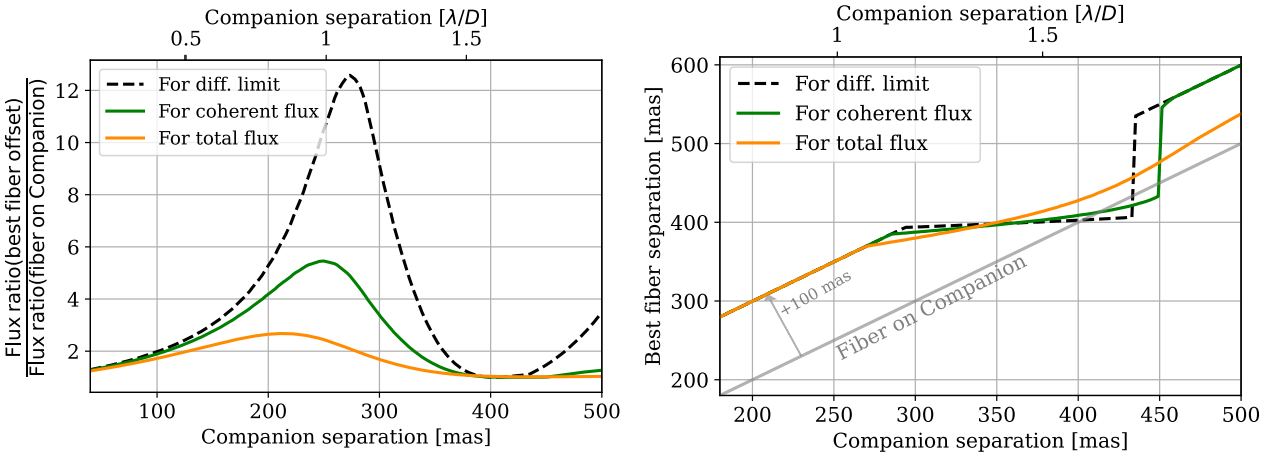

(a) (b)

Figure 5.8 – Fiber off-pointing technique improvement for companions from 40 to 500 mas on the AT. (a) Improvement of the flux ratio compared to fiber pointing on companion. (b) Best fiber positions.

The next step is to validate this off-pointing fiber strategy on-sky.

5.4.2 Validation on sky

In March 2022, I applied (PI) to NAOMI Guaranteed Time Observation in order to observe two companions brown dwarfs, HD 984 B and HD 72946 B. The scientific rationale of the proposal stressed the need for monitoring known brown dwarfs to precise their orbit eccentricity. Bowler et al. (2020) shows a trend towards low eccentricity for giant planet and a uniform distribution of eccentricities for brown dwarfs, highlighting different formation processes between the two populations. I also described the fiber off-pointing technique to use the so called tip-tilt dark holes and emphasized the timeliness with the ongoing GRAVITY+ upgrade. The proposal was reviewed favorably and I performed the observations on GRAVITY and the AT, in delegated visitor mode (ID 0110.C-0182(A)).

These two objects have a well known ephemeris thanks to previous observations (HD 984 B: Meshkat et al. (2015); Franson et al. (2022), HD 72946 B: Bouchy et al. (2016); Balmer et al. (2023)). This is required since I needed to know where to point the SC fiber in GRAVITY at a precision less than 20 mas ($0.08\lambda/D$ on the AT). HD 984 B was at 250 mas separation ($1\lambda/D$) and HD 72946 B was at 140 mas ($0.6\lambda/D$) at the time of the observations. They were both in a separation range where I expected fiber-off-pointing to make a difference in flux ratio (Fig. 5.8).

HD 72946 B was the most challenging target, unresolved by the individual AT and at 6×10^{-4} contrast in K-band. Unfortunately the atmospheric conditions were bad during the run, with seeing up to 2.5", the instrument struggled to track the fringes and the companion was not detected.

HD 984 B observations were scheduled another night, with very good observation conditions. The observing log is presented on Table 5.1. I interleaved observations on the expected position of the brown dwarf (predicted by `http://whereistheplanet.com/`, Wang et al., 2021a) and observations with a fiber offset of +100 mas away from the star. I used the MEDIUM resolution and DUAL-ON-AXIS mode, as it is common for short separation companions observation with GRAVITY. Finally, I reduced the data with the GRAVITY pipeline, and then reduced separately the on-companion and off-companion pointings with the ExoGRAVITY pipeline*.

Table 5.1 – Log for the GRAVITY observations of HD 984 AB on the AT.

Date: 2022-10-24			
Observing time	Airmass	τ_0	Seeing
01:12:17/01:57:20	1.07-1.14	2.5-4.5 ms	0.43-0.66"
Target	ΔRA/ΔDEC†	NFILES/NDIT/DIT	
HD 984 A	0/0 mas	2/8/10 s	
HD 984 B	162/197 mas	3/8/30 s	
HD 984 B	224/273 mas	3/8/30 s	

I estimate the detection SNR (see Sect. 3.3.2) at 7.7 with the pointings on the companion and at 8.7 with the off-pointings. The periodogram from the `astrometry_reduce` script show a clear detection in both cases (Fig. 5.9). Thanks to the technique, the star coherent flux injected in the SC

*For the off-companion pointings, I do not recommend to average NDIT to speed-up the reduction (`gofast` mode). This mode makes the average of NDIT with the fringes centered on the SC fiber, assuming that the companion is close. In specific cases like here, where the companion is not under the fiber, it could result in signal losses.

†Fiber position.

is reduced by ×6 and the total flux by ×3.4 on average. The simulations predicted improvements of ×5.5 and ×2.5. The slightly better flux reduction on-sky was certainly due to the excellent atmosphere conditions.

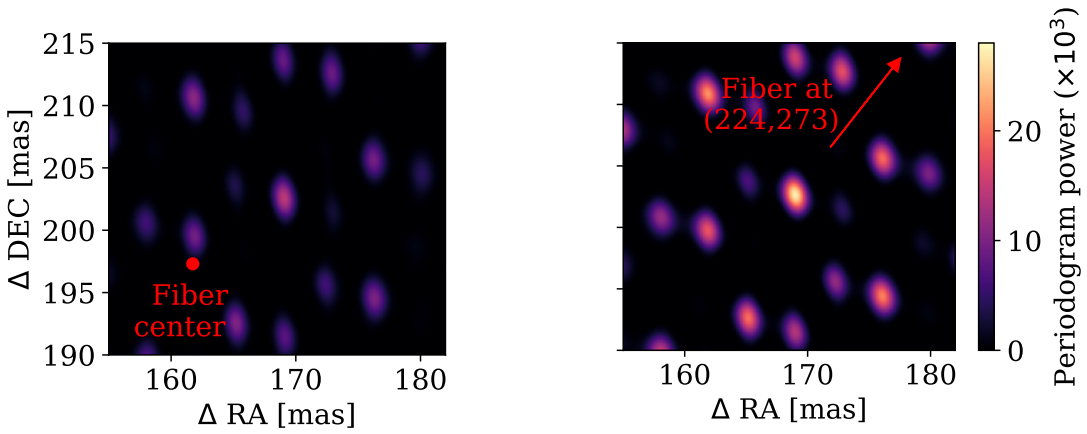

(a) Fiber on-companion (b) Fiber off-companion

Figure 5.9 – Periodogram of the `astrometry_reduce` script, with the fiber on-companion (a) and off-companion to improve the contrast (b). The spot of higher power corresponds to the brown dwarf detection.

The relative astrometry of HD 984 B is pinned down to $\Delta RA = 168.98 \pm 0.02$ mas and $\Delta DEC = 202.64 \pm 0.04$ mas with a parameter covariance $\rho = -0.73$. The relative astrometry measured is consistent in both fiber positions but the uncertainty on ΔRA is reduced by 35% and ΔDEC by 8% thanks to the off-pointing.

The spectrum of the companion is also improved (Fig. 5.10). Assuming the main noise contributor is the photon noise from stellar total flux, I expect a SNR improvement of:

$$\frac{SNR_{\text{off}}}{SNR_{\text{on}}} - 1 = \frac{F_p^{\text{off}}}{F_p^{\text{on}}} \sqrt{\frac{F_s^{\text{on}}}{F_s^{\text{off}}}} - 1 = 0.74 \times \sqrt{3.4} - 1 = 36\% \tag{5.30}$$

with F_p^{off} and F_p^{on} the flux off-companion (including fiber losses) and on-companion respectively, and F_s the stellar flux injected following the same superscripts. On the contrast spectrum produced by the ExoGRAVITY pipeline, the SNR is given by:

$$SNR = \sqrt{C^T \cdot \text{cov} \cdot C} \tag{5.31}$$

with C the contrast spectrum and cov the covariance matrix. I obtain $SNR_{\text{on}} = 120$ and $SNR_{\text{off}} = 164$. This matches the predicted +36% SNR increase due to the technique.

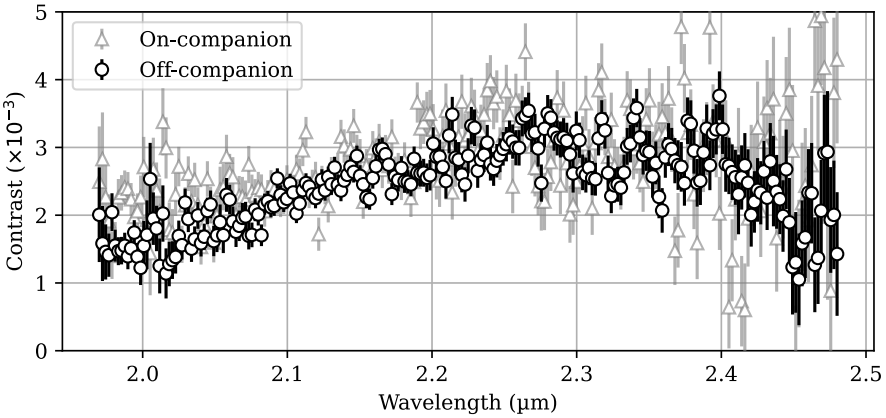

Figure 5.10 – HD 984 B contrast spectrum in K-band. With (black) and without (grey) the tip-tilt dark-hole.

Conclusion With this observation, I proved that the off-pointing technique can bring the expected improvement in flux ratio (total and coherent). It is a valid technique to enable detection and better spectral characterization within the range from 0.5 to 1.3 λ/D separation. The off-axis aberrations in the fiber coupler did not entail astrometry error, since the companion signal is consistent between all baselines. According to GRAVITY Collaboration et al. (2021a), the phase error is at most of 40° at 0.4 λ/D. This is captured by the polynomial fit of the speckle and does not pollute the companion signal. Other possible issue, the FDDL are tracking at the SC fiber position so that an object close to the fiber pointing is integrated coherently over time. If the science object is off-centered with respect to the SC, this might result in losses in coherent flux. A better setup for the future would be to set the FDDL tracking at the expected companion position instead of the SC position. Considering the DIT and the separations, it does not have significant impact though, again the off-pointing technique brings the expected improvement.

This observation proves that a companion at 1 λ/D and 2.7×10^{-3} contrast is easily detected on the AT, with a SNR of more than 7. It opens the way for observations of close-orbit brown dwarfs with the AT instead of the expensive UT. I provided this observation of HD 984 B to Jason Wang so he could add it to the observations of his monitoring programme (5109.C-0779(A)). Thanks to a uniform observation and reduction of 11 brown dwarfs (+HD 984 B) with GRAVITY and the AT, he will be able to comfort or challenge the eccentricity distribution of Bowler et al. (2020).

However, this improved detection cannot fully translate to the UT. As shown in Sect. 3.5.1, the inner working angle of the ExoGRAVITY technique is set by the polynomial order used for speckle fitting. It is around 40 mas separation with a 4^{th} order polynomial on the typical UV plane of the UT (Fig. 3.11b). At 1 λ/D on the AT (250 mas), a companion is still far from the inner working angle and easy to disentangle from the speckles. At 1 λ/D on the UT (57 mas), the signal is already lost in the polynomial on the shortest baselines, making the interferometric deconvolution less efficient.

5.4.3 Use in operation

The off-pointing technique has also been used on the UT. The most spectacular example is the confirmation of the sub-stellar companion Gaia DR3 2728129004119806464 B (later called Gaia ...6464 B) at 34 mas from the host-star and K-band contrast $(3.1 \pm 0.5) \times 10^{-3}$. This is to our knowledge

the substellar companion at the closest separation ever directly observed. This description of the observation method of Gaia ...6464 B detection is part of my paper Pourré et al. (2024).

The observation was taken by Sylvestre Lacour and Thomas Winterhalder during the science verification of the fringe tracker upgrade of GRAVITY in November 2022 (60.A-9102). Thomas had a narrow prediction of a candidate companion position around Gaia ...6464. For this, he used a combination of the Gaia DR3 Non-Single Stars catalog and Markov-chain Monte Carlo (MCMC) technique (described in Winterhalder et al., 2024). The SC fiber was positioned at 60 mas from the star, so 25 mas away from the predicted position for a dark companion. The instrument was set in MEDIUM resolution and DUAL-ON-AXIS mode. We reduced the raw data with the GRAVITY pipeline and then with the ExoGRAVITY pipeline. Exceptionally, and for the first time, we used a 3$^{\text{rd}}$ order polynomial for the speckle fit (due to the reason explained at Sect. 3.5.1), it improved the detection.

Table 5.2 – Log for the GRAVITY observations on the Unit Telescopes.

Date: 2022-11-09			
Observing time	Airmass	τ_0	Seeing
01:51:09 / 02:57:59	1.54-2.16	3.5-9.6 ms	0.35-0.88”
Target	ΔRA/ΔDEC[‡]	NFILES/NDIT/DIT	
Gaia ...6464 A	0/0 mas	4/12/10 s	
Gaia ...6464 B	28/53 mas	16/4/30 s	

At such a small separation, the polynomial captures the planet signal on most baselines. It results in only UT4-UT1 and UT3-UT1 providing a planet signal that stands out of the speckle fit. Still, the planet is detected with SNR=4.5 and an apparent contrast of 2.3×10^{-3}. The actual companion contrast is corrected to 3.1×10^{-3} accounting for the fiber losses due to off-pointing. The measured relative astrometry is $\Delta RA = 15.68 \pm 0.14$ mas and $\Delta DEC = 30.18 \pm 0.15$ mas with a parameter covariance $\rho = -0.94$, in full accordance with Gaia data. Thomas combined this single GRAVITY observation with the Gaia observation using his MCMC tools and checked with Carine Babusiaux and the BINARYS code (Leclerc et al., 2023) that they achieved similar convergence. The GRAVITY direct observation confirms that the companion does not contribute significantly to the Gaia flux, so we can safely assume that the Gaia photocenter is located on the star. Thanks to this information and the precise relative astrometry, the GRAVITY/Gaia association allows to pinpoint the companion mass to $78.34^{+2.62}_{-2.50}\,M_{\text{jup}}$ and the primary mass to $0.53^{+0.02}_{-0.02}\,M_{\odot}$. This is a remarkable example of the power of the synergy between Gaia an GRAVITY. With only one direct observation, the dynamical masses are precisely determined and the companion orbit is improved, especially the period due to Kepler 3$^{\text{th}}$ law. Other than the astrometry, the ExoGRAVITY pipeline provides the K-band spectrum for the companion. However, this spectrum is noisy and probably affected by systematics, there is little or no information to extract from it (Winterhalder et al., 2024).

[‡]Fiber position.

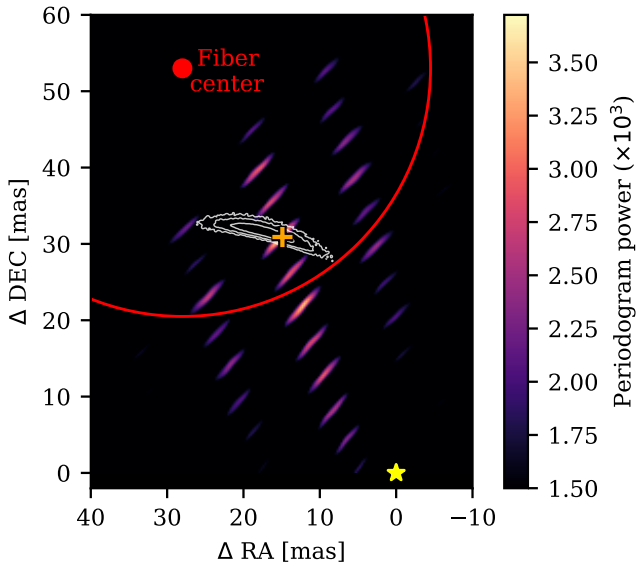

Figure 5.11 – From Pourré et al. (2024). Periodogram for the confirmation of Gaia ...6464 B. (Orange cross) detection of the companion. (White contour) position prediction by Gaia, at 68, 95 and 99.7% in outward order. (Red) Fiber center and 50% injection field of view.

This observation is at the border of the inner working angle for the GRAVITY technique and Fig. 5.11 shows that the detection is not obvious. Several peaks of nearly equal power surround the main detection peak. For comparison, the detection of HD 984 B on Fig. 5.9 is much more clear. I have to note here that the observation on Gaia ...6464 B has been a turning point for my PhD. First unconvinced by the companion detection, I tested the detection with my tools for injection and retrieval of exoplanets. This opened the way for the determination of the detection curves and all the studies around fundamental limits described in Chapter 3. To make sure that we could trust the detection of Gaia ...6464 B, I removed the companion signal from the data and injected in total more than 100 companions at different PA, separation and contrast. All companions injected at the same apparent contrast than Gaia ...6464 B were successfully retrieved. At apparent contrasts of 1.8×10^{-3} (-25% compared to Gaia ...6464 B) I retrieved 90% of the injected planets, and for contrasts of 1.4×10^{-3} (-42%) I retrieved 80% of the injected planets. To conclude, the detection of the brown dwarf is reliable, and would not have been possible at this high level of confidence without the use of the tip-tilt dark hole.

5.5 Wavefront control for GRAVITY+: simulations

GPAO will enable wavefront control possibilities. Then, we can imagine a high contrast mode that allows for a more subtle strategy than using only the tip-tilt with the position of the SC fiber. In this preliminary work on a high-contrast mode for GRAVITY, I investigated for the best modes at pupil plane against diffraction of the UT aperture. So, this study is in the category of static apodization (like Sect. 5.2.2) rather than iterative dark-hole. All these tests are made in an unaberrated case with only 20% bandwidth, 8 mas rms tip-tilt jitter from the VLTI tunnels and realistic model of the SC fiber injection. All these simulations use HCIPy, so without linearization and without assumption on the aberration amplitude.

5.5.1 Find the best apodization

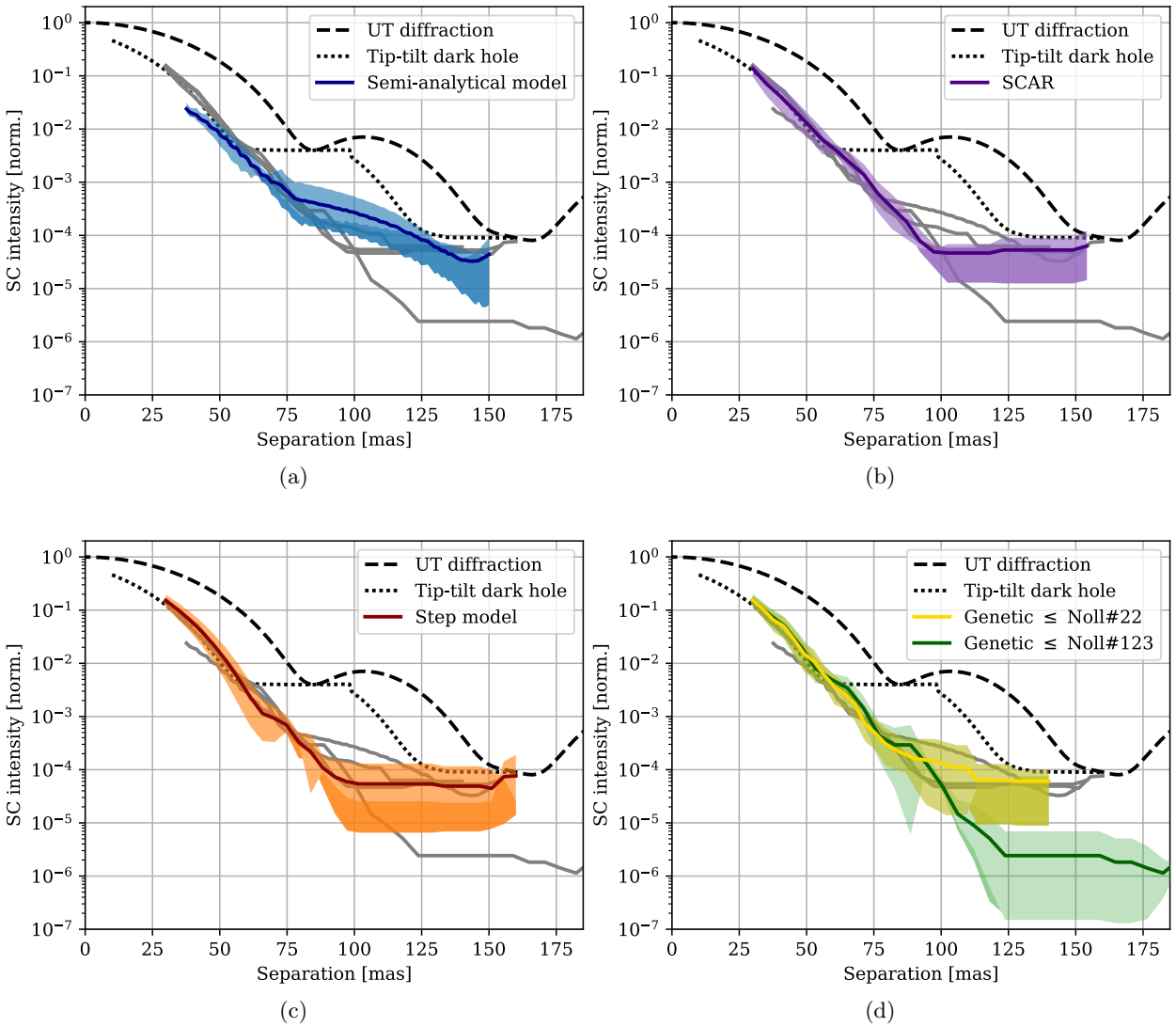

Figure 5.12 – Comparison of the star injection for different OPD apodization families. (Dashed line) UT diffraction with 20% bandwidth and 8 mas rms tip-tilt jitter. (Dotted line) No wavefront control but adding the possibility to offset the SC fiber of ±25 mas to take advantage of tip-tilt dark hole. (a), (b), (c), (d) Highlight of the different OPD apodisations. They all include the tip-tilt dark hole. (Solid colored line) Average injection over the K-band. (Colored area) Wavelength dependency of the injection from 2.0 to 2.4 µm.

My goal here is to find the best OPD pattern to apply on the deformable mirrors of GPAO in order to dig dark holes at separations from 30 to 150 mas (0.5 to 2.6 λ/D). Section 5.2.2 already showed that different phase apodization models exist, either semi-analytical or found thanks to function optimization. I quantified the starlight rejection for the Sylvestre semi-analytical model, for a simple mode inspired by SCAR composed of a coma and a trefoil, for a step-model and I ran optimizations over the lowest order Zernikes with a genetic algorithm. I optimize all OPD patterns to maximize the planet-to-star flux ratio in the fiber. However, there are always runaway solutions that explode the PSF of both the star and the planet, and accidentally create a spot of high-contrast. Thus, I discarded OPD maps of more than 170 nm rms, they affect too much the Strehl. In the

genetic algorithm, I penalized the OPD rms in the cost function to avoid such solutions to occur.

Figure 5.12 shows how these OPD patterns compare to each other in term of injection of starlight in the SC fiber. First, it is striking that almost all models reach a limit along a line from (25 mas, 2×10^{-1}) to (125 mas, 2×10^{-6}). Only the semi-analytical model (Fig. 5.12a) achieves a break of this line below 50 mas, but at the price of strong OPD around 130 nm rms. Otherwise, all methods, except the semi-analytical, bring a two orders of magnitude improvement at 100 mas. At larger separation, the genetic algorithm reveals a apodization that brings an abyssal three orders of magnitude improvement at 125 mas. The modes and the techniques are described in the next section.

5.5.2 Phase apodization families

Semi-analytical model

The semi-analytical model of Sect. 5.2.2 has two free parameters, a and b (Eq. 5.10). I optimized these parameters with the Nelder-Mead algorithm of `scipy.optimize.minimize`. The optimization function minimizes the flux injection at the central wavelength λ =2.2 µm. With this model, the off-pointing of the SC is included as tip-tilt in the OPD maps (Fig. 5.13). Indeed, at short separation the $\sin(k\boldsymbol{\Delta\alpha}\cdot\mathbf{u})$ modulates the phase on a low frequency that is essentially tip-tilt across the pupil (Fig. 5.13a). In the simulation, I force the tip-tilt to stay under ±25 mas to respect the condition stated at Sect. 5.4.1.

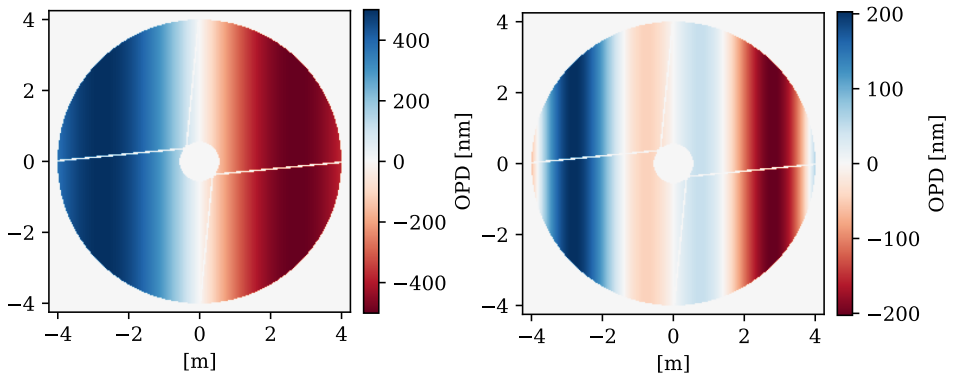

(a) At 40 mas (b) At 90 mas

Figure 5.13 – Optimal OPD patterns of the semi-analytical model, at two different separations.

This model is the most efficient at reducing the stellar flux at separations below 75 mas. It even brings a ×2 improvement at 37 mas compared to pure tip-tilt dark-hole. However, it is outperformed by other methods in the 75 to 125 mas range. According to me, this comes from the fact that tip-tilt is induced by the OPD map shape defined by the sine and cosine in Eq. 5.10 instead of being a free parameter. In all other models, it is a completely free parameter that can take any value at ±25 mas around the planet position and is therefore decoupled from the shape of the apodization.

SCAR mode

I found that a combination of a coma and a trefoil of equal amplitude was the best low-order approximation of the SCAR apodization shown on Fig. 5.1b. It has the same effect of joining the first

and the second zeroes of the diffraction pattern to create a dark-hole at around 120 mas (2 λ/D).

In the simulation, I used the Nelder-Mead minimizer to find the best coma+trefoil amplitude at each separation. However, the minimizer appears to behave poorly with the free condition of the fiber position that can jump anywhere in a 50 mas range around the planet. So, in a first pass, I used the minimizer to identify the best modes without the fiber offset, this creates a collection of optimal modes. In a second pass, I searched for the mode of this collection that provides the best contrast at each separation, but this time including the free parameter on the fiber offset.

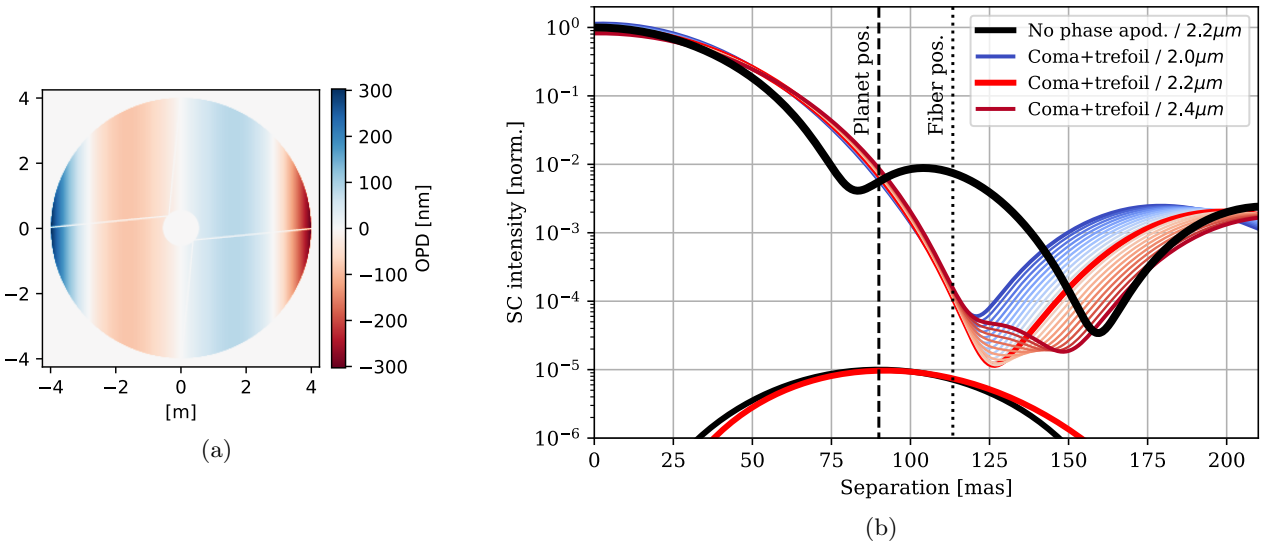

Figure 5.14 – Optimal SCAR mode for a planet at 90 mas. (a) Best OPD apodization of 78 nm rms. (b) Impact of the apodization on SC injection. Lines from blue to dark-red show the injection for different wavelengths across the K-band.

Figure 5.14 shows the optimal low-order SCAR mode for a planet at 90 mas and its impact on focal plane. The dark-hole is created at 125 mas but the offset on the fiber position allows for a star light reduction of two orders of magnitude already at 90 mas. For planets from 100 to 150 mas separation, the best solution is to keep the SC fiber in the dark-hole at 125 mas. This explains the plateau on Fig. 5.12b. In my simulations, the best low-order SCAR modes do not exceed 85 nm rms amplitude, and therefore have moderate chromaticity, and a low impact on the Strehl.

Step model

This model originated from brainstorming with Jean-Baptiste on the best possible modes to reduce stellar injection at the shortest separations. As shown by Eq. 5.5, we need odd modes on the deformable mirror to tackle the pupil diffraction. Moreover, we want this mode to be tip-tilt free, as we choose to inject the tip-tilt by moving the fiber instead of injecting phase slopes on the deformable mirror. From these assumptions, I tested steps modes that are defined by two parameters. As described on Fig. 5.15, one parameter is the width of the inner steps and the other is the amplitude of the inner steps. The amplitude of the outer steps is set to the value that nulls the tip-tilt over the pupil.

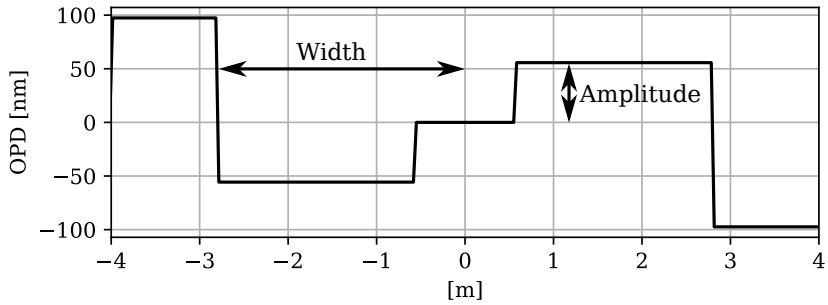

Figure 5.15 – Phase step model across the UT pupil, with the two parameters: width and amplitude. The plateau from -0.55 to 0.55 m is the central obscuration by M2.

As for the SCAR mode, I run a first minimization pass with the Nelder-Mead algorithm but fixing the fiber on planet position (for any planet position from 30 to 160 mas). In a second pass, I enable the fiber off-pointing and I search the best phase map among the phase maps created at the first pass. An example of best step mode is shown on Fig. 5.16. At this separation, the star flux reduction at the central wavelength is ×5 better than with the SCAR mode. However, the dark hole created is more chromatic. Averaging results at the different wavelengths of the K-band, the dark hole depth is similar to the one created with the SCAR mode. This is the takeaway for this phase apodization model, on average similar efficiency at reducing the stellar flux in the fiber, but with more wavelength dependency over the K-band compared to the SCAR mode.

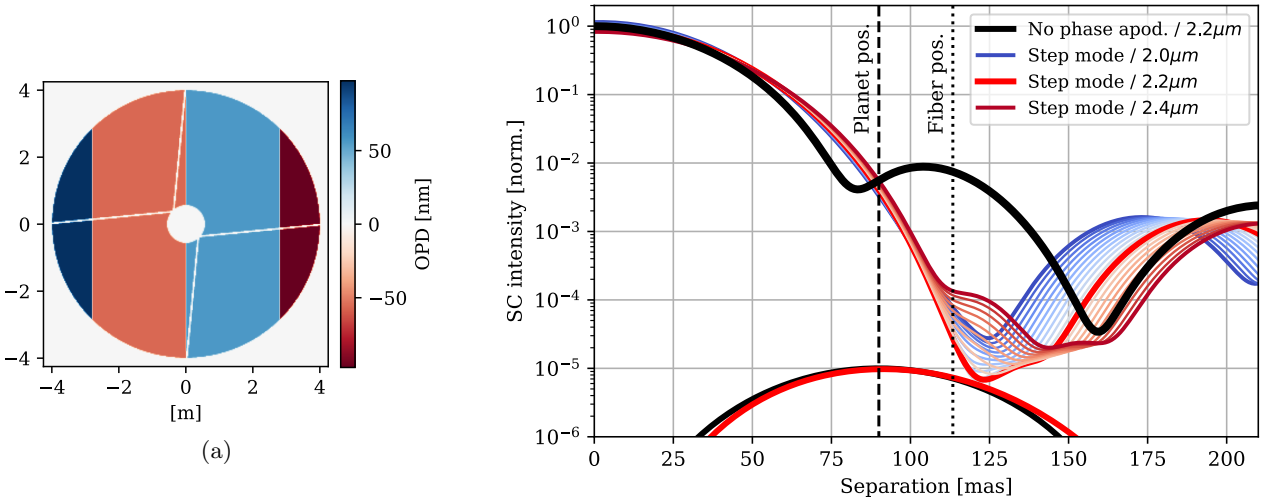

Figure 5.16 – Optimal step mode for a planet at 90 mas. (a) Best OPD apodization of 65 nm rms. (b) Impact of the apodization on SC injection. Lines from blue to dark-red show the injection for different wavelengths across the K-band.

In practice, these modes are impossible to imprint on a continuous deformable mirror surface. I did not investigate the influence on the dark hole of slighly softening the OPD steps. However, when projecting the optimal step modes on the Zernikes of Noll less than 20, we obtain just a coma and trefoil of equal amplitude. Then, we can see our low-order SCAR modes as an edge-soften version of the step modes. Apparently, the sharp edges are not beneficial to the dark hole creation at the separations I investigated.

Genetic algorithms

Finally, I wanted to search for the best apodization without any assumptions on the symmetry and the modal content. For this, it makes sense to use an orthogonal modal decomposition basis. First, I chose the basis formed by Zernike polynomials of lower order or equal order than Noll#22 (secondary spherical aberration). I exclude piston and tip-tilt. This makes a minimization with 19 parameters, with another free parameter for the SC position on the star-planet axis. All these parameters have a non-linear impact on the focal plane. Therefore, it is impossible to converge to anything else than disappointing local minima with the Nelder-Mead algorithm (or any other minimizer available in `scipy.optimize.minimize`). To explore this tricky parameter space, I coded a genetic algorithm. This type of algorithm starts from a set of random solutions that are ranked thanks to a score function. I take the better ranked half of the population and produce a new generation of solution by randomly swapping solution elements (each Zernike mode amplitude). Additionally I added a mutation probability of around 1% to occasionally modify a Zernike mode amplitude by a random amount. Generation after generation, the best ranked solution improves, until reaching convergence to what we hope is the global maximum. In the following, the score function Γ I choose is:

$$\Gamma = r_{p/s}(2.0\ \mu\text{m}, \mathbf{x}) + r_{p/s}(2.2\ \mu\text{m}, \mathbf{x}) + r_{p/s}(2.4\ \mu\text{m}, \mathbf{x}) - \tau \times \text{RMS}\{\phi_{DM}\} \tag{5.32}$$

with $r_{p/s}(\lambda, \mathbf{x})$ the planet/star ratio of injected flux at the wavelength λ and fiber position $\mathbf{x}$ (fiber position is of course the same at all λ) and τ is a weight I set to 1×10^7 m^{-1} after empirical tests.

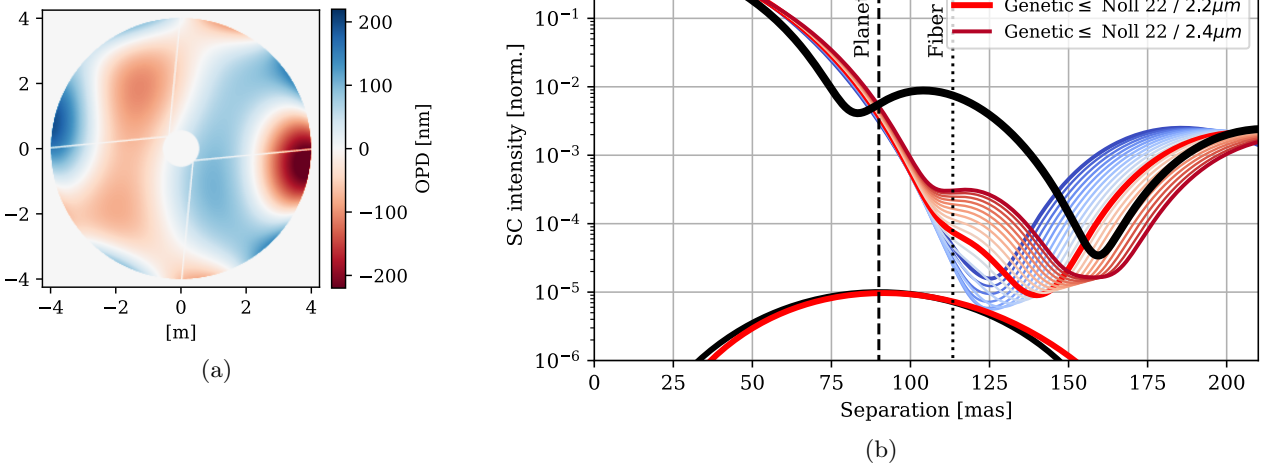

Figure 5.17 – Optimal genetic mode (Noll$\leqslant$ 22) for a planet at 90 mas. (a) Best OPD apodization of 72 nm rms. (b) Impact of the apodization on SC injection. Lines from blue to dark-red show the injection for different wavelengths across the K-band.

The flux ratio improvement thanks to the phase apodization found by the genetic algorithm is shown on Fig. 5.12. For a modal basis composed of Zernike modes up to Noll#22, the best apodization reached the same dark-hole level as the SCAR modes. Figure 5.17 shows the best apodization found for a planet at 90 mas. In the planet direction (horizontally) the apodization shape resembles the

SCAR mode, the OPD rms is 72 mas that is also close to the optimal SCAR. It is difficult for my algorithm to converge to the precise optimal apodization map, hence the solution slightly worse than the best SCAR. However, from these genetic optimizations conducted several times at different separations from 30 to 130 mas, I am convinced that we do not miss a low-order Zernike solution that would be better than SCAR.

To go one step further, I ran two genetic optimizations with all Zernike modes lower or equal to Noll# 123 (piston and tip-tilt excluded). This makes in total 121 free parameters and take several tens of hours to converge on my laptop. For this reason, I ran optimizations for only two planet positions, 90 and 120 mas. At 90 mas, the best solution is still SCAR-like. However, for a planet at 120 mas it converged to an OPD that digs a much deeper dark-hole. Figure 5.18 shows the result of this optimization. The dark-hole created at 140 mas is two orders of magnitude deeper than the SCAR dark-hole at 125 mas. Interestingly, the SCAR mode joined the first two nulls of the diffraction pattern, this mode seems to join the first three zeros. The injection map created by this mode is shown on Fig. 5.19. The dark injection zone created is around 40 mas wide, it is robust to tip-tilt jitter and eventual error in the dark-hole positioning with respect to the planet. Still, I believe that the OPD map is not optimal. I expect the non-horizontally symmetric features to be artifact from the genetic algorithm. A second pass of genetic algorithm with this OPD map as a starting point, and a score function left to determine, would bring us closer to the optimal apodization that joins the first three zeros of the diffraction. Also, very preliminary tests tend to show that this deep dark hole at 150 mas can be achieved with OPD maps composed of the optimal combination of two sinusoids of different frequencies in the planet direction.

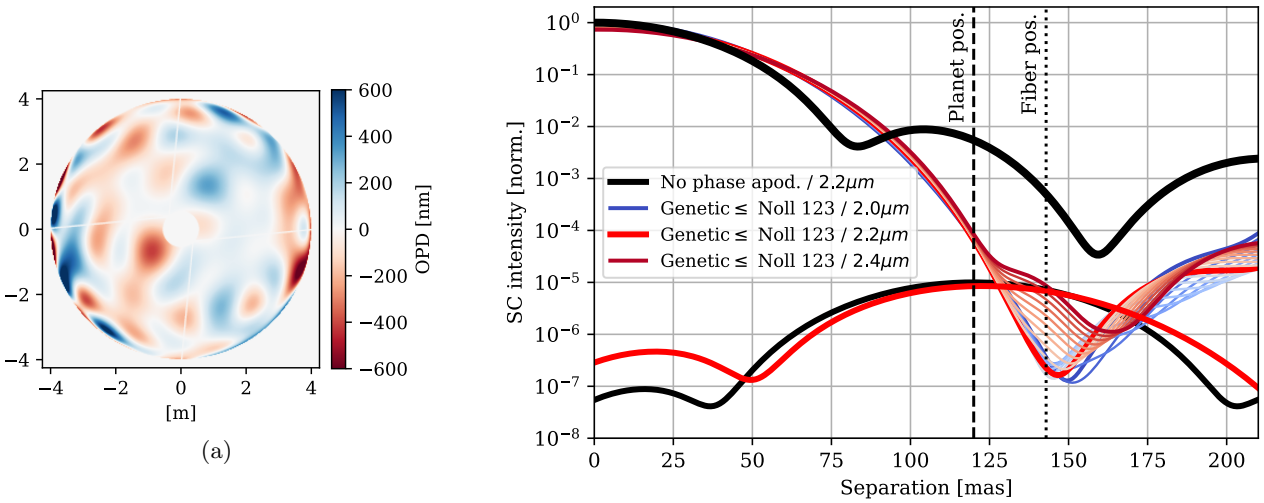

Figure 5.18 – Optimal genetic mode (Noll⩽ 123) for a planet at 120 mas. (a) Best OPD apodization of 165 nm rms. (b) Impact of the apodization on SC injection. Lines from blue to dark-red show the injection for different wavelengths across the K-band.

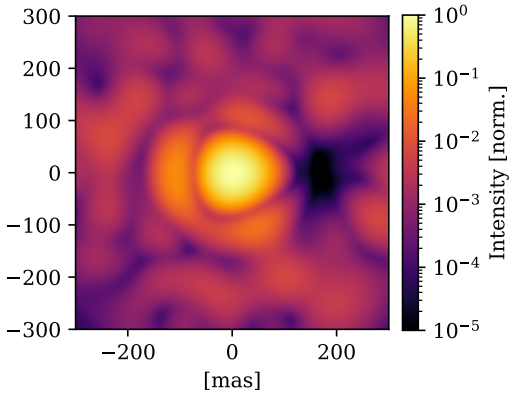

Figure 5.19 – Full injection map for the optimal genetic mode with all lower or equal to Noll#123, and a planet at 120 mas. Include 20% bandwidth and 8 mas rms tip-tilt jitter.

5.5.3 Conclusion

In unaberrated conditions on the UT pupil, the low-order SCAR mode creates the deepest and most achromatic dark hole for observing planets below 100 mas separation. From 100 to 180 mas, another type of mode revealed by the genetic algorithm prevails. The star injection in the fiber at 125 mas reaches 2×10^{-6} of the on-star injection.

I did not investigate for the influence of different pupil orientations. The spiders holding the secondary mirror create diffraction lines that are affecting more certain PA than other. Short preliminary tests tend to show it has a non-negligible impact on the dark hole position and depth. A static apodization model for GRAVITY+ will necessary take into account the pupil orientation.

Finally, this study focused on shortest separation exoplanets, one reason is because this is the region where the Gaia/GRAVITY synergy has an edge (Sect. 3.6). Also, this is where we have a chance that star diffraction dominates the injected flux, and therefore the only region where a static apodization makes sense. It is still interesting to investigate how to create dark hole at longer separations, this is a possible future development of this study.

5.6 Wavefront control for GRAVITY+: tests at VLTI

The next step after the simulations was to confront the real instrument.

5.6.1 Context

The new adaptive optics GPAO will be commissioned at summer 2024 at VLTI. The goal here is to pave the way for an implementation of the wavefront control mode on the new system. Before hand, we expected to have some problems to tackle on the real system, and we want to gather as much knowledge as possible on the "worst offenders" to a high-contrast mode. This means: tests of internal sources of VLTI to prepare for GPAO, but also some tests on-sky to identify if the phase apodization could bring some improvement already on the existing system.

The adaptive optics currently available at VLTI are:

- NAOMI, the adaptive optics of the AT controlling 14 Zernike modes.
- MACAO, the visible adaptive optics of the UT, controlling 50 Zernike modes.

- CIAO, the infrared adaptive optics of the UT, controlling 50 Zernike modes.

Both MACAO and CIAO control the same curvature deformable mirror, but only CIAO offers the possibility to introduce modal offsets. This is why my work on VLTI and GRAVITY focuses on NAOMI and CIAO.

At the VLTI lab (Fig. 5.20), regardless of the telescope (UT or AT), we used three focal planes. Outside GRAVITY, I used the IRIS camera (Gitton et al., 2004) that can make images in J, H or K-band. Inside GRAVITY, I used the acquisition camera in H-band, and the SC arm with the fiber injection in K-band.

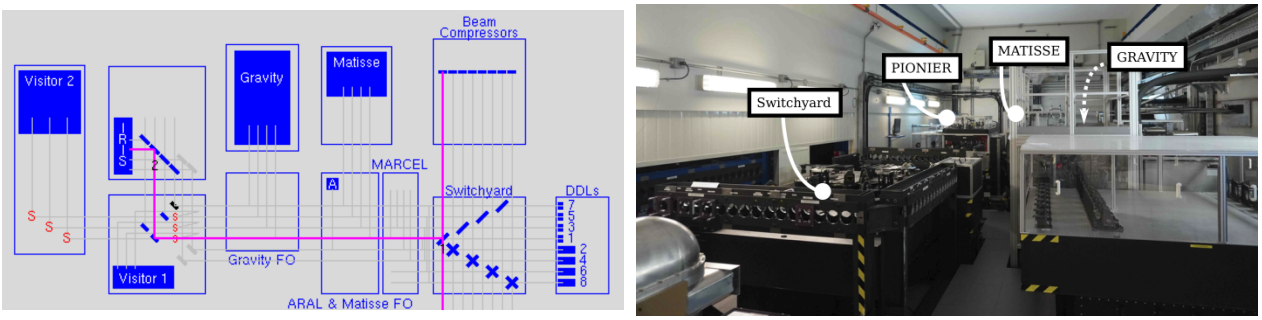

(a) (b)

Figure 5.20 – VLTI lab at Paranal. (a) VLTI lab map on the observer panel. (b) VLTI lab picture (N. Pourré).

For all the following tests, I use the low-order SCAR apodization. The previous section have shown it was the most efficient apodization below 100 mas. Moreover, it is composed of only a coma and a trefoil, that makes it easy to implement.

5.6.2 AT on sky

During the first year of my PhD, I spent three months at ESO Garching with Julien Woillez for testing wavefront control on the AT. It was under a technical time request in the context of the GRAVITY+ commissioning (TTR-109.0013). The ESO headquarters offer the possibility to control the Paranal instruments and telescopes thanks to the Garching Remote Access Facility (GRAF). First, I had access to the VLTI during 4 to 5 hours of daytime, twice a week. It was a great opportunity for me to learn about the finest details of the complex VLTI infrastructure, and to learn how to operate it. From that moment until my last tests in January 2024, I could count on Julien Woillez for guiding me with relentless support and brilliant teaching skills. I want also to acknowledge here the amazing support of the Paranal staff. They would always make everything they could for me to perform my tests in the best conditions despite the numerous other activities on the telescope.

Impossible daytime tests For daytime tests, the goal was to use the internal Nasmyth beacon of one single AT and propagate it through the VLTI tunnels via the delay line, to the IRIS camera. The AT available for my tests depended on the Paranal daytime activities and maintenance. I learned how to inject modal offsets and disturbance in the NAOMI reference slopes, how to collect data from the camera, how to tackle some of the numerous bugs and warnings that spice up the VLTI experience. First, I wanted to bring the system to diffraction limit and obtain the most unaberrated

PSF on IRIS. For this, Julien has a python script that uses NAOMI and the harmonic modulation technique (described later in Sec. 5.7). It is supposed to measure and correct the NCPA between the wavefront sensor and IRIS. Despite a few weeks of attempts, I could not see the Airy rings on IRIS K-band images, only a blurry spot. At one point, we realized that the AT internal lamp was injected by a fiber that was not single-mode but multi-mode. It creates a source that is not a PSF but an extended source, making it easier for NAOMI Shack-Hartmann calibrations, but preventing meaningful wavefront control tests. Then, our only solution was to test the apodization with the AT on-sky. Two half-nights were scheduled for this.

Preparation before on-sky tests Before using some precious on-sky time, I prepared SCAR mode injections on NAOMI. I wanted to make sure the adaptive optics could reproduce the mode, and I wanted to be able to set it at any PA on-sky. The NAOMI control basis is the first 14 Zernike modes (piston excluded). The low-order SCAR mode composed of only a coma and a trefoil is well in the control range. For the angle, this is more complex. The deformable mirror is at the Nasmyth focus and the wavefront sensor is at the coudé focus (Fig. 1 of Woillez et al., 2019). So, the wavefront sensor is stable with respect to IRIS but it rotates with respect to the deformable mirror. The angles are the azimuth angle and the angle of the derotator that lies between the two. The wavefront sensor measurement is rotated numerically before being applied to the deformable mirror. The on-sky north angle θ_n is given in the real-time database (under the key `@wat2tcs:Appl_data:TCS:nmupd:data.northAngle` for AT2). So, the modes amplitude to produce a SCAR mode ($\mathcal{S}$) at any PA on-sky is:

$$\theta_{tot} = \theta_n + \mathrm{PA} - \pi$$

$$\mathcal{S} = \begin{pmatrix} \cos(\theta_{tot}) & -\sin(\theta_{tot}) & 0 & 0 \\ \sin(\theta_{tot}) & \cos(\theta_{tot}) & 0 & 0 \\ [0 & 0 & \cos(3\theta_{tot}) & -\sin(3\theta_{tot}) \\ [0 & 0 & \sin(3\theta_{tot}) & \cos(3\theta_{tot}) \end{pmatrix} \cdot \begin{pmatrix} 0 & a_{\mathrm{h\_coma}} & 0 & a_{\mathrm{o\_trefoil}} \end{pmatrix} \tag{5.33}$$

with $\begin{pmatrix} a_{\mathrm{v\_coma}} & a_{\mathrm{h\_coma}} & a_{\mathrm{v\_trefoil}} & a_{\mathrm{o\_trefoil}} \end{pmatrix}$ the vector of modes amplitude for vertical and horizontal coma, and vertical and oblique trefoil. The NAOMI software includes a command for sending modal offsets to the reference slopes of the Shack-Hartmann (`spaccsServer.Acq.addModesToRef`). Still, during these tests I also developed a basic operational knowledge of SPARTA, the generic software infrastructure of all the adaptive optics of VLT/VLTI.

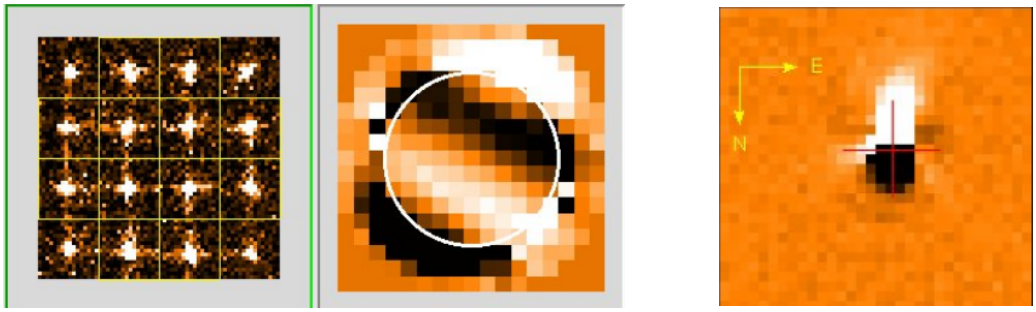

(a) (b)

Figure 5.21 – Preliminary mode injection test on NAOMI, on AT Nasmyth beacon. (a) Image of the Shack-Hartman and estimated deformable mirror shape from the NAOMI panel. The white circle indicates the portion of the mirror that is seen by VLTI. (b) Corresponding IRIS differential image ([image no SCAR] - [image SCAR]).

Figure 5.21 shows the example of a SCAR mode on NAOMI to dig a dark-hole to the north. The angle and the mode shape on the deformable mirror behave as expected. I could not check if the mode was applied with the right amplitude since the internal source do not produce a PSF.

On-sky on IRIS I could then go on-sky for my first half-night of tests on IRIS. The seeing at 500 nm was around 0.8 arcsec. I pointed to the bright star HD 114613 (K=3.27 mag, R=4.28 mag) to make sure that the wavefront sensor had enough flux. On a bright guide star and under 80% seeing conditions, Woillez et al. (2019) predicts a K-band Strehl of 73% with NAOMI. The star hosts a planet detected by radial velocity with a maximal elongation 260 mas and a mass $M_p \sin i = 0.36\, M_{\rm Jup}$, it did not disturb our tests. I tested different SCAR amplitudes on AT2 and recorded 30 s sequences on IRIS. The results are shown on Fig. 5.22. The IRIS pixel scale is 140 $\mathrm{mas_{sky}}$/pixel on the AT, that is a separation sampling every 0.56 λ/D. We can see that the optimal SCAR mode amplitude only improves the contrast by $\times$1.3 at 1.67 λ/D. This is not significative. I used a post-adaptive optics residual cube I generated with HCIPy to deteriorate the simulation shown on Fig. 5.22a and obtain the intensity injected with respect to separation close to Fig. 5.22b. This gives me a Strehl of 45%, well below the expected NAOMI performance. This can be caused by NCPA between NAOMI and IRIS, or, more probably, by uncontrolled high-order patterns on the deformable mirror. Indeed, the deformable mirror has 145 effective actuators but a wavefront sensor that measures only the 14 lowest orders. The arising of high-order artifacts is identified as a probable flaw of NAOMI. In the simulation with Strehl 45%, the improvement by SCAR modes is also non-significative. The rest of my on-sky time this night was dedicated to tip-tilt jitter control tests and tests of control of low-order NCPA with defocus (that was a dead-end briefly described in Sect. 5.7).

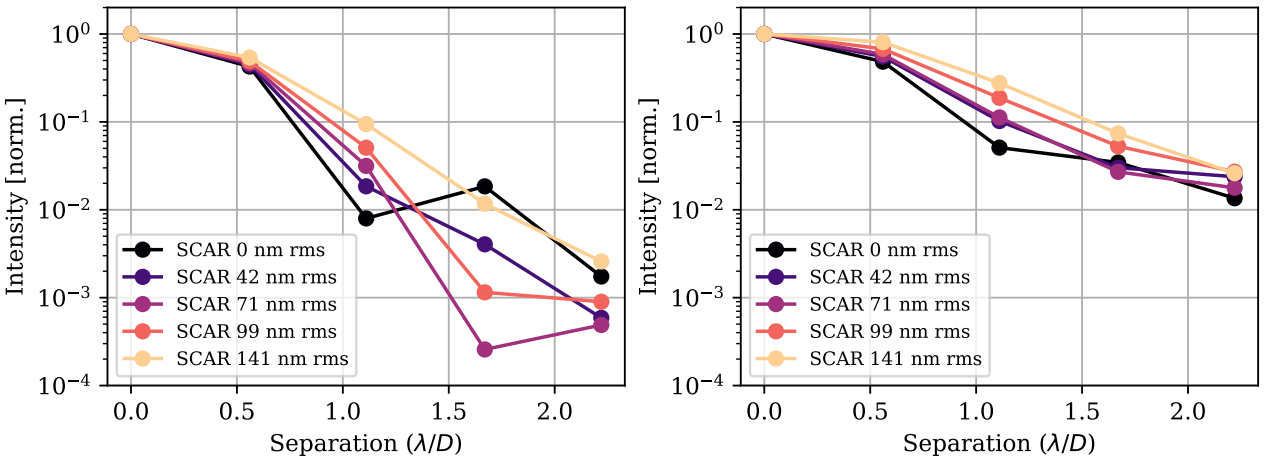

(a) Simulations diff. limit (b) NAOMI on-sky

Figure 5.22 – SCAR apodization impact on K-band image intensity on IRIS. (a) Simulation on the AT pupil, including bandwidth 20%. (b) Intensity measured on-sky on IRIS, averaged over 30 s. SCAR modes injected with NAOMI.

On-sky on GRAVITY My second half-night was scheduled two weeks later. It should have been dedicated to tests on GRAVITY with the AT, but it was canceled due to bad weather (rain!) at Paranal. A few nights later, the VLTI was closed for science operations because of a technical issue on AT4. Thanks to Aaron Labdon (VLTI astronomer at Paranal) I could get some time for my tests at this moment. The atmosphere was exceptional, with an average seeing at 0.45 arcsec. We pointed to HD 191089 (K=6.1 mag, R=7.1 mag), that is bright enough for NAOMI and the FT to operate in the nominal regime. I applied strong SCAR modes on NAOMI and checked on the GRAVITY acquisition camera that the dark hole was applied in the direction I expected. Then I positioned the SC fiber at different separations from 0.6 to 2.2 λ/D along this direction. I estimated in simulation that the optimal SCAR mode for GRAVITY fiber injection on the AT pupil is 50 nm rms. I collected acquisitions with and without the SCAR mode and then reduced the data with the GRAVITY pipeline. The `astroreduced` files contain the flux of individual telescopes. Figure 5.23 shows that the SCAR mode had no beneficial impact on the injection. Simulation confirms that no flux reduction can be obtained with the SCAR mode under this amount of residuals.

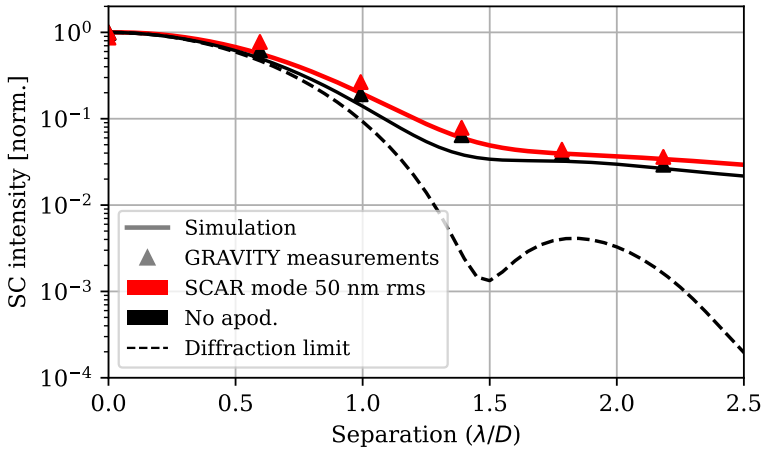

Figure 5.23 – Comparison of the SC injection with and without SCAR mode on the AT. The measured injection is averaged over 2 min.

Conclusion This concludes my tests of wavefront control on the AT. It showed that the AT were not suitable for daytime tests due to the multi-mode beacon injection. Also, I showed that, on-sky, the apodization with SCAR mode brings no stellar flux reduction on NAOMI. However, this was a great opportunity to learn how to operate the VLTI and GRAVITY. After these three months at ESO, the technical time for GRAVITY+ rearranged in one week sessions every three to four month. In these sessions, all GRAVITY+ commissioning and continuous improvement activities are combined.

5.6.3 UT on beacon

AT did not offer the possibility of daytime or nighttime wavefront control tests, so I went to UT for my tests. The main advantage of working with UT is that it is the telescopes we use for exoplanet observations. Most things we learn there can directly apply to GPAO and a future high-contrast mode for GRAVITY. However, it is more difficult to have time on the UT, even daytime. It is mostly because each telescope has three single-telescope instruments that require daily calibration and maintenance, so my daytime tests were really entangled with Paranal operations. Other drawback, using CIAO on the internal source requires to put one UT and VLTI in a non-standard configuration that is difficult and time consuming to set.

Dual-beacon off-axis mode As already discussed in Sect. 5.6.1, each UT has two wavefront sensors and one deformable mirror. MACAO is a curvature sensor that is coupled with the bimorph deformable mirror and do not permit modal offsets injection. On UT, only CIAO allows for injection of modal offsets. The wavefront sensor is a 9×9 Shack-Hartmann in K-band where reference slopes can be modified. But CIAO only works off-axis (Fig. 5.24), namely, it sees a field of view that is different from the 2 arcsec field of view that goes to VLTI. For daytime tests, there are two infrared internal lamps at the Nasmyth focus of the UT. One is injected by a single-mode fiber and the other one is injected by a multi-mode fiber. To run daytime tests on VLTI with CIAO in closed loop, I have to set the Star Separator System (STS) such that the multi-mode beacon is centered on the CIAO wavefront sensor and the single-mode beacon is centered on IRIS or GRAVITY at the VLTI lab (Fig. 5.24). This mode is called dual-beacon-off-axis. An old script ("template" in ESO language) exists to set it automatically but it did not work. Instead of diving into ESO software to repair it (in Tcl programming language), I chose to set the dual-beacon mode manually each time I needed it. It takes 20 min when everything goes well, it takes me up to 5 hours when something, or several things go wrong (examples: one shutter has not been opened, STS startup did not put the mirrors at default position, CIAO real time computer needs reboot, ...). Staring from outdated mirrors' position provided to me by Nicolas Schuhler and Françoise Delplancke-Ströbele, I searched for the good alignment position of the M10, Field Selector Mirrors (FSM) and Variable Curvature Mirrors (VCM) that allows me to see light on both CIAO and IRIS. Finally, I had an updated table of mirrors' position for dual-beacon-off-axis mode on all four UT.

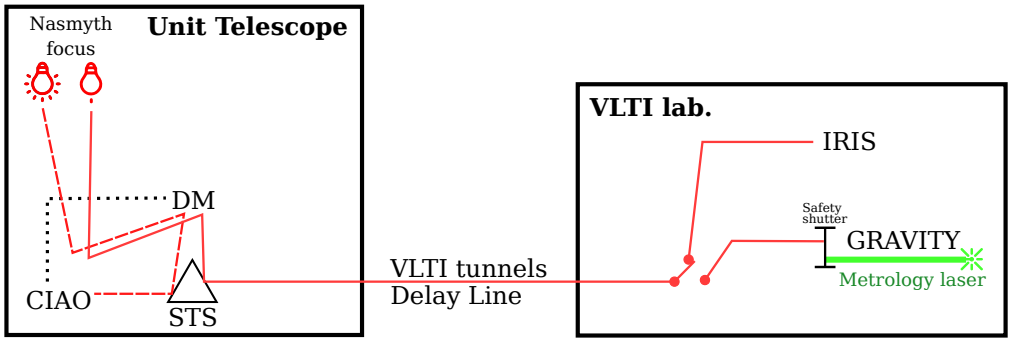

Figure 5.24 – Schematic of dual-beacon-off-axis mode, from UT Nasmyth beacons to VLTI.

For the technical time request of February 2023, I had the opportunity to travel to Paranal and be at the telescope for the first time. It was a valuable experience to see how operations are organized there, and how technical, engineer and astronomer staff work together. Moreover, being on-site facilitated the coordination with the Paranal team, and pushed me higher in the priority list of daytime activities. My primary goal was to test the low-order SCAR apodization impact on GRAVITY injection in SC on one UT Nasmyth beacon.

Apodization tests on IRIS I first worked on IRIS to check if the single-mode Nasmyth beacon really provided a PSF close to the diffraction limit. The PSF obtained is shown on Fig. 5.25 leftmost image. Despite the coarse pixel scale of IRIS (31 mas_{sky}/px on the UT), I got convinced that the size of the PSF core matched well what I obtained in simulation for a point source. Still, the beacon PSF seems not radially symmetric, as it should be for a non-obstructed round pupil. It betrays the presence of low-order aberrations. As a first test, I wanted to inject SCAR modal offsets of different amplitude in CIAO and measure the impact on the IRIS image in K-band. The CIAO software does not provide a command for simple modal offset. For modal injection, I multiply a vector containing the amplitude of the 50 modes controlled with the pseudo-inverse of the matrix `LoopMonitor.WFSSLOPES2MODES` available for each CIAO system. I obtain a set of slopes that I subtract to `Acq.DET1.REFSLP`, and I update the system (`Acq.update`). Figure 5.25 shows the images for SCAR apodizations from 21 to 212 nm rms. The SCAR mode has the expected impact seen on simulations: it removes light from the right side of the PSF and create a trail with vertical dark stripes on the left side. Figure 5.26 displays horizontal slices of the images. It highlights that the PSF without apodizations is indeed aberrated because the profile is not symmetrical. However, it shows that even in these conditions, a SCAR apodization of 85 nm rms reduces the star intensity on the image by $\times 13$ at 90 mas. From simulations, I expect the SCAR amplitude to have most impact on flux reduction at 90 mas at 78 nm rms (for an image and a round pupil unobstructed). This is a promising result, since I obtained it in raw condition: without corrections of the NCPA, and without tip-tilt jitter control for the tunnel seeing.

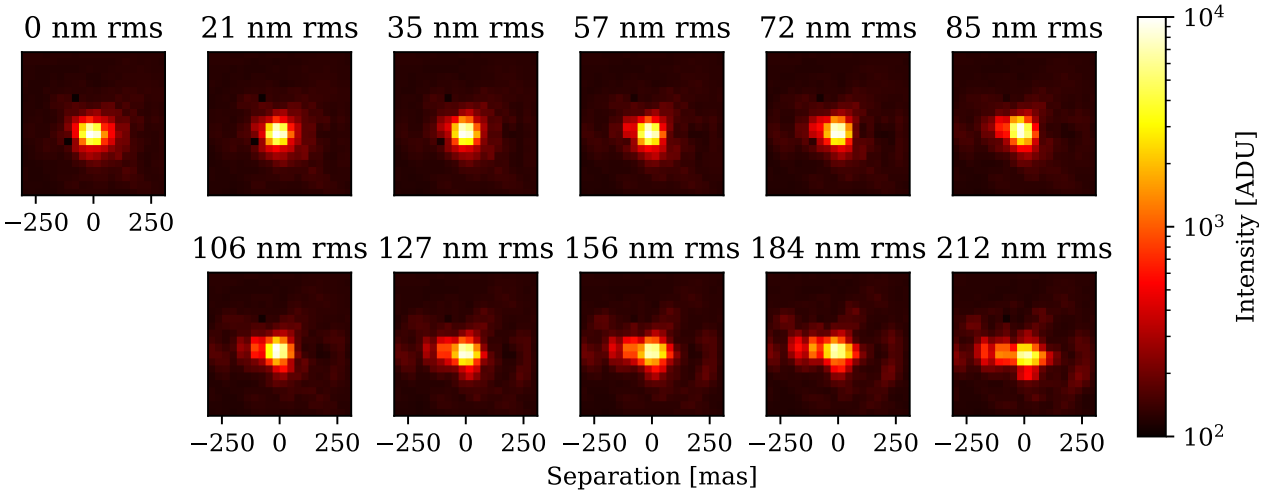

Figure 5.25 – IRIS images of the single-mode Nasmyth beacon of UT2. SCAR modes are injected at different amplitude with CIAO. All images at K-band, 30 s average.

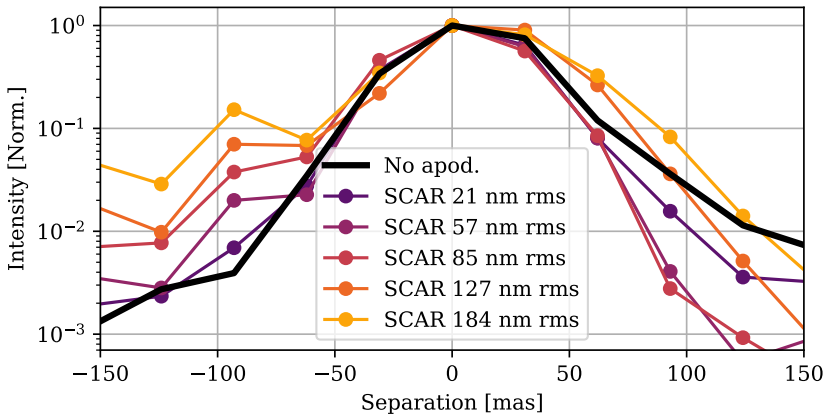

Figure 5.26 – Horitontal slices of IRIS images in K-band for different SCAR amplitudes (Fig. 5.25)

Apodization tests on GRAVITY-SC After these tests on the IRIS camera, I wanted to address my primary goal: test the SCAR mode on the SC fiber injection of GRAVITY. It is operationally heavy to make daytime tests with propagation of a beacon from one UT to GRAVITY. It is not possible to open the GRAVITY shutters to the VLTI without an interlock system armed. As soon as the shutters are open, the metrology lasers propagates from GRAVITY and for safety reasons, nobody is allowed to stay in the VLTI tunnel, or in all UT concerned. It means that, for completing these tests, I had to request for the whole VLT/VLTI for a duration from 2 to 5 hours. Still, from this session in February 2023 to January 2024, I had numerous opportunities to run those heavy tests. I estimate it accumulates to around 50 hours propagation for UT to GRAVITY. This shows how accommodating and helpful the Paranal staff is.

As for IRIS, I first checked that the SCAR mode was applied in the direction I wanted to scan with the SC fiber. To do so, I applied a strong SCAR mode on CIAO that modifies the PSF in a way that is easy to recognize and where the direction is clear. The real-time display of the acquisition camera in GRAVITY shows the PSF and the position of the FT and the SC fibers in the field. Past this preliminary test, I injected the mode on CIAO of UT2. Simulations show that the optimal

SCAR amplitude is 36 nm rms for an unobstructed round pupil. Figure 5.27 shows how the injection in SC is affected. Unfortunately, the SCAR mode brings no improvement, it even causes an increase of the "star" light injection around 100 mas. We have seen that the image on IRIS was affected by low-order aberrations. Also, we know that the fiber coupler in GRAVITY introduces low order aberrations on the order of 100 nm rms. In this environment, it is not surprising that the 36 nm rms SCAR mode do not have the expected effect. The Fig. 5.27 also includes an example of injection curve with 145 mas rms aberrations (defocus, astigmatisms, comas). It matches well the injection measured and gives a realistic example of the NCPA we expect in SC.

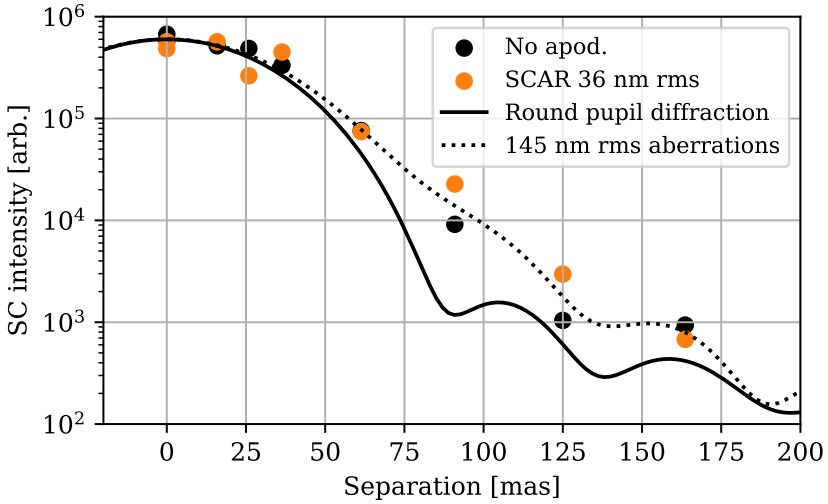

Figure 5.27 – Measured intensity injected in SC on the UT2, with and without SCAR apodization on CIAO. Each round point is an average over 24 s. (Solid line) Simulation, diffraction limit for a 8 m round pupil unobstructed, 20% bandwidth and 8 mas rms tip-tilt jitter. (Dotted line) Simulation, example of injection under 145 nm rms low order aberrations.

Conclusion From these tests on the UT Nasmyth beacon, I concluded that a static apodization would not be efficient for the SC arm of GRAVITY as it is now, even without atmosphere residuals. One way forward could have been to inject SCAR mode of different amplitude and measure the corresponding impact on SC injection (like we did on IRIS). If most of the NCPA are static, we could obtain an internal source model of the best apodization depending on the PA. The internal source is a round pupil, so we would have extrapolate our results to the UT pupil with the M2 obstruction and the spiders. Instead, it appeared more urgent to us to find a way to correct the NCPA as much as possible from the SC. It would increase the injected flux of the science objects (exoplanets, stars of the galactic center, ...), and bring us closer to a system where static phase apodization makes sense.

5.7 Aberrations in GRAVITY

Among instruments providing direct exoplanet observations, GRAVITY has by far the longer non-common path between the adaptive optics and the science detector. Indeed, at VLTI the adaptive optics are at the coudé focus of each telescope and the beam travels up to 250 m in the tunnels before reaching the instrument at the VLTI lab. The aberrations affecting the wavefront along this

path must be treated in a high-contrast mode of GRAVITY. As I published in Pourré et al. (2022c), my initial plan was to optimize the SCAR modes amplitude to correct for odd NCPA, and optimize a defocus amplitude to tackle even NCPA (Eq. 5.5). Defocus is the lowest order even mode, so we expected it to be able to act on the even component of the electric-field at the shortest possible separations. Simulations show that under low order even modes, the right choice of defocus amplitude can dig a dark hole anywhere in the first zero of the injection pattern. However, it brings a significant improvement only in monochromatic case without tip-tilt jitter. I tested it in real conditions on IRIS and GRAVITY, and achieved Strehl deterioration but no contrast improvement. Rather than adding aberrations on top of aberrations, I took the path of NCPA correction in VLTI and in GRAVITY. In this sense, my approach is the same as single-telescope exoplanet imagers where a lot of effort have been put into correcting NCPA over the past few years (N'Diaye et al., 2016; Vigan et al., 2022; Haffert et al., 2023).

5.7.1 Harmonic modulation technique

I used the Zernike harmonic modulation technique to measure NCPA on IRIS and GRAVITY. This method has been used by Julien Woillez on NAOMI/IRIS in 2018 and by Henri Bonnet on CIAO/GRAVITY-FT in 2016. To my knowledge, it has never been published. The method is based on amplitude modulation for rejecting low frequency noise, here are the details. Starting from the Maréchal approximation:

$$\frac{I(\sigma)}{I_{\max}} = e^{-2\pi\sigma^2}, \tag{5.34}$$

with $I_{\max}$ the peak intensity in the image without any aberrations, and σ the rms amplitude of the NCPA in wavelength unit. Under the small σ assumption, the first order expansion gives:

$$I(\sigma) = I_{\max} + p\sigma^2, \tag{5.35}$$

with p a constant. Introducing a temporal modulation of the aberrations as $\mu(t) = R(t) + q\cos(\omega_1 t)$, with $R(t)$ a slow ramp, we obtain:

$$I(\sigma+\mu, t) = I_{\max} + p(\sigma + R(t) + q\cos\omega_1 t)^2 \tag{5.36}$$

$$= I_{\max} + p[\sigma + R(t)]^2 + \frac{pq^2}{2} + 2pq[\sigma + R(t)]\cos(\omega_1 t) + \frac{pq^2\cos(2\omega_1 t)}{2}. \tag{5.37}$$

If we apply a band-pass filter to select the frequency $f_1 = \frac{\omega_1}{2\pi}$, we obtain the signal $W(t)$:

$$W(t) = 2pq[\sigma + R(t)]. \tag{5.38}$$

If there is no NCPA ($\sigma = 0$), the measurement $W(t)$ is in phase with the ramp $R(t)$. If $\sigma \neq 0$, we measure a shift between the measurement and the ramp of the amount of the NCPA amplitude. By modulating with f_1, we take advantage from the lower noise level at high frequency compared to low frequency. This method is especially relevant at VLTI where we measure the NCPA on top of jitters from the tunnels seeing.

Implementation wise, I followed the scripts developed by Julien Woillez for NAOMI. The adaptive optics is used to inject the modulation $\mu(t)$. More specifically, it is injected as a perturbation sequence in the reference slopes. For example for one Zernike mode, the modulation injected is shown on Fig. 5.28. Rather than a simple amplitude ramp, we take a slow sine wave for $R(t)$. It creates ramps that cross the zero at least three times during the modulation. The amplitude of the sine wave determines the maximal NCPA amplitude that is possible to measure.

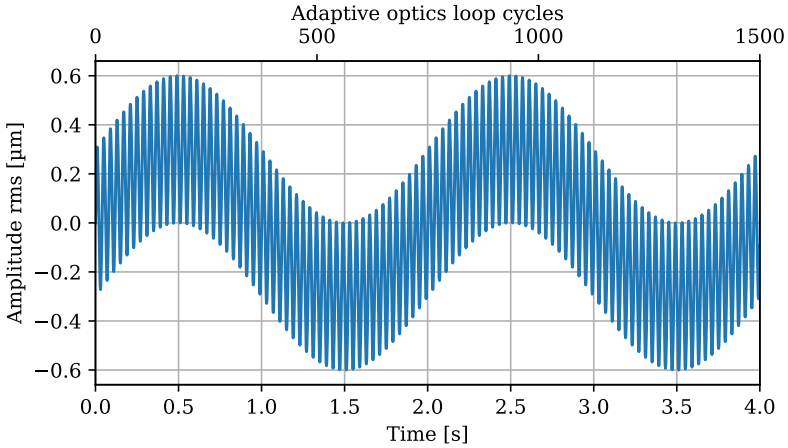

Figure 5.28 – Example of modulation $\mu(t)$ applied for NCPA measurements. f_1 =25 Hz, q = 0.3 µm, and $R(t) = q\sin(\frac{2\pi}{2}t[\text{s}])$.

I coded a simulation model for this NCPA detection technique, again using HCIPy. Figure 5.29 shows the simulated intensity injected in the SC fiber (centered on the beacon) if there is no aberration detected, and if an aberration is detected. The intensity is a quadratic estimator of the wavefront aberration, hence the doubled frequency of the slow ramp modulation. If there is no aberration (5.29a), the maxima of intensity for the slow modulation is reached when the slow modulation crosses zero (t =1, 2 and 3 s). If an aberration is detected (5.29b), the maxima of the slow modulation are not regularly spaced anymore.

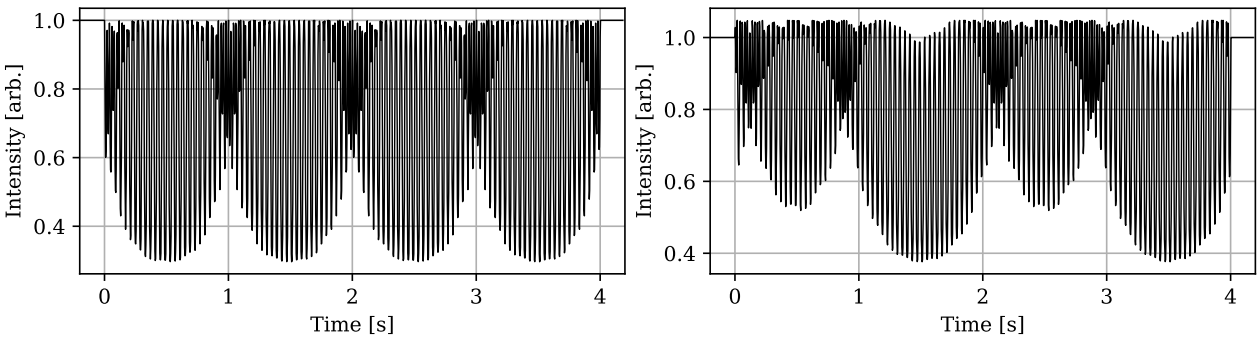

(a) No aberration detected

(b) Aberration detected

Figure 5.29 – (Simulations) Intensity injected in SC during the modulation: without NCPA (a) and with a static NCPA (b).

Using a Butterworth band-pass filter with cutoffs at $f_1 \pm \frac{f_1}{2}$, we obtain the demodulated signal shown on Fig. 5.30. The position of the downward peaks indicate the mode amplitude that maximizes the Strehl along the ramp $R(t)$. Finally, we correct the NCPA with the corresponding opposite offset in the reference slopes.

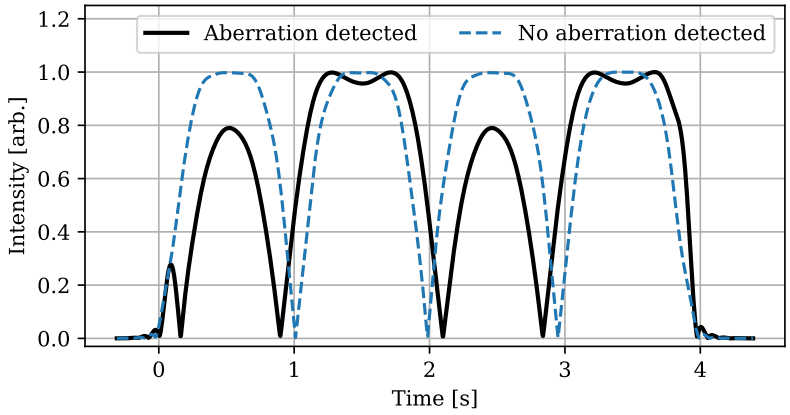

Figure 5.30 – (Simulations) Demodulated signal at f_1 with and without aberration.

During my first three months at ESO learning on NAOMI, I performed a lot of these NCPA measurements on IRIS and the AT. As I was in a training process, I do not want to draw too much conclusion from it. Still, I proved that despite the multi-mode beacon of the AT, the script was able to retrieve the amplitude of injected Zernike modes from Noll#4 to 15. NCPA measurements and correction on the AT are currently not performed on operation, but there is no technical showstopper against it. On AT2, I measured around 40 nm rms NCPA from Noll#4 to 15. On AT3, I measured around 110 nm rms NCPA. These average amplitudes were consistent on a week timescale.

5.7.2 NCPA from UT to IRIS

General setup I used some of my technical daytime to run the NCPA script on IRIS from UT2, with modal injection on CIAO. For this, I ran IRIS at K-band with DIT=5 ms. So the camera provides a sampling rate around 200 Hz that is enough to capture the $f_1 = 25$ Hz without attenuation. There is a tip-tilt tracking mode at VLTI that uses IRIS as a position sensor and sends commands to the FSM of the STS, it is called lab guiding. This mode is not offered when observing with GRAVITY (see Sect. 5.8.1). For this reason, I chose to perform the NCPA tests on IRIS without lab guiding. These tests show if NCPA measurements are possible without tunnel seeing control. On IRIS, I used two different ways to obtain the intensity along the modulation sequence: either taking the value of the brightest pixel at each frame ("max pix." technique), or taking the value of the brightest pixel on the average sequence ("fixed pix." technique). The "max pix." technique follows the brightest pixel along the sequence, and then is expected to be more robust to tip-tilt jitter. The "fixed pix" technique is closer to the situation in GRAVITY, where the SC fiber samples only one fixed position of the field.

NCPA measurement Figure 5.31 shows the demodulated signal for 12 Zernike modes tested in a row with the "fixed pix." flux. The noise level can be seen at the very beginning and end of the sequence. The demodulated signal is obtained well above the noise. After analysis of the position of the downward peaks, it gives the NCPA measurement shown on Fig. 5.32 (blue dotted line).

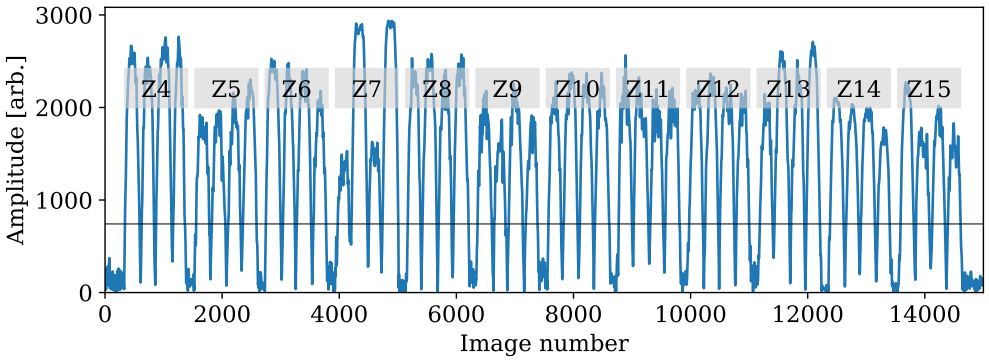

Figure 5.31 – Demodulated IRIS signal sequence with the "fixed pix.", for 12 Zernikes modes from Noll#4 to 15, at 13:12 (CL) on 2023-05-29. UT2.

I performed two NCPA measurements on UT2 at 28 min interval, without applying correction in between. The NCPA measurements at the two times, and using the two "fixed pix." and "max pix." methods, are shown on Fig. 5.32. Measurements are overall consistent in time, apart for Noll#6 (vertical astig.) that is measured with more than 40 nm rms difference. This is comforting for both the measurement method, that seems to bring consistent results, and for the NCPA temporal variation, that seems to not drastically change in 30 min. I did not measure a significant change in the tunnel seeing power spectrum between the two measurements. However, the "fixed pix." reduction is close to the "max pix." reduction at 13:12, and more deviant at 13:40. In this measurement and many others on GRAVITY-SC, I noticed that the astigmatisms and comas are the modes that are the most disturbed by tip-tilt jitter during measurements. The average NCPA of UT2 are measured around 60 nm rms. After iterative correction (1 or 2 iterations), I reduced the NCPA to 30 nm rms. Henri Bonnet conducted similar tests in 2016 and achieved 4 nm rms residuals on the UT. I believe that the difference with my tests comes from the use of a fast lab guiding during the NCPA measurement. I did not test it.

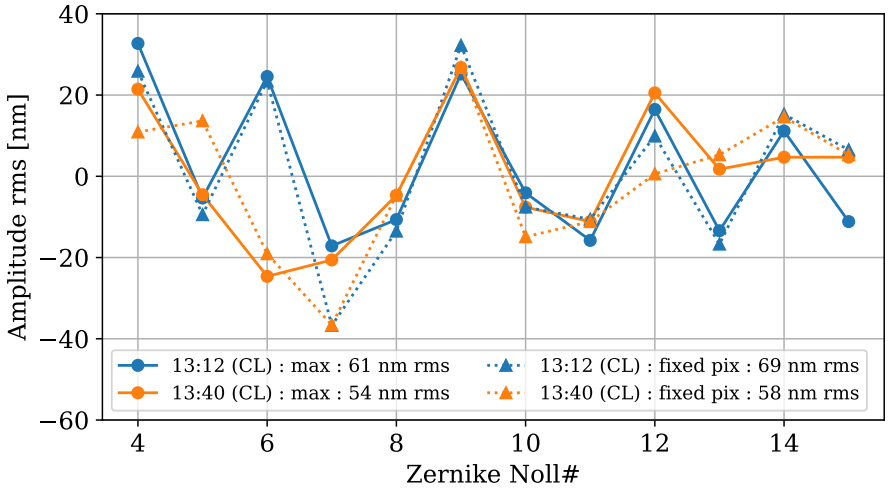

Figure 5.32 – Comparison of NCPA measurements taken 28 min apart on IRIS from UT2 the 2023-05-29.

Another short sanity test, I introduced a 100 nm rms coma on a corrected wavefront to check the method ability to measure and correct a known mode. With both "max pix." and "fixed pix." the coma was retrieved at 75 nm rms. The applied correction fixed part of the coma injected and thus

validated the measurement/correction scripts. As long as the aberrations are measured and corrected with the right sign, iterations of the method shall converge to a flat, unaberrated wavefront.

Conclusion on the tests Technically, I concluded from these tests that the modulation amplitude is better set to $q = 0.2$ µm rms than 0.1 µm rms that gives a weak signal hard to demodulate. Generally, I concluded that NCPA measurements were possible without tunnel seeing control but the correction seems to floor around 30 nm rms residuals.

Future NCPA measurements and correction to IRIS is part of the commissioning plan of GPAO, and this action item is for me. I expect it to be easier than the tests described here. First, it can be conducted in a single-beacon on-axis mode automatically provided by a template, rather than the time consuming manual dual-beacon off-axis used here on CIAO. Second, GPAO has a dedicated command to inject modal offsets in reference slopes (like NAOMI), it makes modal injection more reliable that the multiple step process I use here. Finally, for these measurements I will use the IRIS lab guiding that will stabilize the measurements. Surely, the GPAO NCPA correction on IRIS will be included as an operational step of the VLTI startup performed every afternoon before UT runs.

5.7.3 Enabling NCPA measurements to GRAVITY-SC

Correcting NCPA on IRIS is a first step, but not my goal. I want to correct the aberrations down to the GRAVITY SC arm, and cover the full non-common path between the adaptive optics wavefront sensor and the science injection. These measurements have never been performed before. The closest measurements were made by Henri Bonnet and Frank Eisenhauer during an afternoon of the GRAVITY commissioning in 2016. They used the harmonic modulation technique described earlier to measure the NCPA between CIAO and the GRAVITY-FT arm. They repeated the measurement with different angles of the GRAVITY derotator. They measured low-order aberrations of approximately 100 nm rms amplitude, where a coma following the derotator angle contributes to 75%. They did not venture into correcting these NCPA, and the internal report mentions a possible uncertainty on the scaling of NCPA up to 40%. We expect similar amplitude aberrations in the SC arm that is fed by similar off-axis parabola; however, the aberration content can be different from FT to SC. Either way, it was not an obstacle to science observations since the MACAO residuals on-sky were already around 300 nm rms. This is why during six years there was no further effort in correction of GRAVITY aberrations. But with the GRAVITY+ coming upgrade and my experiments on SCAR modes on internal beacons, we identified it as a serious limitation for high-contrast. The new adaptive optics will provide on-sky residuals around 160 nm rms, and the internal aberrations will be a significant limitation to Strehl.

Need for a fast detector The detector framerate is crucial for the NCPA measurement. Equation 5.37 shows that with a modulation at $f_1 = 25$ Hz the intensity at the focal plane contains the frequency $2f_1$. We want to avoid aliasing and damping in the measurement of these frequencies, so it requires a detector framerate of at least 200 Hz. In 2016, the NCPA measurements were possible on the FT because there are read-out modes of the SAPHIRA detector (Finger et al., 2016b) that

can run at up to 1.2 kHz. Using operational modes, it was possible to record the intensity on the camera during the modulation sequence and deduce the NCPA amplitude. However the SC detector is a HAWAII-2RG (Loose et al., 2003) whose operational modes run at best at 5 Hz. For this reason, the NCPA measurements in SC are more difficult and were never conducted. But this is not the end of the story. There is a way to speed up the HAWAII-2RG framerate and I took it upon myself to implement and test it (with the precious help of Leander Mehrgan and Julien Woillez).

Implementation Indeed, the HAWAII-2RG is a 2048×2048 detector whose maximal frame rate depends on the number of lines read in the direction perpendicular to the outputs (Fig. **??**). The operational modes read 2048×512 pixels and reach minimal DIT of 0.2 s. I did short tests showing that reading only one line (2048×1), we can achieve DIT of 1.1 ms. At ESO, the cameras' software are unified under the New General detector Controller (NGC). On the NGC panel of the SC camera, it is straightforward to take an existing mode and change the read-out window size to speed-up the read-out. What we wanted to do here is less straightforward. We wanted to read six different windows, each centered on the spectrum from one baseline. This has three advantages. First, we collect more flux than reading only one line, as the light from one telescope Nasmyth beacon will light three baselines among the six we read. Second, I do not have to change the windows' parameters when I work on different telescopes. Third, by reading the 6 baselines, it is possible to build an interaction matrix and extract separate flux from each telescope if we measure NCPA on all telescopes at once. I did not test this last point. In all the following tests I worked only on one telescope at a time. However, operationally it would make sense to measure the NCPA on all four UT at once, and save substantial amount of time. Leander Mehrgan had sequencer files to read several separate windows on a HAWAII-2RG in an uncorrelated mode. It has only been tested in laboratory and never on an ESO instrument. With his help and the help of Julien Woillez, I implemented it in the GRAVITY-SC camera software.

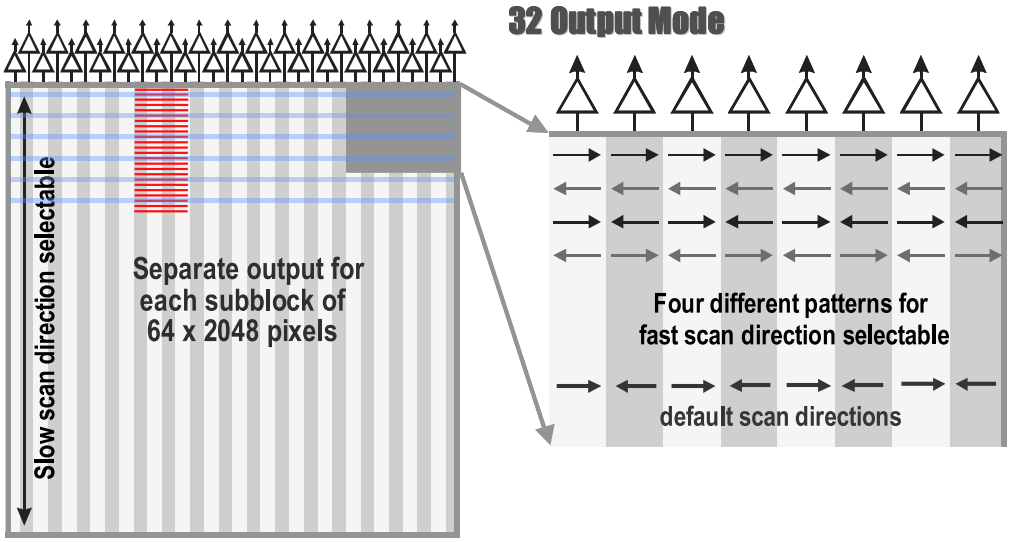

Figure 5.33 – Adapted from Figure 3 of Loose et al. (2003). HAWAII-2RG detector in the 32 output configuration. Red lines represent the position of the 24 GRAVITY spectra (6 baselines × 4 ABCD outputs). Blues lines represent the lines read by my fast-read-out mode.

Fast-SC tests I tested the highest framerate we can achieve with this 2048×6 read-out mode. There is no timestamp associated to the different frames. So, for this, I propagated the Nasmyth beacon from one UT to GRAVITY and ran a NCPA modulation on CIAO. I expected to see the $f_1 = 25$ Hz peaking in the flux. Indeed, computing the power spectral density and adjusting the sampling frequency such that the main peak in the spectrum is at 25 Hz, I found a frame time of 3.06 ms (framerate 327 Hz). It precisely matches the DIT given on the NGC panel. This test proves that the framerate is high enough for the NCPA measurements. I also wanted to make sure that I received enough flux on each frame. In MEDIUM resolution mode, the spectrum is spread over 233 pixels. For my measurements, I rather choose the LOW resolution mode of GRAVITY, this way the light is concentrated on 5 pixels and is higher above the read-out noise (see Fig. 5.35). On a 2048×1 read-out mode with DIT 2 ms, I set the Nasmyth beacon of UT4 at 100% power, and I measured on average 1000 ADU on the brightest pixels. The camera noise was at 34 ADU rms on the same measurement. I conclude that the UT beacon at full power sends enough flux to have a high SNR signal on the SC camera with fast-read-out mode. Still, the transmission can vary by 50% from one UT to another, so I always checked that I received enough flux for my test, and that it did not exceed the 45000 ADU limit. Above this limit the detector can have a non-linear response. However, enough flux on the fast SC camera is too much flux for the acquisition camera that has a DIT=0.7 s. I need the acquisition camera during the NCPA measurement for the slow field guiding to ensure that the SC keeps centered on the beacon. So, I put a neutral density filter before the acquisition camera that reduces the flux by 10 mag. This way, the flux received do not saturate the pixels but is enough for tracking.

Side effects The fast read-out mode for the GRAVITY-SC detector comes with undesired side effects. The most problematic one is frame losses. With the 2048×6 mode at 327 Hz, the FITS files never contain the number of NDIT requested before the acquisition. The actual number of NDIT seems random and from 7 to 10% less than the number of frames requested. I investigated for these lost frames on the GRAVITY calibration unit. Thanks to the Tip-Tilt Piston mirror (TTP) in GRAVITY, I can inject a step function that periodically moves the beacon position in the field to a different position. As the SC fiber position is fixed, the injection in the SC follows the step function injected by the TTP. When I do this test, I can see that the steps recorded by the SC are uneven. This shows that frames are lost during the sequence, and sometimes a group of frames (second oscillation on Fig. 5.34). As we have seen before, the NCPA measurement relies on the position of downward peaks along the sequence. So, the frame losses' problem will certainly impact the position accuracy, and bias the measurement of the Zernike mode amplitude. I observed that increasing the DIT to 55 ms (instead of 3 ms) reduced the number of frame losses to 1 to 2% of the total. We still found no solution against this problem, one possibility is a bad interaction with the SC real time display that cannot follow the high pace. In the following measurements, I will keep the DIT=3 ms despite the frame losses. Another undesired side effect appears, switching from an operation mode to the fast-read-out mode, and back to an operational mode, the real time display of the SC camera appears scrambled. A restart of the NGC server solves the problem, but the cause of this problem must be found if the fast-mode is routinely used in the future.

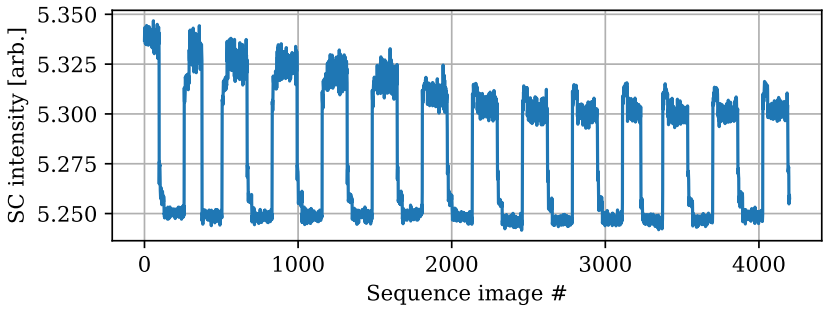

Figure 5.34 – Intensity in SC when a step function is injected with the TTP.

Parameters tuning For NCPA measurements, I obtained the flux injected in the SC by identifying the pixel of the (2048 × 6) image that has the maximal standard deviation along the sequence. Then, I sum all pixels value in a (5 × 6) window centered on the maximal standard deviation pixel (Fig. 5.35).

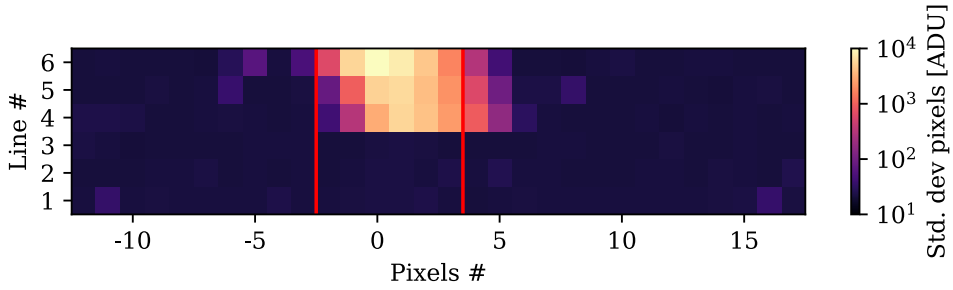

Figure 5.35 – Standard deviation (taken on the temporal axis) of the pixels value on the fast-SC image on a NCPA modulation on one UT. Pixels are numbered relative to the pixel with the highest standard deviation. The vertical red lines delimit the region where I sum the pixels value to extract the flux.

After the implementation of the new read-out mode, I experimented different parameters q, T and f_1, for the NCPA modulation $\mu(t) = q[\sin(\frac{2\pi}{T}t) + cos(2\pi f_1 t)]$. I wanted to find the parameters that provide the cleanest signal. This is compiled in Table 5.3. I call good signal, a demodulated signal where the three downward peaks are clearly identified for all modes from Noll# 4 to 15 (for example Fig. 5.31). I call noisy signal, a demodulated signal where the downward peaks are not easy to identify, and where the beginning and end of the modulation is not clear.

Table 5.3 – Best parameters for the NCPA modulation

Parameter	Values	Comment
q	0.1 µm rms	Noisy signal
	0.2 µm rms	Good signal
	0.3 µm rms	Good signal
The modulation amplitude q determines the highest NCPA amplitude the method can measure. But I expect a too high q amplitude to provide less precise measurements of low amplitude aberrations, because of the steepness of the ramp. In the following, I chose $q = 0.3$ µm rms for modes with Noll#< 7 that are more susceptible of reaching high amplitudes, and $q = 0.2$ µm for higher order modes.		
f_1	10 Hz (SC detector set to DIT=5 ms)	Good signal
	25 Hz (SC detector set to DIT=3 ms)	Good signal
I see no significant influence of the f_1 frequency on the demodulated signal. In the following, I use $f_1 = 25$ Hz to remain in a zone where tunnel seeing has low tip-tilt power (see Sect. 5.8.1).		
T	2 s	Good signal
	4 s	Noisy signal
	8 s	Noisy signal
I found the period T of the slow ramp to provide a better signal when kept short. It makes a steeper ramp and I think that, in a noisy environment, it helps for identifying the ramp point that maximizes Strehl. Even if, like for high amplitude q, it might provide less precise measurements of low amplitude modes. In the following, I use $T = 2$ s.		

With this harmonic modulation method and a fast detector to measure the signal, I could then measure the NCPA down to the GRAVITY-SC.

5.7.4 NCPA from UT to GRAVITY-SC

The two last technical time periods I participated during my PhD were in October 2023 and January 2024. During these sessions I managed to obtain the first NCPA measurements from one UT to the SC. In the following, I specify the UT number together with the GRAVITY input (GV) investigated. Each GRAVITY input leads to a separate fiber coupler, and we expect the off-axis parabolas of the fiber couplers to contribute significantly to NCPA. During technical time, each UT beam can be addressed to any GRAVITY input but I always kept the operational addressing rule (UT1/GV4, UT2/GV3, UT3/GV2, and UT4/GV1). For my first attempts of NCPA measurements in GRAVITY, I was proceeding as on IRIS with 12 Zernikes modes measured per sequence with one modulation for each mode. I soon realized that measurements in GRAVITY-SC were more difficult due to tunnel seeing noise and detector frame losses. So, I rather performed several measurements of each Zernike mode, always starting from the lowest order. Also, I developed a HCIPy simulations of this technique applied to the GRAVITY fibers. It shows that Zernike modes are not orthogonal considering their impact on the injected flux. In these conditions, it is preferable to measure and correct the modes one by one, instead of several modes together.

First defocus measurements In October 2023, I spent a lot of effort in getting the system in the right configuration, and exploring the best modulation parameters (Table 5.3). It paid back at the

end of the technical time week, when I could achieve the first defocus measurement and correction in the SC with the harmonic modulation technique. It was on UT1/GV4 and Fig. 5.36a shows the demodulated signal for 12 measurements in a row. The repetition of two close peaks and a big gap is typical of a strong aberration detected, here a defocus at -140 ± 29 nm rms (the uncertainty is the standard deviation of the 12 measurements, Fig. 5.37). I corrected for this defocus and repeated the measurements. I obtained the demodulated signal of Fig. 5.36b whose regularly spaced peaks are typical of low or zero aberration detected. After correction, I measured a residual 17 ± 37 nm rms defocus (Fig. 5.37).

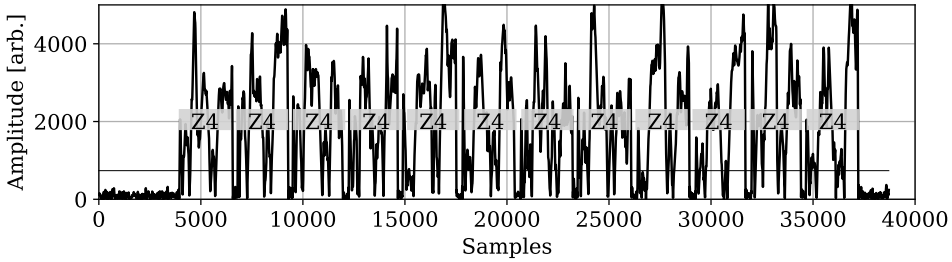

(a) Before defocus correction.

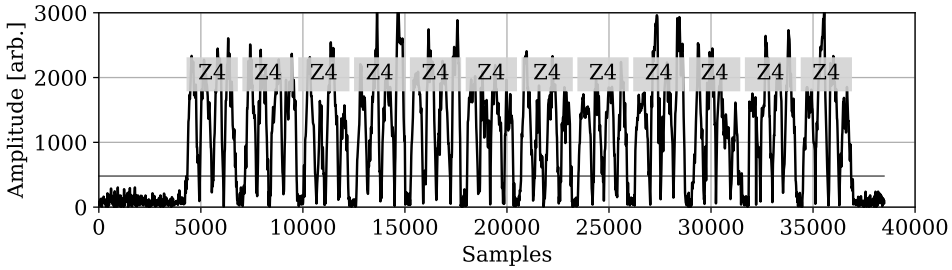

(b) After defocus correction.

Figure 5.36 – Demodulated SC signal sequence with 12 successive defocus measurements. (a) Defocus of -140 nm rms. (b) Defocus of 17 nm rms.

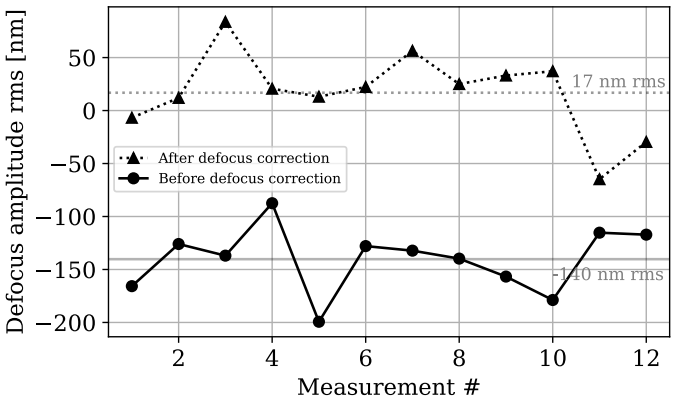

Figure 5.37 – Defocus amplitude measured before and after correction on UT1/GV4 the 2023-10-26. Horizontal lines show the average amplitude for both sequences.

A defocus correction of this amplitude has a drastic impact on the Strehl, and so on the amount of injected flux. Averaging the collected flux over 12 s, outside the modulation sequences, I measured on average $(1.65 \pm 0.24) \times 10^4$ ADU before correction and $(1.96 \pm 0.14) \times 10^4$ ADU after correction. It corresponds to +15% of flux injection and is an additional confirmation that the defocus correction

was effective.

Higher-order NCPA In January 2024, I had some technical time to expand the NCPA measurements to higher order modes and, if possible, several UT. First, I had a run on UT1/GV4 where I measured NCPA from Noll#4 to 9. The summary of the measurements are in Appendix A.5 Table A.1. This time I did not measure a strong defocus but the main aberrations were an astigmatism and a trefoil around 85 nm rms and a coma around 60 nm rms (Fig. 5.38a). For the six modes measured, the total amplitude is 139 ± 9 nm rms. It is an expected amplitude for the NCPA from a UT to the fiber coupler since it is close to the 100 nm rms measured by Henri Bonnet in 2016 on the FT. For some reason, my script for correcting the NCPA via modal offsets in the CIAO slopes was not effective during the January technical time. I could not identify the problem, but extensive debugging was not required since the next time I will make these measurements it will be on GPAO. And GPAO has a dedicated command for modal offsets injection.

The next day, I performed the NCPA measurements on UT3/GV2. This time, I made a first sequence from Noll#4 to 7, and I repeated the measurements from Noll#4 to 11 (spherical). The detailed NCPA amplitudes are in Appendix A.5 Table A.2. I measured a strong defocus of around -220 nm rms. I could also see it on the PSF showed by the acquisition camera, it means that this aberration was not totally caused by the fiber coupler but probably comes from the beam provided by VLTI. During the same technical time week, Julien Woillez and Taro Shimizu investigated a flux problem on the same UT3/GV2; in operation it received significantly less flux than the other UT. My independent measurement of the NCPA seems to point to a focus problem. As shown by Fig. 5.38b, the measurements from the two sequences are consistent. On top of defocus, I measured a 100 nm rms coma and a 50 nm rms trefoil. It adds for a total of 251 ± 7 nm rms, that is much more than expected but certainly because of the strong defocus. Removing the defocus contribution, I obtain total NCPA around 120 nm rms, that is closer to the expected NCPA amplitude in SC.

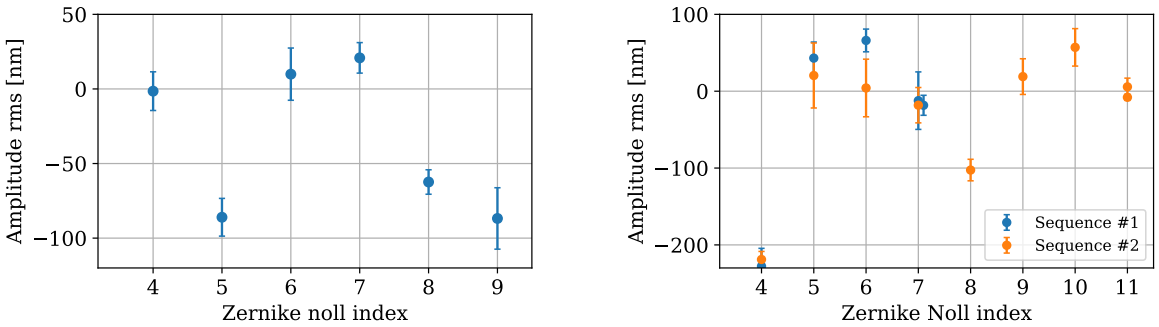

(a) UT1/GV4 (b) UT3/GV2

Figure 5.38 – NCPA measured on Nasmyth beacon of UT1 the 2024-01-23 (a) and UT3 the 2024-01-24 (b) using modulations on CIAO.

Tunnel seeing The measurements on UT1 and UT3 showed the influence of tunnel seeing on the NCPA amplitude error. On UT1 at 22:00 (Paranal time), the average error on modes amplitude was 14 nm. On UT3, 19 hours later, the average error on the same modes' amplitude was 25 nm. I could link it to the variations in the flux injected in the SC during the two sessions. Figure 5.39 shows the power spectral densities of the SC flux for UT1 and UT3. It shows that the flux variation in

UT3 contained more power than in UT1 in the range from 1 to 60 Hz. Specifically, the power is 3 times higher on UT3 than UT1 at the modulation frequency f_1 =25 Hz. The power gap reaches one order of magnitude from 4 to 10 Hz. The conditions in GRAVITY were the same during the two tests, so the difference in the noise amplitude comes from VLTI. It seems that the discrepancy comes from the delay line position that made a longer tunnel path on UT3 measurement than UT1 measurement. An internal document (VLT-TRE-GRA-15880-7501) shows that the path length in the tunnels can have this effect on the tip-tilt power spectral density between 1 and 10 Hz. This test shows that the tunnel seeing has a direct impact on NCPA measurements precision. It highlights why it is preferable to have a modulation frequency at 25 Hz instead of 10 Hz. It also indicates that future NCPA measurements from the coudé adaptive optics to GRAVITY must be performed with delay lines at the shortest path position.

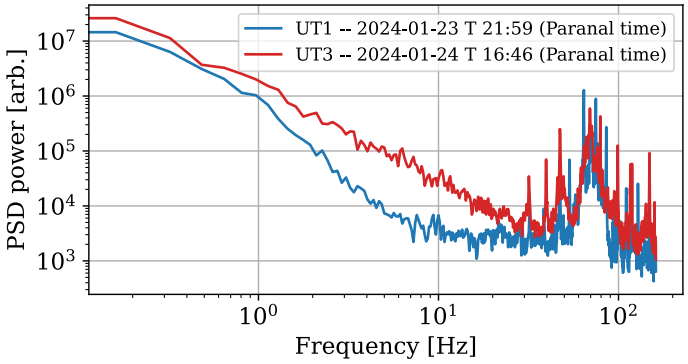

Figure 5.39 – Power spectral densities of the flux injected in SC in UT1 the 2024-01-23 and in UT3 the 2024-01-24. We have no explanation for the 70 Hz peak, but it was also seen in piston by the team working on VLTI vibrations.

Conclusion These NCPA measurements on the UT are a work in progress. It has shown that the frame losses in the SC fast read-out mode did not prevent the NCPA measurements. It has an impact on the measurements error, but I was not able to quantify it. However, the tunnel seeing has certainly an impact that seems to dominate the measurement error budget. Back to our overall goal, we want to pave the way before GPAO. With the new adaptive optics installed, there might be commissioning time to conclude on the temporal variability of the aberrations, and possibly add an operational routine to correct them (Sect. 5.9).

5.8 Stabilize the wavefront

From wavefront control simulations to NCPA measurements on GRAVITY, everything converges to the need for a stable diffraction limited wavefront. The amount of residuals from the rapidly changing atmosphere will be determined by the GPAO design and its successful commissioning by the team. During my PhD, I focused not only on the NCPA but also on other disturbances that are not corrected by the adaptive optics: corrections of the VLTI tunnels seeing (Sect. 5.8.1), and correction of the expected low-wind-effect (Sect. 5.8.2).

5.8.1 Tunnel seeing control

The VLTI tunnels are not in the vacuum: when the UT are open at night, one can even feel a breeze inside due to the chimney effect. This air flow induces turbulence and disturbs the wavefront in a path that is not seen by the adaptive optics. Pfuhl et al. (2014) quantified that tip-tilt represent 90% of the wavefront error caused by the tunnels. In GRAVITY, a slow field guiding (sampling rate 1.4 Hz) is provided by the acquisition camera. It measures the position of a bright object in the field and sends commands to the TTP or the STS mirrors for a correction. Anugu et al. (2018) quantified the typical average residuals to 10 mas rms on-sky on UT.

Limitation for dark-hole depth I have shown in the previous section that the tip-tilt jitter from the tunnels was the main contributor to noise in NCPA measurements on GRAVITY. I ran simulations that show that the dark hole created by phase apodization is also sensitive to the tip-tilt jitter. Figure 5.40 shows how the SC injection is affected by jitter, both in no apodization and SCAR mode apodization conditions. It shows that increasing jitter from 2 to 10 mas rms makes the dark hole created by a SCAR mode less deep by almost two orders of magnitude at 105 mas. Even without apodization, the tip-tilt jitter affects the first zero of the injection pattern at 80 mas by one order of magnitude. This demonstrates that even with no residual aberrations from the adaptive optics, the tip-tilt jitter from the VLTI tunnels can significantly deteriorate the apodization impact on SC injection.

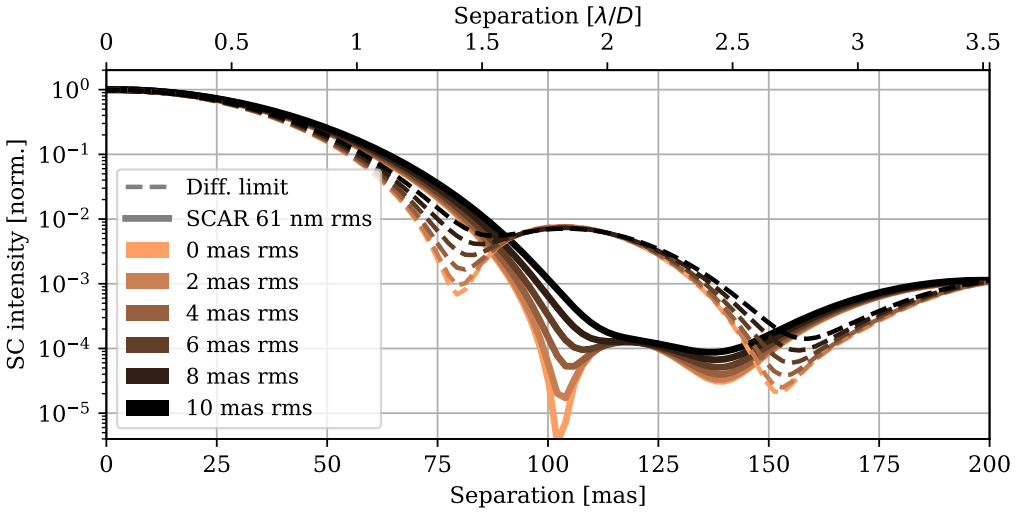

Figure 5.40 – (Simulations) Injection in SC for different amount of tip-tilt jitters. Without and with SCAR apodization over the UT pupil. The curves are the average over the K-band (20% bandwidth).

Limitation for dark-hole implementation Another limitation from the tunnel jitter is huge flux variations in the SC injection when it is not centered on the star (or on the beacon). Figure 5.41 shows the injection variations I measured, on UT beacon, along 45 s sequences at four different separations from 0 to 125 mas. The flux when the fiber is centered on the beacon do not vary by more than 5%. However, when the fiber is at 61 mas separation or more, the flux injected vary by around 40% from one exposure to another (DIT=3 s). It is a big limitation for iterative wavefront control techniques that would require to measure and decrease the off-axis injected flux. This test shows that,

even on the UT internal lamp, it would take averaging exposures on at least one minute to obtain flux values with less than 10% variations. In these conditions, with 3 iterations on 5 acquisitions (e.g. 4 probes plus one flux measurement) and the necessary overheads for reduction and sending commands, it would take 20 to 25 min to dig a dark-hole in the SC. This test was performed without the acquisition camera slow-guiding, further tests would show if it reduces the variations significantly. I checked if the off-axis flux variations on the IRIS camera were of similar amplitude. I measured the pixel values at 60 mas (2 pixels) from the PSF core along sequences with similar DIT=3 s. The flux variations on IRIS are of the same amplitude as on GRAVITY-SC. I conclude that there is not a specific sensitivity of the SC fiber injection to tunnel seeing compared to a focal plane camera.

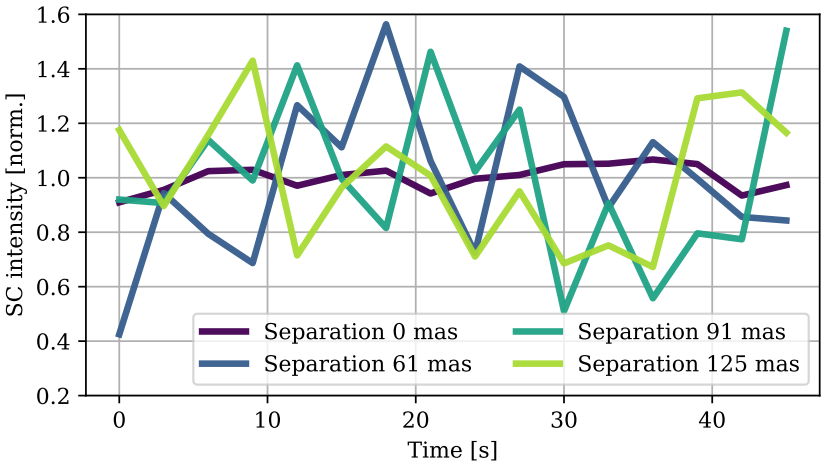

Figure 5.41 – Variations in SC injection measured on the UT2 Nasmyth beacon during sequences of 16×3 s DIT. The intensity of each sequence is normalized by the average of the sequence.

Jitter amplitude According to the ESO internal document already mentioned (VLT-TRE-GRA-15880-7501: GRAVITY Technical Note on VLTI induced tip tilt), the average amount of tip-tilt jitter induced by the VLTI tunnel atmosphere is 15 mas rms (angle of UT on sky) and can peak at 19 mas rms. They measured that the power spectral density of the jitter followed a power law in f^{-2} from 0.01 to 10 Hz, and $f^{-11/3}$ above 10 Hz. It indicates that most of the jitter power lies below 10 Hz. It is in accordance with my measurement of the spectral density of the flux injected in SC on-beacon (Fig. 5.39). These measurements show that a control solution for the frequencies below 10 Hz would already correct most of the jitter.

The abandoned system The initial design of GRAVITY included a fast-guiding system (Pfuhl et al., 2014). The principle was: a laser at 658 nm is focused on the optical axis on the FSM mirror at the STS level (Fig. 5.42). In GRAVITY, a positional sensitive diode collects the laser flux at up to 3.3 kHz and sends the opposite tip-tilt command to the TTP. To avoid vignetting of the science beam, the laser injection makes an angle of 5.8° with respect to the optical axis. So the effective flux that propagates to VLTI is issued from the scattering cone created by mirrors' imperfections. This system was installed in GRAVITY and in all UT and AT. Unfortunately, despite the efforts in adjusting the lasers' position to find the optimal scattering, the flux on two UT was too low to bring any improvement (Table 5.4). As the tip-tilt jitter did not appear to be a major problem in

operation, no more effort has been put to make the fast-guiding system work. The advent of GPAO, together with the growing importance of the exoplanet science case, brings a new interest for this system.

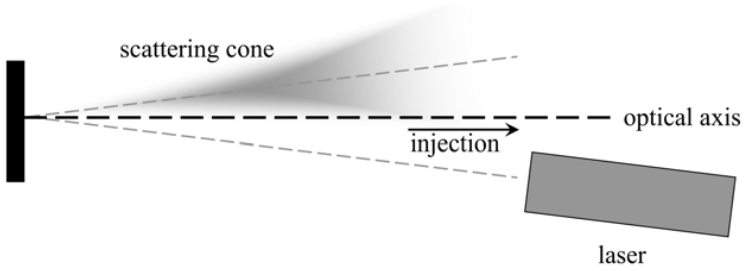

Figure 5.42 – Principle of laser injection on the STS FSM mirror. Flux on the optical axis relies on the non-specular diffusion of the laser spot.

New birth With the precious help of Frank Eisenhauer, I spent some technical time to check if the system was still in place. The last tests were done in 2017 and we wanted to check that lasers and positional diodes were still working. The GRAVITY calibration unit includes a visible source for internal tests of the guiding system. From the internal GRAVITY tests, we saw that the diodes were still operational, receiving from 2.5 to 3.5 V from the visible lamp (nominal on UT is 2 V). We also confirmed that the software for the control loop was still operational. The diode provides measurements at 3.3 kHz but we do not use it at that rate. To go back to the 2017 setup, we adjusted a parameter to smooth the diode signal with a 1.2 ms moving window average. Thanks to this adjustment, we managed to close the fast-guiding loop with the same pure integrator gain as used in previous reports. Then, I ran tests by injecting a tip-tilt disturbance on the TTP (disturbance called "atmosphere normal" in GRAVITY), and corrected it with different integrator gains of the fast-guiding. To have a truth sensor to ensure that the fast-guiding loop reduces the tip-tilt jitter, I modified the number of lines read on the acquisition camera, a Hawaii-2RG also. This way, I was able to run it at 100 Hz framerate on the field image instead of the operational 1.4 Hz. The results of these tests are on Fig. 5.43. It proves that the loop corrects the tip-tilt jitter with a cut-off frequency at 10 Hz. As seen by the acquisition camera, the amount of XY jitter is 50 mas rms on the perturbation alone, and 20 mas rms with the loop at gain 600 (arbitrary). I tested loop gains 1000 and 1200, the loop still converges but the power spectral density shows no significant improvement compared to gain at 600. Without perturbation injected, I measured XY jitter at 1.8 mas rms. Closing the loop at gain 600 adds some noise in the tip-tilt, I measured a total 2.0 mas rms. The noise increases with loop gain, reaching a total 2.8 mas rms at gain 1200. This amount of loop-noise jitter is still below the actual 10 mas rms we have in operation. Reaching this noise floor of 2 mas rms would already be a great improvement. Overall, these tests motivate to use a maximal gain of 600 if the diode receives sufficient flux from the guiding laser (around 2 V).

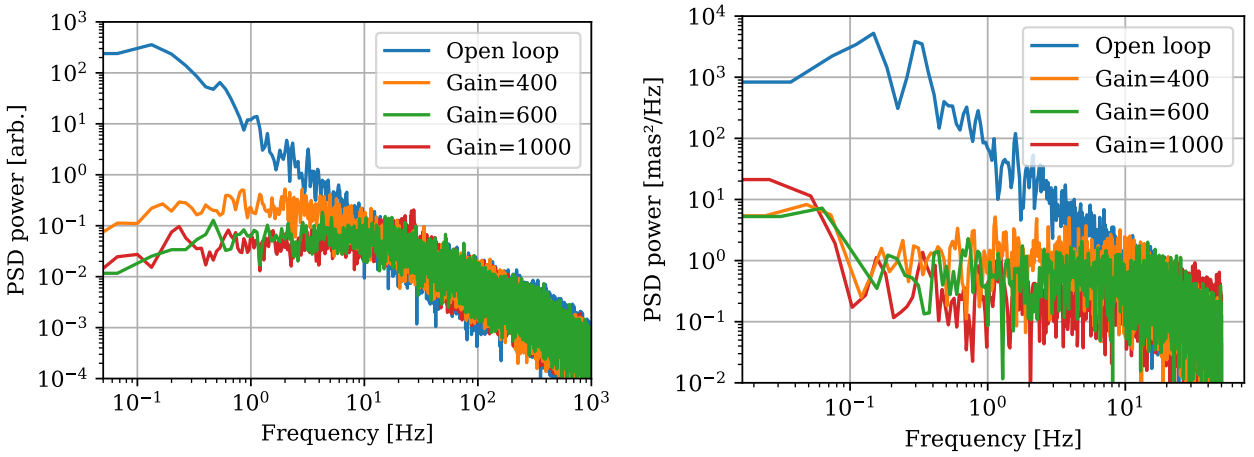

(a) Positional diode signal

(b) Acquisition camera tip-tilt

Figure 5.43 – Power spectral densities of the tip-tilt jitter on the GRAVITY calibration unit, (a) as seen by the positional diode, (b) as seen by the acquisition camera. The TTP injects a perturbation (blue) that the fast-guiding system corrects in function of the gain (arbitrary value).

Injection status I conducted these fast guiding tests in January 2024, during the last technical time week I participated. All these tests were on the GRAVITY calibration unit and I had no time to replicate the fast-guiding tests on the real UT guiding lasers, with the real VLTI tunnel seeing. Still, during a previous technical time, I measured the flux received on the diodes from the four UT and compared it to the values recorded in 2017 during the GRAVITY commissioning (Table 5.4). We still receive enough flux from UT1 and UT2 to close the loop in a nominal regime. The flux from UT3 increased since 2017 but does not reach a value sufficient for effective guiding. The flux from UT4 is detected but at a very low level. Comparing the position of the spot on the diode to the diode field-of-view, I concluded that UT4 is almost off and would need recentering.

Table 5.4 – Voltages received from the guiding laser on the positional sensitive diodes

	Laser off October 2023	Laser on 2017	Laser on October 2023
UT4	0.004 V	0.20 V	0.077 V
UT3	0.005 V	0.46 V	0.68 V
UT2	0.008 V	1.41 V	1.55 V
UT1	0.008 V	2.20 V	2.11 V

Conclusion With this technical time work to revive the fast-guiding system, Frank Eisenhauer and I managed to bring the system back to its 2017 state. Here, we reach the limit of what we can do remotely from Garching, so the next actions will be in Paranal. The limitation is still the amount of flux received from UT3 and UT4. The first thing to do, is to recenter UT4 laser and check if it brings more flux to the corresponding GRAVITY diode; second, try to adjust the laser position on all UT (priority to UT3 and UT4) and see if we can improve the flux received. If these actions prove not sufficient, one way forward will be to use more powerful lasers (actually 60 mW) and adapt the baffling to cancel unwanted scattering effects. It is not officially part of the GPAO commissioning

plan, but I hope I can spend some of my time in Paranal during commissioning to push forward to a fast-guiding system that is ready for operation. On the UT1 and UT2 that receive enough flux, it would be interesting to activate the fast-guiding and measure its impact on-beacon and on-sky.

Alternative solution We also imagined a completely different way to damp the tip-tilt jitter. We thought about using the IRIS lab-guiding in parallel with GRAVITY. There is space between the actual feeding optics that directs the VLTI beams to GRAVITY (Gravity FO in Fig. 5.20a). We could add dichroic beam-splitters to send the H and K-band to GRAVITY but let the J-band go through to IRIS. As discussed previously, IRIS can be used as a sensor for a VLTI lab-guiding system that can operate to 1 kHz if it receives enough flux. IRIS is an infrared camera and I can confirm that it does not see the GRAVITY fast-guiding visible lasers. This guiding method would rely on the star flux. As the favorite targets for ExoGRAVITY are bright nearby stars, there is certainly a range where the IRIS lab-guiding system can be used to reduce the jitter. I made on-sky tests on the AT showing that on a J=5.8 mag star we can close the IRIS guiding loop with DIT down to 40 ms (25 Hz rate). On a J=3.6 mag star, the minimal IRIS DIT was 8 ms (125 Hz). Accounting for the 3 mag difference, on the UT we could run IRIS at 125 Hz framerate on stars brighter than J=6.6 mag. This IRIS+GRAVITY path is not favored at the moment, but it can be a back-up plan if the GRAVITY fast-guiding is a dead-end.

5.8.2 Low-wind effect control

With advent of GPAO, another problem might appear and challenge the wavefront stability: the low-wind effect. It was the topic of my four months Master 2 internship at IPAG with Jean-Baptiste Le Bouquin and Julien Milli in 2021. It also occupied a significant fraction of the first six months of my PhD.

Physical explanation This undesired effect falls under the category of dome-seeing effect. It appears when the wind speed is low at the UT aperture level. The metallic spiders holding the secondary mirror radiate their heat to the clear sky and measurements show that their temperature is 1 to 3° below the ambient air temperature. If the air around the spiders is almost static, the heat exchange with the metallic structure creates a colder laminar flow (Fig. 5.44). The temperature difference creates optical path differences of the order of 100 nm along the spiders and aberrations that are poorly corrected (or even amplified) by the adaptive optics.

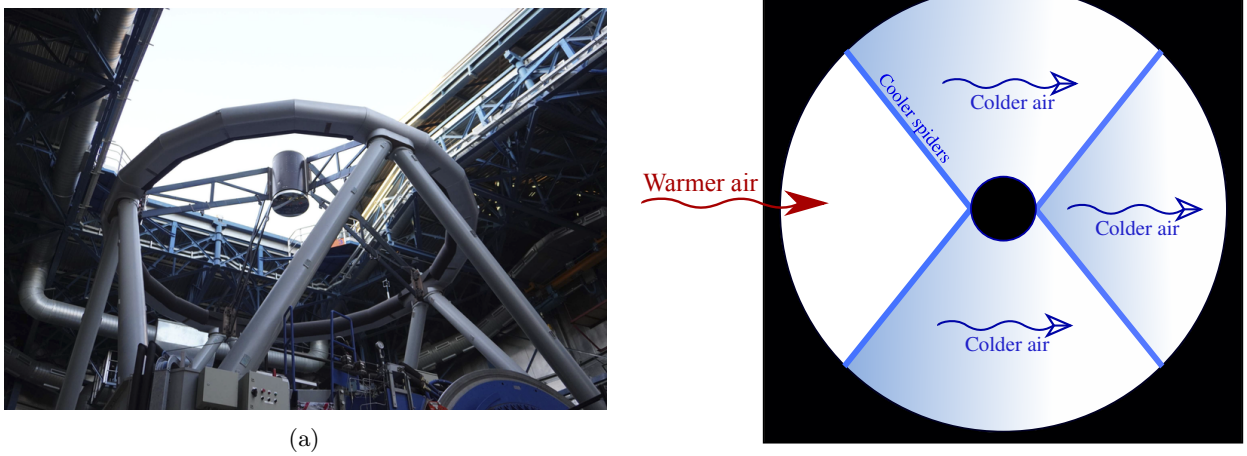

(a) (b)

Figure 5.44 – Illustration for the low-wind effect. (a) Aperture and structure of the secondary mirror (M2) on UT3 (photo N. Pourré). (b) Schematic for the thermal exchange at the spiders in low-wind conditions.

Search for solutions The effect was referenced already 75 years ago in Couder (1949), but it is only when big 8 m telescopes were brought close to their diffraction limit that the effect really obtained the attention of the astronomers. The effect appeared during SPHERE commissioning in 2014 and was identified as the main limitation for the instrument (Sauvage et al., 2016). Later, it also appeared on the other high-contrast imagers of 8 m telescopes like Subaru/SCExAO and Gemini South/GPI. Milli et al. (2018) used wind statistics and temperature measurements on UT3/SPHERE to confirm the physical origin of the effect. They also described how the application of an anti-radiative coating on the spiders reduced the low-wind effect occurence from 20% to 3.4% probability. Other solutions are investigated, including active control via focal plane wavefront sensing (Wilby et al., 2018; Bos et al., 2020), robust coronagraph design (Leboulleux et al., 2022), pyramid wavefront sensor solutions (Schwartz et al., 2018; Bertrou-Cantou et al., 2022; Engler et al., 2022), and photonic lantern sensors (Wei et al., 2023). The low-wind effect limitation is also a major concern for the ELT instrumentation.

The aberrations induced by the low wind effect appears to fragment the PSF core and creates bright side-lobes at the location of the first Airy-ring. Thus, the effect is problematic for direct observations of planetary companions at short separations. For coronagraphic instruments like SPHERE, it generates star light leaks out of the focal plane mask and reduces the maximum achievable contrast level. On an interferometric instrument like GRAVITY+, it is expected to increase the amount of stellar light coupled in the fibers at the planet position and affect the detection limits and spectra SNR.

Simulations: reproduce the effect Before my M2 internship, the impact of low-wind effect on Shack-Hartmann adaptive optics was poorly studied. I used adaptive optics end-to-end simulations with HCIPy to better understand this impact and find active mitigation solutions for SPHERE and GRAVITY+. From this research, I published an Astronomy & Astrophysics paper (Pourré et al., 2022a) and a SPIE proceeding (Pourré et al., 2022b). My work started by creating a realistic simulation of the SPHERE and GRAVITY+ adaptive optics on HCIPy. The two systems have

a Shack-Hartmann wavefront sensor and similar design in term of number of actuators on the deformable mirror (41 in the pupil diameter), in term of loop speed (∼1 kHz), and of course they operate on the same telescopes, the UT. In both cases, the control basis is the Karhunen-Loève modal basis (KL). The benefit of using HCIPy is that it properly simulates the propagation of the wavefront along the system, without linearization and small-phase assumption. It enables us to investigate eventual second-order effects that would cause the bad correction of low-wind effect by adaptive optics. The HCIPy package already includes example of SPHERE-like adaptive optics[§], although it did not include the possibility to inject petal phase discontinuities. With the help of Emiel Por, I developed modifications to include UT pupil segmentation, this add-on was later included in HCIPy. I injected low-wind effect aberrations as separated pistons and tip-tilts on the four quadrants of the UT pupil separated by the spiders. With this simulation, I could reproduce the post-adaptive optics residuals observed on SPHERE during low-wind effect nights (Fig. 5.45). The aberrations were measured in 2014 with a Zernike phase mask called ZELDA on the IRDIS camera (N'Diaye et al., 2013b). In the SPHERE measurement, it was puzzling that the adaptive optics was not able to correct such low-order aberrations. For example, the piston-tip-tilt of Fig. 5.45b are expected to be seen by the wavefront sensor and corrected by the system. Being able to reproduce the effect in simulation was a very encouraging step towards understanding the cause.

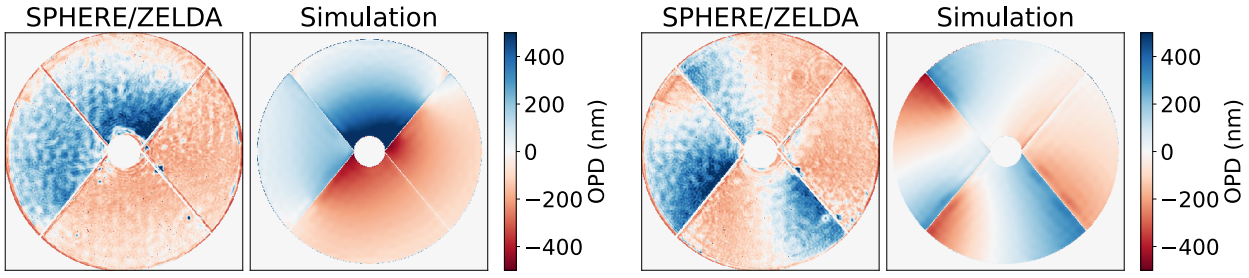

(a) (b)

Figure 5.45 – From Pourré et al. (2022b). Comparison between low-wind effect OPD observed on SPHERE with the ZELDA Zernike sensor, and post-adaptive optics OPD from the HCIPy simulation.

At subaperture scale To understand why such low order aberrations can remain in the residuals of the adaptive optics, I had to look to the wavefront sensor. More, the cause for these residuals appeared at Shack-Hartmann subaperture scale. I ran simulations for the propagation of a wavefront through a squared subaperture and computed the center of gravity of the obtained spot. Then I tested how the spot diffraction and the centroid are affected by phase discontinuities and by the presence of a spider obscuring part of the subaperture. I found that, for a discontinuity, measuring the center of gravity on a restricted field of view brought completely wrong measurements of the local phase difference in the sub-aperture. Figure 5.46 shows an example of these simulations. It can be summarized as:

- Fig. 5.46a: Flat phase in the sub-aperture, the spot is at the center of the field of view.
- Fig. 5.46b: Phase slope of $0.2 \times 2\pi$ amplitude. On an infinite field of view, it would induce a spot displacement of $0.2\lambda/D$. Here, due to the restricted field of view, the centroid is measured at $0.19\lambda/D$ (5% error).

[§]https://docs.hcipy.org/0.5.1/tutorials/ShackHartmannWFS/ShackHartmannWFS.html

- Fig. 5.46c: Same phase slope, a spider obstruct 25% of the subaperture. The centroid is measured at $0.10\lambda/D$ (50% error).
- Fig. 5.46d: Phase discontinuity of $0.2 \times 2\pi$ peak-to-valley amplitude. The centroid is measured $0.14\lambda/D$ (30% error).
- Fig. 5.46e: Same phase discontinuity, obstructed by the spider. The centroid is measured $-0.08\lambda/D$ (140% error, wrong sign).

The presence of the spider obstructing a phase discontinuity breaks the sup-aperture PSF on bright side-lobes. As the side lobes can fall out of the field of view, the measurement can be greatly affected. I investigated the influence of different spider widths on a $3.5\lambda/D$ field of view (like SPHERE). I found that the actual spider width on SPHERE (25% of sub-aperture width) was the worst to measure a phase discontinuity, and we have the same aperture-to-spider width ratio on GPAO.

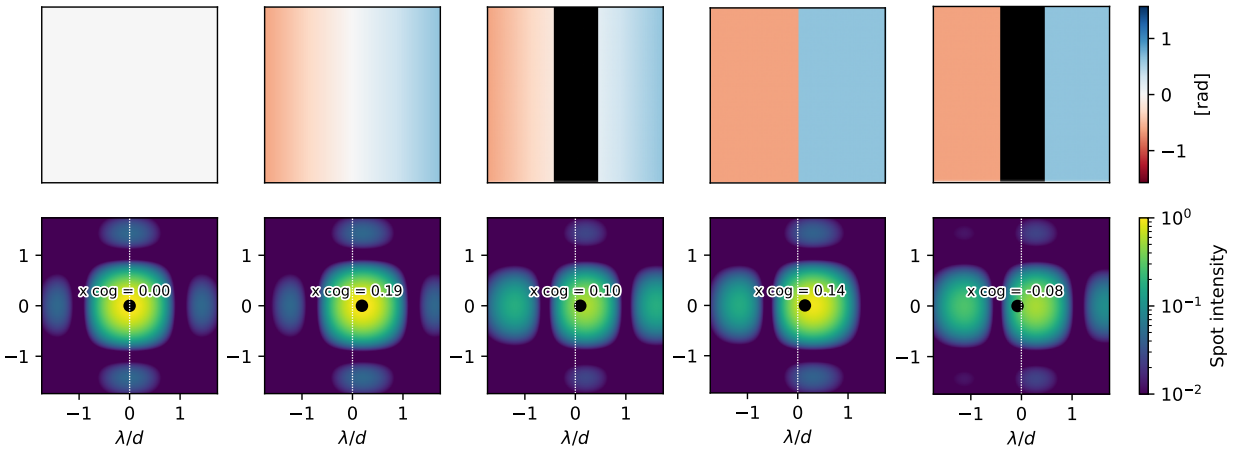

(a) (b) (c) (d) (e)

Figure 5.46 – From Pourré et al. (2022b). Illustration how a Shack-Hartmann spot and the corresponding center of gravity (cog) are affected phase discontinuities and obscuration by a spider. (top) Phase in the Shack-Hartmann sub-aperture. (bottom) corresponding spot. The white dotted line shows the center of the field of view. (a) With flat phase. (b) with a phase slope. (c) with a phase slope obstructed by a spider. (d) with a phase discontinuity. (e) with a phase discontinuity obstructed by a spider. d is the width of the sub-aperture.

At adaptive optics scale To understand why it translates into uncorrected aberrations, we have to zoom back to the entire adaptive optics. The Shack-Hartmann wavefront sensor is sensitive to local phase slopes on the pupil. If one quadrant of the UT pupil is affected by a piston (petal-piston), the sensor will detect it only via the sub-apertures affected by a phase discontinuity: at the edges of the petal-piston. These sub-apertures are partially obstructed by the spiders and I have shown previously that it leads to wrong phase step measurements. Therefore, the petal-piston is almost not seen by the wavefront sensor, and then poorly corrected by the adaptive optics (example Fig. 5 in Pourré et al., 2022a). It was expected that the Shack-Hartmann was a poor piston sensor. For residual petal-tip-tilt, the explanation is more subtle. A petal-tip-tilt is a constant slope over one pupil quadrant and discontinuities on the edges (see Fig. 5.48). The wavefront sensor is sensitive to the phase slope in the quadrant but is poorly sensitive to the edge discontinuities. Figure 5.47 shows that a phase with no rotational (curl=0) over the pupil can generate a slopes map with rotational (curl≠0) after measurement by a Shack-Hartmann. In the first example (figure top), the

phase is composed of a vortex that leads to a sharp discontinuity from π to $-\pi$ rad on the top of the pupil. The Shack-Hartmann makes a wrong measurement of the discontinuity and the slopes are fully rotational. In the second example (figure bottom), the discontinuity is smooth enough to be measured by the Shack-Hartmann, the resulting slopes map is non-rotational. This explains how a bad discontinuity measurements can lead to curl patterns in the Shack-Hartmann slopes. The deformable mirror is a smooth surface, i.e., mathematically, a differentiable scalar field. The curl of a smooth differentiable scalar field is always 0, the deformable mirror cannot generate a mode with a curl. The KL basis is a subspace of the deformable mirror's possible modes, it does not include any curl either. Therefore, a rotational slopes map provided by the Shack-Hartmann does not project on the KL basis and results in no command to the deformable mirror. To summarize, there is two ways for the adaptive optics loop to converge to non-zero low order aberrations on the wavefront: either the aberration is not seen by the sensor, resulting in zero slopes for the command (petal-piston), or the aberration induces a curl pattern in the slopes that do not project onto the control basis (petal-tip-tilt).

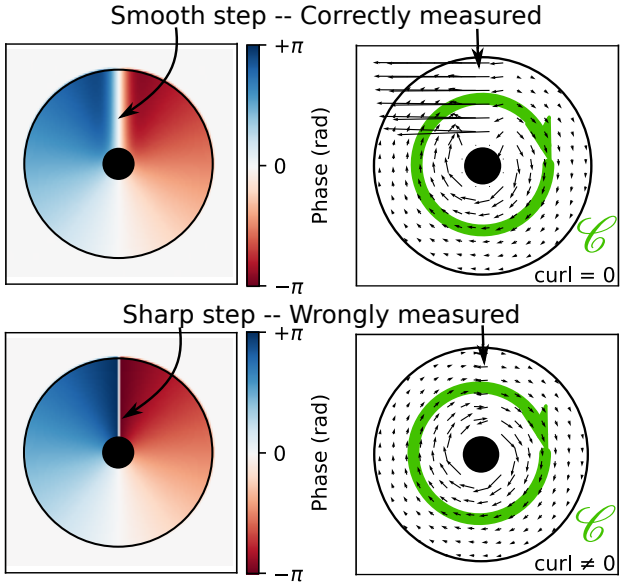

Figure 5.47 – Adapted from Pourré et al. (2022a). Schematic showing how a sharp phase step can be wrongly measured by the Shack-Hartmann and introduce a curl in the slopes (bottom). A smoother phase is correctly measured and result in no curl in the slopes (top).

Mitigation strategy I reproduced the problem of the uncorrected low-wind effect aberrations and understood its origin. Then I developed an active control strategy to mitigate it. The previous active solutions investigated for SPHERE relied totally on focal plane wavefront sensing (Fast & Furious algorithm Wilby et al., 2018). My study shows that the Shack-Hartmann can also be used to measure most of the modes. First, we had to decide which modes to correct. The commonly used low-wind effect basis is composed of 11 modes, the 3 petal-pistons (global piston excluded) and the 8 petal-tip-tilt (Sauvage et al., 2016). After brainstorming sessions with Jean-Baptiste, we found another basis composed of only odd and even combinations of petal-tip-tilts and petal-pistons (Fig. 5.48). Expressed this way, it appears that 2 modes do not contain discontinuities (Mode#4 and Mode#8). It reduces the number of modes to control to 9, 3 petal-pistons modes and 6 petal-tip-tilts

modes.

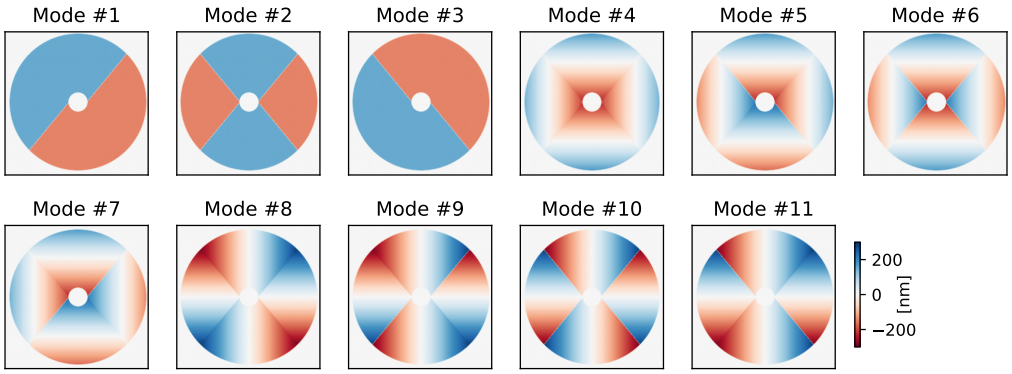

Figure 5.48 – From Pourré et al. (2022b). Proposed decomposition basis in odd and even modes for low-wind effect aberrations.

For the petal-tip-tilts, we have seen previously that the Shack-Hartmann was sensitive to them in the pupil quadrant, but failed to measure them at the quadrant discontinuities. Getting the slopes produced by the wavefront sensor only at the quadrants center, we can obtain a reliable measurement of the petal-tip-tilt modes (Fig. 5.49). This measurement can be projected on our low-wind effect modal basis and applied as a correction to the deformable mirror command.

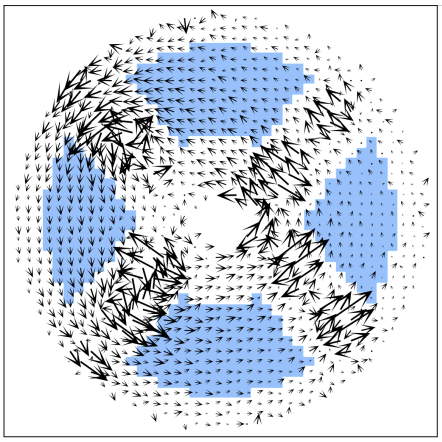

Figure 5.49 – From Pourré et al. (2022a). Shack-Hartmann slopes at adaptive optics convergence under low-wind effect aberrations. (blue) slopes selected for the piston-tip-tilt control.

For the petal-pistons, the Shack-Hartman cannot help. The measurement has to rely on focal plane analysis. The proposed new modal basis (Fig. 5.48) decomposes the petal-piston in 2 odds and one even mode conveniently. For this, I developed a rudimentary focal plane analysis that could directly measure the odd modes#1 and #3. Even modes are inherently difficult to measure with focal plane analysis because of the uncertainty on the mode sign. As we only have one even mode to measure (Mode#2), I implemented a simple trial and error approach to find the right sign. All the theory of this focal plane analysis is described in the Appendix B of Pourré et al. (2022a).

Control loop implementation I implemented both petal-piston and petal-tip-tilt control loops in the end-to-end adaptive optics simulation. Figure 5.50 summarizes how the different loops interact.

For the focal plane sensing, I simulated an H-band camera with 1.5 Hz framerate, in the spirit of the SPHERE Differential Tip Tilt Sensor (Baudoz et al., 2010) and the GRAVITY acquisition camera. In the full adaptive optics simulation, the measurement of odd petal-piston modes proved robust but the measurement of the even petal-piston modes was difficult to converge. The Shack-Hartmann provides a measurement at a 1 kHz rate. I set the gain for the petal-tip-tilt control to 0.005 to temporally decouple the atmosphere control to the low-wind effect control. Julien Milli and Jean-Baptiste Le Bouquin analysed the ZELDA low-wind effect sequences and concluded that the aberrations' variation in time was mostly contained below 0.1 Hz. This is well in the control range of the Shack-Hartman loop and close to the cut-off frequency of the focal plane analysis. We are confident that it would significantly capture and correct the aberrations induced by the low-wind effect.

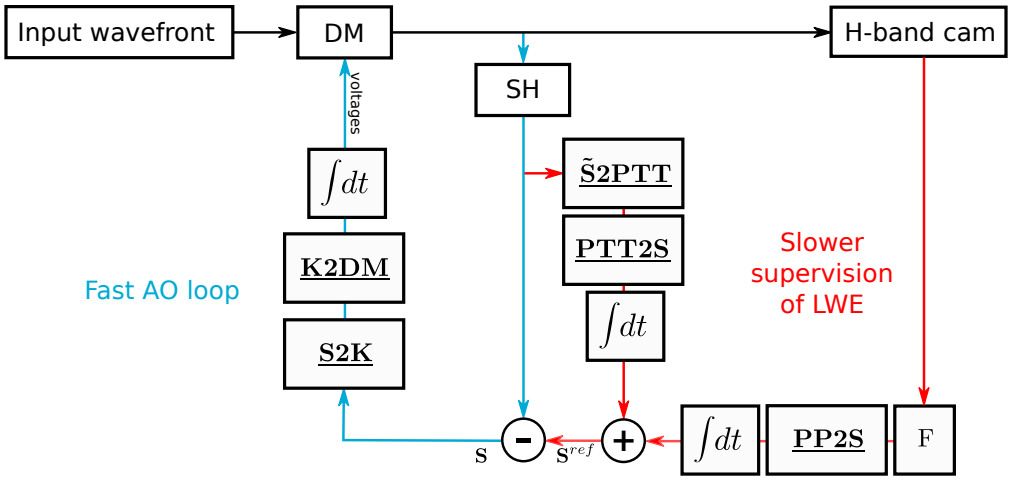

Figure 5.50 – From Pourré et al. (2022a). Schematic of the proposed control loop against low-wind effect. (blue) original adaptive optics loop. (red) slower loop for low-wind effect control. $\int \mathrm{d}t$ is for integrators. F is the operation that extracts the petal-piston modes amplitude from H-band images. SH stands for the Shack-Hartmann. DM for the deformable mirror. **$\tilde{\mathbf{S}}$2PTT** is the matrix from the slopes at the center of quadtrants to the petal-tip-tilt amplitude. **PTT2S** is the matrix from petal-tip-tilt amplitude (KL smoothed) to slopes command. **PP2S** is the matrix from petal-pistons (KL smoothed) to the slopes. **S2K** is the matrix from slopes to KL basis. **K2DM** is the matrix from KL basis to deformable mirror command.

Correction Finally, Fig. 5.51 shows an example of correction in simulation. The simulation includes an atmosphere of 0.6" seeing in frozen flow. The low-wind effect aberrations are injected as a static pattern of petal-pistons and petal-tip-tilts. In this example, the petal-tip-tilt loop converged in 150 ms (150 adaptive optics loop cycles) to +16% Strehl at H-band. The focal plane control loop converge in 1.7 s to additional +4% Strehl. Assuming a perfect aberration sensor that directly projects the phase residuals on the KL basis (best fitting KL) the Strehl reaches 88%. It is only 3% higher than the residuals after our control algorithm and confirms that our general control solution is valid.

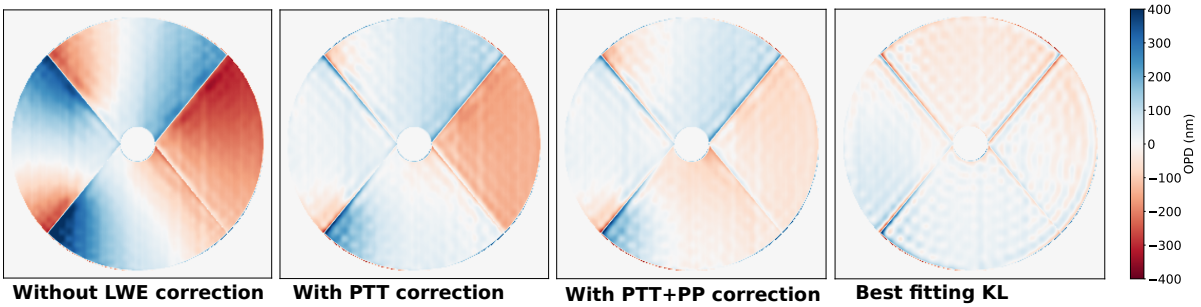

Figure 5.51 – From Pourré et al. (2022b). Result of the low-wind effect control loop implemented in the simulation. Strehl ratios are given at H-band. LWE stands for low-wind effect. PTT stands for petal-tip-tilt. PP stands for petal-piston.

Real telemetry data I never tested this control solution on a bench or on SPHERE. However, thanks to Jean-François Sauvage, I had access to SPHERE telemetry data from the adaptive optics during low-wind effect events. Thanks to Sylvain Oberti, I also had access to AOF (VLT/UT4) telemetry data during low-wind effect. There is still a gap between my simulations and the real phenomenon. In the real data on SPHERE and AOF, I have never been able to detect the curl pattern in the Shack-Hartmann slopes, despite the simultaneous ZELDA sensor showing it in some SPHERE sequences. Also, my simulations predict that the adaptive optics is creating part of the residual aberrations. This is something they investigated during SPHERE commissioning and they saw nothing in the deformable mirror command that could explain the residuals measured with ZELDA. Maybe the slope curl and the deformable mirror wrong commands are too buried under the slopes and commands from the atmosphere control. Some additional analysis of the telemetry data would be required to match simulations with observations.

Conclusion I finished this low-wind effect study and the subsequent communications (A&A paper, WFS in the VLT/ELT ERA VI, SPIE 2022 Montreal) during the first few months of my PhD. After that, my PhD was focused on GRAVITY and GRAVITY+ where low-wind effect is not (yet!) the dominant problem. The spiders on UT3 where SPHERE operates have already been coated against low-wind effect. ESO planned for the application of the anti-radiative coating on the spiders of the other three UT in the coming months. If the passive solution prove not sufficient against low-wind effect, we have my active control strategy that we could implement in GPAO. Following my study, the possibility to send wavefront offsets commands at 1 Hz rate from the VLTI lab was added to the design of GPAO. It would facilitate a future focal plane control of the low-wind-effect, if needed.

5.9 Towards an operational implementation

In this chapter, I described how we could reduce the star light injection in the SC fiber at short separation to allow for lower exoplanet detection limits and higher SNR spectra. This includes NCPA control, tip-tilt jitter and low-wind effect active correction, to finally apply phase apodizations thanks to GPAO. At summer 2024, GPAO will be installed and the question of how it can be implemented in operation is still pending.

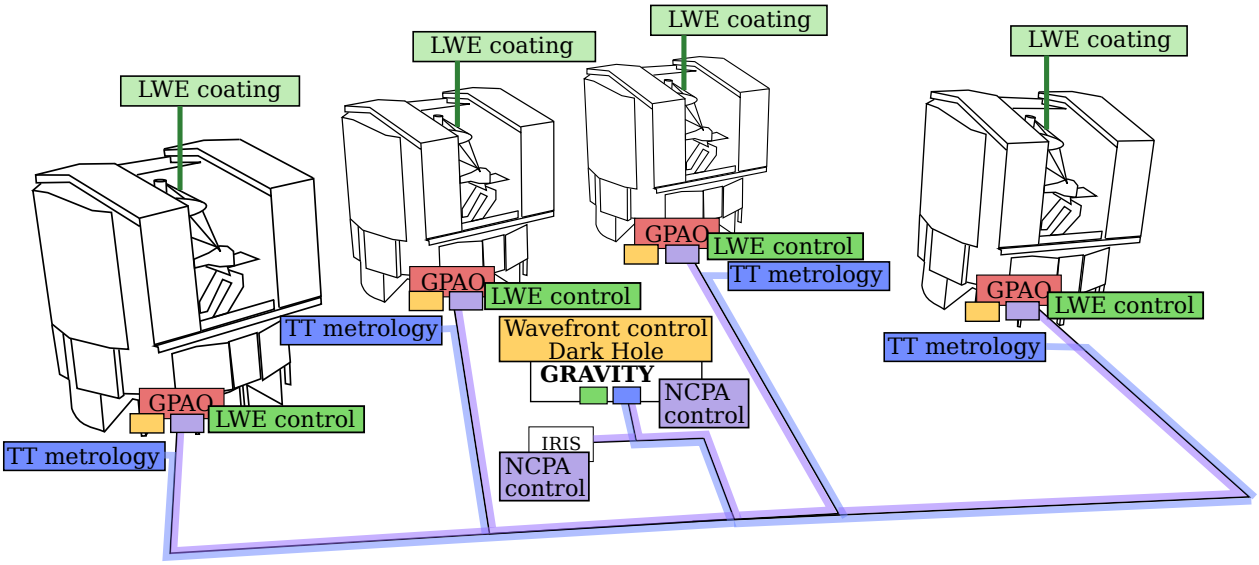

Figure 5.52 – Summary of the building blocks of the high-contrast mode of GRAVITY+. LWE stands for Low Wind Effect, and TT stands for Tip-Tilt.

NCPA For the NCPA at VLTI (down to IRIS), it is still left to determine if it is dominated by tunnel seeing or if a control of static or quasi-static NCPA can reduce the wavefront phase rms. If static NCPA contribute significantly to the aberrations, the plan with GPAO is to routinely correct them down to IRIS before VLTI operation. For the NCPA down to the GRAVITY-SC, I have shown that we can measure and correct them. We still have to determine it is stable in time or if it varies. If it is stable in time but rotates with the GRAVITY K-mirror (as Henri Bonnet showed for the FT aberrations), we could imagine to have a NCPA correction at the beginning of the night, and then apply a model depending on the K-mirror position. For NCPA varying on the timescale of 3 to 4 hours, it would be possible to correct them before the observations requiring high contrast capabilities or optimal flux injection. However, it would be at the cost of night-time overheads from 10 to 30 min depending on the number of Zernike modes we want to control. In case of NCPA drifts at the timescale of a few minutes, there is a solution for real-time aberrations measurement in GRAVITY. As shown on Fig. 2.10, the acquisition camera includes a Shack-Hartman wavefront sensor for each of the four beams. So far, this sensor is not used in operation but there is a growing interest in using it to control NCPA with GPAO. Jens Kammerer is in a post-doctorate position at ESO and this is one of his contributions to the project. With him, I implemented a fast-readout mode for the acquisition camera, reading only the Shack-Hartmann lines, it reaches 18.2 Hz framerate, without frame losses. This sets the maximal control bandwidth we can expect from a control loop driven by the internal Shack-Hartmann. As the acquisition camera and the SC are both in a thermally controlled environment in the GRAVITY cryostat, we can assume that the aberrations between both are static with time. If we reach a good knowledge of the internal differential aberrations, we can imagine using the GRAVITY Shack-Hartmann for tracking the corrections to apply for an optimal correction of the NCPA in SC.

Wavefront stabilization Together with low-wind effect and tip-tilt jitter control, it represents a group of corrective actions that will benefit not only to the exoplanet observations but to all GRAVITY science cases. If the observations on the galactic center, on young-stellar objects, or on distant active galactic nuclei, are not concerned by high-contrast issues, they will still benefit from the Strehl improvement. Overall, a more stable wavefront corrected from most of the low order aberrations leads to higher flux injection of the science target in the SC.

Wavefront control Once the wavefront corrected as much as possible from NCPA and tip-tilt jitter, we expect to be able to use wavefront control techniques to dig a dark hole at specific positions of the focal plane. During my PhD, I focused on using a model of optimal phase apodization to apply as a modal offset to GPAO. This model would adapt to simple parameters, like the position of the UT spiders, but would not require probing and focal plane measurements. This would be easy to implement and would not generate any overheads during the observations. However, it would rely on simulations for finding the best apodization and would not adapt to instrumental changes. For me, this is a solution that we must implement in GPAO, at least as a first try of wavefront control, and see how it reduces the star injection in the SC. For most people I talked to, either in the GRAVITY+ consortium or in the direct imaging community, a static model solution like this is doomed to fail. They would rather go in the direction of an iterative wavefront control relying on probes measurements and adaptive apodization (e.g. speckle nulling). As I showed on Fig 5.41, the flux injected in SC undergoes big variations with time that would make the impact of a probe difficult to measure. For this reason, an iterative dark hole requires to have a fast tip-tilt guiding system. Assuming that this problem will be solved, there is a current effort from Sylvestre Lacour to find how the interferometric nature of the measurement in SC could help identifying the modes to apply to dig the dark hole. In this sense, it would consist in probing the electric field under the SC fiber with the measurement of light coherence between telescope rather than modal probes injected in the adaptive optics of separate telescopes. Future tests during and after GPAO commissioning will tell us what is the solution that digs the deeper dark holes in GRAVITY+.

5.10 Conclusion

I have shown that simple offsets of the SC fiber position was an efficient way to use "tip-tilt dark hole". This way we can already reduce the star light injection in SC by $\times 5$ in coherent flux down to 50 mas. It even already allowed for the confirmation of the Gaia DR3 ...6464 B brown dwarf, the shortest separation sub-stellar companion ever directly observed. With GPAO the SC fiber offset improvement can reach $\times 10 \sim 15$ at 50 mas. Also, the wavefront control solutions are promising in simulations. Close to the diffraction limit, it represent a gain of $\times 100$ at 75 mas in planet-to-star flux ratio, and close to $\times 1000$ at 125 mas. However, I have also shown that actually the SC injection was too aberrated to see any improvement of the phase apodization.

In order to pave the way before a successful wavefront control implementation in GRAVITY+, I focused on NCPA correction, tip-tilt jitter stabilization and low-wind effect mitigation. For the NCPA, I developed the first procedure to measure and correct them down to the SC arm of GRAVITY. More work on technical time is required to measure its amplitude in all GRAVITY inputs, to determine

how it changes in time, and if it is affected by other parameters (e.g. K-mirror position, position in the field). Further work will determine to which precision the NCPA can be corrected, and therefore determine the impact on eventual dark holes.

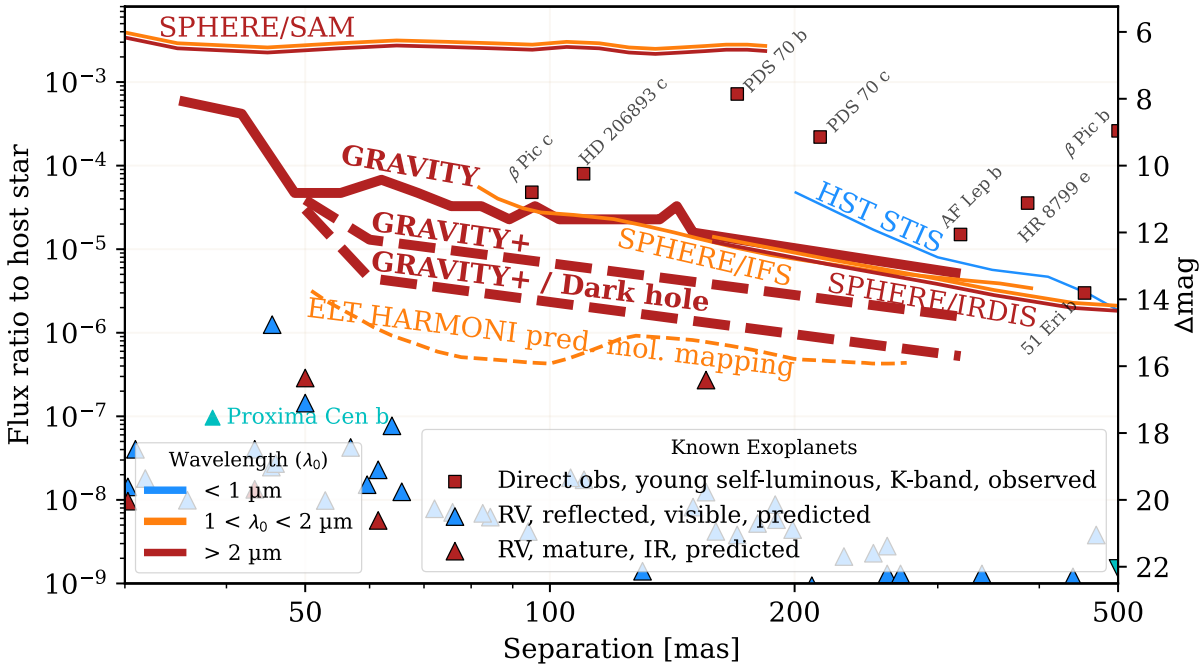

Figure 5.53 – Similar to Fig. 3.19. The predicted detection limits with GPAO and with the wavefront control/dark hole are shown in thick dashed lines.

Most of my work in simulation did not include post-adaptive optics residual from atmosphere. I expect it to be the main limitation to high-contrast, even with the new GPAO. The expected Strehl at K-band is 80%, instead of the actual $\sim$ 30% provided by MACAO. Being conservative, we can assume that the star total and coherent flux injection with separation shown in Fig. 5.5 will be reduced by $\times$3 to 4 from 80 mas. It is more difficult to estimate the final improvement a dedicated high-contrast mode can bring. For this we can rely on the experience on KPIC already mentioned in Sect. 5.2.2. Indeed, Xin et al. (2023) used the speckle nulling technique in KPIC and achieved a $\times$2.8 stellar flux reduction at 90 mas at K-band. Their setup with the injection in a single-mode fiber after a high-order adaptive optics is close to our situation on GRAVITY, so their test is a good benchmark for what we can achieve. Altogether, with the improvement of the higher Strehl and an apodisation (or speckle-nulling) we can expect to improve the planet-to-star flux ratio by $\times$10 down to 60 mas with GRAVITY+. We have shown in Sect. 3 that we were currently limited by systematics. As systematics scale with the stellar flux, we can expect to push the detection limits by $\times$10 with GRAVITY+ and reach 3×10^{-6} contrast at 60 mas. Figure 5.53 shows the predicted detection limits compared to other instruments dedicated to direct observations of exoplanets. It shows that, above 150 mas, the estimated future detection limit of GRAVITY+ is close to the expected detection limit of HARMONI with molecular mapping. But we still have to keep in mind that, apart from any high-contrast considerations, the current lowest magnitude detection of a free floating object with GRAVITY is at K=19 mag. So the expected detection limit of $\Delta K = 16$ mag at 300 mas would only be for the brightest stars like β Pic. Still, the current upgrade from GRAVITY to GRAVITY+ might

allow for direct observations of young Jupiter-mass companions, possibly down to the snow-line at 3 to 5 au, around the closest stars of our galactic neighborhood.

Chapter 6

Conclusion

Contents

6.1 Wrapping up my thesis

The goal of my PhD was to improve exoplanets' observations with GRAVITY and in prevision of GRAVITY+. For this, I followed three paths.

Detection limits

- I developed tools for injection and retrieval of companions in ExoGRAVITY data.
- I proposed a method for quantifying the significance of exoplanets detection with GRAVITY.
- With the injection/retrieval method and archival data, I determined the contrast curve of GRAVITY. It showed that the instrument can detect exoplanets at contrast of 6×10^{-5} down to 50 mas separation. It also showed that below 100 mas there is an influence of the planet's positional angle (PA) orientation with respect to the VLTI UV plane. The PA range from 100° to 180 ° ($\pm$180°) lacks long baselines and the GRAVITY sensitivity to short separation exoplanets is reduced.
- I used archival data and a theoretical noise analysis to show that the ExoGRAVITY observations are currently not limited by stellar photon noise but by systematics that scale with the star's flux.

Systematics in the visibilities

- I showed that the infamous "wiggles" systematics had a limited impact on the measurement of relative astrometry, and therefore on the exoplanet's detection. However, it severely impacts the measurements of exoplanet's spectra.

- I reproduced the wiggles' problem on the GRAVITY calibration unit, and thus, showed that the problem is internal to GRAVITY.
- From analysis of on-sky data of the ExoGRAVITY large programme and on the calibration unit, I confirmed that the wiggles originate from star flux leaking in the SC fiber when observing the companion.
- With numerous tests on on-sky data and on the calibration unit, I searched for the wiggles' source in the instrument. I acquitted most optical elements of GRAVITY (Wollaston prism, SC-FT beam splitter, fibered delay lines,...) and could verify that the problem does not come from the SC camera. Unfortunately, to date I have no satisfactory physical explanation for the wiggles.
- Together with Mathias Nowak, we found a calibration strategy that is very promising for correcting the wiggles' impact on exoplanet spectra and properly compute the covariance error matrix at the data reduction stage.

High-contrast mode

- I developed and tested a method based on off-pointing of the SC fiber that reduces by $\times 5$ the amount of coherent light from the star in the SC when observing companions at separation less than 60 mas on the UT. This method helped to observe a brown dwarf companion around the star Gaia DR3 2728129004119806464. At 34 mas separation, it is to my knowledge the substellar companion at the closest separation ever directly observed.
- I tested in simulation for the best apodization to apply on the GPAO deformable mirrors to reduce the starlight injection in the SC at less than 150 mas separation. Close to the UT diffraction limit, the optimal apodization can reduce by $\times 100$ the amount of star light injected in the SC at 100 mas.
- I tested these apodizations on the AT (on-sky) and the UT (on the internal source) and could see no reduction of the star flux injected in the GRAVITY SC. I concluded that we were currently limited by aberrations in the instrument that are not corrected by the adaptive optics (NCPA).
- On technical time, I enabled the measurement and correction of NCPA in the SC arm of GRAVITY, implying a new read-out mode for the SC camera. I measured NCPA in the SC of the order 130 mas, enough to cancel the benefit of the phase apodization.
- For a high-contrast mode in GRAVITY+, the wavefront stability will be crucial. For this reason, I worked on a correction system against the tip-tilt induced by the VLTI tunnels, and on active mitigation solutions against low-wind effect.

6.2 The way forward for GRAVITY

At short term, the way forward for GRAVITY is clear. We are on the eve of the commissioning of the new GRAVITY+ adaptive optics (summer 2024), which will be a major improvement for exoplanets' observations. I look forward to participating in the upgrade commissioning and trying to make the most of it with the high-contrast mode. Once the system is operational, it will be

interesting to identify the new limitations, especially regarding the wiggles and other systematics limiting the detection.

Moreover, everybody in the ExoGRAVITY consortium is looking forward to the next Gaia Data Release 4 in 2026. The space telescope will identify hundreds of young companions that we will be able to characterize from ground down to 1 M_{Jup} and 1∼2 au. This synergy will be a strong argument for a new Large Programme, and the results from these observations shall be transformative for the field. Before the Gaia DR4, we can already rely on Hipparcos-Gaia proper-motion anomalies to identify planetary mass companions and constrain their position on-sky before observing them with GRAVITY+. In private communication, Anne-Marie Lagrange told me that this technique was already providing AF Lep b-like candidates (∼3 M_{Jup}, < 10 au) that would be good targets once GPAO is operational.

Since 2023, there is a new operating mode at VLTI where GRAVITY serves as a fringe tracker for MATISSE (GRA4MAT, Lagarde et al., 2022). It improves the sensitivity of MATISSE in L (3.4 µm) and M bands (4.7 µm), and makes possible the observation of exoplanets. The spectral characterization in this mid-infrared window is important, for example to study the clouds and dust content in exoplanets' atmospheres (e.g. Skemer et al., 2011). Observations of β Pic b and c have already been carried out and we can expect that more exoplanets will be observed with the GRA4MAT mode in the coming years. We can also imagine GRAVITY serving as a fringe tracker for PIONIER at H-band (1.6 µm) or other future instruments at VLTI, as shorter wavelengths (J or Y bands) will be crucial for short separation observations of mature gaseous giants in reflected light.

On the long haul, some are pushing for building a fifth UT that would provide longer baselines and better UV coverage. I showed that exoplanet observations at VLTI were affected by gaps in the UV coverage, but determining if building a UT5 is realistic or not is out of the scope of my PhD.

6.3 The way forward for direct exoplanet observations

The direct observations of exoplanets are motivating a lot of instrumental developments. At VLTI, the instrument ASGARD/NOTT (Laugier et al., 2023) will be commissioned in a few years. It will be a nulling-interferometer in L-band that is expected to provide exoplanet observations at contrast 10^{-5} and down to separations of 5 mas. The nulling technique is highly sensitive to vibrations, so extensive progress are required on the VLTI to enable such performance. If it delivers the expected performance, it will be complementary with GRAVITY+ by enable direct exoplanet observations at short separations that we cannot access with our instrument.

On single telescopes, the very next developments in years to come are SPHERE+ (Boccaletti et al., 2020b) and RISTRETTO (Lovis et al., 2022) on the VLT. Both will use a two-stage adaptive optics, and both are pathfinder instruments for the Planetary Camera and Spectrograph (PCS) instrument of the ELT, which is planned for the 2040s (Kasper et al., 2021). Together with other instruments on the ELT (e.g. Houllé et al., 2021), they are expected to yield a large number of exoplanet discoveries through direct imaging. GRAVITY+ will be useful to complement these discoveries with precise orbit characterization and spectral analysis that will still be of interest into the ELT era.

There are also space observatory projects that plan to push the boundaries of exoplanet characterization. The Nancy-Grace-Roman telescope will be launched in 2027 and enables direct imaging

of exoplanets in reflected light (Bailey et al., 2023). In the 2050s, there are ambitious projects of space telescopes, as the Habitable World Observatory (HWO, Gaudi et al., 2020) and the Large Interferometer For Exoplanets (LIFE, Quanz et al., 2022). Both aim at resolving terrestrial planets in the habitable zone of their star, and detecting biosignatures on their surface. The challenge is huge, and many technological hurdles need to be overcome before these very large space telescopes see their first light.

However, technical difficulties are not the only challenge on the way for future giant telescopes on the ground or in space. Surely, all these fascinating instrumental projects are the manifestation of the curiosity of human-kind, our enthusiasm to push barriers and discover more about the nature we are part of. But, at the same time, we must acknowledge that our world has finite resources, be it material resource, energy, or funding. Knödlseder (2023) shows that the operation of current facilities and the building of new telescopes is responsible for 36.6 ± 14.0 tCO2e emission per year per astronomer; Stevens et al. (2020) find emissions of about 37 tCO2e per year per astronomer for the Australian community, including flights but not the construction of telescopes. For reference, the average French citizen emits 9 tCO2e per year and this number must be reduced to 2 tCO2e to respect the Paris Agreement and limit the global warming to $+1.5°$C. In this context, it will be more and more difficult to reconcile the environmental impact of astronomy with the imperative global reduction of the carbon footprint of human activities and the necessity for researchers to lead by example regarding efforts to limit climate change (Comité Ethique CNRS et al., 2022).

Public research has a role in our societies, in the broad sense, it is to improve the lives of people through technological, medical and social progress, by answering questions to help understand the world we live in, by giving people the opportunity to dream, and consider the breathtaking richness of our universe. The resources allocated to fundamental research like astronomy have always been balanced with the other needs of society, but we are now facing an environmental crisis. In years to come, more than ever, our societies will have to balance the efforts put in discovering life on other planets with the effort for taking care of every life form on Earth.

Bibliography

Abuter, R., Allouche, F., Amorim, A., et al. (2024a). A dynamical measure of the black hole mass in a quasar 11 billion years ago. *Nature*, 627(8003):281–285. https://www.doi.org/10.1038/s41586-024-07053-4.

Abuter, R., Allouche, F., Amorim, A., et al. (2024b). A dynamical measure of the black hole mass in a quasar 11 billion years ago. *Nature*, 627(8003):281–285. https://www.doi.org/10.1038/s41586-024-07053-4.

Ahn, K., Guyon, O., Lozi, J., et al. (2023). Combining EFC with spatial LDFC for high-contrast imaging on Subaru/SCExAO. *A&A*, 673:A29. https://www.doi.org/10.1051/0004-6361/202244961.

Allard, F., Homeier, D., & Freytag, B. (2012). Models of very-low-mass stars, brown dwarfs and exoplanets. *Philosophical Transactions of the Royal Society of London Series A*, 370(1968):2765–2777. https://www.doi.org/10.1098/rsta.2011.0269.

Anugu, N. (2016). GRAVITY acquisition camera. In *CHARA 2016: Adaptive Optics and Perspectives on Visible Interferometry*.

Anugu, N., Amorim, A., Gordo, P., et al. (2018). Methods for multiple-telescope beam imaging and guiding in the near-infrared. *MNRAS*, 476(1):459–469. https://www.doi.org/10.1093/mnras/sty223.

Argyriou, I., Wells, M., Glasse, A., et al. (2020). The nature of point source fringes in mid-infrared spectra acquired with the James Webb Space Telescope. *A&A*, 641:A150. https://www.doi.org/10.1051/0004-6361/202037535.

Arsenault, R., Alonso, J., Bonnet, H., et al. (2003). MACAO-VLTI: An Adaptive Optics system for the ESO VLT interferometer. In Wizinowich, P. L. & Bonaccini, D., editors, *Adaptive Optical System Technologies II*, volume 4839 of *Society of Photo-Optical Instrumentation Engineers (SPIE) Conference Series*, pages 174–185. https://www.doi.org/10.1117/12.458836.

Ayliffe, B. A. & Bate, M. R. (2009). Circumplanetary disc properties obtained from radiation hydrodynamical simulations of gas accretion by protoplanets. *MNRAS*, 397(2):657–665. https://www.doi.org/10.1111/j.1365-2966.2009.15002.x.

Bailey, V. P., Bendek, E., Monacelli, B., et al. (2023). Nancy Grace Roman Space Telescope coronagraph instrument overview and status. In *Society of Photo-Optical Instrumentation Engineers (SPIE) Conference Series*, volume 12680 of *Society of Photo-Optical Instrumentation Engineers (SPIE) Conference Series*, page 126800T. https://www.doi.org/10.1117/12.2679036.

Balmer, W. O., Pueyo, L., Lacour, S., et al. (2024). VLTI/GRAVITY Provides Evidence the Young, Substellar Companion HD 136164 Ab Formed Like a "Failed Star". *AJ*, 167(2):64. https://www.doi.org/10.3847/1538-3881/ad1689.

Balmer, W. O., Pueyo, L., Stolker, T., et al. (2023). VLTI/GRAVITY Observations and Characterization of the Brown Dwarf Companion HD 72946 B. *ApJ*, 956(2):99. https://www.doi.org/10.3847/1538-4357/acf761.

Barjot, K. (2023). Caractérisation et intégration de composants d'optique intégrée sur l'interféromètre fibré FIRST au télescope Subaru pour l'étude des protoplanètes en accrétion. *arXiv e-prints*, page arXiv:2306.08989. https://www.doi.org/10.48550/arXiv.2306.08989.

Baruteau, C., Crida, A., Paardekooper, S. J., et al. (2014). Planet-Disk Interactions and Early Evolution of Planetary Systems. In Beuther, H., Klessen, R. S., Dullemond, C. P., & Henning, T., editors, *Protostars and Planets VI*, pages 667–689. https://www.doi.org/10.2458/azu_uapress_9780816531240-ch029.

Baudoz, P., Dorn, R. J., Lizon, J.-L., et al. (2010). The differential tip-tilt sensor of SPHERE. In McLean, I. S., Ramsay, S. K., & Takami, H., editors, *Ground-based and Airborne Instrumentation for Astronomy III*, volume 7735 of *Society of Photo-Optical Instrumentation Engineers (SPIE) Conference Series*, page 77355B. https://www.doi.org/10.1117/12.858274.

Benisty, M., Bae, J., Facchini, S., et al. (2021). A Circumplanetary Disk around PDS70c. *ApJ*, 916(1):L2. https://www.doi.org/10.3847/2041-8213/ac0f83.

Benisty, M., Berger, J. P., Jocou, L., et al. (2009). An integrated optics beam combiner for the second generation VLTI instruments. *A&A*, 498(2):601–613. https://www.doi.org/10.1051/0004-6361/200811083.

Bertrou-Cantou, A., Gendron, E., Rousset, G., et al. (2022). Confusion in differential piston measurement with the pyramid wavefront sensor. *A&A*, 658:A49. https://www.doi.org/10.1051/0004-6361/202141632.

Beuzit, J. L., Vigan, A., Mouillet, D., et al. (2019). SPHERE: the exoplanet imager for the Very Large Telescope. *A&A*, 631:A155. https://www.doi.org/10.1051/0004-6361/201935251.

Bidot, A., Mouillet, D., & Carlotti, A. (2024). Exoplanet detection limits using spectral cross-correlation with

spectro-imaging. Analytical model applied to the case of ELT/HARMONI. *A&A*, 682:A10. https://www.doi.org/10.1051/0004-6361/202346185.

Bigioli, A., Courtney-Barrer, B., Abuter, R., et al. (2022). Measuring and compensating vibrations at the VLTI: MANHATTAN-II self-intrinsic noise and hardware extension. In Mérand, A., Sallum, S., & Sanchez-Bermudez, J., editors, *Optical and Infrared Interferometry and Imaging VIII*, volume 12183 of *Society of Photo-Optical Instrumentation Engineers (SPIE) Conference Series*, page 121831Z. https://www.doi.org/10.1117/12.2629168.

Blandford, R. D. & Payne, D. G. (1982). Hydromagnetic flows from accretion disks and the production of radio jets. *MNRAS*, 199:883–903. https://www.doi.org/10.1093/mnras/199.4.883.

Blind, N., Eisenhauer, F., Haug, M., et al. (2014). GRAVITY: the calibration unit. In Rajagopal, J. K., Creech-Eakman, M. J., & Malbet, F., editors, *Optical and Infrared Interferometry IV*, volume 9146 of *Society of Photo-Optical Instrumentation Engineers (SPIE) Conference Series*, page 91461U. https://www.doi.org/10.1117/12.2055542.

Blunt, S., Balmer, W. O., Wang, J. J., et al. (2023). First VLTI/GRAVITY Observations of HIP 65426 b: Evidence for a Low or Moderate Orbital Eccentricity. *AJ*, 166(6):257. https://www.doi.org/10.3847/1538-3881/ad06b7.

Blunt, S., Wang, J. J., Angelo, I., et al. (2020). orbitize!: A Comprehensive Orbit-fitting Software Package for the High-contrast Imaging Community. *AJ*, 159(3):89. https://www.doi.org/10.3847/1538-3881/ab6663.

Boccaletti, A., Chauvin, G., Mouillet, D., et al. (2020a). SPHERE+: Imaging young Jupiters down to the snowline. *arXiv e-prints*, page arXiv:2003.05714. https://www.doi.org/10.48550/arXiv.2003.05714.

Boccaletti, A., Chauvin, G., Mouillet, D., et al. (2020b). SPHERE+: Imaging young Jupiters down to the snowline. *arXiv e-prints*, page arXiv:2003.05714. https://www.doi.org/10.48550/arXiv.2003.05714.

Bopp, J., Felsner, L., Hu, S., Kaeppler, S., & Riess, C. (2018). X-ray phase contrast: Research on a future imaging modality. *Medical Imaging Systems: An Introductory Guide*, pages 191–205.

Borucki, W. J., Koch, D., Basri, G., et al. (2010). Kepler Planet-Detection Mission: Introduction and First Results. *Science*, 327(5968):977. https://www.doi.org/10.1126/science.1185402.

Borucki, W. J. & Summers, A. L. (1984). The photometric method of detecting other planetary systems. *Icarus*, 58(1):121–134. https://www.doi.org/10.1016/0019-1035(84)90102-7.

Bos, S. P., Vievard, S., Wilby, M. J., et al. (2020). On-sky verification of Fast and Furious focal-plane wavefront sensing: Moving forward toward controlling the island effect at Subaru/SCExAO. *A&A*, 639:A52. https://www.doi.org/10.1051/0004-6361/202037910.

Boss, A. P. (1997). Giant planet formation by gravitational instability. *Science*, 276:1836–1839. https://www.doi.org/10.1126/science.276.5320.1836.

Bouchy, F., Ségransan, D., Díaz, R. F., et al. (2016). The SOPHIE search for northern extrasolar planets. VIII. Follow-up of ELODIE candidates: long-period brown-dwarf companions. *A&A*, 585:A46. https://www.doi.org/10.1051/0004-6361/201526347.

Bouvier, J., Perraut, K., Le Bouquin, J. B., et al. (2020). Probing the magnetospheric accretion region of the young pre-transitional disk system DoAr 44 using VLTI/GRAVITY. *A&A*, 636:A108. https://www.doi.org/10.1051/0004-6361/202037611.

Bowler, B. P., Blunt, S. C., & Nielsen, E. L. (2020). Population-level Eccentricity Distributions of Imaged Exoplanets and Brown Dwarf Companions: Dynamical Evidence for Distinct Formation Channels. *AJ*, 159(2):63. https://www.doi.org/10.3847/1538-3881/ab5b11.

Bowler, B. P., Liu, M. C., Kraus, A. L., Mann, A. W., & Ireland, M. J. (2011). A Disk around the Planetary-mass Companion GSC 06214-00210 b: Clues about the Formation of Gas Giants on Wide Orbits. *ApJ*, 743(2):148. https://www.doi.org/10.1088/0004-637X/743/2/148.

Bracewell, R. N. & MacPhie, R. H. (1979). Searching for non-solar planets. *Icarus*, 38(1):136–147. https://www.doi.org/10.1016/0019-1035(79)90093-9.

Cantalloube, F., Farley, O. J. D., Milli, J., et al. (2020). Wind-driven halo in high-contrast images. I. Analysis of the focal-plane images of SPHERE. *A&A*, 638:A98. https://www.doi.org/10.1051/0004-6361/201937397.

Canup, R. M. & Ward, W. R. (2002). Formation of the Galilean Satellites: Conditions of Accretion. *AJ*, 124(6):3404–3423. https://www.doi.org/10.1086/344684.

Carlotti, A., Kasdin, N. J., Vanderbei, R. J., & Riggs, A. J. E. (2013). Hybrid coronagraphic design: optimization of complex apodizers. In Shaklan, S., editor, *Techniques and Instrumentation for Detection of Exoplanets VI*, volume 8864 of *Society of Photo-Optical Instrumentation Engineers (SPIE) Conference Series*, page 88641Q. https://www.doi.org/10.1117/12.2024523.

Carter, A. L., Hinkley, S., Kammerer, J., et al. (2023). The JWST Early Release Science Program for Direct Observations of Exoplanetary Systems I: High-contrast Imaging of the Exoplanet HIP 65426 b from 2 to 16 μm. *ApJ*, 951(1):L20. https://www.doi.org/10.3847/2041-8213/acd93e.

Charnay, B., Bézard, B., Baudino, J. L., et al. (2018). A Self-consistent Cloud Model for Brown Dwarfs and Young Giant Exoplanets: Comparison with Photometric and Spectroscopic Observations. *ApJ*, 854(2):172. https://www.doi.org/10.3847/1538-4357/aaac7d.

Chauvin, G., Lagrange, A. M., Dumas, C., et al. (2004). A giant planet candidate near a young brown dwarf. Direct VLT/NACO observations using IR wavefront sensing. *A&A*, 425:L29–L32. https://www.doi.org/10.1051/0004-6361:200400056.

Chilcote, J., Konopacky, Q., De Rosa, R. J., et al. (2020). GPI 2.0: upgrading the Gemini Planet Imager. In Evans, C. J., Bryant, J. J., & Motohara, K., editors, *Ground-based and Airborne Instrumentation for Astronomy VIII*, volume 11447 of *Society of Photo-Optical Instrumentation Engineers (SPIE) Conference Series*, page 114471S. https://www.doi.org/10.1117/12.2562578.

Chomez, A., Lagrange, A. M., Delorme, P., et al. (2023a). Preparation for an unsupervised massive analysis of SPHERE high-contrast data with PACO. Optimization and benchmarking on 24 solar-type stars. *A&A*, 675:A205. https://www.doi.org/10.1051/0004-6361/202245723.

Chomez, A., Squicciarini, V., Lagrange, A. M., et al. (2023b). An imaged 15 M_{Jup} companion within a hierarchical quadruple system. *A&A*, 676:L10. https://www.doi.org/10.1051/0004-6361/202347044.

Comité Ethique CNRS, ., Askenazy, P., Bustarret, E., et al. (2022). OPINION 2022-43 "Integrating environmental issues into the conduct of research - An ethical responsibility. Technical report, CNRS COMETS.

Couder, A. (1949). Sur un Effet Thermique: Observé dans les Télescopes a Réflexion. *L'Astronomie*, 63:253–258.

Cugno, G., Patapis, P., Banzatti, A., et al. (2024). Mid-Infrared Spectrum of the Disk around the Forming Companion GQ Lup B Revealed by JWST/MIRI. *arXiv e-prints*, page arXiv:2404.07086. https://www.doi.org/10.48550/arXiv.2404.07086.

Cumming, A., Marcy, G. W., & Butler, R. P. (1999). The Lick Planet Search: Detectability and Mass Thresholds. *ApJ*, 526(2):890–915. https://www.doi.org/10.1086/308020.

Davies, R., Absil, O., Agapito, G., et al. (2023). The Enhanced Resolution Imager and Spectrograph for the VLT. *A&A*, 674:A207. https://www.doi.org/10.1051/0004-6361/202346559.

Delorme, J.-R., Jovanovic, N., Echeverri, D., et al. (2021a). Keck Planet Imager and Characterizer: a dedicated single-mode fiber injection unit for high-resolution exoplanet spectroscopy. *Journal of Astronomical Telescopes, Instruments, and Systems*, 7:035006. https://www.doi.org/10.1117/1.JATIS.7.3.035006.

Delorme, J.-R., Jovanovic, N., Echeverri, D., et al. (2021b). Keck Planet Imager and Characterizer: a dedicated single-mode fiber injection unit for high-resolution exoplanet spectroscopy. *Journal of Astronomical Telescopes, Instruments, and Systems*, 7:035006. https://www.doi.org/10.1117/1.JATIS.7.3.035006.

Delplancke, F., Nijenhuis, J., de Man, H., et al. (2004). Star separator system for the dual-field capability (PRIMA) of the VLTI. In Traub, W. A., editor, *New Frontiers in Stellar Interferometry*, volume 5491 of *Society of Photo-Optical Instrumentation Engineers (SPIE) Conference Series*, page 1528. https://www.doi.org/10.1117/12.551873.

Demars, D., Bonnefoy, M., Dougados, C., et al. (2023). Emission line variability of young 10-30 M_{Jup} companions. I. The case of GQ Lup b and GSC 06214-00210 b. *A&A*, 676:A123. https://www.doi.org/10.1051/0004-6361/202346221.

Desidera, S., Chauvin, G., Bonavita, M., et al. (2021). The SPHERE infrared survey for exoplanets (SHINE). I. Sample definition and target characterization. *A&A*, 651:A70. https://www.doi.org/10.1051/0004-6361/202038806.

Duchêne, G. & Kraus, A. (2013). Stellar Multiplicity. *ARA&A*, 51(1):269–310. https://www.doi.org/10.1146/annurev-astro-081710-102602.

Ehrenreich, D., Lovis, C., Allart, R., et al. (2020). Nightside condensation of iron in an ultrahot giant exoplanet. *Nature*, 580(7805):597–601. https://www.doi.org/10.1038/s41586-020-2107-1.

Eisenhauer, F. (2019). GRAVITY+: Towards faint science. In *The Very Large Telescope in 2030*, page 30. https://www.doi.org/10.5281/zenodo.4697646.

Eisenhauer, F., Monnier, J. D., & Pfuhl, O. (2023). Advances in Optical/Infrared Interferometry. *ARA&A*, 61:237–285. https://www.doi.org/10.1146/annurev-astro-121622-045019.

Eisenhauer, F., Perrin, G., Rabien, S., et al. (2005). GRAVITY: The AO assisted, two object beam combiner instrument for the VLTI. *Astronomische Nachrichten*, 326:561–562. https://www.doi.org/10.48550/arXiv.astro-ph/0508607.

Engler, B., Le Louarn, M., Vérinaud, C., Weddell, S., & Clare, R. (2022). Flip-flop modulation method used with a pyramid wavefront sensor to correct piston segmentation on ELTs. *Journal of Astronomical Telescopes, Instruments, and Systems*, 8:021502. https://www.doi.org/10.1117/1.JATIS.8.2.021502.

Eriksson, S. C., Asensio Torres, R., Janson, M., et al. (2020). Strong Hα emission and signs of accretion in a circumbinary planetary mass companion from MUSE. *A&A*, 638:L6. https://www.doi.org/10.1051/0004-6361/202038131.

Esteves, L. J., de Mooij, E. J. W., Jayawardhana, R., Watson, C., & de Kok, R. (2017). A Search for Water in a Super-Earth Atmosphere: High-resolution Optical Spectroscopy of

55Cancri e. *AJ*, 153(6):268. https://www.doi.org/10.3847/1538-3881/aa7133.

Fernandes, R. B., Mulders, G. D., Pascucci, I., Mordasini, C., & Emsenhuber, A. (2019). Hints for a Turnover at the Snow Line in the Giant Planet Occurrence Rate. *ApJ*, 874(1):81. https://www.doi.org/10.3847/1538-4357/ab0300.

Finger, G., Baker, I., Alvarez, D., et al. (2016a). Sub-electron read noise and millisecond full-frame readout with the near infrared eAPD array SAPHIRA. In Marchetti, E., Close, L. M., & Véran, J.-P., editors, *Adaptive Optics Systems V*, volume 9909 of *Society of Photo-Optical Instrumentation Engineers (SPIE) Conference Series*, page 990912. https://www.doi.org/10.1117/12.2233079.

Finger, G., Baker, I., Alvarez, D., et al. (2016b). Sub-electron read noise and millisecond full-frame readout with the near infrared eAPD array SAPHIRA. In Marchetti, E., Close, L. M., & Véran, J.-P., editors, *Adaptive Optics Systems V*, volume 9909 of *Society of Photo-Optical Instrumentation Engineers (SPIE) Conference Series*, page 990912. https://www.doi.org/10.1117/12.2233079.

Finnerty, L., Horstman, K., Ruffio, J.-B., et al. (2023). Characterization of hot Jupiter atmospheres with Keck/KPIC. In *Society of Photo-Optical Instrumentation Engineers (SPIE) Conference Series*, volume 12680 of *Society of Photo-Optical Instrumentation Engineers (SPIE) Conference Series*, page 1268006. https://www.doi.org/10.1117/12.2677777.

Flasseur, O., Denis, L., Thiébaut, É., & Langlois, M. (2020). PACO ASDI: an algorithm for exoplanet detection and characterization in direct imaging with integral field spectrographs. *A&A*, 637:A9. https://www.doi.org/10.1051/0004-6361/201937239.

Franson, K., Bowler, B. P., Brandt, T. D., et al. (2022). Dynamical Mass of the Young Substellar Companion HD 984 B. *AJ*, 163(2):50. https://www.doi.org/10.3847/1538-3881/ac35e8.

Fried, D. L. (1965). Statistics of a Geometric Representation of Wavefront Distortion. *Journal of the Optical Society of America (1917-1983)*, 55(11):1427–1431.

Fusco, T., Sauvage, J. F., Petit, C., et al. (2014). Final performance and lesson-learned of SAXO, the VLT-SPHERE extreme AO: from early design to on-sky results. In Marchetti, E., Close, L. M., & Vran, J.-P., editors, *Adaptive Optics Systems IV*, volume 9148 of *Society of Photo-Optical Instrumentation Engineers (SPIE) Conference Series*, page 91481U. https://www.doi.org/10.1117/12.2055423.

Gaia Collaboration, Prusti, T., de Bruijne, J. H. J., et al. (2016). The Gaia mission. *A&A*, 595:A1. https://www.doi.org/10.1051/0004-6361/201629272.

Gardner, T., Monnier, J. D., Fekel, F. C., et al. (2022). ARMADA. II. Further Detections of Inner Companions to Intermediate-mass Binaries with Microarcsecond Astrometry at CHARA and VLTI. *AJ*, 164(5):184. https://www.doi.org/10.3847/1538-3881/ac8eae.

Gardner, T., Monnier, J. D., Fekel, F. C., et al. (2021). ARMADA. I. Triple Companions Detected in B-type Binaries α Del and ν Gem. *AJ*, 161(1):40. https://www.doi.org/10.3847/1538-3881/abcf4e.

Gaudi, B. S., Seager, S., Mennesson, B., et al. (2020). The Habitable Exoplanet Observatory (HabEx) Mission Concept Study Final Report. *arXiv e-prints*, page arXiv:2001.06683. https://www.doi.org/10.48550/arXiv.2001.06683.

Gillessen, S., Eisenhauer, F., Perrin, G., et al. (2010). GRAVITY: a four-telescope beam combiner instrument for the VLTI. In Danchi, W. C., Delplancke, F., & Rajagopal, J. K., editors, *Optical and Infrared Interferometry II*, volume 7734 of *Society of Photo-Optical Instrumentation Engineers (SPIE) Conference Series*, page 77340Y. https://www.doi.org/10.1117/12.856689.

Gillessen, S., Lippa, M., Eisenhauer, F., et al. (2012). GRAVITY: metrology. In Delplancke, F., Rajagopal, J. K., & Malbet, F., editors, *Optical and Infrared Interferometry III*, volume 8445 of *Society of Photo-Optical Instrumentation Engineers (SPIE) Conference Series*, page 84451O. https://www.doi.org/10.1117/12.926813.

Gilmozzi, R. & Spyromilio, J. (2007). The European Extremely Large Telescope (E-ELT). *The Messenger*, 127:11.

Gitton, P. B., Leveque, S. A., Avila, G., & Phan Duc, T. (2004). IRIS: an infrared tilt sensor for the VLTI. In Traub, W. A., editor, *New Frontiers in Stellar Interferometry*, volume 5491 of *Society of Photo-Optical Instrumentation Engineers (SPIE) Conference Series*, page 944. https://www.doi.org/10.1117/12.551377.

Give'on, A., Kern, B., Shaklan, S., Moody, D. C., & Pueyo, L. (2007). Broadband wavefront correction algorithm for high-contrast imaging systems. In Tyson, R. K. & Lloyd-Hart, M., editors, *Astronomical Adaptive Optics Systems and Applications III*, volume 6691 of *Society of Photo-Optical Instrumentation Engineers (SPIE) Conference Series*, page 66910A. https://www.doi.org/10.1117/12.733122.

Glindemann, A., Algomedo, J., Amestica, R., et al. (2003). The VLTI – A Status Report. In Traub, W. A., editor, *Interferometry for Optical Astronomy II*, volume 4838 of *Society of Photo-Optical Instrumentation Engineers (SPIE) Conference Series*, pages 89–100. https://www.doi.org/10.1117/12.458117.

Gomes, R., Levison, H. F., Tsiganis, K., & Morbidelli, A. (2005). Origin of the cataclysmic Late Heavy Bombardment period of the terrestrial planets. *Nature*, 435(7041):466–469. https://www.doi.org/10.1038/nature03676.

Gonzalez, J. F., Laibe, G., & Maddison, S. T. (2017). Self-induced dust traps: overcoming planet formation barriers. *MNRAS*, 467(2):1984–1996. https://www.doi.org/10.1093/mnras/stx016.

Gould, A., Udalski, A., Shin, I. G., et al. (2014). A terrestrial planet in a ~1-AU orbit around one member of a ∼15-AU binary. *Science*, 345(6192):46–49. https://www.doi.org/10.1126/science.1251527.

Gravity+ Collaboration, Abuter, R., Alarcon, P., et al. (2022). The GRAVITY+ Project: Towards All-sky, Faint-Science, High-Contrast Near-Infrared Interferometry at the VLTI. *The Messenger*, 189:17–22. https://www.doi.org/10.18727/0722-6691/5285.

GRAVITY+ Collaboration, Abuter, R., Allouche, F., et al. (2022). First light for GRAVITY Wide. Large separation fringe tracking for the Very Large Telescope Interferometer. *A&A*, 665:A75. https://www.doi.org/10.1051/0004-6361/202243941.

GRAVITY Collaboration, Abuter, R., Amorim, A., et al. (2018a). Detection of the gravitational redshift in the orbit of the star S2 near the Galactic centre massive black hole. *A&A*, 615:L15. https://www.doi.org/10.1051/0004-6361/201833718.

GRAVITY Collaboration, Abuter, R., Amorim, A., et al. (2020a). Detection of the Schwarzschild precession in the orbit of the star S2 near the Galactic centre massive black hole. *A&A*, 636:L5. https://www.doi.org/10.1051/0004-6361/202037813.

GRAVITY Collaboration, Abuter, R., Amorim, A., et al. (2018b). Detection of orbital motions near the last stable circular orbit of the massive black hole SgrA*. *A&A*, 618:L10. https://www.doi.org/10.1051/0004-6361/201834294.

GRAVITY Collaboration, Abuter, R., Amorim, A., et al. (2021a). Improved GRAVITY astrometric accuracy from modeling optical aberrations. *A&A*, 647:A59. https://www.doi.org/10.1051/0004-6361/202040208.

GRAVITY Collaboration, Abuter, R., Amorim, A., et al. (2024a). Astrometric detection of a Neptune-mass candidate planet in the nearest M-dwarf binary system GJ65 with VLTI/GRAVITY. *arXiv e-prints*, page arXiv:2404.08746. https://www.doi.org/10.48550/arXiv.2404.08746.

GRAVITY Collaboration, Bouarour, Y. I., Garcia Lopez, R., et al. (2024b). The GRAVITY young stellar object survey. XI. Imaging the hot gas emission around the Herbig Ae star HD58647. *A&A*, 682:A165. https://www.doi.org/10.1051/0004-6361/202348059.

Gravity Collaboration, Ganci, V., Labadie, L., et al. (2024). The GRAVITY young stellar object survey. XIII. Tracing the time-variable asymmetric disk structure in the inner AU of the Herbig star HD 98922. *A&A*, 684:A200. https://www.doi.org/10.1051/0004-6361/202346926.

GRAVITY Collaboration, Lacour, S., Nowak, M., et al. (2019). First direct detection of an exoplanet by optical interferometry. Astrometry and K-band spectroscopy of HR 8799 e. *A&A*, 623:L11. https://www.doi.org/10.1051/0004-6361/201935253.

GRAVITY Collaboration, Nowak, M., Lacour, S., et al. (2020b). Peering into the formation history of β Pictoris b with VLTI/GRAVITY long-baseline interferometry. *A&A*, 633:A110. https://www.doi.org/10.1051/0004-6361/201936898.

GRAVITY Collaboration, Perraut, K., Labadie, L., et al. (2021b). The GRAVITY young stellar object survey. VII. The inner dusty disks of T Tauri stars. *A&A*, 655:A73. https://www.doi.org/10.1051/0004-6361/202141624.

GRAVITY Collaboration, Widmann, F., Haubois, X., et al. (2024). Polarization analysis of the VLTI and GRAVITY. *A&A*, 681:A115. https://www.doi.org/10.1051/0004-6361/202347238.

Gravity Collaboration, Wojtczak, J. A., Labadie, L., et al. (2023). The GRAVITY young stellar object survey. IX. Spatially resolved kinematics of hot hydrogen gas in the star-disk interaction region of T Tauri stars. *A&A*, 669:A59. https://www.doi.org/10.1051/0004-6361/202244675.

Greene, T. (2001). Protostars. *American Scientist*, 89(4):316. https://www.doi.org/10.1511/2001.4.316.

Guyon, O. (2003). Phase-induced amplitude apodization of telescope pupils for extrasolar terrestrial planet imaging. *A&A*, 404:379–387. https://www.doi.org/10.1051/0004-6361:20030457.

Haffert, S. Y., Males, J. R., Ahn, K., et al. (2023). Implicit electric field conjugation: Data-driven focal plane control. *A&A*, 673:A28. https://www.doi.org/10.1051/0004-6361/202244960.

Haffert, S. Y., Por, E. H., Keller, C. U., et al. (2020). The Single-mode Complex Amplitude Refinement (SCAR) coronagraph. II. Lab verification, and toward the characterization of Proxima b. *A&A*, 635:A56. https://www.doi.org/10.1051/0004-6361/201731615.

Halbwachs, J.-L., Pourbaix, D., Arenou, F., et al. (2023). Gaia Data Release 3. Astrometric binary star processing. *A&A*, 674:A9. https://www.doi.org/10.1051/0004-6361/202243969.

Hauschildt, P. H., Allard, F., & Baron, E. (1999). The NextGen Model Atmosphere Grid for 3000¡=T_{eff}¡=10,000 K. *ApJ*, 512(1):377–385. https://www.doi.org/10.1086/306745.

Hinkley, S., Lacour, S., Marleau, G. D., et al. (2023). Direct discovery of the inner exoplanet in the HD 206893 system. Evidence for deuterium burning in a planetary-mass companion. *A&A*, 671:L5. https://www.doi.org/10.1051/0004-6361/202244727.

Houllé, M., Vigan, A., Carlotti, A., et al. (2021). Direct imaging and spectroscopy of exoplanets with the ELT/HARMONI high-contrast module. *A&A*, 652:A67. https://www.doi.org/10.1051/0004-6361/202140479.

Johansen, A., Henning, T., & Klahr, H. (2006). Dust Sedimentation and Self-sustained Kelvin-Helmholtz Turbulence in Protoplanetary Disk Midplanes. *ApJ*, 643(2):1219–1232. https://www.doi.org/10.1086/502968.

Jovanovic, N., Martinache, F., Guyon, O., et al. (2015). The Subaru Coronagraphic Extreme Adaptive Optics System: Enabling High-Contrast Imaging on Solar-System Scales. *PASP*, 127(955):890. https://www.doi.org/10.1086/682989.

JWST Transiting Exoplanet Community Early Release Science Team, Ahrer, E.-M., Alderson, L., et al. (2023). Identification of carbon dioxide in an exoplanet atmosphere. *Nature*, 614(7949):649–652. https://www.doi.org/10.1038/s41586-022-05269-w.

Kammerer, J., Lacour, S., Stolker, T., et al. (2021). GRAVITY K-band spectroscopy of HD 206893 B. Brown dwarf or exoplanet. *A&A*, 652:A57. https://www.doi.org/10.1051/0004-6361/202140749.

Kasper, M., Cerpa Urra, N., Pathak, P., et al. (2021). PCS — A Roadmap for Exoearth Imaging with the ELT. *The Messenger*, 182:38–43. https://www.doi.org/10.18727/0722-6691/5221.

Kendrew, S., Hippler, S., Brandner, W., et al. (2012). GRAVITY Coudé Infrared Adaptive Optics (CIAO) system for the VLT Interferometer. In McLean, I. S., Ramsay, S. K., & Takami, H., editors, *Ground-based and Airborne Instrumentation for Astronomy IV*, volume 8446 of *Society of Photo-Optical Instrumentation Engineers (SPIE) Conference Series*, page 84467W. https://www.doi.org/10.1117/12.926558.

Kervella, P., Gitton, P. B., Segransan, D., et al. (2003). VINCI, the VLTI commissioning instrument: status after one year of operations at Paranal. In Traub, W. A., editor, *Interferometry for Optical Astronomy II*, volume 4838 of *Society of Photo-Optical Instrumentation Engineers (SPIE) Conference Series*, pages 858–869. https://www.doi.org/10.1117/12.459345.

Kim, S.-L., Lee, C.-U., Park, B.-G., et al. (2016). KMTNET: A Network of 1.6 m Wide-Field Optical Telescopes Installed at Three Southern Observatories. *Journal of Korean Astronomical Society*, 49(1):37–44. https://www.doi.org/10.5303/JKAS.2016.49.1.37.

Knödlseder, J. (2023). The carbon footprint of astronomical research infrastructures. *arXiv e-prints*, page arXiv:2303.05424. https://www.doi.org/10.48550/arXiv.2303.05424.

Kokubo, E. & Ida, S. (2000). Formation of Protoplanets from Planetesimals in the Solar Nebula. *Icarus*, 143(1):15–27. https://www.doi.org/10.1006/icar.1999.6237.

Kunimoto, M. & Matthews, J. M. (2020). Searching the Entirety of Kepler Data. II. Occurrence Rate Estimates for FGK Stars. *AJ*, 159(6):248. https://www.doi.org/10.3847/1538-3881/ab88b0.

Lacour, S., Dembet, R., Abuter, R., et al. (2019). The GRAVITY fringe tracker. *A&A*, 624:A99. https://www.doi.org/10.1051/0004-6361/201834981.

Lacour, S., Eisenhauer, F., Gillessen, S., et al. (2014). Reaching micro-arcsecond astrometry with long baseline optical interferometry. Application to the GRAVITY instrument. *A&A*, 567:A75. https://www.doi.org/10.1051/0004-6361/201423940.

Lacour, S., Jocou, L., Moulin, T., et al. (2008). Characterization of integrated optics components for the second generation of VLTI instruments. In Schöller, M., Danchi, W. C., & Delplancke, F., editors, *Optical and Infrared Interferometry*, volume 7013 of *Society of Photo-Optical Instrumentation Engineers (SPIE) Conference Series*, page 701316. https://www.doi.org/10.1117/12.789795.

Lacour, S., Wang, J. J., Nowak, M., et al. (2020). The ExoGRAVITY project: using single mode interferometry to characterize exoplanets. In Tuthill, P. G., Mérand, A., & Sallum, S., editors, *Optical and Infrared Interferometry and Imaging VII*, volume 11446 of *Society of Photo-Optical Instrumentation Engineers (SPIE) Conference Series*, page 114460O. https://www.doi.org/10.1117/12.2561667.

Lacour, S., Wang, J. J., Rodet, L., et al. (2021). The mass of β Pictoris c from β Pictoris b orbital motion. *A&A*, 654:L2. https://www.doi.org/10.1051/0004-6361/202141889.

Lafrenière, D., Marois, C., Doyon, R., Nadeau, D., & Artigau, É. (2007). A New Algorithm for Point-Spread Function Subtraction in High-Contrast Imaging: A Demonstration with Angular Differential Imaging. *ApJ*, 660(1):770–780. https://www.doi.org/10.1086/513180.

Lagarde, S., Meilland, A., Lopez, B., et al. (2022). MATISSE, the VLTI mid-infrared imaging spectro-interferometer at the time of the first published astrophysical results. In Mérand, A., Sallum, S., & Sanchez-Bermudez, J., editors, *Optical and Infrared Interferometry and Imaging VIII*, volume 12183 of *Society of Photo-Optical Instrumentation Engineers (SPIE) Conference Series*, page 121830A. https://www.doi.org/10.1117/12.2630164.

Lagrange, A. M., Philipot, F., Rubini, P., et al. (2023). Radial distribution of giant exoplanets at Solar System scales. *A&A*, 677:A71. https://www.doi.org/10.1051/0004-6361/202346165.

Laibe, G., Gonzalez, J. F., & Maddison, S. T. (2012). Revisiting the "radial-drift barrier" of planet formation and its relevance in observed protoplanetary discs. *A&A*, 537:A61. https://www.doi.org/10.1051/0004-6361/201015349.

Langlois, M., Gratton, R., Lagrange, A. M., et al. (2021). The SPHERE infrared survey for exoplanets (SHINE). II. Observations, data reduction and analysis, detection performances, and initial results. *A&A*, 651:A71. https://www.doi.org/10.1051/0004-6361/202039753.

Lapeyrere, V., Kervella, P., Lacour, S., et al. (2014). GRAVITY data reduction software. In Rajagopal, J. K., Creech-Eakman, M. J., & Malbet, F., editors, *Optical and Infrared Interferometry IV*, volume 9146 of *Society of Photo-Optical Instrumentation Engineers (SPIE) Conference Series*, page 91462D. https://www.doi.org/10.1117/12.2056850.

Laugier, R., Defrère, D., Woillez, J., et al. (2023). Asgard/NOTT: L-band nulling interferometry at the VLTI. I. Simulating the expected high-contrast performance. *A&A*, 671:A110. https://www.doi.org/10.1051/0004-6361/202244351.

Le Bouquin, J. B. & Absil, O. (2012). On the sensitivity of closure phases to faint companions in optical long baseline interferometry. *A&A*, 541:A89. https://www.doi.org/10.1051/0004-6361/201117891.

Le Bouquin, J. B., Berger, J. P., Lazareff, B., et al. (2011). PIONIER: a 4-telescope visitor instrument at VLTI. *A&A*, 535:A67. https://www.doi.org/10.1051/0004-6361/201117586.

Leboulleux, L., Carlotti, A., N'Diaye, M., et al. (2022). Redundant apodization for direct imaging of exoplanets. II. Application to island effects. *A&A*, 666:A91. https://www.doi.org/10.1051/0004-6361/202243413.

Lecavelier des Etangs, A. & Lissauer, J. J. (2022). The IAU working definition of an exoplanet. *New A Rev.*, 94:101641. https://www.doi.org/10.1016/j.newar.2022.101641.

Leclerc, A., Babusiaux, C., Arenou, F., et al. (2023). Combining HIPPARCOS and Gaia data for the study of binaries: The BINARYS tool. *A&A*, 672:A82. https://www.doi.org/10.1051/0004-6361/202244144.

Leinert, C., Graser, U., Przygodda, F., et al. (2003). MIDI - the 10 µm instrument on the VLTI. *Ap&SS*, 286(1):73–83. https://www.doi.org/10.1023/A:1026158127732.

Lippa, M., Gillessen, S., Blind, N., et al. (2016). The metrology system of the VLTI instrument GRAVITY. In Malbet, F., Creech-Eakman, M. J., & Tuthill, P. G., editors, *Optical and Infrared Interferometry and Imaging V*, volume 9907 of *Society of Photo-Optical Instrumentation Engineers (SPIE) Conference Series*, page 990722. https://www.doi.org/10.1117/12.2232272.

Llop-Sayson, J., Coker, C. T., Jovanovic, N., et al. (2022). Laboratory demonstration of wavefront control through a single-mode fiber over a 20% bandwidth for the characterization of exoplanet atmospheres. *Journal of Astronomical Telescopes, Instruments, and Systems*, 8:029001. https://www.doi.org/10.1117/1.JATIS.8.2.029001.

Llop-Sayson, J., Ruane, G., Mawet, D., et al. (2019). Demonstration of an electric field conjugation algorithm for improved starlight rejection through a single mode optical fiber. *Journal of Astronomical Telescopes, Instruments, and Systems*, 5:019004. https://www.doi.org/10.1117/1.JATIS.5.1.019004.

Loose, M., Farris, M. C., Garnett, J. D., Hall, D. N. B., & Kozlowski, L. J. (2003). HAWAII-2RG: a 2k x 2k CMOS multiplexer for low and high background astronomy applications. In Mather, J. C., editor, *IR Space Telescopes and Instruments*, volume 4850 of *Society of Photo-Optical Instrumentation Engineers (SPIE) Conference Series*, pages 867–879. https://www.doi.org/10.1117/12.461796.

Lovis, C., Blind, N., Chazelas, B., et al. (2022). RISTRETTO: high-resolution spectroscopy at the diffraction limit of the VLT. In Evans, C. J., Bryant, J. J., & Motohara, K., editors, *Ground-based and Airborne Instrumentation for Astronomy IX*, volume 12184 of *Society of Photo-Optical Instrumentation Engineers (SPIE) Conference Series*, page 121841Q. https://www.doi.org/10.1117/12.2627923.

MacGregor, M. A., Wilner, D. J., Czekala, I., et al. (2017). ALMA Measurements of Circumstellar Material in the GQ Lup System. *ApJ*, 835(1):17. https://www.doi.org/10.3847/1538-4357/835/1/17.

Malbet, F., Duvert, G., Chelli, A., & Kern, P. (2008). AMBER Task Force February 2008 run report. *arXiv e-prints*, page arXiv:0808.1315. https://www.doi.org/10.48550/arXiv.0808.1315.

Malbet, F., Yu, J. W., & Shao, M. (1995). High-Dynamic-Range Imaging Using a Deformable Mirror for Space Coronography. *PASP*, 107:386. https://www.doi.org/10.1086/133563.

Mâlin, M., Boccaletti, A., Charnay, B., Kiefer, F., & Bézard, B. (2023). Simulated performance of the molecular mapping for young giant exoplanets with the Medium-Resolution Spectrometer of JWST/MIRI. *A&A*, 671:A109. https://www.doi.org/10.1051/0004-6361/202245094.

Marion, L., Absil, O., Ertel, S., et al. (2014). Searching for faint companions with VLTI/PIONIER. II. 92 main sequence stars from the Exozodi survey. *A&A*, 570:A127. https://www.doi.org/10.1051/0004-6361/201424780.

Marley, M. S., Fortney, J. J., Hubickyj, O., Bodenheimer, P., & Lissauer, J. J. (2007). On the Luminosity of Young Jupiters. *ApJ*, 655(1):541–549. https://www.doi.org/10.1086/509759.

Marois, C., Lafrenière, D., Doyon, R., Macintosh, B., & Nadeau, D. (2006). Angular Differential Imaging: A Powerful High-Contrast Imaging Technique. *ApJ*, 641(1):556–564. https://www.doi.org/10.1086/500401.

Marois, C., Macintosh, B., & Barman, T. (2007). GQ Lup B Visible and Near-Infrared Photometric Analysis. *ApJ*, 654(2):L151–L154. https://www.doi.org/10.1086/511071.

Marzari, F. & Thebault, P. (2019). Planets in Binaries: Formation and Dynamical Evolution. *Galaxies*, 7(4):84. https://www.doi.org/10.3390/galaxies7040084.

Mayor, M., Marmier, M., Lovis, C., et al. (2011). The HARPS search for southern extra-solar planets XXXIV. Occurrence, mass distribution and orbital properties of super-Earths and Neptune-mass planets. *arXiv e-prints*, page arXiv:1109.2497. https://www.doi.org/10.48550/arXiv.1109.2497.

Mayor, M. & Queloz, D. (1995). A Jupiter-mass companion to a solar-type star. *Nature*, 378(6555):355–359. https://www.doi.org/10.1038/378355a0.

Meshkat, T., Bonnefoy, M., Mamajek, E. E., et al. (2015). Discovery of a low-mass companion to the F7V star HD 984. *MNRAS*, 453(3):2378–2386. https://www.doi.org/10.1093/mnras/stv1732.

Miles, B. E., Biller, B. A., Patapis, P., et al. (2023). The JWST Early-release Science Program for Direct Observations of Exoplanetary Systems II: A 1 to 20 μm Spectrum of the Planetary-mass Companion VHS 1256-1257 b. *ApJ*, 946(1):L6. https://www.doi.org/10.3847/2041-8213/acb04a.

Milli, J., Kasper, M., Bourget, P., et al. (2018). Low wind effect on VLT/SPHERE: impact, mitigation strategy, and results. In Close, L. M., Schreiber, L., & Schmidt, D., editors, *Adaptive Optics Systems VI*, volume 10703 of *Society of Photo-Optical Instrumentation Engineers (SPIE) Conference Series*, page 107032A. https://www.doi.org/10.1117/12.2311499.

Millour, F., Petrov, R. G., Vannier, M., & Kraus, S. (2008). AMBER closure and differential phases: accuracy and calibration with a beam commutation. In Schöller, M., Danchi, W. C., & Delplancke, F., editors, *Optical and Infrared Interferometry*, volume 7013 of *Society of Photo-Optical Instrumentation Engineers (SPIE) Conference Series*, page 70131G. https://www.doi.org/10.1117/12.788689.

Mizuno, H. (1980). Formation of the Giant Planets. *Progress of Theoretical Physics*, 64(2):544–557. https://www.doi.org/10.1143/PTP.64.544.

Monnier, J. D. (2003). Optical interferometry in astronomy. *Reports on Progress in Physics*, 66(5):789–857. https://www.doi.org/10.1088/0034-4885/66/5/203.

Morbidelli, A., Levison, H. F., Tsiganis, K., & Gomes, R. (2005). Chaotic capture of Jupiter's Trojan asteroids in the early Solar System. *Nature*, 435(7041):462–465. https://www.doi.org/10.1038/nature03540.

Muterspaugh, M. W., Lane, B. F., Kulkarni, S. R., et al. (2010). The Phases Differential Astrometry Data Archive. V. Candidate Substellar Companions to Binary Systems. *AJ*, 140(6):1657–1671. https://www.doi.org/10.1088/0004-6256/140/6/1657.

Nasedkin, E., Mollière, P., Lacour, S., et al. (2024). Four-of-a-kind? Comprehensive atmospheric characterisation of the HR 8799 planets with VLTI/GRAVITY. *arXiv e-prints*, page arXiv:2404.03776. https://www.doi.org/10.48550/arXiv.2404.03776.

N'Diaye, M., Dohlen, K., Fusco, T., & Paul, B. (2013a). Calibration of quasi-static aberrations in exoplanet direct-imaging instruments with a Zernike phase-mask sensor. *A&A*, 555:A94. https://www.doi.org/10.1051/0004-6361/201219797.

N'Diaye, M., Dohlen, K., Fusco, T., & Paul, B. (2013b). Calibration of quasi-static aberrations in exoplanet direct-imaging instruments with a Zernike phase-mask sensor. *A&A*, 555:A94. https://www.doi.org/10.1051/0004-6361/201219797.

N'Diaye, M., Vigan, A., Dohlen, K., et al. (2016). Calibration of quasi-static aberrations in exoplanet direct-imaging instruments with a Zernike phase-mask sensor. II. Concept validation with ZELDA on VLT/SPHERE. *A&A*, 592:A79. https://www.doi.org/10.1051/0004-6361/201628624.

Neuhäuser, R., Mugrauer, M., Seifahrt, A., Schmidt, T. O. B., & Vogt, N. (2008). Astrometric and photometric monitoring of GQ Lupi and its sub-stellar companion. *A&A*, 484(1):281–291. https://www.doi.org/10.1051/0004-6361:20078493.

Nielsen, E. L., De Rosa, R. J., Macintosh, B., et al. (2019). The Gemini Planet Imager Exoplanet Survey: Giant Planet and Brown Dwarf Demographics from 10 to 100 au. *AJ*, 158(1):13. https://www.doi.org/10.3847/1538-3881/ab16e9.

Nowak, M. (2019). *The 2017 conjunction of Beta Pictoris b : the life and death of Picsat, followed by a VLTI/GRAVITY observation of the re-emergence*. Theses, Université Paris sciences et lettres.

Nowak, M., Lacour, S., Abuter, R., et al. (2024a). A catalogue of dual-field interferometric binary calibrators. *arXiv e-prints*, page arXiv:2402.05019. https://www.doi.org/10.48550/arXiv.2402.05019.

Nowak, M., Lacour, S., Lagrange, A. M., et al. (2020). Direct confirmation of the radial-velocity planet β Pictoris c. *A&A*, 642:L2. https://www.doi.org/10.1051/0004-6361/202039039.

Nowak, M., Rowther, S., Lacour, S., et al. (2024b). The orbit of HD 142527 B is too compact to explain many of the disc features. *A&A*, 683:A6. https://www.doi.org/10.1051/0004-6361/202347748.

Öberg, K. I., Murray-Clay, R., & Bergin, E. A. (2011). The Effects of Snowlines on C/O in Planetary Atmospheres. *ApJ*, 743(1):L16. https://www.doi.org/10.1088/2041-8205/743/1/L16.

Parmentier, V., Showman, A. P., & Fortney, J. J. (2021). The cloudy shape of hot Jupiter thermal phase curves. *MNRAS*, 501(1):78–108. https://www.doi.org/10.1093/mnras/staa3418.

Pepe, F., Cristiani, S., Rebolo, R., et al. (2021). ESPRESSO at VLT. On-sky performance and first results. *A&A*, 645:A96. https://www.doi.org/10.1051/0004-6361/202038306.

Pepe, F., Mayor, M., Rupprecht, G., et al. (2002). HARPS: ESO's coming planet searcher. Chasing exoplanets with the La Silla 3.6-m telescope. *The Messenger*, 110:9–14.

Perraut, K., Jocou, L., Berger, J. P., et al. (2018). Single-mode waveguides for GRAVITY. I. The cryogenic 4-telescope integrated optics beam combiner. *A&A*, 614:A70. https://www.doi.org/10.1051/0004-6361/201732544.

Perryman, M. (2018). *The Exoplanet Handbook*.

Perryman, M., Hartman, J., Bakos, G. Á., & Lindegren, L. (2014). Astrometric Exoplanet Detection with Gaia. *ApJ*, 797(1):14. https://www.doi.org/10.1088/0004-637X/797/1/14.

Petrov, R. G., Malbet, F., Weigelt, G., et al. (2007). AMBER, the near-infrared spectro-interferometric three-telescope VLTI instrument. *A&A*, 464(1):1–12. https://www.doi.org/10.1051/0004-6361:20066496.

Petrus, S., Chauvin, G., Bonnefoy, M., et al. (2023). X-SHYNE: X-shooter spectra of young exoplanet analogs. I. A medium-resolution 0.65-2.5 μm one-shot spectrum of VHS 1256−1257 b. *A&A*, 670:L9. https://www.doi.org/10.1051/0004-6361/202244494.

Pfuhl, O., Haug, M., Eisenhauer, F., et al. (2014). The fiber coupler and beam stabilization system of the GRAVITY interferometer. In Rajagopal, J. K., Creech-Eakman, M. J., & Malbet, F., editors, *Optical and Infrared Interferometry IV*, volume 9146 of *Society of Photo-Optical Instrumentation Engineers (SPIE) Conference Series*, page 914623. https://www.doi.org/10.1117/12.2055080.

Pfuhl, O., Haug, M., Eisenhauer, F., et al. (2012). GRAVITY: beam stabilization and light injection subsystems. In Delplancke, F., Rajagopal, J. K., & Malbet, F., editors, *Optical and Infrared Interferometry III*, volume 8445 of *Society of Photo-Optical Instrumentation Engineers (SPIE) Conference Series*, page 84451U. https://www.doi.org/10.1117/12.925391.

Pollack, J. B., Hubickyj, O., Bodenheimer, P., et al. (1996). Formation of the Giant Planets by Concurrent Accretion of Solids and Gas. *Icarus*, 124(1):62–85. https://www.doi.org/10.1006/icar.1996.0190.

Por, E. H. & Haffert, S. Y. (2020). The Single-mode Complex Amplitude Refinement (SCAR) coronagraph. I. Concept, theory, and design. *A&A*, 635:A55. https://www.doi.org/10.1051/0004-6361/201731616.

Por, E. H., Haffert, S. Y., Radhakrishnan, V. M., et al. (2018). High Contrast Imaging for Python (HCIPy): an open-source adaptive optics and coronagraph simulator. In *Adaptive Optics Systems VI*, volume 10703 of *Proc. SPIE*. https://www.doi.org/10.1117/12.2314407.

Potier, A., Galicher, R., Baudoz, P., et al. (2020). Increasing the raw contrast of VLT/SPHERE with the dark hole technique. I. Simulations and validation on the internal source. *A&A*, 638:A117. https://www.doi.org/10.1051/0004-6361/202038010.

Potier, A., Mazoyer, J., Wahhaj, Z., et al. (2022). Increasing the raw contrast of VLT/SPHERE with the dark hole technique. II. On-sky wavefront correction and coherent differential imaging. *A&A*, 665:A136. https://www.doi.org/10.1051/0004-6361/202244185.

Pourré, N., Le Bouquin, J. B., Milli, J., et al. (2022a). Low-wind-effect impact on Shack-Hartmann-based adaptive optics. Partial control solution in the context of SPHERE and GRAVITY+. *A&A*, 665:A158. https://www.doi.org/10.1051/0004-6361/202243432.

Pourré, N., Le Bouquin, J. B., Milli, J., et al. (2022b). Understand and correct for the low wind effect on the SPHERE and GRAVITY+ adaptive optics. In Schreiber, L., Schmidt, D., & Vernet, E., editors, *Adaptive Optics Systems VIII*, volume 12185 of *Society of Photo-Optical Instrumentation Engineers (SPIE) Conference Series*, page 121855C. https://www.doi.org/10.1117/12.2629793.

Pourré, N., Le Bouquin, J.-B., Woillez, J., et al. (2022c). Digging a dark hole in GRAVITY: towards Jupiter-like observations at the astronomical unit scale. In Mérand, A., Sallum, S., & Sanchez-Bermudez, J., editors, *Optical and Infrared Interferometry and Imaging VIII*, volume 12183 of *Society of Photo-Optical Instrumentation Engineers (SPIE) Conference Series*, page 121830V. https://www.doi.org/10.1117/12.2629823.

Pourré, N., Palma-Bifani, P., Bonnefoy, M., et al. (in prep.). Constraints on the moon-forming disk around GQ Lup B with VLTI/GRAVITY. *A&A*.

Pourré, N., Winterhalder, T. O., Le Bouquin, J. B., et al. (2024). High contrast at short separation with VLTI/GRAVITY: Bringing Gaia companions to light. *A&A*, 686:A258. https://www.doi.org/10.1051/0004-6361/202449507.

Quanz, S. P., Ottiger, M., Fontanet, E., et al. (2022). Large Interferometer For Exoplanets (LIFE). I. Improved exoplanet detection yield estimates for a large mid-infrared space-interferometer mission. *A&A*, 664:A21. https://www.doi.org/10.1051/0004-6361/202140366.

Racine, R., Walker, G. A. H., Nadeau, D., Doyon, R., & Marois, C. (1999). Speckle Noise and the Detection of Faint Companions. *PASP*, 111(759):587–594. https://www.doi.org/10.1086/316367.

Ren, B., Pueyo, L., Perrin, M. D., Debes, J. H., & Choquet, É. (2017). Post-processing of the HST STIS coronagraphic observations. In Shaklan, S., editor, *Society of Photo-Optical Instrumentation Engineers (SPIE) Conference Series*, volume 10400 of *Society of Photo-Optical Instrumentation Engineers (SPIE) Conference Series*, page 1040021. https://www.doi.org/10.1117/12.2274163.

Ricker, G. R., Winn, J. N., Vanderspek, R., et al. (2015). Transiting Exoplanet Survey Satellite (TESS). *Journal of Astronomical Telescopes, Instruments, and Systems*, 1:014003. https://www.doi.org/10.1117/1.JATIS.1.1.014003.

Roddier, F. (1988). Curvature sensing and compensation: a new concept in adaptive optics. *Appl. Opt.*, 27(7):1223–1225. https://www.doi.org/10.1364/AO.27.001223.

Roddier, F., Northcott, M., & Graves, J. E. (1991). A Simple Low-Order Adaptive Optics System for Near-Infrared Applications. *PASP*, 103:131. https://www.doi.org/10.1086/132802.

Sauvage, J.-F., Fusco, T., Lamb, M., et al. (2016). Tackling down the low wind effect on SPHERE instrument. In Marchetti, E., Close, L. M., & Véran, J.-P., editors, *Adaptive Optics Systems V*, volume 9909 of *Society of Photo-Optical Instrumentation Engineers (SPIE) Conference Series*, page 990916. https://www.doi.org/10.1117/12.2232459.

Schwartz, N., Sauvage, J.-F., Correia, C., et al. (2018). Sensing and control of segmented mirrors with a pyramid wavefront sensor in the presence of spiders. *arXiv e-prints*, page arXiv:1809.08839. https://www.doi.org/10.48550/arXiv.1809.08839.

Seifahrt, A., Neuhäuser, R., & Hauschildt, P. H. (2007). Near-infrared integral-field spectroscopy of the companion to GQ Lupi. *A&A*, 463(1):309–313. https://www.doi.org/10.1051/0004-6361:20066463.

Skemer, A. J., Close, L. M., Szűcs, L., et al. (2011). Evidence Against an Edge-on Disk Around the Extrasolar Planet, 2MASS 1207 b and a New Thick-cloud Explanation for Its Underluminosity. *ApJ*, 732(2):107. https://www.doi.org/10.1088/0004-637X/732/2/107.

Snellen, I., de Kok, R., Birkby, J. L., et al. (2015). Combining high-dispersion spectroscopy with high contrast imaging: Probing rocky planets around our nearest neighbors. *A&A*, 576:A59. https://www.doi.org/10.1051/0004-6361/201425018.

Soummer, R., Perrin, M. D., Pueyo, L., et al. (2014). Five Debris Disks Newly Revealed in Scattered Light from the Hubble Space Telescope NICMOS Archive. *ApJ*, 786(2):L23. https://www.doi.org/10.1088/2041-8205/786/2/L23.

Sozzetti, A. (2010). Astrometry and Exoplanets: The Gaia Era and Beyond. In *EAS Publications Series*, volume 45 of *EAS Publications Series*, pages 273–278. https://www.doi.org/10.1051/eas/1045046.

Stevens, A. R. H., Bellstedt, S., Elahi, P. J., & Murphy, M. T. (2020). The imperative to reduce carbon emissions in astronomy. *Nature Astronomy*, 4:843–851. https://www.doi.org/10.1038/s41550-020-1169-1.

Stolker, T., Haffert, S. Y., Kesseli, A. Y., et al. (2021). Characterizing the Protolunar Disk of the Accreting Companion GQ Lupi B. *AJ*, 162(6):286. https://www.doi.org/10.3847/1538-3881/ac2c7f.

Stolker, T., Kammerer, J., Benisty, M., et al. (2024). Searching for low-mass companions at small separations in transition disks with aperture masking interferometry. *A&A*, 682:A101. https://www.doi.org/10.1051/0004-6361/202347291.

Stone, J. M., Skemer, A. J., Hinz, P. M., et al. (2018). The LEECH Exoplanet Imaging Survey: Limits on Planet Occurrence Rates under Conservative Assumptions. *AJ*, 156(6):286. https://www.doi.org/10.3847/1538-3881/aaec00.

Tallon, M. & Foy, R. (1990). Adaptive telescope with laser probe: isoplanatism and cone effect. *A&A*, 235:549–557.

Tan, X. & Komacek, T. D. (2019). The Atmospheric Circulation of Ultra-hot Jupiters. *ApJ*, 886(1):26. https://www.doi.org/10.3847/1538-4357/ab4a76.

Tatulli, E., Millour, F., Chelli, A., et al. (2007). Interferometric data reduction with AMBER/VLTI. Principle, estimators, and illustration. *A&A*, 464(1):29–42. https://www.doi.org/10.1051/0004-6361:20064799.

Teinturier, L., Charnay, B., Spiga, A., et al. (2024). The radiative and dynamical impact of clouds in the atmosphere of the hot Jupiter WASP-43 b. *A&A*, 683:A231. https://www.doi.org/10.1051/0004-6361/202347069.

Teyssandier, J., Libert, A. S., & Agol, E. (2022). TRAPPIST-1: Dynamical analysis of the transit-timing variations and origin of the resonant chain. *A&A*, 658:A170. https://www.doi.org/10.1051/0004-6361/202142377.

Thatte, N., Tecza, M., Schnetler, H., et al. (2021). HARMONI: the ELT's First-Light Near-infrared and Visible Integral Field Spectrograph. *The Messenger*, 182:7–12. https://www.doi.org/10.18727/0722-6691/5215.

Thompson, A. R., Moran, J. M., & Swenson, George W., J. (2017). *Interferometry and Synthesis in Radio Astronomy, 3rd Edition*.

Traub, W. A. & Oppenheimer, B. R. (2010). Direct Imaging of Exoplanets. In Seager, S., editor, *Exoplanets*, pages 111–156.

Tsiganis, K., Gomes, R., Morbidelli, A., & Levison, H. F. (2005). Origin of the orbital architecture of the giant planets of the Solar System. *Nature*, 435(7041):459–461. https://www.doi.org/10.1038/nature03539.

Udalski, A., Szymański, M. K., & Szymański, G. (2015). OGLE-IV: Fourth Phase of the Optical Gravitational Lensing Experiment. *Acta Astron.*, 65(1):1–38. https://www.doi.org/10.48550/arXiv.1504.05966.

Vievard, S., Huby, E., Lacour, S., et al. (2023). Single-aperture spectro-interferometry in the visible at the Subaru telescope with FIRST: First on-sky demonstration on Keho'oea (α Lyrae) and Hokulei (α Aurigae). *A&A*, 677:A84. https://www.doi.org/10.1051/0004-6361/202245115.

Vigan, A., Dohlen, K., N'Diaye, M., et al. (2022). Calibration of quasi-static aberrations in exoplanet direct-imaging instruments with a Zernike phase-mask sensor. IV. Temporal stability of non-common path aberrations in VLT/SPHERE. *A&A*, 660:A140. https://www.doi.org/10.1051/0004-6361/202142635.

Vigan, A., El Morsy, M., Lopez, M., et al. (2024). First light of VLT/HiRISE: High-resolution spectroscopy of young giant exoplanets. *A&A*, 682:A16. https://www.doi.org/10.1051/0004-6361/202348019.

Vigan, A., Fontanive, C., Meyer, M., et al. (2021). The SPHERE infrared survey for exoplanets (SHINE). III. The demographics of young giant exoplanets below 300 au with SPHERE. *A&A*, 651:A72. https://www.doi.org/10.1051/0004-6361/202038107.

Wang, J. J., Graham, J. R., Dawson, R., et al. (2018). Dynamical Constraints on the HR 8799 Planets with GPI. *AJ*, 156(5):192. https://www.doi.org/10.3847/1538-3881/aae150.

Wang, J. J., Kulikauskas, M., & Blunt, S. (2021a). whereistheplanet: Predicting positions of directly imaged companions. Astrophysics Source Code Library, record ascl:2101.003.

Wang, J. J., Vigan, A., Lacour, S., et al. (2021b). Constraining the Nature of the PDS 70 Protoplanets with VLTI/GRAVITY. *AJ*, 161(3):148. https://www.doi.org/10.3847/1538-3881/abdb2d.

Wardle, M. (2007). Magnetic fields in protoplanetary disks. *Ap&SS*, 311(1-3):35–45. https://www.doi.org/10.1007/s10509-007-9575-8.

Wei, J., Norris, B., Betters, C., & Leon-Saval, S. (2023). Demonstration of a photonic lantern focal-plane wavefront sensor: measurement of atmospheric wavefront error modes and low wind effect in the non-linear regime. *arXiv e-prints*, page arXiv:2311.01716. https://www.doi.org/10.48550/arXiv.2311.01716.

Weidenschilling, S. J. (1977). Aerodynamics of solid bodies in the solar nebula. *MNRAS*, 180:57–70. https://www.doi.org/10.1093/mnras/180.2.57.

Weidenschilling, S. J. (1980). Dust to planetesimals: Settling and coagulation in the solar nebula. *Icarus*, 44(1):172–189. https://www.doi.org/10.1016/0019-1035(80)90064-0.

Wilby, M. J., Keller, C. U., Sauvage, J. F., et al. (2018). Laboratory verification of Fast & Furious phase diversity: Towards controlling the low wind effect in the SPHERE instrument. *A&A*, 615:A34. https://www.doi.org/10.1051/0004-6361/201731958.

Winterhalder, T. O., Lacour, S., Mérand, A., et al. (2024). Combining Gaia and GRAVITY: Characterising Five New Directly Detected Substellar Companions. *arXiv e-prints*, page arXiv:2403.13055. https://www.doi.org/10.48550/arXiv.2403.13055.

Wittrock, J. M., Plavchan, P. P., Cale, B. L., et al. (2023). Validating AU Microscopii d with Transit Timing Variations. *AJ*, 166(6):232. https://www.doi.org/10.3847/1538-3881/acfda8.

Woillez, J., Abad, J. A., Abuter, R., et al. (2019). NAOMI: the adaptive optics system of the Auxiliary Telescopes of the VLTI. *A&A*, 629:A41. https://www.doi.org/10.1051/0004-6361/201935890.

Woillez, J., Abuter, R., Andolfato, L., et al. (2014). Improving the astrometric performance of VLTI-PRIMA. In Rajagopal, J. K., Creech-Eakman, M. J., & Malbet, F., editors, *Optical and Infrared Interferometry IV*, volume 9146 of *Society of Photo-Optical Instrumentation Engineers (SPIE) Conference Series*, page 91461H. https://www.doi.org/10.1117/12.2054723.

Woillez, J. & Lacour, S. (2013). Wide-angle, Narrow-angle, and Imaging Baselines of Optical Long-baseline Interferometers. *ApJ*, 764(1):109. https://www.doi.org/10.1088/0004-637X/764/1/109.

Woitke, P. & Helling, C. (2003). Dust in brown dwarfs. II. The coupled problem of dust formation and sedimentation. *A&A*, 399:297–313. https://www.doi.org/10.1051/0004-6361:20021734.

Wolszczan, A. & Frail, D. A. (1992). A planetary system around the millisecond pulsar PSR1257 + 12. *Nature*, 355(6356):145–147. https://www.doi.org/10.1038/355145a0.

Xin, Y., Xuan, J. W., Mawet, D., et al. (2023). On-sky speckle nulling through a single-mode fiber with the Keck Planet Imager and Characterizer. *Journal of Astronomical Telescopes, Instruments, and Systems*, 9:035001. https://www.doi.org/10.1117/1.JATIS.9.3.035001.

Yang, J.-Y., Xie, J.-W., & Zhou, J.-L. (2020). Occurrence and Architecture of Kepler Planetary Systems as Functions of Stellar Mass and Effective Temperature. *AJ*, 159(4):164. https://www.doi.org/10.3847/1538-3881/ab7373.

Yang, W. & Kostinski, A. B. (2004). One-sided Achromatic Phase Apodization for Imaging of Extrasolar Planets. *ApJ*, 605(2):892–901. https://www.doi.org/10.1086/382586.

Zernike, F. (1934). Diffraction theory of the knife-edge test and its improved form, the phase-contrast method. *MNRAS*, 94:377–384. https://www.doi.org/10.1093/mnras/94.5.377.

Appendix A

Additional material

A.1 Keplerian orbit

An elliptic Keplerian orbit is fully described by seven parameters illustrated on Fig. A.1:

- a: the semi-major-axis of the ellipse.
- e: the eccentricity of the ellipse, defined as $e = \sqrt{1 - \frac{b^2}{a^2}}$ with b the semi-minor-axis. A circular orbit is $e = 0$, a highly eccentric orbit is $e \lesssim 1$.
- P: the orbital period.
- t_p: the date of passage at the periapsis.
- i: the orbit inclination.
- Ω: the longitude of the ascending node.
- ω: the position of the periapsis, in angle with respect to Ω.

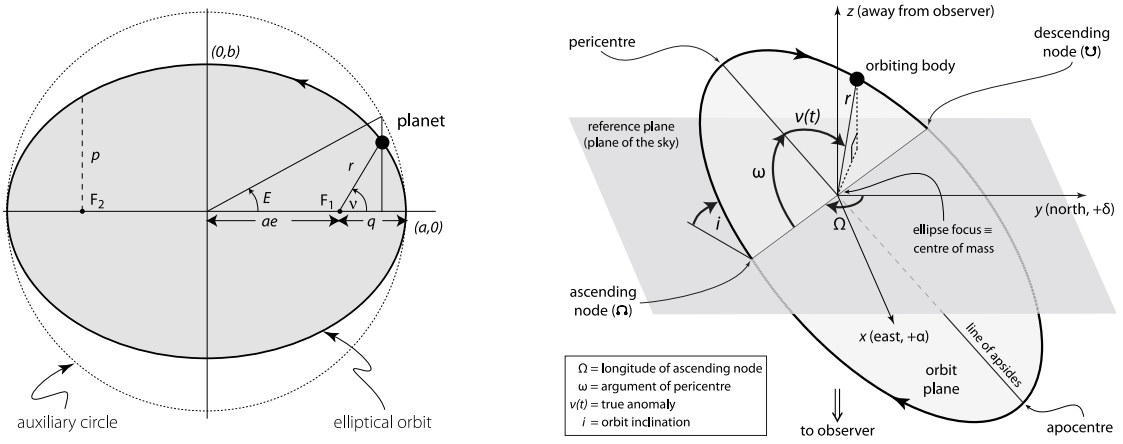

(a) (b)

Figure A.1 – (From Perryman, 2018) (a) Two dimensional description of a Keplerian orbit. (b) Three dimensional Keplerian orbit.

The Keplerian elements are just one set of variable describing an orbit, but it is possible to combine them in a way that forms another set of variables. For example, the Gaia catalogue for non-single stars provides the orbit fits in the Thiele-Innes elements.

A.2 Complex visibilities for a planet detection on GRAVITY

As shown by Eq. (2.42), the coherent flux injected in the SC when observing the companion is the sum of the companion coherent flux and of a star contribution:

$$\underline{V}_{\text{onplanet}}(b,t,\lambda) = \underbrace{\underline{V}_{*}(b,t,\lambda)G(b,\boldsymbol{\Delta\alpha},t,\lambda)}_{\text{speckle}} + \underbrace{\underline{V}_{p}(b,t,\lambda)G(b,\mathbf{0},t,\lambda)}_{\text{planet}}$$

Figure A.2 shows an example of $\underline{V}_{\text{onplanet}}(b,t,\lambda)$ where the complex visibilities are largely dominated by the speckle term. A polynomial modulation of $\underline{V}_{\text{onstar}}$ provide a speckle fit that we can subtract from the data to reveal the exoplanet signal (Fig. A.3). The planet visibility is:

$$\underline{V}_{p}(b,t,\lambda) = S_p(\lambda)\exp\left(i\frac{2\pi}{\lambda}\left[\boldsymbol{\Delta\alpha}\,\mathbf{U}(t)\right]\right)$$

where the exponential term is responsible for modulations at spectral frequencies too high to be captured by the polynomial modulation of the speckles (baselines U4-U2, U4-U1 and U3-U1). On some baseline the planet signal is very weak, the polynomial captured the planet signal (U4-U3 and U3-U1). Still, the information left is sufficient for constraining the planet astrometry and contrast.

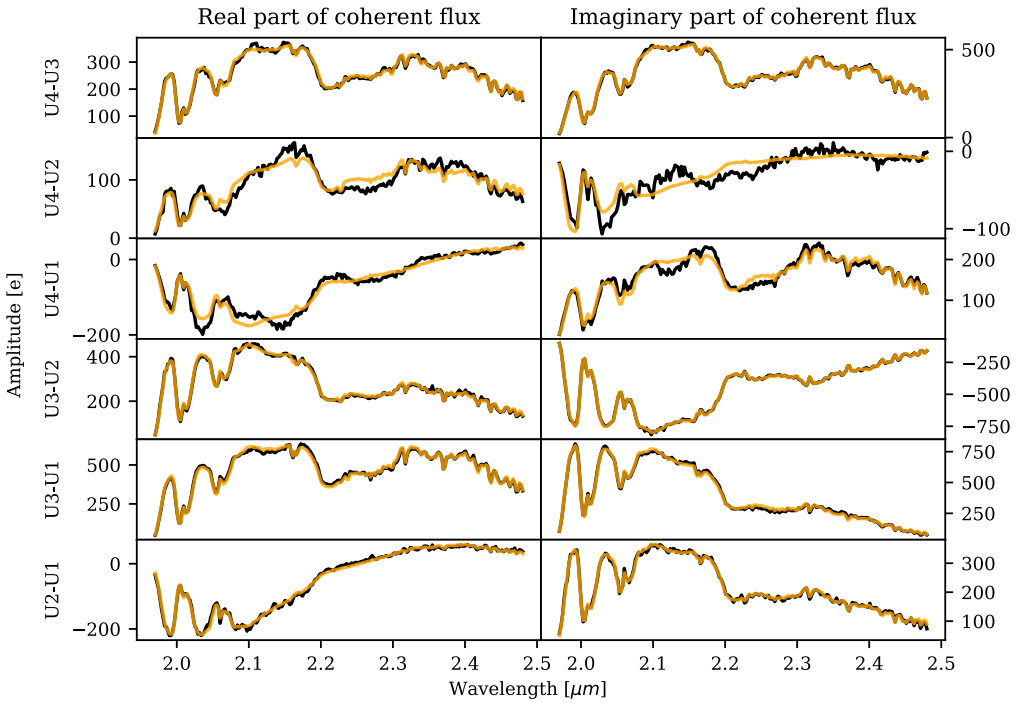

Figure A.2 – Example of $\underline{V}_{\text{onplanet}}$ referenced to the star, for a planet signal injected at 68 mas and 8×10^{-4} contrast. (black) Referenced visibilities. (orange) Speckle fit. (From Pourré et al., 2024)

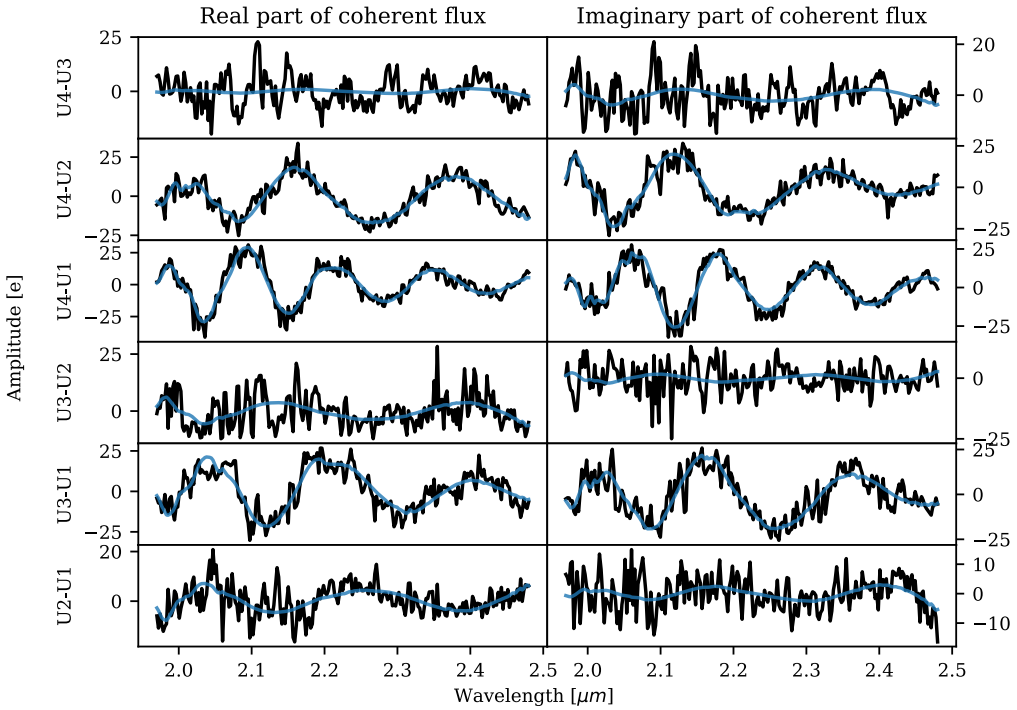

Figure A.3 – Same as Fig.A.2 but once the speckle fit is subtracted from the data. (black) Referenced visibilities with the speckle fit subtracted. (blue) Planet fit. (From Pourré et al., 2024)

A.3 Speckle's and star's referential

The speckle's phase referential is slightly different from the star's phase referential. It is show in Fig. A.4. For the wiggles fit in the `spectrum_reduce` script of the ExoGRAVITY pipeline, we found that the wiggles were better captured when considered static in the speckle's referential.

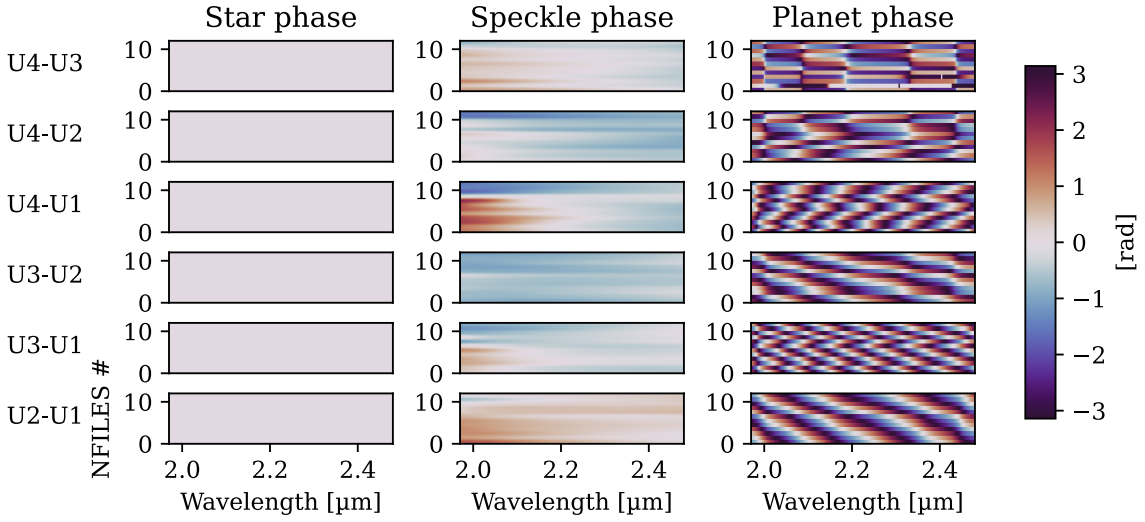

Figure A.4 – Phases referenced to the star, for (left) the observations on-star, (center) the speckles observed on the planet as fitted by the `astrometry_reduce`, (right) the planet.

A.4 Implementation of the wiggle's fit in the ExoGRAVITY pipeline

In Sect. 4.6.4, I test the pipeline solution we found to disentangle the wiggles from the planet spectrum. Here are more details on the implementation. Eqation (4.9) show that we add a wiggle term that resembles the planet term:

$$\underline{V}_{\rm onplanet}(b,t,\lambda) = \underbrace{P(b,t,\lambda)\underline{V}_{\rm onstar}}_{\rm speckles} + \underbrace{C(\lambda)\underline{V}_{\rm onstar}e^{-i\frac{2\pi}{\lambda}[\mathbf{u}(t)\boldsymbol{\Delta\alpha}]}}_{\rm planet} + \underbrace{C_w(b,\lambda)|r(b,t,\lambda)|e^{-i\arg(P(b,t,\lambda))}}_{\rm wiggles} \tag{A.1}$$

To implement it in the `spectrum_reduce` code, we build a new matrix $\underline{\mathbb{R}}_w$ such that:

$$\underline{\mathbb{R}}_w = \begin{pmatrix} \left((\widetilde{\underline{\mathbf{H}}}_{b_1,t_1})_{11} & (\widetilde{\underline{\mathbf{H}}}_{b_1,t_1})_{12}\right)\widetilde{\underline{\mathbf{r}}}_{b_1,t_1} & 0 & 0 \\ 0 & \ddots & 0 & \\ 0 & 0 & \left((\widetilde{\underline{\mathbf{H}}}_{b_6,t_{\rm NDIT}})_{11} & (\widetilde{\underline{\mathbf{H}}}_{b_6,t_{\rm NDIT}})_{12}\right)\widetilde{\underline{\mathbf{r}}}_{b_6,t_{\rm NDIT}} \end{pmatrix} \tag{A.2}$$

and we replace the matrix $\underline{\mathbb{R}}$ of the speckle fit by the matrix $\underline{\mathbb{R}}'$ defined as:

$$\underline{\mathbb{R}}' = \begin{pmatrix} \underline{\mathbb{R}} & \underline{\mathbb{R}}_w & i\underline{\mathbb{R}}_w \end{pmatrix}. \tag{A.3}$$

In the original `spectrum_reduce`, the output is a $\mathbf{C}$ vector of size n_λ corresponding to the planet contrast spectrum $C(\lambda)$. With the modification we propose here, the script produces a $\mathbf{C}'$ vector of size $(n_\lambda + 6\times 2\times n_\lambda)$ including both the planet contrast spectrum and the real/imaginary contrast spectrum $C_w(b,\lambda)$. We recover the planet contrast spectrum by getting the first n_λ elements of $\mathbf{C}'$:

$$\mathbf{C} = \mathbf{C}'\mathbb{I}_c = \begin{pmatrix} \mathbf{C}'_1 & \mathbf{C}'_2 & \cdots & \mathbf{C}'_{n_\lambda} \end{pmatrix}, \tag{A.4}$$

with,

$$\mathbb{I}_c = \underbrace{\left.\begin{pmatrix} 1 & 0 & \cdots & \cdots & \cdots & \cdots & 0 \\ 0 & 1 & 0 & \cdots & \cdots & \cdots & 0 \\ \vdots & 0 & \ddots & 0 & \cdots & \cdots & 0 \\ 0 & \cdots & 0 & 1 & 0 & \cdots & 0 \end{pmatrix}\right\} n_\lambda}_{n_\lambda+6\times2\times n_\lambda} \tag{A.5}$$

Similarly, the original `spectrum_reduce` produces a matrix $\mathbf{C}_{\rm ov}$ of size (n_λ, n_λ) corresponding to the contrast spectrum covariance matrix. With the modification we propose here, the script produces a large covariance matrix $\mathbf{C}'_{\rm ov}$ of size $(n_\lambda + 6\times 2\times n_\lambda,\, n_\lambda + 6\times 2\times n_\lambda)$. We obtain the spectrum covariance matrix $\mathbf{C}_{\rm ov}$ thanks to the linear operation:

$$\mathbf{C}_{\rm ov} = \mathbb{I}_c^\intercal\, \mathbf{C}'_{\rm ov}\, \mathbb{I}_c. \tag{A.6}$$

A.5 Non-common path aberrations in GRAVITY-SC

The NCPA measured on GRAVITY SC with UT Nasmyth beacon and modulations injected with CIAO (Sect. 5.7.4).

A.5.1 UT1 and GRAVITY input 4

For UT1 and GRAVITY input number 4 (GV4).

Table A.1 – NCPA measured on UT1/GV4 the 2024-01-23

Zernike mode	Amplitude rms [nm] $\pm 1\sigma$ error
Noll# 4 (Defocus)	-1±13
Noll# 5 (Oblique astig.)	-86±13
Noll# 6 (Vertical astig.)	10±18
Noll# 7 (Vertical coma)	21±11
Noll# 8 (Horizontal coma)	-62±9
Noll# 9 (Vertical trefoil)	-87±21
Total	139±9

A.5.2 UT3 and GRAVITY input 2

NCPA measured on GRAVITY SC for UT3/GV2:

Table A.2 – NCPA measured on UT3/GV2 the 2024-01-24

Zernike mode	Amplitude rms [nm] $\pm 1\sigma$ error	
	Sequence#1	Sequence#2
Noll# 4 (Defocus)	-228±24	-219±11
Noll# 5 (Oblique astig.)	43±21	20±42
Noll# 6 (Vertical astig.)	66±15	4±37
Noll# 7 (Vertical coma)	-12±37 repeated at -18±13	-18±23
Noll# 8 (Horizontal coma)		-102±14
Noll# 9 (Vertical trefoil)		19±23
Noll# 10 (Oblique trefoil)		57±24
Noll# 11 (Spherical)		-8±4 repeated at 6±11
Total	242±9	251±7

Appendix B

Publications

- (Pourré et al., 2024) : Pourré, N., Winterhalder, T. O., Le Bouquin, J.-B., Lacour, S., et al. (2024). High contrast at short separation with VLTI/GRAVITY: bringing Gaia companions to light. A&A, 686:A258.

- (Pourré et al., 2022c) : Pourré, N., Le Bouquin, J.-B., Woillez, J., et al. (2022c). Digging a dark hole in GRAVITY: towards Jupiter-like observations at the astronomical unit scale. In Mérand, A., Sallum, S., & Sanchez-Bermudez, J., editors, Optical and Infrared Interferometry and Imaging VIII, volume 12183 of Society of Photo-Optical Instrumentation Engineers (SPIE) Conference Series, page 121830V.

- (Pourré et al., 2022a) : Pourré, N., Le Bouquin, J. B., Milli, J., et al. (2022a). Low-wind-effect impact on Shack-Hartmann-based adaptive optics. Partial control solution in the context of SPHERE and GRAVITY+. A&A, 665:A158.

- (Pourré et al., 2022b) : Pourré, N., Le Bouquin, J. B., Milli, J., et al. (2022b). Understand and correct for the low wind effect on the SPHERE and GRAVITY+ adaptive optics. In Schreiber, L., Schmidt, D., & Vernet, E., editors, Adaptive Optics Systems VIII, volume 12185 of Society of Photo-Optical Instrumentation Engineers (SPIE) Conference Series, page 121855C.

A&A, 686, A258 (2024)
https://doi.org/10.1051/0004-6361/202449507

Astronomy & Astrophysics

High contrast at short separation with VLTI/GRAVITY: Bringing *Gaia* companions to light⋆

N. Pourré[1], T. O. Winterhalder[2], J.-B. Le Bouquin[1], S. Lacour[3,2], A. Bidot[1], M. Nowak[4], A.-L. Maire[1], D. Mouillet[1], C. Babusiaux[1], J. Woillez[2], R. Abuter[2], A. Amorim[5,6], R. Asensio-Torres[7], W. O. Balmer[8,9], M. Benisty[1], J.-P. Berger[1], H. Beust[1], S. Blunt[10], A. Boccaletti[3], M. Bonnefoy[1], H. Bonnet[2], M. S. Bordoni[11], G. Bourdarot[11], W. Brandner[7], F. Cantalloube[12], P. Caselli [11], B. Charnay[3], G. Chauvin[13], A. Chavez[10], E. Choquet[12], V. Christiaens[14], Y. Clénet[3], V. Coudé du Foresto[3], A. Cridland[15], R. Davies[11], D. Defrère[17], R. Dembet[3], J. Dexter[16], A. Drescher[11], G. Duvert[1], A. Eckart[18,19], F. Eisenhauer[11], N. M. Förster Schreiber[11], P. Garcia[6,20], R. Garcia Lopez[21,7], E. Gendron[3], R. Genzel[11,23], S. Gillessen[11], J. H. Girard[9], F. Gonte[2], S. Grant[11], X. Haubois[24], G. Heißel[25,3], Th. Henning[7], S. Hinkley[26], S. Hippler[7], S. F. Hönig[22], M. Houllé[13], Z. Hubert[1], L. Jocou[1], J. Kammerer[2], M. Kenworthy[15], M. Keppler[7], P. Kervella[3], L. Kreidberg[7], N. T. Kurtovic[11], A.-M. Lagrange[1,3], V. Lapeyrère[3], D. Lutz[11], F. Mang[11], G.-D. Marleau[27,28,29,7], A. Mérand[2], F. Millour[13], P. Mollière[7], J. D. Monnier[30], C. Mordasini[29], E. Nasedkin[7], S. Oberti[2], T. Ott[11], G. P. P. L. Otten[31], C. Paladini[24], T. Paumard[3], K. Perraut[1], G. Perrin[3], O. Pfuhl[2], L. Pueyo[9], D. C. Ribeiro[11], E. Rickman[32], Z. Rustamkulov[33], J. Shangguan[11], T. Shimizu[11], D. Sing[8,33], F. Soulez[40], J. Stadler[34,35], T. Stolker[15], O. Straub[35], C. Straubmeier[18], E. Sturm[11], C. Sykes[22], L. J. Tacconi[11], E. F. van Dishoeck[15,11], A. Vigan[12], F. Vincent[3], S. D. von Fellenberg[19], J. J. Wang[10], F. Widmann[11], S. Yazici[11]
(GRAVITY Collaboration),
J. A. Abad[2], E. Aller Carpentier[2], J. Alonso[24], L. Andolfato[2], P. Barriga[2], J.-L. Beuzit[12], P. Bourget[24], R. Brast[2], L. Caniguante[24], E. Cottalorda[13], P. Darré[2], B. Delabre[2], A. Delboulbé[1], F. Delplancke-Ströbele[2], R. Donaldson[2], R. Dorn[2], C. Dupuy[2], S. Egner[2], G. Fischer[2], C. Frank[2], E. Fuenteseca[24], P. Gitton[24], T. Guerlet[2], S. Guieu[1], P. Gutierrez[2], P. Haguenauer[2], A. Haimerl[2], C. T. Heritier[36,12], S. Huber[2], N. Hubin[2], P. Jolley[2], J.-P. Kirchbauer[2], J. Kolb[2], J. Kosmalski[2], P. Krempl[37], M. Le Louarn[2], P. Lilley[2], B. Lopez[13], Y. Magnard[1], S. Mclay[2], A. Meilland[13], A. Meister[24], T. Moulin[1], L. Pasquini[2], J. Paufique[2], I. Percheron[2], L. Pettazzi[2], D. Phan[2], W. Pirani[2], J. Quentin[2], A. Rakich[2], R. Ridings[2], J. Reyes[2], S. Rochat[1], C. Schmid[2], N. Schuhler[24], P. Shchekaturov[2], M. Seidel[2], C. Soenke[2], E. Stadler[1], C. Stephan[24], M. Suárez[2], M. Todorovic[2], G. Valdes[24], C. Verinaud[2], G. Zins[2], and S. Zúñiga-Fernández[24,38,39]
(NAOMI Collaboration)

(Affiliations can be found after the references)

Received 6 February 2024 / Accepted 24 March 2024

ABSTRACT

Context. Since 2019, GRAVITY has provided direct observations of giant planets and brown dwarfs at separations of down to 95 mas from the host star. Some of these observations have provided the first direct confirmation of companions previously detected by indirect techniques (astrometry and radial velocities).

Aims. We want to improve the observing strategy and data reduction in order to lower the inner working angle of GRAVITY in dual-field on-axis mode. We also want to determine the current limitations of the instrument when observing faint companions with separations in the 30–150 mas range.

Methods. To improve the inner working angle, we propose a fiber off-pointing strategy during the observations to maximize the ratio of companion-light-to-star-light coupling in the science fiber. We also tested a lower-order model for speckles to decouple the companion light from the star light. We then evaluated the detection limits of GRAVITY using planet injection and retrieval in representative archival data. We compare our results to theoretical expectations.

Results. We validate our observing and data-reduction strategy with on-sky observations; first in the context of brown dwarf follow-up on the auxiliary telescopes with HD 984 B, and second with the first confirmation of a substellar candidate around the star *Gaia* DR3 2728129004119806464. With synthetic companion injection, we demonstrate that the instrument can detect companions down to a contrast of 8×10^{-4} ($\Delta K = 7.7$ mag) at a separation of 35 mas, and a contrast of 3×10^{-5} ($\Delta K = 11$ mag) at 100 mas from a bright primary ($K < 6.5$), for 30 min exposure time.

Conclusions. With its inner working angle and astrometric precision, GRAVITY has a unique reach in direct observation parameter space. This study demonstrates the promising synergies between GRAVITY and *Gaia* for the confirmation and characterization of substellar companions.

Key words. techniques: high angular resolution – techniques: interferometric – planets and satellites: detection – brown dwarfs – planetary systems

⋆ Based on observations collected at the European Southern Observatory under ESO programs 1104.C-0651, 0110.C-0182 (GTO NAOMI), 60.A-9102 (GRAVITY+ commissioning run) and 0112.C-2396(C).

1. Introduction

Thanks to progress in ground-based and space-based direct imaging instrumentation, we can now delve into the specific formation processes leading to substellar companions, such as massive planets and brown dwarfs. It has been proposed that they form by core accretion (Mizuno 1980), disk instability (Boss 1997), or collapse of the prestellar core (Bonnell et al. 2008), and all these models come with different variations. It is still unclear as to which mechanism dominates in each type of object and at what distance. Extensive direct imaging surveys (e.g., Vigan et al. 2021; Nielsen et al. 2019; Stone et al. 2018) have inferred the occurrence rates of massive Jovian planets and brown dwarfs around stars of spectral types from B to M. For intermediate FGK stars, the findings of these surveys favor a dichotomy in the formation processes. The distribution of giant planets within 50 au is consistent with the predictions of the core-accretion model, and the giant planet and brown dwarf populations further out are consistent with the disk-instability pathway. Also, by fitting the orbit of a sample of a dozen substellar companions, Bowler et al. (2020) revealed a difference in the eccentricity distribution of giant planets and brown dwarfs. These authors suggest that planets form in disks and brown dwarfs preferably by core collapse. The most promising way to enlarge the samples for testing the formation theories is to enable direct observations of fainter companions, and to reach the closer-in regions of the systems (below 20 au).

On the one hand, this goal of observing fainter companions at shorter separations triggers the development of faster and higher-order adaptive optics (AO) (Boccaletti et al. 2022; Lozi et al. 2022; GRAVITY+ Collaboration 2022) and deconvolution techniques in high-contrast images (e.g., angular differential imaging: Marois et al. 2006, spectral differential imaging: Racine et al. 1999). So far, ground-based AO-assisted single telescopes and space instruments achieve contrasts down to a few 10^{-7} at 1 arcsec separation (ERIS: Davies et al. 2023, SPHERE: Beuzit et al. 2019, GPI: Macintosh et al. 2014, HiRISE: Otten et al. 2021, KPIC: Jovanovic et al. 2019, JWST: Hinkley et al. 2022). On the other hand, optical long-baseline interferometry with GRAVITY is emerging as a complementary technique because its specific deconvolution capability allows direct observations of planetary companions at separations of as small as 90 mas.

GRAVITY is a second-generation K-band instrument and a two-in-one interferometric combiner in operation at the Very Large Telescope Interferometer (VLTI) since 2016 (GRAVITY Collaboration 2017). The fringe tracker (FT, Lacour et al. 2019) arm operates at 1 kHz on a bright target ($K < 10$) in order to adjust the delay-lines position and correct for atmospheric turbulence. In parallel, the science (SC) arm can integrate up to 300 s, and thus allows for observations of objects as faint as K = 19 mag (GRAVITY Collaboration 2022). In addition, a metrology system measures the angular separation between the FT and the SC in real time. The ability to observe faint objects, together with the robust metrology link between FT and SC, launched optical interferometry into the field of direct imaging of exoplanets. The ExoGRAVITY large program has already provided direct observations of exoplanets orbiting at 3 au from their stars, at challenging separations of down to 95 mas and contrasts of a few 10^{-5} (Nowak et al. 2020; Lacour et al. 2021; Hinkley et al. 2023). GRAVITY provides the relative astrometry with a precision down to 50 μas and a near-infrared K-band spectrometry at R∼500 (medium-resolution mode) or R∼4000 (high-resolution mode). These observations provide unprecedented constraints on the companion's orbit and allow determination of the object's surface temperature and atmospheric composition (GRAVITY Collaboration 2020). However, the field of view of the instrument is limited due to the single-mode nature of modern optical interferometry. For more than 50% injection, it is about 65 mas on the unit telescopes (UTs) and 290 mas on the auxiliary telescopes (ATs). While this is an important drawback when performing blind searches, the situation has completely changed with the release of the *Gaia* space telescope catalog. *Gaia*'s Non-Single-Star (NSS) two-body orbit catalog (Holl et al. 2023; Halbwachs et al. 2023) published within DR3 (Gaia Collaboration 2023) contains astrometry-based orbital solutions for approximately 450 000 stars around each system's center of mass. Assuming that the orbital motion of the star is caused by the presence of a dark and unseen secondary body, the orbital solution constrains the on-sky position of the companion relative to the star with sufficient accuracy to position the single-mode fiber of GRAVITY. A subsequent detection of the companion with GRAVITY can confirm the candidate and provide the dynamical mass – thanks to the astrometry – and a direct measurement of its luminosity and spectrum. This synergy has been identified for a few years now, but there is currently no quantitative assessment of its potential. The actual inner working angle and contrast performance of GRAVITY are still undocumented, and their limitations are still unknown. These questions become even more pressing in the context of the ongoing instrumentation upgrade at the VLTI (Eisenhauer 2019).

The goal of this paper is to demonstrate and quantify the potential of GRAVITY to provide direct confirmations of substellar candidates detected by *Gaia* absolute astrometry and to understand its limitations. In Sect. 2, we describe specific details of substellar companion observations and data reduction with GRAVITY. We outline a strategy to lower the inner working angle. In Sect. 3, we quantify and validate these strategies by observing the brown dwarf HD 984 B and by providing the first direct observation of a brown dwarf companion orbiting the star *Gaia* DR3 2728129004119806464 (hereafter referred to as *Gaia*...6464). Finally, in Sect. 4, we determine the detection limits of GRAVITY by injection and retrieval of synthetic companions in archival ExoGRAVITY observations. We compare the results with expectations from the fundamental statistical noise. We conclude the paper with a summary and a discussion of the synergy with *Gaia* and other direct-imaging instruments (Sect. 5).

2. Method

2.1. The ExoGRAVITY method

The ExoGRAVITY community developed an observation technique and a dedicated pipeline to enable direct observations of exoplanets and brown dwarfs with the GRAVITY instrument down to a few tens of mas close to bright nearby stars (Nowak et al. 2020; GRAVITY Collaboration 2020).

2.1.1. Observing technique

The VLTI recombines either the four relocatable ATs, each of D =1.8 m in diameter, or the four UTs, each of D = 8 m in diameter. The beam from each telescope travels through the VLTI tunnels and delay lines to reach GRAVITY. In the instrument, the two combiners (FT and SC) are fed by separate optical single-mode fibers. In the dual-field mode of the instrument, the fibers of the SC and of the FT can be positioned at different locations on the focal plane of each telescope (Pfuhl et al. 2012).

For separations of less than 0.7 arcsec, the field is separated by a 50/50 beamsplitter before injection into the FT and SC fibers (Appendix A in Nowak et al. 2020). In a typical ExoGRAVITY observation sequence, the FT remains centered on the host star and the SC alternates between long integrations centered on the companion and shorter integrations centered on the star (to avoid saturation). The shape of the fiber mode can be approximated by a Gaussian beam with a full width at half maximum (FWHM) of 65 mas on the UT (290 mas on the AT), which defines the field of view of the instrument. The flux injected into the SC from individual telescopes is recombined in integrated optics (Perraut et al. 2018). The recombination method allows us to measure the total flux of each of the four telescopes, but also the coherent flux of each of the six baselines.

Regarding the total flux (e.g., photometric flux of each telescope), the injected flux is the scalar product between the Gaussian mode of the fiber and the object point-spread function (PSF; Fig. 1). The dependence of the transmission on the distance $\mathbf{s}$ of the object from the center of the fiber is thus given by

$$T(m, \mathbf{s}) = \left| \iint E(\mathbf{x}, m)\, M(\mathbf{x} - \mathbf{s})\, \mathrm{d}\mathbf{x} \right|^2, \quad (1)$$

where m is the telescope, E the incident electric field, M the fiber mode, and $\mathbf{x} = (x, y)$ the coordinates on the focal plane. In the following, we consider that T includes the overall transmission from the atmosphere and the instrument; it therefore depends on the telescope, time, and wavelength. This way, the total flux $F_{\mathrm{oncompanion}}$ injected into the SC for each of the four telescopes when the fiber is centered on the companion can be expressed as

$$F_{\mathrm{oncompanion}}(m, t, \lambda) = F_{\mathrm{s}}(\lambda)\, T(m, \boldsymbol{\Delta\alpha}, t, \lambda) + F_{\mathrm{c}}(\lambda)\, T(m, \mathbf{0}, t, \lambda), \quad (2)$$

where m is the telescope, t the time, λ the wavelength, $\boldsymbol{\Delta\alpha} = (\Delta\mathrm{RA}, \Delta\mathrm{Dec})$ the position of the companion relative to the star, and F_{s} and F_{c} are the total flux from the star and the companion, respectively.

The coherent flux, also called the complex visibility, encodes the amplitude and the phase of the interferometric fringes and provides the useful signal in GRAVITY. We can define the interferometric transmission G as:

$$G(b,\mathbf{s}) = \iint E(\mathbf{x}, m_1)\, M(\mathbf{x} - \mathbf{s})\, \mathrm{d}\mathbf{x} \cdot \iint E^*(\mathbf{x}, m_2) M^*(\mathbf{x} - \mathbf{s})\, \mathrm{d}\mathbf{x}, \quad (3)$$

with the two telescopes m_1 and m_2 composing the baseline b. We can then write the complex visibility $V_{\mathrm{oncompanion}}$ that the instrument measures when the SC fiber is located on the companion as

$$V_{\mathrm{oncompanion}}(b, t, \lambda) = V_{\mathrm{s}}(b, t, \lambda)\, G(b, \boldsymbol{\Delta\alpha}, t, \lambda) + V_{\mathrm{c}}(b, t, \lambda)\, G(b, \mathbf{0}, t, \lambda), \quad (4)$$

where V_{s} and V_{c} are the visibility of the star and the companion, respectively. Here and in the following, the visibility is understood as the complex coherent flux, which matches the definition of Nowak et al. (2020).

The total transmission T and the interferometric transmission G include the flux losses due to the distance of the fiber from the object (star or companion). We estimated the dependence of the transmission on separation using archival observations from the ExoGRAVITY large program 1104.C-0651(A). We selected observations with good atmospheric conditions. In the selected observations, the companion is fainter than contrasts of 10^{-4}, and so the total flux $F_{\mathrm{oncompanion}}$ and the coherent flux $V_{\mathrm{oncompanion}}$ are largely dominated by the star contribution and we neglect the companion contribution. The GRAVITY pipeline (Lapeyrere et al. 2014) outputs an ASTROREDUCED file containing the total flux per telescope and per detector exposure (OI_FLUX table) and the coherent flux per baseline and per detector exposure (OI_VIS table). The ExoGRAVITY pipeline reads these files and normalizes the fluxes measured on-companion by the fluxes measured on-star. Therefore, the output immediately corresponds to the normalized injection curve.

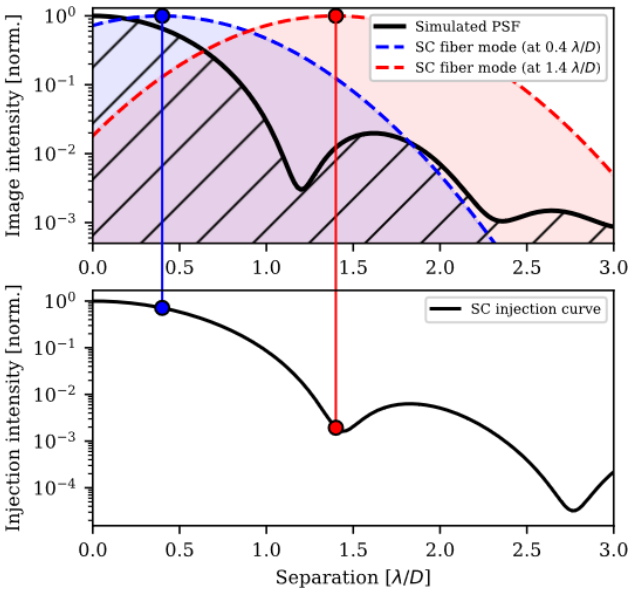

Fig. 1. Injection into the SC arm at the focal plane of GRAVITY. Top: comparison of the Gaussian single mode of the SC fiber with the diffraction-limited PSF at the image plane. This simulation is for 20% bandwidth and the UT aperture. Bottom: injection map given by the convolution of the PSF with the SC fiber mode.

Figure 2 displays the normalized coherent and total fluxes measured at different separations. These are based on archival observations from the ExoGRAVITY large program around bright stars from $K = 7.5$ mag to $K = 3.5$ mag (β Pic, HD 206893, HD 17155, and CD-50 869). This dataset covers SC fiber positions from 55 to 140 mas, and atmosphere conditions from good to normal (seeing from 0.4 to 1.0 arcsec). To obtain continuous injection profiles, we ran AO simulations including single-mode fiber injection with HCIPy (Por et al. 2018). We simulate an atmosphere following Kolmogorov turbulence and a low-order AO controlling 50 modes over an 8 m pupil to mimic the MACAO system at the Coudé focus of the UT (Arsenault et al. 2003). We include 20% bandwidth to account for the spectral range of GRAVITY from 1.95 to 2.4 µm. We also add realistic 10 mas rms tip-tilt jitter residuals from the VLTI tunnels (Anugu et al. 2018). Finally, we adjust the AO loop gain and atmosphere parameters to match the observed total fluxes (coherent and total). The total flux transmission T and the interferometric transmission G are not at the diffraction limit level because of atmospheric residuals not corrected for by the AO, turbulence in the VLTI tunnels, and (quasi-)static aberrations in the instrument. The simulations show that the average Strehl

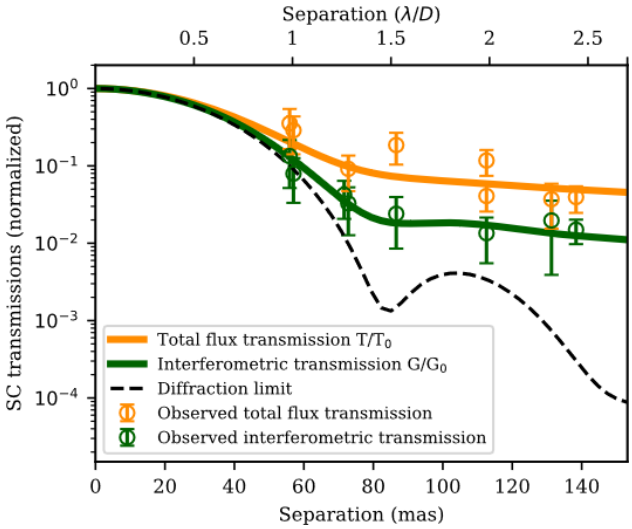

Fig. 2. Total flux transmission (T) and interferometric transmission (G) as a function of the separation from the star on the UT. The points correspond to archival ExoGRAVITY observations around bright stars. The solid lines correspond to simulations matching the observations. The dashed line corresponds to a simulation of the transmission without atmospheric residuals but including a 20% bandwidth and 10 mas rms tip-tilt jitter.

ratio in ExoGRAVITY observations is around 25%, which is a realistic value. In the remainder of the paper, we use the continuous profiles to model the injection of coherent and total flux in GRAVITY.

2.1.2. Unveiling the companion signal

The goal of the ExoGRAVITY reduction pipeline is to extract the companion astrometry and contrast spectrum from the measured complex visibilities $V_{\text{oncompanion}}(b,t,\lambda)$. In the following, "speckle" refers to the flux of the star that couples in the SC combiner while observing the companion. As shown in Eqs. (2) and (4) and in Fig. 2, this speckle light makes a contribution to the total flux, but also to the coherent flux. It is necessary to deconvolve the companion signal (coherent flux) from the coherent speckles. The companion is modeled as a point-source offset with respect to the host star. The complex visibility of the companion is:

$$V_{\text{c}}(b,t,\lambda) = S_{\text{c}}(\lambda)\, e^{-i\frac{2\pi}{\lambda}\,[\mathbf{u}(t)\boldsymbol{\Delta\alpha}]}, \tag{5}$$

where S_{c} is the companion spectrum and $\mathbf{u} = (u, v)$ the coordinates of the array on the UV plane. In the ExoGRAVITY pipeline, the speckle term $V_{\text{s}}G$ of Eq. (4) is modeled as

$$V_{\text{s}}(b,t,\lambda)\, G(b,\boldsymbol{\Delta\alpha},t,\lambda) = P(b,t,\lambda)\, V_{\text{onstar}}(b,t,\lambda), \tag{6}$$

where P is a complex polynomial that captures the spectral dependence of the coupling G at the separation $\boldsymbol{\Delta\alpha}$, and V_{onstar} is the visibility measured with the SC fiber centered on the host star:

$$V_{\text{onstar}} = J(b,t,\lambda)\; G(b,\mathbf{0},t,\lambda)\; S_{\text{s}}(\lambda). \tag{7}$$

Here, S_{s} is the star's spectrum, and J is the function representing the drop in the visibility of the star if the star is resolved by the interferometer. In the following, we assume that the star is not resolved, and so $J = 1$. Introducing the contrast spectrum

$$C(\lambda) = S_{\text{c}}(\lambda)/S_{\text{s}}(\lambda), \tag{8}$$

we can rewrite Eq. (4) phase referenced on the star:

$$V_{\text{oncompanion}}(b,t,\lambda) = P(b,t,\lambda)V_{\text{onstar}} + C(\lambda)V_{\text{onstar}}\mathrm{e}^{-i\frac{2\pi}{\lambda}\cdot[\mathbf{u}(t)\boldsymbol{\Delta\alpha}]}. \tag{9}$$

The first pass through the algorithm requires an assumption on $C(\lambda)$, and so, as a first guess, we assume that $C(\lambda)$ is a flat contrast spectrum. This first pass allows the recovery of the companion astrometry and the average flux ratio, and is the focus of this work. The second part of the pipeline (not described here) uses the astrometry to recover the companion contrast spectrum.

Equation (9) demonstrates the distinction between the speckle signal (first term) and the companion signal (second term). On the one hand, the speckle signal modulates at low spectral frequencies. On the other hand, the companion signal modulates at spectral frequencies that are determined by the projection of the companion separation onto the UV plane. This difference in the spectral oscillations allows the star light to be disentangled from the companion light (see Appendix A for an example). This is the interferometric equivalent of the "spectral deconvolution" first introduced by Sparks & Ford (2002) for high-contrast imaging with single telescopes.

2.2. Aiming for a smaller inner working angle

The previous section describes the standard ExoGRAVITY method. We now describe two modifications designed to improve the inner working angle.

2.2.1. Off-pointing strategy

Figure 2 indicates that it should be possible to improve the flux ratio between the companion and the star by offsetting the position of the fiber when observing the companion. This adds a new degree of freedom in the observation: the offset $\boldsymbol{\delta}$ of the SC fiber with respect to the expected companion position. This way, Eqs. (2) and (4) can be rewritten as

$$\begin{aligned} &F_{\text{oncompanion}}(m,t,\lambda) \\ &\quad = F_{\text{s}}(\lambda)\, T(m,t,\boldsymbol{\Delta\alpha}+\boldsymbol{\delta},\lambda) + F_{\text{c}}(\lambda)\, T(m,t,\boldsymbol{\delta},\lambda), \end{aligned} \tag{10}$$

$$\begin{aligned} &V_{\text{oncompanion}}(b,t,\lambda) \\ &\quad = V_{\text{s}}(b,t,\lambda)\, G(b,t,\boldsymbol{\Delta\alpha}+\boldsymbol{\delta},\lambda) + V_{\text{c}}(b,t,\lambda)\, G(b,t,\boldsymbol{\delta},\lambda). \end{aligned} \tag{11}$$

To reduce the star light without excessively reducing the coupling of the companion light, the offset $\boldsymbol{\delta}$ must be in the direction away from the star and of only a fraction of the PSF central lobe width. The off-pointing technique takes advantage of the sharp decrease in stellar transmission and the moderate decrease in companion transmission when the fiber is moved away from the star by a small offset $\boldsymbol{\delta}$.

2.2.2. Order of the polynomial fit

Section 2.1.2 implies that the degree of the polynomial P used to reject the speckles determines the inner working angle of the ExoGRAVITY technique. There is a trade-off between the quality of the speckle fit, and the self-subtraction of the planet

signal. This is common to most deconvolution techniques. By default, the ExoGRAVITY pipeline uses a fourth-degree polynomial for P. This has proven necessary to deal with the frequent fringe jumps of the fringe tracker. Such phase jumps cause a loss of visibility at the edges of the K-band visibility spectrum. These visibility losses are not necessarily of the same amplitude when observing on the star and on the planet, depending on the non-stationary quality of the fringe tracking. A fourth-degree polynomial is required to capture and remove these features. Consequently, most results published so far with the ExoGRAVITY pipeline have used a polynomial of between fourth and sixth order.

However, the situation recently changed with the commissioning of an improved version of the fringe tracker hardware and tracking algorithm in November 2022 (Abuter et al. 2016; Nowak et al. 2024). The new FT update significantly reduces the occurrence of fringe jumps and thus relaxes the requirements on the degree of the polynomial. It is also interesting to explore the impact of this parameter because the planned upgrade of the AO will stabilize the Strehl, and thus further reduce the occurrence of fringe jumps.

2.3. Empirical detection limit

The standard ExoGRAVITY pipeline lacks a method for determining robust detection limits. The injection of synthetic companions and their retrieval in the data is a classical approach to assessing the limit of direct imaging techniques in realistic conditions. The first step is to create a data set without a companion signal (if the original observation contains one). For this, we extract the companion astrometry ΔRA, ΔDec and the contrast spectrum $C(\lambda)$ exposure by exposure thanks using the ExoGRAVITY pipeline (Sect. 2.1.2). We then subtract the signal of this companion in the VISDATA table of the ASTROREDUCED files. We note that, unlike most other interferometric instruments, this operation is linear because GRAVITY operates with first-order estimators (complex coherent flux) instead of higher-order estimators (power spectrum and bispectrum). We then add synthetic companions at a given contrast C and $\boldsymbol{\Delta\alpha}$ position to the VISDATA:

$$V_{\mathrm{syntheticcomp}} = C\, V_{\mathrm{onstar}}\, \mathrm{e}^{-i\frac{2\pi}{\lambda}[\mathbf{u}(t)\boldsymbol{\Delta\alpha}]}\, e^{i\varphi}. \tag{12}$$

The additional φ phase term is due to the fact that the complex visibilities VISDATA are phased on the fiber position, and that the phase reference is the fringe-tracking phase, which is not necessarily zero. The term φ writes:

$$\varphi = arg(\mathrm{STAR\_REF}) - \mathrm{PHASE\_REF} + \mathrm{PHASE\_MET} + \frac{2\pi}{\lambda}\mathrm{DISP}, \tag{13}$$

following the nomenclature of the GRAVITY pipeline user manual[1], where PHASE_REF is the phase of the fringe tracker, PHASE_MET the differential phase between the fiber coupler and telescope diodes, DISP the fiber differential delay lines (FDDL) delay, and STAR_REF is the average of the two closest acquisitions with the SC on-star. In Eq. (13), we use a STAR_REF expression that has been previously rephrased with the metrology (PHASE_MET) and FDDL delay (DISP). In this paper, we inject companions with a flat contrast spectrum for the sake of simplicity, and so C is scalar. The modified VISDATA are then reduced by the ExoGRAVITY pipeline.

We consider the detection successful if the companion is recovered less than 3 mas away from the injected position and at a contrast with less than 50% relative error compared to the injected contrast. We consider that the detection limit is reached when fewer than 68% (1σ) of the synthetic companions are successfully retrieved.

[1] https://www.eso.org/sci/software/pipelines/index.html#pipelines_table

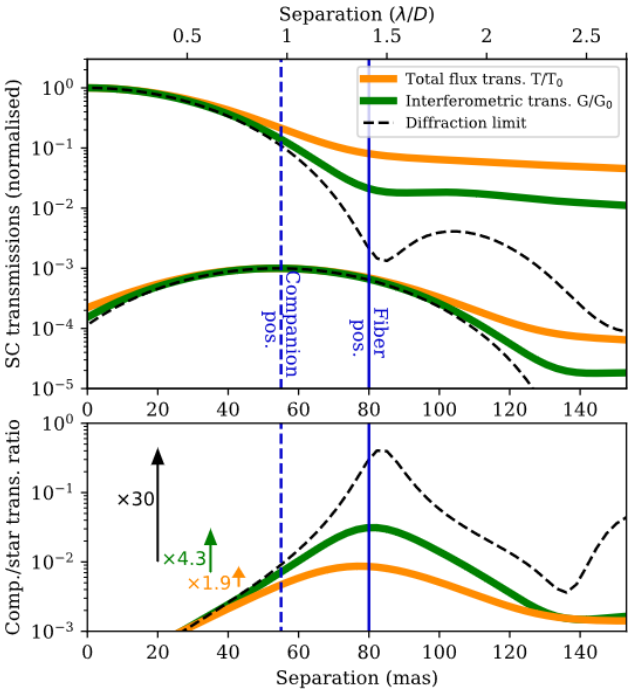

Fig. 3. Quantification of the contrast improvement brought by the off-pointing strategy in the case of a companion at a separation of 55 mas. Top: dependence on separation of both transmission of the total flux (T) and interferometric transmission (G) for a star and a companion. The diffraction limit represents an ideal unaberrated case. Bottom: companion-to-star transmission ratio with respect to separation. The arrows indicate the gain in contrast with a +25 mas SC fiber offset.

3. Results

3.1. Expected performance improvement

3.1.1. Off-pointing technique

We use the injection profiles shown in Fig. 2 to quantify the improvement that can be achieved by the off-pointing technique. Figure 3 shows that an offset of the fiber position can result in a factor 4.3 improvement in the companion/star coherent flux ratio and a factor 1.9 improvement of the total flux ratio. In this example, the companion is at 55 mas from the host star, and the fiber is positioned at 80 mas (55 mas + 25 mas away from the star). The fiber offset from the companion results in an injection efficiency of 67% (it would be 100% if the fiber were centered on the companion). This flux loss due to the offset must be compensated for a posteriori in order to recover the correct companion magnitude (Wang et al. 2021b; Appendix A). We estimate that, with the current AO on the UT, this method can bring a contrast enhancement in coherent flux of up to a factor 6. In terms of the implementation, for companions with a separation of less

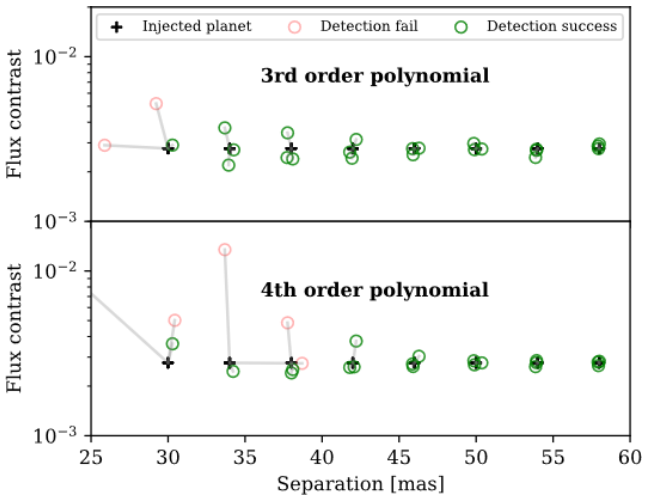

Fig. 4. Planet retrieval at 2.7×10^{-3} raw contrast and separations from 30 to 90 mas. At each separation, three companions are injected at different positional angles to test the robustness of the retrieval. We compare the third-degree (top) and fourth-degree (bottom) polynomials for speckle modeling.

than 55 mas, the SC fiber should be placed at +25 mas from the companion, because a higher offset would result in more planet flux loss and possible errors in the astrometry due to aberrations in the fiber injection (GRAVITY Collaboration 2021). For companions with a separation of between 55 mas and 80 mas, the SC fiber should be placed at 80 mas from the star. The offset method is not valid for companions with separations of greater than 80 mas, and so the SC fiber should be placed on the companion for these targets.

The improvement provided by the off-pointing strategy is currently severely limited by the AO performance. The dashed curve in Fig. 3 represents a realistic improved version of VLTI, with a high-order AO and control of the instrument aberrations. The expected injection profile was computed with the diffraction limit plus a 10 mas tip-tilt jitter, for instance resulting from the VLTI tunnels. The curve also considers a 20% wavelength bandwidth. Under these conditions, off-pointing can bring a contrast enhancement of up to a factor 30. This result emphasizes the need for better AO and instrument aberration control, as will be implemented with GRAVITY+.

3.1.2. Order of the polynomial fit

We used the planet injection and retrieval method described in Sect. 2.3 to define the most relevant polynomial degree when observing at short separation. We injected planets in the data set from the *Gaia*...6464 B run on the UT with the SC fiber at 60 mas of the primary (described in detail in Sect. 3.3). We then determined the best polynomial order to use in the reduction depending on the expected separation of the companion.

Figure 4 compares the performance of the third- and fourth-order polynomials for speckle modeling. The third-order polynomial leads to better planet retrieval below 45 mas separation, for both position and contrast. Beyond 45 mas, the fourth-order polynomial gives slightly better results for contrast retrieval. For completeness, we also ran tests with second-order polynomials. In this case, the retrieval gives erratic results. Thus, we still consider it safer to use the fourth order for separations of greater than 45 mas, as it gives more degrees of freedom for speckle modeling; nevertheless, we recommend using a third-order polynomial below 45 mas separation. This improvement brings the effective innermost working angle of GRAVITY to about 30 mas.

Table 1. Log for the GRAVITY observations of HD 984 AB on the AT.

Date: 2022-10-24			
Observing time	Airmass	τ_0 [a]	Seeing
01:12:17/01:57:20	1.07–1.14	2.5–4.5 ms	0.43–0.66″
Target	ΔRA/ΔDec [b]	NEXP/NDIT/DIT	
HD 984 A	0/0 mas	2/8/10 s	
HD 984 B	162/197 mas	3/8/30 s	
HD 984 B	224/273 mas	3/8/30 s	

Notes. [a]Atmosphere coherence time. [b]SC fiber position relative to the star.

3.2. On-sky validation on the auxiliary telescopes

3.2.1. Observation and data reduction

The star HD 984 A is known to host a companion brown dwarf with a contrast at K-band of 3.7×10^{-3} (Meshkat et al. 2015; Franson et al. 2022). We used this binary system to validate the off-pointing technique described in Sect. 2.2.1. The observation was performed as part of the program 0110.C-0182(A), on the ATs in astrometric configuration, and with the medium spectral resolution of GRAVITY. The off-pointing technique described for the UT is still valid on the AT, but since the ATs are smaller, it requires a ×4.4 scaling on the angular separations. From orbit fits using previous observations (Wang et al. 2021a), the companion was expected at a separation of 255 mas, with ±5 mas uncertainty on the (ΔRA, ΔDec). During the observation, the SC fiber was alternately positioned on the predicted position of the companion and 100 mas further away from the star (+0.4 λ/D), as summarized in Table 1. We chose a detector integration time (DIT) of 30 s, we collected a number of acquisition (NDIT) equal to eight in each of the three files (NEXP), and this for each position of the SC. We reduced the data using the ExoGRAVITY pipeline. The data taken with and without the off-pointing technique were reduced separately to compare the results. After reduction, it appeared that the companion was 9 mas away from the expected position. As this corresponds to only 3% of the fiber field of view on the AT, it did not entail flux losses and had no negative effect on our test.

3.2.2. Contrast improvement

Applying the offset on the fiber position, the coherent flux injected into the SC is reduced by a factor 6 and the total flux is reduced by a factor 3.4 on average. The slightly better improvement compared to expectations (factor 4 in coherent flux) is because the NAOMI AO on the ATs (Woillez et al. 2019) are closer to the diffraction limit than the UT with MACAO. The off-companion observations provide a significantly better detection than the on-companion, with about twice the periodogram power, from 1.4×10^4 to 2.7×10^4, as shown in Fig. 5.

Relative astrometry is improved by the off-pointing technique. With the off-pointing observation, the uncertainty on the ΔRA is reduced by 35% and the uncertainty on ΔDec is reduced by 8% compared to the classical on-companion pointing.

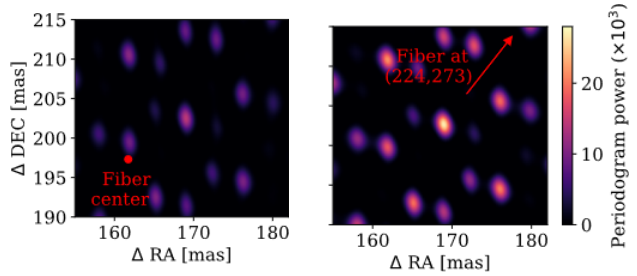

(a) On-companion (b) Off-companion

Fig. 5. Periodogram resulting from the astrometry fit of the GRAVITY data on HD 984 obtained by pointing the fiber at the expected position of the companion (left) and using the off-pointing technique (right). The spot of higher periodogram power corresponds to the detection of HD 984 B.

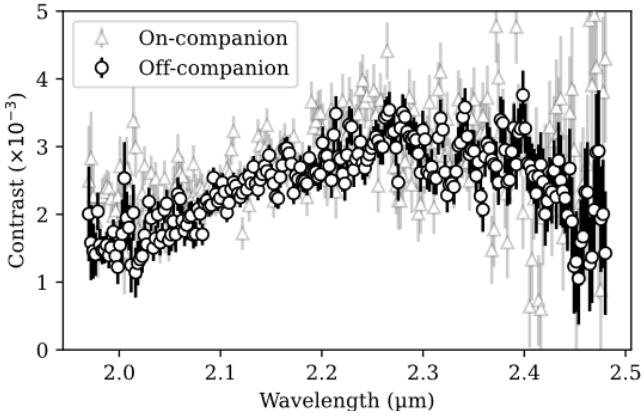

Fig. 6. Contrast spectrum for HD 984 B from our observations with (black) and without (gray) the off-pointing technique.

We also ran the second part of the pipeline to obtain the contrast spectrum. The spectrum quality is expected to improve thanks to the off-pointing. On the one hand, with the reduction of the total flux, we expect the amplitude of the photon noise from star speckles to be reduced by a factor of 1.8. On the other hand, only 72% of the companion flux is injected due to the off-pointing. Overall, we expect an improvement of 30% of the spectrum signal-to-noise ratio (S/N). The resulting contrast spectra are shown in Fig. 6. The total S/N can be calculated as:

$$S/N = \sqrt{C^{\intercal}.\mathrm{COV}^{-1}.C}, \quad (14)$$

where C is the contrast spectrum, $C^{\intercal}$ its vector transpose, and COV is the covariance matrix of the spectrum. The S/N is equal to 120 for the on-companion observations and is equal to 164 (+37%) for the off-companion data. This is fully in line with expectations.

3.2.3. Discussion

The efficiency of the interferometric deconvolution depends on the length of the baselines and the separation. In other words, a companion at 1 λ/D = 252 mas separation on the ATs is easier to disentangle from the speckles than a companion at 1 λ/D = 57 mas on the UTs. Nevertheless, this observation of HD 984 B with the AT demonstrates that a +0.4 λ/D offset brings a significant reduction of the coherent and total stellar flux, a better detection, and a higher S/N spectrum. It also shows that the technique does not introduce significant astrometric errors.

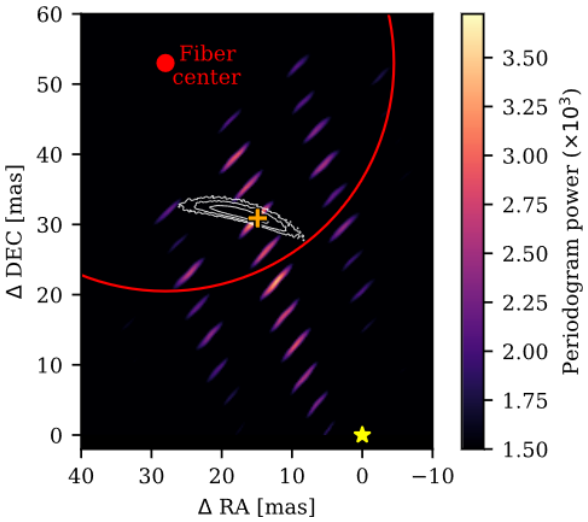

Fig. 7. Periodogram from the astrometry fit of the observations of *Gaia*...6464 B. The best-fit position of the *Gaia*...6464 B according to the ExoGRAVITY pipeline is indicated by the orange plus symbol. The position of the primary star is marked by the yellow symbol. The white contour lines are the *Gaia*-based position probability density of the dark companion (from inside to outside: 68, 95, and 99.7 % of the total set of position predictions). The position of the SC fiber in the field is given by the red dot, while the fiber field of view (50% flux injection limit) is shown by the red circle.

3.3. Application to Gaia... 6464 B on the unit telescopes

We compiled a list of objects from the *Gaia* NSS catalog with candidate substellar companions that are accessible for direct confirmation with GRAVITY (Winterhalder et al. 2024). As a proof of concept, we observed the candidate *Gaia*...6464 with the UTs during a technical time request for the science verification of a GRAVITY FT upgrade (60.A-9102).

3.3.1. Observations and data reduction

We predict the position of *Gaia*...6464 B from the NSS catalog orbital solution, assuming that the companion does not contribute to the flux observed in the *G*-band and that the companion mass is the lower estimate listed in the *Gaia* DR3 `binary_masses` table. We use a randomization procedure to obtain the projected position probability shown in Fig. 7. The companion position is predicted with ±5 mas uncertainty on separation, and ±8° uncertainty on positional angle at 1σ. Given the short predicted separation for the companion (close to 35 mas), we pointed the science fiber 25 mas away from the predicted position to reduce the host star flux injection, as described in Sect. 2.2.1. GRAVITY was set to medium spectral resolution and we used the dual-field on-axis mode. A detailed summary of the observing conditions and exposure time settings can be found in Table 2.

We applied the standard ExoGRAVITY pipeline, except that we reduced the polynomial order to 3 for the speckle fit, as described in Sect. 2.2.2. Figure 7 shows the resulting periodogram. *Gaia*...6464 B is detected at a separation of 34 mas and

Table 2. Log for the GRAVITY observations on the unit telescopes.

Date: 2022-11-09			
Observing time	Airmass	τ_0	Seeing
01:51:09/02:57:59	1.54–2.16	3.5–9.6 ms	0.35–0.88″
Target	ΔRA/ΔDec[(a)]	NEXP/NDIT/DIT	
Gaia...6464 A	0/0 mas	4/12/10 s	
Gaia...6464 B	28/53 mas	16/4/30 s	

Notes. [(a)]SC fiber position relative to the star.

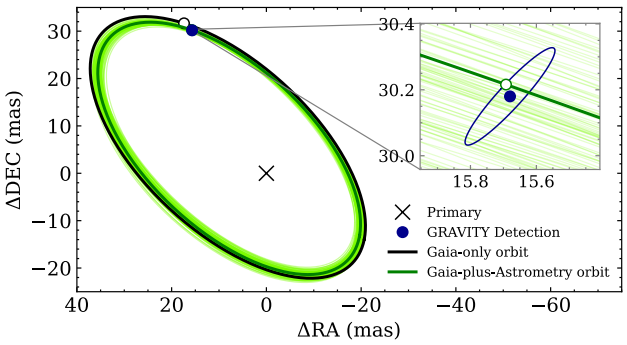

Fig. 8. Orbit of the companion *Gaia*...6464 B. The original *Gaia* orbit is shown in black. The refined orbit resulting from the combination of the *Gaia* solution and the astrometric position measurement provided by GRAVITY is shown in dark green. The light green shows a random subset of the sampled solutions probed during the MCMC run. The blue dot indicates the GRAVITY measurement with the ellipse describing the associated uncertainty. On the main plot, the black circle shows the position of the companion at the time of the observation as predicted by the *Gaia*-only orbital solution. On the inner plot, the green circle shows the position of the companion from the refined orbital solution including the GRAVITY observation.

2.5 mas from the predicted position. The contrast at K-band, corrected for fiber injection loss, is $(3.1 \pm 0.5) \times 10^{-3}$. We confirmed the detection by injecting and recovering synthetic companions in the data at similar contrasts, as described in Sect. 2.3. All the injected companions were correctly retrieved by the pipeline.

3.3.2. Dynamical mass determination

The use of the fiber off-pointing and the lower-order polynomial for speckle fitting allowed a direct observation of *Gaia*...6464 B at the innermost separations possible with the ExoGRAVITY technique. This detection can be used to infer the dynamical masses of the companion and primary, and to further constrain the orbital solution presented in the *Gaia* NSS catalog. To this end, we require two pieces of information from the GRAVITY direct imaging: confirmation of the dark companion hypothesis and the precise relative astrometry.

We used a Markov Chain Monte Carlo (MCMC) framework based on Foreman-Mackey et al. (2013) to combine *Gaia* and GRAVITY data. It should be noted that *Gaia* NSS data must be handled with care when used in combination with MCMC methods, especially for low-eccentricity orbits (Babusiaux et al. 2023). We used BINARYS (Leclerc et al. 2023) to confirm that our MCMC analysis of *Gaia*...6464 B is well-behaved and gives results similar to the those obtained with the local linear approximation technique.

The direct observation provides the companion-to-star flux ratio, which is crucial for mass determination. We compared the mass results under two different assumptions: either the photocenter observed by *Gaia* is fully coincident with the primary position (dark-companion assumption), or the companion-to-primary flux ratio in the *Gaia* band in the visible is the same as the flux ratio measured at K band (faint-companion assumption). We find a companion mass that is $2\,M_{\rm Jup}$ higher under the faint-companion assumption and comparable error bars of the order of $3\,M_{\rm Jup}$ under the two assumptions. As the two hypotheses give similar results, and given that the flux ratio in the G band is expected to be lower than in the K band, the following orbital fit and mass determination remain under the dark-companion assumption.

The MCMC-based combination of observations from *Gaia* and GRAVITY results in an updated set of posterior distributions. In a Bayesian sense, these updated posteriors correspond to a more accurate description of the system, unless the *Gaia* and GRAVITY data conflict in some significant way. The initial and updated orbital solutions projected onto the sky plane are shown in Fig. 8. The *Gaia*-only solution is derived from the NSS catalog, and uses the primary mass derived by isochrone fitting (listed in the *Gaia* DR3 `binary_masses` table). The *Gaia*-only orbit also assumes the lower-limit mass ratio between companion and host. As expected, the *Gaia*-only orbit and the *Gaia*+GRAVITY orbit are in good agreement. While the *Gaia* astrometry alone cannot constrain the individual masses, it is striking that a single observation with GRAVITY is sufficient to narrowly constrain the mass of the companion and the primary. We obtain $M_1 = 0.53^{+0.02}_{-0.02}\,M_\odot$ and $M_2 = 78.34^{+2.62}_{-2.50}\,M_{\rm Jup}$. The detected companion sits at the upper limit of the conventional mass range of brown dwarfs (13 to $80\,M_{\rm Jup}$). A detailed description of the method, along with the study of this companion and other targets are presented in Winterhalder et al. (2024).

4. Detection limits

Evaluation of the instrumental limits of detection is necessary in order to properly use nondetections in a statistically significant manner. Such an evaluation also allows the instrument to be placed in the larger instrumental landscape. This information is not yet available in the literature for GRAVITY. The goal of this section is to provide quantitative numbers on this question. Furthermore, this work allows us to comment on the possible nature of the noise process that limits the achievable contrast.

4.1. Contrast curves

We used the injection and retrieval technique described in Sect. 2.3. The data set consists of five archival ExoGRAVITY observations on the UTs (details in Appendix B) with the position of the SC fiber ranging from 54 to 136 mas. Archival observations are selected based on the criteria of having a bright primary ($K < 6.5$) and good atmospheric conditions (seeing <0.85 arcsec). The integration time for all observations is $5 \times 32 \times 10$ s (27 min) spread over 1 h to take advantage of the rotation of the UV plane. We simulated the fiber off-pointing technique below 80 mas separation (Sect. 2.2.1) by injecting the synthetic companion not at the fiber separation but closer to the host star. The retrieval process is computationally intensive, and so we limited the number of companions injected to five per separation and contrast. The five different injections were

performed at different positional angles to shuffle the possible effects of individual interferometric speckles in the observations. The separation of the injected companions is chosen in a range of maximum ±25 mas around the position of the SC fiber (see Table B.1). The ability to detect companions is significantly affected by the positional angle of the star companion with respect to the UV plane. Therefore, in the following study, we chose the positional angles for planet injection based on the orientation of the VLTI baselines and not on the positional angle of the SC fiber. We tested companion retrieval at the most optimal angle (i.e., parallel to the longest baselines on the UV plane) and at the least optimal angle (i.e., perpendicular to the longest baselines). After the companion injection, we ran the ExoGRAVITY pipeline to retrieve the companion signal. We average the signal from the 32 NDITs of individual exposures before reduction (fast mode of the ExoGRAVITY pipeline) in order to perform hundreds of injections and retrievals within a reasonable time frame.

The results are shown in Fig. 9. The contrast curve is obtained at 1σ when fewer than four out of the five companions are retrieved at the separation and contrast investigated. We cannot significantly determine 2σ or 3σ limits because of the limited number of companions injected. When the positional angle is parallel to the longest VLTI baselines, the sudden loss of sensitivity between 40 and 50 mas is due to the subtraction of the companion signal by the polynomial (Sect. 2.2.2). At separations of greater than 90 mas, the detection limit reaches 3×10^{-5} contrast ($\Delta K = 11.3$ mag). When the positional angle is perpendicular to the longest VLTI baselines, the contrast limit below 70 mas is ten times shallower than in the best position-angle case. The relative orientation must be considered when planning an observation. Beyond 130 mas separations, the contrast limit reaches 3×10^{-5} and the UV plane orientation no longer has any influence.

Finally, we explored the performance at larger separations. To this end, we performed additional injection and retrieval tests at 320 mas separation on AF Leporis b observations. The detection limit is at a contrast of 5.1×10^{-6} ($\Delta K = 13.2$ mag).

4.2. Empirical analysis of limitations

Detection on GRAVITY can be limited by either correlated noise or statistical noise in the measured visibilities. Correlated noise can be caused by stellar speckles that are not correctly fitted by the polynomial modeling. White noise is due to photon noise and detector noise.

We investigated the detection limit for different observing times using archive observations on the UT on HD 206893 (with the fiber at 111 mas separation) and β Pictoris (with the fiber at 92 mas separation). Both data sets have excellent atmospheric conditions and are bright enough for the AO to operate at the nominal regime. The HD 206893 data set has an exposure time of $27 \times 32 \times 10$ s (2.4 h) and spans over 3.5 h. The β Pictoris data set has an exposure time of $13 \times 32 \times 10$ s (1.2 h) and spans over 2.2 h. We select successive exposures in the data set to mimic a shorter observation time.

The results are summarized in Fig. 10. The evolution of the limit contrast roughly follows the inverse square root of the integration time. However, β Pictoris is seven times brighter in K-band than HD 206893. If limited by the photon noise of stellar flux leaking into the SC fiber, we expect the contrast to be $\sqrt{7} \approx 2.6$ deeper on β Pictoris than on HD 206893 at the same

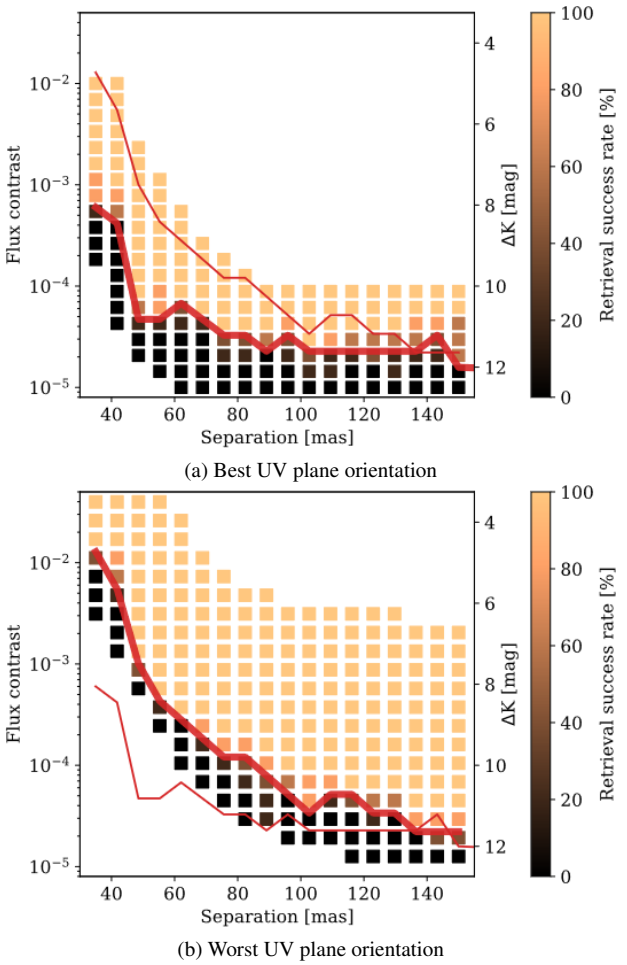

(a) Best UV plane orientation

(b) Worst UV plane orientation

Fig. 9. Rates for successful retrieval of injected companions in ExoGRAVITY observations with 10 s DIT and 27 min exposure time on the UT. (a) Retrieval when the star–companion couple is oriented in the direction of the longest VLTI baselines. (b) Retrieval when the star–companion couple is oriented perpendicular to the longest VLTI baselines. The red curves are the 1σ contrast limits for the best and worst UV plane orientation, shown as thick or thin lines alternatively depending on the background plot.

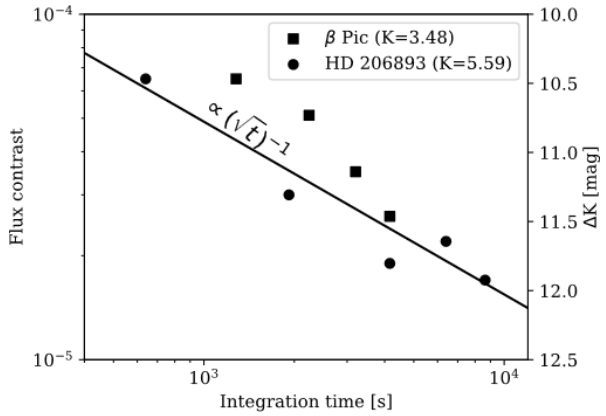

Fig. 10. Limit contrasts at 1σ with respect to the total exposure time (NEXP × NDIT × DIT). The solid line corresponds to the inverse square root of the integration time, with a proportionality constant of 1.5×10^{-3} in flux contrast.

Table 3. Parameters for the computation of the theoretical contrast curve.

Parameter	Value
DIT	10 s
$\mathrm{NDIT_{tot}}$	160
RON	9 photons/DIT
$N_{\mathrm{pixels}}{}^{(a)}$	11 184
Fluxes	
$T_0{}^{(b)}$	1 %
$F_{\mathrm{s}}{}^{(c)}$	7×10^8 photons s^{-1}
$V_{\mathrm{c}}{}^{(d)}$	$0.8 \times F_{\mathrm{c}}$

Notes. [(a)]There are 24 ABCD outputs on the detector, 233 pixels in the spectral direction, and the spectrum is two pixels wide. [(b)]Total transmission of the VLTI and GRAVITY when the SC fiber is at 0 mas separation. [(c)]Flux of HD 206893 for a single telescope. Computed from the star magnitude in K-band and the UT collecting surface. [(d)]We estimate the instrumental visibility to be 0.8.

integration time. Instead, we observe that the detection limit follows a similar $\sqrt{t}^{-1}$ trend for both stars. This indicates that the detection is not limited by photon noise, but by other features that are still averaging over the integration time. The situation is similar in classical imaging where the detection limit evolves with the characteristic lifetime of the speckles in the field. From an operational point of view, we can conclude that extending the integration time up to 90 min is a way to push the contrast limit down to 2×10^{-5} ($\Delta K = 11.7$ mag) at 100 mas.

Overall, GRAVITY seems to be limited by systematic uncertainties that scale with the speckle flux. This explains why the off-pointing technique described in Sect. 2.2.1 has a significant impact on the detection limit, as would any further reduction of the stellar leak.

4.3. Comparison with the theoretical limit

The detection limits can also be determined analytically. Considering the photon noise from the star flux leaking in the fiber at the companion position and the readout noise of the SC camera, we can derive a S/N using

$$S/N = \frac{\eta \sum_{b,\lambda} |G(b,\lambda)\, V_{\mathrm{c}}(b,\lambda)|\, \mathrm{DIT}\, \mathrm{NDIT_{tot}}}{\sqrt{\sum_{m,\lambda} T(m,\lambda)\, F_{\mathrm{s}}(m,\lambda)\, \mathrm{DIT}\, \mathrm{NDIT_{tot}} + RON^2\, N_{\mathrm{pixels}}\, \mathrm{NDIT_{tot}}}}, \quad (15)$$

where η is the fraction of companion signal remaining after subtracting the speckles polynomial, $\mathrm{NDIT_{tot}}$ is the total number of integrations (NEXP × NDIT), RON is the read-out noise of the SC camera (Teledyne H2RG), and N_{pixels} is the number of pixels used on the detector. The other parameters are described in Eqs. (2) and (4).

From Eq. (15) and parameter values listed in Table 3, we can derive a limiting planet-to-star contrast for a given S/N. The results are shown in Fig. 11. The photon noise from the star largely dominates the statistical noise. The detection limit at $S/N = 1$ allows direct comparison with the 1σ empirical contrast curve. This comparison shows that the theoretical detection limits are a factor 12 lower than the empirical detection limits determined from injection and retrieval. We show in Sect. 4.2 that photon noise is not the limitation in actual observations at 100 mas separation. The findings shown in this section confirm that result.

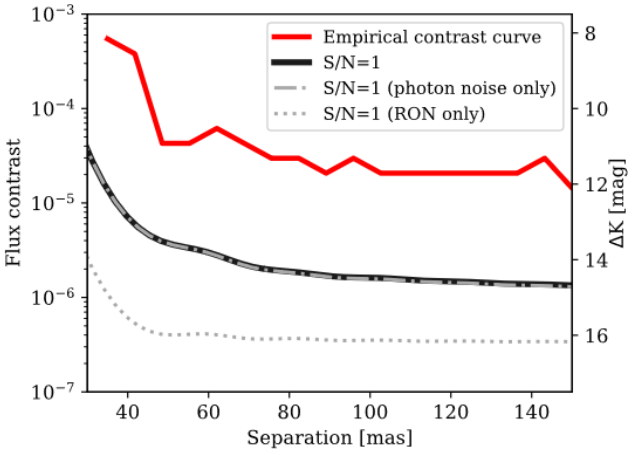

Fig. 11. Theoretical contrast curves for $S/N = 1$ (solid black) compared to the contrast curve derived from the injection and retrieval at a favorable positional angle (red). An indicative contrast curve is given with only the camera readout noise as a noise source (dotted black) and only the photon noise (dashed-dotted black). The theoretical contrast curves are computed for a host star of K-band magnitude 5.6 similar to HD 206893 used in the injection–retrieval data set.

5. Discussion

5.1. Summary

In this paper, we detail a proposed observing strategy and adjustment of the data reduction pipeline required to enable exoplanet observations at shorter separations with GRAVITY. We validated the proposed strategy and demonstrated the *Gaia*–GRAVITY synergy with the detection and mass determination of the short-separation companion *Gaia*...6464 B. We finally explored the actual capabilities of GRAVITY by deriving realistic contrast curves. The most important results of this work can be summarized as follows:

- The fiber off-pointing strategy brings a contrast improvement of up to a factor of six for dual-field observations of companions below 80 mas separation. The implementation of this technique is straightforward;
- The inner working angle has become narrower since the upgrade of the GRAVITY FT. Below 45 mas, fitting the stellar speckles with a third-order polynomial gives better results than the fourth or sixth-order polynomials previously recommended;
- Our detection of the brown dwarf *Gaia*...6464 B shows how the combination of *Gaia* and GRAVITY leads to a precise measurement of the dynamical masses of the companion ($78.34^{+2.62}_{-2.50}\, M_{\mathrm{Jup}}$) and the primary ($0.53^{+0.02}_{-0.02}\, M_{\odot}$). The detection of the brown dwarf is an archetypal example of a GRAVITY observation at the edge of the inner working angle;
- In dual-field mode, GRAVITY can observe companions at contrasts of 4×10^{-5} ($\Delta K = 11$ mag) down to a separation of 75 mas. Due to the limited sampling of the UV plane on the UT, the detection limits below 100 mas are strongly affected by the relative orientation between the primary/secondary and the longest baselines;

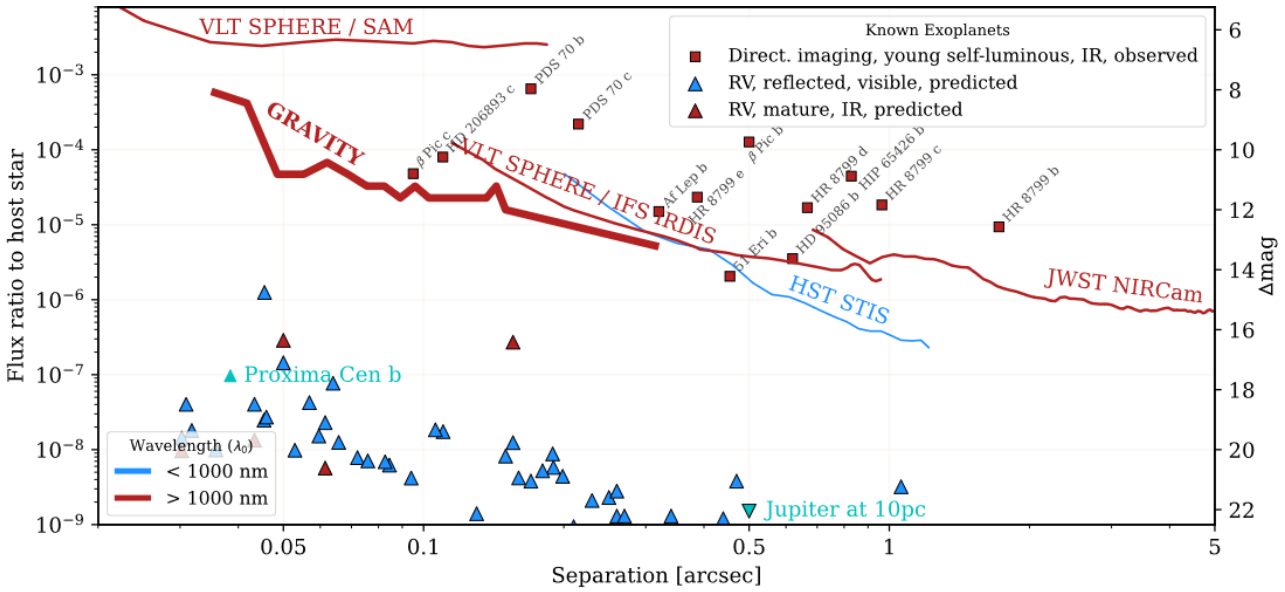

Fig. 12. Detection limits of some representative instruments dedicated to direct observations of exoplanets. GRAVITY detection limit corresponds to the inner part of the on-axis mode of the instrument only. It is limited to 27 min exposure time and companions oriented parallel to the longest baselines of the VLTI. Plot adapted from Dr. Bailey script available at https://github.com/nasavbailey/DI-flux-ratio-plot. The HST/STIS curve is from Ren et al. (2017). VLT SPHERE/IFS IRDIS is from Langlois et al. (2021). VLT SPHERE/SAM is from Stolker et al. (2024). VLT JWST/NIRCam is from Carter et al. (2023). (Blue triangles) Estimated reflected flux in the visible for exoplanets observed using the radial velocity technique. The estimation follows a Lambertian model with radii fixed at 1 $R_{\rm Jup}$ and a geometric albedo of 0.5. (Red triangle) Estimated infrared flux for mature exoplanets observed using the radial velocity technique. Computed from equilibrium temperature estimates and planet radii fixed at 1 $R_{\rm Jup}$. All visible and infrared estimated fluxes are based on Traub & Oppenheimer (2010).

– Observing the same target for about 3h pushes the detection limit down to 2×10^{-5} ($\Delta K = 11.7$ mag) at 100 mas. The limiting factor appears to be speckle structures whose amplitude scales with the coherent flux and that slowly average over time.

These findings are the result of experience gained over 5 yr of exoplanet and brown dwarf observations with GRAVITY. A better understanding of the instrument enabled us to identify promising avenues for improving observations and to consider possible synergies with other instruments.

5.2. Comparison with other direct imaging instruments

Figure 12 compares the contrast curve of GRAVITY estimated in this paper with those of some other exoplanet-imaging instruments. This paper focuses on companion observations with GRAVITY below 300 mas separation. However, it should be noted that the off-axis mode of the instrument allows observations at separations of up to 2 arcsec on the UT. For separations of greater than 200 mas, the detection capabilities of GRAVITY are comparable to single-telescope imagers. Indeed, all exoplanets directly imaged with SPHERE at the VLT have also been detected with GRAVITY. GRAVITY is especially useful because of its 50 μas precision in relative astrometry and its higher spectral resolution. For long-period orbits, the accurate astrometry of GRAVITY can constrain orbital parameters within a few years. Moreover, these accurate astrometric observations will adequately complement further observations at the same level of accuracy as should be achieved by the E-ELT, providing a large time baseline.

Closer than 200 mas, GRAVITY is unique because this region is mostly beyond the reach of current single-telescope instruments. For instance, β Pictoris c and HD 206893 c are easily detected by GRAVITY but have so far remained undetected by SPHERE or GPI. We note that the molecular mapping technique is being increasingly used for exoplanet detection and characterization (Vigan et al. 2024). Molecular mapping has formally no self-subtraction inner working angle (unlike the spectral or angular differential deconvolutions). Instead, the method relies on the signal provided by sharp spectral features in the companion spectra, and is therefore highly photon consuming and requires longer integration times; it is blind to the continuum part of the spectrum, including the absolute flux of the companion. This is complementary to GRAVITY observations at moderate spectral resolution. The question of whether or not the molecular mapping technique can be applied to GRAVITY data themselves remains unanswered.

5.3. Synergy with Gaia

Brown dwarf companion candidates are already available in *Gaia* DR3. The next *Gaia* DR4 will provide the individual epochs of the stellar proper motion and a catalog of possibly thousands of planetary-mass companions suitable for characterization from the ground.

Figure 13 combines the GRAVITY detection limits derived in this paper with the expected *Gaia* sensitivity to substellar companions (Sozzetti 2010). This comparison shows that the GRAVITY sensitivity already overlaps with the *Gaia* sensitivity to companions in the 50 to 100 mas separation range around the nearest stars. Thus, GRAVITY bridges the gap for direct detection of these *Gaia* candidates before the E-ELT instruments (Houllé et al. 2021). We note that Fig. 13 uses the favorable

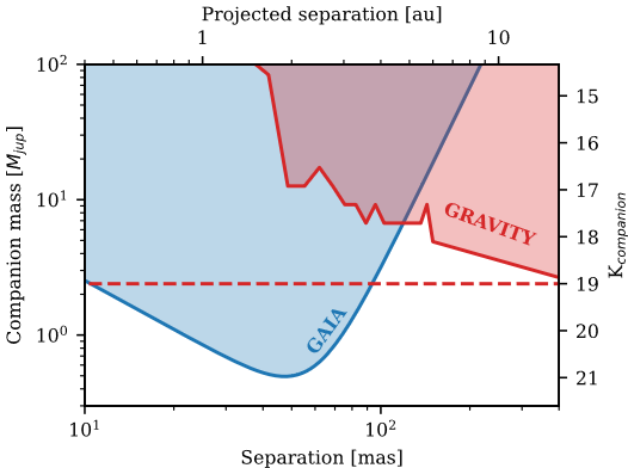

Fig. 13. Comparison of the sensitivity of *Gaia* and GRAVITY for a K=6 mag star at 40 pc. The *Gaia* sensitivity curve is adapted from Sozzetti (2010). The scaling of the K-magnitude with the mass is estimated from the observations of *Gaia*...6464 B analyzed in this paper and previous companion observations from the ExoGRAVITY program. The dashed red line shows the current K-magnitude limit in the SC of GRAVITY.

case of a star located at 40 pc to convert the linear and angular separation. For more distant stars, the *Gaia* sensitivity peak shifts toward even shorter angular separation. This highlights the interest of the unique inner working angle of GRAVITY and emphasizes the importance of pushing the instrument to even shorter separations and deeper contrast.

5.4. Perspectives with GRAVITY+

The GRAVITY+ upgrade includes a faint mode that turns off the metrology lasers during the acquisitions to provide better S/N for faint targets (Widmann et al. 2022) and a new extreme AO at the Coudé focus of the four UTs (Eisenhauer 2019). The replacement of the 20 yr-old MACAO will significantly improve the wavefront correction for atmospheric turbulence and enable correction of instrument internal aberrations (not possible with the current AO). The expected performance is a Strehl ratio of about 0.8 on natural guide stars, compared with the ratio of ∼0.3 presently provided by MACAO. This fact alone will already contribute to limiting the starlight injection at the planet's position by a factor 3 to 4. However, it is possible to go even further. The higher level of AO performance will allow wavefront control techniques to further reduce the starlight at the fiber position when observing the companion (Pourré et al. 2022). The technique consists in injecting offset modes in the AO to tackle diffraction and static aberrations that couple into the SC fiber. Assuming a telescope close to the diffraction limit, and together with the fiber position offset presented in this paper, this technique could reduce the speckle amplitude by up to two orders of magnitude at separations of from 60 to 140 mas. In real conditions on-sky, Xin et al. (2023) showed that wavefront control on KPIC can result in up to a factor 3 reduction in K-band stellar flux injected into a single-mode fiber at 2 λ/D. It indicates that, overall, the developments at VLTI and GRAVITY might push the contrast limits to 3×10^{-6} (ΔK = 13.8 mag) down to 60 mas separation. For the closest stars in our galactic neighborhood, this will enable observations of the young Jupiter-mass planets, possibly down to the snowline at 2 to 5 au from their star.

Acknowledgements. This work is based on observations collected at the European Southern Observatory under ESO programmes 1104.C-0651, 0110.C-0182, 60.A-9102 and 0112.C-2396(C). We would like to thank the Paranal staff, especially the engineers, technicians and astronomers on the VLTI. This work has also made use of data from the European Space Agency (ESA) mission *Gaia* (https://www.cosmos.esa.int/gaia), processed by the *Gaia* Data Processing and Analysis Consortium (DPAC, https://www.cosmos.esa.int/web/gaia/dpac/consortium). Funding for the DPAC has been provided by national institutions, in particular the institutions participating in the *Gaia* Multilateral Agreement. The authors acknowledge the support of the French Agence Nationale de la Recherche (ANR), under grant ANR-21-CE31-0017 (project ExoVLTI). D.D. acknowledges the support from the ERC under the European Union's Horizon 2020 research and innovation program (grant agreement CoG – 866070). G.D.M. acknowledges the support of the DFG priority program SPP 1992 "Exploring the Diversity of Extrasolar Planets" (MA 9185/1) and from the Swiss National Science Foundation under grant 200021_204847 "PlanetsInTime". Parts of this work have been carried out within the framework of the NCCR PlanetS supported by the Swiss National Science Foundation. J.J.W., A.C., and S.B. acknowledge the support of NASA XRP award 80NSSC23K0280. This research has made use of the NASA Exoplanet Archive, which is operated by the California Institute of Technology, under contract with the National Aeronautics and Space Administration under the Exoplanet Exploration Program. This research has also made use of the Jean-Marie Mariotti Center `Aspro` service (Available at `http://www.jmmc.fr/aspro`). This research has also made use of the following python packages: matplotlib (Hunter 2007), numpy (Harris et al. 2020), hcipy (Por et al. 2018) and astropy (Astropy Collaboration 2018).

References

Abuter, R., Dembet, R., Lacour, S., et al. 2016, SPIE Conf. Ser., 9907, 990721
Anugu, N., Amorim, A., Gordo, P., et al. 2018, MNRAS, 476, 459
Arsenault, R., Alonso, J., Bonnet, H., et al. 2003, SPIE Conf. Ser., 4839, 174
Astropy Collaboration (Price-Whelan, A. M., et al.) 2018, AJ, 156, 123
Babusiaux, C., Fabricius, C., Khanna, S., et al. 2023, A&A, 674, A32
Beuzit, J. L., Vigan, A., Mouillet, D., et al. 2019, A&A, 631, A155
Boccaletti, A., Chauvin, G., Wildi, F., et al. 2022, SPIE Conf. Ser., 12184, 121841S
Bonnell, I. A., Clark, P., & Bate, M. R. 2008, MNRAS, 389, 1556
Boss, A. P. 1997, Science, 276, 1836
Bowler, B. P., Blunt, S. C., & Nielsen, E. L. 2020, AJ, 159, 63
Carter, A. L., Hinkley, S., Kammerer, J., et al. 2023, ApJ, 951, L20
Davies, R., Absil, O., Agapito, G., et al. 2023, A&A, 674, A207
Eisenhauer, F. 2019, in The Very Large Telescope in 2030, 30
Foreman-Mackey, D., Hogg, D. W., Lang, D., & Goodman, J. 2013, PASP, 125, 306
Franson, K., Bowler, B. P., Brandt, T. D., et al. 2022, AJ, 163, 50
Gaia Collaboration (Vallenari, A., et al.) 2023, A&A, 674, A1
GRAVITY Collaboration (Abuter, R., et al.) 2017, A&A, 602, A94
GRAVITY Collaboration (Nowak, M., et al.) 2020, A&A, 633, A110
GRAVITY Collaboration (Abuter, R., et al.) 2021, A&A, 647, A59
GRAVITY Collaboration (Abuter, R., et al.) 2022, A&A, 657, A82
GRAVITY+ Collaboration (Abuter, R., et al.) 2022, The Messenger, 189, 17
Halbwachs, J.-L., Pourbaix, D., Arenou, F., et al. 2023, A&A, 674, A9
Harris, C. R., Millman, K. J., van der Walt, S. J., et al. 2020, Nature, 585, 357
Hinkley, S., Carter, A. L., Ray, S., et al. 2022, PASP, 134, 095003
Hinkley, S., Lacour, S., Marleau, G. D., et al. 2023, A&A, 671, A5
Holl, B., Sozzetti, A., Sahlmann, J., et al. 2023, A&A, 674, A10
Houllé, M., Vigan, A., Carlotti, A., et al. 2021, A&A, 652, A67
Hunter, J. D. 2007, Comput. Sci. Eng., 9, 90
Jovanovic, N., Delorme, J. R., Bond, C. Z., et al. 2019, ArXiv e-prints, [arXiv:1909.04541]
Lacour, S., Dembet, R., Abuter, R., et al. 2019, A&A, 624, A99
Lacour, S., Wang, J. J., Rodet, L., et al. 2021, A&A, 654, L2
Langlois, M., Gratton, R., Lagrange, A. M., et al. 2021, A&A, 651, A71
Lapeyrere, V., Kervella, P., Lacour, S., et al. 2014, SPIE Conf. Ser., 9146, 91462D
Leclerc, A., Babusiaux, C., Arenou, F., et al. 2023, A&A, 672, A82
Lozi, J., Ahn, K., Clergeon, C., et al. 2022, SPIE Conf. Ser., 12185, 1218533
Macintosh, B., Graham, J. R., Ingraham, P., et al. 2014, PNAS, 111, 12661
Marois, C., Lafrenière, D., Doyon, R., Macintosh, B., & Nadeau, D. 2006, ApJ, 641, 556
Meshkat, T., Bonnefoy, M., Mamajek, E. E., et al. 2015, MNRAS, 453, 2378
Mizuno, H. 1980, Progr. Theoret. Phys., 64, 544
Nielsen, E. L., De Rosa, R. J., Macintosh, B., et al. 2019, AJ, 158, 13
Nowak, M., Lacour, S., Lagrange, A. M., et al. 2020, A&A, 642, L2
Nowak, M., Lacour, S., Abuter, R., et al. 2024, A&A, in press, https://doi.org/10.1051/0004-6361/202449504

Otten, G. P. P. L., Vigan, A., Muslimov, E., et al. 2021, A&A, 646, A150
Perraut, K., Jocou, L., Berger, J. P., et al. 2018, A&A, 614, A70
Pfuhl, O., Haug, M., Eisenhauer, F., et al. 2012, SPIE Conf. Ser., 8445, 84451U
Por, E. H., Haffert, S. Y., Radhakrishnan, V. M., et al. 2018, Proc. SPIE, 10703, , 1070342
Pourré, N., Le Bouquin, J.-B., Woillez, J., et al. 2022, SPIE Conf. Ser., 12183, 121830V
Racine, R., Walker, G. A. H., Nadeau, D., Doyon, R., & Marois, C. 1999, PASP, 111, 587
Ren, B., Pueyo, L., Perrin, M. D., Debes, J. H., & Choquet, É. 2017, SPIE Conf. Ser., 10400, 1040021
Sozzetti, A. 2010, EAS Pub. Ser., 45, 273
Sparks, W. B., & Ford, H. C. 2002, ApJ, 578, 543
Stolker, T., Kammerer, J., Benisty, M., et al. 2024, A&A, 682, A101
Stone, J. M., Skemer, A. J., Hinz, P. M., et al. 2018, AJ, 156, 286
Traub, W. A., & Oppenheimer, B. R. 2010, in Exoplanets, ed. S. Seager (Tucson, AZ: University of Arizona Press), 111
Vigan, A., Fontanive, C., Meyer, M., et al. 2021, A&A, 651, A72
Vigan, A., El Morsy, M., Lopez, M., et al. 2024, A&A, 682, A16
Wang, J. J., Kulikauskas, M., & Blunt, S. 2021a, Astrophysics Source Code Library, [record ascl:2101.003]
Wang, J. J., Vigan, A., Lacour, S., et al. 2021b, AJ, 161, 148
Widmann, F., Gillessen, S., Ott, T., et al. 2022, SPIE Conf. Ser., 12183, 121830U
Winterhalder, T. O., Lacour, S., Mérand, A., et al. 2024, A&A, submitted [arXiv:2403.13055]
Woillez, J., Abad, J. A., Abuter, R., et al. 2019, A&A, 629, A41
Xin, Y., Xuan, J. W., Mawet, D., et al. 2023, J. Astron. Telescopes Instrum. Syst., 9, 035001

[1] Univ. Grenoble Alpes, CNRS, IPAG, 38000 Grenoble, France
e-mail: nicolas.pourre@univ-grenoble-alpes.fr
[2] European Southern Observatory, Karl-Schwarzschild-Straße 2, 85748 Garching, Germany
[3] LESIA, Observatoire de Paris, PSL, CNRS, Sorbonne Université, Université de Paris, 5 place Janssen, 92195 Meudon, France
[4] Institute of Astronomy, University of Cambridge, Madingley Road, Cambridge CB3 0HA, UK
[5] Universidade de Lisboa – Faculdade de Ciências, Campo Grande, 1749-016 Lisboa, Portugal
[6] CENTRA – Centro de Astrofísica e Gravitação, IST, Universidade de Lisboa, 1049-001 Lisboa, Portugal
[7] Max Planck Institute for Astronomy, Königstuhl 17, 69117 Heidelberg, Germany
[8] Department of Physics & Astronomy, Johns Hopkins University, 3400 N. Charles Street, Baltimore, MD 21218, USA
[9] Space Telescope Science Institute, 3700 San Martin Drive, Baltimore, MD 21218, USA
[10] Center for Interdisciplinary Exploration and Research in Astrophysics (CIERA) and Department of Physics and Astronomy, Northwestern University, Evanston, IL 60208, USA
[11] Max Planck Institute for extraterrestrial Physics, Giessenbachstraße 1, 85748 Garching, Germany
[12] Aix-Marseille Univ, CNRS, CNES, LAM, Marseille, France
[13] Université Côte d'Azur, Observatoire de la Côte d'Azur, CNRS, Laboratoire Lagrange, Bd de l'Observatoire, CS 34229, 06304 Nice cedex 4, France
[14] STAR Institute, Université de Liège, Allée du Six Août 19c, 4000 Liège, Belgium
[15] Leiden Observatory, Leiden University, PO Box 9513, 2300 RA Leiden, The Netherlands
[16] Department of Astrophysical & Planetary Sciences, JILA, Duane Physics Bldg., 2000 Colorado Ave, University of Colorado, Boulder, CO 80309, USA
[17] Institute of Astronomy, KU Leuven, Celestijnenlaan 200D, 3001 Leuven, Belgium
[18] Institute of Physics, University of Cologne, Zülpicher Straße 77, 50937 Cologne, Germany
[19] Max Planck Institute for Radio Astronomy, Auf dem Hügel 69, 53121 Bonn, Germany
[20] Universidade do Porto, Faculdade de Engenharia, Rua Dr. Roberto Frias, 4200-465 Porto, Portugal
[21] School of Physics, University College Dublin, Belfield, Dublin 4, Ireland
[22] School of Physics & Astronomy, University of Southampton, University Road, Southampton SO17 1BJ, UK
[23] Departments of Physics and Astronomy, Le Conte Hall, University of California, Berkeley, CA 94720, USA
[24] European Southern Observatory, Casilla 19001, Santiago 19, Chile
[25] Advanced Concepts Team, European Space Agency, TEC-SF, ESTEC, Keplerlaan 1, 2201 AZ Noordwijk, The Netherlands
[26] University of Exeter, Physics Building, Stocker Road, Exeter EX4 4QL, UK
[27] Fakultät für Physik, Universität Duisburg-Essen, Lotharstraße 1, 47057 Duisburg, Germany
[28] Institüt für Astronomie und Astrophysik, Universität Tübingen, Auf der Morgenstelle 10, 72076 Tübingen, Germany
[29] Center for Space and Habitability, Universität Bern, Gesellschaftsstrasse 6, 3012 Bern, Switzerland
[30] Astronomy Department, University of Michigan, Ann Arbor, MI 48109 USA
[31] Academia Sinica, Institute of Astronomy and Astrophysics, 11F Astronomy-Mathematics Building, NTU/AS campus, No. 1, Section 4, Roosevelt Rd., Taipei 10617, Taiwan
[32] European Space Agency (ESA), ESA Office, Space Telescope Science Institute, 3700 San Martin Drive, Baltimore, MD 21218, USA
[33] Department of Earth & Planetary Sciences, Johns Hopkins University, Baltimore, MD, USA
[34] Max Planck Institute for Astrophysics, Karl-Schwarzschild-Str. 1, 85741 Garching, Germany
[35] Excellence Cluster ORIGINS, Boltzmannstraße 2, 85748 Garching bei München, Germany
[36] DOTA, ONERA, 13661 Salon cedex AIR, France
[37] KRP Mechatec GmbH, Boltzmannstraße 2, 85748 Garching bei München, Germany
[38] Universidad de Valparaíso, Instituto de Física y Astronomía (IFA), Avenida Gran Bretaña 1111, Casilla 5030, Valparaíso, Chile
[39] Núcleo Milenio de Formación Planetaria (NPF), Valparaíso, Chile
[40] Univ. Lyon 1, ENS de Lyon, CNRS, Centre de Recherche Astrophysique de Lyon UMR5574, 69230, Saint-Genis-Laval, France

Appendix A: Complex visibilities for a planet detection on GRAVITY

Figure A.1 shows how we retrieve the companion signal buried in the speckle flux. The ExoGRAVITY reduction script performs a joint fit of the speckles and the planet on the complex visibilities. The correlated and uncorrelated noises can be seen in Fig. A.1b, especially on the U4-U3 and U3-U2 baselines, that provide a weak planet signal.

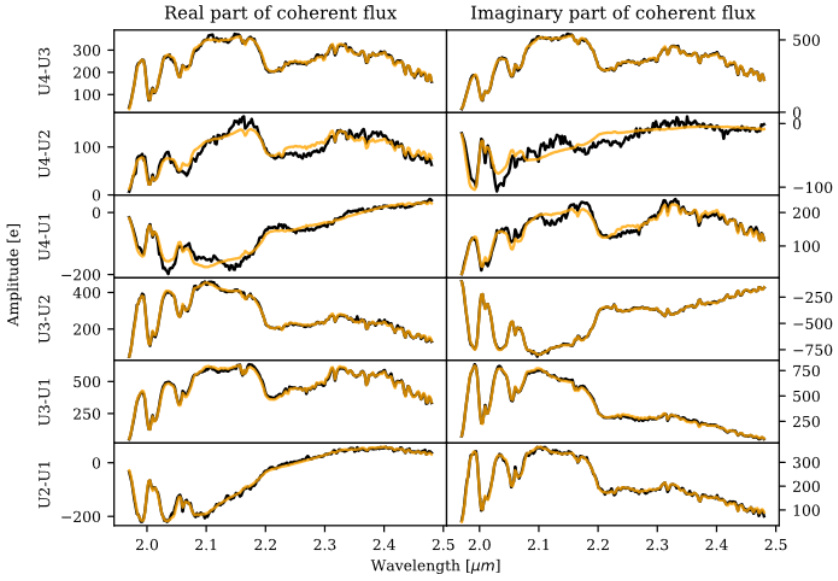

(a) Speckles fit

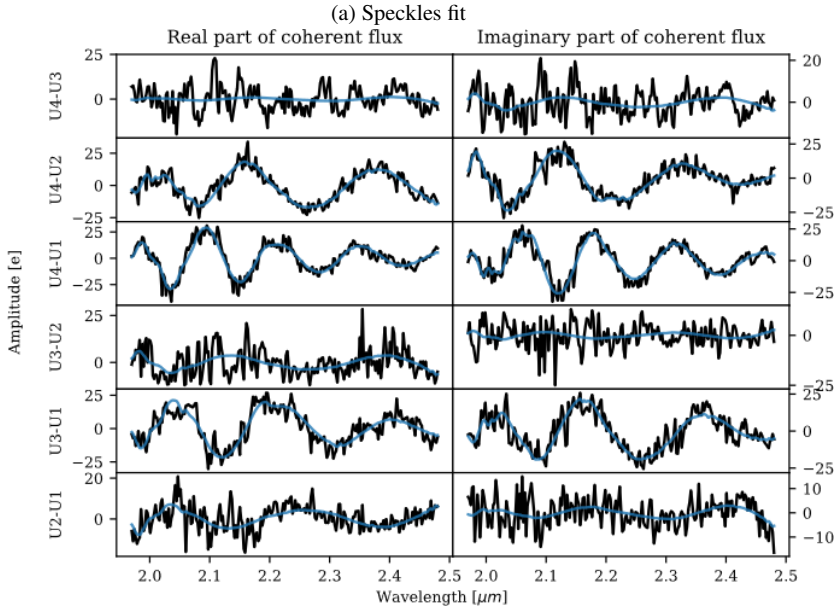

(b) Planet fit

Fig. A.1: Example of speckle fit (a) and planet fit (b) in GRAVITY complex visibilities for an injected companion at 68 mas separation and 8×10^{-4} contrast. (a) Black: Complex visibilities $V_{\text{oncompanion}}$ as outputted by the general GRAVITY pipeline and phase referenced on the star. Orange: Speckles fit with the polynomial modulation corresponding to the first term in Eq. (9). (b) Black: $V_{\text{oncompanion}}$ with the speckle fit subtracted. Blue: Planet fit, corresponding to the second term in Eq. (9)

Appendix B: ExoGRAVITY observations used for detection limits

For the companion injection and retrieval, we used archival ExoGRAVITY observations. We chose the observations based on the criteria of the relative separation of the SC fiber from the star, and good atmospheric conditions. Data sets are detailed in Table B.1.

Table B.1: Details of the ExoGRAVITY observations used for the companion injection and retrievals.

Injection separation limits	30 to 45 mas	45 to 70 mas
SC fiber separation [mas]	54	72
Target star	HD 17155	HD 206893[(a)]
Date	2022-08-19	2021-08-28
K star [mag]	6.5	5.6
Seeing [arcsec]	0.54	0.62
τ_0 [ms]	9-18	2-8
Integration time	$5 \times 32 \times 10$ s	$5 \times 32 \times 10$ s
Injection separation limits	**70 to 100 mas**	**100 to 130 mas**
SC fiber separation [mas]	92	111
Target star	β Pictoris	HD 206893
Date	2021-01-06	2021-10-17
K star [mag]	3.5	5.6
Seeing [arcsec]	0.45	0.50
τ_0 [ms]	8-12	2-4
Integration time	$5 \times 32 \times 10$ s	$5 \times 32 \times 10$ s
Injection separation limits	**130 to 150 mas**	**320 mas**
SC fiber separation [mas]	136	320
Target star	β Pictoris	AF Leporis
Date	2020-02-10	2023-12-23
K star [mag]	3.5	4.9
Seeing [arcsec]	0.81	0.52
τ_0 [ms]	6-15	5-10
Integration time	$5 \times 32 \times 10$ s	$5 \times 12 \times 30$ s

Notes. [(a)]The observations of HD 206893 on 2021-08-28 were performed in a search for the HD 206893 c planet and no planet was detected in this data set.

Digging a dark hole in GRAVITY: towards Jupiter-like observations at the astronomical unit scale

Nicolas Pourré[a], Jean Baptiste Le Bouquin[a], Julien Woillez[b], Alexis Carlotti[a], Lucie Leboulleux[a], Karine Perraut[a], and Sylvestre Lacour[b,c]

[a]Univ. Grenoble Alpes, CNRS, IPAG, 38000 Grenoble, France
[b]European Southern Observatory, Karl-Schwarzschild-Straße 2, 85748 Garching, Germany
[c]LESIA, Observatoire de Paris, PSL, CNRS, Sorbonne Université, Université de Paris, 5 place Janssen, 92195 Meudon, France

ABSTRACT

Since 2019, GRAVITY has obtained unprecedented direct observations of exoplanets at high contrasts (down to 5×10^{-5}) and small angular separations from the host star (down to 110 mas). To access deeper contrast (10^{-6}) at smaller angular separations (less than 100 mas), we propose to dig a dark hole at the planet position. It relies on wavefront control using the adaptive optics deformable mirror to minimize the stellar flux injected in the GRAVITY interferometric combiner. We tested this technique on-sky on the instrument and concluded that the maximal contrast improvement it can achieve is $\times 4$ on the current adaptive optics (NAOMI, MACAO). We also predict that the dark hole technique will bring a contrast improvement up to $\times 100$ at less than 140 mas on the future GRAVITY+ adaptive optics of the Unit Telescopes.

Keywords: high-contrast technique, adaptive optics, infrared interferometry

1. INTRODUCTION

Direct observations of exoplanets allow for both a characterisation of the orbits and of the atmosphere of the objects. Those observations are crucial for understanding the formation process of giant planets and the dynamical history of planetary systems. However, direct imaging instruments are currently restricted to the most massive objects ($> 5M_{jup}$) orbiting far from their host star (> 10 au). More, all the directly observed planets are young giant planets still radiating heat from their formation. In order to complete the picture of the giant planets population, observations of mature objects down to the snowline of planetary systems (~ 5 au) are required. The need for fainter exoplanets observations orbiting closer to their host star motivates a global instrumental effort towards high-contrast at short angular separation.

GRAVITY, a second generation instrument at the Very Large Telescope Interferometer (VLTI), is involved in this race for direct exoplanet observations. Thanks to the interferometric technique the instrument can disentangle stellar speckles from the planet even at short separations where other techniques such as Angular Differential Imaging are less efficient. This interferometric deconvolution provides a 10^3 contrast improvement (Fig. 1) down to a 3 mas separation (minimal angular resolution of the VLTI). GRAVITY already provided disruptive observations of Beta Pictoris c[1] at 130 mas and 4.8×10^{-5} raw contrast and PDS70 b and c[2] at 170 mas and 6.3×10^{-4} raw contrast. The instrument can provide relative astrometry at 60 μas precision and planet K-band spectrum at R=20, 500 or 4000.

The instrument has two fiber optics injection per telescope (before the recombination): the Fringe Tracker (FT) and the SCience fiber (SC). During exoplanets observations at separation smaller than 500 mas use the dual-field on-axis mode of the instrument. The FT is always on-axis, centered on the host-star, and the SC points at the off-axis planet or the star alternatively. The main limitation of GRAVITY compared to classical imaging methods is the restricted field of view of the SC, limited to 60 mas on the Unit Telescopes (UT) and 250 mas on the Auxiliary Telescopes (AT). The planet position must be known at this precision prior to the

Send correspondence to Nicolas Pourré
E-mail: nicolas.pourre@univ-grenoble-alpes.fr

Optical and Infrared Interferometry and Imaging VIII, edited by Antoine Mérand, Stephanie Sallum, Joel Sanchez-Bermudez, Proc. of SPIE Vol. 12183, 121830V · © 2022 SPIE · 0277-786X · doi: 10.1117/12.2629823

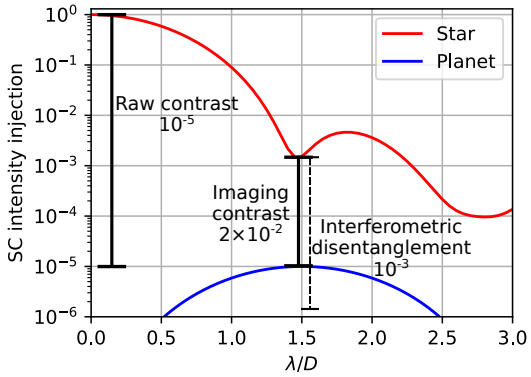

Figure 1. Injection intensity in the SC fiber with respect to the separation at the focal plane. The raw contrast is the ratio between the peak planet intensity and the peak star intensity. The imaging contrast is the ratio between the planet intensity and the star intensity at a given position. The interferometric disentanglement enable to observe planets down to 10^{-3} imaging contrasts.

observations. This is the price to pay on GRAVITY for observing closer than the inner working angle of classical imagers operating at 8-meter class telescopes.

A way to push deeper contrasts at short separation is to use the adaptive optics of the individual telescopes to limit the star injection in the SC. The method is called wavefront control and the goal is to create a dark-hole at the SC position. In this study we investigate the contrast improvement this method can bring on GRAVITY and the expected improvement with the future GRAVITY+ adaptive optics.

2. WAVEFRONT CONTROL FOR FIBER INJECTION AT SHORT SEPARATION

Wavefront control techniques for fiber injection has already been explored by several studies.[3,4] Here we are only interested at separations smaller than 3 λ/D (D being the diameter of individual telescopes). We want to find the modes that can limit the star injection in the fiber close to the diffraction limit.

2.1 Injection maps

The electric field injected E_{inj} in the fiber at the position x_0 of the focal plane is:

$$E_{inj}(x_0) = \int_{focal\ plane} E(x) M_f(x - x_0)\,\mathrm{d}x \tag{1}$$

with x the coordinate in the focal plane, $E(x)$ the electric field at the focal plane and $M_f(x)$ the mode of the fiber at focal plane. From (1) we obtain:

$$E_{inj}(x_0) = \{E(x) * M_f(x)\}(x_0) \tag{2}$$
$$E_{inj}(x_0) = \mathcal{F}[\mathcal{F}\{E(x)\}\mathcal{F}\{M_f(x)\}] \tag{3}$$
$$E_{inj}(x_0) = \mathcal{F}[P(u)M_p(u)] \tag{4}$$

with $P(u)$ the electric field at the pupil plane and $M_p(u)$ the fiber mode at the pupil plane. Equation (4) gives the electric field injected in the fiber at any fiber position (the injection map) directly from the wavefront and the fiber mode at pupil plane (Fig. 2).

We want E_{inj} to be as small as possible at a given position. As we are interested only in the short separations, we will be only interested in low-order modes at the pupil plane.

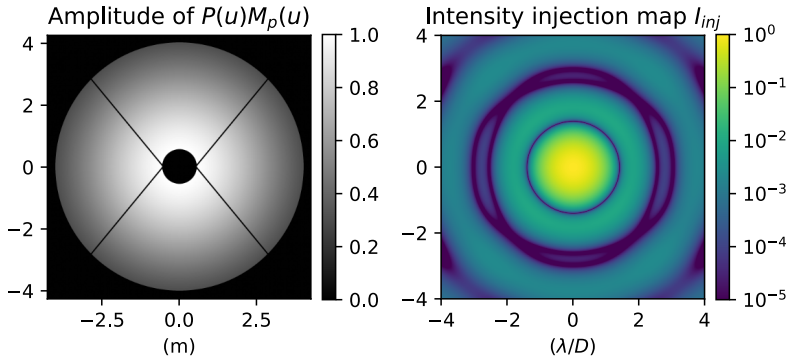

Figure 2. Illustration for the terms in equation (4). Left: The pupil plane term $P(u)M_p(u)$ for the UT aperture. Right: the injection intensity map $I_{inj} = |E_{inj}|^2$.

2.2 Mode #1 : Tip-Tilt

Tip and tilt, the lowest order modes one can think of, play a role in the dark hole on GRAVITY at the shortest separations. We found that the best position for the fiber is not necessarily centered on the planet. We can off-point the SC to reach a position where the imaging contrast $E_{inj}^{planet}/E_{inj}^{star}$ is more favorable. In GRAVITY the fiber position is a chosen parameter. So, we do not apply tip-tilt modes on the deformable mirror but simply choose the optimal SC position in the instrument.

The figure 3 shows that the off-target pointing can lead to $\times 100$ imaging contrast improvement for planets at 1 λ/D.

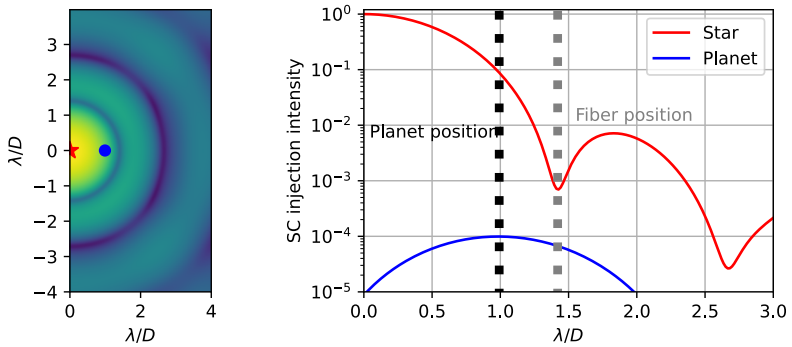

Figure 3. The role of tip-tilt to increase the imaging contrast. Left: injection intensity map on the focal plane with the red star indicating the star position, the blue dot indicate the planet position. Right: slice of the injection map in the planet direction. The injection map includes a 20% wavelength bandwidth.

2.3 Mode #2 : Defocus

The Defocus mode can control the residual aberrations that pollute the first zero of the injection map. We found that applying a Defocus on a static residual patterns can dig the first zero at a given position of the injection map, even if the residual aberrations are higher order modes than defocus.

Figure 4 illustrates how an optimal Defocus can achieve a $\times 10$ imaging contrast improvement in the first zero.

2.4 Mode #3 : SCAR mode

This mode has already been discovered by Por & Haffert in their Single-mode Complex Amplitude Refinement (SCAR).[4] The aim of this mode is to join together the first zero and the second zero of the injection map, and thus create a dark hole at 2 λ/D. In its simplest expression, it is a combination of a Coma and a Trefoil of equal amplitude (Figure 5).

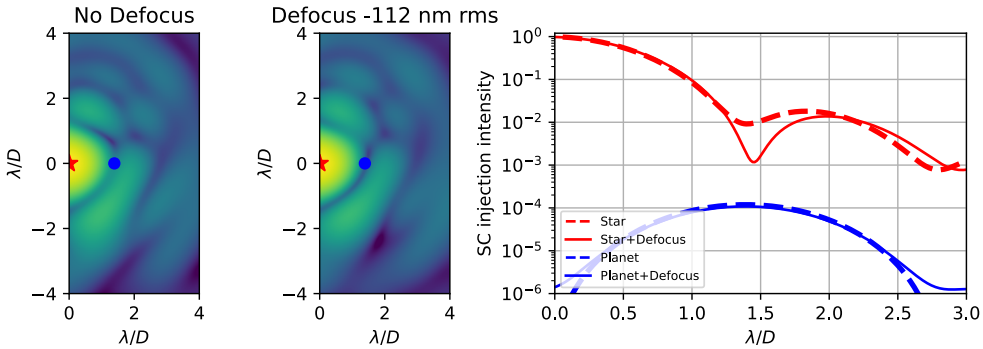

Figure 4. Optimization of the defocus can dig the first zero of the injection map. Left: injection map including 170 nm rms of low order aberrations up to Zernike Noll #30. Center: same injection map with an optimal -170 nm rms defocus. Right: slice of the injection map in the planet direction with dark hole (DH) and without DH. The injection maps includes a 20% wavelength bandwidth.

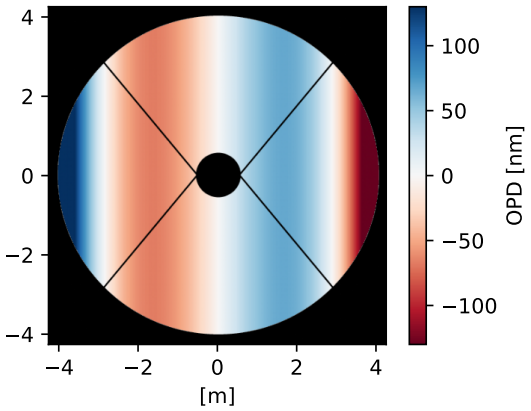

Figure 5. SCAR mode composed of a Coma and a Trefoil on the UT pupil. Here, the mode optical path difference (OPD) is 60 nm rms.

Figure 6 shows that in the diffraction limited case this SCAR mode can improve the imaging contrast by $\times 1000$ around 2 λ/D.

3. OPPONENTS TO HIGH CONTRAST

In the previous section, we have shown that a Defocus control can dig the first zero even in presence of static residual aberrations. In this context, the whole Non-Common Path aberration problem is solved by a simple Defocus optimisation. The contrast killers here will be the non-static residual aberrations such as uncorrected atmosphere turbulence and tip-tilt jitter from the VLTI tunnels.

3.1 Tip-tilt jitter

The residual image field displacement will impact the depth of the dark holes created in the fiber injection map. GRAVITY includes a field guiding at 1 Hz thanks to the acquisition camera. It reduces the on-sky tip-tilt jitter to less than 10 mas rms on the UTs.[5] Figure 7 shows that, even with 10 mas rms tip-tilt jitter, the SCAR mode can still bring a contrast improvement of $\times 100$.

We ran tests on the IRIS infrared camera at the VLTI laboratory. On IRIS, the field guiding in the J-band can operate at a frequency up to 200 Hz and reduce the on-sky tip-tilt jitter to 5 mas rms on the UTs. If the tip-tilt jitter appears to be the main opponent to the dark-hole on GRAVITY, one solution to further reduce the jitter may be to use the IRIS camera at the J-band for additional field guiding in parallel to the GRAVITY observations.

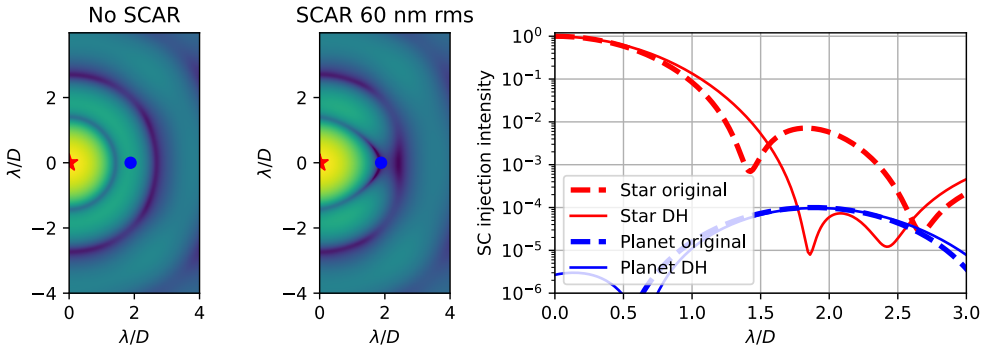

Figure 6. Impact of the SCAR mode on the injection map. Left: original injection map (without SCAR mode). Center: injection map with 60 nm rms SCAR mode. Right: slice of the injection map in the planet direction. The injection maps includes a 20% wavelength bandwidth.

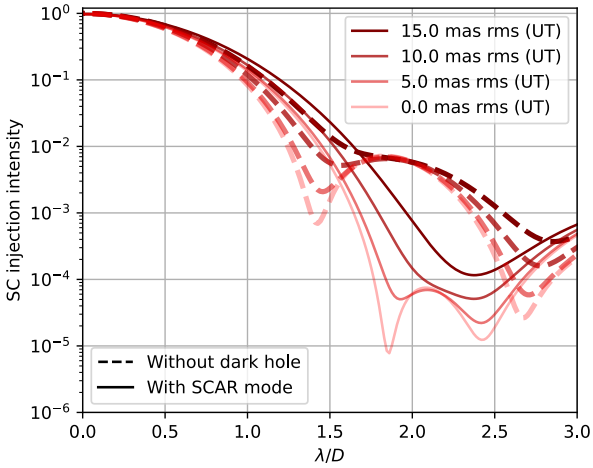

Figure 7. Slice of the injection intensity map with and without dark hole for different tip-tilt jitter amounts.

3.2 Atmosphere residuals

On GRAVITY, the exposure time for exoplanet observations is between 10 and 100 seconds. At this timescale the residual aberrations create a halo of stellar light that makes the zeros of the injection map more shallow. If the atmosphere residuals dominate over the pupil diffraction the dark hole attempts between 1.5 and 3 λ/D are doomed to fail. However, even in the atmosphere dominated regime, the tip-tilt dark hole can still allow for a substantial contrast gain between 1 and 1.5 λ/D.

The amount of uncorrected atmosphere turbulence depends on the frequency of the adaptive optics and the number of modes controlled. The adaptive optics of the UTs, MACAO, control around 60 modes at a frequency of 1000 Hz. The adaptive optics of the Auxiliary Telescopes (ATs) NAOMI controls the first 14 Zernikes modes after piston at 500 Hz. CIAO, the infrared wavefront sensor of the UTs do not operate in the dual-field on-axis mode of the instrument, so it is not convenient for short separation exoplanets observations. In 2024, the GRAVITY+ adaptive optics will upgrade the UTs with extreme adaptive optics controlling around 1000 modes at more than 1 kHz. This new system will be a game changer for high-contrast on GRAVITY and the dark-hole technique will then reach its full potential.

4. TESTS ON THE INSTRUMENT

Before this study, it was not clear if the wavefront entering GRAVITY is diffraction limited or turbulence limited at less than 3 λ/D. We ran on-sky tests on the ATs and NAOMI in June 2022 to test the dark-hole technique on the instrument. We implemented the tip-tilt dark hole by a simple off-pointing of the SC fiber. Defocus by offsets in the Shack-Hartmann reference slopes and the SCAR mode by a combination of Coma and Trefoil in the reference slopes as well.

First, we ran on-sky tests on single stars. Pointing the SC at different separations provided discrete measurements of the injection map and allowed for a quantification of the atmosphere residuals.

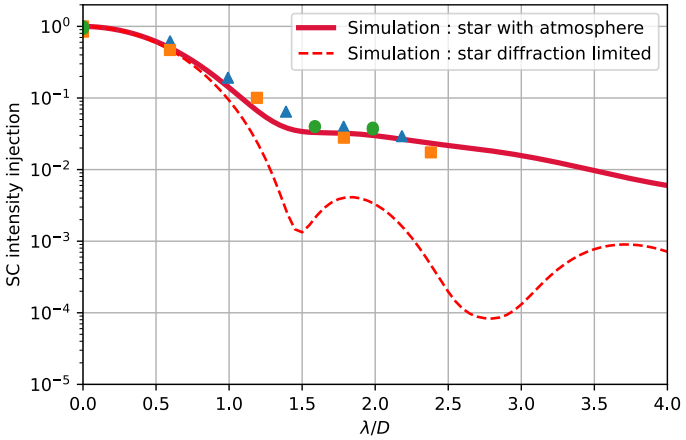

Figure 8. Comparison between the measured stellar flux injected in the SC and injection maps from NAOMI simulations. Points: normalized SC flux measurements on GRAVITY (circles: CN Gru [K=2.1, G=6.7], triangles: HD 191089 [K=6, G=7], squares: HD 191889 [K=5.7, G=6.8]. Lines: SC injection from simulation. The corresponding Strehl ratio at K-band is 0.45. The atmospheric conditions during the observations were excellent (seeing$\sim$ 0.5 arcsec, $\tau_0 \sim 8$ ms).

From Fig. 8, we can see that the first zero of the injection map is not clearly visible. We used an end-to-end simulation of NAOMI to obtain residual phase screens. From these phase screens we computed the SC injection map for long exposure. It shows good agreement with the SC fluxes measured on the instrument and tend to confirm that the injection is dominated by atmosphere residuals.

We made the same measurement with a SCAR mode applied on NAOMI (Fig. 9).

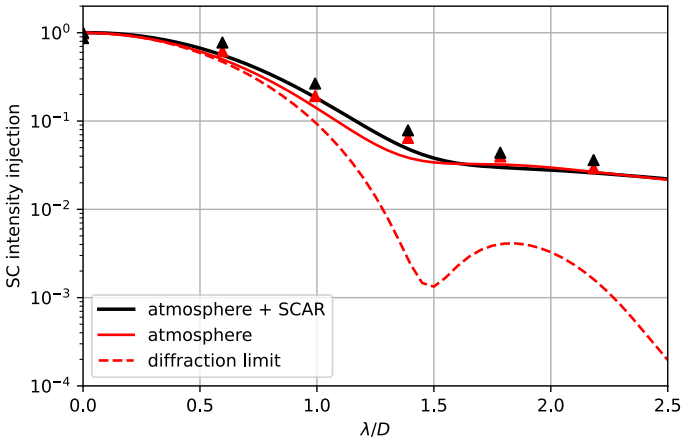

Figure 9. Comparison between the measured stellar flux injected in the SC and injection maps from NAOMI simulations when a SCAR mode of 50 nm rms is applied. Red triangle: normalized SC flux measurements on GRAVITY without SCAR mode. Black triangle: normalized SC flux with a 50 nm rms scar mode applied on NAOMI. Lines: SC injection from simulation.

This mode is supposed to dig a dark hole at 2 λ/D. Our tests show that no injection reduction can be obtained with the SCAR mode under so strong atmosphere residuals. We did not test the Defocus impact on GRAVITY. On-sky tests on the IRIS camera at the K-band showed that $\times 1.3$ is the best contrast improvement we could achieve at 1.5 λ/D with a Defocus optimization.

It leaves us with the simple tip-tilt dark hole. From the injection curves observed on-sky we predict that the off-target pointing enable up to $\times 4$ contrast improvement for companions located between 0.6 and 1.2 λ/D.

5. IMPLEMENTATION ON GRAVITY

5.1 Dark hole on GRAVITY now

Our on-sky tests on GRAVITY have shown that the dark hole technique with the Defocus optimization and the SCAR mode lead to no improvement of the planet/star contrast on NAOMI. We can reasonably extend this conclusion to MACAO on the UTs. However, we have shown that off-target pointing of the SC would lead to $\times 4$ imaging contrast improvement for the closest targets. This "tip-tilt dark hole" technique can be easily implemented since it requires no wavefront control (no modification of the adaptive optics). The observer just need to offset the SC fiber position when observing targets at shorter separation than 1.2 λ/D. A correction of the target flux loss due to the off-target pointing must be applied to obtain the luminosity of the object (similar to Appendix A in Wang et al. 2021[2]).

5.2 Dark hole expectations for GRAVITY+

Simulations displayed in section 3.1 show the contrast improvement that can be obtained in a diffraction limited case including 10 mas tip-tilt jitter. If we assume that the new GRAVITY+ adaptive optics will perfectly correct for the atmosphere at short separation, we predict that the dark-hole technique can bring an imaging contrast improvement of $\times 100$ for exoplanets at separation from 1 to 3 λ/D. How much atmosphere residuals will remain with the GRAVITY+ adaptive optics and how it will compare to the amount of residual tip-tilt jitter is still to be determined.

On operations, the SC off-pointing and the SCAR mode (angle and amplitude) can be automatically determined depending on the exoplanet position. The optimal Defocus can be estimated by measurements of the SC flux in the first zero for different Defocus amplitudes. If the residual aberrations appear to be stable, we could obtain the optimal Defocus amplitude from a model that would not require measurements. The latter solution would result in no overheads for the observer.

6. CONCLUSIONS

The modest contrast improvement achieved on GRAVITY with this technique will be used to push the exoplanets and brown dwarfs observations at raw contrasts down to 5×10^{-5} even at 1 λ/D separation. With GRAVITY+ adaptive optics and the dark hole, planets at raw contrast down to 2×10^{-7} shall be observed with UTs at separations from 60 to 170 mas. This contrast at short separation would enable to observe Jupiter mass planets down to the snow-line.

ACKNOWLEDGMENTS

The research leading to these results has received funding from the European Union's Horizon 2020 research and innovation programme under Grant Agreement 101004719 (ORP). This work was supported by the Action Spécifique Haute Résolution Angulaire (ASHRA) of CNRS/INSU co-funded by CNES. The authors acknowledges the support of the French Agence Nationale de la Recherche (ANR), under grant ANR-21-CE31-0017 (project EXOVLTI). The authors would like to thanks Aaron Labdon and Peter Scicluna for their precious help and expertise during on-sky sessions on GRAVITY. This research has made use of the following python packages: hcipy, numpy, matplotlib, scipy and astropy.

REFERENCES

[1] Nowak, M., Lacour, S., Lagrange, A. M., Rubini, P., Wang, J., Stolker, T., Abuter, R., Amorim, A., Asensio-Torres, R., Bauböck, M., Benisty, M., Berger, J. P., Beust, H., Blunt, S., Boccaletti, A., Bonnefoy, M., Bonnet, H., Brandner, W., Cantalloube, F., Charnay, B., Choquet, E., Christiaens, V., Clénet, Y., Coudé Du Foresto, V., Cridland, A., de Zeeuw, P. T., Dembet, R., Dexter, J., Drescher, A., Duvert, G., Eckart, A., Eisenhauer, F., Gao, F., Garcia, P., Garcia Lopez, R., Gardner, T., Gendron, E., Genzel, R., Gillessen, S., Girard, J., Grandjean, A., Haubois, X., Heißel, G., Henning, T., Hinkley, S., Hippler, S., Horrobin, M., Houllé, M., Hubert, Z., Jiménez-Rosales, A., Jocou, L., Kammerer, J., Kervella, P., Keppler, M., Kreidberg, L., Kulikauskas, M., Lapeyrère, V., Le Bouquin, J. B., Léna, P., Mérand, A., Maire, A. L., Mollière, P.,

Monnier, J. D., Mouillet, D., Müller, A., Nasedkin, E., Ott, T., Otten, G., Paumard, T., Paladini, C., Perraut, K., Perrin, G., Pueyo, L., Pfuhl, O., Rameau, J., Rodet, L., Rodríguez-Coira, G., Rousset, G., Scheithauer, S., Shangguan, J., Stadler, J., Straub, O., Straubmeier, C., Sturm, E., Tacconi, L. J., van Dishoeck, E. F., Vigan, A., Vincent, F., von Fellenberg, S. D., Ward-Duong, K., Widmann, F., Wieprecht, E., Wiezorrek, E., Woillez, J., and Gravity Collaboration, "Direct confirmation of the radial-velocity planet β Pictoris c," *A&A* **642**, L2 (Oct. 2020).

[2] Wang, J. J., Vigan, A., Lacour, S., Nowak, M., Stolker, T., De Rosa, R. J., Ginzburg, S., Gao, P., Abuter, R., Amorim, A., Asensio-Torres, R., Bauböck, M., Benisty, M., Berger, J. P., Beust, H., Beuzit, J. L., Blunt, S., Boccaletti, A., Bohn, A., Bonnefoy, M., Bonnet, H., Brandner, W., Cantalloube, F., Caselli, P., Charnay, B., Chauvin, G., Choquet, E., Christiaens, V., Clénet, Y., Coudé Du Foresto, V., Cridland, A., de Zeeuw, P. T., Dembet, R., Dexter, J., Drescher, A., Duvert, G., Eckart, A., Eisenhauer, F., Facchini, S., Gao, F., Garcia, P., Garcia Lopez, R., Gardner, T., Gendron, E., Genzel, R., Gillessen, S., Girard, J., Haubois, X., Heißel, G., Henning, T., Hinkley, S., Hippler, S., Horrobin, M., Houllé, M., Hubert, Z., Jiménez-Rosales, A., Jocou, L., Kammerer, J., Keppler, M., Kervella, P., Meyer, M., Kreidberg, L., Lagrange, A. M., Lapeyrère, V., Le Bouquin, J. B., Léna, P., Lutz, D., Maire, A. L., Ménard, F., Mérand, A., Mollière, P., Monnier, J. D., Mouillet, D., Müller, A., Nasedkin, E., Ott, T., Otten, G. P. P. L., Paladini, C., Paumard, T., Perraut, K., Perrin, G., Pfuhl, O., Pueyo, L., Rameau, J., Rodet, L., Rodríguez-Coira, G., Rousset, G., Scheithauer, S., Shangguan, J., Shimizu, T., Stadler, J., Straub, O., Straubmeier, C., Sturm, E., Tacconi, L. J., van Dishoeck, E. F., Vincent, F., von Fellenberg, S. D., Ward-Duong, K., Widmann, F., Wieprecht, E., Wiezorrek, E., Woillez, J., and Gravity Collaboration, "Constraining the Nature of the PDS 70 Protoplanets with VLTI/GRAVITY," *AJ* **161**, 148 (Mar. 2021).

[3] Llop-Sayson, J., Ruane, G., Mawet, D., Jovanovic, N., Calvin, B., Levraud, N., Roberson, M., Delorme, J.-R., Echeverri, D., Klimovich, N., and Xin, Y., "Demonstration of an electric field conjugation algorithm for improved starlight rejection through a single mode optical fiber," *Journal of Astronomical Telescopes, Instruments, and Systems* **5**, 019004 (Jan. 2019).

[4] Por, E. H. and Haffert, S. Y., "The Single-mode Complex Amplitude Refinement (SCAR) coronagraph. I. Concept, theory, and design," *A&A* **635**, A55 (Mar. 2020).

[5] Anugu, N., Amorim, A., Gordo, P., Eisenhauer, F., Pfuhl, O., Haug, M., Wieprecht, E., Wiezorrek, E., Lima, J., Perrin, G., Brandner, W., Straubmeier, C., Le Bouquin, J. B., and Garcia, P. J. V., "Methods for multiple-telescope beam imaging and guiding in the near-infrared," *MNRAS* **476**, 459–469 (May 2018).

A&A 665, A158 (2022)
https://doi.org/10.1051/0004-6361/202243432

Astronomy & Astrophysics

Low-wind-effect impact on Shack–Hartmann-based adaptive optics

Partial control solution in the context of SPHERE and GRAVITY+

N. Pourré[1], J.-B. Le Bouquin[1], J. Milli[1], J.-F. Sauvage[2,3], T. Fusco[2,3], C. Correia[4], and S. Oberti[5]

[1] Univ. Grenoble Alpes, CNRS, IPAG, 38000 Grenoble, France
e-mail: nicolas.pourre@univ-grenoble-alpes.fr
[2] DOTA, ONERA, Université Paris Saclay (COmUE), France
[3] Aix Marseille Univ, CNRS, CNES, LAM, Laboratoire d'Astrophysique de Marseille, Marseille, France
[4] Space ODT – Optical Deblurring Technologies, Rua Direita de Francos, 1021, Rés-Do-Cháo Esquerdo 4250-194 Porto, Portugal
[5] European Southern Observatory, Karl-Schwarzschild-str-2, 85748 Garching, Germany

Received 28 February 2022 / Accepted 18 June 2022

ABSTRACT

Context. The low wind effect (LWE) occurs at the aperture of 8-meter class telescopes when the spiders holding the secondary mirror get significantly cooler than the air. The effect creates phase discontinuities in the incoming wavefront at the location of the spiders. Under the LWE, the wavefront residuals after correction of the adaptive optics (AO) are dominated by low-order aberrations, pistons, and tip-tilts, contained in the pupil quadrants separated by the spiders. Those aberrations, called petal modes, degrade the AO performances during the best atmospheric turbulence conditions. Ultimately, the LWE is an obstacle for high-contrast exoplanet observations at a small angular separation from the host star.
Aims. We aim to understand why extreme AO with a Shack-Hartmann (SH) wavefront sensor fails to correct for the petal tip and tilt modes, while these modes imprint a measurable signal in the SH slopes. We explore if the petal tip and tilt content of the LWE can be controlled and mitigated without an additional wavefront sensor.
Methods. We simulated the sensitivity of a single subaperture of a SH wavefront sensor in the presence of a phase discontinuity across this subaperture. We explored the effect of the most important parameters: the amplitude of the discontinuity, the spider thickness, and the field of view. We then performed end-to-end simulations to reproduce and explain the behavior of extreme AO systems based on a SH in the presence of the LWE. We then evaluated the efficiency of a new mitigation strategy by running simulations, including atmosphere and realistic LWE phase perturbations.
Results. For realistic parameters (i.e. a spider thickness at 25% of a SH subaperture, and a field of view of $3.5\lambda/d$), we find that the sensitivity of the SH to a phase discontinuity is dramatically reduced, or even reversed. Under the LWE, a nonzero curl path is created in the measured slopes, which transforms into vortex-structures in the residuals when the loop is closed. While these vortexes are easily seen in the residual wavefront and slopes, they cannot be controlled by the system. We used this understanding to propose a strategy for controlling the petal tip and tilt modes of the LWE by using the measurements from the SH, but excluding the faulty subapertures.
Conclusions. The proposed mitigation strategy may be of use in all extreme AO systems based on SH for which the LWE is an issue, such as SPHERE and GRAVITY+.

Key words. instrumentation: high angular resolution – instrumentation: adaptive optics

1. Introduction

The Spectro-Polarimetric High-Contrast Exoplanet REsearch (SPHERE) instrument at the Very Large Telescope (VLT) is a high-contrast imager optimized for exoplanet hunting (Beuzit et al. 2019). The instrument is equipped with extreme adaptive optics (AO) system (called SAXO, Fusco et al. 2016; Sauvage et al. 2016b) that routinely reaches a Strehl ratio (SR) of 90% in the H band. SPHERE has three scientific arms with different detectors: ZIMPOL (Schmid et al. 2018), allowing for polarimetric observations in the optical, IRDIS (Dohlen et al. 2008), for dual-band imaging and spectroscopy in the near-infrared, and IFS (Claudi et al. 2008), an integral field spectrograph in the near-infrared. Also, the instrument includes cutting-edge coronagraphs at both optical and near-infrared wavelengths, which enable a final contrast of 10^{-5} in the H band for exoplanet observations at a 500 mas separation from the host star (Langlois et al. 2021; Mouillet et al. 2018). Since 2014, SPHERE has achieved groundbreaking observations in the field of exoplanets (e.g., Chauvin et al. 2017; Keppler et al. 2018; Vigan et al. 2021) and circumstellar disks (e.g., van Boekel et al. 2017; Milli et al. 2017; Boccaletti et al. 2020; Ginski et al. 2021).

However, under the best atmospheric conditions, the instrument performances are hampered by the so-called low wind effect (LWE). This effect has been observed since the commissioning of SPHERE in 2014 and it was highlighted very early on as a major limitation of the instrument (Sauvage et al. 2015). The LWE is responsible for differential aberrations (petal modes) between the quadrants of the unit telescope (UT) pupil separated by the four spiders that hold the secondary mirror. Measurements

with the Zernike phase mask ZELDA (N'Diaye et al. 2013, 2016) under LWE conditions on SPHERE have shown typical petal-pistons (hereafter PPs) and petal-tip-tilts (PTTs) in the residual phase screens after the AO correction. The amplitude of the uncorrected aberrations measured with ZELDA ranges from 600 to 800 nm peak-to-valley (ptv) optical path difference (OPD; Sauvage et al. 2015). As a result, the focal plane images are affected by bright side lobes at the location of the first Airy ring responsible for Strehl losses, typically around 30% in the H band (Milli et al. 2018). On a coronagraphic image, the LWE ruins the contrast by a factor of up to 50 at a separation of 0.1″. Unfortunately, the LWE is not restricted to SPHERE, but is also observed with the Adaptive Optics Facility (AOF, Oberti et al. 2018) at the VLT and with SCExAO at Subaru (Bos et al. 2020).

The commonly acknowledged physical explanation for the LWE is the following. At night, the spiders holding the secondary mirror radiate their heat to the clear sky and their temperature drops to 2 ∼ 3 °C below the ambient air temperature. When the wind at the top of the telescope dome drops below 5 m s^{-1}, the air in the dome is not well mixed and a laminar flow can develop around the spiders. Due to thermal exchange, the air efficiently cools down near the spiders, generating layers of colder air in the vicinity of the spiders (Holzlöhner et al. 2021). Ultimately, temperature differences are responsible for optical index differences on each side of the spider, and therefore the discontinuity of the OPD.

A passive mitigation was applied in 2017 on UT3 where SPHERE operates. It consisted in applying a coating on the spiders to limit their thermal emissivity in the mid-infrared. The occurrence frequency of the LWE on SPHERE dropped from ∼20% of the observing time to ∼3.5% of the time (Milli et al. 2018). Still, the LWE continues to degrade the observations when atmospheric conditions are the best. This explains the recent efforts to develop additional mitigation strategies to control the LWE (see Vievard et al. 2019, for an overview of focal plane wavefront sensor strategies). The focal plane wavefront sensing solution called Fast & Furious (F&F, Keller et al. 2012; Korkiakoski et al. 2012, 2014) is one of the most advanced algorithms for LWE control and it has been successfully tested in the laboratory (Wilby et al. 2018) and on-sky using Subaru/SCExAO (Bos et al. 2020). It uses sequential phase diversity (Gonsalves 2002) from an additional focal-plane sensor to measure the PP and PTT aberrations, and the first 50 Zernike modes for non-common path aberrations control. Here, we propose following a complementary approach: understanding the observed behavior of the AO under the LWE in order to propose improvements without requiring a new sensor.

The first purpose of this paper is to understand why the extreme AO of SPHERE fails to correct the PTT aberrations induced by the LWE. Indeed, the PTTs are normal tip-tilts (TTs) on most parts of the pupil. As such, they imprint a recognizable pattern in the slopes measured by the Shack-Hartmann (SH) wavefront sensor. The second purpose is to propose and evaluate a mitigation strategy using, as much as possible, the information already provided by the SH. The paper uses low-level and end-to-end simulations to achieve these goals, and is organized as follows. In Sect. 2, we investigate how bad SH measurements for phase discontinuities lead to uncorrected aberrations. We start in Sect. 2.1 with a low-level study of the slope measured by a single SH subaperture exposed to a phase discontinuity instead of a smooth phase slope. Then, in Sect. 2.2, we link these results with the residuals of an end-to-end AO simulation, and finally reproduce post-AO residuals observed on SPHERE. Section 3 is dedicated to the description of a mitigation algorithm that makes use of the SH information to reliably measure and control the PTT modes. The paper concludes with discussions in Sect. 4 about the interest and limitations of the proposed mitigation, considering the known properties of the LWE.

In the paper, nonbold variables are scalars, bold variables are vectors, and bold-underlined variables are matrices. The symbol $*$ is for element-wise multiplication and $\cdot$ is for matrix product.

2. From bad wavefront measurements to uncorrected aberrations

The LWE induces aberrations that are not corrected by the adaptive optics. In this section we describe how bad measurements by the SH can lead to strong low-order post-AO residuals.

2.1. Shack-Hartmann's sensitivity to a phase discontinuity

The most problematic features of the residual aberrations created by the LWE are the sharp phase discontinuities along the spiders. First, we investigate how such a phase discontinuity affects the measurement from a single SH subaperture. Similar studies have already been performed in the context of detecting phasing errors between primary mirror segments of the W.M. Keck Observatory (Chanan et al. 1998, 2000; van Dam et al. 2017). The conclusion is that, in the weak phase regime, a SH should be able to measure a phase jump. Here, we go further by investigating the influence of the following parameters: the position and amplitude of the discontinuity, the field of view, and the presence of a spider.

We built a basic simulation to propagate the electric field from the pupil plane to the focal plane of the subaperture:

$$\mathbf{I} = |\mathscr{F}\{\mathbf{A}\exp(i\boldsymbol{\phi})\}|^2, \tag{1}$$

where $\mathbf{I}$ is the intensity at the focus of the subaperture, $\mathscr{F}$ is the Fourier transform operation, $\mathbf{A}$ is the pupil transmission (e.g., a simple square of size d for an unobstructed subaperture), and $\boldsymbol{\phi}$ is the phase screen in front of the subaperture. We used a sampling of ≈200 point across the subaperture plane and ≈10 points per λ/d in the image plane. Tests with a finer sampling resulted in no significant changes in the results. We used a center of gravity (CoG) calculation to determine the spot position in the x direction:

$$\mathrm{CoG} = \frac{\int x\,\mathbf{I}\,\mathrm{d}x}{\int \mathbf{I}\,\mathrm{d}x}. \tag{2}$$

The integration for the center of gravity was limited to a given field of view, which was a free parameter.

The expected displacement of the spot in units of λ/d due to a phase slope of ptv amplitude $\Delta\phi = a \times 2\pi$ across the subaperture is given by CoG = a. This relationship does not always hold true, especially when the phase is not a gentle slope, but instead contains a discontinuity. It is the purpose of the following simulations to quantify the extent to which the CoG measurement deviates from the expected value, and under which conditions.

2.1.1. Effect of position and field of view

We first analyze how the measurement is affected by the position of the discontinuity and the field of view used to compute the CoG. We restrict this analysis to the weak-phase regime. Results are given in Fig. 1. When the field of view is wide (e.g., 40 λ/d), the CoG properly estimates the discontinuity, unless when the

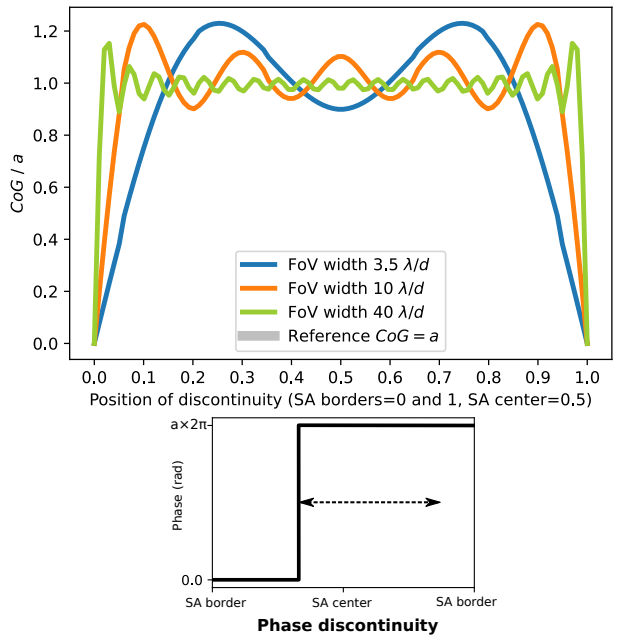

Fig. 1. Impact of the position of the phase discontinuity on the CoG measurement. *Top:* sensitivity to a phase discontinuity with respect to the position of the discontinuity in the subaperture (SA) for different fields of view (FoV). The simulation is carried out for $a = 0.05$ (weak-phase regime). *Bottom:* 1D illustration of the free parameter, the position of the discontinuity.

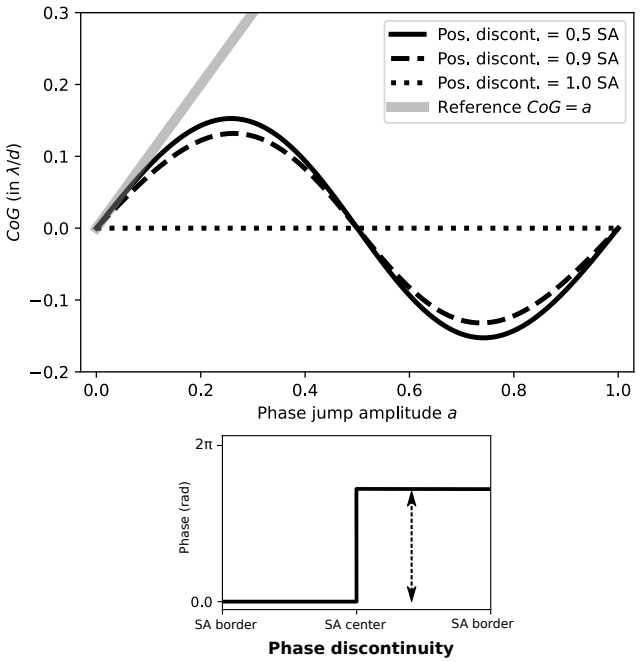

Fig. 2. Impact of the amplitude of the discontinuity on the CoG measurement. *Top*: sensitivity to a phase discontinuity with respect to the amplitude of the discontinuity, where a = 1 corresponds to a 2π rad phase discontinuity. The field of view is restricted to a 3.5 λ/d width. Black lines correspond to different positions of the discontinuity in the pupil plane (0.5 is for the center, 0 and 1 are for the edges). The gray line corresponds to the reference value CoG = a. *Bottom*: 1D illustration of the free parameter, the amplitude of the discontinuity.

discontinuity is located very close to the edge of the subaperture. This is an expected result, as already pointed out in van Dam et al. (2017). However, for a field of view realistically restricted to 3.5 λ/d, the sensitivity significantly depends on the position of the discontinuity. The CoG estimate can be erroneous by up to 20% with respect to the expected value.

2.1.2. Effect of the amplitude

We then analyze the response when the discontinuity amplitude goes beyond the weak-phase regime. The results are presented in Fig. 2. As expected, the CoG measurement evolves nonlinearly with respect to the amplitude of the discontinuity, and wraps with a period of 2π. To put it simply, for an amplitude larger than $\pi/2$ rad ($a \geq 0.25$), there is no hope for the CoG to properly estimate the amplitude of the discontinuity. The relationship with the position of the discontinuity is consistent with the sensibility curves in Fig. 1 for a field of view of 3.5 λ/d. In fact, we found that the effect of amplitude is decoupled from the effect of field of view and position. That is, all configurations can be estimated quantitatively by scaling the results of Fig. 1 with the results of Fig. 2.

2.1.3. Effect of the spider thickness

In practise, phase discontinuities occur at the location of the spiders. It is therefore necessary to investigate how the CoG is affected by a partial obscuration in the subaperture. The results are shown in Fig. 3. The sensitivity to the discontinuity decays dramatically with the thickness of the spider. Moreover, increasing the field of view does not provide a remedy for the missing sensitivity. For a spider size of 25% of the subaperture width, and a field of view of 3.5 λ/d, the CoG provides a measurement with a sign opposite to the applied perturbation.

One could question whether the issue of partial illumination also affects the measurement of slopes for a continuous wavefront, for example when sensing the turbulence without any LWE. Figure 3 shows that the loss in sensitivity is significantly less when considering a phase slope instead of a phase discontinuity. For a field of view of 3.5 λ/d, the loss of sensitivity reaches around 50%. Still, the CoG always provides an estimate with the correct sign. For wider fields of view, the loss in sensitivity due to the spider for the phase slope becomes less prominent.

2.1.4. Application to SPHERE

The SPHERE instrument of the VLT uses a field of view of 3.5 λ/d to compute the CoG. The 5cm thick spiders of the VLT block 25% of a subaperture (40 subapertures across the 8 m pupil). Unfortunately, Fig. 3 shows that it is the worst configuration, that is to say, it is the configuration for which the CoG measurement of a discontinuity is the most different from the expected value. Figure 4 summarizes the resulting effect on the sensitivity around the spider. For a phase discontinuity, the CoG estimate never gets close to the expected value. At best, the sensitivity is 0.1. At worst, the sensitivity reaches –0.5 when the discontinuity is at the center of the subaperture. This result provides an explanation for the "contra-moving spots" observed on SPHERE (SPHERE commissioning report, Sauvage, private communication). Obviously, one expects such reversed sensitivity to have a dramatic effect on the closed-loop operation. For a phase slope, the sensitivity losses are less severe

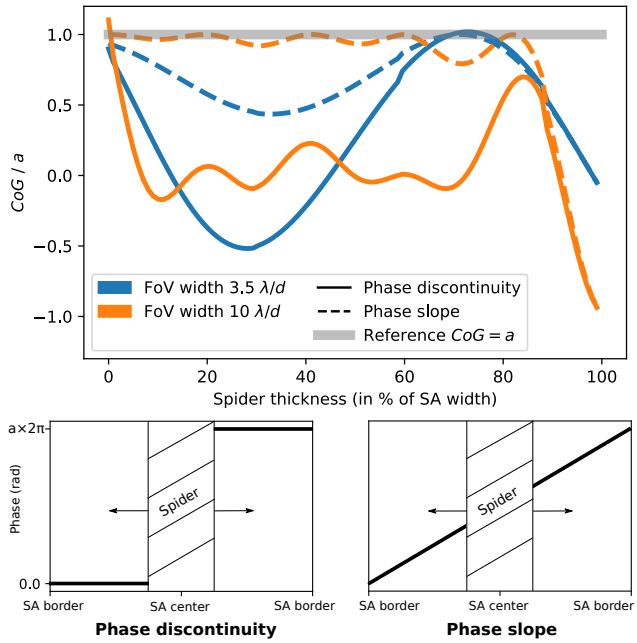

Fig. 3. Impact of the spider thickness on the CoG measurement. *Top:* sensitivity to a phase discontinuity (solid lines) and to a phase slope (dashed lines) with respect to the spider thickness. The simulation is carried out with $a = 0.05$ (weak phase regime). The spider obstructs the subaperture (SA) at the center of the subaperture. The spider thickness varies from 0% (infinitely thin) to 100% of the SA width (full obstruction). Two different fields of view (FoV) are tested. *Bottom:* 1D illustration of the free parameter, the spider thickness, in both the phase discontinuity (*left*) and the phase slope (*right*) cases.

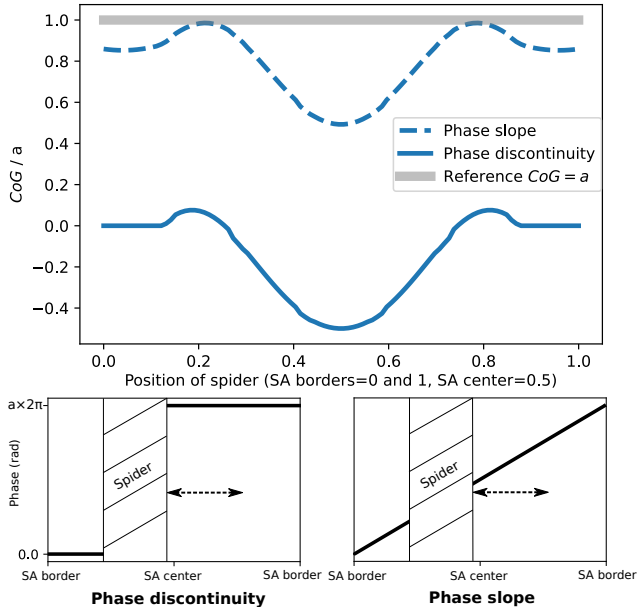

Fig. 4. Impact of the spider position on the CoG measurement. *Top:* sensitivity to a phase discontinuity and a phase slope with respect to the position of the spider in the subaperture (SA). The spider thickness is 25% of the SA width and the field of view is 3.5 λ/d. The simulation is carried out for $a = 0.05$ (weak phase regime). *Bottom:* 1D illustration of the free parameter, the position of the spider, in both the phase discontinuity (*left*) and the phase slope (*right*) cases.

than for the discontinuity; at worst the sensitivity drops to 0.5, but always keeps the correct sign. As long as this sensitivity error remains within the gain margin of the controlled modes, it will be ultimately corrected by the feedback loop.

Overall, the different behavior of the CoG when exposed to a phase discontinuity or a phase slope explains why the presence of spiders in the aperture is not problematic for measuring continuous atmospheric aberrations, but is an issue for measuring discontinuous LWE aberrations.

2.2. Uncorrected aberrations

We expect the bad SH measurement to have an impact on the AO correction. In this section we use end-to-end AO simulations to characterize the uncorrected aberrations and understand why they arise.

2.2.1. Design of the adaptive optics simulation

We used the HCIPy (High-Contrast Imaging for Python, Por et al. 2018) AO simulator to model a high-order AO system. This tool enables a simulation for the spots of each subaperture in the presence of phase discontinuity thanks to a proper treatment of the optical propagation. Electric fields are sampled with 480x480 grid points over the full pupil. Finer sampling resulted in no significant change.

The overall design is similar to SPHERE. The SH wavefront sensor operates at $\lambda = 700$ nm and has 40×40 subapertures in a Fried configuration with respect to the deformable mirror (DM). The DM is composed of 1377 actuators (41 actuators per diameter). The system controls the first 990 Karhunen–Loève (KL) modes (piston excluded). These KL modes are defined by a **K2DM** (KL to DM) 1377×990 matrix. We calibrate the interaction matrix **K2S** (KL to slopes) and take the pseudo-inverse to obtain the reconstruction matrix **S2K**. All modes are controlled with the same leaky integrator (leak $l = 0.01$, and gain $g = 0.3$):

$$\mathbf{DM}_{t+1} = \underline{\mathbf{K2DM}} \cdot [\,(1-l)\,\mathbf{K}_t + g\,\underline{\mathbf{S2K}} \cdot \mathbf{S}_t\,]. \quad (3)$$

The circular telescope pupil has a diameter of 8 m and a central obscuration whose diameter is 1.116 m. The pupil is segmented into four quadrants. We apply a flux criterion to discard the subapertures outside the useful pupil, setting the threshold at 50% of the flux received by a nonobstructed aperture. This selection criterion keeps a total of 1160 subapertures and always keeps the subapertures located behind the spiders.

2.2.2. Simplified perfectly blind configuration

We set up a simplified, symmetric pupil, where the junction between quadrants were aligned with the SH grid and passed between neighboring subapertures. For this configuration, the AO response to a simple PP and a simple PTT perturbation is shown in Fig. 5.

Intuitively, and as seen in Sect. 2.1, this configuration is perfectly blind to discontinuities between quadrants that are pure PPs (top). Yet, the 40×40 SH measures very small nonzero slopes around discontinuities. This comes from the leaking of the diffraction pattern of each subaperture in the field of view of the neighboring subapertures. The subapertures on each side of the discontinuity differ by a piston. Therefore, the diffracted electric fields interfere and slightly bias the CoG positions. This effect explains the small commands applied to the DM and the subsequent small reduction of the wavefront residuals (0.93). It should

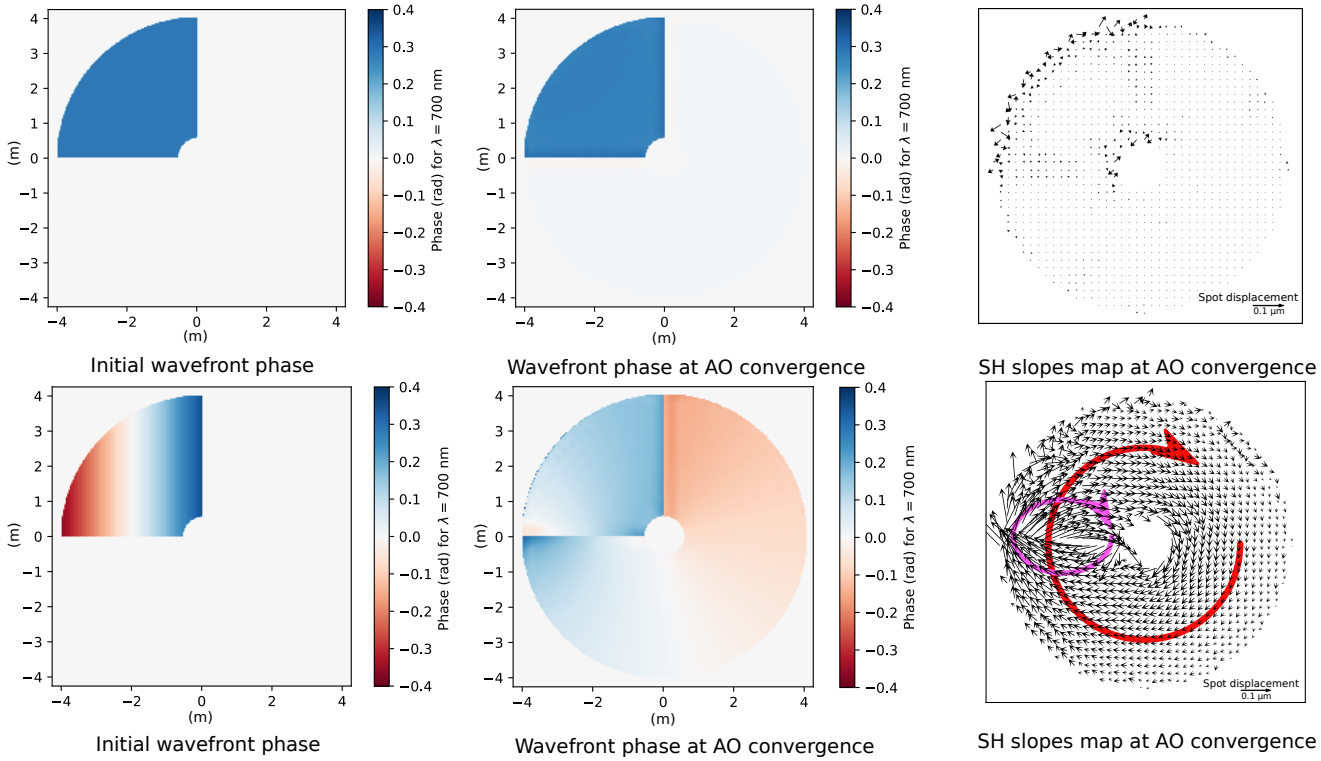

Fig. 5. End-to-end simulation of an AO loop in the presence of discontinuities. Discontinuities pass exactly between SH subapertures. The spider is infinitely thin, and there is no atmosphere. *Top:* static PP of a 32 nm ptv (weak-phase regime) on one quadrant. The ratio between the rms at convergence and the initial rms is 0.93. There are almost no signals in the residual SH slope map. *Bottom:* static PTT of an 80 nm ptv (weak-phase regime) on one quadrant. The ratio between the rms at convergence and the initial rms is 1.02. The red vortex in the residual slopes comes from the nonzero curl of the initial wavefront over a path circling around the central obscuration. The pink vortex in the residual slopes comes from the nonzero curl of the initial wavefront over a smaller path centered in $(-2, 0)$.

be noted that the slope map at the AO convergence contains no global residuals; all that is seen has been corrected.

The situation is different for the PTT perturbation (bottom). The aberration is tentatively corrected, but the applied correction leaks into the entire pupil. The residual wavefront is a vortex phase that shows two prominent curl patterns in the map of residual slopes measured by the SH. Two questions arise from this result, and we thus sought to understand what creates the curl patterns, and why these patterns were not corrected.

The answer to the first question is the loss in sensitivity. This is illustrated in the top panel of Fig. 6. The SH provides an erroneous estimate of the discontinuity amplitude. Therefore, the integration of the slopes along a closed path crossing the discontinuity only once is nonzero. There is an interesting explanation for the double vortex observed in the residual slopes of the bottom panel of Fig. 5. The red vortex in the residual slopes comes from the nonzero curl of the initial wavefront over a path circling around the central obscuration, which is going through $(-2, 0)$, $(0, +2)$, $(+2, 0)$, and $(0, -2)$. This path crosses a discontinuity only once, at $(0, +2)$. The pink vortex in the residual slopes comes from the nonzero curl of the initial wavefront over a smaller path going through $(-3, 0)$, $(-2, +1)$, $(-1, 0)$, and $(-2, -1)$. This path crosses two discontinuities, once at $(-3, 0)$ and once at $(-1, 0)$, but accumulating the losses in the same direction.

The answer to the second question is that curl patterns are out of the control space. It is well known that the curl of the gradient of a scalar differentiable field is zero. The DM being a continuous, smooth surface, it can only create modes without curl. Even the best approximation of a vortex phase map that the DM can create still has a zero curl. This is illustrated by the bottom panel of Fig. 6. This property also applies to the KL modes that form a subspace of the DM space. It explains why any nonzero curl patterns in the residual slopes are not corrected by the AO.

2.2.3. Dependence with the position of the discontinuity

From Sect. 2.1, we expect that the convergence state of the AO loop depends on the exact position of the discontinuity and the possible thickness of the spider. We verified these behaviors by running end-to-end simulations with varying these parameters. The results are presented in Appendix A. The performance of the AO loop is quantified as the ratio between the rms of the residual wavefront at convergence and the rms of the input aberration. The results match the predictions from Fig. 1 (the case with the infinitely thin spider) and Fig. 4 (the case with the 25% thick spider). The correction is best for the setups where the sensitivity is close to one, and worst when the sensitivity has the wrong sign.

This validates our understanding of the link between the local effect (reduced, reversed sensitivity of the discontinuity) and the global effect (unseen piston modes and uncorrectable curl modes), and allows us to make some quantitative conclusions. We find that a SH with thin spiders crossing the subapertures at an adequate position (0.4) could deal with discontinuities up

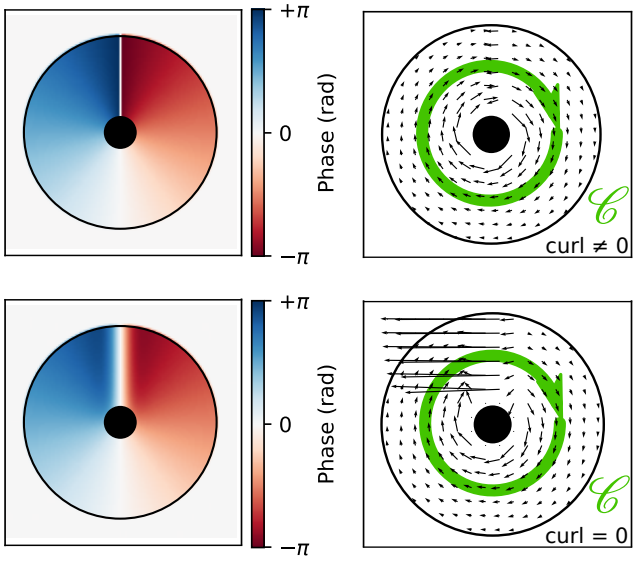

Fig. 6. Schematic for the gradient measured by a SH for a sharp discontinuity (*top*) and for a smoother pattern (*bottom*). In the top case, the amplitude of the discontinuity is not estimated correctly, and consequently the sum of SH slopes along a closed path $\mathscr{C}$ is not equal to zero. In the bottom case, the sum of slopes along the path $\mathscr{C}$ is equal to zero because the strong slope in affected subapertures compensate exactly for the rest of the path.

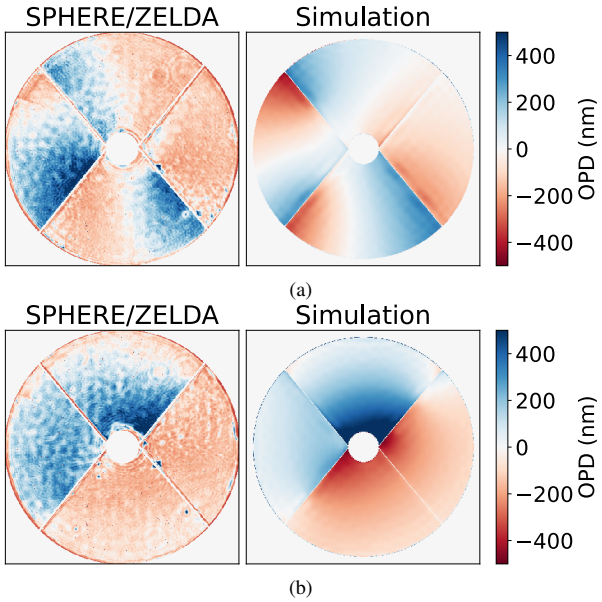

Fig. 7. Qualitative comparison between ZELDA measurements (*left*) and simulated post-AO residuals (*right*) for two LWE events (*a*) and (*b*). The ZELDA measurements have a 1 second detector integration time. They were taken during the night of 2014 October 8. The simulations match the typical SPHERE configuration. The result after convergence of the loop is shown here.

to $\lambda/4$. However, in the presence of a realistic spider obscuration of 25% of a subaperture, the impact of discontinuities is considerable.

2.2.4. Reproduction of SPHERE low-wind-effect residuals

We modified the end-to-end simulations to better match the configuration of SPHERE. We used a realistic VLT pupil with 5 cm thick spiders and with the proper angle for each spider. In this realistic configuration, the spiders (and the discontinuities) cross the SH subapertures at various positions and with different angles. We implemented a spatial filter of $2\lambda/d$ in front of the SH (d being the SH subapertures' width) and a Gaussian weighting on the SH focal-plane spots. We offloaded the TT control on a dedicated TT mirror. We implemented the differential tip-tilt sensor (Baudoz et al. 2010), whose aim is to maintain the centering of the star, behind the coronagraph by measuring, at a slower frequency, the actual position of the star at the focal plane in the H band. In all following simulations, the differential tip-tilt sensor frequency was 1 Hz and the AO loop frequency was 1.2 kHz.

We found that it is interesting to include the differential tip-tilt sensor in our simulation. Indeed, this sensor measurement is a CoG in the H-band focal-plane image. It is sensitive to petal perturbations (e.g., PPs and PTTs) that project on the global TT but are unseen by the SH. Yet, we have shown in Sect. 2.1 that phase discontinuities across an aperture can bias CoG measurements. This conclusion is also true for the differential tip-tilt sensor that makes an erroneous estimate in the case of a discontinuous wavefront, thus enforcing a global TT in the residual phase maps. Simulating the differential tip-tilt sensor is necessary in order to achieve residuals with the same overall structures as the ones observed with the ZELDA sensor, especially the residual global TT.

We used this realistic simulation of SPHERE AO. The LWE was simulated by an injected perturbation in the pupil plane combining discontinuous PP perturbations and discontinuous PTT perturbations. This way, we were able to reproduce some typical PTT and PP structures observed in the post-AO residuals of the instrument (Fig. 7). Figure 7a displays a residual pattern dominated by global vortexes (around the central obscuration) and local vortexes (around the center of individual spiders). Figure 7b displays a residual pattern dominated by strong PPs.

3. Shack–Hartmann-assisted low-wind-effect control

In a weak scintillation regime, the aberration created by the atmospheric turbulence is a continuous and differentiable scalar field (no branch points or branch cuts, Primmerman et al. 1995; Fried 1998). Optical vortexes are thus generally neglected in space-to-ground AO. The problem of vortex reconstruction and branch point identification in the slopes measured by a SH has, however, driven important literature in other contexts (Fried 1998; Tyler 2000; Luo et al. 2015; Wu et al. 2021). Here, we propose building on the successful approaches that made use of petaling modes to correct for the LWE (Sauvage et al. 2016a; Wilby et al. 2018; N'Diaye et al. 2018). These works rely on an additional wavefront sensor to control the petaling modes, generally focal-plane images. Here, we wish to utilize the information encoded inside the nonzero residual slope pattern of the SH sensor as much as possible.

3.1. Description of the algorithm to mitigate the low wind effect

We designed an algorithm that measures the PTTs from the SH and the PPs from a H band focal plane. The corrective command

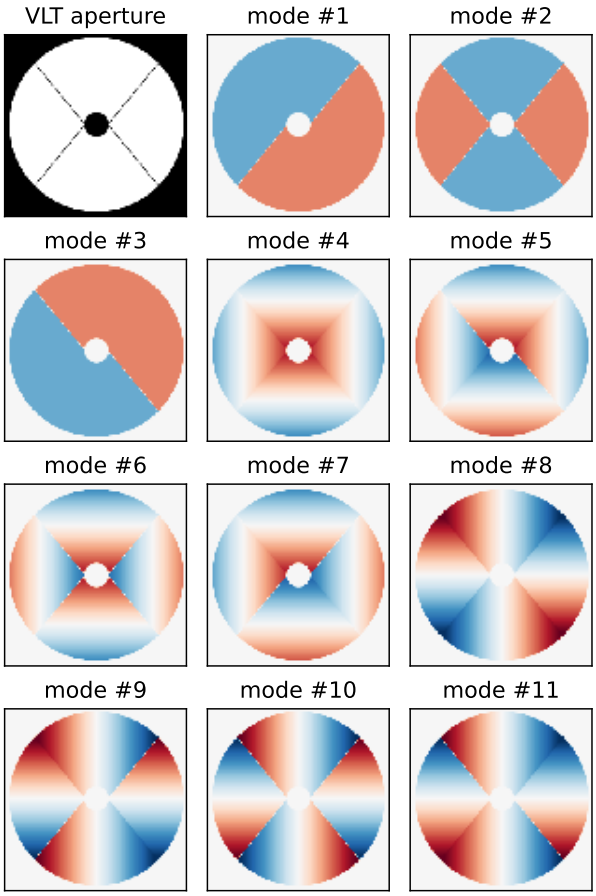

Fig. 8. 11 orthogonal LWE modes of the VLT pupil used in this study as pupil-plane perturbations. This compares to the classical decomposition shown in Fig. 6 of Sauvage et al. (2016a). Modes #1 to #3 are PP modes. Modes #4 to #11 are PTT modes. Odd numbers are for odd modes and even numbers are for even modes. Modes #4 and #8 do not contain discontinuities, and are removed from the control basis. Mode #10 controls the global curl pattern seen in Fig. 5.

is given to the deformable mirror via a modification of the reference slopes.

3.1.1. An alternate modal basis for the low wind effect

The classic basis used to describe the LWE aberrations is composed of 11 modes: the PP and PTT modes in each of the four quadrants of the pupil (three PP modes and eight PTT modes, Sauvage et al. 2016a). We propose decomposing this basis into a new set of odd and even modes (Fig. 8). There are two advantages to this. First, expressing aberrations as odd and even modes is more convenient for a focal-plane analysis, if needed. Second, two of the new PTT modes do not contain phase discontinuities (modes #4 and #8 in Fig. 8). Even if they are not differentiable at the junction between quadrants, those two modes are properly handled by the AO loop. This new basis reduces the number of PTT modes to control from eight to six. To be explicit: modes #4 and #8 are not included in the control matrices, but they are included in the description of the input LWE perturbation.

In practise, the modes of Fig. 8 are not perfectly realizable by the DM. We defined the matrices **PP2K** and **PTT2K**, which are the best approximations of the PP and PTT modes, in phase space, as per the KL basis. We arbitrarily restricted the approximation to the KL space and not the full DM space in order to remain inside the control space of the high-order AO loop. It is important to note, however, that we have not demonstrated that this is a strict requirement. The synthetic interaction matrix of the three PP modes and of the six remaining PTT modes can be constructed from the already known interaction matrix of the KL modes:

$$\mathbf{PTT2S} = \mathbf{K2S} \cdot \mathbf{PTT2K}, \tag{4}$$

$$\mathbf{PP2S} = \mathbf{K2S} \cdot \mathbf{PP2K}. \tag{5}$$

A naive approach is to simply add these modes into the control modal basis. This has been tried in the existing instrument (Sauvage, priv. comm.), and we reproduced the experiment in our simulation. This is doomed to fail, because the issue is not the completeness of the control space. Instead, as demonstrated in previous sections, the issue arises from improperly seen pistons and curl modes. For the PPs, there is nothing we can do with the SH. For the curl modes, it is possible to modify the measurement space in order to improve their visibility by the system.

3.1.2. Measuring the petal-tip-tilt modes with a Shack-Hartmann

The PTT modes are wrongly corrected by the system because the interaction matrix of their best approximation (without curl) does not match their actual imprint in the signal (with curl). This is the effect discussed in previous sections and illustrated in Fig. 6. One way to remedy this is to restrict the measurement space to the subspace for which there is a correct match between the expectation and the actual signal. This subspace is simply made of the subapertures that are not affected by the discontinuities.

On the one hand, discarding too many continuous subapertures will lead to the so-called island effect. It is an issue on the Extremely Large Telescope where spiders are too thick to ensure a continuity between neighboring sections of the pupil (Schwartz et al. 2017; Hutterer et al. 2018; Bertrou-Cantou et al. 2020). We reproduced this unwanted behavior in our simulations when discarding the subapertures partially blocked by the spiders. On the other hand, we have shown in Sect. 2.1.4 that the turbulence is properly seen by subapertures partially blocked by the spiders. Therefore, we decide to use a combination of the two approaches: closing the fast AO loop with all subapertures and all KL modes, to efficiently fight the turbulence and avoid its coupling into the island effect; and controlling specifically the PTT at a slower temporal bandwidth, using only the subaperture not affected by the spiders.

We computed the corresponding reconstruction matrix by restricting the pseudo-inverse $\tilde{\mathbf{S}}\mathbf{2PTT} = (\mathbf{PTT2}\tilde{\mathbf{S}})^{-1}$ to the subapertures that were not crossed, even minimally, by the spiders (see Fig. 9). The tilde in the above equation indicates that the matrix was restricted to selected subapertures. In fact, discarding these subapertures was a way to force curly slope patterns to project onto the controlled modes. Theoretically, it is possible to control the LWE with a higher number of modes than just the PTT (that is, with modes showing curvature across each quadrant). Here, we followed the standard approach of controlling only a small number of flat modes, as expressed in the modified basis of Fig. 8.

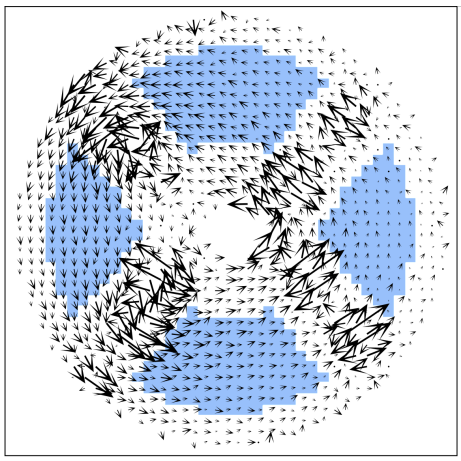

Fig. 9. SH slope map. The blue region highlights the subapertures that are used to estimate the PTT modes. Subapertures located close to the spiders, the secondary mirror, and the outer pupil ring are discarded.

3.1.3. Measuring the petal-piston modes

The PP modes only affect the subapertures that are located at the discontinuities, and for which the actual sensitivity is poor and hardly predictable. It is indeed well known that the SH is not a satisfactory sensor for PPs. The only solution is to rely on an additional sensor.

In the simulation, we modified the SPHERE differential tip-tilt sensor in order to measure the three PPs instead of a single, global TT. For this, we used a simple focal-plane analysis inspired by the literature (Korkiakoski et al. 2014; Wilby et al. 2016; Bos et al. 2020). It should be noted that two out of the three PP modes are odd. They could be linearly estimated from a single image measurement, assuming the corresponding interaction matrix had been calibrated. Therefore, out of the 11 initial LWE modes, only one remains to be estimated by a non-linear analysis (mode #2 in Fig. 8). The derivations are detailed in Appendix B. It is not the purpose of this paper to expand on the well-known focal-plane analysis. We implemented it in the simulation to ensure there was no damaging interplay with the proposed solution to control the PTT modes.

3.1.4. Feedback to the adaptive optics loop

By design, the corrections remain within the controlled space of the AO, and would be then flushed out by the closed loop if applied directly on the DM command. The solution is thus to implement the correction via a modification of reference slopes, as was proposed in the very first studies on the LWE on SPHERE (Sauvage et al. 2015, 2016a).

More precisely, the reference slopes $\mathbf{S}^{\mathrm{ref}}$ are modified thanks to simple integrators:

$$\begin{aligned}\mathbf{S}^{\mathrm{ref}}_{t+1} &= \mathbf{S}^{\mathrm{ref}}_{t} - g_{\mathrm{PTT}}\,\underline{\mathbf{PTT2S}}\cdot\underline{\tilde{\mathbf{S}}\mathbf{2PTT}}\cdot\mathbf{S}_t \\ &\quad - g_{\mathrm{PP}}\,\underline{\mathbf{PP2S}}\cdot\mathrm{F}(\mathbf{I}_t),\end{aligned} \tag{6}$$

where F(**I**) is the operation to extract the PP modes out of the focal plan image **I**. For two out of the three PP modes, this operation is a simple matrix multiplication. The scalar coefficients g_{PTT} and g_{PP} are the gain for the integration of the PTT and PP commands, respectively. We set $g_{\mathrm{PTT}} = 0.005$ (at the same frame rate than the main loop, 1.2 kHz) and $g_{\mathrm{PP}} = 0.1$ (at a frame rate of 1 Hz). The gain values were empirically chosen to optimize the trade-off between control bandwidth and loop stability.

Figure 10 gives a schematic overview of the complete loop, when incorporating the proposed control for the LWE. We recall that, while the correction is implemented in the slope space, the control space of the LWE is in fact restricted to the KL modes. For the sake of completeness, we also ran the algorithm with the PP and PTT modes expressed on a DM zonal basis instead of the KL basis, and we obtained very similar results.

3.2. Simulation parameters

We used the realistic SPHERE simulation described in Sect. 2.2.4. We implemented the proposed control of the PTT modes, as described in 3.1.2. We also modified the differential tip-tilt sensor in order to measure PP modes, as described in Sect. 3.1.3. We included atmosphere turbulence phase screens to verify their possible interplay with the proposed LWE mitigation algorithm. The LWE is only observed under good atmospheric conditions, and we thus simulated such a situation (von Karman power spectral with Fried parameter $r_0 = 16.8$ cm, outer scale $L_0 = 40$ m, coherence time $\tau_0 = 5$ ms, all defined at $\lambda = 500$ nm). We kept the same sequence of atmospheric phase screens in all simulations to permit a direct comparison of the outcome. No noise sources were simulated (no photon noise or read-out noise).

We tested two static LWE phase patterns. The LWE #1 was the input LWE that corresponds to the measured ZELDA post-AO residuals displayed in Fig. 7a. The corresponding input LWE contained a mix of PP and PTT perturbations that displayed a clear curl structure. The simulated post-AO residuals, without any mitigation of the LWE, had 173 nm rms and 650 nm ptv OPD. The LWE #2 was an input LWE that induced very strong PTT in post-AO residuals. The simulated post-AO residuals, without any mitigation of the LWE, had 276 nm rms and 1350 nm ptv OPD. The post-AO residuals for these two LWE perturbations are displayed in Figs. C.1 and C.2 respectively.

3.3. Results

The results from testing the proposed mitigation algorithm are summarized in Table 1. Three input perturbations were tested: no-LWE, LWE#1 and LWE#2. The corresponding map of residual wavefront for the different correction basis can be found in Appendix C.

The no-LWE case demonstrates that the proposed mitigation algorithm does not significantly disturb the AO loop. This is already a very important result. More precisely, the small −0.4% SR when the PP control is activated can be ascribed to the suboptimal try-and-error focal-plane analysis. A phase diversity algorithm (for instance F&F) would be required for a more stable, even PP mode measurement.

The LWE#1 perturbation is responsible for −25% SR if no specific LWE correction is applied. Our proposed PTT control allows us to recover +16% SR in a convergence time of about 150 ms (180 loop time steps). Turning on the PP control leads to recovering another +4% SR. The final SR of 85% is only 3.3% behind the best possible correction allowed by the first 990 KL modes.

The LWE#2 perturbation corresponds to a strong LWE that is responsible for a –59% SR loss. Here the PTT control leads to +30% SR and the additional PP control leads to an additional +16% SR. The final SR after the convergence of our mitigation algorithm is only 8% lower than the best achievable correction in

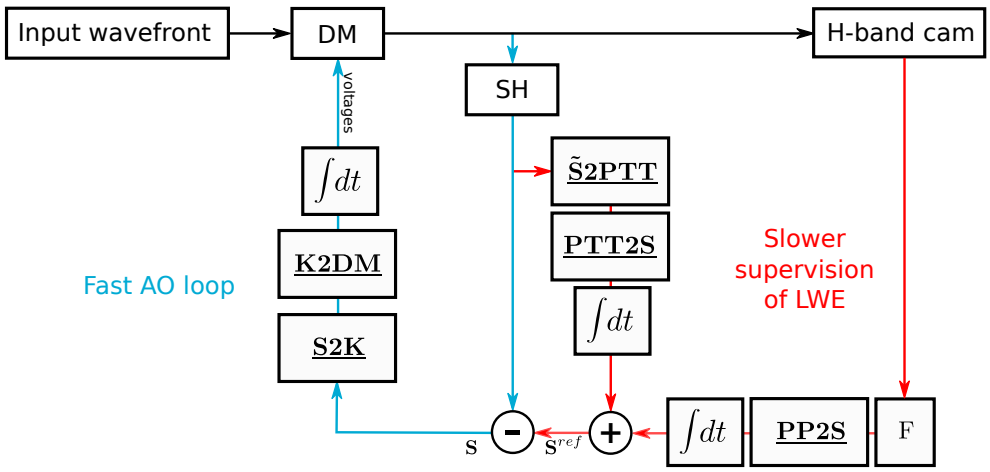

Fig. 10. Block diagram for the proposed LWE correction algorithm. The main AO loop is in cyan. The added supervision algorithm is in red.

Table 1. Results from the corrective algorithm tests performed in simulation.

LWE #	Atmos.	LWE rms/ptv (nm)	LWE corr. basis	Final SR	Final rms (nm)
	Yes		None	90.5 ± 2.0%	81 ± 9
	Yes		PTT	90.6 ± 2.0%	80 ± 9
	Yes		PTT + PP	90.1 ± 1.8%	82 ± 8
1	Yes	173/650	None	65 ± 3%	173 ± 15
1	Yes	173/650	PTT	81 ± 5%	122 ± 18
1	Yes	173/650	PTT + PP	85 ± 4%	106 ± 13
1	Yes	173/650	Best fitting KL [(a)]	88.3 ± 2.7%	92 ± 11
2	Yes	276/1350	None	31.2 ± 2.2%	276 ± 9
2	Yes	276/1350	PTT	61 ± 6%	193 ± 18
2	Yes	276/1350	PTT + PP	77 ± 6%	140 ± 24
2	Yes	276/1350	Best fitting KL [(a)]	85.7 ± 2.7%	107 ± 10

Notes. In Col. 3, entitled "LWE rms/ptv", values correspond to the post-AO residual without LWE correction. SR values are in *H* band, after convergence of the LWE correction. Values after ± correspond to the standard deviation of the SR and rms on a 10-second sample. [(a)]"Best fitting KL" corresponds to the best possible correction in the 990 KL modes space. To obtain it, we projected the post-AO residuals (without LWE correction algorithm) from the phase space to the KL space. We applied the resulting best-KL fit on an additional DM in our simulated system. The additional DM corrects for the static LWE residuals when the original DM in the AO loop corrects for the atmosphere.

the KL space. We investigated this difference and concluded that our basis (Fig. 8) composed of PTT is not sufficient for controlling the curved content of the LWE aberrations. The algorithm corrects for most of the pupil-scale vortex structure but struggles with the correction of smaller, intricate vortexes around spiders. Deliberately, this LWE#2 perturbation induces strong local vortexes, putting our algorithm in a challenging situation. Still, results show that the proposed mitigation provides a very significant improvement. It also demonstrates that the method has a wide linearity range, allowing it to operate even with strong PTT (1350 nm ptv OPD).

Overall, these results validate the proposed measurement and correction strategies to mitigate the PTT content of the LWE. These results also demonstrate that there is no damaging interplay between the proposed correction algorithm and the atmosphere. The proposed algorithm converges in about 200 AO loop iterations, well in agreement with the low gain 0.005 in the integrator. The effective –3dB correction bandwidth is ≈0.6 Hz (about 100 times slower than the main AO loop).

4. Discussion

4.1. Advantages and limitations of the mitigation strategy

The proposed SH-based algorithm dedicated to PTT correction for a partial control of the LWE has some evident advantages. First, the method allows us to recover more than half of the loss of SR due to the LWE, without the use of any additional sensor. Only software modifications are needed to implement it on SPHERE, the AOF or GRAVITY+, for which high-resolution SHs are used. Second, the method is compatible with a subsequent focal-plane analysis in order to control the three PP modes. Even more critically, only one of these three remaining modes is even, and thus requires a fundamentally nonlinear analysis. This simplification is especially interesting when dealing with focal-plane sensing affected by non-common path aberrations. Third, because the method is based on the fast measurement provided by the SH, it has a high temporal bandwidth, sufficient to track LWE temporal evolution (see Sect. 4.2 for a specific discussion on the bandwidth of the LWE). Finally, the method benefits

from the wide linearity range of the SH. In our simulations, the algorithm successfully corrected for PTTs up to 2 µm OPD ptv. This amplitude corresponds to the strongest LWE events documented so far, with less than 10% SR. It is important to notice that the proposed modified controller does not remove the origin of the LWE aberrations (discontinuities), so this notion of capture range does matter.

However, the method obviously suffers from the following limitations. First, it is only a partial solution to tackle the LWE since it only corrects for PTT modes whereas PPs are also significant, low-order contributors. Second, higher-order petal modes (higher than PTTs) are required to correct more complex aberrations introduced by the LWE. Still, their contribution is significantly smaller than the PP and PTT modes (see Appendix D). Third, the correction bandwidths of the turbulence (main AO loop) and of the PTTs (slower modification of the reference slopes) must be sufficiently different to minimize the coupling of the turbulence into the island effect. Indeed, the low orders from the atmosphere, including the TT, project efficiently on the LWE basis. Finally, this mitigation strategy remains in the context of SH spot positioning with CoG, and we have shown that this technique does not provide reliable measurements in LWE conditions (Sect. 2.1). Other positioning techniques such as weighted CoG, thresholding, or match-filtering (Thomas et al. 2006; Ruggiu et al. 1998) might provide a more robust discontinuity measurement and could tackle the LWE problem at the wavefront sensor stage.

4.2. Amplitude and bandwidth of the low wind effect

In order to investigate the typical amplitude of the LWE, we analyzed three sequences of ZELDA measurements taken on SPHERE in 2014 (e.g., left panel of Fig. 7). Each sequence was composed of 100 images, sampled at 1.2 s. We projected PPs and PTTs for each pupil-quadrant on the ZELDA phase-screens to estimate quantitatively the contribution of each modes. Combining the three sequences, we obtained the histogram in Fig. E.1 in the appendix. First, this study confirms that the LWE test cases used in the simulation of this paper have typical shape and amplitudes. The linearity of the proposed method is thus largely sufficient to tackle even the worst PTT events. Secondly, this study confirms that PTT modes are important contributors with OPD up to 750 nm ptv. PPs reach at most 400 nm and their distributions have a much narrower range. The proposed method thus provides a significant gain even when restricted to the PTT modes.

We also computed the power spectral density (PSD) of these three ZELDA sequences. We combined the PSDs of all the PP and PTT modes, and of the three ZELDA sequences, in order to improve the overall signal-to-noise ratio. The averaged PSD is displayed in Fig. E.2 in the appendix. The PSD can be approximated by the following model:

$$f < f_c: \quad P(f) \sim (f/f_c)^{-0.4}, \tag{7}$$
$$f > f_c: \quad P(f) \sim (f/f_c)^{-1.3}, \tag{8}$$

with f the frequency and f_c = 0.06 Hz. The knee at the cut-off frequency f_c corresponds to a typical timescale of 16 s. It is well within the ≈0.6 Hz correction bandwidth of the correction algorithm for the PTTs. This validates the requirement that the PTT control loop runs much slower than the main control loop dedicated to atmosphere correction. Moreover, this frequency separation ensures that the gain for the PTTs is kept much smaller than the gain margin of the main AO loop, thus avoiding instabilities.

Both the SPHERE H-band differential tip-tilt sensor camera and the GRAVITY H-band acquisition camera have frame rates around 1 Hz. Typically, we found that corrections from a focal-plane analysis takes five to ten iterations to converge (gain of 0.1), which corresponds to a -3dB correction bandwidth of ≈0.02 Hz. This is somewhat slower than the LWE cut-off frequency f_c = 0.06 Hz derived above. Again, this highlights the importance of correcting the LWE as much as possible with the information available in the SH.

4.3. Understanding whether the low wind effect is global or local

The first LWE study on SPHERE (Sauvage et al. 2015) suggested that the PP and PTT modes were not created by the DM itself, but instead were fully part of the input perturbations, as unseen modes. The present study draws different conclusions. Our simulations show that the AO loop is not blind to PP and PTT. In particular, the simulations explain how a one-quadrant PTT perturbation can lead to a vortex aberration spread over the whole pupil after AO convergence. It indicates that (part of) the LWE problem originates from a faulty response of the AO loop to a peculiar perturbation.

To explore further this aspect, we ran simulations where the input LWE perturbation was not made of PTT- and PP-like modes, but was instead entirely localized along the spiders (see pictures in Appendix F). According to Figs. F.1 and F.2, without the AO loop, those small perturbations lead to a minor decrease in the Strehl ratio (−3 to −6% for a 500 nm OPD ptv perturbation). When closing the loop, the aberration spreads over the whole pupil because of unseen piston and uncorrectable vortex modes, and gives rise to PP- and PTT-like modes. The SR decrease is, therefore, significant (−25 to −45% for a 500 nm OPD ptv perturbation). These basic simulations demonstrate that a perturbation localized close to the spider is sufficient to create the point spread function and post-AO residuals observed on SPHERE, AOF and SCExAO. In fact, when considering the process of spiders cooling the surrounding air, such localized perturbations may appear more realistic than quadrant-scale perturbations. Further studies on AO telemetry data from the instruments affected by the LWE are required to settle the discrepancy.

4.4. Pyramid wavefront sensor and discontinuities

Many next-generation instruments will use a pyramid wavefront sensor (e.g., the second stage AO of SPHERE+ and the Single Conjugated AO Natural Guide Star (SCAO NGS) modes of the ELT). In this respect, it is important to discuss if our study on discontinuity measurements by a SH applies to the pyramid wavefront sensor too.

The pyramid wavefront sensor has a two measurement regimes (Vérinaud 2004; Guyon 2005). For low-order modes, the pyramid wavefront sensor measures slopes and has a behavior close to the SH. But for high-order modes, the pyramid behavior tends to an interferometric phase measurement. Vérinaud (2004) shows that the sensor response to a sharp phase step is very different from the SH measurement because the information at the pyramid focal plane is not localized, but is instead distributed on a wide range of subapertures. Our study has shown that, on a SH, only the subapertures directly affected by the discontinuities are (partially) sensitive to the phase step,

resulting in a bad measurement. On a pyramid, the spreading of the signal induced by the discontinuity ensures a good measurement, at least in the weak-phase regime. Also, Bertrou-Cantou et al. (2022) show that, during the best seeing conditions where the LWE occurs, the pyramid wavefront sensor can measure LWE-induced petal modes. However, measurements of phase discontinuities beyond the weak-phase regime still suffer a λ phase wrapping. We can conclude that a pyramid in the visible with good seeing conditions (or better, a pyramid in the infrared) is more suitable for the measurement of phase discontinuities than the SH with the classical CoG positioning technique.

Acknowledgements. N.P. was supported by the Action Spécifique Haute Résolution Angulaire (ASHRA) of CNRS/INSU co-funded by CNES. The authors acknowledges the support of the French Agence Nationale de la Recherche (ANR), under grant ANR-21-CE31-0017 (project EXOVLTI). The authors would like to thanks Dr. Eric Gendron for pointing us in the direction of curl structures in AO residuals, Dr. Olivier Lai for a very interesting discussion he initiated on LWE mitigation strategies, and Dr. Emiel Por for his kind assistance in the adaptation of HCIPy to our specific problem. We also would like to thanks the GRAVITY+ AO (GPAO) consortium for their support and expertise, Dr. Christophe Vérinaud and Dr. Cédric Taïssir Héritier for their illuminating discussions on pyramids wavefront sensors, and the anonymous referee that helped us to clarify the paper. This research has made use of the following python packages: matplotlib (Hunter 2007), numpy (Harris et al. 2020), hcipy (Por et al. 2018), astropy (Astropy Collaboration 2018) and scipy (Virtanen et al. 2020).

References

Astropy Collaboration (Price-Whelan, A. M., et al.) 2018, AJ, 156, 123
Baudoz, P., Dorn, R. J., Lizon, J.-L., et al. 2010, SPIE Conf. Ser., 7735, 77355B
Bertrou-Cantou, A., Gendron, E., Rousset, G., et al. 2020, SPIE Conf. Ser., 11448, 1144812
Bertrou-Cantou, A., Gendron, E., Rousset, G., et al. 2022, A&A, 658, A49
Beuzit, J. L., Vigan, A., Mouillet, D., et al. 2019, A&A, 631, A155
Boccaletti, A., Di Folco, E., Pantin, E., et al. 2020, A&A, 637, A5
Bos, S. P., Vievard, S., Wilby, M. J., et al. 2020, A&A, 639, A52
Chanan, G., Troy, M., Dekens, F., et al. 1998, Appl. Opt., 37, 140
Chanan, G., Ohara, C., & Troy, M. 2000, Appl. Opt., 39, 4706
Chauvin, G., Desidera, S., Lagrange, A. M., et al. 2017, A&A, 605, A9
Claudi, R. U., Turatto, M., Gratton, R. G., et al. 2008, SPIE Conf. Ser., 7014, 70143E
Dohlen, K., Langlois, M., Saisse, M., et al. 2008, SPIE Conf. Ser., 7014, 70143L
Fried, D. L. 1998, J. Opt. Soc. Am. A, 15, 2759
Fusco, T., Sauvage, J. F., Mouillet, D., et al. 2016, SPIE Conf. Ser., 9909, 99090U
Ginski, C., Facchini, S., Huang, J., et al. 2021, ApJ, 908, L25
Gonsalves, R. A. 2002, in European Southern Observatory Conference and Workshop Proceedings, 58, 121
Guyon, O. 2005, ApJ, 629, 592
Harris, C. R., Millman, K. J., van der Walt, S. J., et al. 2020, Nature, 585, 357
Holzlöhner, R., Kimeswenger, S., Kausch, W., & Noll, S. 2021, A&A, 645, A32
Hunter, J. D. 2007, Comput. Sci. Eng., 9, 90
Hutterer, V., Shatokhina, I., Obereder, A., & Ramlau, R. 2018, J. Astron. Telescopes Instrum. Syst., 4, 049005
Keller, C. U., Korkiakoski, V., Doelman, N., et al. 2012, SPIE Conf. Ser., 8447, 844721
Keppler, M., Benisty, M., Müller, A., et al. 2018, A&A, 617, A44
Korkiakoski, V., Keller, C. U., Doelman, N., et al. 2012, SPIE Conf. Ser., 8447, 84475Z
Korkiakoski, V., Keller, C. U., Doelman, N., et al. 2014, Appl. Opt., 53, 4565
Langlois, M., Gratton, R., Lagrange, A. M., et al. 2021, A&A, 651, A71
Luo, J., Huang, H., Matsui, Y., et al. 2015, Opt. Express, 23, 8706
Milli, J., Vigan, A., Mouillet, D., et al. 2017, A&A, 599, A108
Milli, J., Kasper, M., Bourget, P., et al. 2018, SPIE Conf. Ser., 10703, 107032A
Mouillet, D., Milli, J., Sauvage, J. F., et al. 2018, SPIE Conf. Ser., 10703, 107031Q
N'Diaye, M., Dohlen, K., Fusco, T., & Paul, B. 2013, A&A, 555, A94
N'Diaye, M., Vigan, A., Dohlen, K., et al. 2016, A&A, 592, A79
N'Diaye, M., Martinache, F., Jovanovic, N., et al. 2018, A&A, 610, A18
Oberti, S., Kolb, J., Madec, P.-Y., et al. 2018, SPIE Conf. Ser., 10703, 107031G
Por, E. H., Haffert, S. Y., Radhakrishnan, V. M., et al. 2018, in Proc. SPIE, Vol. 10703, Adaptive Optics Systems VI
Primmerman, C. A., Price, T. R., Humphreys, R. A., et al. 1995, Appl. Opt., 34, 2081
Ruggiu, J.-M., Solomon, C. J., & Loos, G. 1998, Opt. Lett., 23, 235
Sauvage, J.-F., Fusco, T., Guesalaga, A., et al. 2015, in Adaptive Optics for Extremely Large Telescopes IV (AO4ELT4), E9
Sauvage, J.-F., Fusco, T., Lamb, M., et al. 2016a, SPIE Conf. Ser., 9909, 990916
Sauvage, J.-F., Fusco, T., Petit, C., et al. 2016b, J. Astron. Telescopes Instrum. Syst., 2, 025003
Schmid, H. M., Bazzon, A., Roelfsema, R., et al. 2018, A&A, 619, A9
Schwartz, N., Sauvage, J.-F., Correia, C., et al. 2017, AO4ELT5 Proceedings, https://doi.org/10.26698/AO4ELT5.0015
Thomas, S., Fusco, T., Tokovinin, A., et al. 2006, MNRAS, 371, 323
Tyler, G. A. 2000, J. Opt. Soc. Am. A, 17, 1828
van Boekel, R., Henning, T., Menu, J., et al. 2017, ApJ, 837, 132
van Dam, M. A., Raglandb, S., & Wizinowichb, P. L. 2017, AO4ELT5 Proceedings
Vérinaud, C. 2004, Opt. Commun., 233, 27
Vievard, S., Bos, S., Cassaing, F., et al. 2019, ArXiv e-prints, [arXiv:1912.10179]
Vigan, A., Fontanive, C., Meyer, M., et al. 2021, A&A, 651, A72
Virtanen, P., Gommers, R., Oliphant, T. E., et al. 2020, Nat. Methods, 17, 261
Wilby, M. J., Keller, C. U., Sauvage, J. F., et al. 2016, SPIE Conf. Ser., 9909, 99096C
Wilby, M. J., Keller, C. U., Sauvage, J. F., et al. 2018, A&A, 615, A34
Wu, T., Berto, P., & Guillon, M. 2021, Appl. Phys. Lett., 118, 251102

Appendix A: Adaptive optics residuals with respect to the position of the discontinuity

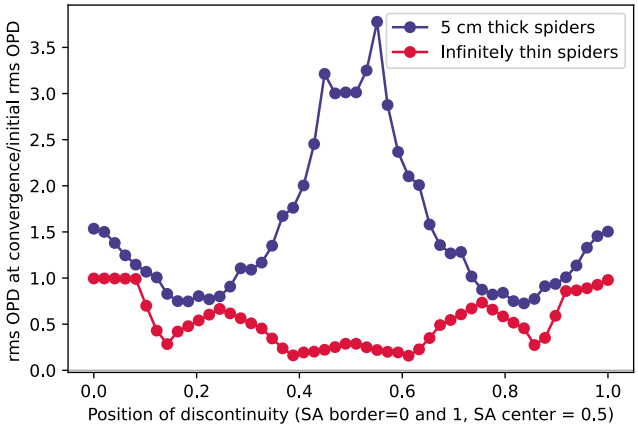

Fig. A.1: Ratio between the rms of the input aberration and the rms of the residual wavefront at convergence, when varying the position of the spiders with respect to the subapertures. The AO simulation is described in Sect. 2.2.1. The input aberration is the 80 nm OPD ptv PTT displayed in Fig. 5. The residual wavefront detailed in Fig. 5 corresponds to the leftmost red point (position = 0, infinitely thin spiders).

Appendix B: Derivations for the focal-plane analysis

In order to estimate the PP modes from the focal-plane images, we implemented a simple algorithm based on F&F, the derivations of which can be found in Korkiakoski et al. (2014). In our case the focal-plane analysis is restricted to the three PPs. We analytically derived the Fraunhofer approximation (Eq. (B.1)) in the weak-phase regime (Eq. (B.2)), thus limiting to first order:

$$\mathbf{I} = |\mathscr{F}\{\mathbf{A}\exp(i\boldsymbol{\phi})\}|^2, \tag{B.1}$$

$$\mathbf{I} \approx |\mathscr{F}\{\mathbf{A} + i\mathbf{A}\boldsymbol{\phi})\}|^2, \tag{B.2}$$

where $\mathbf{I}$ is the image, $\mathscr{F}$ is the Fourier transform operation, $\mathbf{A}$ is the pupil transmission, and $\boldsymbol{\phi}$ is the phase screen. Reducing to the three PP modes of Fig. 8 we get:

$$\boldsymbol{\phi} = P_1\,\boldsymbol{\phi}_1 + P_2\,\boldsymbol{\phi}_2 + P_3\,\boldsymbol{\phi}_3,$$

where $\boldsymbol{\phi}_1$, $\boldsymbol{\phi}_2$, and $\boldsymbol{\phi}_3$ are the normalized wavefronts of the three PP modes, and P_1, P_2, and P_3 are the corresponding amplitudes of these modes. Then,

$$\mathbf{I} \approx |\mathscr{F}\{\mathbf{A} + i\,P_1\mathbf{A}\boldsymbol{\phi}_1 + i\,P_2\mathbf{A}\boldsymbol{\phi}_2 + i\,P_3\mathbf{A}\boldsymbol{\phi}_3)\}|^2.$$

We define the following Fourier Transforms:

$$\tilde{\mathbf{A_0}} = \mathscr{F}\{\mathbf{A}\},$$
$$\tilde{\mathbf{A_1}} = \mathrm{Im}\{\mathscr{F}\{\mathbf{A}\boldsymbol{\phi}_1\}\},$$
$$\tilde{\mathbf{A_2}} = \mathscr{F}\{\mathbf{A}\boldsymbol{\phi}_2\},$$
$$\tilde{\mathbf{A_3}} = \mathrm{Im}\{\mathscr{F}\{\mathbf{A}\boldsymbol{\phi}_3\}\}.$$

The focal plane image $\mathbf{I}$ can be decomposed into the sum of an even image $\mathbf{I}_e$ and an odd image $\mathbf{I}_o$:

$$\mathbf{I} = \mathbf{I}_e + \mathbf{I}_o. \tag{B.3}$$

By investigating the symmetry of the various terms, we obtain:

$$\mathbf{I}_e \approx \tilde{\mathbf{A_0}}^2 + P_1^2\tilde{\mathbf{A_1}}^2 + P_2^2\tilde{\mathbf{A_2}}^2 + P_3^2\tilde{\mathbf{A_3}}^2 + 2\,P_1\,P_3\,\tilde{\mathbf{A_1}}\,\tilde{\mathbf{A_3}}, \tag{B.4}$$

$$\mathbf{I}_o \approx -2\,P_1\,\tilde{\mathbf{A_0}}\tilde{\mathbf{A_1}} - 2\,P_3\,\tilde{\mathbf{A_0}}\tilde{\mathbf{A_3}}. \tag{B.5}$$

Equation (B.5) defines a linear transform between the unknowns P_1 and P_3, and the observable $\mathbf{I}_o$. The set of two vectors $-2\tilde{\mathbf{A_0}}\tilde{\mathbf{A_1}}$ and $-2\tilde{\mathbf{A_0}}\tilde{\mathbf{A_3}}$ defines an interaction matrix, which can be calibrated by playing known perturbations. With the inverted interaction matrix, we obtain amplitudes of the two odd PP modes for each frame.

Equation (B.4) is nonlinear and has a fundamental sign ambiguity. To deal with the nonlinearity, we rearrange Eq. (B.5) and Eq. (B.4) into:

$$P_2\tilde{\mathbf{A_2}} \approx \sqrt{\mathbf{I}'_e - \tilde{\mathbf{A_0}}^2 - \frac{\mathbf{I}_o^2}{4\tilde{\mathbf{A_0}}^2}}, \tag{B.6}$$

where we applied the necessary normalization on $\mathbf{I}_e$ (described in Korkiakoski et al. (2014)):

$$\mathbf{I}'_e = \mathbf{I}_e + \left(1 - \frac{\max(\mathbf{I}_e)}{\max(\tilde{\mathbf{A_0}}^2)}\right)\tilde{\mathbf{A_0}}^2. \tag{B.7}$$

We found that the median of the right-hand side of Eq. (B.6) is a robust estimator of P_2. This estimate is multiplied by an unknown, constant scalar factor (the median of $\tilde{\mathbf{A_2}}$), which is calibrated manually. To lift the sign ambiguity, we implemented a (suboptimal) try-and-error approach.

Appendix C: Wavefronts corrected by the mitigation algorithm

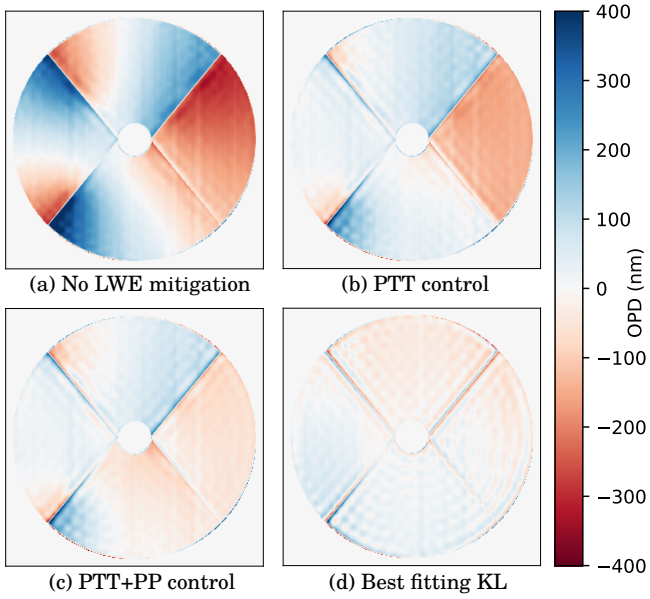

Fig. C.1: Post-AO residuals for the LWE#1 perturbation. Each (a), (b), (c), and (d) wavefront shows the OPD at the mitigation algorithm convergence for the corresponding line in Table 1. Wavefronts are averaged over 2 s to wash out the atmosphere contribution.

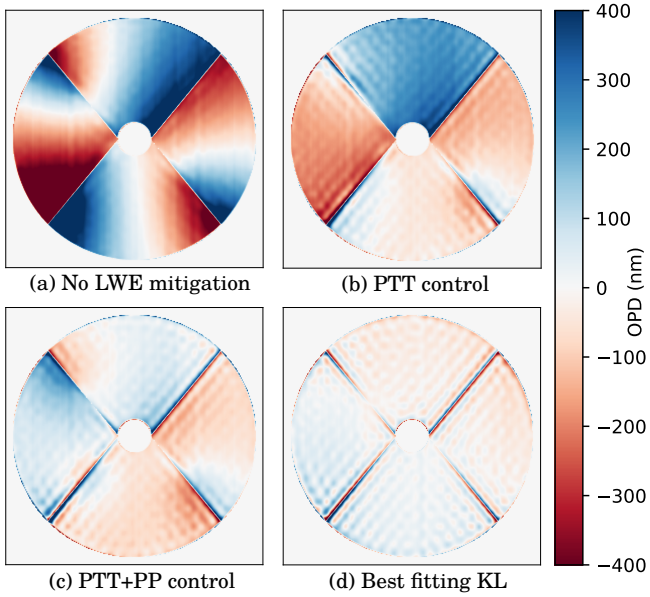

Fig. C.2: Post-AO residuals for the LWE#2 perturbation. Each (a), (b), (c), and (d) wavefront shows the OPD at the mitigation algorithm convergence for the corresponding line in Table 1. Wavefronts are averaged over 2 s to wash out the atmosphere contribution.

Appendix D: Power in the petaling modes higher than petal-tip-tilts

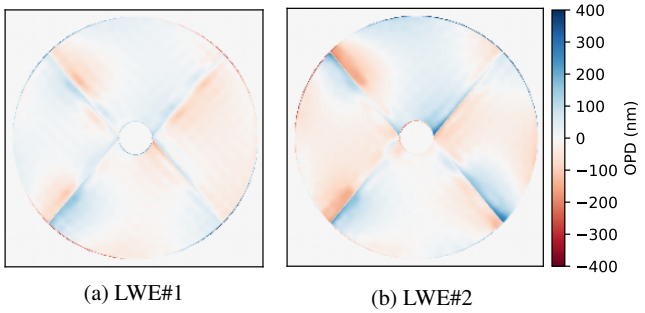

Fig. D.1: Post-AO residuals for LWE#1 and LWE#2 when assuming an ideal correction of PP and PTT. All that remains is the higher-order content composed of vortexes around the spiders.

Table D.1. Comparison of the post-AO residuals for the LWE#1 and LWE#2 perturbations, with and without an ideal PP and PTT correction.

LWE #		SR	rms (nm)
1	Uncorrected post-AO residuals	70 %[a]	160[a]
1	PP+PTT ideal correction	98 %[b]	37[b]
2	Uncorrected post-AO residuals	34 %[c]	263[c]
2	PP+PTT ideal correction	96 %[d]	55[d]

Notes. Residuals after the ideal PP+PTT correction give the power of the higher-order LWE petaling modes. These values are taken without atmosphere. SR values are in H band. [(a)] corresponds to Fig. C.1.a but without the atmosphere contribution. [(b)] corresponds to the OPD screen on Fig. D.1a. [(c)] corresponds to Fig. C.2.a but without the atmosphere contribution. [(d)] corresponds to the OPD screen on Fig. D.1b.

Appendix E: Analysis of ZELDA low-wind-effect sequences

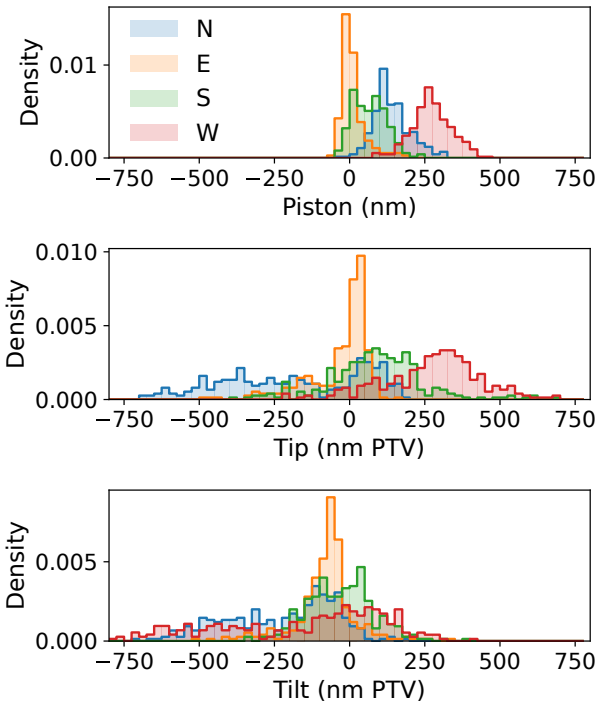

Fig. E.1: Distribution of piston, tip and tilt per quadrant (north, east, south and west) for a combination of three ZELDA sequences measured on SPHERE during the LWE. The piston reference is arbitrarily set to be 0 on average on the east quadrant.

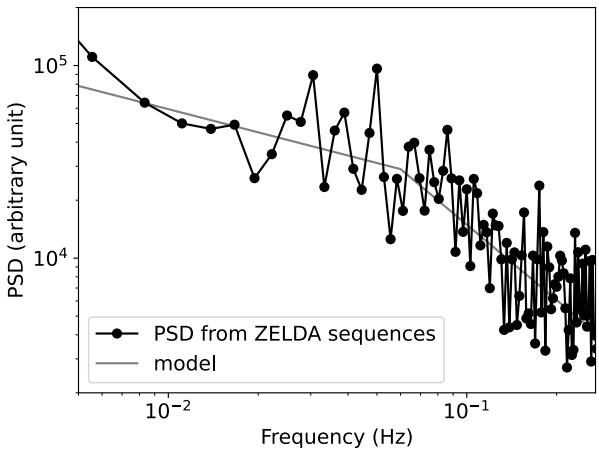

Fig. E.2: Power spectral density calculated from three sequences of wavefront measurements with the ZELDA sensor, during LWE events on SPHERE. ZELDA measurements are projected on a PP and PTT basis, and the power spectra of each mode is summed. The PSD model displays a knee at $f_c = 0.06$ Hz.

Appendix F: Adaptive optics response to local low wind effect

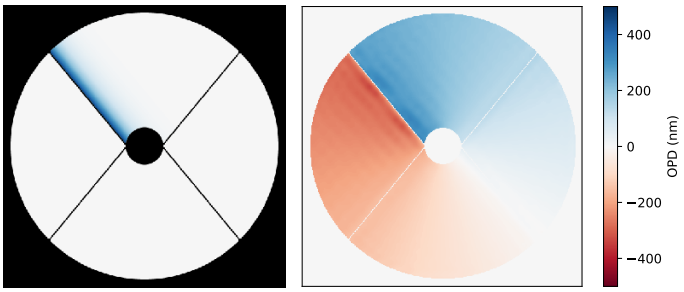

(a) Perturbation (b) Post-AO residuals

Fig. F.1: AO response to an OPD gradient localized along a spider with 500 nm OPD ptv. The OPD has a discontinuity at the position of the spider, and decreases exponentially with the distance to the spider. There is no atmosphere. The SR at H-band for the perturbation before closing the AO loop is 97% (a). The SR at AO convergence is 75% (b).

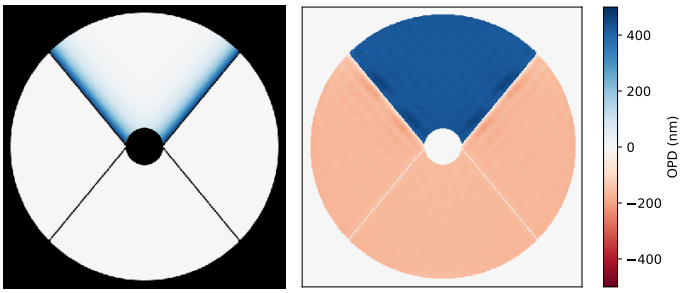

(a) Perturbation (b) Post-AO residuals

Fig. F.2: AO response to two OPD gradients localized along different spiders with 500 nm OPD ptv each. The OPD has a discontinuity at the position of the spider, and decreases exponentially with the distance to the spider. There is no atmosphere. The SR at H-band for the perturbation before closing the AO loop is 94% (a). The SR at AO convergence is 55% (b).

Understand and correct for the low wind effect on the SPHERE and GRAVITY+ adaptive optics

Nicolas Pourré[a], Jean Baptiste Le Bouquin[a], Julien Milli[a], Jean-François Sauvage[b,c], Thierry Fusco[b,c], Carlos Correia[d], and Sylvain Oberti[e]

[a]Univ. Grenoble Alpes, CNRS, IPAG, 38000 Grenoble, France
[b]DOTA, ONERA, Université Paris Saclay (COmUE), France
[c]Aix Marseille Univ, CNRS, CNES, LAM, Laboratoire d'Astrophysique de Marseille, Marseille, France
[d]Space ODT - Optical Deblurring Technologies, Rua Direita de Francos, 1021, Rés-Do-Chão Esquerdo 4250-194 Porto, Portugal
[e]European Southern Observatory, Karl-Schwarzschild-Straße 2, 85748 Garching, Germany

ABSTRACT

The low wind effect is responsible for uncorrected aberrations that reduce the contrast of exoplanet observations during the nights where the atmospheric conditions are the best. This effect arises at the aperture of 8 meter telescopes such as the Very Large Telescope (on SPHERE, Adaptive Oprics Facility (AOF)), Subaru (on SCExAO) and Gemini South (GPI). It is a thermal effect occuring at the spiders that hold the secondary mirror. We use numerical simulations to understand why the high-order adaptive optics fail to correct for low wind effect. Our simulations show that the adaptive optics might amplify/create most of the undesired residuals. We propose a mitigation strategy based on both Shack-Hartmann measurements and H-band focal plane images. We speculate that, contrary to a common belief, the low wind effect could be a local effect on the pupil that is spread out by the adaptive optics loop.

Keywords: low wind effect, high-contrast, adaptive optics

1. INTRODUCTION

The goal of obtaining direct images of exoplanets orbiting their host star has driven tremendous efforts in designing instruments. Instruments tended toward high order extreme Adaptive Optics to bring the biggest existing telescopes to their diffraction limit. On the way, numerous obstacles appeared such as the vibrations and the non-common-path aberrations. Additionally, in this race for high angular resolution and high contrast, an unexpected hurdle has became of prime concern: the low wind effect (LWE). It have been first detected during the commissioning of the Spectro-Polarimetic High contrast imager for Exoplanets REsearch (SPHERE) at the Very Large Telescope (VLT)[1] and has been considered as the main limitation of the instrument at that time.[2]

The LWE have first been detected because of its strong impact on focal plane images. When the effect is present, near-infrared images display bright lobes at the location of the first Airy ring and even a fragmentation of the core of the point-spread-function in the strongest cases. On SPHERE, these secondary lobes are responsible for starlight leaking through the coronagraphs and degrade the raw contrast by a factor 50 at 100 mas.[3] Also, the degradation of the point-spread-function prevents non-coronagraphic exoplanets direct observations at short angular separation. The bright lobes location and intensity vary in a timescale between 1 and 2 seconds on the VLT but the analysis of longer image sequence show that part of the effect is consistent over around one minute. To further investigate the LWE, measurements have been performed on SPHERE with the Zernike phase mask ZELDA[4,5] . It allows for a conversion of pupil phase aberrations into intensity on the image plane (Fig. 2). The ZELDA measurements during LWE events revealed sharp optical path difference (OPD) discontinuities at the spiders and piston, tip, tilt aberrations restricted to the four pupil quadrants.

Send correspondence to Nicolas Pourré
E-mail: nicolas.pourre@univ-grenoble-alpes.fr

Adaptive Optics Systems VIII, edited by Laura Schreiber, Dirk Schmidt, Elise Vernet,
Proc. of SPIE Vol. 12185, 121855C · © 2022 SPIE
0277-786X · doi: 10.1117/12.2629793

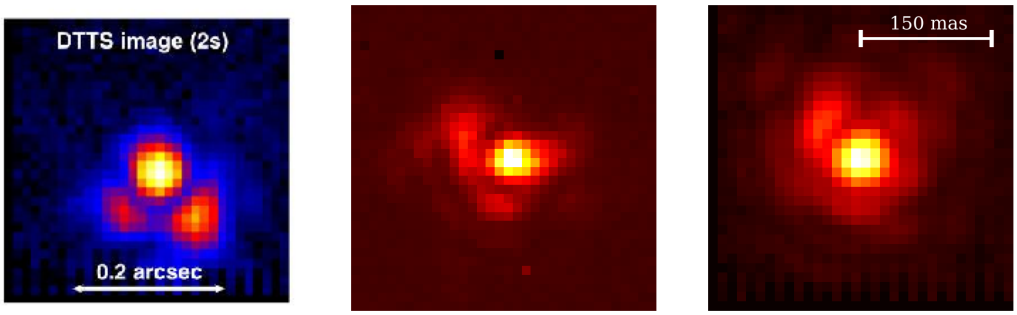

(a) (b) (c)

Figure 1: Three LWE point spread functions averaged over different durations. (a) Image from the Differential Tip Tilt Sensor (DTTS) on SPHERE taken from Milli et al. 2018. The image is at H-band and is averaged over 2 seconds. (b) Image with IRLOS at H-band from the AOF. Averaged over 10 seconds. (c) Image from the DTTS, average over 1.5 minute.

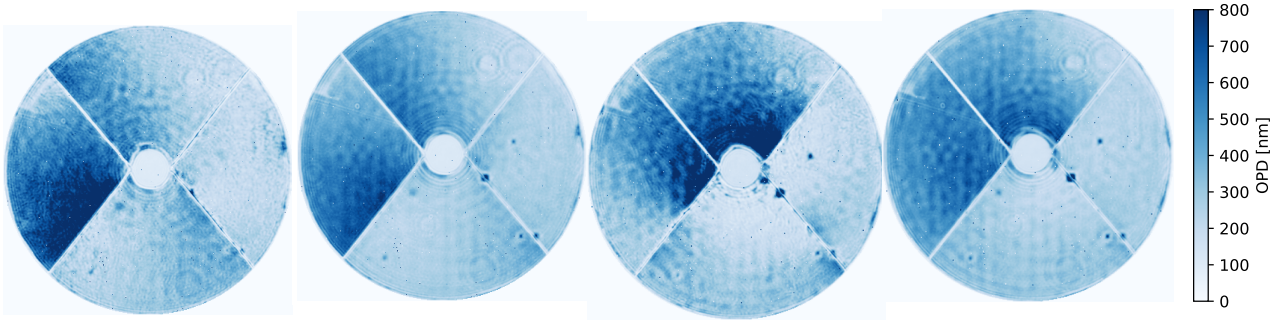

(a) 1 s DIT at 1:52 UT (b) 2 min average at 1:52 UT (c) 1 s DIT at 2:44 UT (d) 2 min average at 2:44 UT

Figure 2: Pupil OPD measurement with the Zernike phase mask ZELDA on SPHERE. Taken during the LWE night of 8 October 2014 during SPHERE commissioning.

The low wind effect appears during the nights with surface wind below 4 m.s^{-1}.[3] In this condition, the air is not well mixed at the telescope aperture and a laminar air flow can develop around the spiders holding the secondary mirror. The air cools down at the contact of the spiders and this thermal exchange is responsible for layers of colder air (and lower optical index) in the telescope pupil, creating aberrations with sharp OPD discontinuities. The LWE is present during the nights where otherwise the atmospheric conditions are the best, therefore this effect has to be mitigated. There has been efforts in various directions to correct for LWE. First of all, at the VLT a coating has been applied on the spiders of the Unit Telescopes 3 to limit emissivity in the mid-infrared. This passive solution limited the occurrence of the phenomenon from 20% to 3.5% of the observing time.[3] There are also mitigation strategies relying on a focal plane measurement of the LWE aberrations and a correction by the adaptive optics (see Vievard et al. 2019[6] for an overview). Some of these active techniques have already been tested in laboratory and on-sky (e.g. Fast & Furious algorithm[7,8]).

Here we investigate the effect of the LWE phase discontinuities on a Shack-Hartmann based adaptive optics. This investigation will bring an explanation for the post-AO residuals observed on SPHERE during LWE events. Also we will propose an active mitigation strategy that uses the SH measurements and a focal plane analysis. This mitigation algorithm can be implemented on any instrument with a high-resolution SH and affected by the LWE such as SPHERE and GRAVITY+ at the VLT. In the paper, non-bold variables are scalars, bold variables are vectors and bold-underlined variables are matrices. $\cdot$ is for matrix product.

2. SHACK-HARTMANN MEASUREMENT OF DISCONTINUITIES

The most striking feature of the LWE aberrations measured by the ZELDA sensor is the sharp OPD discontinuities. We will investigate how discontinuities are measured by the SH wavefront sensor. For this, we will

use numerical simulations at the SH sub-aperture scale and study the sensitivity to phase discontinuities. We will stay in the SPHERE and GRAVITY+ configuration with spiders obstructing 25% of the SH sub-aperture and with a sub-aperture field of view of 3.5 λ/d, with d the width of the sub-apertures. The focal plane is oversampled compared to the realistic 6x6 pixels per spot.

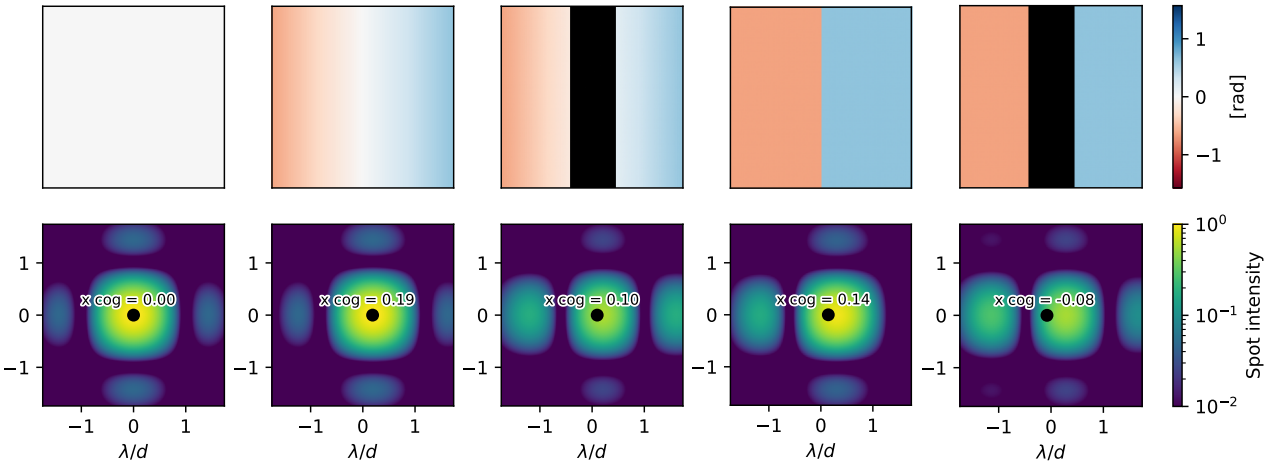

(a) (b) (c) (d) (e)

Figure 3: Square aperture phase (top) and corresponding SH spot (bottom) in different configurations. (a) no aberration. (b) phase slope of $0.2 \times 2\pi$ amplitude. (c) phase slope obstructed by a spider. (d) phase discontinuity with same peak-to-valley amplitude as the slope. (e) phase discontinuity obstructed by a spider. The black dot displays the center-of-gravity measured in the 3.5 λ/d field of view.

Figure 3 displays how a spot can be distorted by a phase discontinuity across the sub-aperture and how the center-of-gravity of the spot can be affected. A phase slope of amplitude $\Delta\varphi = a \times 2\pi$ rad induces a spot displacement of $a \times \lambda/d$ at the focal plane. In this example $a = 0.2$, so the measurement accuracy is given by the difference between the `x cog` value displayed and 0.2. Regarding morphological features, we can see that the difference between a phase slope and a phase discontinuity (Fig. 3b and 3d) is that the discontinuity is responsible for a bright secondary lobe. For this reason, the center-of-gravity in the restricted field of view do not measure the right value (on a infinite field of view it would measure 0.2 λ/d, the right value for the phase step introduced). This phenomenon is even more prominent when the discontinuity is obstructed by a spider (Fig. 3c and 3e). In this case the sub-aperture sensitivity to the phase discontinuity is reduced and can even be reversed.

A more detailed study of the sub-aperture sensitivity to a phase discontinuity at different positions is displayed on Fig. 4. It shows that the sensitivity is different depending on the discontinuity location in the sub-aperture. We recover an expected result, if the discontinuity is located at the border of the sub-aperture the ability of the sub-aperture to measure the phase step is dramatically reduced. For a non-obstructed discontinuity the sensitivity varies by up to 20% depending on the location of the discontinuity. For a discontinuity obstructed by a spider, the measurement never gets close to the expected value a, leading to a greatly erroneous estimation of the phase step amplitude.

The erroneous measurement by the SH does not come from the wrapping for phase discontinuities with amplitudes higher than $\lambda/4$. Figure 5 shows that even in the weak phase regime the sub-aperture sensitivity to the phase step depends on the position of the step. As expected, this bad sensitivity is even worse when the discontinuity is obstructed by a spider. Here the sensitivity is reversed even in the weak-phase regime. Overall, it demonstrates the inability of the center of gravity to measure obstructed phase discontinuities on a restricted field of view. Unfortunately this is precisely the kind of aberrations the LWE induces.

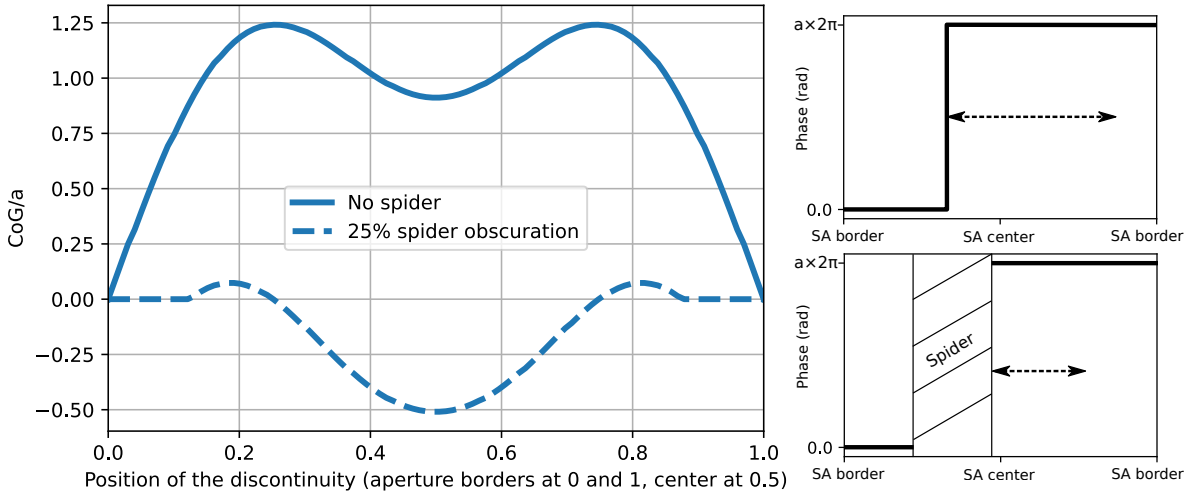

(a) (b)

Figure 4: (a) Center-of-gravity (CoG) with respect to the position of the discontinuity in the sub-aperture (SA), with and without spider. The center-of-gravity is scaled by the discontinuity amplitude a. $CoG/a = 1$ corresponds to a perfect measurement of the phase step. The simulations are carried out in the weak-phase regime ($a = 0.02$) (b) 1D sketches for the both cases with and without spider.

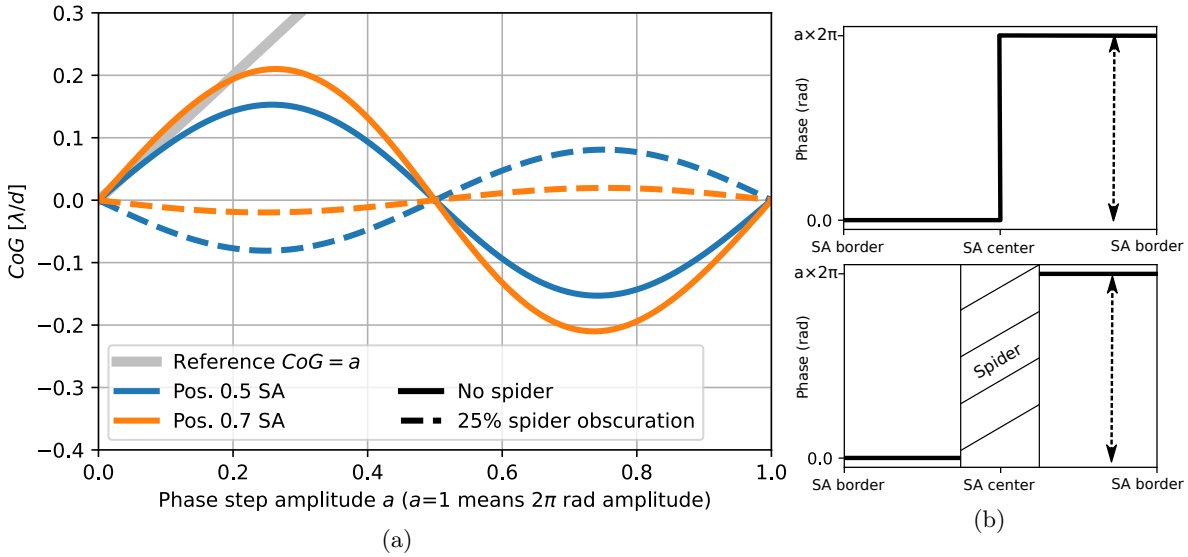

(a) (b)

Figure 5: (a) Center-of-gravity (CoG) with respect to the amplitude of the discontinuity for two positions in the sub-aperture (SA), with and without spider. The grey line shows the ideal measurement for $CoG = a$. (b) 1D sketches for the both cases with and without spider at position 0.5 SA.

3. IMPACT ON THE ADAPTIVE OPTICS

3.1 The uncorrected modes

In this section, we will use an end-to-end simulation with HCIPy[9] to investigate for the post-AO residuals when the pupil phase contains discontinuities at the spiders. The design of the AO simulation is close to the SPHERE and GRAVITY+ design with a deformable mirror (DM) of 1377 actuators (41 actuators in a pupil diameter) controlled by the firsts 990 Karhunen-Loève (KL) modes. The wavefront sensor is a 40x40 SH at λ =700 nm and each sub-aperture spot is sampled by 6x6 pixels. For now we use no spatial filter and no spot weighting. We exclude sub-apertures that receive less than 50% of the nominal flux but always keep sub-apertures located behind the spiders. Only sub apertures located behind (or too close) to the secondary mirror central obscuration

or the pupil border are excluded. The pupil is the VLT Unit Telescopes pupil with a 8 m diameter, 1.1 m central obscuration and four spiders of 5 cm width.

To simulate LWE, we will inject aberrations at the pupil-plane in the shape of pistons restricted to the four pupil quadrants separated by the spiders (petal-pistons thereafter called PP) and tip-tilts restricted to the four pupil quadrants (petal-tip-tilts thereafter called PTT). Figure 6 shows that a PP is not corrected by the AO. Even if it stays in the weak-phase regime. The PP do not induce any SH response in the quadrant and is only seen through its impact at the discontinuities obstructed by spiders. The previous section have shown that this measurement is greatly faulty, therefore the PP modes are unseen and uncorrected.

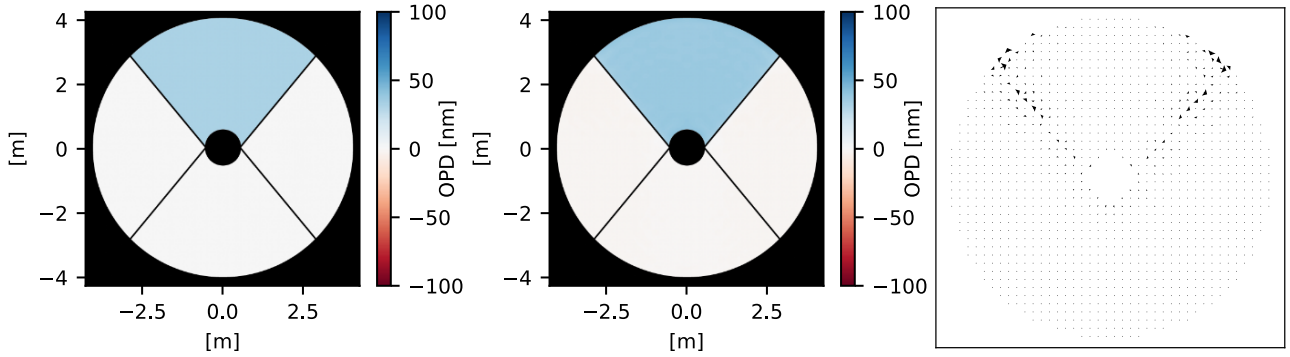

(a) PP perturbation before AO (b) Residuals after AO convergence (c) SH slopes at AO convergence

Figure 6: AO response to a petal-piston of 32 nm peak-to-valley amplitude (weak-phase regime) as perturbation. (a) perturbation before AO, the OPD is 21 nm rms. (b) post-AO residuals after convergence, the OPD rms is 24 nm rms. (c) SH slopes at convergence.

Figure 7 shows that the AO loop behaviour is different when the perturbation is a PTT. Here again, the SH response to the perturbation at the discontinuities is faulty but the SH is sensitive to the tip-tilt inside the quadrant that is a constant phase slope. When we close the loop, the AO converges to a state where neither the slopes nor the OPD is equal to zero. Rather, we see that the residual slopes pattern is composed of a global curl around the central obscuration and of local curl on the top-right spider.

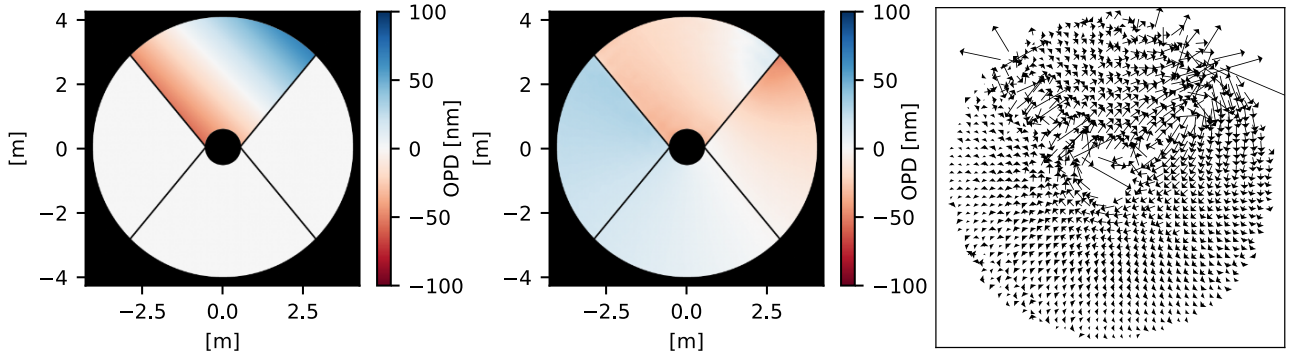

(a) PTT perturbation before AO (b) Residuals after AO convergence (c) SH slopes at AO convergence

Figure 7: AO response to a petal-tip-tilt of 100 nm peak-to-valley amplitude (weak-phase regime) as perturbation. (a) perturbation before AO, the OPD is 16 nm rms. (b) post-AO residuals after convergence, the OPD rms is 19 nm rms. (c) SH slopes at convergence.

There is a fundamental reason for these residuals. A well known vector operators law states that:

$$\overrightarrow{curl}\ \overrightarrow{grad}\ \mathscr{S} = 0 \tag{1}$$

with $\mathscr{S}$ a continuous surface. In our AO system, the $\mathscr{S}$ is the DM surface and the $\overrightarrow{grad}$ operator is the SH. Then we understand that the DM cannot induce a curl in the SH slopes. The other way around, a curl in the

SH slopes do not projects on the Karhune-Loève basis (or any other DM subspace) and remains uncorrected. This statement is true for any curl structure, be it global (at the pupil scale) or local (around a spider). Then, the question arises: why this curl structure appeared in our SH slopes if the DM cannot create it? The Figure 8 helps to understand the process. A perfect wavefront sensor (Fig. 8b) would measure the right amplitude for the discontinuity. Over a closed path, the phase step amplitude would compensates for the slope induced by the rest of the pupil and the resulting slope map would not contain any curl. The SH is not this perfect sensor, we have shown in the previous section that the SH has a reduced sensitivity to phase discontinuities. It will make a good measurement of the phase slopes on the pupil but will underestimate the phase discontinuities amplitude (Fig. 8c). For this reason the SH slopes will contain a curl component that will remain uncorrected even after the AO loop convergence. Interestingly, through this process a perturbation initially restricted to one quadrant can spread over the whole pupil after the AO convergence.

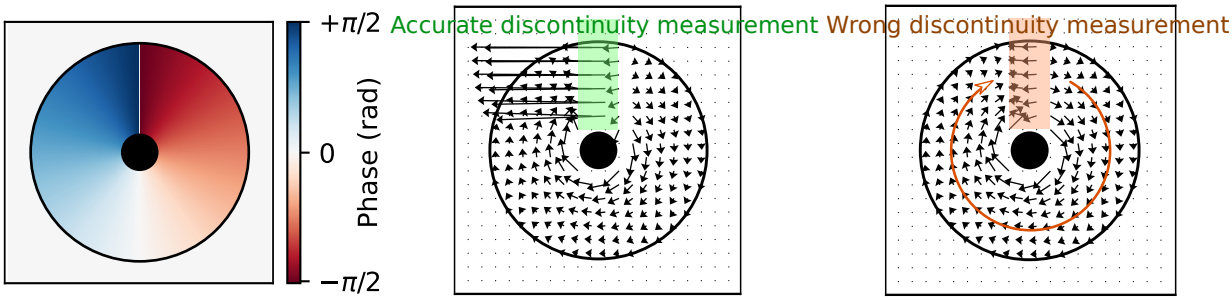

(a) Wavefront to measure (b) Good SH measurement. $\overrightarrow{curl} = 0$ (c) Wrong SH measurement. $\overrightarrow{curl} \neq 0$

Figure 8: Explanation for how a curl structure can arise in the slopes from a bad discontinuity measurement.

With the explanations for the badly corrected PP and PTT we can now reproduce the post-AO residuals observed with the ZELDA sensor on SPHERE during LWE nights. To achieve this, we refine the AO to make it closer to the SPHERE AO. We included a spatial filter of 2 λ/d, d being the width of one SH subaperture. We also included a Gaussian weighting of the SH spots for the center of gravity calculations. Finally, we included the Differential Tip-Tilt Sensor (DTTS) of the instrument.[10] In SPHERE, the goal of this sub-system is to ensure the centering of the central star behind the coronagraph. It measures the residual tip-tilt thanks to a centre of gravity measurement on a dedicated H-band camera and send a corrective command to a specific tip-tilt mirror before the SH. In our simulations the DTTS appeared to be responsible for residual tip-tilts when the system is exposed to a LWE perturbation. It is expected since we have shown that phase discontinuities can mislead a center of gravity mesurement on a spot. With this improved AO simulation, we are able to reproduce qualitatively the post-AO residuals observed on SPHERE (Fig. 9).

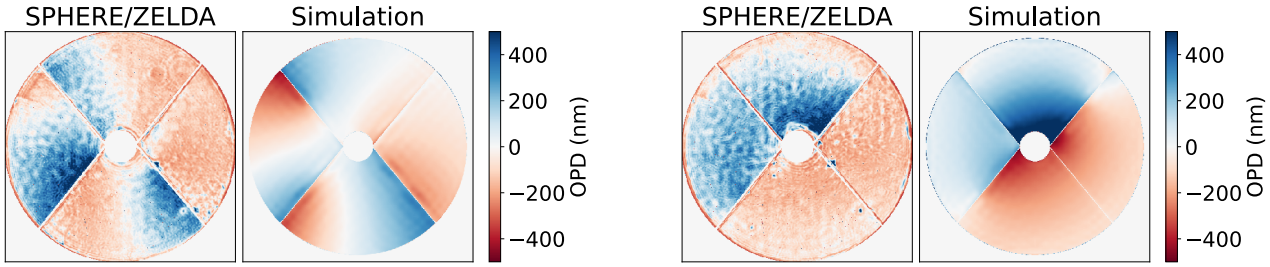

(a) (b)

Figure 9: Qualitative reproduction of the LWE post-AO residuals observed on SPHERE with the ZELDA sensor.

3.2 Local perturbations

So far, we have simulated LWE with petal-pistons and petal-tip-tilts perturbations at the pupil plane. However, it would be surprising if the cooling of the spiders on the ambient air was creating regular pistons or tip-tilt on a whole pupil quadrant. We would expect the colder layer to be localized along the spiders and have a limited

spatial extension. We ran simulations with perturbations composed of OPD gradients along the spiders rather than full quadrant PP and PTT (Fig. 10). We have shown in our analysis that the bad correction of LWE aberrations come from an erroneous measurement of discontinuities by the SH. Our simulations with a local OPD gradient confirms that a discontinuity is enough to create all the post-AO residuals observed on SPHERE. If the sum of all OPD gradient along the spiders contribute in the same rotation direction there will be a curl pattern in the residual SH slopes and a vortex pattern in the phase. Two OPD gradients contributing in an opposite direction will induce petal-pistons in the vortex phase. These simulations show that the AO can be responsible for creating most of the residual aberrations that degrade focal plane images during LWE events. It contradicts the observations of the DM voltages on SPHERE[2] that show no sign of the DM creating the petal aberrations. More work is required to settle this discrepancy.

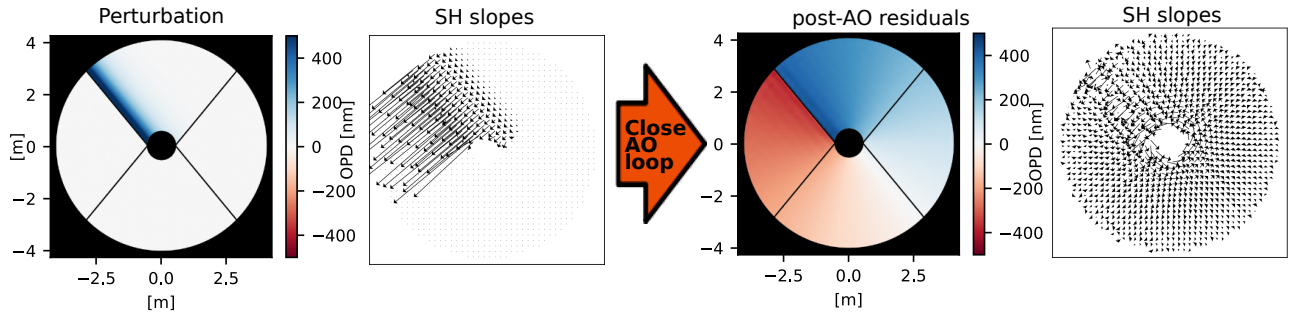

(a)

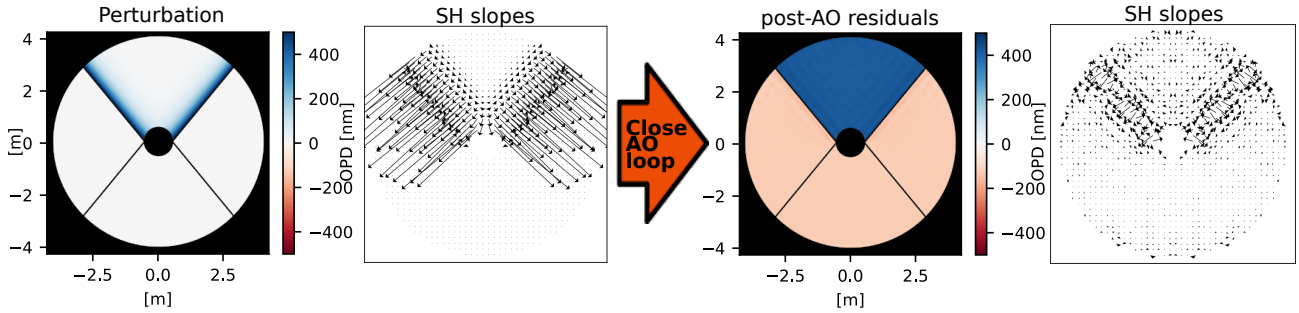

(b)

Figure 10: Closing the AO loop on OPD gradients along the spiders. (a) one OPD gradient along a spider. The perturbation is of 89 nm rms (Strehl H-band 92%). After AO convergence the residuals are of 225 nm rms (Strehl H-band 69%). (b) two OPD gradients along two different spiders. The perturbation is of 81 nm rms (Strehl H-band 92%). After AO convergence the residuals are of 243 nm rms (Strehl H-band 63%).

3.3 What can we expect on the next generation telescopes?

Next generation giant telescopes (e.g. ELT) have thicker spiders. If the spiders are thicker than the SH subapertures, the wavefront sensor cannot ensure continuity between the separated parts of the pupil and uncorrected petal-pistons appear, this is called the island-effect. In this context there is no phase discontinuity problem since no sub-aperture see two quadrants at the same time but petal-pistons are undetectable by the SH. How does a LWE perturbation is treated by the AO for this kind of pupil?

We ran simulations with SPHERE's AO configuration (1377 actuators, 40x40 SH) but without spatial filter and without weighting of SH spots. To mimic the ELT case, we use the VLT UT pupil but with spiders 40 cm thick. Our study shows that petal-tip-tilts never occur in the post-AO residuals in such a configuration, no matter if we simulate LWE with PP and PTT in the pupil phase or with OPD gradients localized along the spiders (Sect. 3.2). It was expected since PTT come from uncorrected curl structures in the slopes that arise when the SH make a bad measurement of a discontinuity across a sub-aperture. Here no sub-apertures are affected by discontinuities, and so no PTT are visible.

Yet, it does not mean that the LWE perturbation is corrected by the AO. Even worse, the adaptive optics converges to strong PP that are responsible for a degradation of the residual OPD (Fig. 11). Still, these simulations show that in this large spiders configuration the LWE becomes PP problem only.

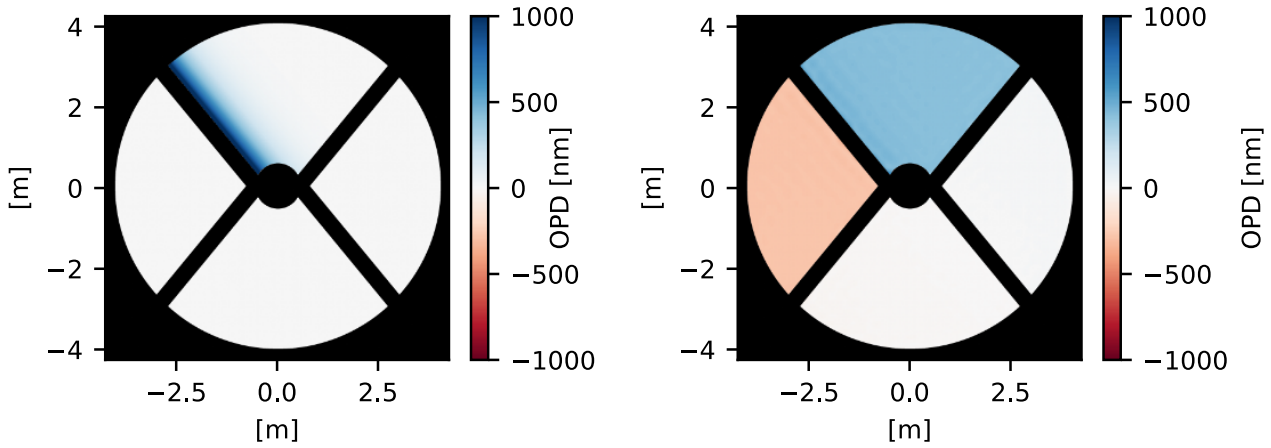

(a) Before AO (b) After AO convergence

Figure 11: (a) Perturbation at the pupil plane composed of an OPD gradient along the top-left spider. The OPD is 150 nm rms. (b) Residuals after AO convergence. The OPD is 255 nm rms.

4. MITIGATION STRATEGY

We describe here a mitigation strategy that uses the SH to measure the PTT modes and a focal plane analysis to measures the PP modes. LWE mitigation algorithms usually control 11 modes (3 petal-pistons and 8 petal-tip-tilt).[8,11,12] Excluding the control of the global piston reduces the number of PP modes to three. Here we propose to use a modified basis where we rearranged the PP and PTT modes into odd and even modes (Fig. 12). Thanks to this new basis, we see that two PTT modes do not contain discontinuities (modes #4 and #8), they are naturally corrected by the AO. Only 9 modes leave to correct, 3 PP modes and 6 PTT modes.

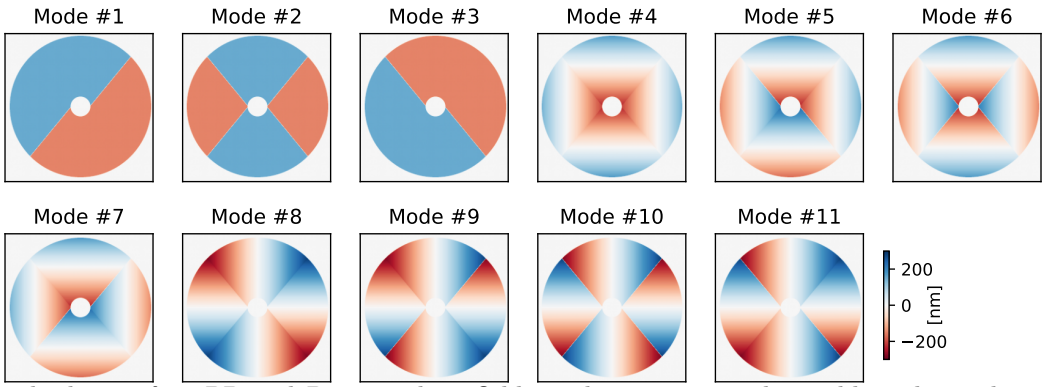

Figure 12: The basis of 11 PP and PTT modes. Odd numbers correspond to odd modes and even numbers correspond to even modes.

For the PTT modes measurement, we propose to use the information in the SH slopes. As we have seen before, the SH is sensitive to the PTT inside the quadrant but poorly sensitive at the discontinuity. Our measurement strategy relies only on the slopes located in the quadrant and discards the slopes located too close to the discontinuity. We select the sub-apertures located in the blue area on Fig. 13 and project the slopes on the 6 PTT modes at each iteration of the AO loop. It gives a measurement at a frequency of 1200 Hz and benefits from the wide SH capture range (PTT up to 2 μm peak-to-valley).

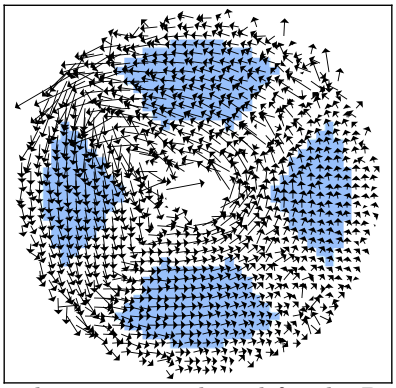

Figure 13: Blue: sub-apertures selected for the PTT measurement.

For a full measurement of the 9 LWE modes, we propose to measure the petal-pistons with a focal plane analysis. The focal plane approach has already been studied extensively for measuring petal modes. It requires a phase diversity or an asymmetric pupil to lift the sign ambiguity on the even modes. But here there are only three PP modes left to measure and, in the basis shown on Fig. 12, we can see that there is only one even PP mode (mode #2). The other two odd PP modes can be measured from a single image as long as the mode amplitude remains in the algorithm capture range (typically OPD peak-to-valley $< \lambda/2$). The method for the PP modes measurement at focal plane is inspired from the Fast & Furious algorithm.[13] In the Fraunhofer approximation the image $\mathbf{I}$ expression is:

$$\mathbf{I} = |\,\mathscr{F}\{\mathbf{A}\exp(i\boldsymbol{\phi})\}\,|^2, \tag{2}$$

with $\mathscr{F}$ the Fourier transform operation, $\mathbf{A}$ the pupil amplitude, $\boldsymbol{\phi}$ the pupil plane phase. If we consider only the three PP modes:

$$\boldsymbol{\phi} = P_1\,\boldsymbol{\phi}_1 + P_2\,\boldsymbol{\phi}_2 + P_3\,\boldsymbol{\phi}_3, \tag{3}$$

with P_1, P_2 and P_3 the modes amplitudes, in the weak-phase regime we can write:

$$\mathbf{I} \approx |\,\mathscr{F}\{\mathbf{A} + i\,P_1\mathbf{A}\boldsymbol{\phi}_1 + i\,P_2\mathbf{A}\boldsymbol{\phi}_2 + i\,P_3\mathbf{A}\boldsymbol{\phi}_3)\}\,|^2. \tag{4}$$

Let us define the following notations:

$$\begin{aligned}
\tilde{\mathbf{A_0}} &= \mathscr{F}\{\mathbf{A}\},\\
\tilde{\mathbf{A_1}} &= \mathrm{Im}\{\,\mathscr{F}\{\mathbf{A}\boldsymbol{\phi}_1\}\,\},\\
\tilde{\mathbf{A_2}} &= \mathscr{F}\{\mathbf{A}\boldsymbol{\phi}_2\},\\
\tilde{\mathbf{A_3}} &= \mathrm{Im}\{\,\mathscr{F}\{\mathbf{A}\boldsymbol{\phi}_3\}\,\}.
\end{aligned}$$

Finally, splitting the image into an odd and an even component we obtain:

$$\mathbf{I}_e \approx \tilde{\mathbf{A_0}}^2 + P_1^2\tilde{\mathbf{A_1}}^2 + P_2^2\tilde{\mathbf{A_2}}^2 + P_3^2\tilde{\mathbf{A_3}}^2 + 2\,P_1\,P_3\,\tilde{\mathbf{A_1}}\,\tilde{\mathbf{A_3}}, \tag{5}$$

$$\mathbf{I}_o \approx -2\,P_1\,\tilde{\mathbf{A_0}}\tilde{\mathbf{A_1}} - 2\,P_3\,\tilde{\mathbf{A_0}}\tilde{\mathbf{A_3}}. \tag{6}$$

The equation 6 is linear, so the amplitudes of the odd modes P_1 and P_3 can be determinate without ambiguity. In the equation 5, the only unknown is the amplitude of the even mode P_2 but the sign cannot be measured from a single image. In our algorithm we implemented a trial-and-error approach to deal with this sign ambiguity.

Once measured, the 9 LWE modes correction is applied in the AO loop via a modification of the reference slopes. As described in the previous section, the petal modes in the phase space contain phase discontinuities that are badly seen by the SH. In order to smooth the discontinuities, we project the LWE petal modes into

the KL basis to obtain the matrices **PTT2K** and **PP2K**. Then we use the interaction matrix **K2S** to obtain **PTT2S** and **PP2S**, the best expression of the LWE modes in the slopes space:

$$\mathbf{PTT2S} = \mathbf{K2S} \cdot \mathbf{PTT2K}, \tag{7}$$

$$\mathbf{PP2S} = \mathbf{K2S} \cdot \mathbf{PP2K}. \tag{8}$$

Finally, using the PTT amplitudes measured with the SH and the PP amplitudes measured at the focal plane we can modify the reference slopes during the AO loop operation and correct for the 9 LWE modes (Fig. 14).

Regarding the temporal aspects, it is necessary to decouple the PTT correction to the atmosphere correction by the AO loop. If we do not, the PTT control will come into conflict with the atmosphere correction and disturb the nominal AO loop operation. To avoid this, we apply the LWE PTT correction with a low gain at 0.005 when the full KL atmosphere correction is applied with a gain of 0.3. This way the PTT algorithm take 170 ms to converge, that is enough to control for the LWE that evolves on a timescale of a few seconds. On the petal-piston side, the DTTS on SPHERE and the acquisition camera on GRAVITY can provide H-band images at a frequency around 1 Hz. It means that the PP correction algorithm can converge on a timescale of 10 s. At this timescale there is no risk to disturb the atmosphere correction but it is also too slow to correct for the fast LWE evolution on a timescale of 1∼2 sec. Still, it can correct for the quasi-static component of the LWE. The low measurement frequency of focal plane analysis justifies the use of the faster SH to measure as much as possible LWE modes.

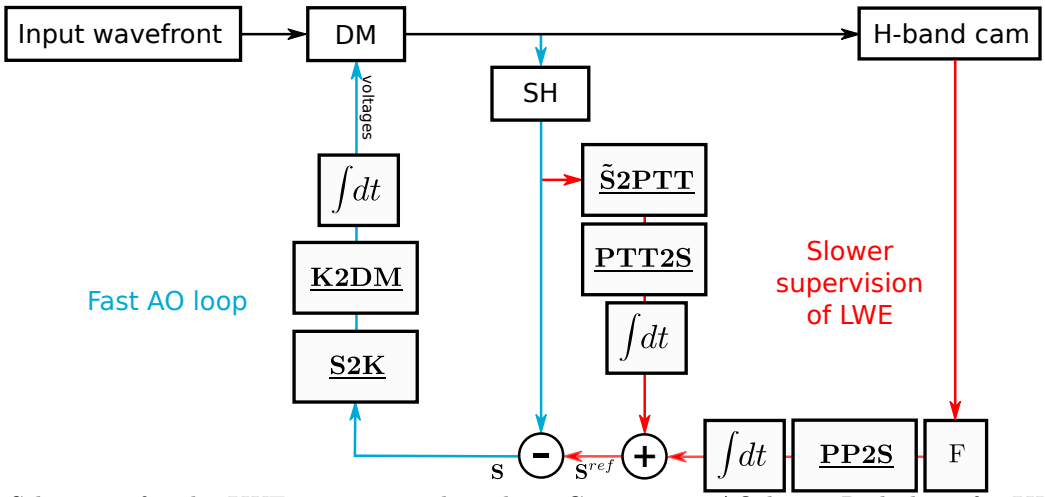

Figure 14: Schematic for the LWE mitigation algorithm. Cyan: main AO loop. Red: loop for LWE control. $\int dt$ are integrators. F is the operation that extracts the three PP modes amplitudes from the H-band images. $\tilde{\mathbf{S}}$ refers to the slopes selected inside the quadrants for PTT measurement (Fig. 13).

We tested our mitigation strategy in simulations. We used the SPHERE-like end-to-end AO simulation described at the previous section. The only difference is that we do not use the DTTS as a tip-tilt sensor but has a PP sensor (as described previously). We simulate LWE with two static phase patterns containing PP and PTT as perturbations. The LWE#1 induce post-AO residuals that correspond to what has been observed on SPHERE (Fig. 9a). The post-AO residuals contain 173 nm rms and 650 nm peak-to-valley OPD. The LWE#2 induces stronger PTT in the post-AO residuals. For this pattern the residuals are of 276 nm rms and 1350 nm peak-to-valley OPD. This pattern is meant to test the algorithm limit in the PTT correction. Additionally, we included a simulated atmosphere with Fried parameter $r_0 = 16.8$ cm and coherence time $\tau_0 = 5$ ms (both defined at $\lambda = 500$ nm). Adding an atmosphere permit to check that the SH PTT control and the atmosphere control are well decoupled in the AO loop.

The tests results for the mitigation algorithm are displayed on Fig. 15. For both LWE#1 and LWE#2 perturbations the algorithm converged to weaker PTT modes in a timescale around 150 ms. For LWE#1 the Strehl at H-band before the algorithm correction is 65% and the PTT control algorithm allow for a +16% Strehl

recovering. After the algorithm convergence virtually no PTT are visible in the post-AO residuals anymore. If we run the PP control on LWE#1 we recover an additional +4% Strehl. The best fitting of the LWE modes in the 990 KL space (directly projecting the AO residuals from the phase space to the KL space, thus avoiding the measurement stage) reach 88% Strehl. Our correction algorithm reaches 85% Strehl, only 3 points below the best achievable correction. It validates our measurement strategy. For LWE#2 the Strehl before the algorithm correction is 31% and the PTT control recovers +30% Strehl. With the PP control the algorithm reaches 77% Strehl, 9 points below the best achievable correction in the KL space. The residuals after PTT+PP correction contain local vortexes around the spiders that are not captured by our SH-based measurement.

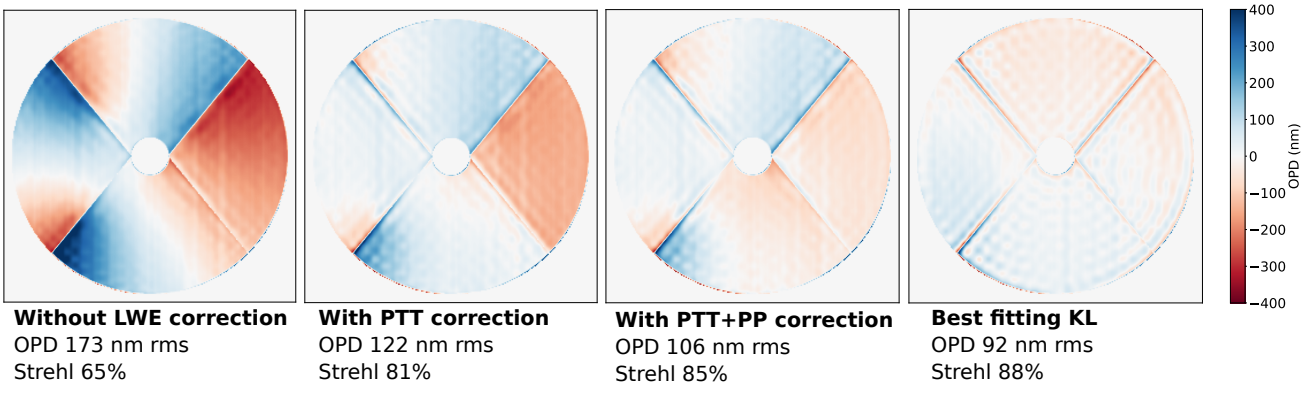

(a) LWE#1

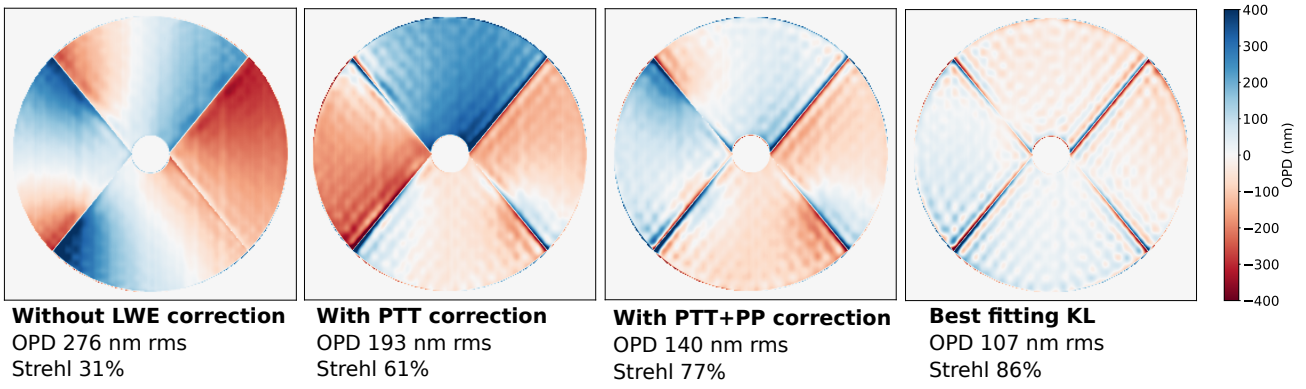

(b) LWE#2

Figure 15: Post AO residuals for (a) LWE#1 and (b) LWE#2 in different configurations. The residual are averaged over 2 seconds to reduce the atmosphere contribution. The Strehl ratios are given at H-band.

5. CONCLUSIONS

Our study shows that the SH is unable to measure obstructed discontinuities. In LWE conditions, these faulty measurements are responsible for uncorrected petal-pistons and petal-tip-tilts in the post-AO residuals. We also show that a local perturbation along the spiders is enough to reproduce the full pupil uncorrected aberrations observed on SPHERE. In this framework, the AO is responsible for most of the wavefront degradation. Then, we predict that on the next generation telescopes like the ELT the LWE will be a petal-piston problem only since with spiders thicker than the SH sub-apertures no petal-tip-tilt can arise in the AO residuals. Finally, we found that 8 out of 11 LWE modes can be corrected with the SH in AO similar to SPHERE's or GRAVITY+. We successfully tested in simulations a mitigation strategy that uses both the SH and a focal plane analysis for the measurement of the LWE modes.

ACKNOWLEDGMENTS

N. P. was supported by the Action Spécifique Haute Résolution Angulaire (ASHRA) of CNRS/INSU co-funded by CNES. The authors acknowledges the support of the French Agence Nationale de la Recherche (ANR), under grant ANR-21-CE31-0017 (project EXOVLTI). The authors would like to thanks Dr. Eric Gendron for pointing us in the direction of curl structures in AO residuals, Dr. Olivier Lai for a very interesting discussion he initiated on LWE mitigation strategies and Dr. Emiel Por for his kind assistance in the adaptation of HCIPy to our specific problem. We also would like to thanks the GRAVITY+ AO (GPAO) consortium for their support and expertise. This research has made use of the following python packages: matplotlib, numpy, hcipy, astropy and scipy.

REFERENCES

[1] Beuzit, J. L., Vigan, A., Mouillet, D., Dohlen, K., Gratton, R., Boccaletti, A., Sauvage, J. F., Schmid, H. M., Langlois, M., Petit, C., Baruffolo, A., Feldt, M., Milli, J., Wahhaj, Z., Abe, L., Anselmi, U., Antichi, J., Barette, R., Baudrand, J., Baudoz, P., Bazzon, A., Bernardi, P., Blanchard, P., Brast, R., Bruno, P., Buey, T., Carbillet, M., Carle, M., Cascone, E., Chapron, F., Charton, J., Chauvin, G., Claudi, R., Costille, A., De Caprio, V., de Boer, J., Delboulbé, A., Desidera, S., Dominik, C., Downing, M., Dupuis, O., Fabron, C., Fantinel, D., Farisato, G., Feautrier, P., Fedrigo, E., Fusco, T., Gigan, P., Ginski, C., Girard, J., Giro, E., Gisler, D., Gluck, L., Gry, C., Henning, T., Hubin, N., Hugot, E., Incorvaia, S., Jaquet, M., Kasper, M., Lagadec, E., Lagrange, A. M., Le Coroller, H., Le Mignant, D., Le Ruyet, B., Lessio, G., Lizon, J. L., Llored, M., Lundin, L., Madec, F., Magnard, Y., Marteaud, M., Martinez, P., Maurel, D., Ménard, F., Mesa, D., Möller-Nilsson, O., Moulin, T., Moutou, C., Origné, A., Parisot, J., Pavlov, A., Perret, D., Pragt, J., Puget, P., Rabou, P., Ramos, J., Reess, J. M., Rigal, F., Rochat, S., Roelfsema, R., Rousset, G., Roux, A., Saisse, M., Salasnich, B., Santambrogio, E., Scuderi, S., Segransan, D., Sevin, A., Siebenmorgen, R., Soenke, C., Stadler, E., Suarez, M., Tiphène, D., Turatto, M., Udry, S., Vakili, F., Waters, L. B. F. M., Weber, L., Wildi, F., Zins, G., and Zurlo, A., "SPHERE: the exoplanet imager for the Very Large Telescope," *A&A* **631**, A155 (Nov. 2019).

[2] Sauvage, J.-F., Fusco, T., Guesalaga, A., Wizinowitch, P., O'Neal, J., N'Diaye, M., Vigan, A., Girard, J., Lesur, G., Mouillet, D., Buezit, J.-L., Kasper, M., Le Louarn, M., Mlli, J., Dohlen, K., Neichel, B., Bourget, P., Heigenauer, P., and Mawet, D., "Low Wind Effect, the main limitation of the SPHERE instrument," in [*Adaptive Optics for Extremely Large Telescopes IV (AO4ELT4)*], E9 (Oct. 2015).

[3] Milli, J., Kasper, M., Bourget, P., Pannetier, C., Mouillet, D., Sauvage, J. F., Reyes, C., Fusco, T., Cantalloube, F., Tristam, K., Wahhaj, Z., Beuzit, J. L., Girard, J. H., Mawet, D., Telle, A., Vigan, A., and N'Diaye, M., "Low wind effect on VLT/SPHERE: impact, mitigation strategy, and results," in [*Adaptive Optics Systems VI*], Close, L. M., Schreiber, L., and Schmidt, D., eds., *Society of Photo-Optical Instrumentation Engineers (SPIE) Conference Series* **10703**, 107032A (July 2018).

[4] N'Diaye, M., Dohlen, K., Caillat, A., Costille, A., Fusco, T., Jolivet, A., Madec, F., Mugnier, L., Paul, B., Sauvage, J.-F., Soummer, R., Vigan, A., and Wallace, J. K., "Design optimization and lab demonstration of ZELDA: a Zernike sensor for near-coronagraph quasi-static measurements," in [*Adaptive Optics Systems IV*], Marchetti, E., Close, L. M., and Vran, J.-P., eds., *Society of Photo-Optical Instrumentation Engineers (SPIE) Conference Series* **9148**, 91485H (Aug. 2014).

[5] N'Diaye, M., Vigan, A., Dohlen, K., Sauvage, J. F., Caillat, A., Costille, A., Girard, J. H. V., Beuzit, J. L., Fusco, T., Blanchard, P., Le Merrer, J., Le Mignant, D., Madec, F., Moreaux, G., Mouillet, D., Puget, P., and Zins, G., "Calibration of quasi-static aberrations in exoplanet direct-imaging instruments with a Zernike phase-mask sensor. II. Concept validation with ZELDA on VLT/SPHERE," *A&A* **592**, A79 (Aug. 2016).

[6] Vievard, S., Bos, S., Cassaing, F., Ceau, A., Guyon, O., Jovanovic, N., Keller, C. U., Lozi, J., Martinache, F., Montmerle-Bonnefois, A., Mugnier, L., NDiaye, M., Norris, B., Sahoo, A., Sauvage, J.-F., Snik, F., Wilby, M. J., and Wong, A., "Overview of focal plane wavefront sensors to correct for the Low Wind Effect on SUBARU/SCExAO," *arXiv e-prints* , arXiv:1912.10179 (Dec. 2019).

[7] Wilby, M. J., Keller, C. U., Sauvage, J. F., Dohlen, K., Fusco, T., Mouillet, D., and Beuzit, J. L., "Laboratory verification of Fast & Furious phase diversity: Towards controlling the low wind effect in the SPHERE instrument," *A&A* **615**, A34 (July 2018).

[8] Bos, S. P., Vievard, S., Wilby, M. J., Snik, F., Lozi, J., Guyon, O., Norris, B. R. M., Jovanovic, N., Martinache, F., Sauvage, J. F., and Keller, C. U., "On-sky verification of Fast and Furious focal-plane wavefront sensing: Moving forward toward controlling the island effect at Subaru/SCExAO," *A&A* **639**, A52 (July 2020).

[9] Por, E. H., Haffert, S. Y., Radhakrishnan, V. M., Doelman, D. S., van Kooten, M., and Bos, S. P., "High Contrast Imaging for Python (HCIPy): an open-source adaptive optics and coronagraph simulator," in [*Adaptive Optics Systems VI*], Close, L. M., Schreiber, L., and Schmidt, D., eds., *Society of Photo-Optical Instrumentation Engineers (SPIE) Conference Series* **10703**, 1070342 (July 2018).

[10] Baudoz, P., Dorn, R. J., Lizon, J.-L., Fusco, T., Dohlen, K., Charton, J., Beuzit, J.-L., Puget, P., Mouillet, D., Felt, M., Wildi, F., Barufolo, A., Kasper, M., and Hubin, N., "The differential tip-tilt sensor of SPHERE," in [*Ground-based and Airborne Instrumentation for Astronomy III*], McLean, I. S., Ramsay, S. K., and Takami, H., eds., *Society of Photo-Optical Instrumentation Engineers (SPIE) Conference Series* **7735**, 77355B (July 2010).

[11] Sauvage, J.-F., Fusco, T., Lamb, M., Girard, J., Brinkmann, M., Guesalaga, A., Wizinowich, P., O'Neal, J., N'Diaye, M., Vigan, A., Mouillet, D., Beuzit, J.-L., Kasper, M., Le Louarn, M., Milli, J., Dohlen, K., Neichel, B., Bourget, P., Haguenauer, P., and Mawet, D., "Tackling down the low wind effect on SPHERE instrument," in [*Adaptive Optics Systems V*], Marchetti, E., Close, L. M., and Véran, J.-P., eds., *Society of Photo-Optical Instrumentation Engineers (SPIE) Conference Series* **9909**, 990916 (July 2016).

[12] N'Diaye, M., Martinache, F., Jovanovic, N., Lozi, J., Guyon, O., Norris, B., Ceau, A., and Mary, D., "Calibration of the island effect: Experimental validation of closed-loop focal plane wavefront control on Subaru/SCExAO," *A&A* **610**, A18 (Feb. 2018).

[13] Korkiakoski, V., Keller, C. U., Doelman, N., Kenworthy, M., Otten, G., and Verhaegen, M., "Fast & Furious focal-plane wavefront sensing," *Applied Optics* **53**, 4565 (July 2014).

Annexe C

Résumé en français / Summary in French

Table des matières

C.1 Introduction

Plus de 5600 planètes extrasolaires ont été découvertes à ce jour (2 avril 2024) et ce nombre continue de grandir. L'étude de ces exoplanètes est un domaine de recherche très actif qui nous permet de comprendre comment les systèmes planétaires se forment et comment ils évoluent. La découverte de ces milliers d'exoplanètes nous permet aussi de déterminer si notre système solaire est unique en son genre, ou s'il est représentatif des systèmes planétaires dans notre galaxie.

Toutes ces découvertes sont permises par une instrumentation de pointe et des techniques d'analyse de données toujours plus sophistiquées qui repoussent les limites de ce que l'on est capable d'observer. Chaque instrument et chaque technique d'observation ouvre une fenêtre sur des exoplanètes dans une certaine gamme de masse, de distance à l'étoile, d'âge, etc. Toutes prises ensemble, ces méthodes d'observation nous permettent d'avoir une vue de plus en plus complète sur la diversité des mondes dans notre voisinage galactique.

C.1.1 Définition d'une exoplanète

Selon l'union astronomique internationale (IAU, Lecavelier des Etangs and Lissauer, 2022), une exoplanète est :

- un objet de moins de 13 fois la masse de Jupiter ($M_{\rm Jup}$),
- en orbite autour d'une étoile, d'une naine brune ou de résidus d'étoile. Le rapport de masse doit être de moins de 1/25 entre la planète et la masse centrale,
- assez massive pour correspondre aux critères qui définissent une planète dans notre système solaire (forme sphérique due à son équilibre hydrostatique, orbite libre d'autres corps).

C'est la définition que j'ai suivie dans ce manuscrit.

C.1.2 Sujets de recherche actuels

Formation planétaire

Nous savons que l'existence des systèmes planétaires commence lorsque l'effondrement d'un nuage moléculaire génère une surdensité, la protoétoile. Au cours des centaines de millier d'années qui suivent, la poussière en orbite autour de la jeune étoile s'organise en disque où se forment des corps de plus en plus massifs. L'accrétion des poussières commence grâce aux forces de Van der Waals (Weidenschilling, 1980) mais, quand ces corps deviennent assez massifs, ils finissent par pouvoir s'accréter gravitationnellement. Pour les plus massifs l'accrétion peut s'emballer et permettre de former des protoplanètes (Kokubo and Ida, 2000).

De nombreuses questions restent en suspens, notamment pour la formation de planètes géantes gazeuses qui nous intéressent tout particulièrement ici. Plusieurs mécanismes peuvent expliquer la formation de planètes de type Jupiter (ou plus massives) sans que l'on parvienne encore à déterminer précisément quel processus domine en fonction des circonstances. D'après le modèle d'accrétion de cœur (Mizuno, 1980), une protoplanète qui accrète assez de solides pour atteindre la masse critique de 10 $M_\oplus$ (masse terrestre) entre ensuite dans une phase d'emballement de l'accrétion de gaz (Pollack et al., 1996) qui permet à la protoplanète d'atteindre des masses de plusieurs fois la masse de Jupiter. Par ailleurs, le modèle d'instabilité gravitationnelle (Boss, 1997) décrit que, sous

certaines conditions de pression et de température, le disque protoplanétaire peut devenir localement instable et s'effondrer pour former une planète géante gazeuse. Ce dernier mécanisme de formation semble être favorisé pour former des exoplanètes très massives (plus de 1 $M_{\rm Jup}$) et loin de leur étoile (plus de 10 UA). Marley et al. (2007) montre que ces mécanismes de formation conduisent à différentes relations masse-luminosité et luminosité-âge. Grâce à ces différences entre modèles, on peut espérer que davantage d'**observation de la lumière** nous provenant directement de ces exoplanètes géantes nous permette de déterminer quel mécanisme a été à l'œuvre dans leur formation.

Populations et migrations

Grâce aux études de Yang et al. (2020) et Kunimoto and Matthews (2020) sur la statistique des planètes détectées par transit (Sect. C.1.3), on sait maintenant que 75% des étoiles de type FGK sont entourées de planètes, avec en moyenne 2.7 planètes par système. Le relevé SHINE (Vigan et al., 2021) a montré que seulement environ 6% des étoiles de type FGK ont un compagnon plus massif que 1 $M_{\rm Jup}$ au delà de 5 UA. De plus, l'étude de Fernandes et al. (2019) se basant sur des observations par transit et par vitesse radiale montre un pic à 2 UA dans la population de géantes gazeuses. En effet, il est communément admis que les géantes gazeuses se forment au delà de la ligne des glaces (2$\sim$ 5 UA), suffisamment loin de l'étoile pour que l'eau soit à l'état solide. Mais dans ce cas, on peut trouver étonnant que l'on détecte autant de Jupiter-chaudes (ex. Mayor and Queloz, 1995), des géantes gazeuses en orbite à moins de 0.1 UA de leur étoile.

L'existence de Jupiter-chaudes trouve son explication dans les phénomènes de migration planétaire. Les planètes ne restent pas nécessairement sur l'orbite où elles se sont formées, l'interaction gravitationnelle avec le disque protoplanétaire ou avec les autres planètes ou protoplanètes du système (Baruteau et al., 2014) peut faire changer la planète d'orbite au cours du temps. Notre système solaire a probablement connu un phénomène de migration majeure des planètes géantes, se réorganisant pour former le système que l'on connait aujourd'hui. Ce phénomène est décrit par le modèle de Nice (Tsiganis et al., 2005; Morbidelli et al., 2005; Gomes et al., 2005) et pourrait expliquer la forte activité météoritique et cométaire que notre système a connu quand il était agé de 600 millions d'années. C'est une des raisons pour lesquelles l'**observation des orbites des planètes géantes** est important pour comprendre la dynamique des systèmes exoplanétaires.

Atmosphères

Enfin, l'amélioration des techniques d'observation permet d'étudier les atmosphères d'exoplanètes de plus en plus finement. Par example, la spectroscopie de transit donne des résultats spectaculaires sur les processus dynamiques et chimiques dans l'atmosphère des Jupiter-chaudes (Tan and Komacek, 2019; Parmentier et al., 2021; JWST Transiting Exoplanet Community Early Release Science Team et al., 2023; Ehrenreich et al., 2020). Mais la spectroscopie par absorption n'est pas la seule méthode d'observation des atmosphères. L'observation directe de la lumière des exoplanètes géantes permet d'obtenir le spectre de géantes gazeuses jeunes ($<$ 15 Myr), qui rayonnent encore fortement dans l'infrarouge proche du fait de leur formation récente. Ces observations directes n'ont pas encore le pouvoir de résolution spectrale de la spectroscopie de transit, mais elle permettent d'obtenir la

température de surface, la métallicité et éventuellement le rapport C/O d'exoplanètes à plus de 5 UA de leur étoile.

Le télescope spatial James Webb (JWST) a déjà permis un grand bond en avant dans la caractérisation des atmosphères d'exoplanètes (ex. Miles et al., 2023). Dans les décennies qui viennent, des grands projets de télescopes spatiaux comme le Habitable World Observatory (HWO : Gaudi et al., 2020) ou le Large Interferometer For Exoplanets (LIFE : Quanz et al., 2022) se donnent pour but de caractériser des atmosphères de planètes telluriques pour y rechercher des bio-signatures.

C.1.3 Méthodes d'observation

Plusieurs techniques co-existent pour l'observation d'exoplanètes. Chaque technique a sa spécificité en terme de masse et demi-grand axe des planètes qu'elle peut observer. La Figure C.1 montre la répartition des exoplanètes découvertes à ce jour.

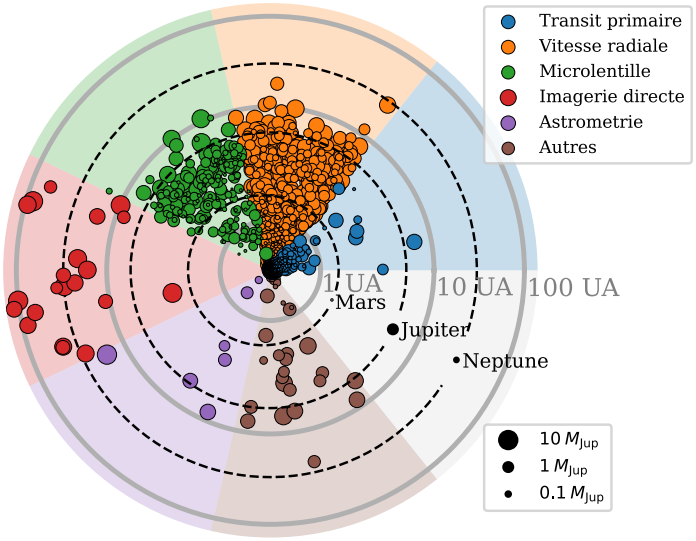

FIGURE C.1 – Comparaison des détections d'exoplanètes en fonction des principales méthodes de détection. (cercles) toutes les exoplanètes confirmées avec une estimation du demi grand axe de leur orbite et de leur masse, selon `https://exoplanet.eu`.

Transit primaire La méthode de détection par transit primaire est celle qui a amené le plus de détections. C'est une méthode indirecte qui se base sur la mesure de la chute de luminosité de l'étoile centrale lorsqu'elle est partiellement éclipsée par le passage d'un compagnon sur la ligne de visée. Pour des raisons géométriques, cette méthode détecte des planètes très proches de leur étoile (50% des détections sont plus proche que 0.07 UA).

Vitesse radiale La méthode de détection par vitesse radiale a permis la première détection d'une exoplanète autour d'une étoile de type solaire (Mayor and Queloz, 1995). Il s'agit également d'une méthode indirecte qui mesure grâce à l'effet Doppler le déplacement périodique de l'étoile-hôte sous l'attraction gravitationnelle d'un compagnon. Cette méthode peut détecter des géantes et des planètes de quelques fois la masse de la Terre (super-Terres) à l'échelle de 1 UA autour de leur étoile.

Microlentille gravitationnelle La matière déforme l'espace-temps, et donc peut courber les rayons lumineux comme le ferait une lentille. La méthode des microlentilles gravitationnelles utilise cette propriété prédite par la relativité générale pour détecter des exoplanètes. Le principe est le suivant, on observe la photométrie au cours du temps de milliers d'étoiles situées à plusieurs kiloparsec (kpc), appelons les "étoiles A". Parfois, une étoile B passe proche de la ligne de visée entre nous et une étoile A. Ce passage induit un phénomène de microlentille qui modifie la photométrie de l'étoile A. Si l'étoile B a une planète en orbite, elle laisse également une empreinte dans la courbe photométrique de l'étoile A. Cette méthode peut détecter des exoplanètes de seulement 2 $M_\oplus$ (Gould et al., 2014) et beaucoup plus loin de nous que les autres méthodes d'observation (pic à 7 kpc).

Imagerie directe La méthode d'observation par imagerie directe est la plus simple sur le principe : faire une image des systèmes planétaires. Cependant elle requiert une instrumentation de pointe, et ce pour deux raisons principales. Premièrement, les instrument doivent avoir la haute résolution angulaire nécessaire pour distinguer la lumière qui provient de l'étoile-hôte de celle qui provient de la planète. Deuxièmement, les instrument doivent permettre des observations à haut-contraste, dû au rapport de luminosité entre l'étoile et la planète de l'ordre de 1 pour 100 000 à 1 000 000 pour les exoplanètes les plus brillantes. Le rapport de flux est favorable pour des exoplanètes géantes jeunes observées dans l'infrarouge. Pour ces raisons, les exoplanètes détectées par imagerie directe sont toutes de moins de 15 Myr, très massives (plusieurs $M_{\rm Jup}$) et sur des orbites à plus de 5 UA de leur étoile. Les principaux instruments qui permettent ces observations sont SPHERE sur le VLT (Beuzit et al., 2019), GPI sur Gemini south (Nielsen et al., 2019) et SCExAO sur Subaru (Jovanovic et al., 2015). Ils se basent tous sur des optiques adaptatives permettant de corriger les aberrations optiques induites par l'atmosphère terrestre, et sur des techniques de coronographie pour diminuer le flux de l'étoile et révéler les planètes en orbite.

Astrométrie La méthode astrométrique se propose de détecter des planètes en mesurant des déplacement périodique de l'étoile-hôte par rapport à un référentiel fixe. Comme pour la méthode des vitesse radiales, cette technique mesure la faible attraction gravitationnelle qu'exerce l'exoplanète sur son étoile. À ce jour, cette méthode a détecté des compagnons sub-stellaires dans le domaine des naines-brunes mais encore peu d'exoplanètes. La situation devrait changer en 2026 lorsque les équipes du télescope spatial Gaia (Gaia Collaboration et al., 2016) publieront leur quatrième fournée de données (DR4) couvrant plus de 5 ans d'observations. Les retombées attendues sont de l'ordre de milliers de détections d'exoplanètes plus massives que 100 $M_\oplus$ avec un pic de sensibilité autour de 2∼3 UA (Sozzetti, 2010; Perryman et al., 2014).

D'autres méthodes existent, dont certaines mesurent directement la lumière des exoplanètes mais sans pour autant produire une image. C'est le cas des observations directes par interférométrie qui sont au cœur de ma thèse.

C.2 Observations d'exoplanètes avec GRAVITY

C.2.1 L'instrument GRAVITY sur l'interféromètre du très grand télescope

GRAVITY (Gillessen et al., 2010) est un instrument installé sur l'interféromètre du très grand télescope (VLTI) au sommet du mont Paranal au Chili. Il permet des observations en bande K ($\lambda \sim 2.2$ µm) en recombinant soit les quatre télescopes de 8 mètres de diamètre (Unit Telescopes, UT), soit les quatre télescopes mobiles de 1.8 mètres de diamètre (Télescopes Auxiliaires, AT). Grâce à son suiveur de frange (Lacour et al., 2019) qui corrige les turbulences atmosphériques à l'échelle de l'interféromètre, GRAVITY a significativement poussé les limites de magnitude (K<19 mag) qui cantonnaient par le passé l'interférométrie optique à l'observation d'objets brillants (K ou H<6 mag). Aussi, grâce à son système de métrologie (Gillessen et al., 2012), GRAVITY permet de mesurer l'astrométrie relative entre deux objets avec une précision de 50 µas.

Conçu en priorité pour les observations d'étoiles proche du centre galactique (GRAVITY Collaboration et al., 2018a, 2020a), l'instrument s'est aussi avéré être sans égal pour les observations de noyaux actifs de galaxies (Abuter et al., 2024a), les observations d'étoiles jeunes (Bouvier et al., 2020; GRAVITY Collaboration et al., 2021b) et les observations exoplanètes.

En effet, c'est sur GRAVITY que les premières observations directes d'exoplanètes par interférométrie optique ont été réalisées (HR 8799 e GRAVITY Collaboration et al., 2019). Par la suite, le Large Programme ExoGRAVITY qui a duré de février 2020 à septembre 2023 a permis d'observer la plupart des exoplanètes détectées par imagerie directe et d'apporter les premières observations directes d'exoplanètes découvertes par vitesse radiales (voir Sect. C.2.3).

C.2.2 Principe interférométrique

Le principe des observations sur GRAVITY peut s'expliquer à partir d'un formalisme d'optique ondulatoire basique. Imaginons un champ électromagnétique qui est collecté sous forme d'ondes plane par deux télescopes T_1 et T_2 :

$$E_{\mathrm{T}_1}(t,\lambda) = E_0 \ \exp\left(i\frac{2\pi}{\lambda}(\mathbf{k}(t)\cdot\mathbf{x}_{\mathbf{T_1}})\right) \ \exp(-i\omega t) \tag{C.1}$$

$$E_{\mathrm{T}_2}(t,\lambda) = E_0 \ \exp\left(i\frac{2\pi}{\lambda}(\mathbf{k}(t)\cdot\mathbf{x}_{\mathbf{T_2}})\right) \ \exp(-i\omega t) \tag{C.2}$$

avec E_0 l'amplitude du champ, $\mathbf{k}(t)$ un vecteur unitaire orienté dans la direction du pointage des deux télescopes, $\mathbf{x}_{\mathbf{T_1}} = (x_{\mathrm{T}_1}, y_{\mathrm{T}_1}, z_{\mathrm{T}_1})$, $\mathbf{x}_{\mathbf{T_2}} = (x_{\mathrm{T}_2}, y_{\mathrm{T}_2}, z_{\mathrm{T}_2})$ la position des deux télescopes dans l'espace, et $\omega = 2\pi f$ la pulsation de l'onde lumineuse. En combinant ces deux champs électriques, on obtient l'intensité :

$$I_{\mathrm{T}_1\mathrm{T}_2}(t,\lambda) = |E_{\mathrm{T}_1}(t,\lambda) + E_{\mathrm{T}_2}(t,\lambda)|^2 \tag{C.3}$$

$$= 2I_0 + 2I_0 \ \cos\left(\frac{2\pi}{\lambda}[\mathbf{k}(t)\cdot(\mathbf{x}_{\mathbf{T_2}} - \mathbf{x}_{\mathbf{T_1}})]\right). \tag{C.4}$$

L'intensité telle qu'elle peut être mesurée par un détecteur est donc la somme de deux termes : un terme qui correspond à la simple somme des intensités collectées par les deux télescopes, et un terme

oscillant en cosinus qui correspond à l'interférence des deux champs électriques. En exprimant $\mathbf{k}$ dans le système de coordonnées approprié et en introduisant $U_b = x_{\mathrm{T}_2} - x_{\mathrm{T}_1}$ et $V_b = y_{\mathrm{T}_2} - y_{\mathrm{T}_1}$, on obtient une expression de l'Eq. (C.4) plus éloquente dans un contexte d'astronomie :

$$I_{\mathrm{T}_1\mathrm{T}_2}(t,\lambda) = 2I_0 + 2I_0 \cos\left(\frac{2\pi}{\lambda}[\Delta\mathrm{RA}\, U_b(t) + \Delta\mathrm{Dec}\, V_b(t)]\right). \tag{C.5}$$

avec ΔRA et ΔDec, respectivement la différence d'ascension droite et de déclinaison entre la source du champ électromagnétique et la direction de pointage $\mathbf{k}$. Le terme en $z_{\mathrm{T}_2} - z_{\mathrm{T}_1}$ correspondant au délai géométrique entre l'arrivée au télescope 1 et 2 disparaît car il est compensé par les lignes à retard du VLTI. L'ensemble des U_b et V_b pour toutes les lignes de bases formées par tous les télescopes forme le plan UV de l'interféromètre.

Le pouvoir de l'interférométrie vient du fait que la plus petite résolution angulaire qu'il soit possible de distinguer entre deux objets est déterminé par la longueur des lignes de bases, et non par le diamètre des télescopes. Ainsi, en terme de résolution angulaire, le VLTI équivaut à la limite de diffraction d'un télescope de 130 mètres de diamètre.

Pour révéler le terme d'interférence dans l'Eq. (C.5), GRAVITY utilise la technique de recombinaison ABCD qui consiste à séparer l'intensité $I_{\mathrm{T}_1\mathrm{T}_2}$ en quatre voies qui chacune se voit affecter une phase différente séparée de $\pi/2$ radians. Cette recombinaison particulière est réalisée par une puce d'optique intégrée (Perraut et al., 2018). La lumière est ensuite dispersée en longueur d'onde par des grismes pour être enregistrée par le détecteur de la voie scientifique. L'observable fournie par GRAVITY sont les visibilités complexes (phase et amplitude), référencées (la phase représente une position sur le ciel) pour chaque longueur d'onde sondée dans la bande K.

C.2.3 ExoGRAVITY

Genèse du projet

ExoGRAVITY est d'abord né comme un programme d'observation dirigé par Sylvestre Lacour (Lacour et al., 2020). Avec le temps, de plus en plus de chercheur·euse·s ont rejoint le groupe pour apporter leur expertise en terme d'interprétation des observations, en terme d'instrumentation, ou de réduction de données. Depuis septembre 2023, le large programme d'observation est terminé mais ExoGRAVITY continue d'exister en tant que consortium ouvert qui échange sur les programmes d'observation en cours, qui guide les programmes d'observation futurs et aide les observateurs avec le traitement de leurs données.

GRAVITY a beau être un instrument très puissant pour l'observation en bande K d'objets ponctuels, il fallait développer des techniques d'observation adaptées et des codes de réduction de donnée spécifique au cas scientifique des exoplanètes.

Outils

GRAVITY propose plusieurs modes d'observation. L'écrasante majorité des observations que j'ai réalisé et analysé pendant ma thèse sont en résolution MEDIUM (R∼500) et dans le mode DUAL ON-AXIS. Dans GRAVITY, la lumière est injectée simultanément dans le suiveur de frange

(FT) et dans la voie scientifique (SC). L'injection se fait dans des fibres optique mono-mode qui ont un champ de vue limité (65 mas de diamètre sur les UT, 290 mas sur les AT). En mode DUAL ON-AXIS, la fibre du FT reste centré sur l'étoile hôte tandis que la fibre du SC observe un autre champ de vue séparé au maximum de 600 mas par une lame séparatrice 50/50.

Le code de réduction de données ExoGRAVITY (tel que décrit dans GRAVITY Collaboration et al., 2020b) intervient après un premier niveau de réduction général par le code GRAVITY (Lapeyrere et al., 2014). Le code ExoGRAVITY est séparé en deux parties :

- `astrometry_reduce` qui permet d'obtenir l'astrométrie relative (ΔRA, ΔDec) entre la planète et l'étoile,
- `spectrum_reduce` qui permet d'obtenir le spectre de contraste entre la planète et l'étoile de 1.97 à 2.48 µm.

Tous deux déconvoluent la lumière de l'étoile-hôte de la lumière de la planète à partir des visibilités complexes issues du terme d'interférence de l'Eq. (C.5) et de la recombinaison ABCD. Cette déconvolution interférométrique s'avère très efficace, et ce même à des séparations angulaires planète-étoile de l'ordre de 100 mas où les techniques d'imagerie directe classiques peinent à révéler des planètes.

Résultats

Depuis 2019, de nombreuses exoplanètes ont été observées et suivies avec GRAVITY. La précision astrométrique permet de fortement contraindre les orbites même avec des observations espacées de 1 ou 2 ans seulement. Les spectres en bande K obtenus permettent de déterminer la magnitude absolue de l'objet, sa température ainsi que, parfois, le rapport C/O dans leur atmosphère. Ce sont autant d'informations cruciales pour déterminer le processus de formation des exoplanètes et des naines brunes.

En plus des célèbres exoplanètes découvertes par imagerie directe comme β Pictoris b (GRAVITY Collaboration et al., 2020b), PDS 70 b et c (Wang et al., 2021b) et HR8799 b, c, d et e (Nasedkin et al., 2024), GRAVITY a aussi permis les première observation directe de β Pictoris c (Nowak et al., 2020) et HD 206893 c (Hinkley et al., 2023) qui jusque là n'avaient été observées que indirectement par la méthode des vitesses radiales.

Jusqu'à maintenant, l'exoplanète de plus faible masse détectée par GRAVITY est 51 Eri b qui est estimée à 2 $M_{\rm Jup}$ et située à 10 UA de son étoile. Plus proche de son étoile, à 2.7 UA, β Pictoris c a une masse d'environ 8 $M_{\rm Jup}$. Actuellement, l'instrument ne semble pas capable de détecter des Jupiter jeunes (1 $M_{\rm Jup}$, 5 UA). L'observation de ces jumelles de Jupiter constitue un objectif pour les développements futurs de l'instrument.

De plus, du fait de son champ de vue limité, GRAVITY est peu performant pour la découverte de nouvelles exoplanètes. En revanche, lorsqu'une autre technique d'observation nous aide à déterminer la position de la planète autour de son étoile, GRAVITY s'avère être un instrument de caractérisation très puissant. En 2026, l'équipe du télescope spatial Gaia fournira la position de milliers d'exoplanètes dont les plus massives et les plus jeunes pourront être observées et caractérisée finement depuis le sol avec GRAVITY. Cette synergie Gaia/GRAVITY est très attendue par la communauté (Winterhalder et al., 2024; Pourré et al., 2024) et devrait permettre de faire un bond dans notre compréhension de

la formation et de l'évolution des système planétaires contenant des géantes gazeuses.

C.2.4 GRAVITY+

Les nombreux succès de GRAVITY et les échéances prometteuses à venir ont motivé une mise à jour de l'instrument depuis 2019 (Eisenhauer, 2019). Cette mise à jour contient plusieurs axes, notamment l'amélioration de la sensibilité de l'instrument, la réduction des vibrations du VLTI et la possibilité d'étendre la distance entre le FT et le SC (GRAVITY+ Collaboration et al., 2022). Mais les deux améliorations majeures sont de nouvelles optiques adaptatives et des étoiles guide laser pour les quatre UT.

Pour les observations d'exoplanètes, ce sont les nouvelles optiques adaptatives, GPAO, qui sont le plus attendues. Elles viennent remplacer les optiques adaptatives MACAO qui ont plus de vingt ans (Arsenault et al., 2003). Le dimensionnement de GPAO est proche des meilleures optiques adaptatives d'imageurs comme SPHERE (Fusco et al., 2014) et promet à GRAVITY de faire un grand bond en avant dans les observations d'exoplanètes.

Ma thèse se situe dans ce contexte, centrée sur cette nouvelle technique d'observation directe d'exoplanète qu'est l'interférométrie optique, avec les nouvelles optiques adaptatives GPAO installées dès l'été 2024 et la synergie très prometteuse avec Gaia dans les années à venir. Ma thèse a eu pour but de déterminer les limites actuelles de GRAVITY pour les observations d'exoplanètes (Sect. C.3), de trouver la cause de bruits systématiques dans les données et de proposer une solution de correction (Sect. C.4), et de développer un mode haut-contraste dédié aux observations d'exoplanètes pour tirer le meilleur parti de la mise à jour GRAVITY+ (Sect. C.5).

C.3 Limites de détection ExoGRAVITY

Il est important pour tout instrument d'observation de connaître ses limites de détection. Cela aide à défendre des nouveaux programmes d'observation et à identifier des synergies fructueuses avec d'autres instruments. Ce travail n'avait pas encore été conduit dans le cadre d'ExoGRAVITY. J'ai développé des outils d'injection de signal de planète dans les données qui m'ont permis de déterminer la courbe de contraste de GRAVITY ainsi que la nature des bruits limitant les observations de compagnons faibles.

C.3.1 Déterminer ce qu'est une détection

Avant ma thèse, dans ExoGRAVITY il n'y avait pas de méthode pour quantifier la robustesse des détections de compagnons (exoplanète ou naine brune). Le choix de déterminer si une détection était crédible ou non se basait sur l'analyse visuelle des cartes périodogramme produites par le code `astrometry_reduce`. Ces cartes regroupent les $\delta\chi^2$ (différence entre le χ^2 sans planète et le χ^2 avec une planète à la position testée) pour différente astrométrie relative (ΔRA, ΔDec). La position de la planète est indiquée par le pic de $\delta\chi^2$ dans la carte périodogramme. Comme illustré par la Fig. C.2a, une détection robuste est constituée d'un pic central entouré de pics secondaires dont la disposition dépend du plan UV de l'interféromètre. Cependant, il y a des cas où la détection est moins claire et

où il est difficile d'identifier un pic de $\delta\chi^2$ qui serait proéminent par rapport au reste de la carte. Dans ces cas là, nous regardions les carte périodogramme individuelles, produites pour les différents fichiers d'observation et vérifions si les différents fichiers semblaient s'accorder sur une détection. De la même manière, nous regardions les meilleurs ajustements sur les différentes lignes de base et vérifiions s'ils s'accordaient entre eux. Cette méthode qualitative permettait de déterminer si un compagnon avait été détecté ou non, mais, en particulier dans les cas limite, elle ne permettait pas de déterminer si la détection était suffisamment robuste pour être publiée.

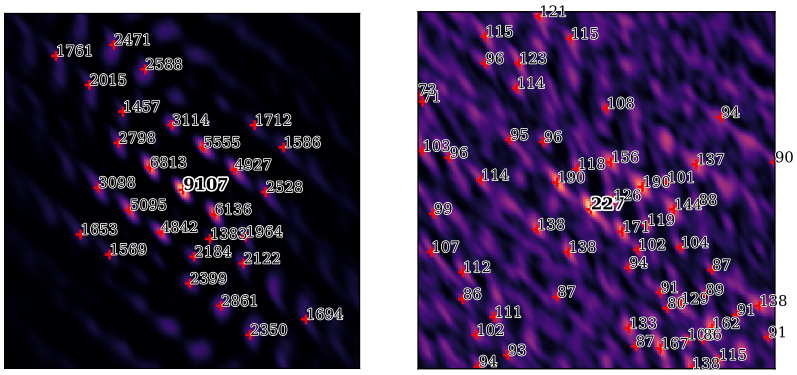

(a) AF Lep b (b) Planète soustraite

FIGURE C.2 – Carte periodogramme pour l'observation d'AF Lep b le 2023-12-23. (a) Periodogramme original, avec les pics supérieurs à 1000 indiqués par des croix rouges. (b) Periodogramme après soustraction du meilleur ajustement de AF Lep b. Les pics indiqués sont ceux au dessus de 60.

Je propose donc une méthode pour quantifier la proéminence d'un signal de planète dans les carte périodogramme. Cette méthode se base sur la mesure du pic $p_{\max}$ dans la carte périodogramme de tous les fichiers combinés (comme Fig. C.2a). Ensuite, je supprime le meilleur ajustement de signal planète correspondant à $p_{\max}$ dans les données puis je relance une réduction. Cela produit une nouvelle carte périodogramme, différente car le signal planète principal a été soustrait (Fig. C.2b). J'extrais le nouveau pic $p_{0,\max}$ qui, s'il y avait bel et bien une planète dans les données, est bien inférieur à $p_{\max}$. Le rapport signal à bruit de la détection ($\mathrm{RSB}_{\mathrm{det}}$) peut être estimé par :

$$\mathrm{RSB}_{\mathrm{det}} = \sqrt{\frac{p_{\max}}{p_{0,\max}}} \tag{C.6}$$

Pour le cas de l'observation de AF Lep B présenté en Fig. C.2, le RSB vaut $\sqrt{9107/227} = 6.3$. La détection de cette exoplanète est donc robuste. On peut répéter cette procédure en supprimant le signal correspondant au pic $p_{0,\max}$ pour s'assurer s'il s'agit d'un artefact ou d'une seconde planète dans les données.

C.3.2 Courbe de contraste ExoGRAVITY

Grâce à ma technique de suppression de planète dans les données d'observation, j'ai pu constituer un jeu de données dépourvu de planète et uniforme en terme de durée d'observation, de temps d'intégration, de magnitude de l'étoile hôte et de conditions atmosphériques. Ce jeu de données comprend des observations autour de HD 17155, HD 206893, β Pic et AF Lep prises dans des bonnes conditions de seeing allant de 0.45 à 0.81 arcsec. Dans ces observations, la fibre du SC est positionnée

de 54 mas à 320 mas de l'étoile.

J'ai utilisé des injections de planète à différentes séparations et à différents contrastes pour déterminer lesquelles étaient retrouvées avec succès par les codes de réduction ExoGRAVITY. Le critère de détection réussie que j'ai appliqué était plus rudimentaire que celui décrit précédemment en Sect. C.3.1. J'ai considéré qu'une planète était retrouvée avec succès si elle était détectée à moins de 3 mas (largeur caractéristique des pics des périodogrammes) de la position où je l'avais injectée et avec moins de 50% d'erreur sur le contraste.

Cela m'a permis de déterminer la limite de contraste de la méthode ExoGRAVITY de 35 à 320 mas pour 30 minutes de temps d'intégration. Cette limite pour les séparations plus faibles que 100 mas s'est avérée sensiblement affectée par l'orientation du couple étoile-planète par rapport aux plus longues bases du VLTI. Si la planète est à un angle de position (PA) parallèle aux plus grandes lignes de base (UT1-UT4, UT2-UT4, UT1-UT3), la détection est plus robuste ; si le PA est perpendiculaire aux grandes lignes de bases la déconvolution interférométrique est moins efficace et la limite de contraste est moins profonde.

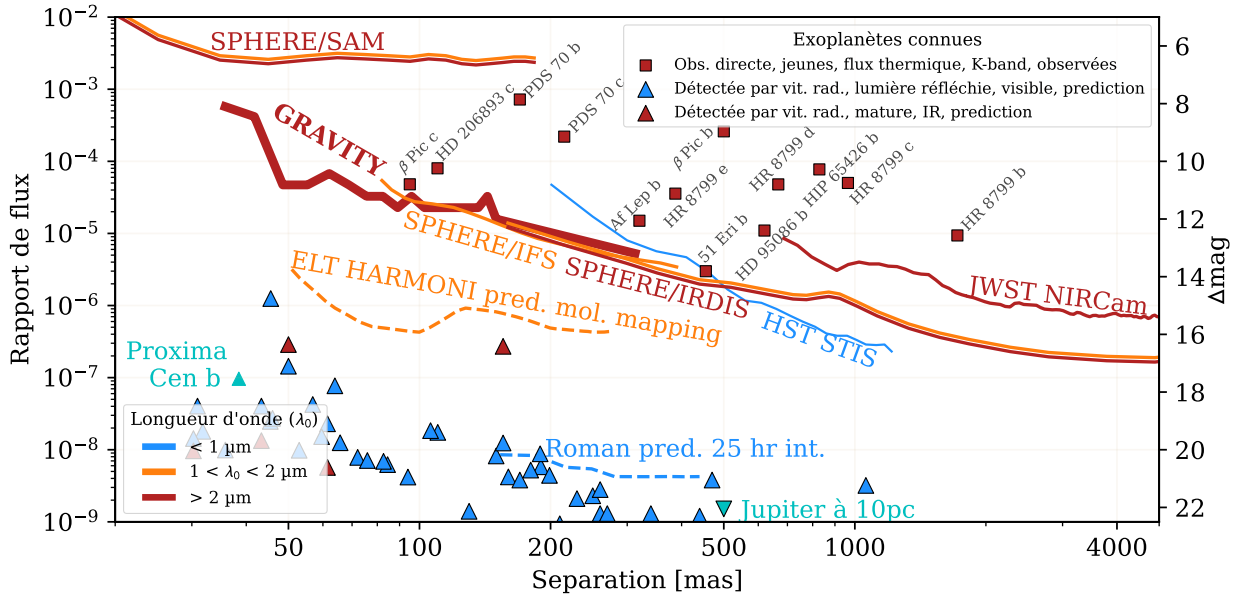

FIGURE C.3 – Courbe de contraste de certains des instruments dédiés à l'observation directe d'exoplanètes. Adapté de `https://github.com/nasavbailey/DI-flux-ratio-plot`. SPHERE/IFS en bande YJH et IRDIS en bande HK de Chomez et al. (2023a). SPHERE/SAM de Stolker et al. (2024). ELT/HARMONI de Houllé et al. (2021). HST/STIS de Ren et al. (2017). JWST/NIRCAM de Carter et al. (2023). Prédiction pour le télescope spatial Roman pour 25 heures d'exposition (communication personnelle de V. Bailey). (carrés rouges) Exoplanètes observées directement avec GRAVITY. (triangles bleus) Contraste estimé en lumière visible pour les exoplanètes détectées par la méthode des vitesses radiales cataloguées dans la NASA exoplanet archive. L'estimation utilise un modèle Lambertien faisant l'hypothèse d'un rayon de 1 R_{Jup} et un albédo géométrique de 0.5. (triangles rouges) Estimation du contraste dans l'infrarouge proche des planètes détectées par la méthode des vitesses radiales. Flux calculé à partir d'une estimation de leur température d'équilibre et en faisant aussi l'hypothèse d'un rayon de 1 R_{Jup}. Les prédictions de flux visible et infrarouge sont basées sur les formules de Traub and Oppenheimer (2010).

La Figure C.3 montre la courbe de contraste que j'ai obtenu pour GRAVITY dans le cas d'une planète orientée parallèlement aux grandes lignes de base (orientation optimale). Cette courbe

confirme que les exoplanètes à faible séparation, β Pictoris c et HD 206893 c, sont bien accessibles par la méthode ExoGRAVITY. La courbe montre aussi que l'instrument pourrait détecter des exoplanètes à quelques 10^{-5} de contraste jusqu'à 50 mas. Jamais une exoplanète n'a été observé en dessous de 90 mas avec GRAVITY, mais les capacités de l'instrument jusqu'à 50 mas sont de bon augure pour les futures caractérisations de planètes découvertes par Gaia qui sont attendues majoritairement entre 10 et 100 mas.

La Figure C.3 permet aussi de comparer la sensibilité de GRAVITY à la sensibilité d'autres instruments dédiés à l'observation directe d'exoplanètes. Premièrement, cela confirme que GRAVITY est le seul instrument capable d'observer des compagnons de masse planétaire à des contrastes de quelques 10^{-5} à moins de 100 mas. Le mode de pupille segmentée de SPHERE (SAM) permet d'observer des compagnons à très faible séparation mais pas d'atteindre des contrastes permettant les observations d'exoplanètes. Au delà de 100 mas, la courbe de sensibilité de GRAVITY est similaire à celle de SPHERE. Les télescope spatiaux JWST et HST ne permettent pas encore l'imagerie directe d'exoplanètes à faible séparation, mais la situation pourrait changer avec le télescope spatial Roman (Bailey et al., 2023) qui devrait permettre dès 2027 d'observer des exoplanètes géantes en lumière réfléchie à moins de 500 mas. Depuis le sol, les travaux de Houllé et al. (2021) montrent que la technique de "molecular mapping" appliquée à l'instrument HARMONI sur l'ELT devrait permettre de sonder des séparations similaires à GRAVITY, et même d'atteindre des contrastes plus profonds.

Il reste à déterminer comment la mise à jour GRAVITY+, et en particulier les nouvelles optiques adaptatives, permettra de repousser les limites de contraste de l'instrument (éléments de réponse à la Sect. C.5).

C.3.3 Limites fondamentales

Après la détermination de la courbe de contraste de la méthode ExoGRAVITY, la question s'est posée de la nature des bruits qui limitent les détections d'exoplanètes. Il était assez clair que la limite devait provenir du flux de l'étoile qui s'injecte dans la fibre du SC quand on observe la planète, mais nous ne savions pas s'il s'agissait de bruit de photon ou de bruits systématiques.

Pour tenter de déterminer la nature du bruit dans les données j'ai commencé par comparer la limite de contraste à 100 mas dans deux jeux de donnée autour d'étoiles de magnitude différentes (HD 206893 et β Pictoris). Les limites observées empiriquement indiquent que les bruits fondamentaux dans les données sont proportionnel à la quantité de flux de l'étoile injecté. Cela indique donc que les bruits fondamentaux sont des systématiques et non du bruit de photon (dont le niveau serait en racine carrée du nombre de photons injectés dans le SC).

Une analyse du bruit théorique menée avec mon camarade thésard Alexis Bidot confirme que le bruit de photon attendu est environ $\times 10$ sous le niveau de bruit qui nous limite actuellement. Aussi, cette étude nous a permis de conclure que le bruit de lecture de la caméra est négligeable dans les observations à faible séparation autour d'étoile brillantes que l'on considère ici.

Conclusion

Mon étude basée sur des injection de planètes dans de vraies données d'observation a permis de dériver la courbe de contraste de GRAVITY et de mettre en lumière la place privilégiée qu'à

l'inteférométrie infrarouge pour l'observation directe d'exoplanètes à moins de 100 mas.

L'étude empirique et théorique d'observations m'a permis de conclure que les détections sont actuellement limitées par des bruits systématiques qui sont proportionnels au flux de l'étoile qui s'injecte dans la fibre du SC lorsque l'on observe la planète.

Cette étude constitue une partie d'une publication acceptée dans la revue Astronomy & Astrophysics (Pourré et al., 2024).

C.4 Systématiques dans les visibilités en bande K

Dès le début du large programme ExoGRAVITY en 2020, il est apparu que les observations à moins de 150 mas autour d'étoiles brillantes (K<6 mag) étaient polluées par un signal d'origine inconnue. Ce signal apparaît comme des oscillations dans les visibilités que l'on appelle "wiggles" en anglais et que je traduirais ici par "tortillons".

C.4.1 Des "tortillons" dans les données

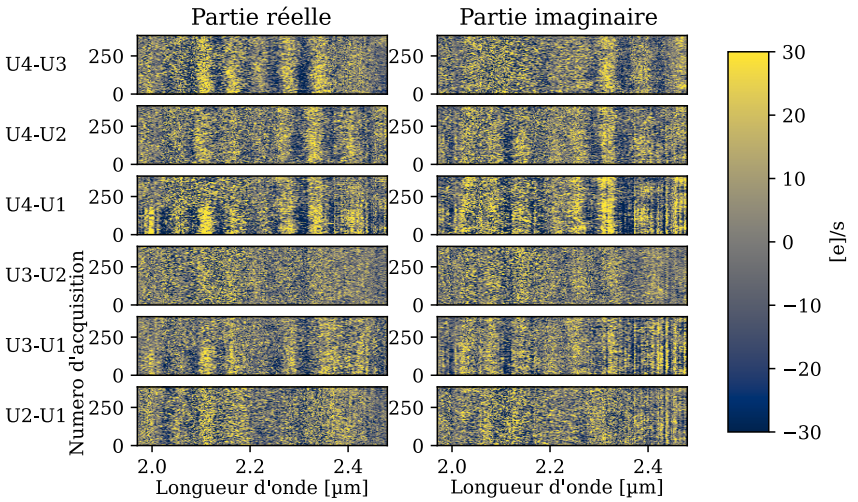

FIGURE C.4 – Résidus des visibilités complexes après ajustement du signal de la planète et de l'étoile. Pour chaque ligne de base, les 384 acquisitions successives sont sur l'axe vertical. Issu d'une observation de β Pic c le 2020-03-07.

L'exemple typique de tortillons dans les observations ExoGRAVITY est l'observation de β Pictoris c du 2020-03-07. Durant cette observation les conditions atmosphériques étaient assez favorables (seeing de 0.49 à 0.99 arcsec) et la fibre de science était placée à 138 mas de l'étoile. Après réduction par le code de réduction GRAVITY, les visibilités complexes sont ajustées par un modèle de la contribution du flux stellaire et par un modèle de planète dans le code `astrometry_reduce`. Si l'on soustrait le meilleur ajustement de la contribution stellaire et le meilleur ajustement de la planète aux visibilités, on s'attendrait à ce qu'il ne reste que du bruit Gaussien dans les données. Au lieu de cela, dans ces observations de β Pictoris c, les résidus sont dominés par un bruit structuré sous forme d'oscillations d'amplitude variable mais de forme similaire sur toutes les lignes de base (Fig. C.4). Ce signal ne ressemble ni à une contribution de l'étoile ni à une planète (voir Fig. 2.16).

D'ailleurs, le fait que les tortillons aient une fréquence spectrale similaire sur toutes les bases nous indique qu'il ne provient pas d'une source sur le ciel.

Ces tortillons peuvent être modélisés par une cavité Fabry-Perot qui induirait une différence de marche d'environ 80 µm. Avec ce modèle de cavité, j'ai analysé l'impact de ce bruit corrélé sur les observables. Il apparaît que la détection et astrométrie de la planète est robuste contre les tortillons, il faudrait qu'ils soient 10 fois plus intenses pour perturber la détection de β Pic c. En revanche, le spectre de contraste obtenu pour la planète est très affecté par cette oscillation systématique. C'est ce qui a motivé la recherche de la cause de ces tortillons et la recherche d'une solution de correction de son effet sur les spectres.

C.4.2 Rechercher la source des "tortillons"

J'ai pu analyser des dizaines d'observations ExoGRAVITY autour d'étoiles brillantes (β Pictoris, HD 206893, HR 8799). De ces observations j'ai pu conclure trois choses :

- les tortillons apparaissent seulement entre 50 et 140 mas de séparation,
- l'amplitude des tortillons semble être corrélée au flux de l'étoile qui rentre dans la fibre du SC,
- les observations avec la fibre du SC sur l'étoile (séparation 0 mas) ne sont pas affectées par les tortillons.

Ces observations permettent d'éliminer une cause du problème dans une réflexion partielle de la lumière de l'étoile. En effet, si le problème vient d'une réflexion, on imagine mal comment il pourrait être absent lorsqu'on observe l'étoile et qu'une grande quantité de flux stellaire rentre dans la fibre du SC.

Au détour d'un fenêtre de temps technique sur GRAVITY, j'ai pu tester avec Sylvestre Lacour de reproduire le problème sur l'unité de calibration de GRAVITY (Blind et al., 2014). L'unité de calibration est située juste à la sortie de l'instrument, dans le laboratoire du VLTI. Elle est utilisé chaque fin d'après-midi et chaque matinée pour calibrer l'instrument et vérifier que tout les sous-systèmes fonctionnent bien. Elle peut aussi servir à réaliser des observations sur lampe interne dans un environnement contrôlé. C'est ce que nous avons fait avec Sylvestre Lacour, nous avons réussi à reproduire des observations internes dans un mode proche de celui utilisé pour ExoGRAVITY, et les tortillons apparaissaient bel et bien dans les données. C'est un résultat important, il montre que le problème des tortillons provient de l'instrument GRAVITY lui-même et pas du VLTI. Il permet aussi de réaliser de nombreux tests de jour pour identifier la source du problème.

Les tortillons apparaissent avec un haut RSB dans les observations sur l'unité de calibration. Grâce à cela, j'ai pu mener à bien des tests qui montrent que le problème ne vient pas de la réduction de données mais a bien une cause instrumentale. Je me suis donc attelé à tenter de trouver la source des tortillons dans GRAVITY en modifiant un par un les paramètres des différents sous systèmes et en analysant leur éventuel impact sur les résidus. Cela m'a permis d'exclure la plupart systèmes de GRAVITY (half-wave plate, lignes à retard différentielles fibrées (FDDL), prisme de Wollaston, miroir en toit), seuls les dérotateurs situés à l'entrée de l'instrument semblent avoir un impact sur la présence des tortillons, mais c'est un résultat préliminaire qui demande à être confirmé.

En déplaçant la fibre de science à différentes positions autour de la lampe de calibration (qui joue le rôle d'étoile), j'ai pu réaliser une carte de l'amplitude des tortillons en fonction de la position

autour de l'étoile (Fig. C.5). Elle montre que plus on est proche de l'étoile, plus les tortillons sont forts et il s'avère que l'amplitude des oscillations suit assez bien l'amplitude du flux cohérent de l'étoile qui s'injecte dans la fibre. L'amplitude des tortillons représente environ 0.5% du flux injecté à 100 mas et semble tomber autour de 0.15% à 50 mas. L'amplitude relative entre le flux injecté des les tortillons diminue avec la séparation, ce qui est logique compte tenu du fait que l'on n'observe pas le problème à séparation 0 mas (sur l'étoile).

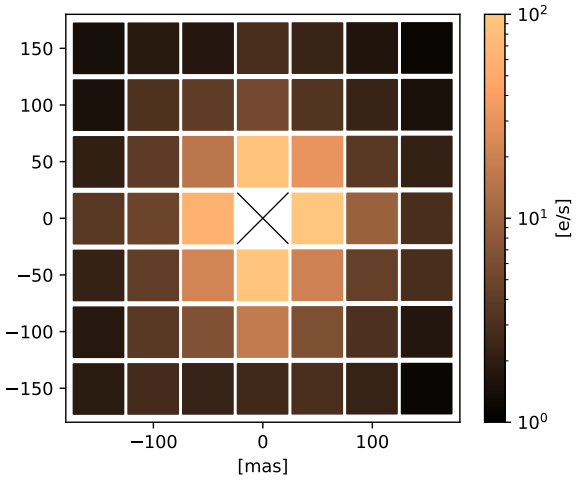

FIGURE C.5 – Carte d'amplitude des tortillons à différentes positions autour de la lampe de calibration (qui fait office d'étoile).

Malgré tout mes efforts pour trouver la source des tortillons, jusqu'à manipuler l'instrument lui-même, je n'ai pas encore pu trouver de cause convaincante.

C.4.3 Calibration

Faute de corriger le problème à la racine, il est toujours possible d'essayer de limiter son impact sur les spectres d'exoplanètes au moment de la réduction des données. Cela a été la motivation de très nombreuses discussions avec Mathias Nowak et Jean-Baptiste Le Bouquin dès le début de ma thèse et cette étude de solutions de calibration m'a amené à me plonger dans le détail du code de réduction ExoGRAVITY. Après de très nombreuses tentatives de calibrations qui n'avaient que peu d'impact sur le spectre obtenu, nous avons fini par converger sur une stratégie de calibration prometteuse.

Cette stratégie se base sur deux hypothèses : que les tortillons sont statiques en phase par rapport au flux de l'étoile qui rentre dans le SC, et que les tortillons peuvent avoir une amplitude différente en fonction des lignes de base. Ces hypothèses nous ont conduit à rajouter un élément au script `spectrum_fit` du code ExoGRAVITY. Dans ce code, la contribution de l'étoile et de la planète sont ajustées simultanément au traver d'un ajustement linéaire qui assure la meilleure correspondance entre les données et le modèle. Pour débarrasser le spectre de la planète de la contribution des tortillons, nous ajoutons un élément à l'ajustement linéaire qui ressemble à l'ajustement de la planète, mais qui capture tout ce qui est statique en phase par rapport au flux de l'étoile.

Pour tester cette méthode de calibration, j'ai injecté une planète à 111 mas et à un contraste de 8×10^{-5} dans un long jeu de donnée de 2.4 heures autour de HD 206893. La planète que j'ai

injecté a un spectre connu, ce qui permet avec la matrice de covariance des erreurs de calculer un χ^2 indiquant la correspondance du spectre retrouvé avec le spectre injecté. La Figure C.6 montre qu'avec la nouvelle version du code (qui comprend une correction des tortillons) le spectre retrouvé se trouve plus proche du spectre injecté. Le χ^2 réduit qui vaut 2.18 dans la version originale du code se trouve réduit à 1.14 dans la nouvelle version qui comprend la calibration des tortillons. Cette diminution du χ^2_{red} provient à la fois d'une diminution de la différence entre le spectre retrouvé et le spectre injecté, ce qui est visible dans la Fig. C.6. Mais cette diminution du χ^2_{red} vient aussi d'une modification de la matrice de covariance qui semble mieux capturer les erreurs statistiques et corrélées dans le spectre.

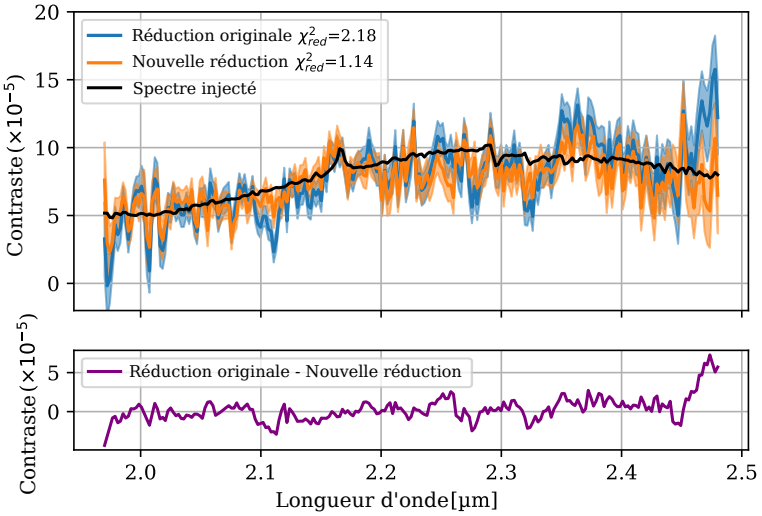

FIGURE C.6 – Comparaison de spectres de contraste entre la réduction de donnée originale et la nouvelle réduction incluant une correction des tortillons. Les aplats bleu et orange montrent les barres d'erreur.

Cette correction de l'effet des tortillons dans le spectre de la planète semble très efficace. Mes tests montrent que le spectre corrigé n'est plus dominé par les erreurs corrélées mais est maintenant limité par les bruits statistiques (bruit de photon).

Conclusion

La correction du problème des tortillons est une priorité pour obtenir des spectres moins biaisés, et donc de meilleures estimations des paramètres de l'atmosphère des exoplanètes.

Malgré tous mes efforts, je n'ai pas pu déterminer la cause de l'apparition des tortillons dans les données. Cependant, j'ai montré que le problème venait de l'instrument lui même et pas du VLTI.

Avec Mathias Nowak, nous avons trouvé une méthode pour limiter fortement l'impact des tortillons sur les spectres d'exoplanètes en modifiant le code de réduction ExoGRAVITY.

C.5 Mode haut-contraste pour GRAVITY+

Les nouvelles optiques adaptatives de GRAVITY+, GPAO, vont être grandement bénéfique aux observations d'exoplanètes. Premièrement, elles vont apporter une meilleure correction des aberrations induites par la turbulence atmosphérique terrestre. Le rapport de Strehl attendu en

bande K est de 80% contre actuellement 30% sur les actuelles MACAO. Deuxièmement, elles vont permettre de compenser les aberrations internes de GRAVITY, ce que les optiques adaptatives actuelles ne permettent pas. Enfin, troisièmement, elles permettront d'appliquer des techniques de contrôle de front d'onde qui créent des zones spécifiques de haut-contraste en plan focal (appelées "dark holes").

Tout ceci réduira l'injection de la lumière de l'étoile qui s'injecte dans la fibre de science et réduira d'autant le bruit dans les données. Ceci permettra de repousser les limites de détection et d'obtenir des spectres d'exoplanètes à plus haut RSB.

C.5.1 Creuser des "dark hole"

Les techniques de contrôle de front d'onde consistent à injecter des aberrations dans le front d'onde afin de réduire l'intensité lumineuse de la diffraction de la lumière stellaire dans une zone spécifique où l'on souhaite observer une planète. Cette technique a d'abord été proposée par Malbet et al. (1995) et elle est à l'étude depuis quelques années sur les instruments imageurs d'exoplanète les plus performants (SPHERE : Potier et al. (2020, 2022), SCExAO : Ahn et al. (2023)). À ma connaissance, cette technique est encore à l'état de test et n'est pas encore utilisée de manière systématique pour les observations.

Les imageurs d'exoplanètes ne sont pas les seuls à pouvoir bénéficier de cette technique. Les instrument d'observation directe d'exoplanète basés sur une injection dans une fibre optique peuvent aussi tirer parti des "dark holes" pour réduire l'injection indésirable de l'étoile dans leur fibre. Ces techniques sont à l'étude sur l'instrument Keck/KPIC (Delorme et al., 2021b) avec des développement prometteurs (Llop-Sayson et al., 2019, 2022; Xin et al., 2023).

C'est un des objectifs de ma thèse : préparer l'implémentation d'un mode haut-contraste pour GRAVITY+ qui utiliserait le contrôle du front d'onde pour creuser un "dark hole" sous la fibre de science. Je l'ai montré sur la Fig. C.3, GRAVITY est un instrument particulièrement intéressant pour sa capacité à observer des exoplanètes à faible séparation (<100 mas). Étant donné que les exoplanètes géantes sont relativement rare à grande séparation (Vigan et al., 2021) et que les exoplanètes révélées par Gaia sont attendues en dessous de 100 mas, j'ai concentré mon travail sur les "dark holes" à faible séparation.

C.5.2 GRAVITY : "dark hole" positionnel

Pour obtenir un impact à faible séparation de l'étoile en plan focal, il faut injecter des modes de bas ordre. C'est pourquoi, avec Jean-Baptiste Le Bouquin, notre réflexion a commencé autour des modes de "tip-tilt" qui constituent une simple pente de phase dans la pupille et induisent une translation de l'image en plan focal. En effet, nous avous identifié un régime à faible séparation où il était possible qu'un simple "tip-tilt" permette d'améliorer le rapport de flux en faveur de la planète. En réalité, plutôt qu'ajouter une pente de phase grâce au miroirs déformables de l'optique adaptatives, il nous est apparu beaucoup plus simple de modifier la position de la fibre pour la placer à l'endroit optimal.

Pour tester cette hypothèse de "dark hole" positionnel, j'ai utilisé une simulation d'optique adaptative et d'injection fibrée avec HCIPy (Por et al., 2018) que j'ai calibré sur des observations

ExoGRAVITY sur les UTs. Cela m'a permis d'obtenir un modèle réaliste de l'intensité du flux de l'étoile injecté dans la fibre du SC en fonction de la séparation (Fig. C.7), et ce séparément pour le flux total et le flux cohérent (la fraction de flux qui contribue aux visibilités complexes). Sur la figure, il apparaît clairement qu'en éloignant la fibre du SC de l'étoile on diminue le flux de l'étoile injecté tout en diminuant relativement peu le flux de la planète injecté (Pourré et al., 2022c). Ces courbes d'injection m'ont permis de déterminer qu'un déplacement de la fibre de science pouvait apporter une amélioration du rapport de flux planète-étoile jusqu'à ×5 en flux cohérent en dessous de 83 mas. Mes recommandations pour les observations sur les UTs avec GRAVITY sont donc les suivantes :

- planète à moins de 58 mas : fibre à la position de la planète +25 mas dans la direction opposée à l'étoile
- planète entre 58 et 83 mas : fibre à 83 mas
- planète à plus de 83 mas : fibre centrée sur la planète.

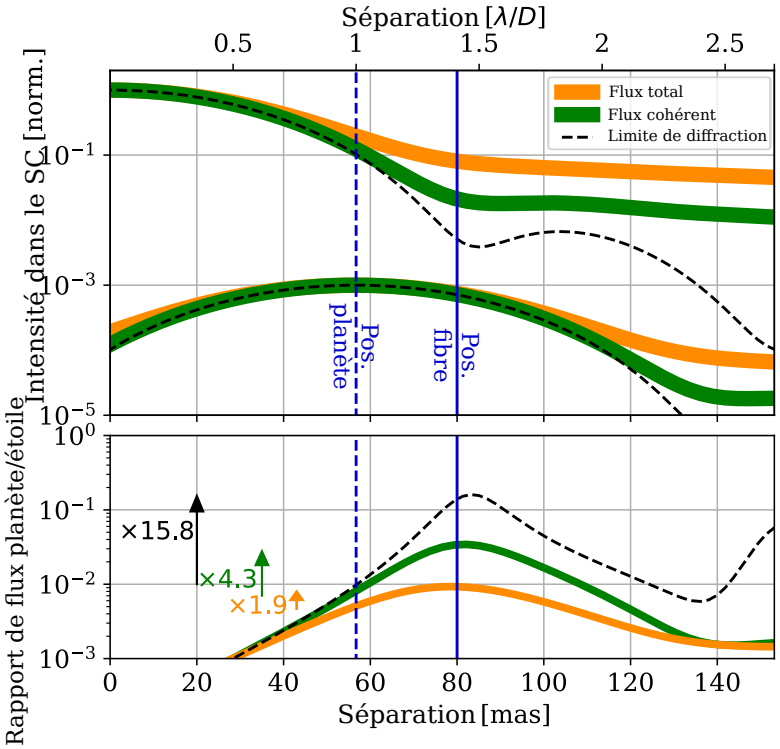

FIGURE C.7 – Exemple d'amélioration du rapport de flux en pointant la fibre à 25 mas d'une planète située à 57 mas de son étoile. (haut) Coupes du flux total, du flux cohérent et de la limite de diffraction. (bas) Rapport de flux pour toutes les séparations possibles de la fibre du SC. La position optimale est indiquée par la ligne bleue en trait plein

J'ai pu valider cette stratégie sur les ATs en obtenant du temps d'observation en tant que PI sur le temps garanti (GTO) du projet NAOMI (ID 0110.C-0182(A)). Les ATs sont 4.4 fois plus petits que les UTs, donc les séparations doivent être mises à l'échelle avec un rapport de 4.4. Mon programme avait pour but l'observation de deux naines brunes bien connues HD 984 B et HD 72946 B. Pour des raisons de mauvais temps, les observations de HD 72946 B n'ont pas été fructueuses. En revanche, les observations de HD 984 B à une séparation de 250 mas m'ont permis de confirmer que la méthode du "dark hole" positionnel apportait l'amélioration attendue du rapport de flux sans pour autant

générer d'erreur d'astrométrie (Pourré et al., 2024).

Cette technique est maintenant systématiquement utilisée pour les observations de compagnons à faible séparation menées par le consortium ExoGRAVITY. En 2022, elle a même permis à Sylvestre Lacour et Thomas Winterhalder d'observer la naine brune Gaia DR3 2728129004119806464 B de 78 M_{Jup} à une séparation de 35 mas sur les UTs (Winterhalder et al., 2024; Pourré et al., 2024). À ma connaissance, il s'agit du compagnon substellaire à la plus faible séparation jamais observée directement.

Donc, un simple déplacement de la fibre de science est efficace pour améliorer le contraste. Mais nous pouvons aller plus loin que cela.

C.5.3 GRAVITY+ : contrôle du front d'onde

Grâce à GPAO qui sera installé cet été 2024, nous pourront envisager l'utilisation de techniques de contrôle de front d'onde pour réduire encore plus le flux de l'étoile qui s'injecte dans le SC pendant les observations ExoGRAVITY.

Simulations

Encore une fois, j'ai utilisé HCIPy pour réaliser des simulations permettant de prédire quels seraient les modes optimaux pour creuser un "dark hole" à la plus faible séparation possible dans GRAVITY+. Mes simulations font l'hypothèse d'une atmosphère parfaitement corrigée par GPAO, ce qui ne sera pas le cas, mais elles permettent tout de même de déterminer quels modes sont les plus efficaces pour contrer l'injection de la lumière stellaire à la limite de diffraction des UTs.

J'ai testé plusieurs forme de mode différentes, j'ai même réalisé des minimisations par un algorithme génétique pour m'assurer de bien identifier les modes optimaux. Il s'avère que le mode le plus efficace pour creuser un "dark hole" à faible séparation est un mélange d'aberration de coma et de trefoil (Fig. C.8a). Ce mode a la propriété de faire se rejoindre le premier et le second zéro de la figure de diffraction pour creuser un "dark hole" à 125 mas (Fig. C.8) qui réduit $\times 1000$ le flux injecté. Il s'agit d'un mode qui avait déjà été identifié par Por and Haffert (2020) dans leur concept instrumental "Single-mode Complex Amplitude Refinement" (SCAR).

Mes simulations, en particulier les minimisations par algorithme génétique, montrent que certains modes peuvent creuser un "dark hole" très profond (contraste 10^{-7}) à 150 mas en faisant se rejoindre les trois premiers zéros de la figure de diffraction. Je n'ai pas poussé cette étude plus loin car je me suis concentré sur la réduction du flux stellaire aux plus faibles séparations possibles, cependant c'est une piste à explorer dans le futur.

Tous mes travaux sur les modes optimaux pour le contrôle de front d'onde dans GRAVITY se placent dans le contexte d'une apodisation statique en phase : on applique un mode théorique provenant de simulations répliquant notre connaissance de l'instrument et on espère qu'il va avoir l'effet escompté sur le plan focal. Cette méthode a ses limites, l'instrument est complexe et on s'attend à ce qu'il soit affecté par de nombreuses aberrations statiques et semi-statiques qui peuvent dégrader l'efficacité de l'apodisation en phase. Pour cette raison, Sylvestre Lacour travaille actuellement à un modèle semi-analytique de mode à appliquer sur GPAO pour creuser des "dark hole". Ce modèle comprend des paramètres qu'il est possible d'optimiser, par exemple en se basant sur des mesures

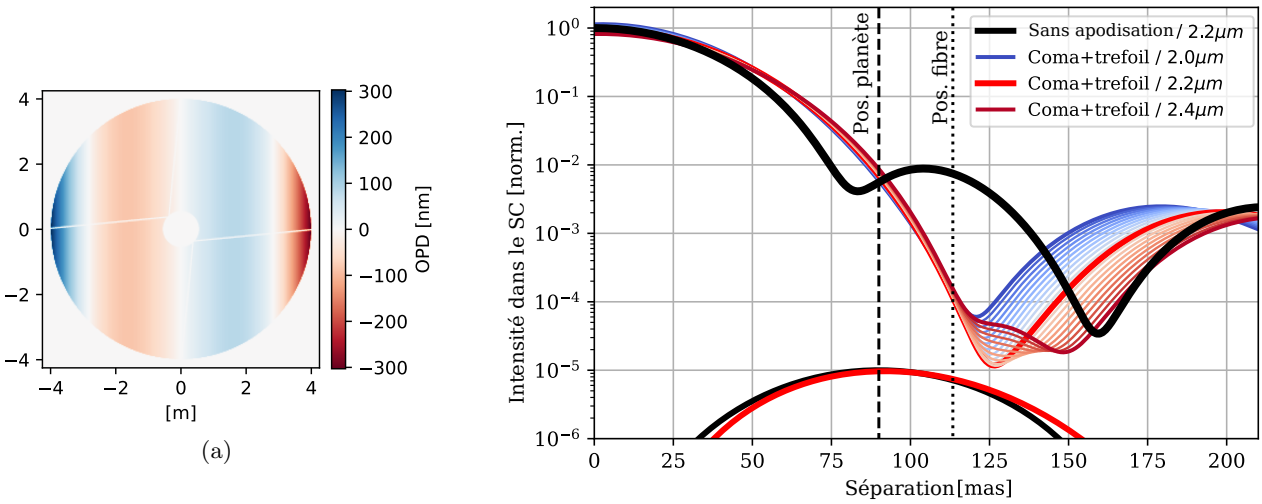

(a) (b)

FIGURE C.8 – Mode SCAR optimal pour observer une planète à 90 mas. (a) Meilleure apodisation en OPD, 78 nm rms. (b) Impact de l'apodisation sur l'injection dans le SC.

du flux injecté dans le SC, pour correspondre au mieux à l'état de l'instrument au moment de l'observation. Cette communication entre GRAVITY et l'optique adaptative n'est pas sans poser des problèmes, et il reste à déterminer si une optimisation d'un modèle semi-analytique est faisable ou non.

Tests au VLTI

J'ai pu utiliser du temps technique sur GRAVITY et le VLTI pour tester les modes SCAR sur le ciel (sur les ATs) et sur source interne des UTs.

Les tests sur le ciel sur les ATs m'ont permis de conclure que les modes SCAR n'apportaient aucune amélioration du contraste dans le SC du fait de fort résidus de turbulence atmosphérique.

J'ai pu ensuite réaliser des tests sur la source interne située au foyer Nasmyth des UTs. J'ai injecté les modes grâce à l'optique adaptative CIAO (Kendrew et al., 2012) qui a senseur de front d'onde de Shack-Hartmann qui permet d'injecter des modification de pentes de référence. Tout d'abord, j'ai regardé l'impact des modes SCAR sur les images produites par la caméra IRIS (Gitton et al., 2004) située à côté de GRAVITY dans le laboratoire du VLTI. Ces mesures sont résumées sur la Fig. C.9. Elles montrent que le mode SCAR a l'effet attendu, il réduit l'intensité lumineuse proche de l'étoile (ici à droite du lobe principal). Pour un mode SCAR de 85 nm d'amplitude rms, je mesure une réduction $\times 13$ de l'intensité lumineuse de l'étoile à 90 mas. Ceci est prometteur, mais il faut garder à l'esprit que IRIS n'est pas GRAVITY. Il reste encore à démontrer l'impact des modes SCAR dans l'instrument lui-même.

C'est pourquoi j'ai conduit des tests similaires sur source interne des UT jusqu'à la voie scientifique de GRAVITY. J'ai réalisé ces tests sur l'UT2 en comparant l'injection à différentes séparations de 60 à 160 mas avec et sans apodisation appliqué sur CIAO. Ces tests ont montré que le mode SCAR n'avait pas d'impact bénéfique sur l'injection de l'étoile dans la fibre de science. Ce résultat n'est pas si surprenant étant donné qu'il est connu que les optiques internes de GRAVITY sont responsable d'aberrations de l'ordre de 100 nm rms dans l'injection fibrée du FT et du SC. Dans ces conditions,

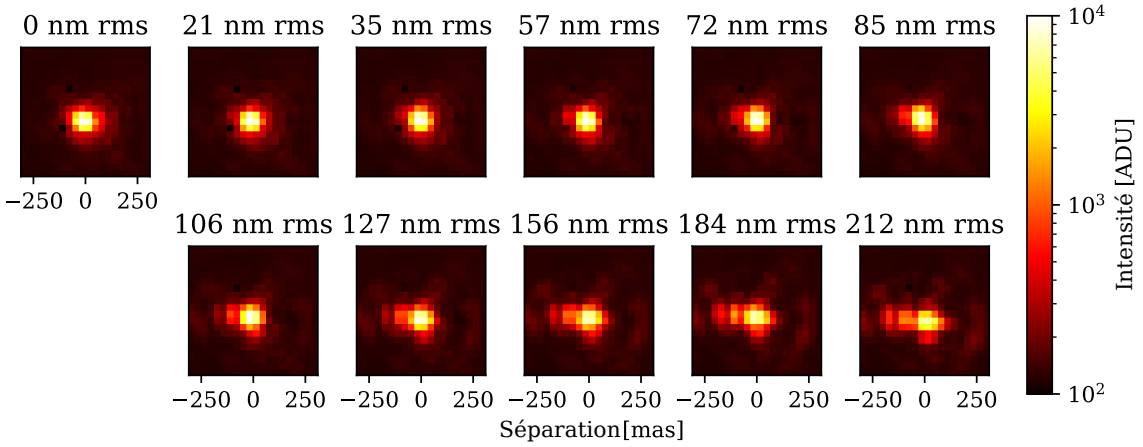

FIGURE C.9 – Images de la caméra IRIS sur la lampe mono-mode du foyer Nasmyth de l'UT2. Les modes SCAR sont injectés à des amplitudes différentes avec CIAO. Toutes les images sont en bande K et moyennées sur 30 secondes.

un mode d'amplitude de quelques dizaines de nm rms sera fortement perturbé et ne pourras pas avoir l'effet attendu en plan focal.

Si le contrôle de front d'onde est inefficace sur source interne pendant des tests de jour, il sera bien entendu aussi inefficace sur le ciel avec GPAO. Il est donc apparu comme une priorité de corriger les aberrations de l'instrument qui ne sont pas vues par les optique adaptatives (aberrations de chemin non-commun, NCPA).

C.5.4 Aplanir et stabiliser le front d'onde

NCPA Mes travaux ont montré que les NCPA sont un problème majeur pour l'implémentation d'un mode haut-contraste pour les observations d'exoplanètes à faible séparation dans GRAVITY+. Après mes tests sur les modes SCAR, je me suis concentré sur la mesure et la correction des aberrations non-communes jusqu'à l'injection dans la voie SC de GRAVITY. Pour cela j'ai utilisé une méthode qui consiste à moduler des modes de Zernike grâce à une optique adaptative et à mesurer l'impact de cette modulation sur le flux qui s'injecte dans la fibre. Pour rendre cette mesure possible, il a fallu que je modifie la caméra du SC pour permettre l'enregistrement du flux à un fréquence proche de 300 Hz (avec l'aide précieuse de Leander Mehrgan et Julien Woillez). La mesure s'est avérée difficile à réaliser du fait de la turbulence interne des tunnels du VLTI. Malgré tout, j'ai pu réaliser des mesures préliminaires qui ont montré que les NCPA sont de l'ordre de 139±9 nm rms sur l'UT1 et de l'ordre de 250 nm rms sur l'UT3. Maintenant que l'on a une méthode pour mesure l'amplitude des différents modes de Zernike qui composent les NCPA, il est possible de les corriger en appliquant une compensation dans les pentes de référence de CIAO et dans un futur proche, de GPAO.

Contrôle du tip-tilt L'air dans les tunnels du VLTI induit une perturbation du front d'onde qui s'exprime surtout sous forme d'instabilité en tip-tilt de l'ordre de 10 mas rms. Cette perturbation est un problème pour la mesure des NCPA, mais surtout, elle limite la profondeur des "dark holes" réalisés et est responsable de fortes variations d'intensité dans la fibre de science. Jusqu'à présent, la correction de la turbulence dans les tunnels du VLTI n'était pas apparu comme une priorité, mais la

situation est en train de changer avec l'arrivée de GPAO et notre volonté d'implémenter un mode haut-contraste. Pour corriger cette instabilité en tip-tilt, nous avons choisi de travailler à mettre en fonctionnement un système qui avait été conçu mais jamais mis en service dans GRAVITY (Pfuhl et al., 2014). Il s'agit d'envoyer un laser visible au pied de chaque UT pour récupérer ce flux grâce à des diodes sensibles à la position installées dans GRAVITY. Malheureusement, actuellement le flux en provenance du laser est trop faible sur deux des UTs pour permettre une mesure et une correction efficace. Dans les mois qui viennent et pendant la mise en service de GPAO, je continuerai d'optimiser le flux reçu, quitte à changer les lasers pour de plus puissants. L'objectif est de mettre en service ce système de correction du tip-tilt qui serait bénéfique aux observations d'exoplanètes sur GRAVITY.

Effet de vent faible Tout comme SPHERE (Sauvage et al., 2016) et Subaru, on s'attend qu'en amenant les UT à leur limite de diffraction on rencontre un problème qui s'appelle l'effet de faible vent (Low Wind Effect, LWE). Il s'agit d'un effet thermique qui apparaît à cause des structures qui tiennent le miroir secondaire des télescopes (appellées les araignées). Ce problème génère des aberrations de bas ordre qui ont un temps caractéristique de quelque secondes et qui pourraient contribuer à rajouter beaucoup de flux de l'étoile dans le SC pendant les observations. Une solution contre le LWE est d'appliquer un revêtement qui limite le rayonnement thermique des araignées. Cette méthode a été appliquée avec succès sur l'UT3 pour SPHERE (Milli et al., 2018) et dans les mois qui viennent elle sera aussi appliquée aux autres UTs dans le cadre du projet GRAVITY+. Si, malgré cette solution passive, nous identifions que le LWE est toujours un problème sur GRAVITY+, nous pourront envisager un solution active utilisant l'optique adaptative. C'était le sujet de mon stage de Master 2 avec Jean-Baptiste Le Bouquin et Julien Milli. Mon étude a permis de comprendre pourquoi les aberrations induites par le LWE ne sont pas automatiquement corrigées par les optiques adaptatives et j'ai pu développer une méthode de mesure et de contrôle qui permettrait de forcer les optiques adaptatives à corriger ce problème. Ce travail a donné lieu à une publication dans Astronomy & Astrophysics (Pourré et al., 2022a).

Conclusion

Mon étude pour l'implémentation d'un mode haut-contraste pour GRAVITY+ m'a amené à étudier comment un simple déplacement de la fibre du SC peut augmenter le contraste de manière bénéfique et quels sont les modes qui permettent de creuser la diffraction de l'étoile aux plus faibles séparations. Cependant, les tests aux VLTI ont montré qu'il était impératif de corriger le front d'onde contre les NCPA et la turbulence des tunnels. Enfin, on s'attend à devoir appliquer des mesures correctives contre l'effet de vent faible qui viendra probablement perturber les observations d'exoplanètes avec GRAVITY+. Tout ceci dessine un mode haut-contraste composé de plusieurs blocs qui est résumé sur la Fig. C.10.

En terme de performance, grâce à GPAO, on peut s'attendre à ce que la meilleure correction de la turbulence atmosphérique réduise de $\times 3 \sim 4$ le flux de l'étoile qui s'injecte dans le SC à 100 mas. De plus, l'expérience récente de Xin et al. (2023) montre que la technique de contrôle de front d'onde sur KPIC peut apporter une diminution de l'ordre de $\times 3$ du flux de l'étoile. KPIC est un instrument

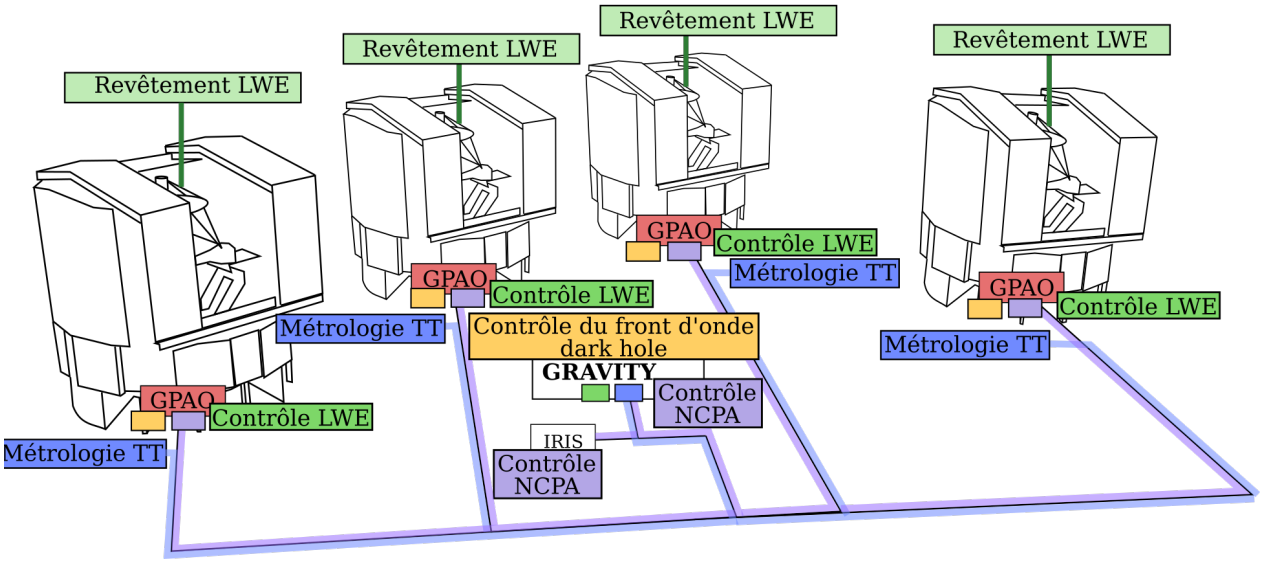

FIGURE C.10 – Résumé des différentes composantes du mode haut-contraste de GRAVITY+. LWE est l'acronyme de "low wind effect", l'effet de vent faible. TT est l'acronyme de tip-tilt.

non-interférométrique qui ressemble à GRAVITY+ car il utilise également une injection en bande-K dans une fibre mono-mode après une optique adaptative extrême. On peut donc s'attendre à des performances similaires, ce qui amènerait à $\times 10$ la réduction du flux de l'étoile injecté dans le SC avec un mode haut-contraste pour GRAVITY+.

C.6 Conclusion

Durant ma thèse, j'ai étudié les limites fondamentales de détection d'exoplanètes avec GRAVITY. Cela m'a permis de conclure que nous sommes actuellement limités à un contraste de 2×10^{-5} à 100 mas du fait de bruits systématiques qui sont proportionnels au flux de l'étoile qui s'injecte dans la fibre de science de l'instrument.

J'ai aussi travaillé à corriger le bruit systématique visible dans les données sous forme de "tortillons". Ceux-ci polluent les observations de spectres d'exoplanète à moins de 150 mas et représente donc un obstacle à la caractérisation d'exoplanètes à faible séparation. Faute d'avoir pu trouver la cause instrumentale du problème, j'ai participé à l'élaboration d'un méthode efficace pour corriger l'effet de ces "tortillons" au moment de la réduction de données.

De plus, j'ai étudié l'implémentation d'un mode haut-contraste pour GRAVITY+. Celui ci devra comprendre une méthode de contrôle du front d'onde pour créer des "dark holes" où la lumière de l'étoile est réduite, mais aussi comprendre un contrôle des NCPA, de la turbulence dans les tunnels du VLTI et probablement un contrôle des aberrations induites par l'effet de faible vent. Mis bout à bout, tous ces sous-systèmes devraient permettre de réduire de $\times 10$ le flux de l'étoile injecté dans le SC par rapport au système actuel.

Étant donné que la limite de détection de GRAVITY est proportionnelle à la quantité de flux de l'étoile qui s'injecte dans la fibre de science, on peut s'attendre que GRAVITY+ permette des détections d'exoplanètes à des contrastes autour de 2×10^{-6} entre 60 et 200 mas. Ceci devrait rendre

possible les premières détections directes d'exoplanètes jeunes de la masse de Jupiter à seulement quelques UA de leur étoile.